Process Intensification and Integration for Sustainable Design

Process Intensification and Integration for Sustainable Design

Edited by

Dominic C. Y. Foo
Mahmoud M. El-Halwagi

WILEY-VCH

Editors

Dominic C. Y. Foo
University of Nottingham Malaysia
Department of Chemical and
Environmental Engineering
Broga Road
43500 Semenyih, Selangor
Malaysia

Mahmoud M. El-Halwagi
Texas A&M University
Department of Chemical Engineering
3122 TAMU Room 200
TX
United States

All books published by **Wiley-VCH** are carefully produced. Nevertheless, authors, editors, and publisher do not warrant the information contained in these books, including this book, to be free of errors. Readers are advised to keep in mind that statements, data, illustrations, procedural details or other items may inadvertently be inaccurate.

Library of Congress Card No.:
applied for

British Library Cataloguing-in-Publication Data
A catalogue record for this book is available from the British Library.

Bibliographic information published by the Deutsche Nationalbibliothek
The Deutsche Nationalbibliothek lists this publication in the Deutsche Nationalbibliografie; detailed bibliographic data are available on the Internet at <http://dnb.d-nb.de>.

© 2021 WILEY-VCH GmbH, Boschstr. 12, 69469 Weinheim, Germany

All rights reserved (including those of translation into other languages). No part of this book may be reproduced in any form – by photoprinting, microfilm, or any other means – nor transmitted or translated into a machine language without written permission from the publishers. Registered names, trademarks, etc. used in this book, even when not specifically marked as such, are not to be considered unprotected by law.

Print ISBN: 978-3-527-34547-2
ePDF ISBN: 978-3-527-81870-9
ePub ISBN: 978-3-527-81872-3
oBook ISBN: 978-3-527-81873-0

Cover Design Adam-Design, Weinheim, Germany
Typesetting SPi Global, Chennai, India
Printing and Binding

Printed on acid-free paper

10 9 8 7 6 5 4 3 2 1

Dominic C. Y. Foo would like to dedicate this book to his wife Cecilia and kids Irene, Jessica, and Helena. Mahmoud M. El-Halwagi would like to dedicate this book to his parents, his wife Amal, and sons Omar and Ali.

Contents

Preface

The chemical process industry involves a broad spectrum of manufacturing sectors and facilities around the world. With increased global competition, escalating environmental concerns, dwindling energy, and material resources, it is imperative for industry to seek continuous process improvement. Process intensification and integration are among the most effective strategies leading to improved process designs and operations with enhancement in cost effectiveness, resource conservation, efficiency, safety, and sustainability. Process integration is a holistic framework for designing and operating industrial facilities with an overarching focus on the interconnected nature of the various pieces of equipment, mass, energy, and functionalities. On the other hand, process intensification involves efficiency improvement through effective strategies such as increasing throughput for the same physical size or decreasing the physical size for the same throughput, coupling units and phenomena, enhancing mass and energy utilization, and mitigating environmental impact. There is a natural synergism between process integration and intensification. For instance, mass and energy integration (two key pillars of process integration) are ideal approaches for enhancing mass and energy intensities.

This book is intended to provide a compilation of the various recent developments in the fields of *process intensification* and *process integration* with focus on enhancing sustainability of the chemical processes and products. It includes state-of-the-art contributions by world-renowned leaders in process intensification and integration. It strikes a balance between fundamental techniques and industrial applications. Both academic researchers and industrial practitioners will be able to use this book as a guide to optimize their respective plants and processes.

The 14 chapters in the book are classified into two broad areas: process intensification and process integration. As expected, several intensification chapters include integration and vice versa. These chapters may be read independently of each other, or with no particular sequence. Synopses of all chapters are given as follows.

Section 1 – Process Intensification

The first section of the book consists of six chapters focusing on process intensification. Chapters 1 and 2 focus on process intensification for the shale gas industry. Chapter 1 entitled "Shale Gas as an Option for the Production of Chemicals and Challenges for Process Intensification" (by *Ortiz-Espinoza and Jiménez-Gutiérrez*) discusses alternatives to produce chemicals from shale gas, and opportunities for process intensification. In Chapter 2 entitled "Design and Techno-Economic Analysis of Separation Units to Handle Feedstock Variability in Shale Gas Treatment" (by *Bohac and coworkers*), a systematic approach is proposed for the design of a processing plant to treat raw shale gas with variable composition. Chapters 3–5 focuses on various process intensification aspect of membrane separation processes. In Chapter 3 entitled "Sustainable Design and Model-Based Optimization of Hybrid RO–PRO Desalination Process" (by *Lu and coworkers*), a dimensionless model-based optimization approach was developed to evaluate the performance of a hybrid systems consisting of *reverse osmosis* and *pressure retarded osmosis* processes. In Chapter 4, entitled "Techno-Economic and Environmental Assessment of Ultrathin Polysulfone Membranes for Oxygen-Enriched Combustion" (by *Lock and coworkers*), multiscale simulation was used for techno-economic feasibility study of ultrathin polysulfone membrane for oxygen-enriched combustion; the multiscale simulation covers molecular scale, mesoscale, and eventually process optimization and design. Chapter 5, entitled "Process Intensification of Membrane-Based Systems for Water, Energy, and Environment Applications" (by *Md Nordin and coworkers*), outlined three important applications of membrane technology in process intensification, i.e. membrane electrocoagulation flocculation for dye removal, membrane diffuser in photobioreactor, and forward osmosis/electrolysis. Chapter 6, entitled "Design of Internally Heat-Integrated Distillation Column (HIDiC)" (by *Harvindran and Foo*), discussed the use of process simulation software for the design of an internal HIDiC.

Section 2 – Process Integration

The second section of the book features eight chapters on process integration. Chapters 7–9 present some latest advancements in *heat exchanger network* (HEN) synthesis. While Chapters 7 and 8 are based on *pinch analysis* techniques, Chapter 9 is based on mathematical programming technique. Chapter 7 entitled "Graphical Analysis and Integration of Heat Exchanger Networks with Heat Pumps" (by *Yang and Feng*), presents pinch analysis-based strategies for the integration with heat pumps as well as heat pump-assisted distillation with HEN. In Chapter 8 that is entitled "Insightful Analysis and Integration of Reactor and Heat Exchanger Network" (by *Zhang and coworkers*), a *combined multi-parameter optimization diagram* (CMOD) is proposed to allow better integration of reactors with the HEN, taking into consideration of energy consumption, temperature, selectivity, and reactor conversion. Next, a new methodology named as *velocity optimization* is proposed in Chapter 9, entitled

"Fouling Mitigation in Heat Exchanger Network Through Process Optimization" (by *Wang and Feng*). This new methodology allows the correlation of fouling, pressure drop, and heat transfer coefficient of heat exchangers with velocity; this allows velocity distribution to be determined among all the heat exchangers in the HEN. Chapter 10 entitled "Decomposition and Implementation of Large-Scale Interplant Heat Integration" (by *Song and coworkers*) proposed a three-step strategy for the decomposition of large-scale inter-plant heat integration problem. The chapter also proposes a new pinch analysis technique to identify the maximum interplant heat recovery potential, while minimizing the corresponding flow rates of heat transfer fluids. Chapter 11 entitled "Multi-objective optimisation of integrated heat, mass and regeneration networks with renewables considering economics and environmental impact" (by *Isafiade and coworkers*) presents a mathematical programming method for multi-period *combined heat and mass exchange networks* (CHAMENs) in which a regeneration network is included; the latter consists of multiple recyclable mass separating agents and regenerating streams. In Chapter 12 entitled "Optimization of Integrated Water and Multi-regenerator Membrane Systems Involving Multi-contaminants: A Water-Energy Nexus Aspect" (by *Abass and Majozi*), another mathematical approach was presented for the synthesis of integrated water and membrane network; the latter consists of detailed models of electrodialysis and reverse osmosis units that are embedded within a water regeneration network. Chapter 13 entitled "Optimization Strategies for Integrating and Intensifying Housing Complexes" (by *Núñez-López and Ponce-Ortega*) provides an overview of process integration and intensification for housing complexes, the latter is typically a much larger scale as compared to industrial processes. In the last chapter entitled "Sustainable Biomass Conversion Process Assessment Contributing to 'Process Intensification and Integration for Sustainable Design'" (by *Tan*), a multi-objective process sustainability evaluation methodology known as GREENSCOPE (*Gauging Reaction Effectiveness for ENvironmental Sustainability of Chemistries with a multi-Objective Process Evaluator*) is demonstrated to track process sustainability performance for a biomass conversion process.

These 14 chapters cover some of the most recent and important developments in process intensification and process integration. We hope the book will serve as a useful guide for researchers and industrial practitioners who seek to develop tools and applications for process improvement and sustainable development.

Kajang, Malaysia — *Dominic C. Y. Foo*
College Station, United States — *Mahmoud M. El-Halwagi*
January 2020

1

Shale Gas as an Option for the Production of Chemicals and Challenges for Process Intensification

Andrea P. Ortiz-Espinoza and Arturo Jiménez-Gutiérrez

Tecnológico Nacional de México, Instituto Tecnológico de Celaya, Chemical Engineering Department, Ave Tecnologico y Garcia Cubas, Celaya 38010, Mexico

1.1 Introduction

Shale gas is unconventional natural gas trapped or adsorbed in shale rock formations. As opposed to conventional natural gas, shale gas is difficult to extract because of the low porosity of the rock formations in which it is confined. This particular characteristic implied a high cost for the extraction of this gas, so that its production remained unfeasible until the development of more suitable extraction technologies, such as hydraulic fracturing and horizontal drilling [1]. Hydraulic fracturing is a stimulation technique used to increase the flow rate of gas and oil in low permeability reservoirs. This method consists in injecting high-pressurized fluids into the well to create fractures and maintain them opened to allow the flux of gas and oil [1, 2]. Hydraulic fracturing is generally combined with horizontal drilling to increase the area covered with a lower number of wells. These two technologies have led to an increase in the net production of natural gas in the United States (US) for more than a decade, which has been referred to as the shale gas revolution [1, 3].

The aim of this chapter is to give an overview of shale gas and its potential to produce value-added chemicals. This chapter addresses the following aspects: shale gas composition and places where deposits are located, effect of shale gas discoveries on natural gas prices, alternatives to produce chemicals from shale gas, and opportunities for process intensification.

1.2 Where Is It Found?

Although shale gas has been known for a while, the first shale gas well was drilled in 1821 in Chautauqua, NY, its exploitation was possible only until the development of hydraulic fracturing and horizontal drilling technologies. After the oil crises of the 1970s, the US government and some oil and gas companies, separately, initiated the investment in research projects to evaluate and make shale gas extraction possible. From the beginning of the 2000s, technical

Process Intensification and Integration for Sustainable Design, First Edition.
Edited by Dominic C. Y. Foo and Mahmoud M. El-Halwagi.
© 2021 WILEY-VCH GmbH. Published 2021 by WILEY-VCH GmbH.

Table 1.1 Major shale gas plays in the United States.

Shale play	State(s)	Percentage of dry shale gas production in 2018
Marcellus	PA, WV, OH, and NY	32.7
Permian	TX and NM	12.3
Utica	OH, PA, and WV	11.3
Haynesville	LA and TX	11.0
Eagle Ford	TX	7.1
Woodford	OK	5.0
Barnett	TX	4.4
Mississippian	OK	3.8
Niobrara–Codell	CO and WY	3.4
Bakken	ND and MT	2.7
Fayetteville	AR	2.3
Rest of the United States "shale"		4.0

Source: Adapted from EIA 2018 [4].

and economic factors promoted the idea to produce natural gas from shale formations. The Barnett shale play was the first basin to be exploited in a large scale, with the hydraulic fracturing technology being tested there. Following the success to extract natural gas from the Barnett shale play, shale gas extraction began in other locations. Table 1.1 gives basic information about the major shale gas plays in the United States.

Apart from US reserves, recoverable shale gas resources around the world have been found in countries such as China, Argentina, Algeria, Canada, Mexico, Australia, South Africa, and Russia [3, 5]. Despite these discoveries, several factors such as geological aspects and the lack of the necessary infrastructure have curbed the development of the shale gas industry in those other countries [6, 7].

Table 1.2 Recent shale gas reserves and production in for the six countries with more shale gas reserves.

Country	Unproved recoverable reserves by 2013 (Tcf)	Production in 2018 (Bcf/yr)	References
China	1115.20	353.15	[8]
Argentina	801.50	365.00	[9]
Algeria	706.90	No production	[10]
United States	662.50 (by 2015)	7079.62	[4]
Canada	572.90	182.80	[11]
Mexico	545.20	No production	[12]

Source: From EIA 2015 [13].

Table 1.2 shows the production rates in 2018 for the six countries with more unproved technically recoverable shale gas resources.

1.3 Shale Gas Composition

One particular characteristic of shale gas is its varying composition. Shale gas composition depends heavily on the location of the sources, and it may variate even within wells in the same play. The primary component of shale gas is methane, but it also contains considerable quantities of natural gas liquids (NGLs) such as ethane and propane. Apart from these components, shale gas also contains acid gases such as CO_2, H_2S, and inorganic components such as nitrogen [5, 14]. The separation of NGLs from methane has induced industries to look for alternatives to transform them into more valuable products, but at the same time the varying composition of shale gas represents a challenge for the treatment plants, which have to be robustly designed to handle such variations in the gas composition.

1.4 Shale Gas Effect on Natural Gas Prices

The high availability of natural gas, generated as a result of the increasing production of shale gas, has caused a noticeable drop of its price in the United States. Moreover, the ability to extract natural gas from deposits that are not associated to crude oil reservoirs has uncoupled natural gas and crude oil prices [1]. These facts have contributed to what has been defined as the new era of cheap natural gas, in which it has been priced consistently under US$5 per million Btu for almost a decade in the United States [15]. In particular, natural gas prices in 2019 have shown a decrease from 3.18 at the beginning of the year to US$2.07 per million Btu in September [16]. Even more, in an extreme situation, producers at the Waha hub in the Permian basin in West Texas had to pay the pipeline to take the excess of gas, showing a negative US$9 in April, which contributed to an average price of only 73 cents per million Btu for the first eight months of 2019, compared with an average market price of US$2.10 in 2018 (which is also lower than the five year average from 2014 to 2018 of US$2.80) [17]. These trends create an opportunity for the development of technologies to transform shale/natural gas into value-added chemicals. One additional point to consider is the increasing amount of liquefied natural gas that is being exported from the United States [18]. As this quantity grows, international natural gas prices may also get affected.

The main consumers of natural gas are the electricity generation industry, the residential sector, the industrial sector, and the chemical industry. Low natural gas prices have incentivized the electric power plants to switch from coal to natural gas, with an impact not only on the economy of these systems but also on the environment by reducing the total greenhouse gas emissions [1].

Another sector that has shown interest in switching from oil-based feedstocks, such as naphtha or crude oil, to natural gas is the chemical industry. The availability of inexpensive natural gas and NGLs has boosted the chemical industry to create new plants for the production of value-added chemicals using methane and NGLs as feedstock [5, 19].

1.5 Alternatives to Produce Chemicals from Shale Gas

Due to the increasing availability of low-cost natural gas, the chemical industry has started to invest in the research and development of chemical routes that can transform methane into value-added chemicals. Some of the chemical compounds that have received special attention are methanol, ethylene, propylene, and liquid fuels obtained from syngas. Some of the processes to produce the aforementioned chemicals are discussed next.

1.6 Synthesis Gas

Synthesis gas is a mixture of carbon monoxide and hydrogen typically needed for the production of chemicals such as a methanol, ammonia, or gas-to-liquid (GTL) products. The production process for synthesis gas varies depending on the oxidizing agent selected for the reforming of the natural gas. The main reforming processes are steam reforming (SR), partial oxidation (POX), and dry reforming (DR) [20]. The characteristics of these processes are listed in Table 1.3.

Although these processes may be used separately, combinations of two or more of the main reforming options have been proposed to enhance the overall performance of the reforming task. One such process is the autothermal reforming (ATR) in which the exothermic nature of the POX reforming is combined with the endothermic SR [21].

In all of these reforming alternatives, energy and water usage and generation are key points to consider when selecting the appropriate technology. Studies regarding heat and mass integration potential for the SR, POX, and ATR options can be consulted in the work of Martínez et al. [21] and Gabriel et al. [22].

Table 1.3 Reforming options and their characteristics.

Reforming option	Oxidizing agent	Conditions	Chemistry	Type
Steam reforming	H_2O	Endothermic	$CH_4 + H_2O \rightarrow CO + 3H_2$	Catalytic
Partial oxidation	O_2	Exothermic	$CH_4 + \frac{1}{2}O_2 \rightarrow CO + 2H_2$	Catalytic/non catalytic
Dry reforming	CO_2	Endothermic	$CH_4 + CO_2 \rightarrow 2CO + 2H_2$	Catalytic

Source: Adapted from Noureldin et al. 2014 [20].

1.7 Methanol

Typically, methanol is used as an intermediate to produce other chemicals such as acetic acid, formaldehyde, and MTBE, among others [23]. The production process for methanol consists of three stages, reforming, synthesis, and purification. In the first stage, the main goal is to transform methane into syngas. For this purpose a reforming process is selected. One important factor to consider when selecting the reforming process is that the ratio of H_2 to CO to feed the methanol synthesis reactor has to be equal to 2.

For the synthesis of methanol, compression of the syngas obtained from the reforming stage is needed. Then, the compressed syngas is fed to a catalytic reactor in which the following reactions take place:

$$CO_2 + 3H_2 \rightarrow CH_3OH + H_2O$$

$$CO + 2H_2 \rightarrow CH_3OH$$

The synthesis reactor operates at 83 bar and 260 °C. The outlet of the reactor is cooled and sent to a flash unit to separate the unreacted syngas and recirculate it. Additionally, a fraction of the recycled syngas is purged, with a potential use as fuel. The crude methanol obtained from the flash unit is purified using one or two distillation columns [23].

This process has been analyzed to assess its environmental impact and its safety characteristics [23, 24]. The main drawbacks of the process are the high pressure required for the operation of the synthesis reactor and the wasted fraction of non-recycled syngas. Ortiz-Espinoza et al. [24] studied the effect of different operating pressures for the methanol synthesis reactor on the safety, environmental, and economic characteristics of the methanol production process using POX reforming. The high operating pressure is related to the profitability of the process, but safety properties may be hindered by such operating conditions. Greenhouse emissions are an additional item of relevance for consideration. Figure 1.1 shows the results of the analysis conducted by Ortiz-Espinoza et al. [24], in which values of three metrics used for profitability, inherent safety, and sustainability are reported for different reactor pressures and recycling fractions for the unreacted syngas. Such metrics were the return on investment (ROI) for economic performance, process route index (PRI) for inherent safety, and total emissions of CO_2 equivalents for process sustainability. One can observe the gradual trend of the three metrics that reflect their conflicting behavior. In summary, the economic potential of the process is better at high pressures and high recycling fractions, but if safety is of primary concern, a lower pressure would favor the process characteristics.

It should also be noticed that the methanol synthesis reaction is exothermic; therefore, heat integration options may be considered to further enhance the environmental and economic performance of the process.

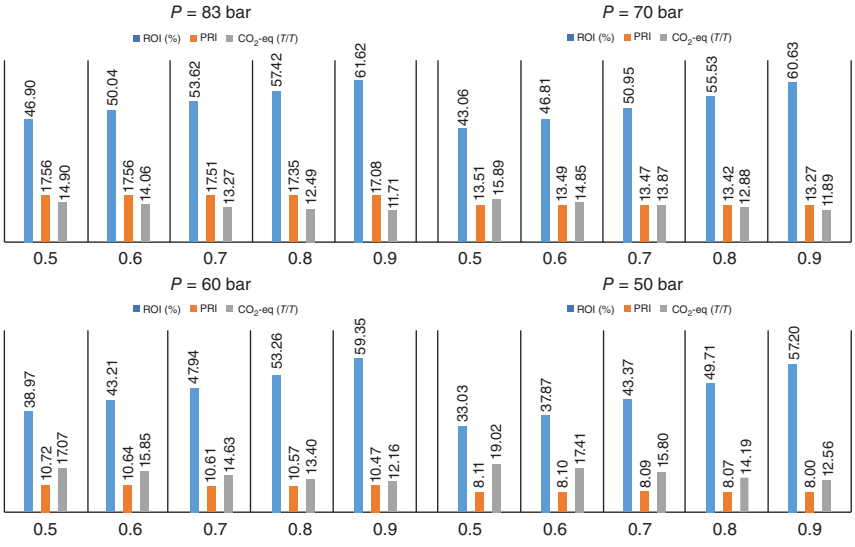

Figure 1.1 Safety, sustainability, and economic indicator for different pressures and recycling fractions in the methanol production process.

1.8 Ethylene

Ethylene is a major building block used in the chemical industry to produce a wide variety of important chemicals. The increasing availability of shale gas has boosted the ethylene industry as several ethylene production plants have been planned to be built in the United States [5]. The alternatives to produce ethylene include processes that use NGLs as feedstock, such as ethane cracking or propane dehydrogenation [25], and processes that transform methane to ethylene [26, 27]. Among the processes that convert methane to ethylene, two important options are the oxidative coupling of methane (OCM) and the methanol to olefins (MTO) technology. OCM is a direct process in which methane and oxygen are fed to a catalytic reactor, with the products of the reaction being separated in a purification stage that consists of the removal of water and CO_2 and a cryogenic distillation train [26]. Although this process is known for the low yield achieved in the reactor, which render a process option with low profitability, the development of new catalyst structures has made possible the construction of demonstration facilities for this technology that offer better economic perspectives [28].

The other alternative for ethylene production is MTO, which is a more complex process as it involves several stages. First, the reforming of natural gas and the production of methanol take place. After the methanol synthesis, the crude methanol is sent to a catalytic reactor where low-weight olefins are produced. In the reactor a variety of components are produced, such as ethylene and propylene, butylene, C_5s, hydrogen, low-weight hydrocarbons, water, and CO_2. The effluent of the reactor is then sent to separation and purification units, which start with CO_2 removal and dehydration units. Then, the remaining stream is sent to a distillation train consisting of demethanizer, deethanizer, and depropanizer columns, as well as C_2 and C_3 splitters. A column to separate C_4s and C_5s is also

needed. The overall process is very energy intensive, as it involves a reforming stage and a large distillation train.

Even when the MTO technology has been reported to be more profitable than the OCM option [26], the latter technology is less complex and avoids the need to transform the natural gas to intermediate products such as syngas. That provides an incentive to develop improvements to this technology in order to enhance its overall performance and profitability. Proposed ideas to achieve such improvements include the use of membranes in the CO_2 separation system and modifications to the ethylene fractionation column to reduce heating and condenser duties [29, 30].

1.9 Benzene

Benzene is an important starting molecule in the petrochemical industry. The production of benzene from shale gas was considered in Pérez-Uresti et al. [31], and a process based on the direct methane aromatization (DMA) route was designed. In this process, methane is fed to a DMA reactor operating at 800 °C and atmospheric pressure. The main products of the reaction are benzene and hydrogen. The effluent from the DMA reactor is sent to a membrane unit to separate the hydrogen. Then, the remaining stream is cooled and compressed to be separated in a flash tank. The gas stream obtained from the flash separator is methane-rich and is recycled to the DMA reactor. The liquid stream is fed to a distillation column where benzene is obtained as a top product. Although the DMA process competes with the traditional production routes based on catalytic reforming or steam cracking of liquid petroleum feedstocks, it represents an attractive alternative given the low prices of natural gas.

1.10 Propylene

Propylene has typically been produced as a byproduct either from the steam cracking of naphtha to produce ethylene or from the fluid catalytic cracking to produce gasoline. With the shale gas boom and the excess of NGLs such as ethane, the production of ethylene has switched the feedstock from naphtha to ethane. This action has eliminated the production of propylene as a byproduct, opening an opportunity for the development of on-purpose propylene production processes. The alternatives to produce propylene from shale gas include two options via methanol and one using the propane obtained from the purification of shale gas [32, 33]. The processes to produce propylene via methanol are the MTO route and the methanol to propylene (MTP) process [33]. The MTO process is described earlier in the ethylene section. MTP follows a similar path. First, natural gas is transformed into syngas gas using a reforming alternative, and then the syngas is transformed into methanol. As opposed to the MTO process, where crude methanol is sent to the MTO reactor, methanol has to be purified for its use as feedstock for the MTP process. Therefore, the crude methanol obtained from

the methanol synthesis reactor is sent to a flash unit and purified using a distillation column. The purified methanol is then fed to a reactor, where it is converted to dimethyl ether and water. Then, the outlet stream of the reactor is sent to a fixed bed catalytic reactor to produce propylene. The effluent from the fixed bed reactor contains propylene, gasoline, and LPG, as well as water. It is sent to a flash unit to remove water and the remaining stream is purified using distillation columns.

Another alternative for the production of on-purpose propylene is the propane dehydrogenation process, in which a depropanizer column is used to separate C^{4+} compounds that may be present in the fresh material. The purified propane enters a cold box to refrigerate the effluent from the propylene production reactor. Then, the propane stream is mixed with hydrogen and sent to a fired-heater before being fed to a fluidized catalyst bed reactor. The reaction is highly endothermic. The outlet stream of the reactor contains propylene, propane, light gases, ethane and ethylene, and some heavier hydrocarbons. The reactor effluent is cooled, compressed, and sent to a cool box where hydrogen is separated from the hydrocarbons. The liquid stream from the cold box is sent to a selective hydrogenation process (SHP) to further improve the production of propylene. The effluent from the SHP is fed to a deethanizer column to remove light gases. Finally, the remaining stream is fed to a C_3-splitter column to produce the propylene. The propane obtained at the bottom of the splitter column is recycled to the depropanizer column [32].

These processes represent an excellent opportunity for the independent production of propylene instead of obtaining it as a byproduct of other processes.

1.11 Process Intensification Opportunities

The incentive for shale gas monetization can also be viewed as an opportunity to develop intensified processes for shale gas transformation technologies. Recent efforts to design intensified processes have been observed. Process intensification is understood here as a search for more competitive process alternatives via the development of more compact flowsheets (i.e. with fewer pieces of equipment or smaller sizes of the same number of equipment units) and/or with a reduction on the consumption of basic resources (raw materials, energy) through more efficient designs.

The first efforts to develop formal design methodologies for intensified processes were due to the work by Gani and his research group [34–36]. Such initial methodologies make use of the concepts of tasks and phenomena, giving rise to the concepts of phenomena building blocks (PBBs), which represent the tasks involved in a process unit such as reaction, heating, cooling, mass transfer, and so forth; the combination of PBBs provides simultaneous phenomena building blocks (SPBBs), which are used to model the operations involved in a process. For instance, in a distillation column, the following SPBBs can be observed. Each tray shows a mixture with two phases, with contact, transfer, and separation between the two phases (vapor and liquid), while the condenser adds cooling and the reboiler adds heating to the previous SPBBs, as shown in Figure 1.2 for a column with five trays.

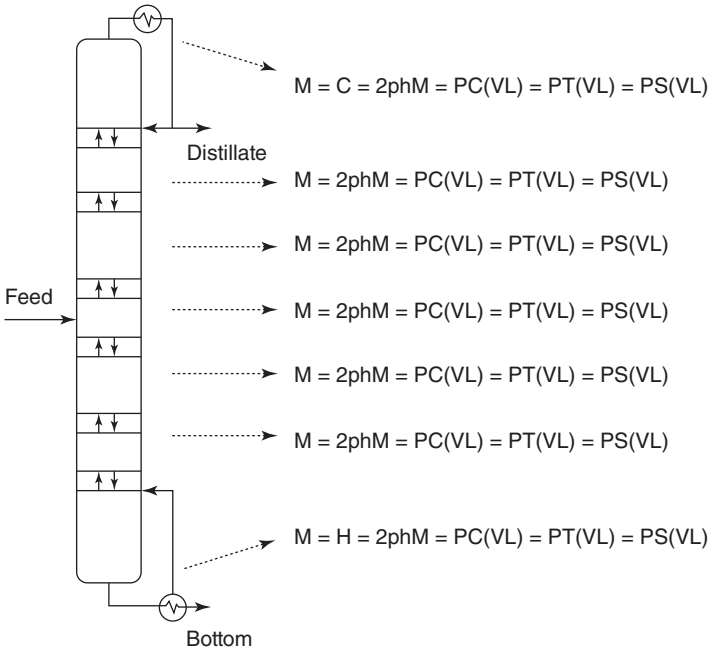

Figure 1.2 Simultaneous phenomena building blocks in a conventional distillation column.

Using these concepts, Lutze et al. [36] developed a methodology for process design of intensified processes, consisting of three stages. In the first one, a basic process flowsheet is synthesized. In the second stage, SPBBs are developed and a superstructure that contains all the possible tasks of the system is formulated. The problem is then solved as a mixed-integer nonlinear programming (MINLP) model to obtain the intensified structure that minimizes a given objective function such as the total annual cost of the system. Babi et al. [34] applied an extended formulation of that model that included sustainability metrics to a case study dealing with the production of dimethyl carbonate. In the work by Castillo-Landero et al. [37], such a methodology was taken as a basis, but instead of formulating an MINLP model to search for the optimal intensified configuration, a sequential approach with gradual intensification of the process was conducted until a final structure with a minimum number of equipment units was obtained. One advantage of this procedure is that one can assess individual levels of process intensification so that a structure that favors a given metric of interest can be selected.

Interesting challenges arise when shale gas processes are considered for process intensification. Let us take, for instance, the basic flowsheet for the production of ethylene from shale gas, or natural gas, shown in Figure 1.3. As discussed earlier, this process shows a fairly simple structure but an adverse profitability, which poses a particular incentive to explore potential benefits that an effective process intensification task could provide. Nonetheless, noticeable challenges exist for its transformation into an intensified process that combines

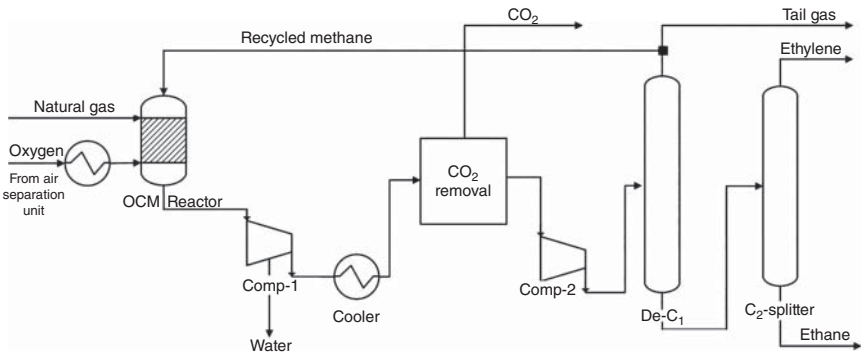

Figure 1.3 Basic flowsheet for ethylene production from shale/natural gas.

the process tasks, namely, reaction and several separation tasks. First of all, the reactor performs a catalytic, gas-phase reaction task, which consists of a complex reaction mechanism. Secondly, the separation tasks consist of a combination of compression for water condensation and absorption for CO_2 removal (typically carried out with an amine such as MEA). Combination of absorption and membrane could possibly be considered. The distillation train, finally, is highly energy intensive. Given the tasks identified for this process, and the aim to intensify it, the use of membrane units would be of special consideration. Membrane units could conceptually be designed first to carry out the individual tasks. Then, combinations of reaction and separation tasks based on such membrane units could be considered. The resulting structure would include innovative gas-phase membrane-reactive-separation units. The design of effective membranes that, among other things, could separate the gas mixture that requires cryogenic distillation systems could provide a significant impact on the process economics. It should be mentioned that some efforts to combine reactive distillation with membrane separation have been reported (e.g. [38]). However, the reaction for which the intensification with membrane units has been considered has been typically implemented for liquid-phase reactions. In such cases, membranes aid in improving the effectiveness of the process, for instance, by releasing one of the products of the reversible reaction to improve its yield. The problem posed by shale gas processes is the gas-phase reaction that requires special membrane materials for its effective application. The aspects outlined here taking the OCM transformation technology as an example provide a clear incentive toward the design of more competitive alternatives based on more compact, innovative shale gas-intensified technologies.

1.12 Potential Benefits and Tradeoffs Associated with Process Intensification

Although intensification opportunities for shale gas technologies remain to be explored, it is worthy of mention its potential benefits and possible tradeoffs based on the results from research and applications of intensification methodologies. First, it could be mentioned that a direct economic impact that would

favor investment and operating costs could be observed. A notable example is the intensified process design developed by Eastman Chemicals for the production of 400 kT/yr of methyl acetate that transformed a flowsheet with 10 units (one reactor and nine separation columns) into a single reactive-distillation piece of equipment. The resulting intensified process had 1/5 of capital investment and 1/5 of energy costs with respect to the original process [39]. One could also expect improvements in other factors such as carbon footprint and global warming metrics [37]. However, tradeoffs with other aspects such as process inherent safety and process controllability remain to be assessed. In an initial work to account for process inherent safety for a case study dealing with the intensification of an isoamyl acetate process, it was found that a partially intensified process could provide a better alternative in terms of inherent safety expectations with respect to a fully intensified process [40]. On the other hand, the effect of losing degrees of freedom for process control that arises from intensifying an original process and how it affects the process operability and controllability is an item that remains to be addressed.

1.13 Conclusions

An analysis of shale gas availability and its potential implications to support a shale gas industry that expands its use as an energy source to include transformation processes into value-added chemical products has been presented. Designs for shale gas transformation into valuable chemicals such as methanol and ethylene are examples of current efforts to produce higher value-added molecules particularly valuable as precursors of important end products. The development of extraction technologies has provided the basis for the development of shale gas monetization strategies. It has been shown how the profitability of shale gas processes may be in conflict with other important considerations such as the process safety, which sets the incentive for the development of multi-objective optimization formulations to obtain designs that offer the best compromises between such conflicting metrics. Another interesting challenge, in addition to the development of efficient and profitable shale gas flowsheets, lies in the design of intensified processes for flowsheets originally based on conventional reaction and separation units. Current intensification methodologies could be taken as a basis, with the challenge of its application for cases based on gas-phase reactions that involve complex reaction mechanisms and different types of separation processes. The development of membrane-based processes seems like a promising alternative in the search for innovative shale gas intensified processes.

References

1 Wang, Q., Chen, X., Jha, A.N., and Rogers, H. (2014). Natural gas from shale formation – the evolution, evidences and challenges of shale gas revolution in United States. *Renewable and Sustainable Energy Reviews* 30: 1–28. https://doi.org/10.1016/j.rser.2013.08.065.

2 EPA (2018). *The Process of Unconventional Natural Gas Production*. U.S. Environmental Protection Agency. https://www.epa.gov/uog/process-unconventional-natural-gas-production (accessed 7 March 2019).
3 Gao, J. and You, F. (2017). Design and optimization of shale gas energy systems: overview, research challenges, and future directions. *Computers and Chemical Engineering* 106: 699–718. https://doi.org/10.1016/j.compchemeng.2017.01.032.
4 EIA (2018). *Where Our Natural Gas Comes From*. U.S. Energy Information Administration. https://www.eia.gov/energyexplained/index.php?page=natural_gas_where (accessed 4 March 2019).
5 Al-Douri, A., Sengupta, D., and El-Halwagi, M.M. (2017). Shale gas monetization – a review of downstream processing to chemical fuels. *Journal of Natural Gas Science and Engineering* 45: 436–455. https://doi.org/10.1016/j.jngse.2017.05.016.
6 Hu, D. and Xu, S. (2013). Opportunity, challenges and policy choices for China on the development of shale gas. *Energy Policy* 60: 21–26. https://doi.org/10.1016/j.enpol.2013.04.068.
7 Lozano Maya, J.R. (2013). The United States experience as a reference of success for shale gas development: the case of Mexico. *Energy Policy* 62: 70–78. https://doi.org/10.1016/j.enpol.2013.07.088.
8 OGJ-editors (2019). *WoodMac Lowers China Gas Production Forecast*. Oil and Gas Journal. https://www.ogj.com/drilling-production/article/14038976/woodmac-lowers-china-gas-production-forecast (accessed 18 September 2019).
9 EIA (2019a). *Growth in Argentina's Vaca Muerta Shale and Tight Gas Production Leads to LNG Exports*. U.S. Energy Information Administration. https://www.eia.gov/todayinenergy/detail.php?id=40093 (accessed 17 September 2019).
10 EIA (2019b). *Background Reference: Algeria*. U.S. Energy Information Administration. https://www.eia.gov/beta/international/analysis_includes/countries_long/Algeria/background.htm (accessed 18 September 2019).
11 National Energy Board (2018). *Canada's Energy Future 2018 Supplement: Natural Gas Production*. National Energy Board. https://www.cer-rec.gc.ca/nrg/ntgrtd/ftr/2018ntrlgs/nrgftrs2018spplmntsntrlgs-eng.pdf (accessed 18 September 2019).
12 Duhalt, A., Mikulska, A., and Maher, M.D. (2019). *A Proposed Shale Ban in Mexico*. Baker Institute Issue Brief No. 05.03.19. Houston, TX: Rice University's Baker Institute for Public Policy.
13 EIA (2015). *World Shale Resource Assessments*. U.S. Energy Information Administration. https://www.eia.gov/analysis/studies/worldshalegas (accessed 17 September 2019).
14 Bullin, K.A. and Krouskop, P.E. (2009). Compositional variety complicates processing plans for US shale gas. *Oil and Gas Journal* 107: 50–55.
15 EIA (2019c). *Henry Hub Natural Gas Spot Prices*. U.S. Energy Information Administration. https://www.eia.gov/dnav/ng/hist/rngwhhdm.htm (accessed 7 March 2019).

16 Business Insider. (2019). Natural gas (Henry hub) prices. https://markets.businessinsider.com/commodities/natural-gas-price (accessed 17 September 2019).
17 Reuters. (2019). Texas Waha natural gas prices. https://www.reuters.com/article/us-usa-texas-permian-prices/texas-waha-natgas-prices-rise-ahead-of-gulf-coast-pipeline-start-up-idUSKCN1VR27U (accessed 17 September 2019).
18 EIA (2019d). *Annual Energy Outlook 2019*. U.S. Energy Information Administration. https://www.eia.gov/outlooks/aeo/pdf/aeo2019.pdf (accessed 7 March 2019).
19 He, C. and You, F. (2014). Shale gas processing integrated with ethylene production: novel process designs, exergy analysis, and techno-economic analysis. *Industrial and Engineering Chemical Research* 53: 11442–11459. https://doi.org/10.1021/ie5012245.
20 Noureldin, M.M.B., Elbashir, N.O., and El-Halwagi, M.M. (2014). Optimization and selection of reforming approaches for syngas generation from natural/shale gas. *Industrial and Engineering Chemistry Research* 53: 1841–1855. https://doi.org/10.1021/ie402382w.
21 Martínez, D.Y., Jiménez-Gutiérrez, A., Linke, P. et al. (2014). Water and energy issues in gas-to-liquid processes: assessment and integration of different gas-reforming alternatives. *ACS Sustainable Chemistry & Engineering* 2: 216–225. https://doi.org/10.1021/sc4002643.
22 Gabriel, K.J., Linke, P., Jiménez-Gutiérrez, A. et al. (2014). Targeting of the water-energy nexus in gas-to-liquid processes: a comparison of syngas technologies. *Industrial and Engineering Chemical Research* 53: 7087–7102. https://doi.org/10.1021/ie4042998.
23 Julián-Durán, L.M., Ortiz-Espinoza, A.P., El-Halwagi, M.M., and Jiménez-Gutiérrez, A. (2014). Techno-economic assessment and environmental impact of shale gas alternatives to methanol. *ACS Sustainable Chemistry & Engineering*. 2: 2338–2344. https://doi.org/10.1021/sc500330g.
24 Ortiz-Espinoza, A.P., Jiménez-Gutiérrez, A., and El-Halwagi, M.M. (2017). Including inherent safety in the design of chemical processes. *Industrial and Engineering Chemistry Research* 56: 14507–14517. https://doi.org/10.1021/acs.iecr.7b02164.
25 Yang, M. and You, F. (2017). Comparative techno-economic and environmental analysis of ethylene and propylene manufacture from wet shale gas and naphta. *Industrial & Engineering Chemistry Research* 56: 4038–4051. https://doi.org/10.1021/acs.iecr.7b00354.
26 Ortiz-Espinoza, A.P., Noureldin, M.M.B., Jiménez-Gutiérrez, A., and El-Halwagi, M.M. (2017). Design, simulation and techno-economic analysis of two processes for the conversion of shale gas to ethylene. *Computers and Chemical Engineering* 107: 237–246. https://doi.org/10.1016/j.compchemeng.2017.05.023.
27 Thiruvenkataswamy, P., Eljack, F.T., Roy, N. et al. (2016). Safety and techno-economic analysis of ethylene technologies. *Journal of Loss Prevention in the Process Industries* 39: 74–84. https://doi.org/10.1016/j.jlp.2015.11.019.

28 Peplow, M. (2017). How fracking is upending the chemical industry. *Nature* 550 (7674): 26–28. https://www.nature.com/news/how-fracking-is-upending-the-chemical-industry-1.22753.

29 Salerno, D., Arellano-García, H., and Wozny, G. (2011). Ethylene separation by feed-splitting from light gases. *Energy* 36: 4518–4523. https://doi.org/10.1016/j.energy.2011.03.064.

30 Stünkel, S., Illmer, D., Drescher, A. et al. (2012). On the design, development and operation of an energy efficient CO_2 removal for the oxidative coupling of methane in a miniplant scale. *Applied Thermal Engineering* 43: 141–147. https://doi.org/10.1016/j.applthermaleng.2011.10.035.

31 Pérez-Uresti, S.I., Adrián-Mendiola, J.M., El-Halwagi, M.M., and Jiménez-Gutiérrez, A. (2017). Techno-economic assessment of benzene production from shale gas. *Processes* 5: 1–10. https://doi.org/10.3390/pr5030033.

32 Agarwal, A., Sengupta, D., and El-Halwagi, M. (2018). Sustainable process design approach for on-purpose propylene production and intensification. *ACS Sustainable Chemistry & Engineering* 6: 2407–2421. https://doi.org/10.1021/acssuschemeng.7b03854.

33 Jasper, S. and El-Halwagi, M.M. (2015). A techno-economic comparison between two methanol-to-propylene processes. *Processes* 3: 684–698. https://doi.org/10.3390/pr3030684.

34 Babi, D.K., Holtbruegge, J., Lutze, P. et al. (2015). Sustainable process synthesis-intensification. *Computers and Chemical Engineering* 81: 218–244. https://doi.org/10.1016/j.compchemeng.2015.04.030.

35 Bertran, M.O., Frauzem, R., Sańchez-Arcilla, A.S. et al. (2017). A generic methodology for processing route synthesis and design based on superstructure optimization. *Computers and Chemical Engineering* 106: 892–910. https://doi.org/10.1016/j.compchemeng.2017.01.030.

36 Lutze, P., Babi, D.K., Woodley, J.M., and Gani, R. (2013). Phenomena based methodology for process synthesis incorporating process intensification. *Industrial and Engineering Chemistry Research* 52: 7127–7144. https://doi.org/10.1021/ie302513y.

37 Castillo-Landero, A., Jiménez-Gutiérrez, A., and Gani, R. (2018). Intensification methodology to minimize the number of pieces of equipment and its application to a process to produce dioxolane products. *Industrial and Engineering Chemistry Research* 57 (30): 9810–9820. https://doi.org/10.1021/acs.iecr.7b05229.

38 Buchaly, C., Kreis, P., and Górak, A. (2007). Hybrid separation processes – combination of reactive distillation with membrane separation. *Chemical Engineering and Processing: Process Intensification* 46 (9): 790–799. https://doi.org/10.1016/j.cep.2007.05.023.

39 Siirola, J.J. (1996). Industrial applications of process synthesis. *Advances in Chemical Engineering* 23: 1–62. https://doi.org/10.1016/S0065-2377(08)60201-X.

40 Castillo-Landero, A., Ortiz-Espinoza, A.P., and Jiménez-Gutiérrez, A. (2019). A process intensification methodology including economic, sustainability and safety considerations. *Industrial and Engineering Chemistry Research* 58 (15): 6080–6092. https://doi.org/10.1021/acs.iecr.8b04146.

2

Design and Techno-Economic Analysis of Separation Units to Handle Feedstock Variability in Shale Gas Treatment

Eric Bohac[1], Debalina Sengupta[2], and Mahmoud M. El-Halwagi[1,2]

[1] Texas A&M University, Department of Chemical Engineering, University Drive at Spence Street, College Station, 77840, USA
[2] Texas A&M Engineering Experiment Station, Gas and Fuels Research Center, University Drive at Spence Street, College Station, 77840, USA

2.1 Introduction

Over the past decade, the shale gas boom has caused significant industrial development in the United States, with the promise of significant monetization opportunities for the manufacturing sector to produce various value-added chemicals and fuels [1]. Shale gas is a form of natural gas where the gas is trapped within low permeability shale formations [2]. One major challenge with shale gas however is the wide variability in the composition and flow rate of the gas. The composition and flow rate, both between wells and within the same well over time, can differ significantly [3–5].

Dynamic and spatial variability in flow rate and composition pose major challenges when designing a gas processing plant of optimal size. In general, plants with larger process equipment are more flexible and are able to handle a wider range of inlet compositions. Nonetheless, these plants also have higher fixed and variable costs. A gas processing plant is needed to purify and separate natural gas and natural gas liquids (NGLs) and to isolate various possible containments including water, sulfur species, carbon dioxide, mercury, and oxygen [6]. Such separation operations may include acid gas removal, to remove sulfur species and carbon dioxide, dehydration, nitrogen rejection, mercury removal, NGL recovery, and NGL separation. One issue currently facing the gas production industry is a lack of capacity to handle greatly increased production [7]. Another issue is frequent unplanned shutdowns and a lack of efficiency in operations [8]. Regardless of the dynamic and spatial variability in shale gas flow rate and composition, gas processing facilities must have the ability to handle such variations and render a set of products with consistent qualities to satisfy pipeline constraints

Process Intensification and Integration for Sustainable Design, First Edition.
Edited by Dominic C. Y. Foo and Mahmoud M. El-Halwagi.
© 2021 WILEY-VCH GmbH. Published 2021 by WILEY-VCH GmbH.

and downstream-processing requirements [9–12]. In this chapter, the aim is to determine a method to find the optimal size of a plant and a strategy to process wellhead gas when feeds of various compositions are available to the facility. Process synthesis, simulation, and techno-economic analysis were used to determine the optimal configuration and capacity of the gas treatment plant.

The approach will also incorporate safety into the early stages of process design, before changes in design become more costly and difficult to make [13–15]. The concept of inherent safety is that, by eliminating or reducing the sources of hazards in a chemical plant, the severity and likelihood of process safety incidents will be reduced [8]. One challenge of implementing inherent safety is the lack of information in early design stages. Most existing safety assessment tools are used retroactively, after the process design is completed or near completion [16]. In order to quantify the inherent safety of alternative process designs during the early design stages, a number of safety indices have been developed [14, 15, 17]. In this work the safety of different process designs will be compared using a modified version of the process route index (PRI) [18]. This safety index was chosen because the chemicals involved in natural gas processing are highly flammable and explosive [18, 19].

Another important consideration is environmental impact. While natural gas is considered to be cleaner than coal and oil (from an emissions and energy consumption standpoint), there is potential for further reduction in environmental impact [20, 21]. However to the author's knowledge fluctuating feedstock compositions have not been considered in literature for shale gas processing.

2.2 Problem Statement

The problem to be addressed in this work is stated as follows:

- A set of shale gas wells with anticipated profiles for variable flow rates and compositions and known, temperature, and pressure
- A known set of feedstock and product prices

It is desired to develop a systematic design and optimization approach for gas treatment plant. Although the processing steps for treating raw shale gas can vary depending on the composition of the wellhead gas, a common process flowsheet (shown by Figure 2.1) is considered. First, condensates and free water are separated. Then, acid gases (CO_2 and H_2S) are removed. Acid gas content must be lowered to permissible levels to prevent corrosion issues during additional processing and/or during pipeline transport [6]. Dehydration is then carried out to remove bound water. This water must be removed to low levels because (i) it may form hydrates with natural gas components such as methane, ethane, and carbon dioxide, and (ii) it may freeze in later processing steps. In either case, the formed solids may plug piping and separation units [6]. Next, methane (sales gas) is separated from the other NGLs. Finally the latter is fractionated into their individual components as they typically have high economic value.

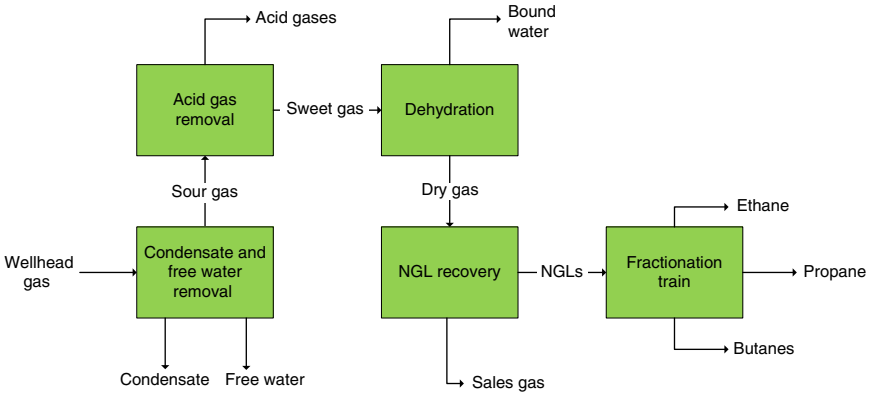

Figure 2.1 Shale gas treatment process.

2.3 Methodology

Figure 2.2 gives an overview of the proposed approach. First, a statistical analysis is carried out for the composition data. Several feeds are chosen, and process simulations are performed using a set of given assumptions to meet product specifications. Then, a process design is developed for each feed. Next, fixed and variable costs are estimated using simulation results, which include equipment sizing, mass and energy balances, operating conditions, and utility consumption as well as detailed cost data. Finally economic calculations are performed, and when combined with revenue information enable analysis of economic results.

2.4 Case Study

To illustrate the applicability of the proposed approach, a case study is solved based on representative data for the Barnett Shale Play in Texas. The key objectives of the case study include:

- Design of a base case and several additional process designs for different feed compositions
- Economic evaluations of the proposed designs
- Process safety evaluation of the proposed designs
- Sensitivity analysis where product and feedstock prices are varied based on standard deviations from historical price data

To streamline the study, the following assumptions are made:

- *Average flow rate, temperature, and pressure*: Although the flow rate, temperature, and pressure of shale gas coming out of the well can vary significantly, it was assumed that wellhead gas is sent to a centralized processing facility where these values on average would be relatively constant, and only composition would vary. Additionally it is common for gas to be saturated

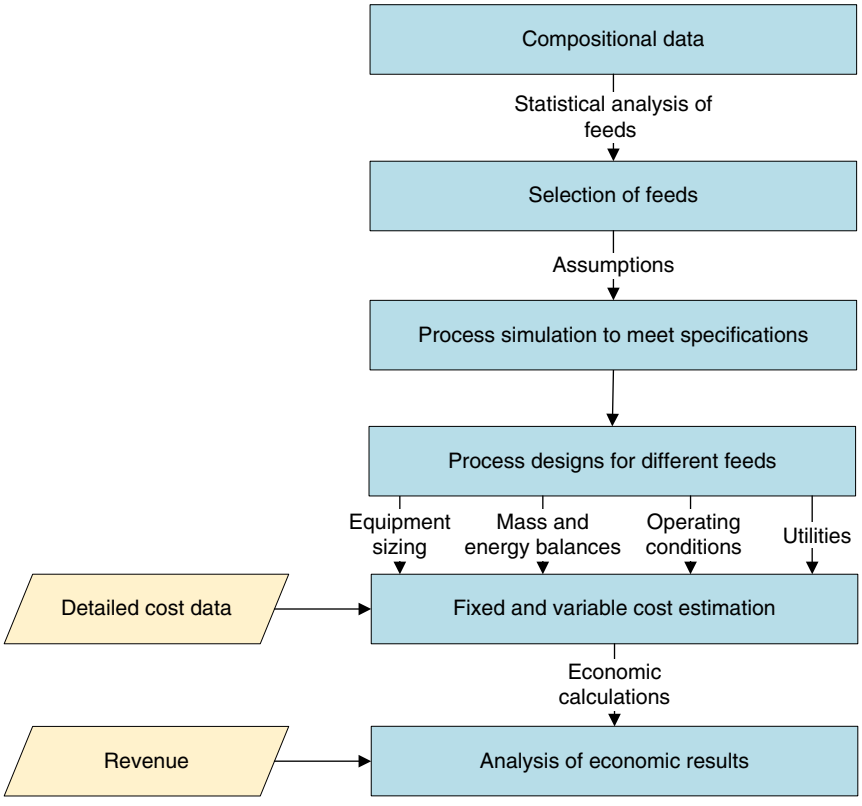

Figure 2.2 Overview of the methodology.

with water because water is sent down the well to maintain well pressure. It is not uncommon for there to also be free water in the incoming gas stream; however this is easily removed using a knockout drum on the front end of the process at minimal cost.

- Inlet feeds enter the processing plant at a standard vapor volumetric flow of 150 million standard cubic feet per day (MMSCFD), 100 °F, and 1000 psig. The Peng–Robinson equation of state was used in the process simulation model.
- The gas feedstock is saturated with water.

2.4.1 Data

First, compositional data was obtained for the Barnett Shale region (located in the Dallas, TX, area) [3]. Next, minor components such as nitrogen, oxygen, and hydrogen were removed from the data sets so that only the major components (CO_2 and the hydrocarbons) were considered. The compositional data sets were classified into different types. This was done based on the methane composition in each data set. There were five types of data sets as shown in Table 2.1. Table 2.1 also shows the probability of each feed type as determined from the literature data [3].

Table 2.1 Feed types as determined by methane composition.

Feed type	Methane composition (mol%)	Probability of feed type (%)
1	>87	7.50
2	81–87	28.33
3	75–81	28.33
4	69–75	28.33
5	<69	7.50

Table 2.2 Selected cases.

Composition (mol%)	Feed #1	Feed #2	Feed #3	Feed #4	Feed #5
Methane	94.11	83.62	77.78	71.94	56.34
Ethane	2.59	7.54	9.42	11.55	16.13
Propane	0.02	4.68	7.26	9.60	16.06
n-Butane	0.25	2.11	2.65	3.15	4.96
i-Butane	0.26	1.08	1.27	1.61	2.62
n-Pentane	0.02	0.30	0.60	0.82	1.60
i-Pentane	0.03	0.30	0.53	0.76	1.44
Neopentane	0.00	0.00	0.00	0.02	0.04
Carbon dioxide	2.71	0.38	0.49	0.56	0.81

Next, one case from each feed type was selected from among the data sets. The case chosen for each feed type was a case found near the middle of the distribution. A total of five cases were selected (see Table 2.2). From among these cases, the base case was selected as type 3 case since it falls nearest to the middle of the distribution and is representative of the most commonly found composition in this region.

Finally one additional case is considered. As mentioned in the introduction, sulfur species, predominately hydrogen sulfide, may also be found in shale gas [6]. The goal of considering this case is to determine if the additional processing needed for a gas with a high acid (HA) loading would significantly affect the economics of treating such a stream. This inlet composition of this case was chosen such that the methane and NGL content would be similar to that of the base case (Feed #3) (Table 2.3).

2.4.2 Process Simulations and Economic Evaluation

Process simulation was performed to meet the required specifications (sales gas gross heating value of 950–1150 Btu/SCF [British thermal unit/standard cubic feet], 1000 psig, and CO_2 content of 2–3 mol% maximum, 0.3 g H_2S/100 SCF gas)

Table 2.3 High acid (HA) gas feed composition.

Composition (mol%)	HA feed
Methane	74.35
Ethane	9.00
Propane	6.94
n-Butane	2.54
i-Butane	1.22
n-Pentane	0.57
i-Pentane	0.51
Neopentane	0.00
Carbon dioxide	4.78
Hydrogen sulfide	0.10

[22, 23], and process designs were developed for each feed. ProMax simulation software [24] was used to simulate this process.

The simulation results were then used to size process equipment, develop mass and energy balances, and determine operating conditions and utility consumption of process equipment. Aspen process economic analyzer [25] was used to estimate the equipment purchase costs. The Hand factor was utilized to account for installation and other costs. The fixed capital investment (FCI) for each processing unit was then estimated [26].

$$\mathrm{FCI}_i = \sum_{q=1}^{N_{equipment}} f_q^{Hand} C_q^{Purchased} \tag{2.1}$$

where FCI_i, fixed capital investment for a given processing unit; f_q^{Hand}, Hand factor for equipment q; and $C_q^{Purchased}$, the purchased cost of equipment q.

Table 2.4 shows the values and assumptions used to estimate the variable costs (raw material costs were considered separately):

The only additional equations used were those to estimate the number of workers based on the number of processing steps [28]:

$$N_{np} = \sum \text{Equipment} \tag{2.2}$$

where N_{np}, the number of non-particulate processing steps, which is related with the number of operators per shift (N_{OL}), given as in Eq. (2.3):

$$N_{OL} = (6.29 + 31.7 \times P^2 + 0.23 \times N_{np})^{0.5} \tag{2.3}$$

where P, the number of processing steps where particulate solids are handled.

2.4.2.1 Changes in Fixed and Variable Costs

Additional cases were fed through the base case process design, and any needed modifications were made to meet product specifications. Therefore, fixed and variable costs were first estimated as before, and then only the change in each of

Table 2.4 Parameters used for the techno-economic analysis.

Parameter	Values	Units	References
Variable cost parameters			
TEG price	0.93	$/lb	[27]
Refrigerant price	13.11	$/GJ	[28]
Electricity price	0.049	$/kWh	[29]
Fuel price	2.98	$/MSCF	[30]
Plant operator rate	32.74	$/h	[31]
Plant supervisor rate	68.13	$/h	[32]
Maintenance	5	% of FCI	[25]
Operating charges	25	% of operating labor cost	[25]
Plant overhead	50	% of operating labor + maintenance cost	[25]
General administrative	8	% of all other operating costs	[25]
Stream factor	0.96	—	—

Table 2.5 Price of different commodities.

Commodity	Units	Base case
Heat value[a)]	$/MMBtu	2.98
Ethane	$/gal	0.262
Propane	$/gal	0.632
n-Butane	$/gal	0.691

a) Methane and wellhead gas are priced in terms of their heat value ($/MMBtu).

these costs was used in the subsequent calculations. For fixed costs, the change was only used in cases where the costs were higher, since the need for smaller equipment does not result in any savings for an existing plant.

2.4.2.2 Revenue

Table 2.5 shows the price of each component [33]:

2.4.2.3 Economic Calculations

The next step was to calculate the return on investment (ROI) [26]:

$$\text{ROI} = \text{Annual Net Profit}/\text{TCI} \times 100\% \tag{2.4}$$

where TCI, total capital investment.

First, the quantities in Eqs. (2.5)–(2.11) must be calculated.

$$\mathrm{FCI} = \sum \mathrm{FCI}_i \tag{2.5}$$

where FCI, total fixed capital investment:

$$\mathrm{TCI} = \mathrm{FCI} + \mathrm{WCI} \tag{2.6}$$

where WCI, working capital investment (assumed to be 15% of FCI):

$$\mathrm{AFC} = (\mathrm{FCI} - \mathrm{FCI}_S)/N \tag{2.7}$$

where AFC, annualized fixed cost (depreciation); FCI_S, the salvage value of the FCI (assumed to be 10% of FCI); and N, plant lifetime (assumed to be 10 years):

$$\mathrm{AOC} = \sum \mathrm{VC}_i \tag{2.8}$$

where AOC, annual operating cost; VC_i, total variable cost for each process unit:

$$\mathrm{TAC} = \mathrm{AFC} + \mathrm{AOC} \tag{2.9}$$

where TAC, total annualized cost:

$$\text{Annual income} = \text{Annual sales of methane} + \text{Annual sales of NGLs} \tag{2.10}$$

$$\text{Annual Net Profit} = (\text{Annual Income} - \text{Depreciation} - \text{AOC}) \times (1 - \text{Tax Rate}) + \text{Depreciation} \tag{2.11}$$

where the tax rate is assumed to be 30%.

For the other cases, the calculations are similar, except instead of fixed and variable costs only the additional costs were determined. This is done because we are considering only the additional costs for processing a new composition. Similarly instead of ROI, incremental return on investment (IROI) is calculated instead:

$$\mathrm{IROI} = \text{Annual Net Profit}/\Delta\mathrm{TCI} \times 100\% \tag{2.12}$$

where ΔTCI, the change in total capital investment for a given additional case.

Finally, the total ROI can be determined for treating multiple feeds from the following:

$$\text{Total ROI} = \sum_{1}^{5} p_f \times \text{Annual Profit}_f/\mathrm{TCI}_{total} \tag{2.13}$$

where p, probability or likelihood of obtaining a particular feed, and the subscript f denotes feed.

2.4.3 Safety Index Calculations

A modified version of the PRI was used to evaluate each case in order to incorporate safety considerations into the design process. These calculations were done

following the method of Leong and Shariff [18], but the flow rate of each stream was incorporated as follows:

$$\mathrm{PRI} = [(\mathrm{HV}_m) \times (\rho) \times (P) \times (\Delta \mathrm{FL}_{mix}) \times (\dot{m})]/10^8 \tag{2.14}$$

where $\dot{m}$, mass flow rate (kg/h); HV_m, average mass heating value (kJ/kg); ρ, average fluid density (kg/m^3); P, average pressure (bar); and $\Delta \mathrm{FL}_{mix}$, average explosiveness (%), where the explosiveness for each stream is given as the difference between UFL_{mix} and LFL_{mix}:

$$\mathrm{UFL}_{mix} = 1/\left(\sum_{i=1}^{n} y_i/\mathrm{UFL}_i\right) \tag{2.15}$$

$$\mathrm{LFL}_{mix} = 1/\left(\sum_{i=1}^{n} y_i/\mathrm{LFL}_i\right) \tag{2.16}$$

2.5 Discussion

First the process simulation for the six cases is discussed. Specifically the dehydration, the turboexpander, and the fractionation train processes are discussed for all cases. Additionally acid gas removal is considered for the high acid gas case. Acid gas removal is not needed for Feeds #1–5 as acid gas levels (CO_2 and H_2S) already meet specifications. Free water removal is not needed, as it is assumed only bound water is present (see Section 2.4).

2.5.1 Process Simulations

2.5.1.1 Dehydration Process

For all five cases, the first unit operation of the gas treatment process is dehydration. The typical dehydration process used in natural gas processing is glycol dehydration, with the flowsheet shown in Figure 2.3. As mentioned previously, the goal of the glycol dehydration process is to remove thermodynamically bound water from the gas to permissible levels. Triethylene glycol (TEG) is the most commonly used solvent in industry for water removal. This process contains two loops, i.e. the contactor loop (where wet gas is contacted with TEG to remove water) and the regenerator loop (where water is removed from TEG in order to recycle the TEG back to the contactor).

2.5.1.2 NGL Recovery Process

Figure 2.4 shows a typical NGL recovery process used in natural gas processing.

In all cases except for Feed #1 (for reasons discussed later), NGL recovery is done via the turboexpander process. This process is used to separate methane from the NGLs. A key feature of this process is the turboexpander, which is used to recover some recompression work done by the gas (see Figure 2.4). Another key feature of the process is the compact (brazed aluminum) heat exchanger. These exchangers can achieve much closer approach temperatures and can operate at much lower temperatures than can shell-and-tube exchangers [34].

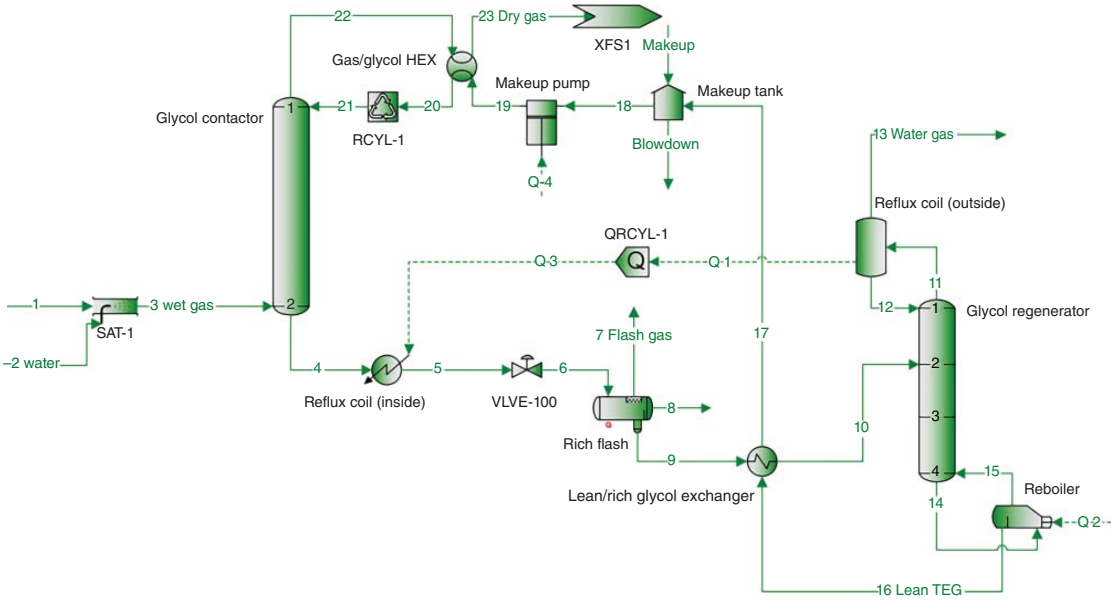

Figure 2.3 Glycol dehydration process.

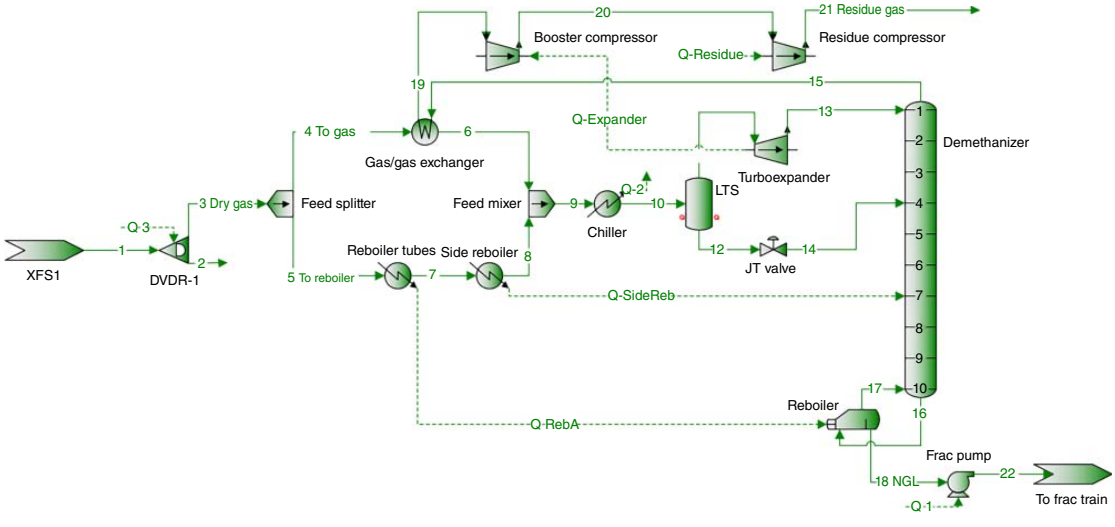

Figure 2.4 Turboexpander process (stream 19 shows the recovery of recompression work).

2.5.1.3 Fractionation Train

As seen in Figure 2.5, NGLs may be further separated into their components using this distillation column sequence. This distillation column sequence is chosen such that components are removed in order from lightest to heaviest. This enables easy separation because it reduces the flow rate sent to subsequent columns more than would separate the components in the opposite order. The columns operate at very high pressure (from 120 to 285 psig) because at low pressures all of these components are gases. This is done for all cases except for Feed #1.

2.5.1.4 Acid Gas Removal

The acid gas removal unit simulated for this case is shown in Figure 2.6. This unit is similar to the dehydration unit (Section 2.5.1.1). The solvents (methyl diethanolamine [MDEA] and piperazine) are used to remove acid gases, CO_2 and H_2S, from the incoming sour gas in the absorber column, and the solvents are stripped of the impurities in the stripper.

2.5.2 Profitability Assessment

Figure 2.7 shows the annual revenue associated with the five feeds and compares the revenue with the composition of methane in the feed.

The total revenue increases with increasing quantity of NGLs in the feed, despite the fact that each feed is primarily methane (Figure 2.7).

Methane sales prices (heat value) are typically reported in $/MMBtu (see Table 2.5), which may be converted into an average price of US$0.02 gal/yr as shown in Table 2.6. This price is significantly less than the price of the NGLs as listed in Table 2.6. Thus, feeds with high NGL content generate higher revenue.

Table 2.7 shows the results from the economic calculations for the base case. The ROI exceeded 10%, meeting the minimum criteria for potential profitability (ROI > 10%).

As discussed previously, the base case was considered an existing plant. Additional cases were considered from a standpoint of whether needed modifications were justified by amount of additional revenue made. This was assessed by calculating the IROI. The results are displayed in Figure 2.8. Figures 2.8 and 2.10 do not include the base case (Feed #3) as they examine only additional cases.

Higher methane composition feeds generally require fewer modifications to the existing plant. As a result, the TCI change for these feeds is very low (Figure 2.8). However, the additional annual net profit for these feeds is also low. The necessary modifications are justified economically, using the criteria of IROI > 10%, for all the cases except for the high methane case (Feed #1).

We next explain the condition for Feed #1. The content of NGLs in Feed #1 is very low (see Table 2.2), such that the gas already meets pipeline quality, except for the quantity of water in the gas. Therefore the turboexpander and fractionation train separation units are not needed. NGLs are very valuable, and therefore it is worth considering keeping these separation units. However this is determined to be infeasible, due to the fact that for the given inlet pressure of 1000 psig, the stream can never be in the two-phase region regardless of the

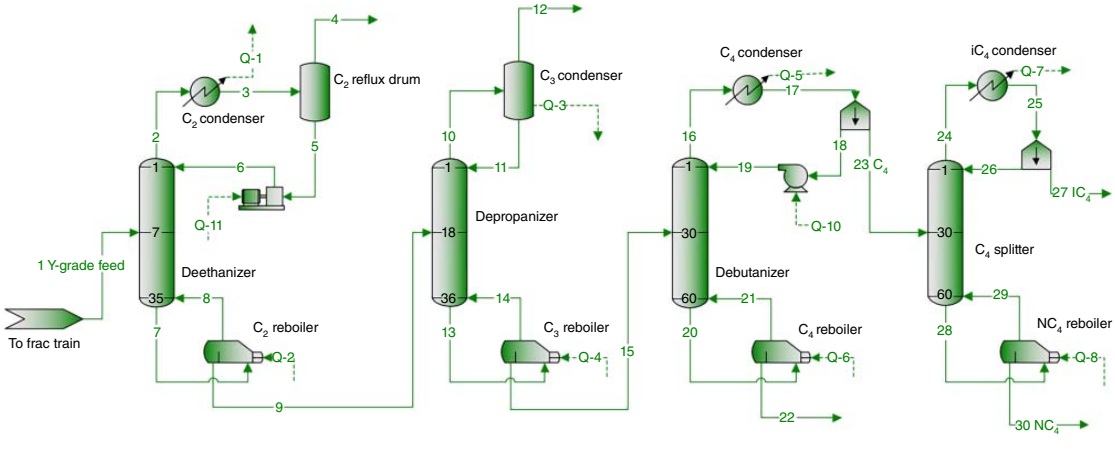

Figure 2.5 Fractionation train.

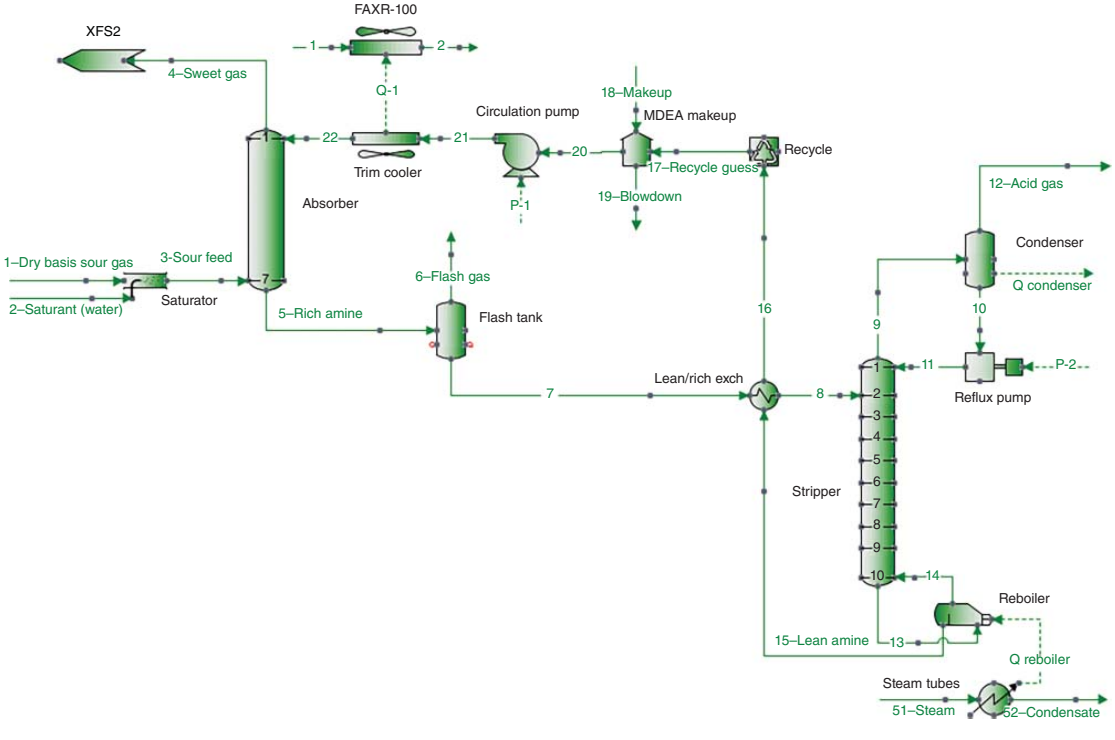

Figure 2.6 Acid gas removal unit.

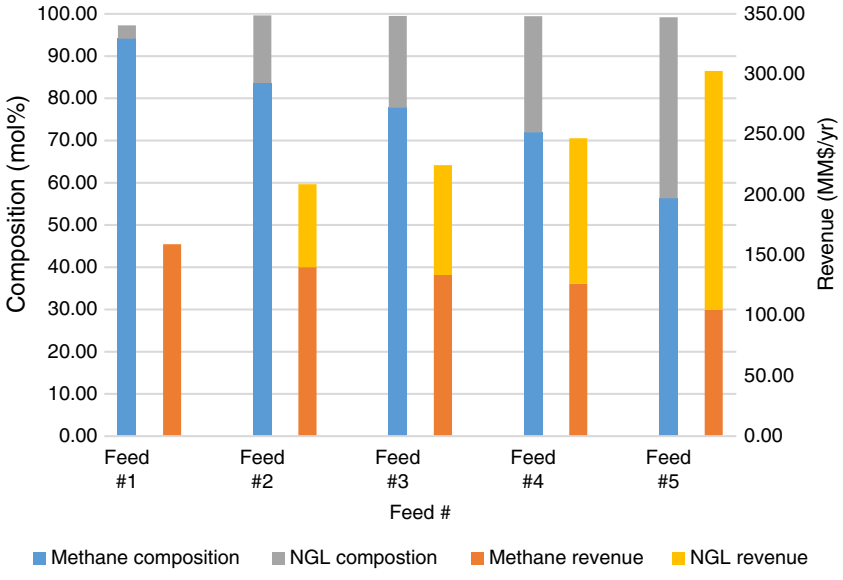

Figure 2.7 Comparison of gas composition with revenue.

Table 2.6 Effective prices for products ($/gal).

Commodity	Units	Base case
Heat value	$/gal	0.02
Ethane	$/gal	0.262
Propane	$/gal	0.632
n-Butane	$/gal	0.691

stream temperature. Thus it is not possible to remove the NGLs from the gas in a profitable way (see the phase envelop in Figure 2.9). Besides, the sales gas and wellhead gas have the same price (the heat value price), and almost the same heat value (approximately 1015 Btu/SCF), so there is no way to make a profit.

Some feeds are more likely to occur than others. To obtain a more accurate picture of whether or not each stream is worth treating, its IROI is multiplied by the probability for it to occur (see Table 2.2 for details). Next, the IROI based on probability of occurrence was calculated (Figure 2.10).

As can be seen all of the listed feeds are still worth treating based on the IROI > 10%. Despite the fact that Feed #5 generates the most additional revenue, it is only barely worth making the additional needed capital investment because the probability of this feed occurring is very low (7.50%).

The total ROI calculated for these five feeds based on their likelihood to occur is determined from Eq. (2.13).

The total ROI is found to be 24.4%, which is greater than the 15.9% for treating only the base case.

Table 2.7 Return on investment for the base case.

	Base case
Total fixed cost (MM$)	29.5
Total variable cost (MM$/yr)	13.6
Feedstock cost (MM$/yr)	204
Total revenue (MM$/yr)	225
Annual net profit (MM$/yr)	5.50
Total capital investment (MM$/yr)	34.6
ROI (%)	15.9

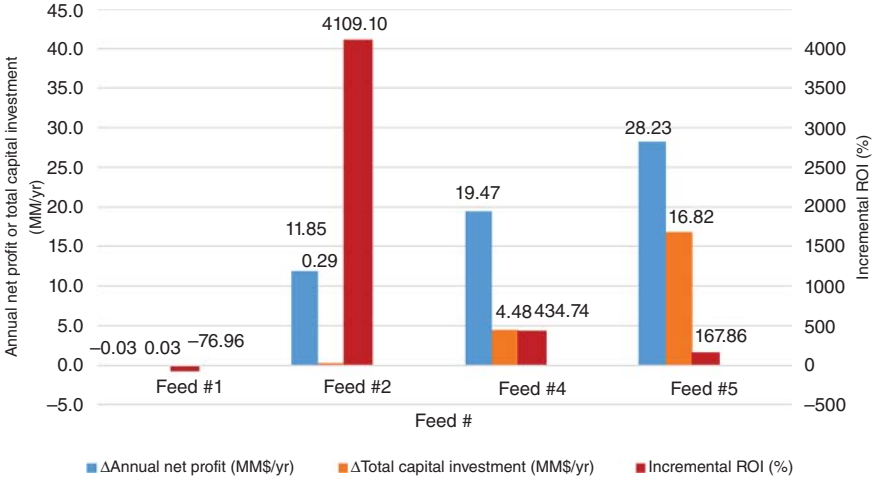

Figure 2.8 Economic metrics for the additional cases.

2.5.3 High Acid Gas Case Economics

Figure 2.11 shows the revenue for the base case and high acid gas case. There is only a slight decrease in revenue compared with the base case for the high acid case. This is because only a small percentage of the incoming gas is acid gases, while the remainder of the feed composition is similar to that for the base case feed.

As shown in Table 2.8, the additional TCI required to treat this stream is not significant, as compared with the additional revenue, and therefore this stream is clearly worth treating (IROI > 10%).

2.5.4 Safety Index Results

PRI is a relative comparison. The exact values from the calculations are not meaningful, only the relative comparison between different process routes, or in this

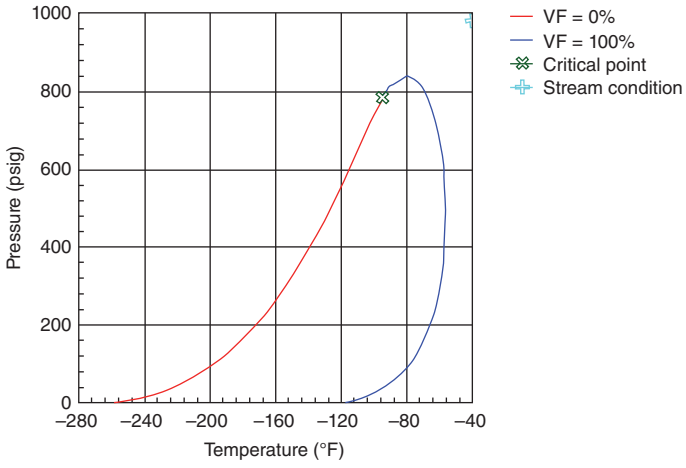

Figure 2.9 Phase envelope for Feed #1 before the demethanizer column (generated from process simulation).

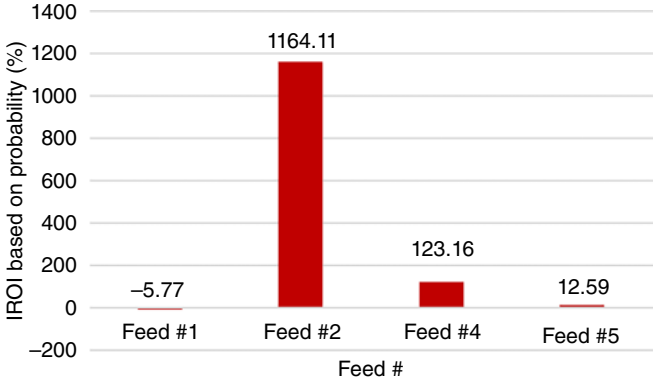

Figure 2.10 IROI based on feed probability.

case different incoming feeds. Only streams where a significant change in composition, pressure, or fluid density occurs were included in the calculation.

One significant weakness of PRI is that is uses the overall average value of each property for all the streams, effectively treating every stream considered as if it has the same flow rate (and thus same potential risk). This leads to misleading results; to give a more truthful picture, the values of each of the four properties used to calculate PRI (mass heating value, fluid density, pressure, and explosiveness) were multiplied by their flow rates as presented in Table 2.9.

The lower methane cases are less safe to process. This is because the flows are generally larger in these designs because dehydration is more difficult, and because the fractionation process has higher flow rates due to higher NGL content. Nonetheless there is really not a significant difference in these process designs from a safety perspective. Therefore economic criteria should be the main concern for deciding whether or not to treat streams.

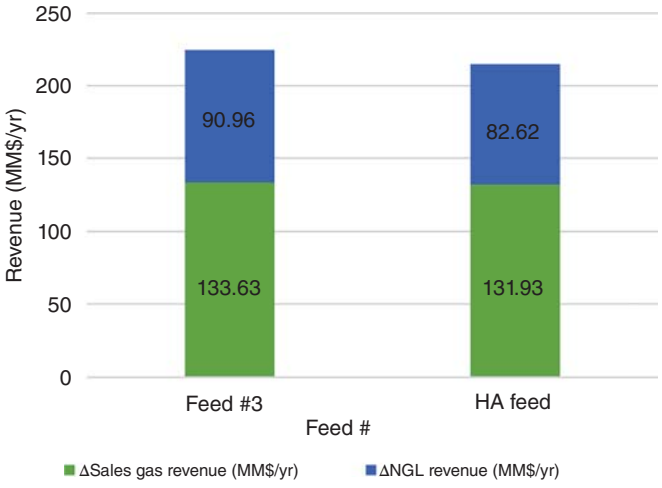

Figure 2.11 Revenue for the high acid gas case and base case (MM$/yr).

Table 2.8 Incremental return on investment for high acid case.

	HA feed
ΔAnnual net profit (MM$/yr)	11.8
ΔTotal capital investment (MM$/yr)	6.15
Incremental ROI (%)	192

Table 2.9 Results from modified process route index calculations.

	Feed #1	Feed #2	Feed #3	Feed #4	Feed #5	HA feed
Overall	19.48	27.85	31.83	34.03	34.43	26.83

2.5.5 Sensitivity Analysis

One issue of great concern for shale gas producers is price volatility. The price of heating value and of NGLs has fluctuated significantly over the last 15 years [33]. The average and standard deviation for NGL and heating value price data were determined assuming a normal distribution (see Table 2.10) [25].

A Monte Carlo simulation with 10 000 iterations was performed to find the probability of not being profitable for the base case (when ROI < 10%). Variables were set to be distributed normally in the simulation program. The probability of losing money was about 36%. The average ROI was about 59%; however the standard deviation from the Monte Carlo was approximately 135%. Clearly the shale gas processing business is potentially very profitable, but also very risky. The measured contributions to variance on ROI are shown in Figure 2.12.

Table 2.10 Maximum, minimum, average, and standard deviation for price data.

	Maximum	Minimum	Average	Standard deviation
Heating value ($/MMBtu)	US$13.42	US$1.72	US$4.40	US$2.22
Ethane ($/gal)	US$1.39	US$0.14	US$0.43	US$0.27
Propane ($/gal)	US$1.89	US$0.36	US$0.97	US$0.37
n-Butane ($/gal)	US$2.31	US$0.49	US$1.26	US$0.47

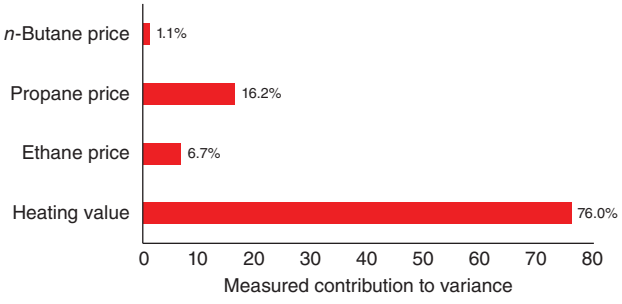

Figure 2.12 Measured contributions to variance on ROI for the inputs.

Table 2.11 Description of Cases 1–3 for sensitivity analysis.

	Case 1	Case 2	Case 3
Heating value	−1 Standard deviation	Average	+1 Standard deviation
NGL prices	Average	Average	Average

By far the biggest contributor is the heating value, which affects both raw material cost and the sales gas price. This makes sense because methane is the predominant component for this feed (77.78 mol%).

2.5.5.1 Heating Value Cases

Next a few specific cases are considered as shown in Table 2.11. The heating value price affects both the methane and the feedstock price. A higher price for heating value increases both the methane sales prices (which increases potential profitability) and increases the feedstock price (which decreases potential profitability). A sensitivity analysis is used to show which of these counteracting effects is more significant.

The results in Figure 2.13 show the process is more profitable at lower heating value prices. This means the methane is being sold for less; however this reduction in revenue is more than offset by the reduction in feedstock cost. A further calculation shows, assuming average NGL prices, the heating value price must be less than US$5.42 per MMBtu to achieve an ROI of more than 10%.

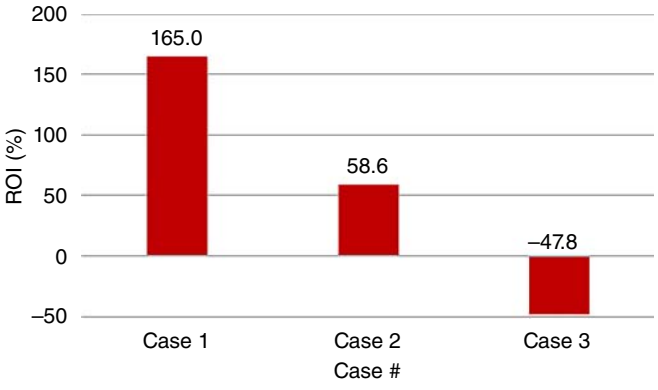

Figure 2.13 Results for Cases 1–3 for the sensitivity analysis.

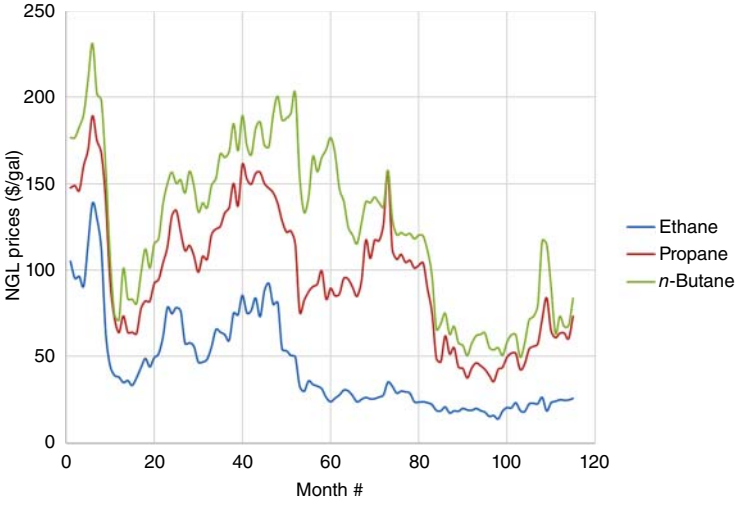

Figure 2.14 Price of products over time [34].

2.5.5.2 NGL Price Cases

Figure 2.14 shows NGL prices over time are correlated. Therefore cases where the NGL product prices fluctuated together were considered (Table 2.12). Since for a normal distribution 99.7% of the values lie within 3 standard deviations of the mean, ±3 standard deviations were chosen for the cases (prices were not allowed to be negative). Since the main question is whether the process will be profitable or not, only the deviations in the direction that would make the process less profitable were examined.

As can be seen in Figure 2.15, for even a drop of 1 standard deviation in NGL prices, the ROI value will become negative. This occurs because the standard deviations of the product prices are very high. An additional calculation shows

Table 2.12 Description of cases for sensitivity analysis.

	Case 4	Case 5	Case 6
Heating value	Average	Average	Average
NGL prices	−1 Standard deviation	−2 Standard deviation	−3 Standard deviation

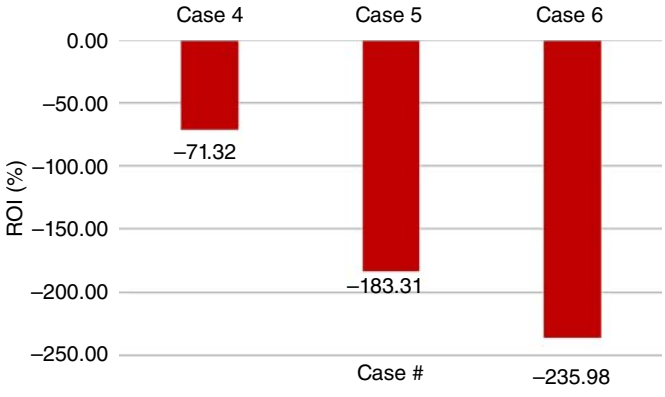

Figure 2.15 Results for Cases 4–6 for the sensitivity analysis.

that to achieve an ROI of more than 10%, product prices cannot drop more than 16.5%, assuming an average heating value price.

2.6 Conclusions

A methodology was developed for process design under uncertainty for a shale gas treatment plant. An integrated approach of process simulation, design under uncertainty, techno-economic analysis, and safety assessment was used to determine the optimal design of the gas treatment plant. A number of feeds with varying inlet compositions were examined to represent the uncertain compositions of shale gas. A case study was carried out for data from the Barnett Shale Play.

A key observation is the increase of both revenue and processing costs with increasing NGL content. As measured by ROI, all feeds (including the high acid case) are worth treating, except the high methane case (Feed #1). From the sensitivity analysis, it can be concluded that for the base case, shale gas processing is still profitable for even the highest feedstock prices. However, a drop of one standard deviation in product prices will make processing highly unprofitable.

Appendices

Included in the Appendix are key parameters for the process simulations. Further guidance can be found in the Bryan Research & Engineering guide [24].

2.A Appendix A: Key Parameters for the Dehydration Process

Table 2.A.1 Dehydration column parameters for the base case (Feed #3).

Column	Feed flow rate (MMSCFD)	*T* (°F)	*P* (psig)	Number of trays
Contactor	150	101	996–998	2
Regenerator	0.830	214–308	0–4	4

Feed flow rate is a standard vapor volumetric flow rate.

Table 2.A.2 Makeup composition for the base case (Feed #3).

Stream	Water (mass%)	TEG (mass%)
Makeup	0.1	99.9

Table 2.A.3 Glycol circulation rate for the base case (Feed #3).

Stream	Circulation rate (gal/lb)
21	2–5 gal glycol/lb water in stream 1

2.B Appendix B: Key Parameters for the Turboexpander Process

Table 2.B.1 Demethanizer column parameters.

Column	Total feed flow rate (MMSCFD)	*T* (°F)	*P* (psig)	Number of trays	Light/heavy key
Demethanizer	202	−111 to 65.4	250–254	10	Methane/ethane

Feed flow rate is a standard vapor volumetric flow rate.

Table 2.B.2 Low temperature separator (LTS) inlet temperature.

Stream	*T* (°F)
10	−25

Table 2.B.3 Outlet pressure for the pressure changing equipment.

Stream	*P* (psig)
13	250
14	255
21 Residue gas	900

2.C Appendix C: Key Parameters for the Fractionation Train

Table 2.C.1 Fractionation train column parameters for the base case (Feed #3).

Column	Feed flow rate (MMSCFD)	*T* (°F)	*P* (psig)	Number of trays	Light/heavy key
Deethanizer	27.1	38.8–159	285–292	35	Ethane/propane
Depropanizer	17.9	104–187	190–193	36	Propane/*i*-butane
Debutanizer	8.09	163–219	135–140	60	*n*-Butane/pentane
C_4 splitter	5.74	147–179	120–140	60	*i*-Butane/*n*-butane

Feed flow rate is a standard vapor volumetric flow rate.

2.D Appendix D: Key Parameters for the Acid Gas Removal System

Table 2.D.1 Acid gas removal column parameters.

Column	Feed flow rate (MMSCFD)	*T* (°F)	*P* (psig)	Number of trays
Contactor	150	100–110	796–800	7
Regenerator	150.18	210	8–12	10

Feed flow rate is a standard vapor volumetric flow rate.

Table 2.D.2 Makeup composition.

Stream	Water (mass%)	MDEA (mass%)	Piperazine (mass%)
18 – Makeup	55	40	5.0

Table 2.D.3 Key heat exchange equipment outlet temperatures.

Stream	*T* (°F)
8	210
22	110[a)]

a) Set at 10 °F warmer than inlet gas.

Abbreviations

AFC	annualized fixed cost (depreciation)
AOC	annual operating cost
Btu	British thermal unit
CO_2	carbon dioxide
$C_q^{Purchased}$	purchased cost of equipment q
FCI	fixed capital investment
FCI_i	fixed capital investment for a given processing unit
FCI_S	salvage value of the fixed capital investment
ΔFL_{mix}	average explosiveness of a mixture
f_q^{Hand}	Hand factor for equipment q
gal	gallons
GJ	gigajoules
h	hours
H_2S	hydrogen sulfide
HA	high acid
HV_m	average mass heating value
IROI	incremental return on investment
kWh	kilowatt hours
lb	pounds
LFL_{mix}	lower flammability level of a mixture
$\dot{m}$	mass flow rate
MDEA	methyl diethanolamine
MM$	million dollars
MMBtu	million British thermal units
MMSCFD	million standard cubic feet per day
MSCF	thousand standard cubic feet
N	plant lifetime (number of years)
N_2	nitrogen
NGL	natural gas liquid
N_{np}	number of non-particulate processing steps
N_{OL}	number of operators per shift
P	number of processing steps where particulate solids are handled
P	average pressure
PRI	process route index
psig	pounds per square inch of gauge pressure

ROI	return on investment
SCF	standard cubic feet
TAC	total annualized cost
TEG	triethylene glycol
TCI	total capital investment
ΔTCI	change in total capital investment for a given additional case
UFL_{mix}	upper flammability limit of a mixture
VC_i	total variable cost for each process unit
WCI	working capital investment
yr	years
ρ	average fluid density

References

1 Al-Douri, A., Sengupta, D., and El-Halwagi, M.M. (2017). Shale gas monetization – a review of downstream processing to chemicals and fuels. *Journal of Natural Gas Science and Engineering* 45: 436–455. https://doi.org/10.1016/j.jngse.2017.05.016.

2 WVU. (2016) Uncoventional resources. http://pages.geo.wvu.edu/~jtoro/Petroleum/24_Unconventional-1.pdf (accessed 08 January 2017).

3 Hill, R.J., Jarvie, D.M., Zumberge, J. et al. (2007). Oil and gas geochemistry and petroleum systems of the fort worth basin. *AAPG Bulletin* 91: 456–457. https://doi.org/10.1306/11030606014.

4 Bullin, K.A. and Krouskop, P.E. (2009). Compositional variety complicates processing plans for us shale gas. *Oil & Gas Journal* 107: 50–55.

5 Martini, A.M., Walter, L.M., and McIntosh, J.C. (2008). Identification of microbial and thermogenic gas components from Upper Devonian black shale cores, Illinois and Michigan basins. *AAPG Bulletin* 92: 327–339. https://doi.org/10.1306/10180706037.

6 Kidnay, A.J., Parrish, W.R., and McCartney, D.G. (2011). *Fundamentals of Natural Gas Processing*, 2e. Boca Raton: CRC Press.

7 Farley, T. and Hutchinson, T. (2018). Overcome engineering challenges for multi-well gathering facilities. *Gas Processing News*. http://www.gasprocessingnews.com/features/201404/overcome-engineering-challenges-for-multi-well-gathering-facilities.aspx (accessed 1 August 2018).

8 Khan, F.I. and Amyotte, P.R. (2005). I2SI: a comprehensive quantitative tool for inherent safety and cost evaluation. *Journal of Loss Prevention in the Process Industries* 18: 310–326. https://doi.org/10.1016/j.jlp.2005.06.022.

9 Duran, L.M.J., Ortiz-Espinoza, A.P., El-Halwagi, M.M., and Jiménez-Gutiérrez, A. (2014). Techno-economic assessment and environmental impact of shale gas alternatives to methanol. *ACS Sustainable Chemistry & Engineering* 2: 2338–2344. https://doi.org/10.1021/sc500330g.

10 Ortiz-Espinoza, A.P., Jiménez-Gutiérrez, A., Noureldin, M., and El-Halwagi, M.M. (2017). Design, simulation and techno-economic analysis of two processes for the conversion of shale gas to ethylene. *Computers and Chemical*

Engineering 107: 237–246. https://doi.org/10.1016/j.compchemeng.2017.05.023.

11 Pérez-Uresti, S.I., Adrián-Mendiola, J.M., El-Halwagi, M.M., and Jiménez-Gutiérrez, A. (2017). A techno-economic assessment of benzene production from shale gas. *Processes* 5: 33–42. https://doi.org/10.3390/pr5030033.

12 Zhang, C. and El-Halwagi, M.M. (2017). Estimate the capital cost of shale-gas monetization projects. *Chemical Engineering Progress* 113: 28–32.

13 Kidam, K., Sahak, H.A., Hassim, M.H. et al. (2016). Inherently safer design review and their timing during chemical process development and design. *Journal of Loss Prevention in the Process Industries* 42 https://doi.org/10.1016/j.jlp.2015.09.016.

14 Roy, N., Eljak, F., Jiménez-Gutiérrez, A. et al. (2016). A review of safety indices for process design. *Current Opinion in Chemical Engineering* 14: 42–48. https://doi.org/10.1016/j.coche.2016.07.001.

15 Guillen-Cuevas, K., Ortiz-Espinoza, A.P., Ozinan, E. et al. (2018). Incorporation of safety and sustainability in conceptual design via a return on investment metric. *ACS Sustainable Chemistry & Engineering* 6: 1411–1416. https://doi.org/10.1021/acssuschemeng.7b03802.

16 Hurme, M. and Rahman, M. (2005). Implementing inherent safety throughout process lifecycle. *Journal of Loss Prevention in the Process Industries* 18: 238–244. https://doi.org/10.1016/j.jlp.2005.06.013.

17 Rahman, M., Heikkila, A.M., and Hurme, M. (2005). Comparison of inherent safety indices in process concept evaluation. *Journal of Loss Prevention in the Process Industries* 18: 327–334. https://doi.org/10.1016/j.jlp.2005.06.015.

18 Leong, C.T. and Shariff, A.M. (2009). Process route index (PRI) to assess level of explosiveness for inherent safety quantification. *Journal of Loss Prevention in the Process Industries* 22: 216–221. https://doi.org/10.1016/j.jlp.2008.12.008.

19 Johnson, J. (2016). U.S. Chemical Safety Board investigates Mississippi natural gas plant accident. *Chemical & Engineering News*. https://cen.acs.org/articles/94/i28/US-Chemical-Safety-Board-investigates.html (accessed 1 August 2018).

20 BP (2018). *BP Energy Outlook*, 2018e. BP.

21 AlNouss, A., Ibrahim, M., and Al-Sobhi, S.A. (2018). Potential energy savings and greenhouse gases (GHGs) emissions reduction strategy for natural gas liquid (NGL) recovery: process simulation and economic evaluation. *Journal of Cleaner Production* 194: 525–539. https://doi.org/10.1016/j.jclepro.2018.05.107.

22 Gas Processors Supply Association (2004). *Engineering Data Book*, 2.1–2.3. Tulsa, OK: Gas Processors Suppliers Association.

23 (2013). *Purity Product Specifications*. Lone Star NGL LLC. https://cms.energytransfer.com/wp-content/uploads/2018/12/LST_Purity_Specifications-Combined_03-04-2013.pdf.

24 (2015). *Promax Foundations*. Bryan Research & Engineering, Inc. http://www.bre.com/PDF/Foundations-Manual-En.pdf.

25 (2012). *Aspen Capital Cost Estimator User's Guide*, 608–610. Aspentech.

26 El-Halwagi, M.M. (2012). *Sustainable Design Through Process Integration: Fundamentals and Applications to Industrial Pollution Prevention Resource Conservation, and Profitability Enhancement*. Oxford: Butterworth-Heinemann.

27 ICIS Chemical Business (2008). *Triethylene Glycol*, vol. 273, 54–55. ICIS Chemical Business. https://www.icis.com/resources/news/2008/01/28/9095618/chemical-profile-triethylene-glycol.

28 Turton, R., Bailie, R.C., Whiting, W.B., and Shaeiwitz, J.A. (2011). *Analysis, Synthesis and Design of Chemical Processes*, 3e. Upper Saddle River, NJ: Pearson Education.

29 (2016). *Typical Bills and Average Rates Report – Summer 2016*. Edison Electric Institute. http://www.eei.org/resourcesandmedia/products/Pages/ProductDetails.aspx?prod=6B4E01F2-84AE-4EFA-AEB8-57B0199F2B90&type=P.

30 EIA. (2017) Henry Hub natural gas spot price. https://www.eia.gov/dnav/ng/hist/rngwhhdm.htm (accessed 27 October 2017).

31 Bureau of Labor Statistics. (2016) Occupational employment and wages, May 2016 – 51-8092 gas plant operators. https://www.bls.gov/oes/current/oes518092.htm (accessed 2 September 2017).

32 Bureau of Labor Statistics. (2016) Occupational employment and wages, May 2016 – 11-3051 industrial production managers. https://www.bls.gov/oes/current/oes113051.htm (accessed 2 September 2017).

33 Bloomberg L.P. 2017. Mont Belvieu LST Prices.

34 Polasek, J.C., Donnelly, S.T., and Bullin, J.A. (1989). *Process Simulation and Optimization of Cryogenic Operations Using Multi-stream Brazed Aluminum Exchangers*, 100–106. Tulsa, OK: Gas Processors Association.

3

Sustainable Design and Model-Based Optimization of Hybrid RO–PRO Desalination Process

Zhibin Lu[1], *Chang He*[2], *Bingjian Zhang*[2], *Qinglin Chen*[2], *and Ming Pan*[1]

[1] *Sun Yat-sen University, School of Chemical Engineering and Technology, No. 2, Daxue Road, Zhuhai 519082, China*
[2] *School of Materials Science and Engineering, Guangdong Engineering Technology Research Center for Petrochemical Energy Conservation, Sun Yat-sen University, No. 135, Xingang Xi Road, Guangzhou 510275, China*

3.1 Introduction

The shortage of freshwater has become an increasingly prominent issue around the world owing to the growing population and industrialization [1, 2]. The rapid growth in demand of freshwater far exceeds our capacity for sustainable production. It is reported that the global water demand will continue to increase at a steady rate until 2050, accounting for an increase of 20–30% above the current level of water use, mainly due to rising demand in the industrial and domestic sectors [3, 4]. Due to the limited surface water resources, current global withdrawals are already close to their maximum sustainable levels at about 4600 km^3/yr and a third of the world biggest groundwater systems are already facing with exhaustion [5, 6]. Thus, stress levels will continue to increase as demand for water grows and the effects of climate change intensify.

In the process industry, note that water and energy are closely interlinked and interdependent. It is a well-known fact that water is essential for energy extraction and conversion, while energy is crucial for water purification and production. This relationship is termed as the *water–energy nexus* and their water–power tradeoff should be considered during the development of new desalination processes [7]. Note that the prolonged reliance on fossil fuels as energy sources is not a long-term solution due to the drawbacks of greenhouse gases emissions and finite reserves [8]. Therefore, freshwater scarcity coupling with energy requirements has seriously restricted the sustainable development of human society.

It has been reported that 97% of the total water resources on earth is saline water in the oceans, which leave only 3% as freshwater [9]. For a long time, various seawater desalination technologies have been extensively researched in order to produce drinkable water, which include multi-effect distillation, multi-stage flash, electrodialysis, membrane distillation, and *reverse osmosis* (RO), [10].

Process Intensification and Integration for Sustainable Design, First Edition.
Edited by Dominic C. Y. Foo and Mahmoud M. El-Halwagi.
© 2021 WILEY-VCH GmbH. Published 2021 by WILEY-VCH GmbH.

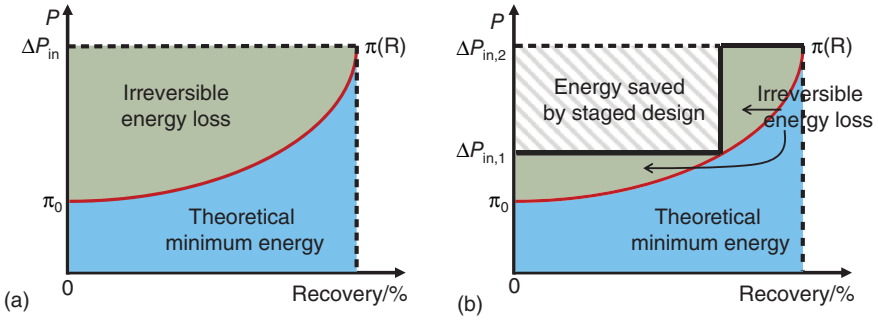

Figure 3.1 Energy use of (a) a single-stage RO and (b) two-stage RO desalination. ΔP_{in}, $\Delta P_{in,1}$ and $\Delta P_{in,2}$ represent the inlet operating pressures of the single-stage RO, the first and second stages of two-stage RO, respectively. The osmotic pressure curve expressed as a function of the recovery rate.

Compared with other technologies, RO desalination has been regarded as one of the most promising technology with relatively high water recovery and operation flexibility [11, 12]. However, its energy consumption remains as the current focus of technological innovation, since it requires high operating pressure and accounts for a significant portion of the total cost [13, 14]. The feasible solutions include the adoption of highly semi-permeable membrane and efficient energy recovery device (ERD), as well as the exploration of RO driven by renewable energies (such as solar, wind, wave, geothermal heat, etc.) [15].

From the viewpoint of *process integration*, a large quantity of energy can be further saved through innovative system designs. As shown in Figure 3.1a, the theoretical minimum energy required for RO desalination is indicated by the blue area under the *osmotic pressure curve* [16]. Due to the thermodynamic restriction, the minimum applied pressure to feed must be equal to the osmotic pressure of the exit brine, when pressure losses along the membrane channel are neglected. This part of energy can be represented by the area of the rectangle. Thus, the difference between these areas represents the *irreversible energy loss* in a single-stage RO process. To overcome this drawback, staged RO design is hence proposed. Figure 3.1b shows a two-stage RO process with the smaller hatched rectangle represents its saved energy. For an infinite multi-stage RO, the process would in theory operate immensely approximate to the thermodynamic limit. However, this assumption is impractical since the additional capital costs outweigh the energy saved. Another RO design with *closed-circuit configuration* (closed-circuit reverse osmosis [CCRO]) has been proposed as shown in Figure 3.2, which can achieve the goal of energy saving by recirculating the pressurized feed with various applied pressures. In spite of the capital costs saved by CCRO, recirculation loop operation is a huge challenge for membrane stability [17, 18]. Besides, brine management is another major issue in the case of RO as brine discharge to the surrounding sea results in the negative consequences for the pollution of marine environment [19].

Among the various renewable energy sources, *osmotic energy* (also known as salinity-gradient energy) has gradually emerged as the research hotspot. Natural

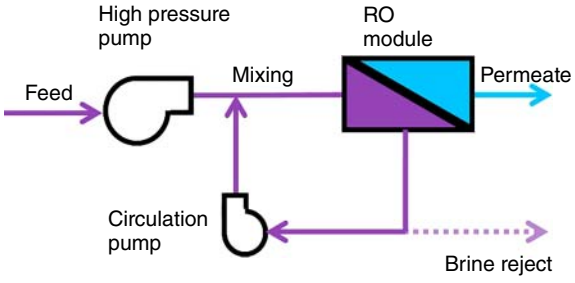

Figure 3.2 Schematic diagram of a closed-circuit reverse osmosis process. Source: Warsinger et al. 2016 [17]. Reproduced with permission of Elsevier.

salinity gradient energy usually arises from the mixing of freshwater rivers flowing into oceans. The principle of osmotic power is the exploitation of the mixing entropy. The osmotic power possesses several advantages [20]: (i) it was estimated that salinity power is potentially one of the largest sources of renewable energy on earth, (ii) it is environmental friendly because there is no greenhouse gas emission to the atmosphere during its operation, and (iii) compared with other renewable energy sources (such as solar and wind), osmotic energy is less affected by environmental factors. Therefore, the successful utilization of this renewable energy is evidently significant to address energy and environment related problems. Several technical processes including *pressure retarded osmosis* (PRO) and reverse electrodialysis and capacitive mixing can be used to generate this chemical energy [21–23]. In this regard, PRO is one of the most explored technologies so far. As a membrane-based separation process firstly proposed in the 1970s, PRO harvests Gibbs free energy of mixing by allowing water to flow through a semi-permeable membrane, from a low-salinity feed solution (FS) to a pressurized high-salinity draw solution (DS), i.e. against an applied hydraulic pressure. This work has drawn significant attention in the recent years [24].

In the past decades, the development of PRO process has been greatly hindered by the lack of proper semi-permeable membranes. The major challenge is to fabricate a membrane with robust mechanical strength, superior structural stability, desirable water permeability, and high salt rejection [25]. It has been proven that the conventional RO membranes are not suitable for PRO applications, due to its severe *internal concentration polarization* (ICP) effect. The latter dramatically reduces the effective osmotic driving force and ultimately results in a low water flux and power density (PD). Although the commercial cellulose acetate membrane designed for *forward osmosis* (FO) suffers from relatively less ICP effect, its low water permeability and operational limitations of this membrane restrict its application in PRO [8]. A number of advancements have been made in the fabrication of hollow fiber thin-film composite (TFC) membranes tailored for PRO processes, resulting in desired power densities. It has been reported that the newly developed hollow fiber TFC membranes exhibit the high PD of 38 W/m^2 at 30 bar, using 1.2 M NaCl solution and deionized water as the draw and feed solutions, respectively [26, 27]. Furthermore, new models for local mass transfer across the membrane and the hydrodynamics along the flow channels have also been developed and validated [20, 28].

In 2009, the world's first pilot PRO osmotic power plant was built by Statkraft in Norway, which demonstrated the technical capability of PRO, and the PD of 5 W/m^2 was the breakeven value for commercially applications [29]. Subsequently, more bench- and pilot-scale experiments have been carried out to evaluate the economic performance of the PRO processes [30]. Even as PRO is making progress in improving its overall process stability, there remains a huge space for process design and development. For example, the capacity of power generation of PRO strongly depends on the concentration difference of mixing solution, thus the PD generated by river-to-sea PRO is finite. For achieving a higher power generation efficiency, staged PRO process has been suggested [31]. Theoretical studies showed that the staged PRO has many advantages over the conventional PRO process, such as decreasing the impact of feed salinity and improving flexibility by using different membranes in different stages. However, staged PRO processes also require additional membrane costs than conventional processes, which may become a major obstacle to their further application.

Much higher energy can be generated if the high salinity brine of RO plants is served as the draw solution, thus forming the RO–PRO hybrid process. Theoretically, coupling PRO with RO creates the superiority of two aspects. Not only that it cuts down the energy consumptions of RO desalination and pretreatment, but also features zero brine discharge to the environment [32]. As a consequence, the hybrid processes have received considerable attentions and a great number of studies are currently involved in investigating its feasibility. For example, thermodynamic analysis on the feasibility of RO–PRO hybrid system was assessed by Wang et al. [33], He et al. [34], and Sharqawy et al. [35]. In the Japan Mega-ton project, a pilot PRO system was constructed using the seawater RO brine as the draw solution [36]. Achilli et al. [37] constructed an RO–PRO experimental system and confirmed that the reduction of RO energy consumption can be achieved using PRO. Prante et al. [38] proposed a novel RO–PRO system in which the diluted draw solution from the PRO unit is exchanged with RO unit feed by pressure exchanger, in order to offset the energy consumed by the RO unit. The minimum specific energy consumption (SEC) for this unit was reported as 1.2 kWh/m^3 for 50% water recovery [38]. Thus, design and optimization of RO–PRO model are necessary, in order to provide engineering perspectives for the future application.

This chapter aims to describe the state-of-the-art RO–PRO hybrid process in detail and to develop useful guidelines for model-based optimization methods that are beneficial to enhance system sustainability. A fundamental theoretical introduction is first presented on PRO and RO. A general description of RO–PRO hybrid process is then provided, including open- and closed-loop configurations. Next, nonlinear numerical models of these two configurations are established using dimensionless groups for system-level optimization. Finally, the comparative analysis and discussion of computational results will be given and conclusions are summarized. It is hoped that this work will provide good insights for sustainability research of the desalination process.

3.2 Unit Model Description and Hybrid Process Design

3.2.1 The Process Description

The osmosis phenomenon describes the spontaneous water transport across a semi-permeable membrane from a feed stream of higher chemical potential (i.e. low solute concentration) into another stream of lower chemical potential (i.e. high solute concentration). The latter solution with lower water chemical potential is termed as the *draw solution*, while the former one as feed [39]. Due to the differences in solubility and diffusivity between water and salt ions, most salt ions are retained by the semi-permeable membrane [38]. When two solutions of different concentration are separated by a semi-permeable membrane, which is permeable to the solvent but impermeable to the solute, osmotic pressure (π) arises due to the difference in the chemical potential [40]. During the osmosis process, the draw solution is diluted by the permeate, while the feed is concentrated until equilibrium is reached. The osmotic pressure of a solution may be defined as the *hydrostatic pressure* that would cease the solvent (i.e. water) transport across the membrane when applied to the draw solution. This pressure can be calculated via van't Hoff equation, as shown in Eq. (3.1):

$$\pi = icRT \tag{3.1}$$

where c is the molar concentration (mol/l), R is the ideal gas constant (8.314 J/mol/K), T is the absolute temperature (K), and i is the number of osmotically active particles in the solution. Note that i is usually called as the van't Hoff factor, given as $i = 1 + \alpha(\nu - 1)$ with α being the degree of dissociation and ν, the stoichiometric coefficient of dissociation reaction (for NaCl, $\alpha = 1$ and $\nu = 2$, thus $i = 2$) [41]. The hydrodynamic pressure difference across the membrane is the osmotic pressure difference $\Delta\underline{\pi}$.

There are three types of possible osmotic processes occurring between freshwater (or solution with low concentration, LC) and saline water (or solution with high concentration, HC) partitioned by a semi-permeable membrane, given as in Figure 3.3. As shown in Figure 3.3a, in FO water transports across the membrane from freshwater to saline water driven by the osmotic pressure gradient ($\Delta\pi$) between the two solutions. As a hydrostatic pressure differential (ΔP) is applied to the saline water, the permeate flux is gradually decreasing to zero until $\Delta P = \Delta\pi$.

At any stage as ΔP lies between 0 and $\Delta\pi$, water still flows into the saline water because $\Delta\pi$ remains larger than ΔP, resulting in a net driving force of $\Delta\pi - \Delta P$. This phenomenon is illustrated in Figure 3.3b and is defined as PRO. When the transmembrane pressure difference ΔP is greater than $\Delta\pi$, the direction of water permeation is reversed. This is because water is forced to permeate through the membrane from the saline water into the fresh water, as shown in Figure 3.3c. This phenomenon is referred to as RO, because the water moves in the opposite direction to that of a natural osmotic process. The relationship between the three cases described earlier in terms of water fluxes and pressures is shown in Figure 3.3d. The flux reversal point occurs where $\Delta P = \Delta\pi$.

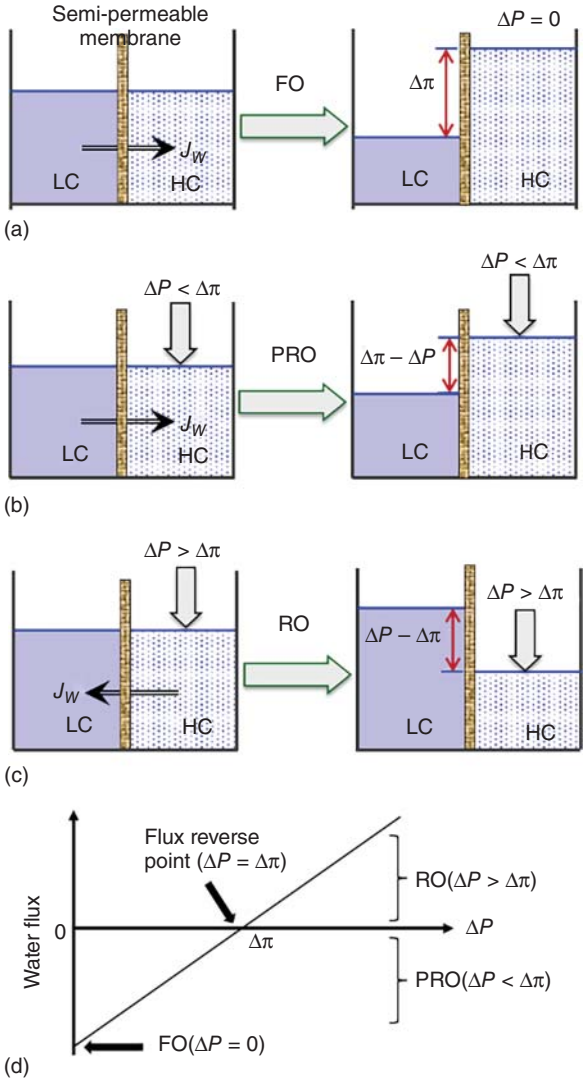

Figure 3.3 Schematic representations of (a) FO, (b) PRO, (c) RO processes, and (d) water flux as a function of applied pressure in these three osmotic processes.

In principle, no extra energy is required for FO, while RO requires a great amount of energy to create the high hydrostatic pressure necessary to produce fresh water. When mixing two solutions with different compositions and concentrations, the Gibbs free energy of mixing is released, which is the source of osmotic pressure gradient energy. In PRO process, as water transfers from the low-salinity side to the pressurized high-salinity side, chemical potential is converted into hydraulic pressure along with the increased volumetric flow on the salty water. The additional flow can be used to spin a turbine and to generate power by utilizing the excess pressure. The energy available from the reversible PRO exactly equals to the Gibbs free energy of mixing, ΔG_{mix}. For aqueous solutions with strong electrolyte, the Gibbs free energy of mixing per mole of the

system can be determined as

$$-\frac{\Delta G_{mix}}{RT} = \left[\sum_i x_i \ln(\gamma_i x_i)\right]_M - \phi\left[\sum_i x_i \ln(\gamma_i x_i)\right]_{LC} - (1-\phi)\left[\sum_i x_i \ln(\gamma_i x_i)\right]_{HC} \tag{3.2}$$

where x_i is the mole fraction of species i in mixture, low, and high concentration solutions, denoted by subscripts M, LC, and HC, respectively. The ratio of the total moles in low concentration solution to that in the system is denoted by ϕ. The activity coefficient, γ, accounts for non-ideal behavior of the species and is a function of temperature, pressure, and solution composition. The Gibbs free energy of mixing represents the theoretical maximum energy that can be extracted from the salinity gradient, regardless of pathway.

Theoretically, water permeation flux J_w across an ideal semi-permeable thin film can be expressed as follows:

$$J_w = A(\Delta\pi - \Delta P) \tag{3.3}$$

where A is the water permeability coefficient of the membrane. However, with a realistic membrane, a small amount of salt permeates the membrane from the draw solution to the feed solution due to the concentration gradient across the membrane, and the effect of reverse salt diffusion should be discussed. *Concentration polarization* is a phenomenon that can severely reduce the effective osmotic pressure difference across the membrane, due to the accumulation or depletion of solutes near an interface. Three types of concentration polarization phenomena of a PRO membrane occur at steady state, as indicated in Figure 3.4. The ICP takes place within the porous support and increases the local concentration at the active-support interface from $C_{F,m}$ to C_i. Due to the ICP effect, the osmotic pressure of the feed solution at the interface active-support layers (π_i) is enhanced, thus reducing the transmembrane driving force. The dilutive external concentration polarization (ECP) occurs at the mass transfer boundary layer of the draw solution, diluting the local concentration at the active layer from $C_{D,b}$ to $C_{D,m}$; this lowers the osmotic pressures of the draw active layer surface membrane ($\pi_{D,m}$). Similar to the dilutive ECP, the concentrative ECP appears as a consequence of the increase in feed concentration, giving a rise to the osmotic pressure at the feed side. In summary, both ICP and ECP reduce the effective osmotic pressure difference across the membrane, despite the ECP exhibiting a relatively small effect [40]. Besides, in FO the active layer of the membrane faces the feed solution, while in RO and PRO the dense layer faces the draw solution. It is necessary to ensure that the membrane can sustain the hydraulic pressure induced on the high concentration solution side [24].

3.2.2 Unit Model and Performance Metrics

3.2.2.1 RO Unit Model

Figure 3.5 shows a typical single-stage RO process installed with ERD (e.g. pressure exchanger). In this process, feed solution (e.g. seawater) is continuously pressurized by the ERD and high pressure pump before entering the RO system.

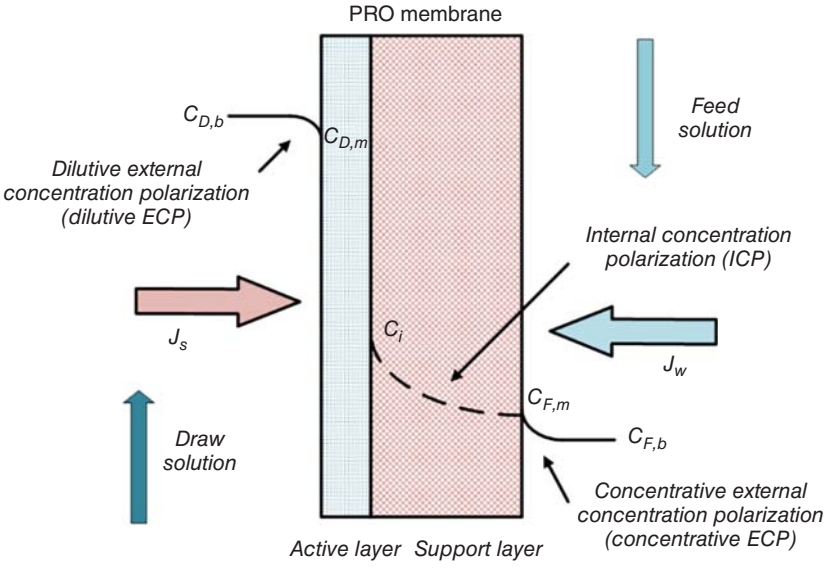

Figure 3.4 Schematics of the ICP, concentrative ECP, and dilutive ECP. Herein $C_{F,m}$ and $C_{D,m}$ are concentrations of salt on the feed and draw sides of the membrane interfaces, $C_{F,b}$ and $C_{D,b}$ are the bulk concentrations of the feed and draw solutions, respectively [8, 40].

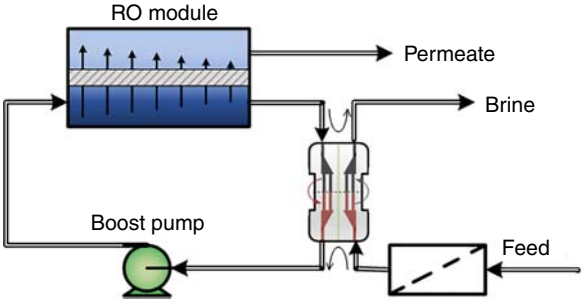

Figure 3.5 Schematic of a single-stage RO unit with ERD.

In the latter, the feed solution is separated into relatively pure permeate and concentrated brine. This brine solution then goes through ERD to recover its energy, which is then used to pressurize the feed solution, so to compensate the energy consumption of the high pressure pump. It's worth noting that feed solution is firstly pretreated by means of physical and chemical methods before entering the RO system so to remove the impurity (e.g. ions), which is harmful to the RO membrane.

Nanofiltration (NF) offers a potential solution to hardness-related fouling owing to its selective rejection of divalent ions relative to monovalent ions [42]. Kaya et al. [43] investigated the performance of different NF–RO relative to a single-stage RO, demonstrating improved permeate recovery as well as reduced RO scaling as NF was employed. Thus, the pretreatment step via NF is one of the determining factors for a successful seawater desalination.

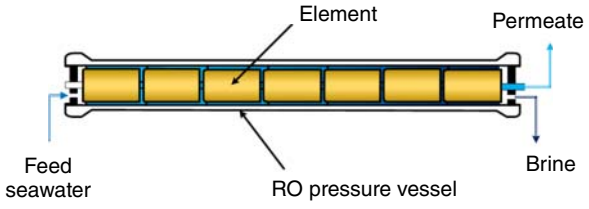

Figure 3.6 Schematic diagram of RO pressure vessel [14].

In practice, an RO plant may consist of multiple trains. Each RO train will consist of multiple pressure vessels connected in parallel, and a certain number of standard spiral wound membrane elements (usually seven to nine elements) are arranged in series in a pressure vessel. The number of membrane modules per pressure vessels is determined based on the required recovery, and the number of pressure vessels per train is decided to meet the targeted production rate [44]. The detailed structure of a pressure vessel is shown in Figure 3.6. As shown, the feed seawater is introduced at the front of the pressure vessel, and both permeate and concentrate are obtained from the outlet. Herein, the arrangement of the elements is such that the concentrate from an element becomes the feed of the subsequent element. The permeate from each of the elements is collected in a central permeate tube [45]. Furthermore, the first membrane element is exposed to the entire vessel feed flow and operates under a maximum applied pressure, hence obtaining more permeate than the subsequent elements [46].

In general, the goal of RO desalination is to produce more permeate with reduced energy consumption and costs. The main performance metric is the SEC (often in kWh/m^3), which gives the energy consumption per volume of fresh water produced. It is one of the most important indexes characterizing the performance of the desalination process particularly from the viewpoint of process sustainability. SEC is comprised of the all contributions of a desalination project, i.e. (i) feed water intake facility, (ii) pretreatment, (iii) desalination section (includes high pressure pumps, RO membrane trains, and ERD), (iv) product posttreatment section, and (v) brine treatment/disposal facility. Among them, the main contributor is the desalination section whose share usually varies between 60% and 80% depending on the feed water type, local conditions, and technology employed. In this section, energy is consumed to overcome hydraulic osmotic pressure, resistance to fluid permeation through the membrane, friction losses in the permeate channels of membrane, and non-ideal operation of equipment. Note that, in addition to minimum SEC at the limit of thermodynamic restriction, the SEC can be minimized through appropriate improvements in process design and equipment [47].

Based on the aforementioned analysis and energy balance, a general expression for the SEC is defined in Eq. (3.4) as follows:

$$\mathrm{SEC} = \frac{W_{total}}{Q_p} \tag{3.4}$$

where Q_p is the permeate flow rate and W_{total} is the rate of work done over the entire process. The total work is associated with the required electrical energy assuming all the equipment is driven by electricity. For the case of ideal operation

without ERD, W_{total} is assumed to be equal to the work done by the pump. The permeate product water recovery ratio (RR) for the RO process is an important indicator of the process productivity, and is defined as:

$$\mathrm{RR} = \frac{Q_p}{Q_f} \times 100\% \tag{3.5}$$

where Q_f is the volumetric feed flow rate. Zhu et al. [48] proposed to combine the SEC with recovery ratio. For a single-stage RO without ERD, the SEC under ideal conditions can be rewritten as follows [48]:

$$\mathrm{SEC} = \frac{\pi_0}{\eta_{pump}\mathrm{RR}(1-\mathrm{RR})} \tag{3.6}$$

where π_0 and η_{pump} represent the feed osmotic pressure and the efficiency of pump, respectively. The water recovery ratio is an essential parameter determining the energy consumption in desalination process. In fact, since high RO recovery ratio will accelerate membrane fouling, the overall recovery in most RO desalination plants is <50% [49].

In general, cost analysis can be carried out from the perspective of capital and production costs. Energy consumption is a major contribution of the total production cost for water desalination. Besides, production cost also consists of the cost of membranes, labor, equipment, maintenance, and financial charges. For a built plant, the capital cost (i.e. equipment and membranes) is fixed. Although the feed is pretreated in the process of manufacture, membrane elements still need to be replaced after reaching their service lifetime due to unavoidable membrane fouling, which is accounting for maintenance cost. Moreover, fluctuations in electricity and water prices have an impact on costs and profits. To achieve sustainable development, high concentration RO brine cannot be discharged directly without being treated to meet environmental emission standards.

3.2.2.2 PRO Unit Model

Figure 3.7 shows a generic flowsheet for a PRO model. The feed solution (e.g. freshwater or brackish water) and draw solution (e.g. seawater) flow in the opposite direction with the same velocity. The reason why the counter-current being selected instead of co-current is that the former scheme performs better with higher effectiveness. In a practical counter-current scheme, the draw solution is on the bore side of the hollow fiber tube, while the feed solution is on the shell side of the module.

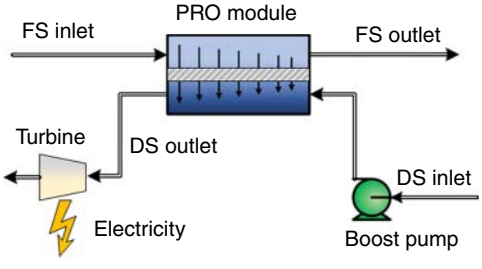

Figure 3.7 Schematic representation of a PRO unit (FS, feed solution; DS, draw solution).

In a PRO unit, the feed solution with low concentration enters the system at ambient pressure. If the hydraulic pressure applied at the draw solution lowers than the osmotic pressure difference, water will permeate through the semi-permeable membrane into the pressurized draw solution through osmosis from the feed solution. The diluted draw solution exiting from the PRO unit is sent to the hydro-turbine for power generation. After that, the exhausted draw solution is processed in a regeneration unit that can extract fresh water and create the concentrated draw solution for recycling. It should be noted that a thermal process is a preferable choice for regeneration when a waste heat source is available [50].

The major aim of a PRO process is to extract sustainable power from salinity gradient energy economically. The performance metrics can be measured directly by water flux and reverse salt flux in the experiment. In addition, a key performance metric is the PD, which defines the amount of power that can be extracted per unit of membrane area in the system. Increasing the PD enables high power output systems with low membrane area. Meanwhile, the investment on membranes will be one of the largest capital costs, and the membrane replacement will constitute a significant operating cost [51]. Owing to the fact that the PD is directly proportional to the hydraulic pressure differential (ΔP) and water flux across the membrane (J_w), it can be calculated using Eq. (3.7) that follows:

$$\mathrm{PD} = \Delta P J_w = A\Delta P(\Delta\pi - \Delta P) \tag{3.7}$$

By differentiating Eq. (3.7) with respect to ΔP, the maximum power density (PD_{max}) can be obtained as $\Delta P = \Delta\pi/2$. Substituting this value for ΔP in Eq. (3.7) yields:

$$\mathrm{PD}_{\max} = A(\Delta\pi)^2/4 \tag{3.8}$$

Therefore, theoretically, operating a PRO process at a pressure close to $\Delta\pi/2$ is recommended in order to harvest the maximal power output. Increasing the osmotic pressure difference is attractive as the dependence of the maximum power in Eq. (3.8) on $\Delta\pi$ is quadratic. For a full-scale system, the PD cannot be considered constant along the module, due to several facts such as the variations of the applied pressure and the solution concentration. In this case, the average power density $\overline{\mathrm{PD}}$ is recommended, which is expressed by dividing system power output, $\Delta P\Delta Q$, by the membrane area A_m, given as in Eq. (3.9).

$$\overline{\mathrm{PD}} = \Delta P\Delta Q/A_m \tag{3.9}$$

where ΔQ is the transmembrane water flow rate for the entire module. To guarantee the maximum energy production in PRO, the operating condition should be well-controlled.

In PRO, another important performance metric is the specific energy production (SEP), which measures the extractable energy per unit volume of initial draw and feed solution. SEP can be calculated by dividing the power output, $\Delta P\Delta Q$, by sum of the initial feed flow rate $Q_{F,0}$ and the initial draw flow rate $Q_{D,0}$:

$$\mathrm{SEP} = \frac{\Delta P\Delta Q}{Q_{F,0} + Q_{D,0}} \tag{3.10}$$

In practice, the PRO process normally extracts a lower specific energy than the theoretical maximum, making it necessary to calculate the energy conversion efficiency of salinity gradient. Thus, the SEP of a system and the efficiency of energy extraction are directly related.

3.2.3 The RO–PRO Hybrid Processes

RO is an energy-consuming process, while PRO is energy-generating; thus allowing them the possibility of coupling. Thermodynamic analysis of the RO–PRO hybrid system shows that the operation is only feasible when the extra energy generated by the PRO is higher than the overall energy consumed by RO. Through the integration of PRO and RO process in which RO brine is used as the draw solution of PRO, it can reduce the required pumping cost and energy consumption of RO. Furthermore, the RO–PRO can make full use of the energy of RO pressurized brine for power generation, further increasing the extent of water recovery to more than 50% [50].

The RO–PRO system has numerous advantages. Compared with a single RO system, RO energy consumption is compensated by energy production from PRO. In addition, the RO brine can be diluted to a lower concentration, minimizing the environmental impacts. Compared with a single PRO system, PRO energy production in the RO–PRO system is augmented by the higher concentration of the RO brine. Furthermore, the RO brine entering the PRO subsystem is relatively free of foulant because it receives prior treatment by the RO pretreatment system, which eliminates additional energy expenditure. Note that in the river-to-sea PRO system, the energy and chemical costs of pre-treating seawater is a substantial operating expenditure. In conclusion, the fact that RO–PRO system uses concentrated RO brine as PRO draw solution not only minimizes pretreatment and posttreatment costs but also eases the environmental burden. Thus, RO–PRO hybrid configuration is widely investigated because of the inherently reciprocal advantages of the two processes.

The RO–PRO hybrid process can be divided into two categories, namely, open- and closed-loop RO–PRO configurations, on the basis of whether the draw solution is recirculated or not. Preliminary studies by Kim et al. [52] suggested that placing the RO unit before the PRO unit and using the RO brine to augment the draw solution was preferred.

3.2.3.1 Open-Loop Configuration

Figure 3.8a presents a schematic diagram of the open-loop RO–PRO system, which mainly consists of RO, PRO, booster pump, and two ERDs. As shown, the pretreated feed water is pressurized first via ERD-2 by the diluted draw solution and then via ERD-1 by the high pressure RO brine. After that, it is sent to a booster pump to reach the desired pressure for RO desalination. The pressurized stream enters the RO unit to produce salt-free water. The resulting concentrated brine at high pressure is sent to ERD-1 to exchange pressure energy with the inter-stage seawater. Herein, although the brine in the ERD-1 outlet is depressed by ERD-1, its applied hydraulic pressure is still suitable for the operation of PRO unit as a draw solution, and thereby, it is unnecessary to add a booster pump for this

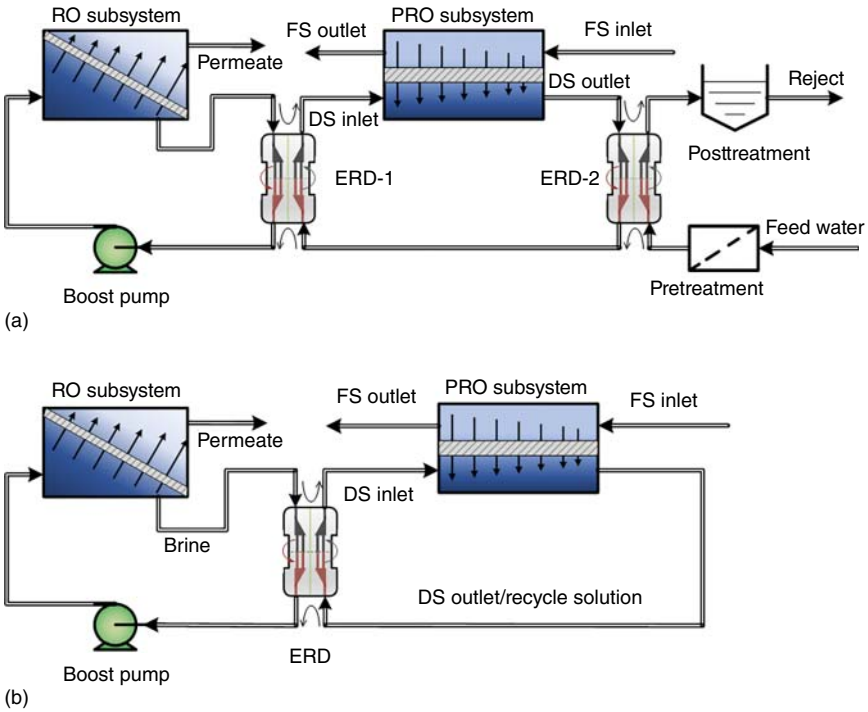

Figure 3.8 Schematic diagrams of the RO–PRO hybrid system with (a) open-loop configuration and (b) closed-loop configuration (FS, feed solution; DS, draw solution).

stream. In the PRO unit, water permeates from the low-salinity feed solution into the draw solution and the concentrated brine gets diluted. The hydraulic energy gained from the draw solution outlet is harvested by the ERD-2. Therefore, the RO–PRO configuration not only recovers the pressure energy of streams but also utilizes the salinity gradient energy between brine and feed solution [53].

Since it usually takes a huge membrane area to transport the same amount of water in PRO as in RO, the permeate volume in PRO is usually less than that in RO in the actual application. When the amount of water permeating into the draw solution of PRO unit is less than that of RO unit, the diluted draw solution from PRO has a salinity that is higher than the pretreated seawater. At this case, it is not economical to recycle the outlet draw solution as the feed solution to RO, because this will require a higher energy input to achieve the same recovery in RO and also result in salt accumulation in the seawater feed. Hence, the diluted draw solution is discharged after pressure exchanging with the pretreated seawater feed and follow-up treatment [54].

3.2.3.2 Closed-Loop Configuration

Taking into account the disposal of concentrated draw solution from the PRO outlet, a closed-loop RO–PRO hybrid system is proposed, as shown in Figure 3.8b. By means of recycling the diluted draw solution, energy consumption for pretreatment of feed water is greatly reduced. This configuration obviously

differs from the typical one, which is reflected in the number of ERD required and the recycling draw solution. Herein, the number of ERDs reduces by half as compared with the typical one, and the seawater shown in Figure 3.8a is replaced by the recycling draw solution. It is worth mentioning that the precise control of the amount and salt concentration of the recycling medium are vital to maintain this kind of hybrid process. In particular, a purge valve is required to prevent the accumulation of salinity. In this process, the amount of permeate of PRO unit is the same as that of RO unit. Note that the flow rate and salt concentration of draw solution at the exit of the PRO unit must be equal to those at the entrance of the RO unit as the diluted draw solution of PRO is directly used as the feed of RO. To some extent, the process design of closed-loop configuration is not as flexible as that of open-loop one due to its low robustness, which is easily influenced by changing operation conditions. Though the recycled draw solution can be saline water prepared in laboratory, pretreatment seawater is preferred because it requires less modification of the existing and heavily optimized RO system.

3.3 Unified Model-Based Analysis and Optimization

In order to investigate the performance of the RO–PRO hybrid system with open-loop and closed-loop configurations, a dimensionless nonlinear constraint optimization model is proposed. For the purpose of simplifying the optimization model, several assumptions are made as follows: (i) pressure drop across the membrane channel is ignored; (ii) salt leakage in the modules is neglected; in other words, the membrane is assumed to reject salt completely; (iii) both the ICP and ECP in the RO unit are not considered, while only ECP in the PRO unit is negligible, herein note the ICP in the PRO model should be taken into consideration due to its significant impact on mass transfer across the membrane; and (iv) the change in the salt concentration of feed solution is negligible since the salinity of feed solution is much lower than that of draw solution in the PRO unit.

3.3.1 Dimensionless Mathematical Modeling

It can be found from Figure 3.8 that the two hybrid configurations are composed of almost similar RO and PRO units. The most important constraints in the mathematical modeling are the characteristic equations of RO and PRO units. As for the RO unit, according to Eq. (3.3), the flow rate of permeate across a membrane area of dS is given by

$$\frac{dQ}{dS} = A_{RO}(\Delta\pi_{RO} - \Delta P_{RO}) = A_{RO}\left(\pi_0 \frac{Q_0}{Q} - \Delta P_{RO}\right) \tag{3.11}$$

where dQ is water flow across membrane area, π_0 and Q_0 are the osmotic pressure and volumetric flow rate at the inlet of the RO, respectively, and Q is the flow rate of draw solution. Using the dimensionless parameters defined by Li [13, 55, 56]

and integrating Eq. (3.11) from inlet to outlet of the membrane channel gives

$$\gamma_{RO} = \frac{1}{\theta_{RO}} \left[\mathrm{RR} + \frac{1}{\theta_{RO}} \ln \left(\frac{\theta_{RO} - 1}{\theta_{RO} - \theta_{RO}\mathrm{RR} - 1} \right) \right] \tag{3.12}$$

$$\mathrm{RR} = \Delta Q_{RO} / Q_0 \tag{3.13}$$

$$\theta_{RO} = \Delta P_{RO} / \pi_0 \tag{3.14}$$

$$\gamma_{RO} = A_{RO} S_{RO} \pi_0 / Q_0 \tag{3.15}$$

where RR, θ_{RO}, and γ_{RO} are identified as the performance parameter (i.e. recovery ratio), operational parameter (i.e. dimensionless operating pressure), and design parameter (i.e. dimensionless total membrane area), respectively. The subscripts *RO* and 0 in Eqs. (3.12)–(3.15) represent RO unit and initial state, respectively. Equation (3.12) is a dimensionless characteristic equation for RO, in which RR, θ_{RO}, and γ_{RO} are closely interlinked, and arbitrary two parameters would determine the remaining one.

In the presence of ICP and absence of ECP, the solution–diffusion model of water transport across the membrane in PRO can be simplified as in Eq. (3.16).

$$J_{w,PRO} = \frac{dQ}{dS_{PRO}} = A_{PRO} \left[\sigma \left(\frac{\pi_{D,in} Q_{D,in}}{Q} - \pi_F \right) - \Delta P_{PRO} \right] \tag{3.16}$$

$$\pi_{D,in} = (1 - \mathrm{RR}) Q_0 \tag{3.17}$$

$$Q_{D,in} = \pi_0 / (1 - \mathrm{RR}) \tag{3.18}$$

where σ is defined as an ICP factor whose value is determined by the solute resistance coefficient K and mass transfer coefficient B of the membrane, $\sigma = 1/(1 + BK)$. Similar to the derivation of Eq. (3.12), integrating Eq. (3.16) with the dimensionless parameters, we can obtain the dimensionless characteristic equation for PRO:

$$\gamma_{PRO} = \frac{1}{\theta_{PRO}} \left[1 - q + \frac{(1 - \mathrm{RR})\sigma}{\theta_{PRO}} \ln \left(\frac{\sigma - (1 - \mathrm{RR})\theta_{PRO}}{\sigma - q\theta_{PRO}} \right) \right] \tag{3.19}$$

$$q = [\Delta Q_{PRO} + (1 - \mathrm{RR}) Q_0] / Q_0 \tag{3.20}$$

$$\theta_{PRO} = (\Delta P_{PRO} + \pi_F) / \pi_0 \tag{3.21}$$

$$\gamma_{PRO} = A_{PRO} S_{PRO} \pi_0 / Q_0 \tag{3.22}$$

Similarly, θ_{PRO} and γ_{PRO} are regarded as the operational and design parameters, while q is represented as the dilutive factor (flow rate at the membrane outlet divided by the one at the membrane inlet), which is strongly dependent on the membrane performance. Note that there are close similarities between Eqs. (3.12) and (3.19), revealing the close relationship among q, θ_{PRO}, and γ_{PRO}.

3.3.2 Mathematical Model and Objectives

For the open-loop configuration, the total energy recovered by the two ERDs is given as follows:

$$W_{ERD} = \eta_{ERD} Q_0 (1 - \mathrm{RR})[\Delta P_{RO} + (q - 1 + \mathrm{RR})\Delta P_{PRO}] \tag{3.23}$$

where η represents the efficiency and the subscript *ERD* represents the ERD. This portion of recovered work will be directly used to pressurize the feed water. Nevertheless, the feed pressure cannot reach the required high pressure in RO process after being pressurized by pressure exchangers. Thus, the booster pump is added to provide extra pressure for the feed solution, of which the energy consumption is calculated as follows:

$$W_{pump} = \frac{Q_0 \Delta P_{RO} - W_{ERD}}{\eta_{pump}} \tag{3.24}$$

Considering the energy consumption for the pretreatment of RO feed and the posttreatment of brine discharged from PRO, the *normalized specific energy consumption* (NSEC) can be computed by

$$\begin{aligned} \mathrm{NSEC}_{OL} &= \frac{W_{pump} Q_0}{\Delta Q_{RO} \pi_0} + \frac{W_{pre} Q_0}{\Delta Q_{RO}} + \frac{W_{post} Q_0 q}{\Delta Q_{RO}} \\ &= \frac{\theta_{RO} - \eta_{ERD}(1 - \mathrm{RR})[\theta_{RO} + (q - 2 + 2\mathrm{RR})(\theta_{PRO} - r)]}{\eta_{pump} \mathrm{RR}} + \frac{W_{pre} + W_{post} Q_0 q}{\mathrm{RR}} \end{aligned} \tag{3.25}$$

where the subscripts *pre* and *post* represent the steps of the pretreatment and posttreatment, respectively; r is the osmotic pressure ratio of the concentration of feed solution to that of feed water, $r = \pi_F / \pi_0$.

To minimize NSEC with regard to the open-loop RO–PRO system, a dimensionless optimization model is established as

$$\begin{aligned} \min \quad & \mathrm{NSEC}_{OL} \\ \text{s.t.} \quad & \text{Eqs. (3.12) and (3.19)} \\ & 0 = \gamma_{tot} - \gamma_{RO} - \gamma_{PRO} \\ & 0 \le \theta_{RO} - 1 \\ & 0 \ge \theta_{PRO} - 1/(1 - \mathrm{RR}) \\ & 0 \le q - 1 + \mathrm{RR} \end{aligned} \tag{3.26}$$

In this model, the first two equality constraints are dimensionless characteristic equations of RO and PRO units. The third equality constraint is aimed at allocating the total membrane area of the integrated system, in which $\gamma_{PRO} = AS_{tot} \pi_0 / Q_0$ is defined as the total dimensionless membrane area. The remaining inequality constraints are set to guarantee non-negative driving force in each unit.

For the closed-loop configuration, the amount of energy recovered by ERD is equivalent to $\eta_{\mathrm{ERD}} Q_0 (1 - \mathrm{RR})(\Delta P_{RO} - \Delta P_{PRO})$. The energy harvested in the draw solution at the outlet of the PRO unit, $Q_0 \Delta P_{PRO}$, circulates infinitely within the

system with the recycling solution. Note that the energy consumption of pretreatment is unnecessary in the closed-loop system. Accordingly, the NSEC of closed-loop configuration is

$$\mathrm{NSEC}_{CL} = \frac{W_{pump} Q_0}{\Delta Q_{RO} \pi_0} = \frac{[1 - \eta_{ERD}(1 - \mathrm{RR})][\theta_{RO} - (\theta_{PRO} - r)]}{\eta_{pump} \mathrm{RR}} \tag{3.27}$$

$$W_{pump} = [(Q_0 \Delta P_{RO})/(\Delta Q_{RO} - \pi_0) - W_{ERD}] \tag{3.28}$$

In summary, the dimensionless optimization model for the closed-loop configuration is formulated as

$$\begin{aligned} &\min \mathrm{NSEC}_{CL} \\ &\text{s.t. Eqs. (3.12) and (3.19)} \\ &\quad 0 = \gamma_{tot} - \gamma_{RO} - \gamma_{PRO} \\ &\quad 0 \le \theta_{RO} - 1 \\ &\quad 0 \ge \theta_{PRO} - 1 \\ &\quad 0 = q - 1 \end{aligned} \tag{3.29}$$

It is worth pointing out that the last equality constraint is used to guarantee the identical flow rates and concentrations of the draw (at PRO outlet) and the feed solution (RO entrance).

3.3.3 Optimization Results and Comparative Analysis

According to the actual operating data of seawater RO desalination plants, the variation ranges of the total dimensionless membrane areas (γ_{tot}) and water RR in this work are considered as 0.6–1.6 and 0.3–0.7, respectively. In addition, the energy consumption of pretreatment (W_{pre}) and posttreatment (W_{post}) are 0.25 and 0.05 kWh/m^3, respectively, which are consistent with the practical data. Moreover, the efficiencies of pump and ERD are assumed as $\eta_{pump} = 0.86$ and $\eta_{ERD} = 0.98$, along with osmotic pressure ratio $r = 0.1$.

Figure 3.9 shows that the NSECs of both configurations decrease when γ_{tot} increases and RR decreases. In Figure 3.9a, the minimum NSEC of the closed-loop configuration decreases sharply when the dimensionless membrane area is small ($\gamma_{tot} = 0.6$–0.8) and the recovery ratio is high (RR = 0.55–0.7). For example, when $RR = 0.7$ and $\gamma_{tot} = 0.6$ the NSEC increases rapidly to 9.56, while at the same recovery ratio and γ_{tot} increases to 0.8, the corresponding NSEC reduces by nearly half to only 4.75. This reduction indicates that the performance of the closed-loop configuration is sensitive to the change of the membrane area and recovery ratio in the aforementioned ranges. Thus, as designing a closed-loop configuration, it is advised to avoid operating in the range of $\gamma_{tot} = 0.6$–0.8 and RR = 0.55–0.7, where system performance fluctuates considerably. The optimal operating range of the closed-loop configuration is γ_{tot} = 0.9–1.2 and RR = 0.3–0.55, where the NSECs are at a relatively low level, thus having more advantages in energy conservation compared with the open-loop configuration.

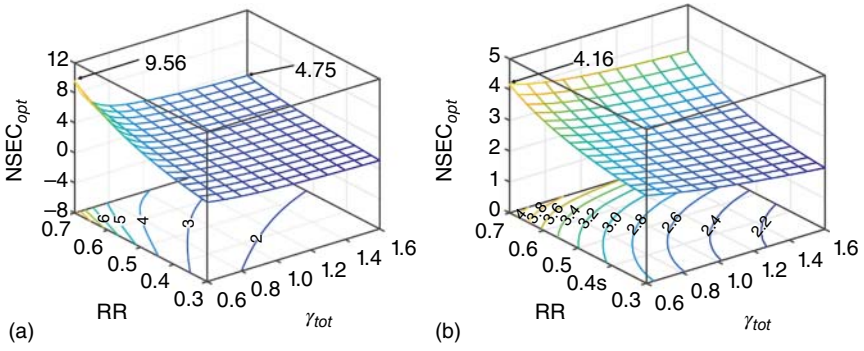

Figure 3.9 Optimal NSECs of the (a) closed-loop and (b) open-loop RO–PRO configurations as a function of γ_{tot} and *RR*.

Through the comparison of Figure 3.9a,b, it can be concluded that the open-loop configuration has the advantage of saving energy, as the water recovery ratio is high and the total semi-permeable membrane area is small. For instance, as RR = 0.7 and $\gamma_{tot} = 0.6$, the minimum NSEC of open-loop configuration is only 4.16, while in the closed-loop one it has tripled to 9.56. However, RR = 0.23–0.4 and $\gamma_{tot} = 0.56$–1.61 are generally used in desalination plants at present. At this operating level, the closed-loop configuration outperforms the open-loop one in terms of reducing energy consumption, which has a greater potential for energy conservation in the practical application.

During optimization, the model will optimize the dimensionless membrane area allocation ratio of RO and PRO, in order to minimize the NSEC. Figure 3.10 shows that the two configurations have obvious differences in membrane area allocation. For the closed-loop one, Figure 3.10a shows that membrane area allocated by the PRO unit increases with the increase in the recovery ratio and the total membrane area. Figure 3.10c indicates that the proportion of the membrane area occupied by the RO unit is close to 50% under most conditions. Note however that, in the case of RR > 0.55 and $\gamma_{tot} < 0.8$, the optimal S_{RO}/S_{tot} will drop sharply and eventually to zero. In the corresponding region of Figure 3.10a, the change of γ_{PRO} is minimal and even negligible in the direction of γ_{tot} due to the limited driving force. In this case, there is a minimum dimensionless membrane area ($\gamma_{PRO,min}$), ensuring that volumetric flow rate of permeated water in the PRO unit is exactly equal to that in the RO unit. To be more specific, the dimensionless total membrane area in the system needs to be greater than $\gamma_{PRO,min}$ ($\gamma_{PRO,\min} = \pi_0 \mathrm{RR}/\overline{\Delta\pi_{PRO}}$, where $\overline{\Delta\pi_{PRO}}$ is the average transmembrane osmotic pressure difference in the PRO unit). As γ_{tot} decreases continuously until it is equal to $\gamma_{PRO,min}$, the closed-loop configuration cannot be capable of operating under specified constraints.

As shown in Figure 3.10b, the open-loop configuration of the membrane area allocated to PRO unit (γ_{PRO}) increases monotonically with the increase in γ_{tot}, but decreases at first and then increases with the increase in recovery ratio. The corresponding proportion of the membrane area of RO unit is shown in Figure 3.10d. The increase in γ_{RO} makes the RO's operation approach the thermodynamic limit,

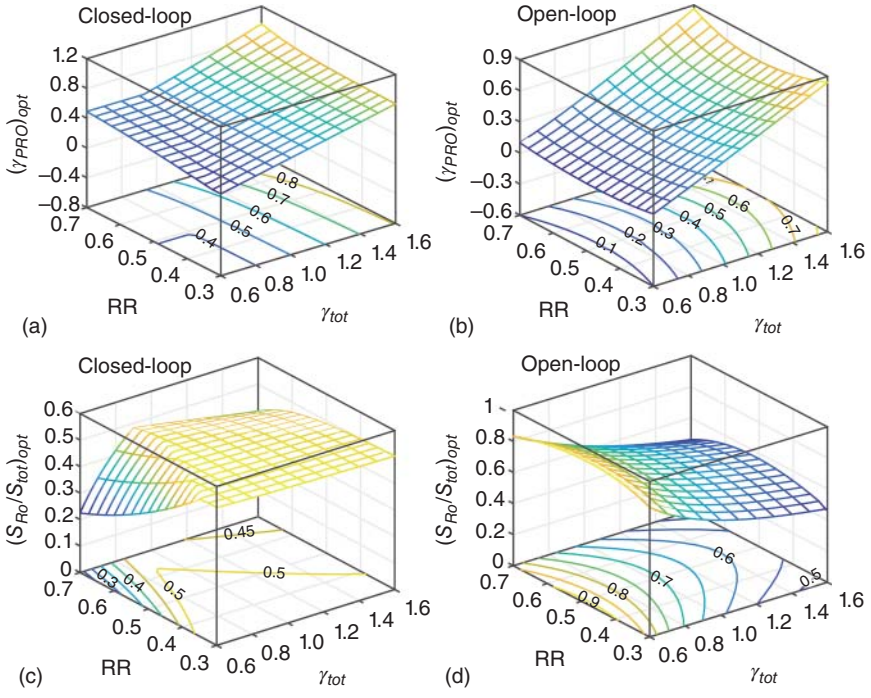

Figure 3.10 The optimal γ_{PRO} in (a) closed-loop configuration and (b) open-loop configuration and the optimal S_{RO}/S_{tot} in (c) closed-loop configuration and (d) open-loop configuration at varied γ_{tot} and *RR*.

and a further increase would play a negligible role in reducing the energy consumption of the system. Thereby, as γ_{tot} increases, more dimensionless membrane area is allocated to the PRO unit to reduce its NSEC. In the case of $\gamma_{tot} > 1.2$, more than half of the membrane area tends to be distributed to the PRO unit, indicating that the PRO unit makes a greater contribution to energy saving.

As shown in Figure 3.11a,b, the optimized dimensionless operating pressure ($\Delta P_{RO}/\pi_0$) decreases continuously with the increase in γ_{tot} and the decrease in RR, and the downward trend of closed-loop configuration is more pronounced. With the growth of γ_{tot}, the decreasing rate of $\Delta P_{RO}/\pi_0$ slows down gradually. By comparing Figure 3.11a,b with Figure 3.9a,b, it can be found that the $\Delta P_{RO}/\pi_0$ and NSEC have a similar trend, indirectly indicating that the operation of RO unit plays a more important role in the overall energy consumption of the hybrid system. The optimum results of dimensionless operating pressure $\Delta P_{PRO}/\pi_0$ for PRO unit under different γ_{tot} and RR are shown in Figure 3.11c,d. As shown, the variation tendencies in $\Delta P_{PRO}/\pi_0$ of open- and closed-loop configurations are completely opposite. In the open-loop configuration, $\Delta P_{PRO}/\pi_0$ decreases with the increase in γ_{tot} and decrease in RR. In Figure 3.11d, as the membrane area of PRO unit increases gradually, its optimal operating pressure decreases gradually to achieve the goal of maximizing SEP. In the closed-loop configuration, however, the optimized $\Delta P_{PRO}/\pi_0$ appears a growing trend in general. This is because the

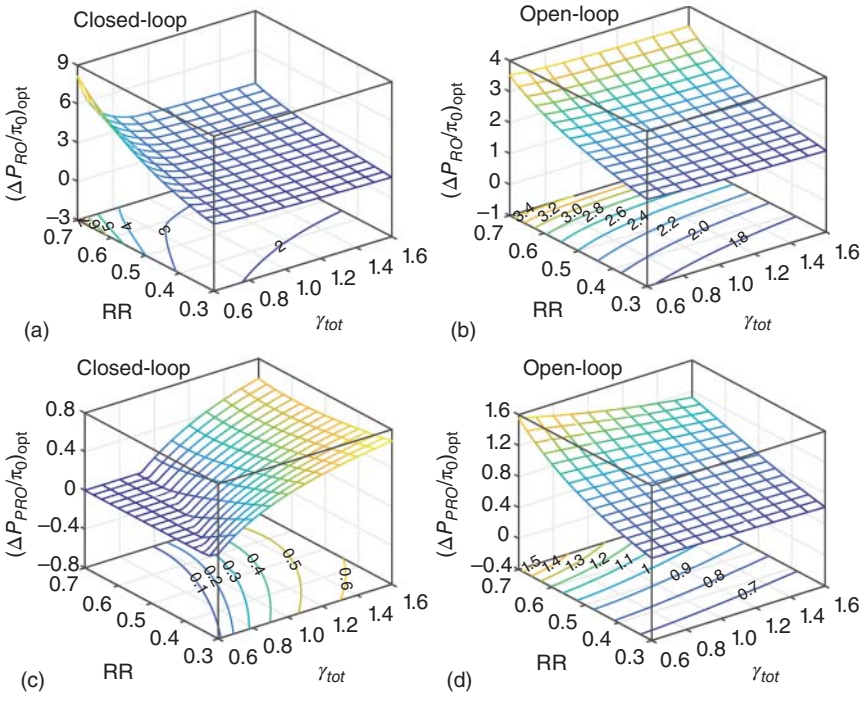

Figure 3.11 Optimal $\Delta P_{RO}/\pi_0$ in (a) closed-loop configuration and (b) open-loop configuration and the optimal $\Delta P_{PRO}/\pi_0$ in (c) closed-loop configuration and (d) open-loop configuration at varied γ_{tot} and *RR*.

water flux of PRO unit (Q_0RR) will be changed to a fixed value under the fixed recovery ratio, i.e. the increase of energy recovery via PRO (Q_0RRΔP_{PRO}) can only be realized by the rise of $\Delta P_{PRO}/\pi_0$. In Figure 3.11c, as RR ≥ 0.55 and $\gamma_{tot} \leq 0.9$, $\Delta P_{PRO}/\pi_0$ is equal to zero, which reveals that the PRO is actually operating as FO process in this case. From Figures 3.10c and 3.11c, it can be seen that in the closed-loop configuration the anomalous phenomenon $\Delta P_{PRO}/\pi_0 = 0$ occurs in case of a small membrane area. This is due to the fact that as $\Delta P_{PRO}/\pi_0 = 0$, the required membrane area will no longer to be reduced by changing the operating pressure of the PRO unit. Thus, PRO cannot recover the salinity gradient energy (Q_0RR$\Delta P_{PRO} = 0$). In other words, a large amount of total membrane area is occupied by PRO to dilute the draw solution from the outlet of RO unit when total membrane area is small.

3.4 Conclusion

In this chapter, fundamental theory of an RO–PRO hybrid system with open-loop and closed-loop configurations has been provided. The energy efficiencies of two configurations in terms of normalized SEC were explored through using a dimensionless model-based optimization approach. The optimization results indicated that both configurations have the capability to obtain renewable

energy from salinity gradients for compensating their energy consumption. In particular, the comparative assessment indicated that the closed-loop configuration has greater superiority in energy conservation under the normal level of water recovery ratio (RR ≥ 0.55) and abundant membrane area ($\gamma_{tot} \leq 0.9$), although the practical operating flexibility of the closed-loop configuration is inferior to that of the open-loop configuration.

Nomenclature

Greek Symbols

π	osmotic pressure (kPa)
π_0	feed osmotic pressure (kPa)
$\Delta\pi$	osmotic pressure difference/gradient across the membrane (kPa)
ΔP	hydraulic pressure difference across the membrane (kPa)
α	degree of dissociation (dimensionless)
ΔG_{mix}	Gibbs free energy of mixing, J
ϕ	ratio of the total moles in low concentration solution to that in the system (dimensionless)
γ	activity coefficient (dimensionless)
η	efficiency (dimensionless)
ΔQ	transmembrane water flow rate (m^3/s)
θ_{RO}	$\Delta P_{RO}/\pi_0$ (dimensionless)
θ_{PRO}	$(\Delta P_{PRO} + \pi_F)/\pi_0$ (dimensionless)
σ	internal concentration polarization $1/(1 + BK)$ (dimensionless)
γ_{RO}	$A_{RO}S_{RO}\pi_0/Q_0$ (dimensionless)
γ_{PRO}	$A_{PRO}S_{PRO}\pi_0/Q_0$ (dimensionless)
γ_{tot}	$S_{tot}A\pi_0/Q_0$ (dimensionless)

Roman Symbols

c	molar concentration (mol/l)
R	ideal gas constant (8.314 J/mol/K)
T	absolute temperature (K)
i	van't Hoff factor (dimensionless)
ν	stoichiometric coefficient of dissociation reaction (dimensionless)
x_i	mole fraction of species i in the solution (dimensionless)
J_w	water permeation flux (m/s)
A	water permeability coefficient of the membrane (m/(s·kPa))
Q	volumetric flow rate (m^3/s)
W	work (kWh)
RR	recovery ratio of permeate water (dimensionless)
A_m	membrane area (m^2)
q	dilute ratio Q/Q_0 (dimensionless)

r	osmotic pressure ratio π_F/π_0 (dimensionless)
B	salt permeability (m/s)
K	solute resistivity (s/m)

Subscripts

M	resultant mixture solution
LC	low concentration solution
HC	high concentration solution
w	water
s	dissociated ions of the salt
F/f	feed solution property
D	draw solution property
b	bulk property
p	permeate property
0	initial condition
pump	pump
max	maximum
min	minimum
in	inlet
OL	open-loop configuration
CL	closed-loop configuration
pre	pretreatment
post	posttreatment
tot	total

Abbreviations

CCRO	closed-circuit reverse osmosis
DS	draw solution
ECP	external concentration polarization
ERD	energy recovery device
FO	forward osmosis
FS	feed solution
PD	power density
RO	reverse osmosis
PRO	pressure retarded osmosis
NF	nanofiltration
NSEC	normalized specific energy consumption
ICP	internal concentration polarization
SEC	specific energy consumption
SEP	specific energy production
TFC	thin-film composite

References

1 Gude, V.G. (2015). Energy storage for desalination processes powered by renewable energy and waste heat sources. *Applied Energy* 137: 877–898.

2 Tarnacki, K., Meneses, M., Melin, T. et al. (2012). Environmental assessment of desalination processes: reverse osmosis and Memstill®. *Desalination* 296: 69–80.

3 United Nations Water. (2019) World Water Development Report, 18 March 2019. https://www.unwater.org/publications/world-water-development-report-2019.

4 Burek, P., Satoh, Y., Fischer, G., et al. (2016). Water futures and solution – fast track initiative. Final report WP-74-041.

5 United Nations Water. (2018) World Water Development Report. https://www.unwater.org/publications/world-water-development-report-2018 (accessed 20 July 2019).

6 Richey, A.S., Thomas, B.F., Lo, M.H. et al. (2015). Quantifying renewable groundwater stress with GRACE. *Water Resources Research* 51 (7): 5217–5238.

7 Gabriel, K.J., El-Halwagi, M.M., and Linke, P. (2016). Optimization across the water-energy nexus for integrating heat, power and water for industrial processes coupled with hybrid thermal-membrane desalination. *Industrial and Engineering Chemistry Research* 55 (12): 3442–3466.

8 Yip, N.Y., Tiraferri, A., Phillip, W.A. et al. (2011). Thin-film composite pressure retarded osmosis membranes for sustainable power generation from salinity gradients. *Environmental Science and Technology* 45 (10): 4360–4369.

9 Eltawil, M.A., Zhengming, Z., and Yuan, L. (2009). A review of renewable energy technologies integrated with desalination systems. *Renewable and Sustainable Energy Reviews* 13 (9): 2245–2262.

10 Burn, S., Hoang, M., Zarzo, D. et al. (2015). Desalination techniques – a review of the opportunities for desalination in agriculture. *Desalination* 364: 2–16.

11 Greenlee, L.F., Lawler, D.F., Freeman, B.D. et al. (2009). Reverse osmosis desalination: water sources, technology, and today's challenges. *Water Research* 43 (9): 2317–2348.

12 Wang, Y., Wang, Z., and Wang, J. (2018). Lab-scale and pilot-scale fabrication of amine-functional reverse osmosis membrane with improved chlorine resistance and antimicrobial property. *Journal of Membrane Science* 554: 221–231.

13 Li, M. (2017). Reducing specific energy consumption of seawater desalination: staged RO or RO–PRO? *Desalination* 422 (Supplement C): 124–133.

14 Voutchkov, N. (2018). Energy use for membrane seawater desalination – current status and trends. *Desalination* 431: 2–14.

15 Khan, M.A.M., Rehman, S., and Al-Sulaiman, F.A. (2018). A hybrid renewable energy system as a potential energy source for water desalination using

reverse osmosis: a review. *Renewable and Sustainable Energy Reviews* 97: 456–477.

16 Elimelech, M. and Phillip, W.A. (2011). The future of seawater desalination: energy, technology, and the environment. *Science* 333 (6043): 712–717.

17 Warsinger, D.M., Tow, E.W., Nayar, K.G. et al. (2016). Energy efficiency of batch and semi-batch (CCRO) reverse osmosis desalination. *Water Research* 106: 272–282.

18 Werber, J.R., Deshmukh, A., and Elimelech, M. (2017). Can batch or semi-batch processes save energy in reverse-osmosis desalination? *Desalination* 402: 109–122.

19 Li, W., Krantz, W.B., Cornelissen, E.R. et al. (2013). A novel hybrid process of reverse electrodialysis and reverse osmosis for low energy seawater desalination and brine management. *Applied Energy* 104: 592–602.

20 Wang, Y., He, W., and Zhu, H. (2016). Computational fluid dynamics (CFD) based modelling of osmotic energy generation using pressure retarded osmosis (PRO). *Desalination* 389: 98–107.

21 Lin, S., Yip, N.Y., Cath, T.Y. et al. (2014). Hybrid pressure retarded osmosis–membrane distillation system for power generation from low-grade heat: thermodynamic analysis and energy efficiency. *Environmental Science and Technology* 48 (9): 5306–5313.

22 Ramon, G.Z., Feinberg, B.J., and Hoek, E.M.V. (2011). Membrane-based production of salinity-gradient power. *Energy and Environmental Science* 4 (11): 4423–4434.

23 Yip, N.Y., Brogioli, D., Hamelers, H.V.M., and Nijmeijer, K. (2016). Salinity gradients for sustainable energy: primer, progress, and prospects. *Environmental Science and Technology* 50 (22): 12072–12094.

24 Achilli, A., Cath, T.Y., and Childress, A.E. (2009). Power generation with pressure retarded osmosis: an experimental and theoretical investigation. *Journal of Membrane Science* 343 (1): 42–52.

25 Zhang, S., Fu, F., and Chung, T.-S. (2013). Substrate modifications and alcohol treatment on thin film composite membranes for osmotic power. *Chemical Engineering Science* 87: 40–50.

26 Wan, C.F., Li, B., Yang, T., and Chung, T.-S. (2017). Design and fabrication of inner-selective thin-film composite (TFC) hollow fiber modules for pressure retarded osmosis (PRO). *Separation and Purification Technology* 172: 32–42.

27 Wan, C.F., Yang, T., Gai, W. et al. (2018). Thin-film composite hollow fiber membrane with inorganic salt additives for high mechanical strength and high power density for pressure-retarded osmosis. *Journal of Membrane Science* 555: 388–397.

28 Xiong, J.Y., Cai, D.J., Chong, Q.Y. et al. (2017). Osmotic power generation by inner selective hollow fiber membranes: an investigation of thermodynamics, mass transfer, and module scale modelling. *Journal of Membrane Science* 526: 417–428.

29 She, Q., Jin, X., and Tang, C.Y. (2012). Osmotic power production from salinity gradient resource by pressure retarded osmosis: effects of operating conditions and reverse solute diffusion. *Journal of Membrane Science* 401–402: 262–273.

30 Higa, M., Shigefuji, D., Shibuya, M. et al. (2017). Experimental study of a hollow fiber membrane module in pressure-retarded osmosis: module performance comparison with volumetric-based power outputs. *Desalination* 420: 45–53.

31 Altaee, A. and Hilal, N. (2015). Design optimization of high performance dual stage pressure retarded osmosis. *Desalination* 355: 217–224.

32 Chung, H.W., Nayar, K.G., Swaminathan, J. et al. (2017). Thermodynamic analysis of brine management methods: zero-discharge desalination and salinity-gradient power production. *Desalination* 404: 291–303.

33 Wang, S., Kang, L., Zhang, B. et al. (2019). Energy minimization in hybrid desalination system of reverse osmosis and pressure retarded osmosis. *CIESC Journal* 70 (2): 617–624.

34 He, W., Wang, Y., Sharif, A., and Shaheed, M.H. (2014). Thermodynamic analysis of a stand-alone reverse osmosis desalination system powered by pressure retarded osmosis. *Desalination* 352: 27–37.

35 Sharqawy, M.H., Zubair, S.M., and Lienhard, V.J.H. (2011). Second law analysis of reverse osmosis desalination plants: an alternative design using pressure retarded osmosis. *Energy* 36 (11): 6617–6626.

36 Kurihara, M. and Hanakawa, M. (2013). Mega-ton water system: Japanese national research and development project on seawater desalination and wastewater reclamation. *Desalination* 308: 131–137.

37 Achilli, A., Prante, J.L., Hancock, N.T. et al. (2014). Experimental results from RO–PRO: a next generation system for low-energy desalination. *Environmental Science and Technology* 48 (11): 6437–6443.

38 Prante, J.L., Ruskowitz, J.A., Childress, A.E., and Achilli, A. (2014). RO–PRO desalination: an integrated low-energy approach to seawater desalination. *Applied Energy* 120: 104–114.

39 Han, G., Zhang, S., Li, X., and Chung, T.-S. (2015). Progress in pressure retarded osmosis (PRO) membranes for osmotic power generation. *Progress in Polymer Science* 51: 1–27.

40 Touati, K. and Tadeo, F. (2016). Green energy generation by pressure retarded osmosis: state of the art and technical advancement – review. *International Journal of Green Energy* 14 (4): 337–360.

41 Helfer, F., Lemckert, C., and Anissimov, Y.G. (2014). Osmotic power with pressure retarded osmosis: theory, performance and trends – a review. *Journal of Membrane Science* 453: 337–358.

42 Labban, O., Liu, C., Chong, T.H., and Lienhard, J.H. (2018). Relating transport modeling to nanofiltration membrane fabrication: navigating the permeability–selectivity trade-off in desalination pretreatment. *Journal of Membrane Science* 554: 26–38.

43 Kaya, C., Sert, G., Kabay, N. et al. (2015). Pre-treatment with nanofiltration (NF) in seawater desalination – preliminary integrated membrane tests in Urla, Turkey. *Desalination* 369: 10–17.

44 Senthil, S. and Senthilmurugan, S. (2016). Reverse osmosis–pressure retarded osmosis hybrid system: modelling, simulation and optimization. *Desalination* 389: 78–97.

45 Karuppiah, R., Bury, S.J., Vazquez, A., and Poppe, G. (2012). Optimal design of reverse osmosis-based water treatment systems. *AIChE Journal* 58 (9): 2758–2769.

46 Du, Y., Xie, L., Liu, Y. et al. (2015). Optimization of reverse osmosis networks with split partial second pass design. *Desalination* 365: 365–380.

47 Karabelas, A.J., Koutsou, C.P., Kostoglou, M., and Sioutopoulos, D.C. (2018). Analysis of specific energy consumption in reverse osmosis desalination processes. *Desalination* 431: 15–21.

48 Zhu, A., Christofides, P.D., and Cohen, Y. (2009). Energy consumption optimization of reverse osmosis membrane water desalination subject to feed salinity fluctuation. *Industrial and Engineering Chemistry Research* 48 (21): 9581–9589.

49 Peñate, B. and García-Rodríguez, L. (2012). Current trends and future prospects in the design of seawater reverse osmosis desalination technology. *Desalination* 284: 1–8.

50 Altaee, A., Millar, G.J., and Zaragoza, G. (2016). Integration and optimization of pressure retarded osmosis with reverse osmosis for power generation and high efficiency desalination. *Energy* 103: 110–118.

51 Straub, A.P., Deshmukh, A., and Elimelech, M. (2016). Pressure-retarded osmosis for power generation from salinity gradients: is it viable? *Energy and Environmental Science* 9 (1): 31–48.

52 Kim, J., Park, M., Snyder, S.A., and Kim, J.H. (2013). Reverse osmosis (RO) and pressure retarded osmosis (PRO) hybrid processes: model-based scenario study. *Desalination* 322: 121–130.

53 Wang, S., Zhu, Q., He, C. et al. (2018). Model-based optimization and comparative analysis of open-loop and closed-loop RO–PRO desalination systems. *Desalination* 446: 83–93.

54 Wan, C.F. and Chung, T.-S. (2016). Energy recovery by pressure retarded osmosis (PRO) in SWRO–PRO integrated processes. *Applied Energy* 162: 687–698.

55 Li, M. (2015). Analysis and optimization of pressure retarded osmosis for power generation. *AIChE Journal* 61 (4): 1233–1241.

56 Li, M. (2018). Systematic analysis and optimization of power generation in pressure retarded osmosis: effect of multistage design. *AIChE Journal* 64 (1): 144–152.

4

Techno-economic and Environmental Assessment of Ultrathin Polysulfone Membranes for Oxygen-Enriched Combustion

Serene Sow Mun Lock, Kok Keong Lau, Azmi Mohd Shariff, Yin Fong Yeong, and Norwahyu Jusoh

Universiti Teknologi PETRONAS, CO_2 Research Center (CO2RES), Department of Chemical Engineering, 32610 Seri Iskandar, Malaysia

4.1 Introduction

In order to optimize O_2/N_2 gas separation for oxygen-enriched combustion, it is required to increase O_2 membrane permeance while maintaining good selectivity for sieving capability of O_2 over N_2. The high O_2 permeance is required since O_2 that is more permeable in membrane separation constitutes a minority of 21% in the air feed [1]. Additionally, sufficient selectivity is necessary to minimize the existence of N_2 that contributes no heating value [1]. It has been reported that polymeric membranes have to exhibit an ideal O_2/N_2 selectivity of 3–6 and optimum O_2 permeance value in order to be commercially viable in oxygen-enriched combustion [2]. The restraint in trade-off between permeance and selectivity inherit in polymeric membranes can be circumvented by fabricating the thickness of dense active layer within polymeric membrane to the ultrathin dimension (<5000 Å) [3, 4].

Ultrathin polymeric membrane dominates industrial application due to its improved gas transport properties, while being economically feasible by requiring mere reduction in active film thickness [3, 4]. Nonetheless, the challenge associated to adaptation of ultrathin polymeric membrane is that it inherits different morphological and permeability properties, $\overline{P}$, as compared with bulk polymeric structure that has received most scholarly attention [5]. It is found that by reducing the thickness of a film appropriately beneath a certain dimension, the conformation of polymeric chains in membrane is perturbed when it is located in the vicinity closer to surface boundary. The restrictions consequently affect the polymer's properties, which are known as *confinement* effects [6]. The length scales of interest associated to the thickness dependent confinement in ultrathin films are summarized in Figure 4.1 [7].

To date, the studies of thickness dependent physical and gas transport properties upon confinement have received less scrutiny due to challenges to fabricate defect-free ultrathin polymeric membrane at laboratory scale. Among the major challenges in experimental scale testing for ultrathin membranes are summarized

Process Intensification and Integration for Sustainable Design, First Edition.
Edited by Dominic C. Y. Foo and Mahmoud M. El-Halwagi.
© 2021 WILEY-VCH GmbH. Published 2021 by WILEY-VCH GmbH.

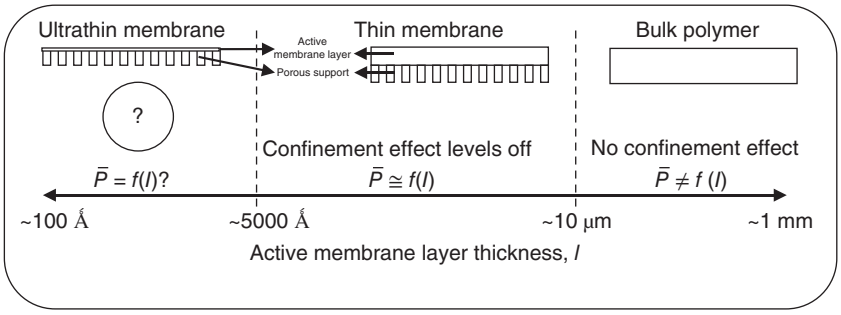

Figure 4.1 Schematic defining the length scales of interest associated to the thickness dependent behavior [7]. Source: Adapted from Rowe et al. (2009).

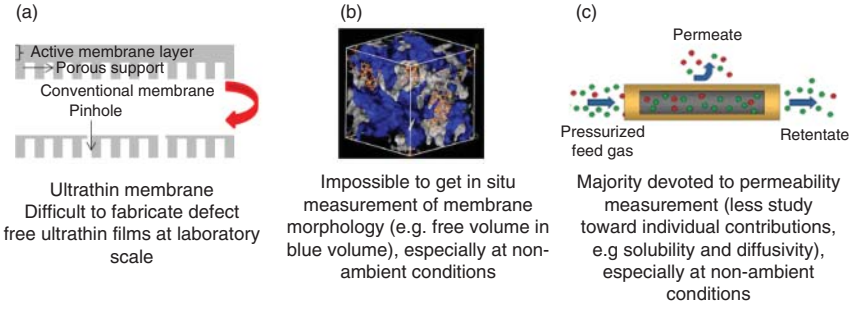

Figure 4.2 Experimental challenges that restraint the elucidation toward confinement in ultrathin polymeric membranes with (a) difficulties in fabricating defect-free films, (b) limitation in in situ measurement to study membrane morphology, and (c) inconveniency to measure gas transport properties at different operating conditions.

in Figure 4.2. As shown, the difficulties can be attributed to fabrication [8, 9], in situ measurement to study membrane morphology [10], and inconveniency to measure gas transport properties typically at different ranges [11].

4.2 Numerical Methodology for Membrane Gas Separation Design

Due to advancement in computational machines over recent years, simulation tools have been widely employed to circumvent the challenges inherent within experimental scale testing for membrane. The hierarchical modeling from molecular to process simulation in membrane processes at different scales has been provided in Figure 4.3 [12]. In this context, the evolution of computational capacity allows membrane characteristic to be investigated over different length and time scales, namely, nanoscale, mesoscale, macroscale, and process optimization and design.

Nanoscale simulation of membrane involves the study of essential that constitutes to fundamentals of interaction between atoms. In this context, end effect of membrane morphology as a direct consequence of operating and feed conditions that are difficult to be obtained from in situ measurement can be

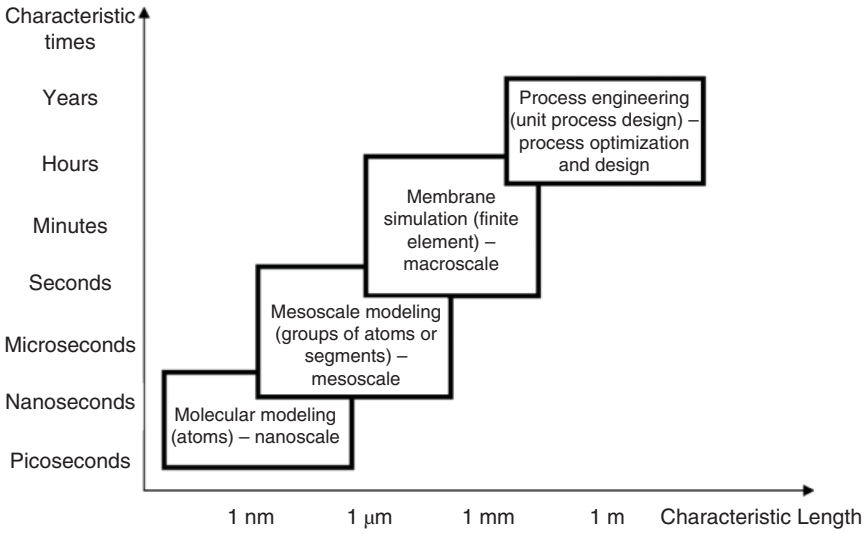

Figure 4.3 Time and distance in multiscale modeling of membrane [12]. Source: Adapted from He at al. (2017).

elucidated [13]. *Nanoscale simulation* can be used to develop empirical equations that describe intrinsic material properties of ultrathin films [13]. To date, most nanoscale simulation work has assumed an idealistic preposition of uniform characteristic of membrane material through the periodic boundary condition (PBC) [14, 15]. Nonetheless, the assumption is merely valid for bulk polymer and not for ultrathin structure, whereby confinement that arises from the polymer membrane surface plays an important role to chain relaxation [16]. Over recent years, published literatures have emerged to construct ultrathin polymer films adopting different methodologies by simulating interaction between the polymer and interfaces [17, 18]. Most of the works have been devoted to the study of methodology to construct ultrathin films at a fixed dimension and ambient operating conditions.

Mesoscale simulation of membrane is deduced as the simulation scale that operates at dimension for modeling complex membrane behavior with both atom-like effects and properties of the entire structure through adaptation of groups of atoms or segments together [19]. This includes transport of gas molecules within the membrane [19]. Although simulation has been demonstrated to be rather successful to model transport properties in membrane, majority of the study has been similarly confined to sorption and trajectory of gas molecules using assumption of PBC. Limited number of works has emerged that tested the dependence of gas transport on simulated size dimension [20, 21]. Their studies have been dedicated to simulating confined polymeric film in the thickness dimension through adaptation of different molecular techniques and tested whether this had an effect on the relaxation and gas permeation properties of ultrathin film at a fixed dimension [22, 23]. In addition, their simulations have been devoted to demonstrating confinement effect to gas transport behavior qualitatively in membrane model length of comparatively small dimension (merely ~100 Å) as compared with actual polymeric membrane employed in

industrial application. Moreover, majority of the works have been focused on elucidation of pure gas at ambient operating conditions.

Macroscale simulation is defined as modeling at dimension aimed to quantify separation performance and efficiency of a membrane (e.g. stage cut and product recovery) through finite element ideology by dividing the membrane module into many predefined independent entities [24]. Over the last decade, the attention has been diverted to incorporation of non-ideal effects within the macroscopic mathematical models in order to increase prediction accuracy. It is found that elucidation of the non-ideal effects has emerged from divergence of operating parameters from ambient condition since membrane gas separation is often operated at a wide range of operating conditions [25, 26]. Among the most common non-ideal effects include the following: (i) real gas behavior due to interaction of gases at high operating pressure [27, 28], (ii) pressure drop within the narrow channels in membrane for gas flow [25, 29], (iii) the Joule–Thomson cooling when gas permeates from high to low pressure end through the confined restriction of membrane pores under adiabatic expansion [28, 30], and (iv) flow configuration that is affected by design of membrane module, which alters the direction for permeation driving force [29, 31]. Recently, published mathematical modeling works have been diverted to quantification of membrane mixed gas transport property as a direct consequence of change in temperature and pressure [25, 32]. However, the membrane transport property as a function of operating conditions has majorly being obtained through empirical fitting at laboratory scale using bulk polymer that can be fabricated easily in comparison to ultrathin films.

In *process optimization and design* scale, membrane unit can be linked with other unit operations in order to evaluate an entire industrial process [32, 33]. The incorporation of mathematical model in process simulator is typically applicable for industrial process that requires auxiliary equipment or hybrid process, such as O_2/N_2 gas separation. Most of the published literatures have assumed ideal condition in membrane performance, whence the evaluation of techno-economic and feasibility of industrial process is typically independent of operating conditions and thickness. Only over recent years, process simulation work has been devoted to incorporate temperature- and pressure-dependent gas transport property in process simulator, in order to study the impact toward separation and process economics of natural gas sweetening process [32]. The temperature- and pressure-dependent gas transport properties have been obtained from experimental empirical fitting using polymer membrane at a fixed dimension. In addition, the work has been focused on application of natural gas sweetening that has received considerable attention over recent years. All the studies that have devoted to process optimization and design in oxygen-enriched combustion have employed constant membrane transport that is independent of operating conditions [1, 34].

This work contributes to a body of knowledge that demonstrates recent advances in multiscale simulation for ultrathin polysulfone (PSF) polymeric membranes applied in oxygen-enriched combustion. The modeling framework can be used to increase prediction accuracy of ultrathin polymeric membrane utilized in industrial application with minimal intervention from time-consuming, costly, and challenging experimental work, which enhances energy and environmental sustainability in a long run.

4.3 Methodology

This section describes the methodology used to evaluate ultrathin PSF membranes applied in oxygen-enriched combustion using multiscale simulation approach.

4.3.1 Simulation and Elucidation of Mixed Gas Transport Properties of Ultrathin PSF Membranes (Molecular Scale)

The Soft Confining Methodology for Ultrathin Film (SCMUF) as outlined in our earlier works has been used to simulate ultrathin PSF polymeric membranes at varying operating conditions [35]. Methodology and basis in current work are provided in Figure 4.4. Biovia Materials Studio 8.0 has been adapted with Condensed-phase Optimized Molecular Potentials for Atomistic Simulation Studies (COMPASS) force field [37]. COMPASS has been used because it is able to simulate PSF membrane with close agreement to actual observations [36].

The effect of mixed gas behavior, 20% O_2 and 80% N_2 gas molecules, has been incorporated in the PSF ultrathin films, which is analogous to approximate composition of air [36, 38]. The incorporation of mixed gas molecules has been applied consistently based upon protocols in Figure 4.5 to simulate mixed gas diffusivity [39] and solubility [36] using a combination of the Grand Canonical Monte Carlo and Metropolis algorithms [36, 41], and finally permeance [40].

The effect of real gas behavior has been modeled through incorporation of mixing properties for diffusivity, solubility, and permeability based upon

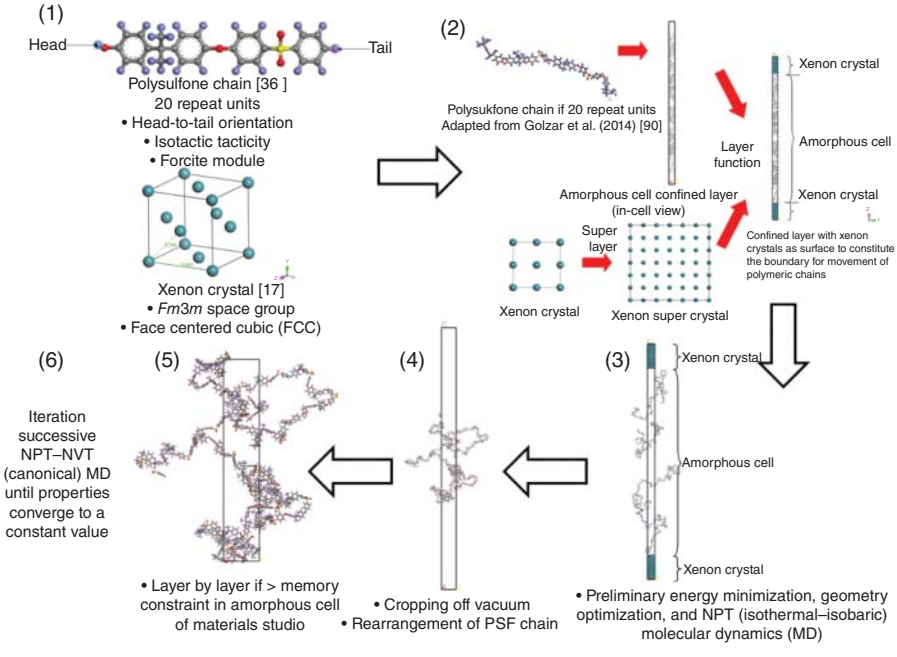

Figure 4.4 Preparation of PSF polymeric layer [35]. Source: Adapted from Lock et al. (2017).

(a) Diffusion coefficient

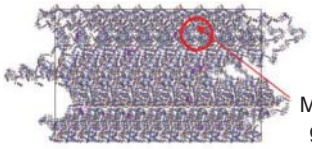

Mixture of O_2/N_2 gas molecules

• Einstein self diffusion correlation [40];

$$D_t = \frac{1}{6N} \lim_{t\to\infty} \frac{d}{dt} \sum_{t=1}^{N} \langle |r_t(t)^2 - r_t(t)^2| \rangle$$

(b) Solubility coefficient

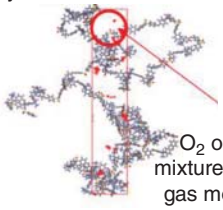

O_2 or N_2 or mixture of O_2/N_2 gas molecules

• Slope of the straight line connecting a point on the solubility isotherm to the origin [36]

$$S_t = \lim_{f_t \to 0} \left(\frac{C_t}{f_t} \right)$$

(c) Permeance coefficient

• Fickian law of diffusion [40];

$$J_t = -D_t \frac{dC_i}{dx}$$

• Definition of gas permeance:

$$P_i = \frac{J_i l}{p_n - p_i} = \left(\frac{c_{h,i} - c_{l,i}}{p_n - p_i} \right) D_i$$

$$\bar{P}_i = \frac{P_i}{i} = \frac{S_i D_i}{i}$$

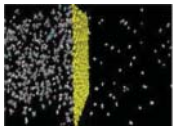

Figure 4.5 Methodology and basis to elucidate mixed gas (a) diffusivity, (b) solubility, and (c) permeance of studied ultrathin film.

published empirical models from our previous work [42], such as those shown in Eqs. (4.1)–(4.3), respectively.

$$D_i(l, T, P, x_i) = A_{i0} \exp\left(\frac{-\Delta H_A}{RT}\right) \times \exp\left(-\frac{B_{i,x_j}\left(l - \frac{b_0}{\varnothing_1 \tau_0 \exp \varnothing_2}\right)}{l - \varnothing_1 \cdot \frac{b_0}{\tau_0 \exp \varnothing_2} - \nu_o \cdot \varnothing_1 \cdot l}\right), B_{i,x_i} < B_i \tag{4.1}$$

$$S_i(l, T, P, x_i) = k_{Di0} \exp\left(\frac{-\Delta H_k}{RT}\right) + \frac{22414 \nu_{eq}}{\nu_0 \nu_i} \frac{b_{i0} \exp\left(\frac{-\Delta H_b}{RT}\right)}{1 + \sum_{i=1}^{N} b_{i0} \exp\left(\frac{-\Delta H_b}{RT}\right) f_i} \times \left(\frac{l - \frac{b_0}{\varnothing_1 \tau_0 \exp \varnothing_2} - \nu_o \cdot {\varnothing_1}^{-1} \cdot l}{l - \frac{b_0}{\varnothing_1 \tau_0 \exp \varnothing_2}} \right) - \frac{22\,414(\nu_{eq} - \nu_0)}{\nu_0 \nu_i} \frac{b_{i0} \exp\left(\frac{-\Delta H_b}{RT}\right)}{1 + \sum_{i=1}^{N} b_{i0} \exp\left(\frac{-\Delta H_b}{RT}\right) f_i} \tag{4.2}$$

$$\overline{P_i}(l,T,P,x_i)[\mathrm{GPU}]$$
$$= \frac{10^{14}}{l} A_{i0} \exp\left(\frac{-\Delta H_A}{RT}\right) \exp\left(-\frac{B_{i,x_j}\left(l - \dfrac{b_0}{\varnothing_1 \tau_0 \exp \varnothing_2}\right)}{l - \varnothing_1 \cdot \frac{b_0}{\tau_0 \exp \varnothing_2} - \nu_o \cdot \varnothing_1 \cdot l}\right)$$
$$\times \frac{10^{14}}{l}\left[\frac{1}{76} k_{Di0} \exp\left(\frac{-\Delta H_k}{RT}\right) + \frac{22414 \nu_{eq}}{76 \nu_0 \nu_i} \frac{b_{i0} \exp\left(\dfrac{-\Delta H_b}{RT}\right)}{1 + \sum_{i=1}^{N} b_{i0} \exp\left(\dfrac{-\Delta H_b}{RT}\right) f_i}\right.$$
$$\times \left(\frac{l - \dfrac{b_0}{\varnothing_1 \tau_0 \exp \varnothing_2} - \nu_o \cdot {\varnothing_1}^{-1} \cdot l}{l - \dfrac{b_0}{\varnothing_1 \tau_0 \exp \varnothing_2}}\right) - \frac{22414(\nu_{eq} - \nu_0)}{76 \nu_0 \nu_i}$$
$$\left. \times \frac{b_{i0} \exp\left(\dfrac{-\Delta H_b}{RT}\right)}{1 + \sum_{i=1}^{N} b_{i0} \exp\left(\dfrac{-\Delta H_b}{RT}\right) f_i}\right), B_{i,x_i} < B_i \tag{4.3}$$

In Eqs. (4.1)–(4.3), the definition of $\varnothing_1$ and $\varnothing_2$ similarly have been provided in Eqs. (4.4) and (4.5), respectively.

$$\varnothing_1 = (0.8051 + 1.756 \times 10^{-4} T) \times \left\{1 - 0.0894 \ln\left[1 + \frac{P}{4408 \exp(-1.543 \times 10^{-3} T)}\right]\right\} \tag{4.4}$$

$$\varnothing_2 = \frac{\varphi T_0}{T\left[1 - \frac{f_P(T)}{g_T(P)} \frac{1}{S_\infty} \int_{P_{atm}}^{P} \Delta\left(\frac{\partial V}{\partial T}\right)_{P'} dP'\right] - T_0} \tag{4.5}$$

4.3.2 Simulation of Mathematical Model Interfaced in Aspen HYSYS for Mass and Heat Balance (Mesoscale)

A mathematical model to characterize separation mechanism of ultrathin polymeric membrane under countercurrent flow configuration has been developed in the present work. The basis and assumption to solve the macroscopic mass and heat balances have been outlined in detailed in our previous works [43, 44].

4.3.3 Design of Oxygen-Enriched Combustion Using Ultrathin PSF Membranes

In this section, simulation system with incorporation of confinement effect in ultrathin polymeric membranes is considered as a non-ideal model. On the other hand, ideal simulation is dedicated for system that conventionally ignores confinement effect through assumption of uniform characteristic in bulk polymer

system. In order to attain objective of determining significance of the non-ideal effect as compared with its ideal counterpart, the two simulation models are compared in terms of separation performance and process economics applied in oxygen-enriched-air combustion. The configuration of a single stage membrane module without any recycling system has been adapted consistently to characterize the simulation conditions. The purpose is to isolate the complexity of membrane area ratio at different stages and recycle streams, which play a pivotal role in quantifying separation performance of membrane [45, 46]. Overall process design using Aspen HYSYS version 8.0 that simulates utilization of membrane to produce oxygen enriched air has been shown in Figure 4.6 [47].

The process simulation design encompasses those of a natural gas stream at industrial delivery pressure and an air stream at atmospheric condition, which have been treated prior to introduction to a combustion chamber for subsequent heat generation. In order to quantify the quality of heat produced, it has been fed to a simple Rankine steam cycle for electricity production. The Rankine steam cycle is consisted of steam side with steam turbine, steam condenser, condensate pump, and steam side of a boiler, in which the heat released from the combustion chamber has been introduced in order to extract electricity power. The permeance for ideal model has been obtained by ignoring confinement within ultrathin membrane ($l \rightarrow \infty$) in Eqs. (4.1)–(4.5) for mixed air gas system. As for permeance of the non-ideal model, Eqs. (4.1)–(4.5) have been employed consistently. Internal rate of return (IRR) of a single staged membrane in oxygen-enriched combustion has been computed through employment of economic parameters as outlined in Figure 4.7.

Air has been assumed to be delivered to the oxygen-enriched-air combustion plant at 35 °C and 1 bar (ambient operating condition). Higher operating temperature has been achieved via a heater, while higher pressure through a compressor. The heating or compression costs have been included in process economics study. The range of temperature and pressure have been altered between 35 and 55 °C and 2–50 bar, respectively, which are typical operating conditions encountered in industrial applications. The membrane area requirement has been defined as

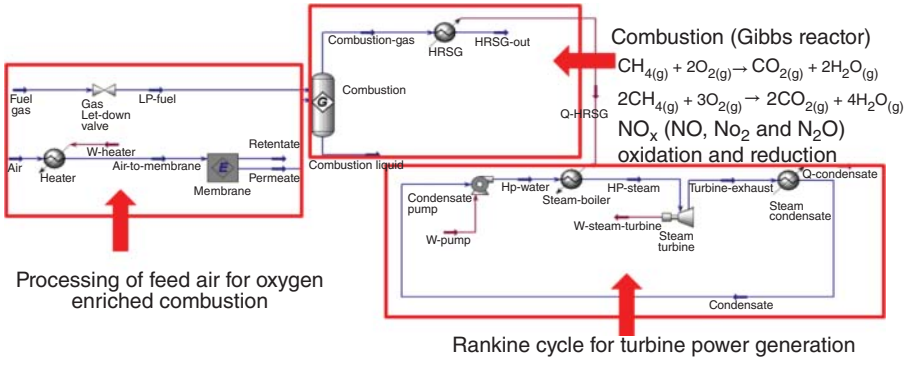

Figure 4.6 Schematic representation of process flow in Aspen HYSYS to study performance and economics of oxygen-enriched-air combustion. HRSG, heat recovery steam generators; NPT, isobaric-isothermal; NVT, canonical. [47]. Source: Adapted from Brunet et al. (2012).

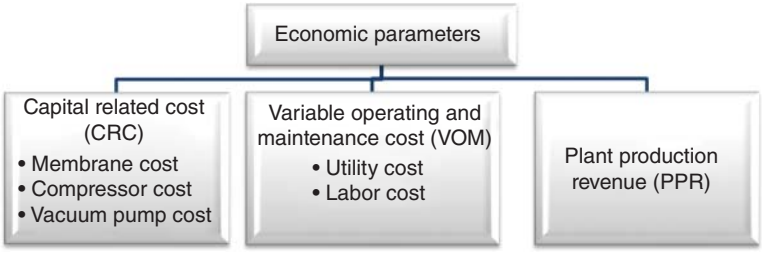

Figure 4.7 Economic parameters involved in computation of IRR for process economic studies.

the active permeation area necessary to achieve oxygen recovery of 90% in the enriched-air gas streams for the ideal model since this recovery has been proposed to be the composition required to be competitively viable with conventional adsorption or cryogenic technologies [48]. Later, the same membrane area is plotted for a particular membrane thickness and operating conditions to quantify the impact of non-ideal model based on deviation from conventional assumption of ignorance in confinement.

4.4 Results and Discussion

This section describes the results from multiscale simulation of ultrathin PSF films to preliminary evaluate techno-economic feasibility in oxygen-enriched combustion. Similarly, it is initiated with discussion of gas transport properties at the molecular level, followed by macroscopic separation performance and finally process design and optimization in industry application.

4.4.1 Simulation and Elucidation of Mixed Gas Transport Properties of Ultrathin PSF Membranes (Molecular)

The gas transport properties of O_2/N_2 gas mixture have been investigated in a ~500 Å PSF polymeric membranes. Empirical equations for mixed gas diffusivity and solubility derived in Eqs. (4.1) and (4.2) have been fitted with simulated data with the parameters summarized in Tables 4.1 and 4.2, respectively. Applicability of the empirical equations for air mixture has been evaluated in Figure 4.8.

Table 4.1 Values of constants determined from curve fitting with revised Doolittle-thickness empirical equation (Eq. (4.1)).

Gas	Parameter of revised Doolittle-thickness model							
	b_0 (ps)	T_0 (K)	τ_0 (ps)	φ	$\frac{f_p(T)}{g_T(P)}\frac{1}{S_\infty}$	$A_{i,0}$ ($\times 10^{-8}$ cm^2/s)	ΔH_A (J/mol)	B_i
O_2	5760	209	70	2.32	11	1.7309×10^6	1.6374×10^4	0.9483
N_2						3.2850×10^6	1.9370×10^4	1.0705

Table 4.2 Values of physical parameters for solubility–thickness empirical equation (Eq. (4.2)).

Gas	Parameter of revised solubility–thickness model								
	b_0 (ps)	T_0 (K)	τ_0 (ps)	φ	$\frac{f_P(T)}{g_T(P)}\frac{1}{S_\infty}$	$k_{Di,0}$ (cm^3STP/cm^3 atm)	ΔH_k (J/mol)	$b_{i,0}$ (atm^{-1})	ΔH_b (J/mol)
O_2	5760	209	70	2.32	11	6.7431×10^{-6}	2.5496×10^{4}	1.2845×10^{-3}	7.1175×10^{3}
N_2						9.8052×10^{-5}	1.4143×10^{4}	3.5457×10^{-4}	1.0587×10^{4}

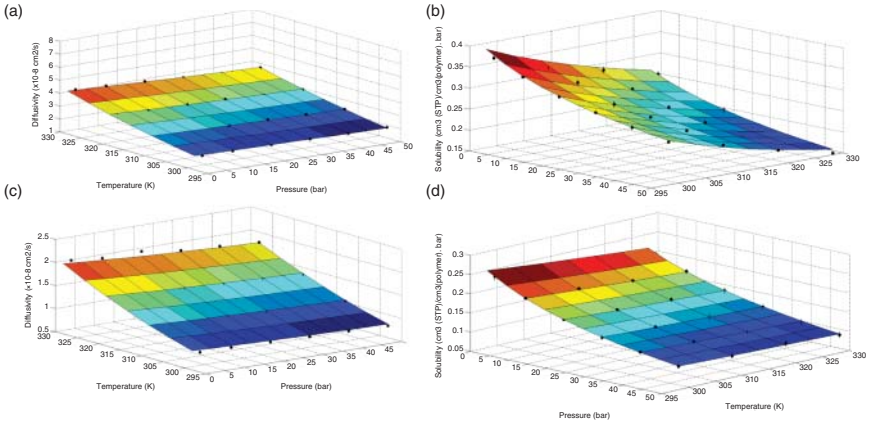

Figure 4.8 Gas transport properties of ~500 Å ultrathin PSF films under varying operating temperature and pressure for (a) oxygen diffusivity ($R^2 = 0.9961$), (b) oxygen solubility ($R^2 = 0.9905$), (c) nitrogen diffusivity ($R^2 = 0.9978$), and (d) nitrogen solubility ($R^2 = 0.9852$) under mixed gas condition. Surface plot characterizes empirical equations (4.1) and (4.2) with fitted parameters in Tables 4.1 and 4.2.

It is found that the empirical equations are able to provide good characterization for the solubility and diffusivity under mixed gas condition with high coefficient of determination ($R^2 = 0.99$), which reaffirms their applicability using the physical parameters and Eq. (4.3).

Based upon the mixed gas physical properties summarized in Tables 4.1 and 4.2 and Eq. (4.3), the effect of membrane thickness toward mixed gas permeance at varying operating pressure and temperature has been elucidated in Figures 4.9 and 4.10 for O_2 and N_2, respectively. Gas permeance of the faster permeating components (O_2) is found to be consistently higher than their lower counterparts (N_2). The observation is in accordance with observation in published literature that elucidated gas permeability of mixtures in PSF membranes [49]. The greater permeability of O_2 as compared with N_2 can be deduced through smaller kinetic diameter that reduces the resistance for transport of gas molecule. The explanation has been supported in Figure 4.11 whereby sorption sites and density distribution of air mixture within PSF polymeric membrane have been illustrated. It is apparent in Figure 4.11 that although similar sorption sites are involved in

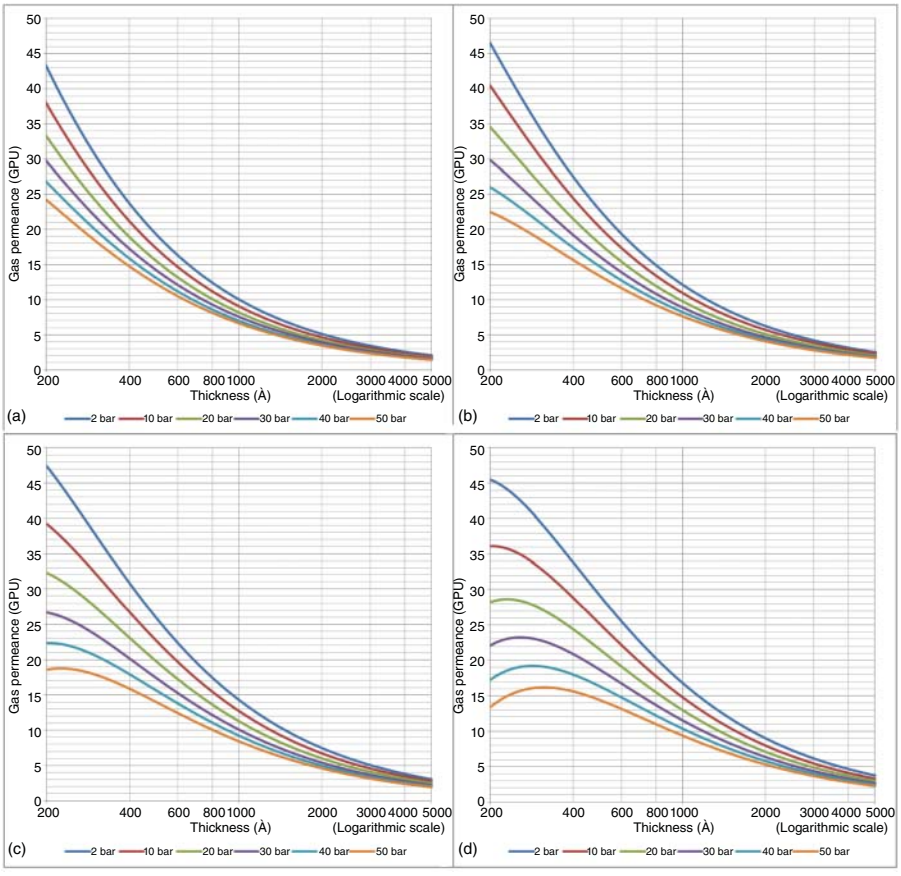

Figure 4.9 Effect of thickness upon confinement toward O_2 permeance (mixed gas) under varying operating pressures of (a) 25 °C, (b) 35 °C, (c) 45 °C, and (d) 55 °C.

the process of absorption for O_2 and N_2 sorbates, the saturation of O_2 in a particular location is found to be consistently higher than N_2, which demonstrates the higher transport affinity of O_2. The mixed gas permeances are found to exhibit decrement in sorption sites with decrement in film thickness, decrement in sorption sites with increment in operating temperature, and decrement in sorption sites with increment in operating pressure. The trend of effect of thickness and operating parameters toward number and density distribution of sorption sites is similarly depicted in Figure 4.11.

4.4.2 Simulation of Mathematical Model Interfaced in Aspen HYSYS for Mass and Heat Balance (Mesoscale)

Macroscopic separation performance, which includes stage cut, permeate composition, and temperature drop, has been elucidated. This section involves using ideal model that ignores confinement and non-ideal simulation model developed in Eq. (4.3) coupled with mathematical model outlined in Section

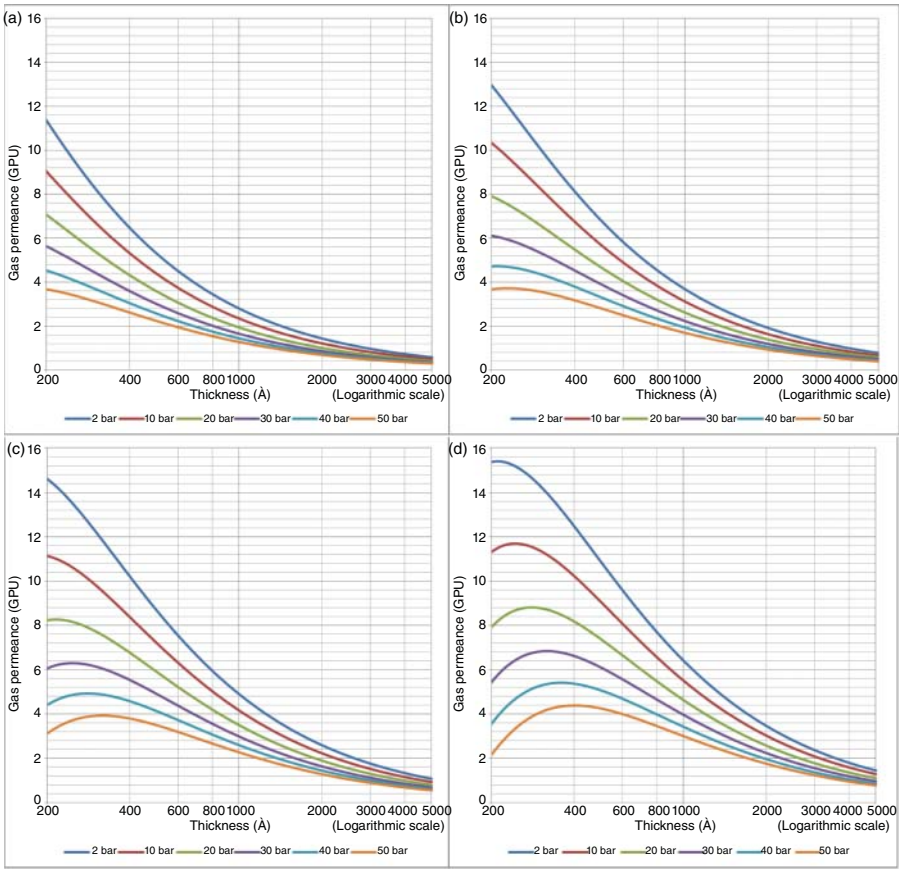

Figure 4.10 Effect of thickness upon confinement toward N_2 permeance (mixed gas) under varying operating pressures of (a) 25 °C, (b) 35 °C, (c) 45 °C, and (d) 55 °C.

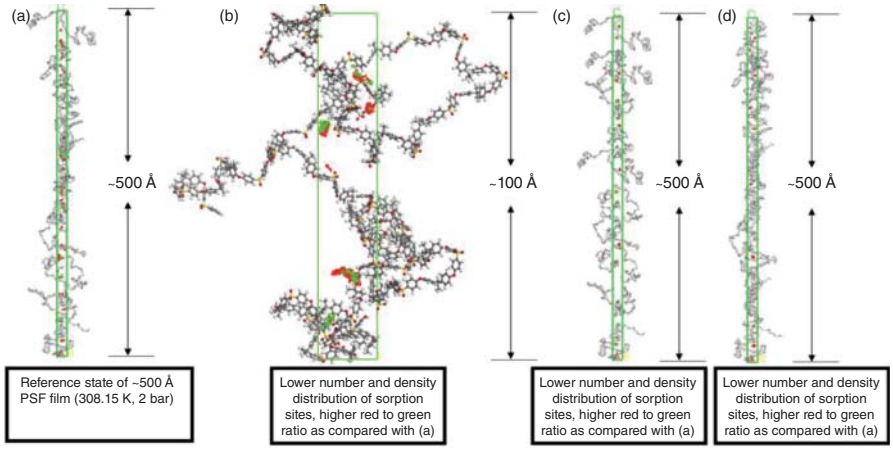

Figure 4.11 Sorption sites and density distribution, shown in red and green color for oxygen and nitrogen, respectively, in (a) ~500 Å PSF film (308.15 K, 2 bar), (b) ~100 Å PSF film (308.15 K, 2 bar), (c) ~500 Å PSF film (328.15 K, 2 bar), and (d) ~500 Å PSF film (308.15 K, 50 bar).

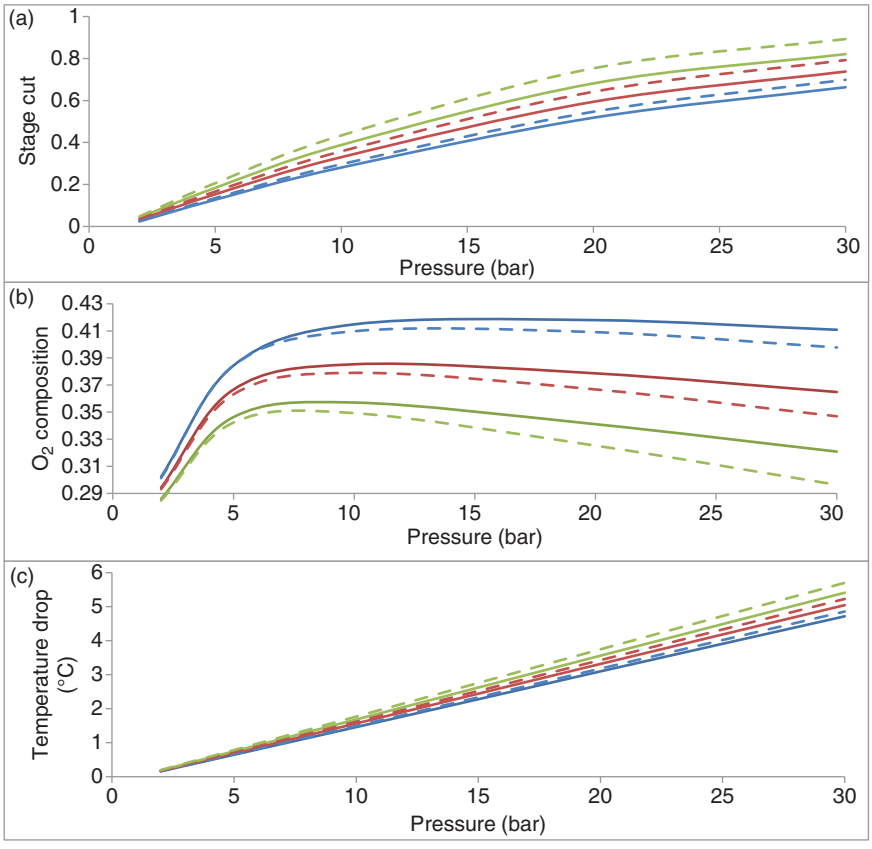

Figure 4.12 Prediction of macroscopic membrane separation performance, which includes (a) stage cut, (b) O_2 permeate composition, and (c) temperature drop across the membrane (35 °C – non-ideal 35 °C – ideal 45 °C – non-ideal 45 °C – ideal 55 °C – non-ideal 55 °C – ideal).

4.3.2. The results are summarized in Figure 4.12. It is found that under all circumstances, stage cut increases with operating pressure due to higher driving force for permeation. In addition, stage cut of membrane operated under higher operating temperature is also greater attributed to higher activation energy to form polymeric membrane matrix with more void spaces that promote the permeance of gas molecules. Stage cut predicted from ideal model is consistently higher than its counterpart under non-ideal condition typically under higher operating pressure and temperature, which has been rationalized through pronounced densification and confinement under such conditions, further reducing the free channels for gas permeation.

As for the effect of operating pressure to oxygen permeate concentration, it is found to be increasing gradually until a certain concentration before experiencing a decrement when pressure is further increased. The increment at lower operating pressure has been rationalized through higher driving force

for permeation of oxygen into the permeate stream. Nonetheless, attributed to the considerably low concentration of oxygen in air mixture, the permeable oxygen has depleted at the retentate side when operating pressure is further increased. Thereby, the increased driving force contributes to permeation of nitrogen existing in abundant to the permeate end, causing a decrement in oxygen concentration in a whole with increment in operating pressure. It is also seen that oxygen permeate concentration predicted from the non-ideal simulation model is consistently higher than that of the ideal model, which is more apparent under condition of higher operating temperature and pressure. The observation can be explained through consideration of confinement in an ultrathin polymeric film under condition of greater operating temperature and pressure, which has been taken into account within the non-ideal simulation model, further constituting to polymeric membrane films with smaller void spaces and hence higher sieving capability. Viewing from the aspect of effect of feed pressure toward temperature drop across the membrane, it is depicted to be increasing attributed to the larger Joule–Thomson effect when feed gas undergoes more prominent impact of adiabatic expansion through the membrane. The temperature drop increases with operating temperature since there is more permeation across the membrane under such circumstance. In a similar manner to stage cut behavior, temperature drop predicted by the ideal model is consistently higher than its counterpart under non-ideal condition. The observation can be rationalized through higher permeance under the ideal model that further constitutes to more cooling effect.

4.4.3 Design of Oxygen-Enriched Combustion Using Ultrathin PSF Membranes

The performance of the ultrathin polymeric membrane under varying operating conditions has been evaluated with respect to their separation efficiency and process economics.

4.4.3.1 Membrane Area Requirement

Figure 4.13 depicts the effect of operating temperature and pressure to membrane area requirement in order to achieve a recovery of 90% O_2 in the product stream for membrane at the smallest membrane specification of 200 Å for ideal simulation model. The 200 Å specification has been chosen as benchmark since it has been reported to be the most commonly defect free and thinnest thickness for ultrathin membrane, which has been adapted in commercial application [50].

The membrane area requirement has been employed as basis for other specification at higher membrane thickness as well as non-ideal simulation model to determine the effect of thickness upon confinement toward separation performance and process economics. Intuitively, the membrane area requirement decreases with increment in operating pressure, which can be explained through higher driving force that promotes permeation of more oxygen to achieve the designated recovery. In addition, the membrane area requirement is also smaller for ultrathin membrane operated at higher operating temperature, which has been

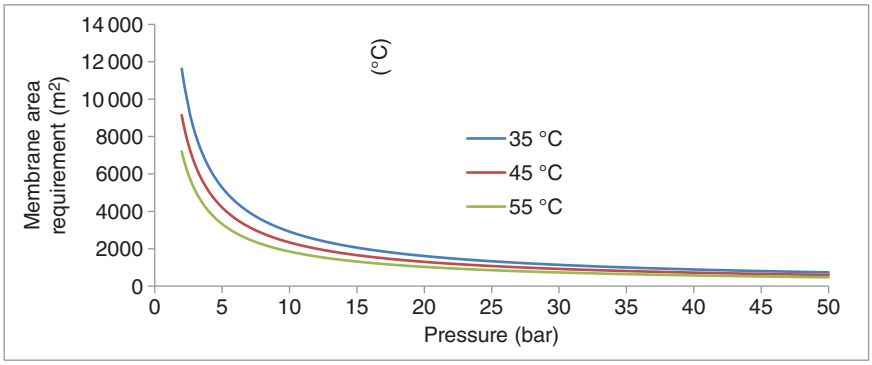

Figure 4.13 Membrane area requirement to achieve product quality of 90% recovery of oxygen in permeate stream for varying operating temperature and pressure.

attributed to its higher permeance that enables acquirement of 90% oxygen recovery under a smaller membrane area.

Nonetheless, the rate of decrement in membrane area requirement is found to experience a decline with increment in operating pressure. In addition, advancement of operating temperature effect toward reduction in membrane area is found to be typically apparent at lower operating pressure. Thereafter, the difference diminishes at higher operating pressure. The reasoning has been attributed to oxygen existing in minority within the air mixture, which has been depleted when most of the permeable oxygen has been transported through the membrane barrier. This further contributes to least impact to the membrane area requirement when operating pressure is increased.

4.4.3.2 Compressor Power Requirement

The effect of thickness upon confinement to the compressor power requirement has been investigated for the proposed oxygen-enriched combustion plant design under varying operating temperature and pressure, as shown in Figure 4.14.

Firstly, the ideal simulation model that neglects the effect of thickness upon confinement toward gas transport performance in oxygen-enriched combustion plant has been investigated. Viewing from the aspect of membrane thickness effect to stage cut, the latter is shown to be decreasing with the increase in membrane thickness. The membrane's productivity is quantified by its permeance, which is a measure of flux through the membrane, normalized with the membrane thickness and pressure driving force. Such observation can be rationalized as a smaller resistance through the barrier that controls relative rate of transport of various species, which constitutes to larger permeation under the same membrane area. The result supports the general contention of current research work to make the selective membrane layer as thin as possible to improve the transfer of the permeating substance [4]. It is also found that the stage cut is larger for higher operating temperature of 55 °C (Figure 4.14b) in comparison with temperature of 35 °C (Figure 4.14a). The observation has been attributed to higher activation energy that forms membrane structure of higher void channels, which

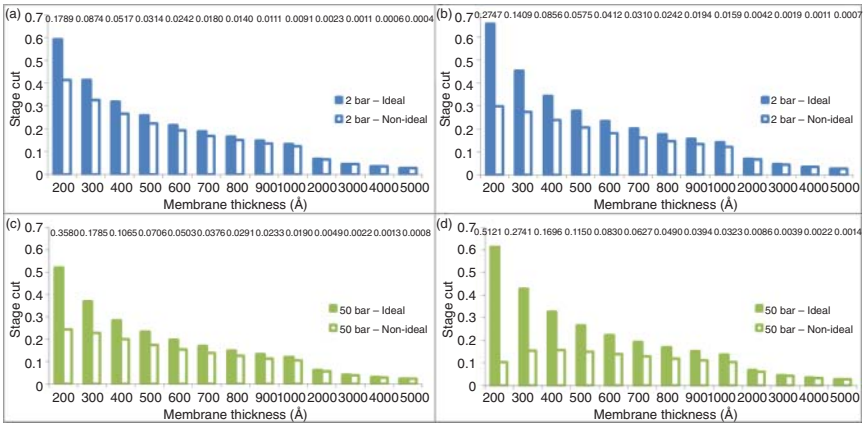

Figure 4.14 Effect of operating conditions to the stage cut of ultrathin polymeric membrane under varying thicknesses operated at (a) 2 bar, 35 °C, (b) 2 bar, 55 °C, (c) 50 bar, 35 °C, and (d) 50 bar, 55 °C.

is also facilitated with higher energetic state for diffusion jump. In addition, viewing from the aspect of operating pressure effect to stage cut (Figure 4.14a,c), it is found to be lower than its counterpart at lower operating pressure.

Similar observation has been demonstrated at higher operating temperature with pressure of 50 bar (Figure 4.14d) as compared with performance at operating pressure of 2 bar (Figure 4.14b). The behavior can be rationalized through higher driving force that commits a lower membrane area requirement, further allowing smaller amount of permeation and stage cut.

Owing to the same analogy that characterizes the effect of membrane thickness upon confinement to stage cut, similar behavior has been noticeable for compressor power requirement since it is directly correlated to the flow rate as shown in Figure 4.15.

The compressor power requirement at higher operating pressure (Figure 4.15c,d) at 50 bar pressure is higher in comparison to its lower operating pressure of 2 bar (Figure 4.15a,b). The behavior is intuitively reasonable due to higher compression power to compress the air mixture from atmospheric condition to higher operating pressure.

Analogously, the non-ideal simulation model that takes into consideration the thickness upon confinement to stage cut and compressor power requirement has been studied and included in Figures 4.14 and 4.15, respectively. It is seen that the stage cut is consistently lower for non-ideal simulation model in comparison to its counterpart that assumes no effect of thickness upon confinement toward membrane morphology and hence gas transport properties. In addition, the difference between stage cut and compressor power requirement predicted between the ideal and non-ideal models has been provided alongside in Figures 4.14 and 4.15. It is observed that the deviation between ideal and non-ideal simulation conditions is exemplified with decrement in membrane thickness. The observation can be explained through enhanced confinement attributed to more drastic loss of free volume to the film free surface, which has been rationalized through shorter

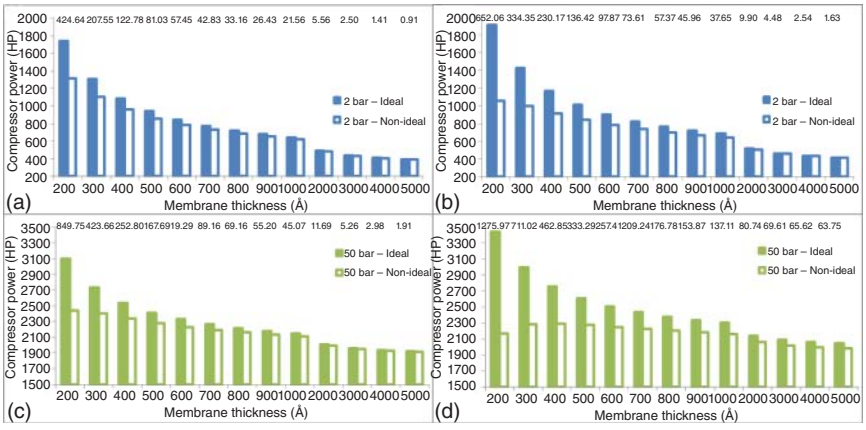

Figure 4.15 Effect of operating conditions to the compressor power of ultrathin polymeric membrane under varying thicknesses operated at (a) 2 bar, 35 °C, (b) 2 bar, 55 °C, (c) 50 bar, 35 °C, and (d) 50 bar, 55 °C.

distance traveled between membrane matrix and surface. The more prominent deviation from bulk polymer with decrement in membrane thickness has contributed to larger prediction discrepancy between the ideal and non-ideal simulation conditions.

4.4.3.3 Turbine Power Requirement

This section describes the effect of thickness upon confinement to oxygen recovery in Figure 4.16 for oxygen-enriched combustion through employment of polymeric membrane films under various operating conditions. Oxygen recovery quantifies the amount of heat that is generated from oxygen-enriched combustion that consequently results in production of power through turbine work.

Similarly, oxygen recovery for ideal simulation model that disregards the effect of thickness upon confinement has been evaluated. It is seen that the oxygen recovery in the permeate stream reduces when the active film thickness is increased attributed to the increment in pathway for transport that reduces the gas permeance substantially, and hence smaller amount of recovered product under a same membrane area requirement. With regard to the operating temperature, product recovery is depicted to be lower for higher operating temperature of 55 °C (Figure 4.16b) as compared with 35 °C (Figure 4.16a). The observation can be explained through higher activation energy that promotes gas permeance for not only oxygen but also nitrogen that exists abundantly in the air feed stream. Thereby, more nitrogen is also permitted to pass through the polymeric membrane, further reducing recovery of oxygen in the permeate stream. Additionally, the effect of operating pressure of 50 bar as shown in Figure 4.16c in comparison with 2 bar as shown in Figure 4.16a has been investigated. It is found that increment in operating pressure contributes to reduction in product lost, which has been attributed to smaller membrane area requirement to achieve 90% oxygen recovery for the reference state. Same behavior has been reported

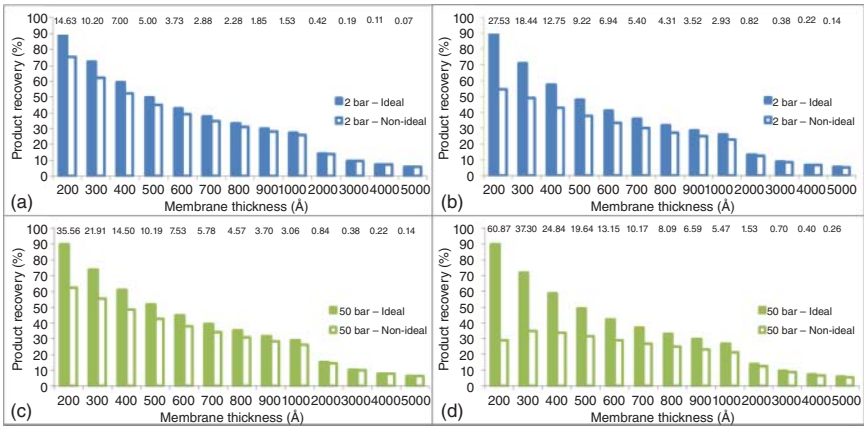

Figure 4.16 Effect of operating conditions to the product recovery of ultrathin polymeric membrane under varying thicknesses operated at (a) 2 bar, 35 °C, (b) 2 bar, 55 °C, (c) 50 bar, 35 °C, and (d) 50 bar, 55 °C.

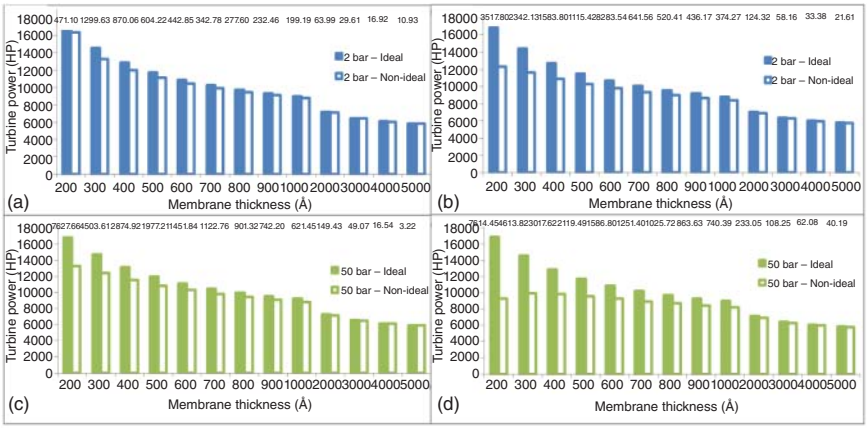

Figure 4.17 Effect of operating conditions to the turbine power of ultrathin polymeric membrane under varying thicknesses operated at (a) 2 bar, 35 °C, (b) 2 bar, 55 °C, (c) 50 bar, 35 °C, and (d) 50 bar, 55 °C.

for polymeric membrane operated at higher operating temperature of 50 bar (Figure 4.16d) in comparison with that at 2 bar (Figure 4.16b), owing to the same analogy of smaller membrane area provided.

The effect of turbine power generation has been provided in Figure 4.17.

With regard to the effect of thickness, operating temperature, and pressure to turbine power generation predicted by the ideal simulation model, it is shown to be a direct consequence of the amount of recovered oxygen. The observation has been rationalized through higher amount of oxygen that contributes to efficient combustion in the reactor, further constituting to higher heat recovery and ultimately the power generated by turbine as end product.

The non-ideal simulation model with consideration of confinement highlighted in current study is shown in the unfilled bars (Figures 4.16 and 4.17). From these figures, it is demonstrated that the product recovery from the non-ideal model is consistently lower than the prediction by ideal simulation model. Smaller prediction by the non-ideal simulation model has been attributed to densification upon confinement that contributes to smaller permeance of oxygen to the product stream. With respect to product recovery and turbine power generation (Figures 4.16 and 4.17), the deviation between ideal and non-ideal simulation models is found to be more apparent in decrement of thickness of active skin layer. At smaller thickness, the confinement is more prominent, which further refines the free channel for permeation and hence a more exemplified depression in product recovery.

When comparing the product recovery operated at 35 °C (Figure 4.16a) and 55 °C (Figure 4.16b), respectively, it is higher at lower operating temperature due to the higher sieving capability of the membrane when void spaces that form pathway for transport decreases. In the contrary, at higher operating temperature, the selectivity reduces due to increment in empty channels that allow permeation of oxygen and nitrogen. Since nitrogen is the species available in abundant within the feed stream, the enhancement of membrane permeance at higher operating temperature and reduction in selectivity of O_2/N_2 promotes transport of nitrogen, further leading to less oxygen recovery when temperature is increased. In addition, difference between the product recovery predicted by the non-ideal and ideal simulation models is consistently higher with increment of operating temperature at all membrane thickness. The observation can be rationalized through the exemplification of impact of membrane selectivity, which is not captured by the ideal simulation model, further promoting prediction significance between the two simulation models.

As for the effect of operating pressure to the product recovery at 2 bar (Figure 4.16a) and 50 bar (Figure 4.16c) for non-ideal simulation model operated at 35 °C, product recovery is lower at higher operating pressure. This has been attributed to the smaller membrane area that enables lower permeation of recovered oxygen at membrane thickness < 1000 Å. The depression in recovery decreases until the product recovery at higher operating pressure of 50 bar is greater than its counterpart at 2 bar when film thickness exceeds that of 1000 Å. The observation has been rationalized through enhanced densification at higher operating pressure that confines the permeance of major component in the feed stream, which is nitrogen, further contributing to greater oxygen recovery. Viewing from the aspect of effect of operating pressure, i.e. 2 bar (Figure 4.16b) and 50 bar (Figure 4.16d) at 55 °C, it is found that the product recovery is consistently lower at higher operating pressure. This has been attributed to the fact that at higher operating temperature, the sieving capacity of polymeric membrane by allowing transport of more permeable oxygen to permeate and retaining the less permeable nitrogen in the retentate stream has been largely reduced. The reduction is pronounced to the extent that compression at higher pressure to increase the membrane selectivity has not been able to counterfeit the implication from operating temperature. Consistently, at all active film thickness, the deviation between ideal and non-ideal simulation models is

consistently greater for higher operating pressure, which has been observed typically at lower film thickness. The behavior has been rationalized through higher reduction in permeance when free volume for permeation decreases at higher compaction. The decrement in permeance is found to be drastically observed at membrane thickness of 200 Å until effect of confinement surpasses the reduction in transport resistance, further constituting to a behavior of increment in product recovery with membrane thickness beneath 200 Å before continuing on the normal trajectory of decline in recovery when membrane thickness increases.

With respect to the effect of turbine power generation to the non-ideal simulation model as shown in Figure 4.17, it is projected to exhibit the same behavior as the ideal model, whereby an increment in oxygen recovery contributes to an overall increment in turbine power generation. The observation is intuitively reasonable since a higher oxygen recovery entails higher combustion efficiency and finally a larger power generation in a whole. It is found that turbine power is not much affected by the operating conditions of the permeate stream being fed into the combustion factor. In this context, the amount of oxygen is found to be the dominating factor.

4.4.3.4 Economic Parameter

This section describes the IRR that has been computed on a basis of four years for oxygen-enriched combustion employing varying ultrathin membrane thicknesses and operating conditions. The IRR is used since it is a common metric used in capital budgeting that can provide a straightforward estimate of profitability of potential investments. The effect of membrane thickness to the IRR for both ideal and non-ideal simulation conditions have been elucidated and tabulated in Figure 4.18. Figure 4.18 shows that for ideal simulation model, the IRR experiences a decreasing fashion when the polymeric membrane thickness is increased.

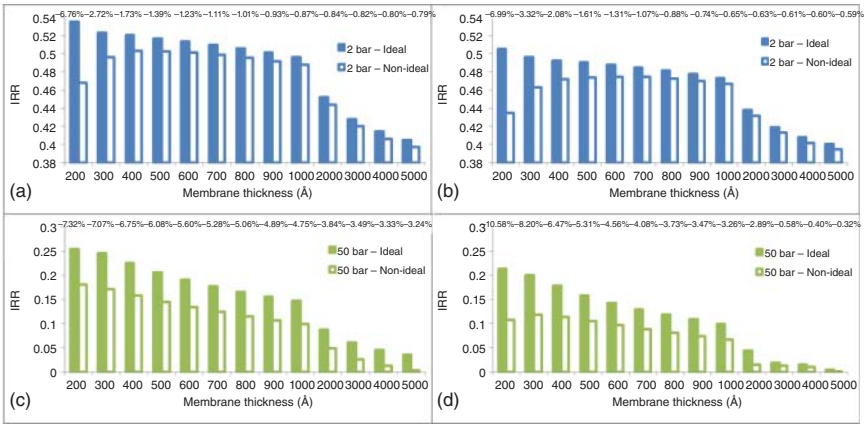

Figure 4.18 Effect of operating conditions to the IRR of ultrathin polymeric membrane under varying thicknesses operated at (a) 2 bar, 35 °C, (b) 2 bar, 55 °C, (c) 50 bar, 35 °C, and (d) 50 bar, 55 °C.

Investment with the highest IRR value is usually preferable in industrial application since it resembles a greater profitability and attractiveness of the business. Therefore, it is found that thinner polymeric membrane generally inherits advantages in terms of operability and economic prospect by demonstrating the higher IRR as compared with its thicker counterpart. The higher IRR has been attributed to higher product recovery, which can be rationalized through increasing permeance of O_2 that enhances the turbine generation despite an increment in compressor power requirement to maintain operability of the plant. When operating temperature is increased (Figure 4.18a,b), it is found that the IRR decreases due to the higher utility cost to heat the feed to higher temperature. The polymeric membrane at higher operating temperature inherits higher activation energy for diffusion jump, which reduces the membrane area requirement to achieve the product recovery. Nonetheless, the sieving capability, which is the ability to allow permeation of oxygen gas while withholding the transport of nitrogen that provided no heating advantages in the permeate stream, reduces simultaneously at higher operating temperature. This condition circumvented the advantage of smaller membrane area that reduces capital cost of the oxygen-enrichment combustion plant. With respect to the effect of operating pressure, it is found that the IRR reduces at higher operating pressure. Despite the advantage of higher driving force when polymeric membrane is operated at higher operating pressure that reduces the membrane area requirement, the low concentration of oxygen of merely 21% in air feed mixture constitutes to redundant compressor to power requirement maintain operability of the combustion plant that allows merely smaller improvement in oxygen recovery.

From Figure 4.18, it is found that the IRR predicted by non-ideal simulation model is consistently lower in comparison with its ideal counterpart. The condition has been attributed to the lower recovery in oxygen that leads to reduced turbine power generation and hence profitability of the plant in a whole. It is found that depression in IRR predicted by the non-ideal simulation model is typically perceptible under lower film thickness when confinement is most apparent, whereby the deviation between the ideal and non-ideal simulation models gradually decreases when thickness is increased. Unlike the ideal simulation model that has observed constant decrement of IRR with increment in film thickness, the non-ideal simulation model predicted increment in IRR followed by decrement when film thickness is increased further at lower operating pressure (Figure 4.18a,b). The behavior has been attributed to densification that reduces the gas permeability of oxygen for sufficient plant profitability but higher stage cut that constitute to higher compressor power requirement at the same time. At higher film thickness, the reduction in oxygen gas transport is too substantial until the IRR decreases as a whole. At operating temperature of 35 °C (Figure 4.18a), the optimum membrane thickness that optimizes IRR is ~400 Å, while at operating temperature of 55 °C (Figure 4.18b), the membrane thickness with the highest IRR is observed at ~600 Å. The findings of present study reckons with effort of current research. It has been reported that key to the extensive application of membrane system in industry is polymeric layer with superior performance has been fabricated in the magnitude of ultrathin size upon nanoscale dimension. Simultaneously, there are continuous effects to

make the selective membrane area as thin as possible [51]. Nonetheless, it is also found from present study that the film thickness has to be optimized at varying operating conditions since the general contention of thinnest ultrathin polymeric membrane structure is not necessarily the most profitable option. At higher operating pressure of 50 bar (Figure 4.18c,d), the non-ideal simulation demonstrates a remarkable decline in IRR with increment in active film thickness. This has been rationalized to enhanced depression in oxygen permeance at higher operating pressure that subsequently reduces feasibility of the plant typically at higher film thickness. Under 50 bar pressure, the optimum film thicknesses that optimize IRR at 35 and 55 °C are at ~200 and ~300 Å, respectively. The optimum IRR at 300 Å for film thickness operated at 50 bars and 35 °C has been attributed to enhanced densification that reduces gas permeability that offsets the advantage of reduced transport resistance at thickness < 300 Å.

With regard to the effect of operating temperature, the deviation between non-ideal and ideal simulation models is more apparent at higher operating temperature in thinner film. The observation has been proclaimed via higher void channels that further reduces the membrane selectivity at higher operating temperature. The reduction in membrane selectivity contributes to lower oxygen/nitrogen ratio in the product stream, whereby oxygen is the required element for optimum combustion efficiency, while the nitrogen carries no heating value and favors merely the undesired side reaction. At higher film thickness, the difference between non-ideal and ideal simulation models levels off faster attributed to large void spaces that contribute to less impact toward the critical size of oxygen and nitrogen by allowing permeation of oxygen and detention of nitrogen. Viewing from the aspect of operating pressure, it is seen that the depression observed in non-ideal simulation model is more noticeable at higher operating pressure, which has been assigned to compaction effect at higher pressure that further increases the difference between non-ideal and ideal models. The IRR operated at higher operating pressure is found to exhibit lower value at higher operating pressure due to higher maintenance cost to operate the plant with higher compressor power requirement.

4.5 Conclusion

The performance of ultrathin polymeric membrane in industrial scale oxygen-enriched combustion has been evaluated with the consideration of separation performance and process economics using a multiscale simulation approach. The design sensitivity has been investigated by altering the active film thickness, operating temperature and operating pressure, which results in different gas permeance as well as membrane selectivity and hence varying outputs. It is found that generally a thinner polymeric membrane structure constitutes to lower resistance in gas permeation across the membrane under a same membrane area requirement, which ultimately causes greater oxygen recovery for turbine generation at the expense of larger compressor power requirement to sustain operability of the plant with higher flow rate. With increment in operating temperature, although a smaller membrane area is

required to achieve the designated product recovery that reduces capital cost, the reduction in membrane selectivity reduces the ratio of oxygen over nitrogen in the product stream. The condition contributes to higher stage cut when membrane permeance is increased at higher operating temperature that increases the load of compressor power, but not sufficient profitability from combustion of oxygen to counterfeit the maintenance cost since amount of nitrogen that carries no heating value also increases in the product stream. With respect to operating pressure, despite lower membrane area requirement due to the higher driving force for permeation, the low concentration of oxygen of merely 21% in air feed mixture constitutes to redundant compressor power to operate the oxygen combustion plant, which permits merely small improvement in oxygen recovery when operating pressure is increased. The difference between prediction of non-ideal and ideal simulation models is found to be typically substantial under condition of lower membrane thickness and higher operating temperature and operating pressure. The percentage deviation can reach as high as ~10% in IRR prediction, which urges the need to incorporate the thickness upon confinement to enhance accuracy of simulation model for ultrathin membrane applied in industrial scale application. In addition, it is also found that the general contention of fabricating ultrathin polymeric membrane with thinnest possible active layer, as well as increasing the operating pressure and operating temperature of the membrane in order to reduce transport resistance, to promote driving force and to enhance activation energy for greater gas transport is not always the most economical. The thinner film experiences enhanced densification till the extent of not sufficient profitability to overcome the liability in compressor power, further reducing its economic prospect in comparison with the thicker counterpart. In addition, in contrary to other gas separation applications that requires operation at higher operating temperature and pressure to increase the flux across the membrane due to high impurities content, oxygen-enriched combustion favors operation at lower operating temperature to enhance membrane selectivity and lower operating pressure to minimize redundant load to compressor power. Therefore, a trade-off must be determined among these parameters. In this study, the optimum condition for optimization of process economics of ultrathin PSF polymeric film applied in oxygen-enriched combustion is at ~400 Å, 35 °C, and 2 bar.

Acknowledgment

This work is done with the financial support from Murata Science Foundation (Grant No. 18 MP04).

References

1 Habib, M.A., Nemitallah, M.A., Afaneh, D., and Mezghani, K. (2017). Characteristic of air separation in hollow-fiber polymeric membrane for oxygen enriched air clean combustion applications. *Journal of Cleaner Production* 143: 960–972.

2 Lin, H., Zhou, M., Ly, J. et al. (2013). Membrane-based oxygen-enriched combustion. *Industrial and Engineering Chemistry Research* 52 (31): 10820–10834.
3 Baker, R.W. (2002). Future directions of membrane gas separation technology. *Industrial and Engineering Chemistry Research* 41 (6): 1393–1411.
4 Khulbe, K.C., Feng, C.Y., and Matsuura, T. (eds.) (2007). Synthetic membranes for membrane processes. In: *Synthetic Polymeric Membranes: Characterization by Atomic Force Microscopy*, 5–14. Leipzig, Germany: Springer-Verlag Berlin Heidelberg.
5 Singh, L., Ludovice, P.J., and Henderson, C.L. (2004). Influence of molecular weight and film thickness on the glass transition temperature and coefficient of thermal expansion of supported ultrathin polymer films. *Thin Solid Films* 449 (1–2): 231–241.
6 Forrest, J.A., Dalnoki-Veress, K., and Dutcher, J.R. (1997). Interface and chain confinement effects on the glass transition temperature of thin polymer films. *Physical Review E* 56 (5): 5705–5716.
7 Rowe, B.W., Freeman, B.D., and Paul, D.R. (2009). Physical aging of ultrathin glassy polymer films tracked by gas permeability. *Polymer* 50 (23): 5565–5575.
8 Ismail, A.F. and Yean, L.P. (2003). Review on the development of defect-free and ultrathin-skinned asymmetric membranes for gas separation through manipulation of phase inversion and rheological factors. *Journal of Applied Polymer Science* 88 (2): 442–451.
9 Wang, D., Wang, Z., Wang, L. et al. (2015). Ultrathin membranes of single-layered MoS_2 nanosheets for high-permeance hydrogen separation. *Nanoscale* 7 (42): 17649–17652. https://doi.org/10.1039/C5NR06321C.
10 Horn, N.R. and Paul, D.R. (2011). Carbon dioxide plasticization of thin glassy polymer films. *Polymer* 52 (24): 5587–5594.
11 Costello, L.M. and Koros, W.J. (1992). Temperature dependence of gas sorption and transport properties in polymers: measurement and applications. *Industrial and Engineering Chemistry Research* 31 (12): 2708–2714.
12 He, X., Nieto, D.R., Lindbråthen, A., and Hägg, M. (2017). Membrane system design for CO_2 capture: from molecular modeling to process simulation. In: *Process Systems and Materials for CO_2 Capture: Modelling, Design, Control and Integration* (eds. A.I. Papadopoulos and P. Seferlis), 249–276. Wiley.
13 Mottet, C. (2011). Relaxations on the nanoscale: an atomistic view by numerical simulations. In: *Mechanical Stress on the Nanoscale: Simulation, Material Systems and Characterization Techniques* (eds. M. Hanbücken, P. Müller and R.B. Wehrspohn), 83–106. Wiley-VCH Verlag GmbH & Co. KGaA.
14 Modi, N., Winterhalter, M., and Kleinekathofer, U. (2012). Computational modeling of ion transport through nanopores. *Nanoscale* 4 (20): 6166–6180. https://doi.org/10.1039/C2NR31024D.
15 Lu, R., Meng, Z., Rao, D. et al. (2014). A promising monolayer membrane for oxygen separation from harmful gases: nitrogen-substituted polyphenylene. *Nanoscale* 6 (17): 9960–9964. https://doi.org/10.1039/C4NR02315C.
16 Forrest, J.A., Dalnoki-Veress, K., Stevens, J.R., and Dutcher, J.R. (1996). Effect of free surfaces on the glass transition temperature of thin polymer films. *Physical Review Letters* 77 (10): 2002–2005.

17 Liu, H., Li, Y., Krause, W.E. et al. (2012). The soft-confined method for creating molecular models of amorphous polymer surfaces. *The Journal of Physical Chemistry B* 116 (5): 1570–1578.

18 Wu, H. and Xin, Y. (2017). Molecular dynamics simulation of gas diffusion behavior in polyethylene terephthalate/aluminium/polyethylene interface. *Composite Interfaces* 24 (9): 915–926.

19 Glotzer, S.C. and Paul, W. (2002). Molecular and mesoscale simulation methods for polymer materials. *Annual Review of Materials Research* 32 (1): 401–436.

20 Frentrup, H., Hart, K.E., Colina, C.M., and Müller, E.A. (2015). In silico determination of gas permeabilities by non-equilibrium molecular dynamics: CO_2 and He through PIM-1. *Membranes* 5 (1): 99–119.

21 Ozcan, A., Perego, C., Salvalaglio, M. et al. (2017). Concentration gradient driven molecular dynamics: a new method for simulations of membrane permeation and separation. *Chemical Science* 8 (5): 3858–3865. https://doi.org/10.1039/C6SC04978H.

22 Neyertz, S., Douanne, A., and Brown, D. (2005). Effect of interfacial structure on permeation properties of glassy polymers. *Macromolecules* 38 (24): 10286–10298.

23 Neyertz, S., Douanne, A., and Brown, D. (2006). A molecular dynamics simulation study of surface effects on gas permeation in free-standing polyimide membranes. *Journal of Membrane Science* 280 (1–2): 517–529.

24 Girdauskaite, L., Haasemann, G., and Krzywinski, S. (2016). Modeling and simulation. In: *Textile Materials for Lightweight Constructions: Technologies – Methods – Materials – Properties* (ed. C. Cherif), 537–598. Berlin, Heidelberg: Springer Berlin Heidelberg.

25 Safari, M., Ghanizadeh, A., and Montazer-Rahmati, M.M. (2009). Optimization of membrane-based CO_2-removal from natural gas using simple models considering both pressure and temperature effects. *International Journal of Greenhouse Gas Control* 3 (1): 3–10.

26 Huang, Y. and Paul, D.R. (2005). Effect of temperature on physical aging of thin glassy polymer films. *Macromolecules* 38 (24): 10148–10154.

27 Scholz, M., Harlacher, T., Melin, T., and Wessling, M. (2013). Modeling gas permeation by linking nonideal effects. *Industrial and Engineering Chemistry Research* 52 (3): 1079–1088.

28 Hosseini, S.S., Dehkordi, J.A., and Kundu, P.K. (2016, 33). Gas permeation and separation in asymmetric hollow fiber membrane permeators: mathematical modeling, sensitivity analysis and optimization. *Korean Journal of Chemical Engineering* (11): 3085–3101.

29 Marriott, J. and Sørensen, E. (2003). A general approach to modelling membrane modules. *Chemical Engineering Science* 58 (22): 4975–4990.

30 Hosseini, S.S., Najari, S., Kundu, P.K. et al. (2015). Simulation and sensitivity analysis of transport in asymmetric hollow fiber membrane permeators for air separation. *RSC Advances* 5 (105): 86359–86370. https://doi.org/10.1039/C5RA13943K.

31 Wang, R., Liu, S.L., Lin, T.T., and Chung, T.S. (2002). Characterization of hollow fiber membranes in a permeator using binary gas mixtures. *Chemical Engineering Science* 57 (6): 967–976.

32 Ahmad, F., Lau, K.K., Shariff, A.M., and Yeong, Y.F. (2013). Temperature and pressure dependence of membrane permeance and its effect on process economics of hollow fiber gas separation system. *Journal of Membrane Science* 430: 44–55.

33 Murad Chowdhury, M.H., Feng, X., Douglas, P., and Croiset, E. (2005). A new numerical approach for a detailed multicomponent gas separation membrane model and AspenPlus simulation. *Chemical Engineering Technology* 28 (7): 773–782.

34 Belaissaoui, B., Le Moullec, Y., Hagi, H., and Favre, E. (2014). Energy efficiency of oxygen enriched air production technologies: cryogeny vs membranes. *Seperation and Purification Technology* 125: 142–150.

35 Lock, S.S.M., Lau, K.K., Shariff, A.M. et al. (2017). Computational insights on the role of film thickness on the physical propertes of ultrathin polysulfone membranes. *RSC Advances* 7 (70): 44376–44393.

36 Golzar, K., Amjad-Iranagh, S., Amani, M., and Modarress, H. (2014). Molecular simulation study of penetrant gas transport properties into the pure and nano sized silica particles filled polysulfone membranes. *Journal of Membrane Science* 451: 117–134.

37 Biovia Materials Studio, Materials Studio Overview [Internet]. Available from: http://accelrys.com/products/collaborative-science/biovia-materials-studio (accessed 20 March 2020).

38 Hu, H., Du, L., Xing, Y., and Li, X. (2017). Detailed study on self- and multicomponent diffusion of CO_2-CH_4 gas mixture in coal by molecular simulation. *Fuel* 187: 220–228.

39 Einstein, A. (1949). Autobiographical notes. In: *Albert Einstein: Philosopher Scientist* (ed. P.A. Schilpp), 1–96. Open Court Publishing Company.

40 Fick, A. (1855, 86). Ueber diffusion. *Annalen der Physik* (in German) 94: 59.

41 Metropolis, N., Rosenbluth, A.W., Rosenbluth, M.N. et al. (1953). Equation of state calculations by fast computing machines. *The Journal of Chemical Physics* 21 (6): 1087–1092.

42 Lock, S.S.M., Lau, K.K., Shariff, A.M. et al. (2018). Thickness dependent penetrant gas transport properties and separation performance within ultrathin polysulfone membrane: insights from atomistic molecular simulation. *Journal of Polymer Science Part B Polymer Physics* 56 (2): 131–158.

43 Lock, S.S.M., Lau, K.K., Shariff, A.M., and Yeong, Y.F. (2017). Preliminary techno-economic and environmental assessment of thickness dependent physical aging in oxygen enriched combustion using polymeric membranes. *Journal of Cleaner Production* 162: 914–937.

44 Lock, S.S.M., Lau, K.K., Shariff, A.M., and Yeong, Y.F. (2017). Joule Thomson effect in a two-dimensional multi-component radial crossflow hollow fiber membrane applied for CO_2 capture in natural gas sweetening. In: *Process Systems and Materials for CO_2 Capture* (eds. A.I. Papadopoulos and P. Seferlis), 371–397. John Wiley & Sons, Ltd.

45 Chen, B., Ruan, X., Xiao, W. et al. (2015). Synergy of CO_2 removal and light hydrocarbon recovery from oil-field associated gas by dual-membrane process. *Journal of Natural Gas Science and Engineering* 26: 1254–1263.
46 Belaissaoui, B., Willson, D., and Favre, E. (2012). Membrane gas separations and post-combustion carbon dioxide capture: parametric sensitivity and process integration strategies. *Chemical Engineering Journal* 211–212: 122–132.
47 Brunet, R., Cortés, D., Guillén-Gosálbez, G. et al. (2012). Minimization of the LCA impact of thermodynamic cycles using a combined simulation-optimization approach. *Applied Thermal Engineering* 48: 367–377.
48 Drioli, E. (2006). Gas separation membranes: a potential dominant technology. *Membranes* 31 (2): 95–97.
49 Ettouney, H. and Majeed, U. (1997). Permeability functions for pure and mixture gases in silicone rubber and polysulfone membranes: dependence on pressure and composition. *Journal of Membrane Science* 135 (2): 251–261.
50 Lin, L., Feng, C., Lopez, R., and Coronell, O. (2016). Identifying facile and accurate methods to measure the thickness of the active layers of thin-film composite membranes – a comparison of seven characterization techniques. *Journal of Membrane Science* 498: 167–179.
51 Sanders, D.F., Smith, Z.P., Guo, R. et al. (2013). Energy-efficient polymeric gas separation membranes for a sustainable future: a review. *Polymer* 54 (18): 4729–4761.

5

Process Intensification of Membrane-Based Systems for Water, Energy, and Environment Applications

Nik A. H. M. Nordin[1], Zulfan A. Putra[2], Muhammad R. Bilad[1], Mohd D. H. Wirzal[1], Lila Balasubramaniam[1], Anis S. Ishak[1], and Sawin Kaur Ranjit Singh[1]

[1] *Universiti Teknologi PETRONAS, Chemical Engineering Department, Bandar Seri Iskandar, Perak, 32610, Malaysia*
[2] *PETRONAS Group Technical Solutions (Process Simulation and Optimization), Kuala Lumpur, 50088, Malaysia*

5.1 Introduction

A membrane, in the process separation context, is defined as a "selective barrier between two phases" that enables separation under a driving force, such as pressure, concentration, temperature, etc. Membrane processes are attractive because of several advantages. The separation can be carried out in either batch, semi-batch, or continuous, depending on the objectives, with low energy input. The prime example of established membrane process is reverse osmosis (RO) for seawater desalination that offers much lower energy input than multistage evaporation [1]. The operational conditions are generally mild, principally because of mechanical limitations of module assembly and the limitation of membrane materials that are mostly polymeric, which limits the allowable operating temperature below the melting point of polymer. Membranes are assembled in modules, in rather simple units, which allow easy scale-up, capacity extensions, and hybridizations with other processes via *membrane engineering* [2].

Membrane processes have a much wider spectrum of applications in chemical and bioengineering. It can separate molecules/particles based on their size as in microfiltration (MF) and ultrafiltration (UF) and based on solution–diffusion as in RO and gas separation. It can facilitate chemical reactions as in enzymatic, catalytic, and biological reactors. It can also facilitate mass and energy transfer between different phases as contactor, crystallizer, emulsifier, stripper, scrubber, or diffuser [3]. The role of membranes as a thin interface between two phases makes it very attractive for enhancements of energy and mass transfer in chemical and biochemical operations.

Membrane processes have been widely demonstrated in many applications, including water production, wastewater treatment, energy generation, and the separations and purification of chemicals [4]. Therefore, membrane technologies gain higher recognitions and are competing with other conventional separation technologies in terms of energy efficiency, separation selectivity, and capital investments [3].

Process Intensification and Integration for Sustainable Design, First Edition.
Edited by Dominic C. Y. Foo and Mahmoud M. El-Halwagi.
© 2021 WILEY-VCH GmbH. Published 2021 by WILEY-VCH GmbH.

One of the recent examples of a success story of process intensification involving membrane is membrane bioreactor (MBR) for wastewater treatment [5]. MBR combines the conventional activated sludge process with micro-/ultrafiltration, in which are treated traditionally as two separated units of secondary and tertiary treatments. Process intensification substantially improves the overall process efficiency and effluent quality to a level that the effluents can directly be reused [6]. Under effluent reuse scenarios, the MBR is economically more attractive than the two conventional standalone units. With an increasing number of large-scale ($\geq$10 000 m^3/d) and super-large-scale ($\geq$100 000 m^3/d) plants put into operation, MBR technology is taking a considerable share in the field of wastewater treatment [7]. The technology is increasingly favored especially for effluent reuse purposes. MBRs have been implemented worldwide in more than 200 countries with global market growth rates of about 15% [5].

MBR technologies for wastewater treatment have been developed for over three decades, mainly under the motivation to combine two process units. Throughout these years, MBR has been receiving extensive academic attentions and has achieved rapid growths in worldwide installations. The main highlights of the MBR developments include high effluent quality, small footprint, and improved biological performances [8], whereas a major weakness in the MBR developments resides in energy consumption, mainly to accommodate membrane fouling management [8].

Several review articles are available for discussions on how membrane processes can be included in process intensification [3, 9]. They are mainly in the area of desalination, RO pre- and post-treatment, distillation, bioreactor, etc. Generally, process intensification can be achieved by combining membrane with other units to meet process requirements. For example, MBR combines reaction and separation units. Membrane distillation (MD) has a heat transfer unit, while forward osmosis (FO) and pressure retarded osmosis require draw solution recovery units [10].

This chapter briefly discusses several examples of emerging process intensification techniques involving membrane process. The focus is on the proof of concept for the respective intensification units and how they enhance the overall performance of their respective system. In membrane electrocoagulation flocculation (MECF) system, the process efficiency of a conventional electrocoagulation flocculation (ECF) can be substantially increased by allowing rapid separation of micro-sized flocculants. In another case, membrane has recently been applied as diffuser to create micro-sized air bubbles for enhancing mass transfer of carbon dioxide (CO_2) into water for microalgae growth. Lastly, a case study on the combination of FO and electrolysis for the recovery of draw solution is also presented. For the latter, hydrogen and oxygen are by-products of the feed treatment, while electrolysis enhances the solute concentration in the draw solution. These three examples demonstrate how membranes can be used and reflect their flexibility in process intensification.

5.2 Membrane Electrocoagulation Flocculation for Dye Removal

This section highlights the combination of membrane with conventional ECF to form MECF and demonstrate how process intensification enhances the overall performance (dye removal efficiency), while maintaining energy input. The concept has been proven in lab-scale experiment for the removal of Celestine Blue dye. The systems were tested under certain feed pH and dosing of NaCl [11].

Discharge of dye-containing wastewater creates an esthetically undesirable aqueous environment that affects the penetration of sunlight for photosynthetic and biological activities of aquatic organisms. Some of the dyes are also carcinogenic, mutagenic, and toxic to human and aquatic lives [12]. On top of that, since dyes are aromatic compounds, they are highly stable against lights, oxidants, and biological degradation, which make the treatment process difficult [13].

Currently, there are few established methods for dye removal, i.e. chemical coagulation/flocculation, Fenton reagent, electro-kinetic coagulation, standalone membrane filtration, oxidation processes, and biological treatments [14]. Nonetheless, they have merits and limitations and show superiority under certain circumstances, which open the avenue for process development. For example, chemical processes such as Fenton reagent and electro-kinetic coagulation produce large amount of sludge [15]. Advanced oxidation processes using ultraviolet/hydrogen peroxide (UV/H_2O_2), ozonation, and photo-catalysis have limitations due to toxic by-products [16]. On the other hand, biological treatments are slow as most of the dyes are toxic to the microorganisms, which then inhibit biological degradation [17]. Membrane process, such as nanofiltration and RO, can also be used as a standalone unit to remove dye from wastewater. However, these processes operate at higher pressure and susceptible from membrane fouling and require series of pretreatments before it can be implemented.

Recently, ECF has been identified as an efficient and simple method to treat dye-containing wastewater [18]. It is an electrochemical process that, depending on the design, induces removal mechanisms via coagulation–flocculation, adsorption, and flotation. The electrolytic reaction at the anode surface releases ions that neutralize the charge of particulates in wastewater; the latter initiates the formation of coagulants in the aqueous solution. The electro-generated coagulants can then adsorb the dissolved contaminants [19]. During electrocoagulation, indirect oxidation also occurs by generating oxidants from agents such as chlorine, hydroxide ions, hypochlorite, and hydrogen peroxide, which are usually originated from the electrolytes used [20]. Chlorines can electrochemically degrade the dyes in the solution quickly and the reaction is irreversible due to the strong oxidative activity [21]. However, the main drawback of ECF is its high specific energy consumption, which can be addressed by using MECF. A new combination of ECF and MF to form MECF in treating dye-containing wastewater is next described.

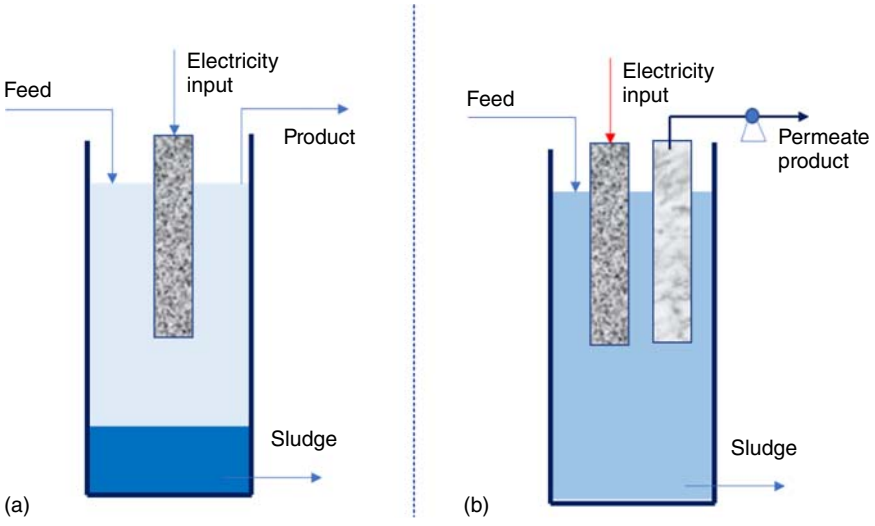

Figure 5.1 Illustration of membrane electrocoagulation flocculation where (a) standalone electrocoagulation flocculation (ECF), and (b) membrane electrocoagulation flocculation (MECF) process.

Figure 5.1 illustrates the schematic of the MECF. ECF is responsible for dye degradation and its flocculation, while membrane is responsible for the removal suspended coagulants. In this combined process, membrane enhances the treatment process by simultaneously separating micro-sized coagulants without having to wait for their settling, as in the standalone ECF.

Figure 5.2 shows the energy consumption and dye removal under different operational parameters in a lab-scale ECF unit [11]. The experiments were done for removal of 10 ppm Celestine Blue set at pH 7 by exploring different electrolyte loadings and electrical inputs of 1 and 2 V. As shown, the energy consumption increases with increasing amount of NaCl added in the dye solution. Figure 5.2 also shows that there is a significant difference in energy consumption, whereby electrical input of 2 V consumes much higher energy than that at 1 V. However, the difference in terms of dye removal rate trend at both voltages is not that significant. Generally, high dye removal is desired under low energy input, which in this case falls under 0.8 g/l of NaCl at 1 V. This condition requires 0.75 kWh/m^3 of energy input and the dye removal efficiency is 43.2%. It is worth noting that the removal efficiency is still rather low, even under optimum condition.

Because of the poor removal efficiency, membrane process is introduced in the system (Figure 5.1b) to improve the dye removal efficiency. As a reference, filtration of dye solution using standalone membrane only removes up to 8% of dye. The removal of dye is mainly due to irreversible adsorption, and under prolonged filtration would offer no rejection. Therefore, combination with ECF to form MECF is necessary to enhance dye removals.

Figure 5.3 shows the performance of MECF for the removal of 10 ppm of Celestine Blue solution at pH of 7 and under different electrolyte (NaCl) loadings. As

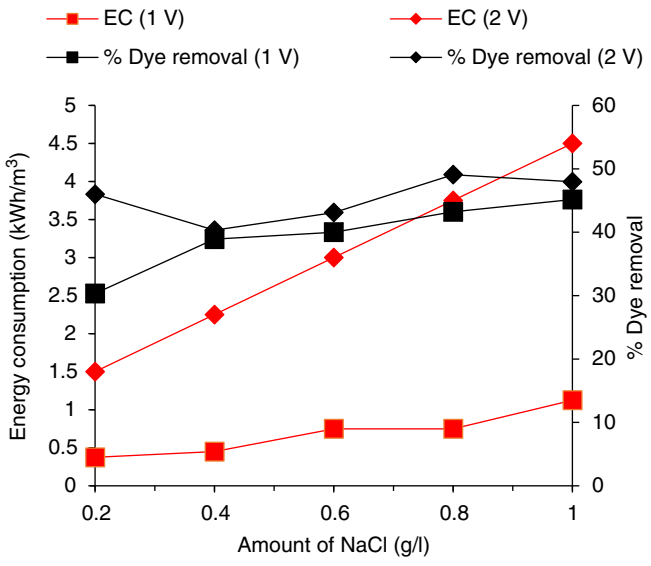

Figure 5.2 Effect of NaCl loading and energy input on dye removal efficiency and energy consumption (EC) of feed containing 10 ppm Celestine Blue at pH 7. Source: From Balasubramaniam 2018 [11].

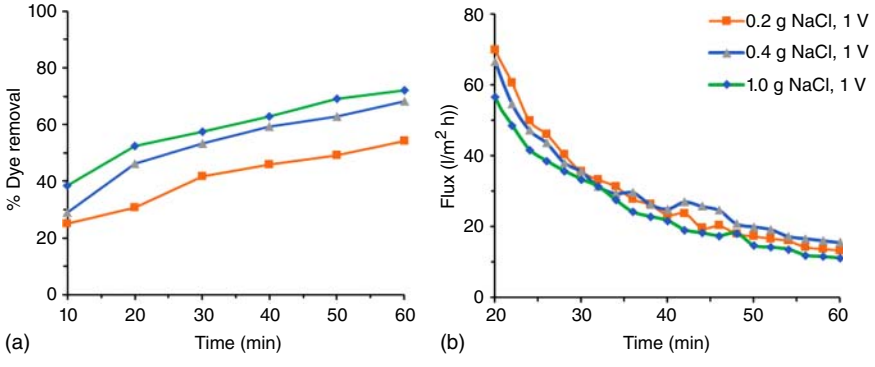

Figure 5.3 Effect of electrocoagulation time on dye removal (a) and flux in MECF system (b). The feed contained 10 ppm of Celestine Blue solution at pH = 7. Source: From Balasubramaniam 2018 [11].

shown in Figure 5.3a, the highest removal efficiency is 72% using 1.0 g of NaCl. The removal efficiency is the highest when the highest amount of NaCl is used, i.e. is 1.0 g/l. This is because higher amount of Cl^- ions in the dye solution increases the rate of anode dissolution, hence producing more metal coagulant in the solution. The highly available anions (Cl^-) can decrease the positive charge of iron ions produced that causes bigger flocs to formed, as compared with the flocs formed when low NaCl is used [22].

Figure 5.3b also shows that the flux drops gradually over time and begin to reach steady state. This clearly indicates that membrane fouling has taken place

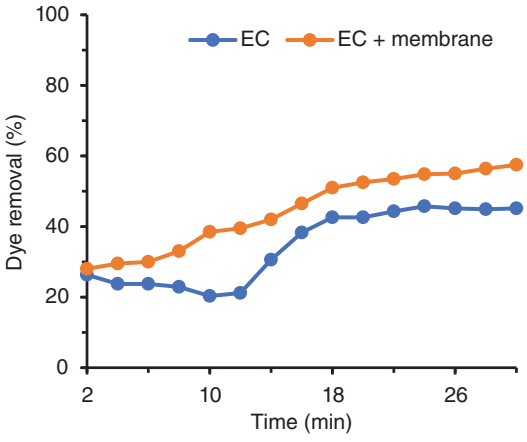

Figure 5.4 Comparison between dye removal efficiency in ECF and MECF using 10 ppm of Celestine Blue solution as feed and at 1.0 g of NaCl at 1 V and at pH 7. Source: From Balasubramaniam 2018 [11].

due to the membrane pore clogging and formation of cake layer. The initial permeate flux was high because there is no flocs in the beginning of ECF [23]. Further decline in flux is due to cake layer accumulation from the flocs generated via electrocoagulation, creating additional resistance to the permeate flow. Membrane fouling is the drawback of MECF and will become the energy consumer factor when overall energy input is assessed.

Figure 5.4 compares dye removal efficiency of ECF and MECF using 1.0 g NaCl at 1 V. It shows that the proficiency of MECF in enhancing dye removal is superior as compared with ECF. The enhanced performance in MECF is due to the simultaneous electrochemical oxidation and adsorption of flocs by electrostatic affinity and physical entrapment [24]. This proves that the dye removal process can be optimized through this hybrid technology. Overall results show the advantage of combining membrane filtration in the MECF system. ECF only achieves 43.2% of dye removal with energy input of 0.75 kWh/m^3. Integrating membrane to ECF improves the dye removal efficiency to 70% without affecting the energy input.

5.3 Carbonation Bioreactor for Microalgae Cultivation

Microalgae cultivation is an emerging application in which it provides mean for carbon dioxide (CO_2) dissolution into the algae growth medium. Algae cultivation-based technology is an environment sustainable approach, which uses direct sunlight for rapid growth. Besides, it also co-produces high value-added biomass-based materials. The CO_2 consumption intensity is reported at 1.83 kg of CO_2/kg biomass produced [25], which makes it essential in the context of CO_2 fixation. Microalgae can double their body mass as rapid as 24 hours of cultivation, with oil content exceeding 50% of their dry weight. This section illustrates a case study in which membrane material is used for a new application (e.g. air diffuser) where it is combined with microalgae cultivation system.

Aeration is crucial in algae cultivation where it serves to supply CO_2, to sweep gas for the O_2 removal in photosynthesis, and to provide mixing and circulation [26]. The three functions are hindered by their specific bottlenecks. The mass transfer of CO_2 is often restricted by low mass transfer coefficient at the gaseous and liquid sides, causing insufficient photosynthesis capabilities of the algae under carbon limited growth. The presence of excessive O_2 in the culture would leads to photooxidation of the algae cell and reduces the biomass viability [27]. Therefore, effective O_2 sweeping is crucial to minimize the saturated O_2 presence in the culture. Supplying high flow rate of CO_2 may seem as an ideal solution. In a detailed study focusing on the effect of shear rates on algae cultivation, Mirón et al. [28] reported that biomass yield of *Phaeodactylum tricornutum* increases up to 47% when the aeration rate is increased in the presence of shear protectant. High radial mixing within the cultures (at high aeration velocity) provides effective O_2 sweeping and CO_2 delivery, which will benefit the algae growth. Whereas, without shear protectant, high aeration velocity reduces biomass yield to 60% as shear stress leads to cell death almost instantly [28]. Thus, supplying high aeration rate without inducing high shear stress is desirable to overcome those bottlenecks. Hence, it is important to consider the trade-off with high aeration rate to improve CO_2 transport and O_2 sweeping efficiency to the culture, but high shear stresses for the algae.

Membrane technology has been matured over the years, and their potential microalgae cultivation has been explored. The membranes in the context of microalgae harvesting are used to concentrate the algae species by removing water from the cultivation media. While extensive research on membrane pore properties and surface chemistry has been explored as filtration media, utilizing the technology as gas diffuser is rarely investigated.

Comparative analysis between conventional perforated tube diffuser and MF has been established [29]. The MF membrane produced significantly smaller air bubble (mean diameter = 0.3 cm), whereas the perforated tube produced significantly larger air bubble (mean diameter = 1.2 cm) under similar inlet air flow rate of 4 l/min (Table 5.1). It was estimated that the membrane aerator produces 64 times more bubbles, thus total contact interfacial area is four times higher. This resulted in higher biomass content (*Staurastrum* sp.) of 277 mg/l for membrane aerator, while only 203 mg/l when using perforated tube (Figure 5.5). The authors also applied 50 vol% of CO_2 in air as inlet at 4 l/min and further improves biomass concentration to 325 mg/l for membrane and 249 mg/l for perforated tube [29]. It should be noted that using the membrane as aerator produces higher biomass content consistently than conventional perforated tube. This result implies that using membrane as an aerator is highly beneficial in supplying CO_2 to the culture medium, as compared with the conventional approach, even at low CO_2 concentration (pure air as inlet).

Aside from diffuser extrusion size, the surface chemistry also plays major roles in controlling bubble size formation. Wesley et al. [30] used modified porous steel sinter and observed that hydrophobic surface tends to have higher affinity with air, allowing bubble to grow bigger until it gains sufficient buoyancy forces to

Table 5.1 Comparative analysis of bubble size and total contact area produced between perforated tube and MF membrane under air flow rate of 4 l/min.

Aerator	Mean radius (cm)	Cross-section area of bubble (cm^2)	Total amount of bubbles (min^{-1})	Total contact area (cm^2/min)
Perforated tube	1.2	4.52	552	2 499.74
MF membrane	0.3	0.28	35 363	10 007.78

Source: From Lutfi et al. 2018 [29].

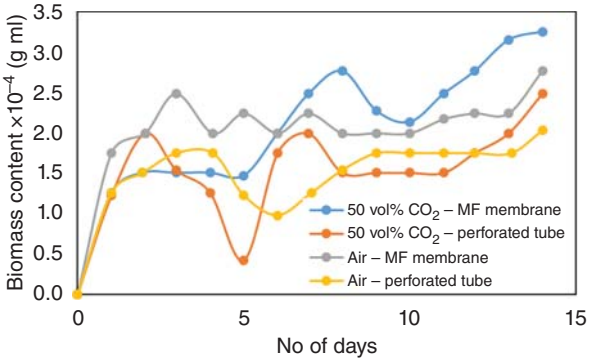

Figure 5.5 Biomass concentration produced using perforated and membrane aerator under inlet flow rate of 4 l/min. Source: From Lutfi et al. 2018 [29].

overcome the surface tension, before it is released to the liquid. The findings suggested altering the hydrophilicity and size of the opening would produce smaller bubble size.

To further understand the roles of the hydrophilicity and pore size, preliminary static analysis of forces acted on bubble formed can be hypothesized (Figure 5.6). For air bubble to detach from the membrane surface, its buoyancy forces (F_B) and the pump force from the inlet air (F_{air}) should overcome the hydrostatic pressure (F_H) and surface adhesion ($F_{surface}$). Based on force analysis, it can be postulated that altering the surface properties is crucial in controlling the bubble size. Combination of surface tension (S), wettability (through contact angle, θ), and pore sizes of membrane (R_{pore}) directly influences the size of the formed bubbles, based on the *Young–Laplace* theory. Controlling these three properties would enable one to fully control the size of the formed bubble.

Applying hydrophilic coating onto the existing membrane is among feasible methods to control the bubble size formed (Figure 5.7) [31]. It can alter the surface wettability to have higher affinity toward water, hence reducing both surface tension and contact angle. Controlling coating parameters (i.e. coating concentration and coating cycles) are crucial to avoid very small pore size bubble (that would require high capillary pressure for inlet air to overcome) and membrane's pore blockage.

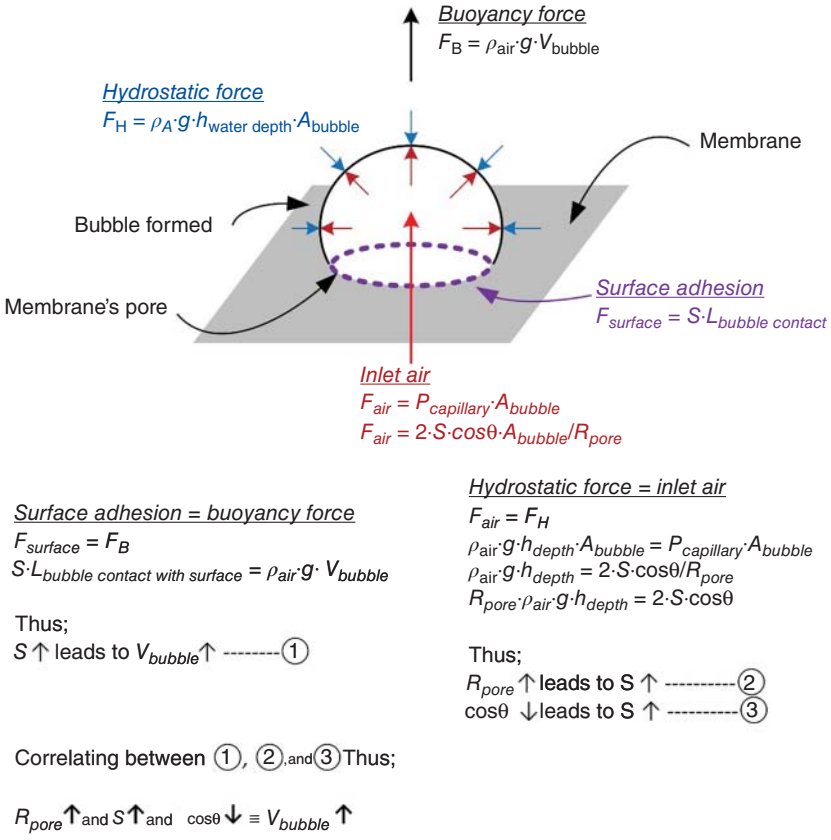

Figure 5.6 Preliminary static force analysis on bubble formed through membrane pores based on the *Young–Laplace* theory.

The effect of surface hydrophilicity on bubble formation has been explored by using polyvinylidenefluoride (PVDF) MF membrane coated with polyether block amide (PEBAX® 1657) at different concentrations [31]. The presence of ether and amide functional groups from PEBAX coating, containing rich –OH and –NH, leads to membrane hydrophilicity to improve from 111.19° ± 0.10° (without coating) to 40.57° ± 1.29° for PEBAX 2.0 wt%. The bubble formed for PEBAX 2.0 wt% is notably smaller than the ones without coating (Figure 5.8). Their impact on algae cultivation is evaluated using *Chlorella vulgaris* algae for growth duration of 14 days. Concentration of biomass is the highest (1.107 g/l) when PVDF/PEBAX 2.0 wt% is used due to small air bubbles delivered into culture medium that promotes higher contact between air and culture medium. The algae growth is superior when using an almost identical parameter that was approximately only 0.6 g/l of *C. vulgaris* concentration after 14 days of cultivation.

It should be highlighted that small pore sizes of the membrane aerator would require higher pressure to overcome both capillary and hydrostatic pressure, thus may impact the processing cost. In addition, smaller bubble sizes may lead to low

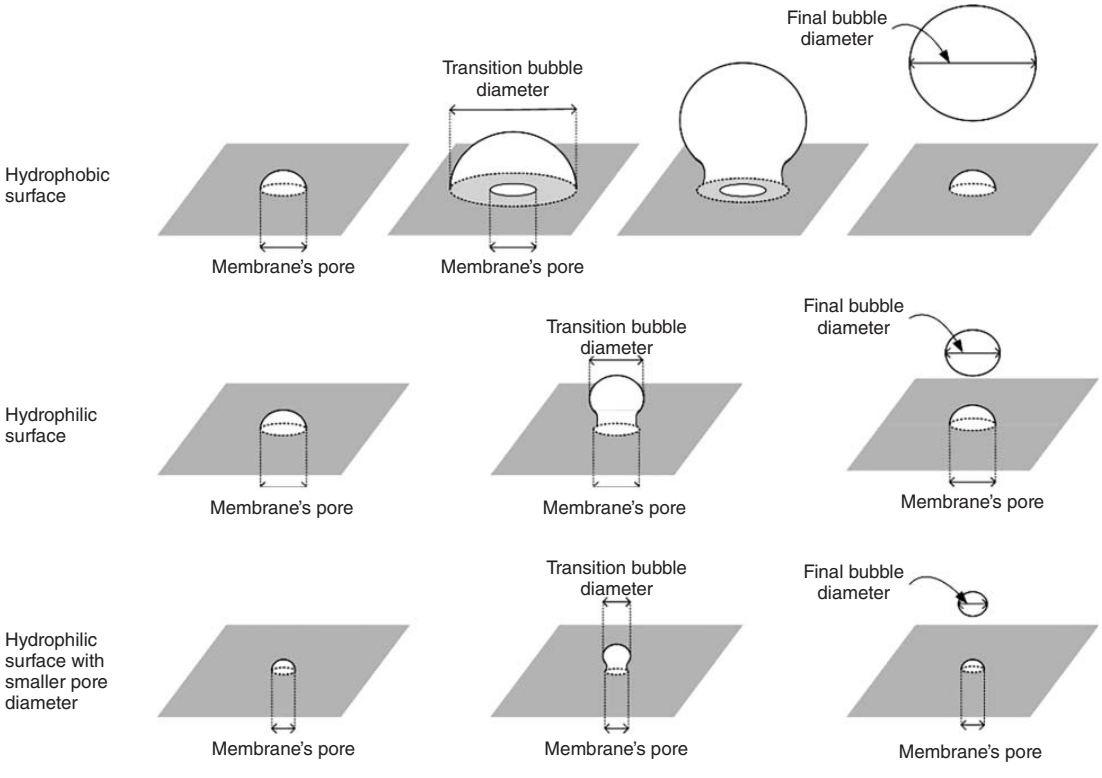

Figure 5.7 Conceptual bubble formation under different surface wettability and pore sizes. Source: Adapted from Wesley et al. 2016 [30].

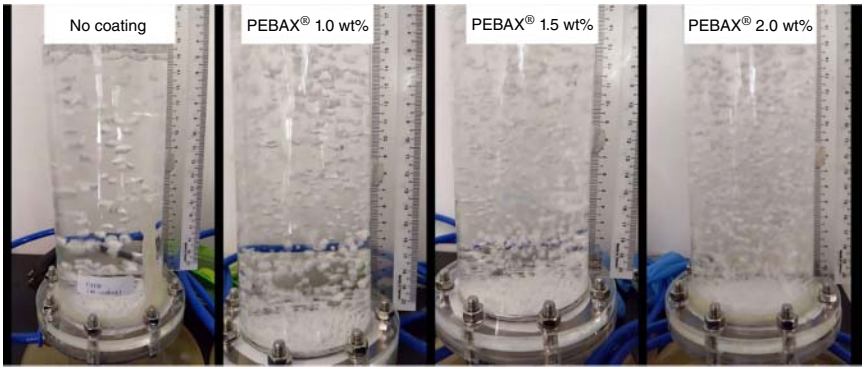

Figure 5.8 Impact of hydrophilic coating (PEBAX®) at different concentration on bubble size formation. Source: From Ishak 2019 [31].

turbulence mixing and unable to sweep dissolved oxygen. The latter could reduce their photosynthesis activity due to cell damaging photooxidations [27].

In the combination of small pore size and hydrophilicity, small air bubbles can be produced to maximize the contact between air and culture medium, improving the CO_2 mass transfer and enhance biomass productivity. While it is undeniably beneficial, extensive study specifically on their sensitivity analysis and economic feasibility should be conducted. This case study demonstrates the effective combination of membrane as a diffuser in microalgae cultivation reactor. Via this case study, a new application is introduced, which opens a new avenue for further studies.

5.4 Forward Osmosis and Electrolysis for Energy Storage and Treatment of Emerging Pollutant

FO process is known as the direct osmosis process, which utilizes osmotic pressure differences between lower and higher salinity water, whereby water permeates through a semi-permeable membrane [32]. In Figure 5.9, a wastewater stream that has a higher osmotic pressure permeates through the membrane to a draw solution side. FO has advantages when compared with other membrane separation processes. Unlike conventional pressure-driven RO and thermal-driven MD processes, FO operates at very low hydraulic pressures and ambient temperature. This significantly reduces both capital and operating costs [33]. Various potential applications of FO including seawater desalination [34], water and wastewater treatment [35], food processing [36], and power generation [37] have been widely studied.

As water permeates through the membrane, the draw solution becomes more diluted. Hence, the flux reduces over time. To maintain a constant flux of water, the draw solution needs to be regenerated by removing the permeating water. Some of the attempts to do so are shown in Figure 5.10. Integrating it with an RO system (Figure 5.10a) requires a high-pressure pump and the RO membrane

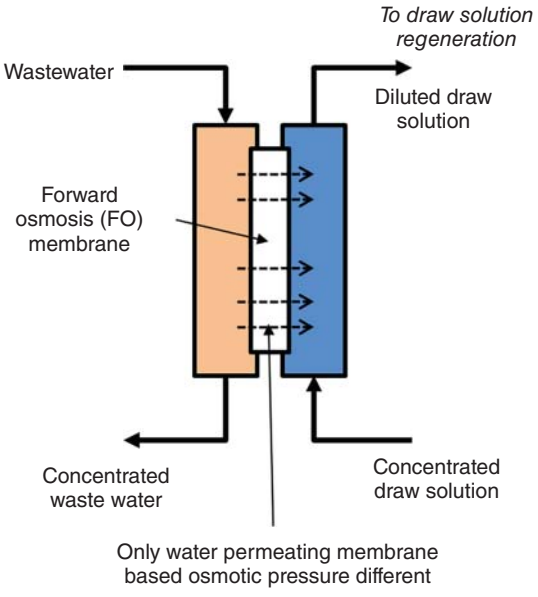

Figure 5.9 Forward osmosis process.

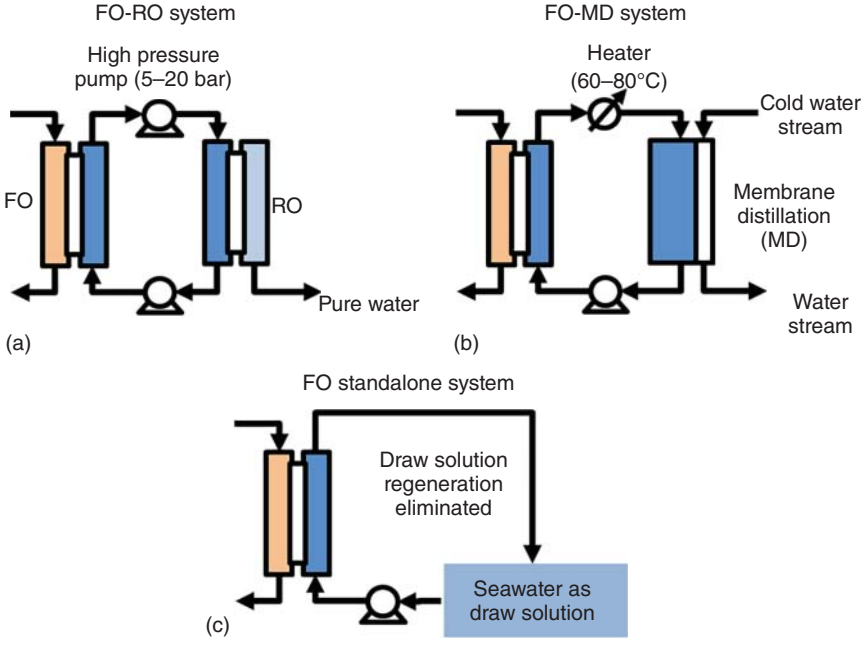

Figure 5.10 Alternatives of draw solution regeneration methods of FO using (a) reverse osmosis (RO), (b) membrane distillation (MD), and (c) without regeneration.

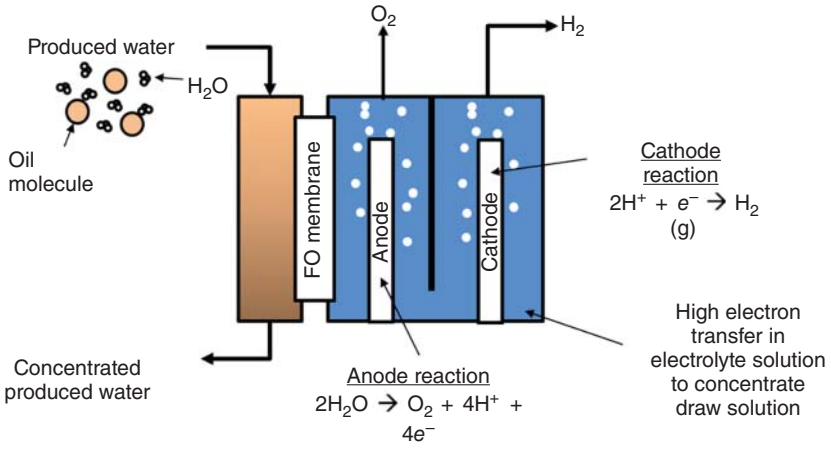

Figure 5.11 Integrated FO membrane with an electrolysis unit. Source: Adapted from Singh 2019 [38].

easily degrades. In Figure 5.10b, an MD system is limited by the availability of the cold water stream, which is typically an ambient water stream. Lastly, Figure 5.10c uses the abundance of seawater as the draw solution, which may need additional water treatment prior to entering the FO unit.

Another attempt to regenerate the draw solution is to integrate the FO system with an electrolysis unit, as shown in Figure 5.11. This integrated system is expected to continuously regenerate the draw solution while simultaneously produce hydrogen and oxygen gas by-products. Sulfuric acid is commonly used as the electrolyte solution because it is a strong acid that dissociates to produce hydrogen ions in water solution. In this regard, hydrogen will be produced at the negative electrode (cathode) and oxygen at the positive electrode (anode).

Experimental setup for this FO–electrolysis process is shown in Figure 5.12. This setup was used to study consecutively the performances of FO with and without the integration of electrolysis [38]. Furthermore, variations of concentrations

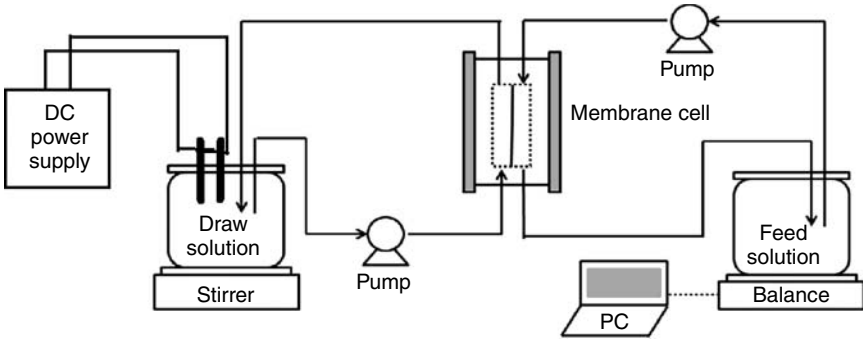

Figure 5.12 Experimental lab setup for forward osmosis–electrolysis unit. Source: Adapted from Singh 2019 [38].

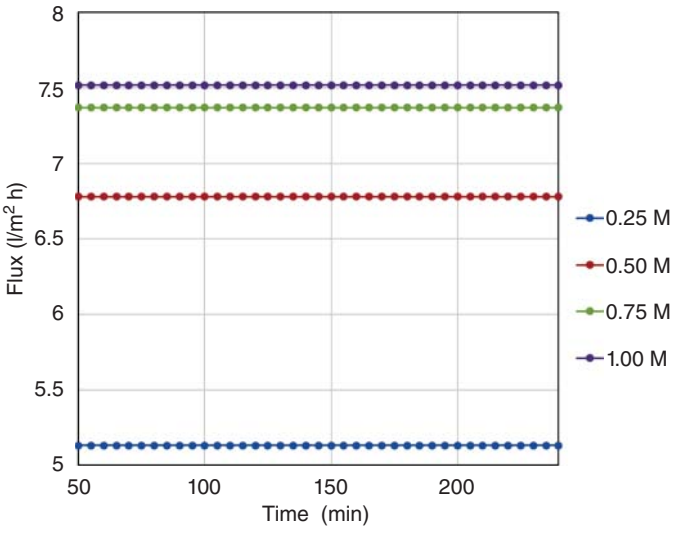

Figure 5.13 Performance of forward osmosis (FO) unit with non-circulated (once through) draw solution. Source: Adapted from Singh 2019 [38].

and voltages on the draw solution were also studied to observe the performance of the system.

Figure 5.13 shows steady-state situations for a standalone FO system by using non-circulated (once through) draw solutions at different concentrations. It can be seen that at higher concentration of draw solutions, osmotic pressure gradient increases, and hence higher water fluxes is observed from the wastewater to the draw solution.

Figure 5.14 shows the results at two different initial concentrations of draw solution, i.e. 0.25 and 0.5 M. The figure shows results from the 50th minute, where the fluxes are already stable. For non-circulated (once through) draw solution, a higher concentration of draw solution obviously yields higher water flux. For circulated FO, i.e. without using the electrolysis unit to regenerate the draw solution, the flux decreases over time because the osmotic pressure gradient reduces as well [38].

It can be seen also that at lower voltages, the fluxes decrease. This happens because at lower voltages, the amount of water permeating the membrane is not fully electrolyzed. Thus, the draw solution is getting more diluted. Hence, the osmotic pressure gradient gets reduced. Nonetheless, the fluxes achieve higher steady-state points than the one without the electrolysis unit.

For the draw solution with 0.25 M initial concentration, higher voltages (e.g. 5.5 V), the fluxes reach the steady-state value of the non-circulated draw solution. In this regard, the same amount of water permeating through the membrane is electrolyzed to produce H_2 and O_2 gases. Increasing the voltages above this value should increase the water flux. However, due to equipment limitation, the voltage cannot be set at higher than 6 V. Furthermore, the carbon electrodes have already started to decompose at this value.

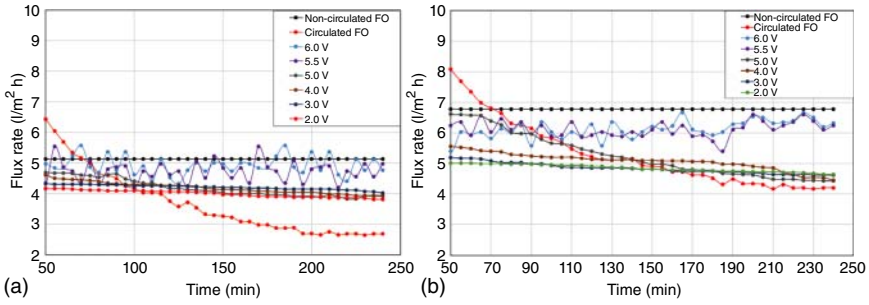

Figure 5.14 Performances of the FO–electrolysis unit with draw solution initial concentrations of (a) 0.25 M and (b) 0.5 M. Source: Adapted from Singh 2019 [38].

On the other hand, for the draw solution with initial concentration of 0.5 M, the applied highest voltage of 6 V could not fully achieve the steady-state value of the non-circulated FO. In this regard, due to this higher initial concentration, a higher voltage is needed to electrolyze the same amount of water permeating into the draw solution. As mentioned earlier, equipment limitation has restricted the voltage, and hence, the steady-state value of non-circulated draw solution cannot be fully achieved while the carbon electrode already starts to decompose.

Nonetheless, this result proves that the concept of integrating the FO–electrolysis unit can be used to concentrate wastewater, hence reducing the amount of wastewater to be treated. This leads to reduced capital expenditures of wastewater treatment. Note also that H_2 is produced as an energy source at the same time. By mass balance, the molar amount of H_2 produced is equal to that of the treated water.

Overall, it can be seen that the electrolysis unit can be integrated with FO for the regeneration of draw solution. Higher concentration of draw solutions will require higher voltages to achieve the steady-state values of once-through draw solution system. In this regard, the system can be further optimized to achieve higher water removal by adjusting the voltages and the use of proper electrode materials. On the other hand, high-energy requirement for the splitting of water in electrolysis, membrane stability under the electrolysis process, and potential harmful gas by-product should be considered for further developments. Nevertheless, possible future extension of this concept is seen in Figure 5.15 where wastewater treatment plant is not merely an obligation for environmental protection, but also a means to produce clean energy such as hydrogen.

5.5 Conclusions and Future Perspective

This chapter highlights the membrane engineering aspects in several process intensification applications. Three emerging cases are discussed in great details. Membranes can be used to separate the floc formed from electro-coagulation and flocculation of dye-containing feed. In this case, inclusion of membrane enhances process efficiency by up to 70%. The membrane allows the floc separation in an earlier stage and thus offers energy saving as well as enhances the dye removal

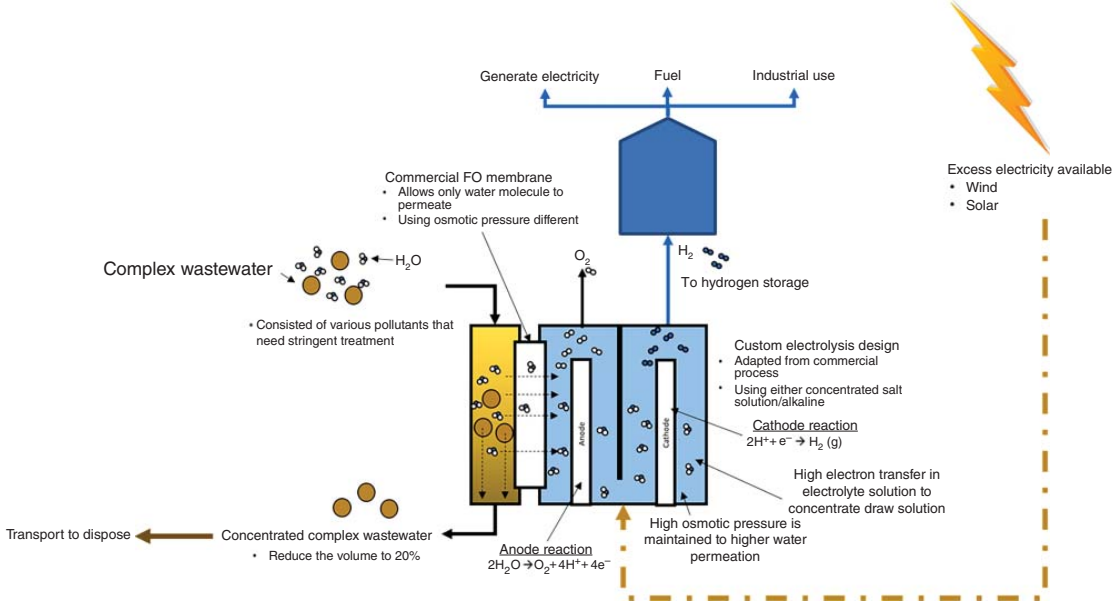

Figure 5.15 Future possible application of integrated forward osmosis–electrolysis process.

efficiency. In membrane carbonation system, a porous membrane can be used as a micro-bubble diffuser, which is a rather new application for the MF membrane. The advantage of small pore sizes of the membrane allows formation of small bubbles to increase interfacial areas for enhancing the mass transport. As the results, when combined with microalgae cultivation reactor, the membrane diffusers enhance the cultivation rate by almost double. Recovery of draw solution in FO can be achieved by introducing electrolysis of the draw solution. Doing this allows water splitting to form oxygen and hydrogen gases, which helps to maintain high draw solution concentration and sustain the FO process for concentration of wastewater. The gases can be used as fuel and sold as by-product. All three cases discussed in this chapter demonstrate the flexibility of membrane engineering for process intensifications.

List of Abbreviations and Symbols

CO_2	carbon dioxide
EC	energy consumption
ECF	electrocoagulation flocculation
FO	forward osmosis
MBR	membrane bioreactor
MD	membrane distillation
MF	microfiltration
MECF	membrane electrocoagulation flocculation
PVDF	polyvinylidenefluoride
RO	reverse osmosis
UF	ultrafiltration
F_B	buoyancy forces
F_{air}	pump force from the inlet air
F_H	hydrostatic pressure
$F_{surface}$	surface adhesion
R_{pore}	pore size of membrane
S	surface tension
θ	contact angle

References

1 Fritzmann, C., Löwenberg, J., Wintgens, T., and Melin, T. (2007). State-of-the-art of reverse osmosis desalination. *Desalination* 216 (1–3): 1–76.

2 Drioli, E. and Curcio, E. (2007). Membrane engineering for process intensification: a perspective. *Journal of Chemical Technology and Biotechnology* 82 (3): 223–227.

3 Drioli, E., Stankiewicz, A.I., and Macedonio, F. (2011). Membrane engineering in process intensification – an overview. *Journal of Membrane Science* 380 (1–2): 1–8.

4 Rios, G.M., Belleville, M.-P., and Paolucci-Jeanjean, D. (2007). Membrane engineering in biotechnology: quo vamus? *Trends in Biotechnology* 25 (6): 242–246.

5 Lay, W.C.L., Lim, C., Lee, Y. et al. (2017). From R&D to application: membrane bioreactor technology for water reclamation. *Water Practice Technology* 12 (1): 12–24.

6 Bilad, M.R. (2017). Membrane bioreactor for domestic wastewater treatment: principles, challenges and future research directions. *Indonesian Journal of Science and Technology* 2 (1): 97–123. https://doi.org/10.17509/ijost.v2i1.5993.

7 Judd, S. and Judd, C. (eds.) (2011). Commercial technologies, Chapter 4. In: *MBR Book*, 2e, 289–357. Oxford: Butterworth-Heinemann.

8 Bilad, M.R., Mezohegyi, G., Declerck, P., and Vankelecom, I.F.J. (2012). Novel magnetically induced membrane vibration (MMV) for fouling control in membrane bioreactors. *Water Research* 46 (1): 63–72.

9 Sirkar, K.K., Fane, A.G., Wang, R., and Wickramasinghe, S.R. (2015). Process intensification with selected membrane processes. *Chemical Engineering and Processing Process Intensification* 87: 16–25.

10 Drioli, E., Brunetti, A., Di Profio, G., and Barbieri, G. (2012). Process intensification strategies and membrane engineering. *Green Chemistry* 14 (6): 1561–1572.

11 Balasubramaniam, L. (2018). *Electrocoagulation Assisted Membrane for Celestine Blue Dye Removal*. Universiti Teknologi PETRONAS (UTP).

12 Gürses, A., Açıkyıldız, M., Güneş, K., and Gürses, M.S. (2016). Dyes and pigments: their structure and properties. In: *Dyes and Pigments* (eds. A. Gürses, M. Açıkyıldız, K. Güneş and M.S. Gürses), 13–29. Cham: Springer International Publishing.

13 Chequer, F.M.D., de Oliveira, G.A.R., Ferraz, E.R.A. et al. (2013). Textile dyes: dyeing process and environmental impact. In: *Eco-Friendly Textile Dyeing and Finishing*, vol. 6 (ed. M. Gunay), 151–176. IntechOpen.

14 Holkar, C.R., Jadhav, A.J., Pinjari, D.V. et al. (2016). A critical review on textile wastewater treatments: possible approaches. *Journal of Environmental Management* 182: 351–366.

15 Yeap, K.L., Teng, T.T., Poh, B.T. et al. (2014). Preparation and characterization of coagulation/flocculation behavior of a novel inorganic–organic hybrid polymer for reactive and disperse dyes removal. *Chemical Engineering Journal* 243: 305–314.

16 Miralles-Cuevas, S., Oller, I., Agüera, A. et al. (2017). Combination of nanofiltration and ozonation for the remediation of real municipal wastewater effluents: acute and chronic toxicity assessment. *Journal of Hazardous Materials* 323: 442–451.

17 Jonstrup, M., Kumar, N., Guieysse, B. et al. (2013). Decolorization of textile dyes by *Bjerkandera* sp. BOL 13 using waste biomass as carbon source. *Journal of Chemical Technology and Biotechnology* 88 (3): 388–394.

18 Zou, J., Peng, X., Li, M. et al. (2017). Electrochemical oxidation of COD from real textile wastewaters: kinetic study and energy consumption. *Chemosphere* 171: 332–338.

19 Singh, S., Srivastava, V.C., and Mall, I.D. (2013). Mechanism of dye degradation during electrochemical treatment. *Journal of Physical Chemistry C* 117 (29): 15229–15240.

20 Zaviska, F., Drogui, P., Blais, J.-F., and Mercier, G. (2009). In situ active chlorine generation for the treatment of dye-containing effluents. *Journal of Applied Electrochemistry* 39 (12): 2397–2408.

21 Hassan, M.A. and El Jamal, M.M. (2012). Kinetic study of the electrochemical oxidation of methylene blue with Pt electrode. *Portugaliae Electrochimica Acta* 30 (5): 351–359.

22 Donneys-Victoria, D., Marriaga-Cabrales, N., Camargo-Amado, R.J. et al. (2018). Treatment of landfill leachate by a combined process: iron electrodissolution, iron oxidation by H_2O_2 and chemical flocculation. *Sustainable Environment Research* 28 (1): 12–19.

23 Abdelrasoul, A., Doan, H., and Lohi, A. (2013). Fouling in membrane filtration and remediation methods. In: *Mass Transfer – Advances in Sustainable Energy and Environment Oriented Numerical Modeling*, vol. 195 (ed. H. Nakajima), 195–218. IntechOpen.

24 Vinduja, V. and Balasubramanian, N. (2013). Electrocoagulation-integrated hybrid membrane processes for the treatment of tannery wastewater. *Environmental Science and Pollution Research* 20 (10): 7441–7449.

25 Cheah, W.Y., Show, P.L., Ling, T.C., and Juan, J.C. (2015). Biosequestration of atmospheric CO_2 and flue gas-containing CO_2 by microalgae. *Bioresource Technology* 184: 190–201.

26 Pires, J.C.M., Alvim-Ferraz, M.C.M., Martins, F.G., and Simões, M. (2012). Carbon dioxide capture from flue gases using microalgae: engineering aspects and biorefinery concept. *Renewable and Sustainable Energy Reviews* 16 (5): 3043–3053.

27 Molina, E., Fernández, J., Acién, F.G., and Chisti, Y. (2001). Tubular photobioreactor design for algal cultures. *Journal of Biotechnology* 92 (2): 113–131.

28 Mirón, A.S., Garcıa, M.C.C., Gómez, A.C. et al. (2003). Shear stress tolerance and biochemical characterization of *Phaeodactylum tricornutum* in quasi steady-state continuous culture in outdoor photobioreactors. *Biochemical Engineering Journal* 16 (3): 287–297.

29 Lutfi, U.A.M.I., Hizam, S.M., Lau, K.S. et al. (2018). Microfiltration membrane assisted CO_2 diffuser for algae cultivation. *Journal of Applied Membrane Science and Technology* 22 (1): 1–10.

30 Wesley, D.J., Smith, R.M., Zimmerman, W.B., and Howse, J.R. (2016). Influence of surface wettability on microbubble formation. *Langmuir* 32 (5): 1269–1278.

31 Ishak, A.S. (2019). *Effect of Hydrophilic Coating for Membrane Assisted Air Diffuser for Chlorella vulgaris Cultivation*. Universiti Teknologi PETRONAS (UTP).

32 Cath, T.Y., Childress, A.E., and Elimelech, M. (2006). Forward osmosis: principles, applications, and recent developments. *Journal of Membrane Science* 281 (1–2): 70–87.

33 McGinnis, R.L. and Elimelech, M. (2007). Energy requirements of ammonia–carbon dioxide forward osmosis desalination. *Desalination* 207 (1–3): 370–382.

34 Phuntsho, S., Hong, S., Elimelech, M., and Shon, H.K. (2013). Forward osmosis desalination of brackish groundwater: meeting water quality requirements for fertigation by integrating nanofiltration. *Journal of Membrane Science* 436: 1–15.

35 Achilli, A., Cath, T.Y., Marchand, E.A., and Childress, A.E. (2009). The forward osmosis membrane bioreactor: a low fouling alternative to MBR processes. *Desalination* 239 (1–3): 10–21.

36 Dova, M.I., Petrotos, K.B., and Lazarides, H.N. (2007). On the direct osmotic concentration of liquid foods. Part I: Impact of process parameters on process performance. *Journal of Food Engineering* 78 (2): 422–430.

37 Yip, N.Y., Tiraferri, A., Phillip, W.A. et al. (2011). Thin-film composite pressure retarded osmosis membranes for sustainable power generation from salinity gradients. *Environmental Science and Technology* 45 (10): 4360–4369.

38 Singh, S.K. (2019). *Feasibility Study on Using Electrolysis to Regenerate Draw Solution from Forward Osmosis (FO) System*. Universiti Teknologi PETRONAS (UTP).

6

Design of Internally Heat-Integrated Distillation Column (HIDiC)

Vasu Harvindran and Dominic C. Y. Foo

University of Nottingham Malaysia, Department of Chemical and Environmental Engineering/Center of Excellence for Green Technologies, Broga Road, Semenyih, Selangor 43500, Malaysia

6.1 Introduction

Distillation is one of the main energy-intensive processes in the chemical process industry. However, conventional distillation usually results in huge degradation of energy due to high temperature differences between its condenser and reboiler. The enormous loss of energy reduces the thermodynamic efficiency of a distillation process by about 10% [1, 2]. This simply means that a conventional column uses a large amount of energy with relatively low efficiency [3]. Numerous advanced distillation designs have been proposed to improve the energy efficiency [4], including the heat-integrated distillation column (HIDiC) configuration. The concept of HIDiC was originally proposed by Fitzmorris and Mah [5], with a different name termed as "secondary reflux and vaporization" (SRV). Iwakabe et al. [6] carried out a study on an HIDiC pilot plant and reported up to 60% of energy saving as compared with conventional column. Gadalla et al. [3] evaluated the conceptual design and feasibility of an HIDiC using commercial simulation software. Several recent works based on process simulation were also reported independently by Gutiérrez-Guerra et al. [7] and Cong et al. [8]. In the former, energy savings reported for 50–87% for the separation of isomer mixtures [7]. In the work of Cong et al. [8], performance analysis and structural optimization were performed for multi-tube type HIDiC. In a more recent work, Rix et al. [9] reported some heuristic guidelines for the design of heat-integrated columns.

Unlike the conventional column with only one column shell, the HIDiC configuration consists of two separate columns for its rectifying and stripping sections respectively (see Figure 6.1). The working principle of HIDiC is contradicting to that of conventional column, as the rectifying section is operated at higher temperature and pressure as compared with the stripping section, in order to carry out internal heat transfer. Top vapor from the stripping column is compressed and fed to the bottom of the rectifying column. Bottom liquid from the rectifying column is recycled and mixed with the feed stream that enters the top of the stripping column. Pressure of the recycled stream is reduced with a throttling valve to meet the pressure requirement of the stripping column. Top product of

Process Intensification and Integration for Sustainable Design, First Edition.
Edited by Dominic C. Y. Foo and Mahmoud M. El-Halwagi.
© 2021 WILEY-VCH GmbH. Published 2021 by WILEY-VCH GmbH.

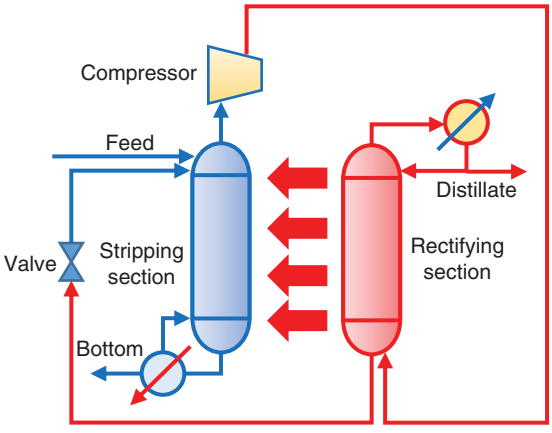

Figure 6.1 Conceptual design of HIDiC. Source: Suphanit 2010 [4]. Reproduced with permission of Elsevier.

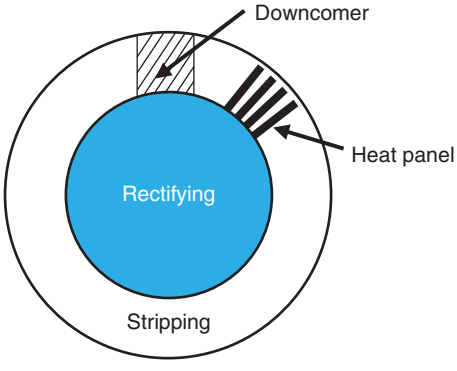

Figure 6.2 Heat panels in the stripping section. Source: From de Rijke [1].

the rectifying column is the desired light product whereas the bottom product of the stripping column is the heavy product. The idea of raising pressure of the rectifying column is to promote heat transfer between hot vapor from the rectifying section with the cold liquid from the stripping section through heat panels. This eventually leads to reduced duties of the reboiler and condenser [3].

In a concentric distillation column, the rectifying section is built within the annular stripping section as shown in Figure 6.2. The residual heat from the rectifying section is transferred to the stripping section by the heat panels that are placed in the stripping sections [1]. As shown in Figure 6.3, the working principle of the heat panels in HIDiC is such that the hot vapor from the rectifying section enters the panels located in the stripping section and condenses due to heat exchange with the cold liquid stream in the stripping section. The condensate flows back into the rectifying section. The cold liquid in the stripping section flows down over the heat panels and evaporates as heat is transferred from the rectifying section through the panel walls. The vapor generated flows upward through the sieve trays [10].

This chapter aims to improvise the energy efficiency of the conventional column by implementing an advanced design technology based on HIDiC. The design feasibility and economic potential of the new design are taken into consideration. Heat integration is performed at two different configurations (top

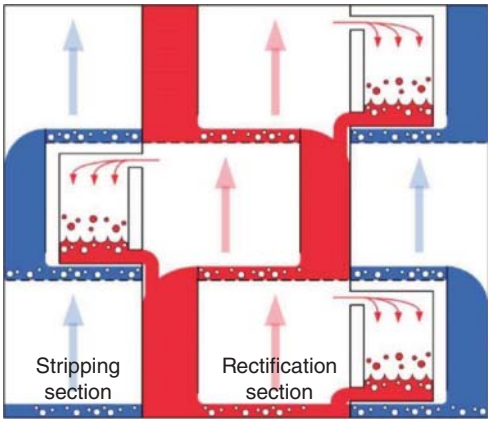

Figure 6.3 Cross section of HIDiC with heat panels in the stripping section. Source: Olujić et al. [10]. Reproduced with permission of Elsevier.

Figure 6.4 Hierarchy for HIDiC design.

and bottom integration) in HIDiC, in order to determine the best configuration with higher energy saving and lower total annualized cost (TAC), with respect to the conventional column.

The chapter is structured as follows. In the section that follows, conceptual design of conventional distillation column is first performed. The latter is needed in order to provide basic data for HIDiC design in the following stage (see Figure 6.4). Best heat integration configuration between the rectifying and stripping columns of HIDiC is next determined. Finally, economic evaluation is performed for conventional column and HIDiC, before the chapter is concluded.

6.2 Example and Conceptual Design of Conventional Column

A conventional binary distillation is used to separate a feed mixture of methanol and water. The feed is a saturated liquid mixture that enters the column at 125.7 °C and 3.65 bar. The column is designed to recover 99% of methanol as top product (with 97% purity) and 99% of water as bottom product (with 99% purity). Process simulation study is performed (with Aspen HYSYS V8.8) of the conventional column, with results shown in Table 6.1.

HIDiC is next simulated based on the simulation results of the conventional column. Firstly, basic design of HIDiC is simulated with no heat integration between the two column sections. This is to ensure that the heat transfer per stage is equivalent to zero and a maximum reboiler duty can be obtained as comparable with the conventional design. Then, the design procedure proceeds to the HIDiC complete design with heat transfer between the rectifying and stripping sections until the reboiler duty is reduced to a minimal value (partial

Table 6.1 Simulation results of conventional column.

Parameters	Simulation study
Distillate flow rate (kmol/h)	42.348
Bottom flow rate (kmol/h)	123.212
Distillate temperature (°C)	99.34
Bottom temperature (°C)	143.25
Mole fraction of methanol in distillate	0.970
Mole fraction of water in distillate	0.030
Mole fraction of methanol in bottom	0.003
Mole fraction of water in bottom	0.996
Recovery of methanol in distillate (%)	0.989
Recovery of water in bottom (%)	0.990
Rectifying trays	5
Stripping trays	8

HIDiC) or even zero (ideal HIDiC) [11]. At this point, the positions of heat transfer from the rectifying section to the stripping section are varied to determine the configuration that yields the highest energy saving as compared with the conventional column. Simulation study reveals that the reboiler and condenser duties are 7314 and 7063 MJ/h, respectively.

6.3 Basic Design of HIDiC

HIDiC basic design proceeds based on the output parameters acquired from the simulation of the conventional column (Figure 6.5). Basic design simply means the column configuration of both rectifying and stripping sections without heat integration between them. This procedure is essential to determine the maximum reboiler duty, which is comparable with the conventional design with heat transfer per stage, Q_{stage} equivalent to zero [11]. In order to begin with the simulation of HIDiC in Aspen Plus V8.8, few assumptions have to be considered such as

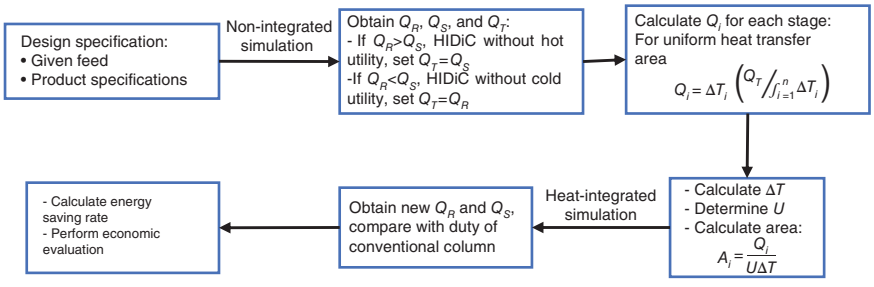

Figure 6.5 Design procedure of HIDiC with constant heat transfer area per stage.

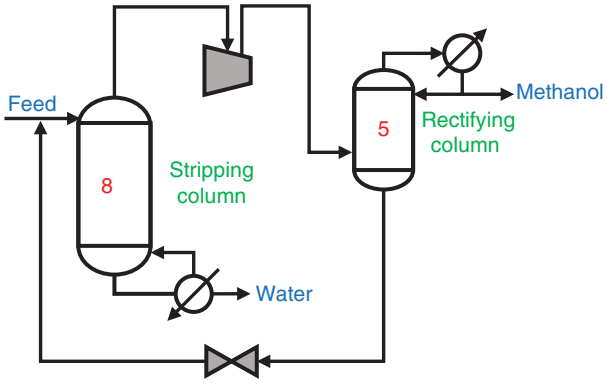

Figure 6.6 HIDiC basic design configuration (8 trays in stripping column and 5 trays in rectifying column). Source: Gadalla [11]. Reproduced with permission of Elsevier.

- Feed entry stage in HIDiC
- Number of stages in the rectifying and stripping columns
- Compression ratio of compressor

Therefore, the data obtained from the conventional design is actually the key for HIDiC design. The conventional column will be split around the feed entry stage into the rectifying and stripping columns (Figure 6.6). The feed enters at the top stage of the stripping column. The compression ratio of the compressor is set at 1.8 in order to ensure the rectifying column is operating at a higher pressure as compared with the stripping column. This ensures that the temperature of the rectifying column is much higher than the temperature of the stripping column allowing for reasonable and logical temperature difference for heat integration. Compression ratio below 1.8 is not practical for this basic design case study as the corresponding temperature difference between certain trays shows negative values implying insufficient thermal gradient between the columns. On the other hand, compression ratio above 1.8 is not advisable as the compressor may consume more electricity leading to higher operating cost.

Simulation exercise reveals that the reboiler and condenser duties of the HIDiC basic design are reduced to 6573 and 6371 MJ/h (Table 6.2), respectively, which are slightly lower as compared with the conventional column.

The temperature for each stage in the rectifying and stripping columns is obtained from the simulation study and tabulated in Table 6.3. According to Gadalla et al. [3], the temperature profile of the rectifying section has to be located well above the temperature profile of the stripping section in order to ensure possible heat integration between the columns. The temperature

Table 6.2 Reboiler and condenser duty of HIDiC basic design.

	Reboiler, Q_S	Condenser, Q_R
Duty (MJ/h)	6573	6371

Table 6.3 Temperature profile for rectifying and stripping columns.

Rectifying column		Stripping column	
Stage number	**Temperature (°C)**	**Stage number**	**Temperature (°C)**
1	121.6	1	112.8
2	122.6	2	112.5
3	123.8	3	112.3
4	125.7	4	112.6
5	128.4	5	114.1
		6	118.8
		7	124.3
		8	134.2

difference actually creates a thermal driving force to transfer heat from the rectifying column to the stripping column.

6.4 Complete Design of HIDiC

The next step is to design the HIDiC complete design configuration. Two different scenarios are considered:

1. Top-integrated column (heat transfer from rectifying column to the top section of the stripping column)
2. Bottom-integrated column (heat transfer from rectifying column to the bottom section of the stripping column)

6.4.1 Top-Integrated Column

Simulation is first carried out by extracting the necessary energy streams from the rectifying column at any given stages and adding them to the specified stages in the stripping column. The amount of heat transfer per stage, Q_i, is calculated based on constant heat transfer area approach by Suphanit [4], given as in Eq. (6.1).

$$\text{Heat transfer per stage, } Q_i = \Delta T_i \left(\frac{Q_T}{\int_{i=1}^{n} \Delta T_i} \right) \tag{6.1}$$

The heat transfer area per stage, A_i, is then calculated based on the Q_i obtained, following Eq. (6.2).

$$\text{Heat transfer area per stage, } A_i = \frac{Q_i}{U \Delta T_i} \tag{6.2}$$

According to Suphanit [4], if the condenser duty, Q_R, of HIDiC basic design is less than its reboiler duty, Q_S, the total amount of heat transfer between the

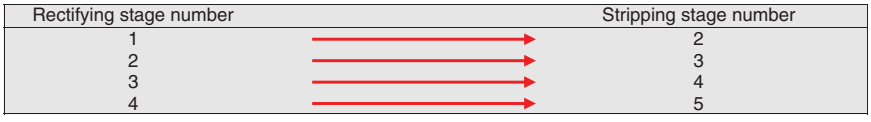

Figure 6.7 Heat transfer between stages for top-integrated column configuration.

Table 6.4 Calculation of Q_i and A_i for top-integrated column configuration.

Rectifying column		Stripping column			Q_T = 6371 MJ/h	Let total heat transfer coefficient, U = 3600 kJ/m² h °C	
Stage	Rectifying temperature (°C)	Stage	Stripping temperature (°C)	Heat-integrated stage, i	Temperature difference, ΔT_i	Heat transfer per stage, Q_i (MJ/h)	Heat transfer area, A_i (m²)
1	121.6	2	112.5	1	9.11	1377	42.00
2	122.6	3	112.3	2	10.25	1550	42.00
3	123.8	4	112.6	3	11.26	1702	42.00
4	125.7	5	114.1	4	11.52	1742	42.00
				Total	42.14	6371	168.00

sections, Q_T, will be set equivalent to Q_R. This is to ensure that the maximum heat integration between the two columns is provided by the total heat rejection from the rectifying column. The heat transfer between the rectifying and stripping sections is shown in Figure 6.7. Note that heat integration is only done up to four stages of the rectification column due to the limitation of the simulation software.

The heat transfer per stage, Q_i, calculated in Table 6.4 is used to determine the new Q_R and Q_S. As observed from Table 6.4, the heat transfer per stage, Q_i, increases as the temperature difference, ΔT_i, between the rectifying and stripping sections increases. The total heat transfer area required for top-integrated column configuration is determined as 168.00 m². The energy saving of the HIDiC with respect to the conventional column is calculated using Eqs. (6.3–6.5) [12].

$$\text{Standard energy duty} = (\text{Reboiler load in conventional column}) \tag{6.3}$$

$$\text{Energy duty of HIDiC} = (\text{Heater load} + \text{reboiler load} + \text{compressor power}) \tag{6.4}$$

$$\text{Energy saving rate (\%)} = \left[1 - \frac{\text{Energy duty of HIDiC}}{\text{Standard energy duty}}\right] \times 100 \tag{6.5}$$

6.4.2 Bottom-Integrated Column

The procedure for calculating the heat transfer per stage, Q_i, and heat transfer area per stage, A_i, for the bottom-integrated column configuration is similar to those of top-integrated column configuration. The heat transfer between the rectifying and stripping sections is shown in Figure 6.8.

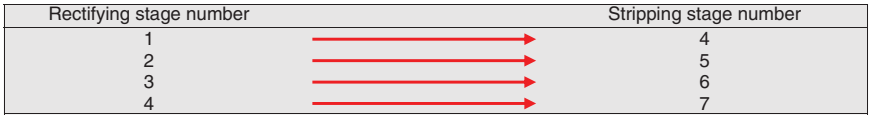

Figure 6.8 Heat transfer between stages for bottom-integrated column configuration.

Table 6.5 Calculation of Q_i and A_i for bottom-integrated column configuration.

Rectifying column		Stripping column			Q_T = 6371 MJ/h	Let U = 3600 kJ/m² h °C	
Stage	Rectifying temperature (°C)	Stage	Stripping temperature (°C)	Heat-integrated stage, i	Temperature difference, ΔT_i	Heat transfer per stage, Q_i (MJ/h)	Heat transfer area, A_i (m²)
1	121.6	4	112.6	1	9.01	2414	74.45
2	122.6	5	114.1	2	8.41	2253	74.45
3	123.8	6	118.8	3	5.03	1348	74.45
4	125.7	7	124.3	4	1.33	3563	74.45
				Total	23.78	6371	297.80

Similarly, the heat transfer per stage, Q_i, calculated in Table 6.5 is used in the simulation of the bottom-integrated column configuration to determine the new Q_R and Q_S. The total heat transfer area required for bottom-integrated column configuration is determined as 297.80 m² (see Table 6.5).

6.4.3 Geometrical Analysis for Heat Panels

Gadalla et al. [3] proposed a hydraulic model to evaluate the heat transfer area available for the heat panels based on the availability of physical space on the stages (Figure 6.9). The specified model is built based on the hydraulic diameter obtained from the flooding limits of the column, configuration of the rectifying and stripping columns, and area of heat panels. The dimensions and layout of heat panels located on the column stages are used to determine all physical space areas available to place the heat panels. The heat panels are placed in the stripping side, which is the external annular space outside the rectifying column, as the diameter of the stripping column is much larger as compared with the rectifying column [3]. However, the model proposed by Gadalla et al. [3] is used to determine the heat transfer area per stage, A_i, by assuming a fixed height, H, and thickness, w, for the heat panel. The model can be approached in a different way as A_i is already determined by using the constant heat transfer area approach proposed by Suphanit [4]. The new technique performed for the geometrical analysis of heat panels is still the same but only the height of heat panels, H, is fixed in this case to determine the thickness of the panel, w, and the number of heat panels in each stage, N_{HP}. A new stripping diameter, d_{str}, has to be calculated, as the rectifying section is actually nested in the stripping section and this new stripping diameter, d_{str}, will be used for the rest of the calculations.

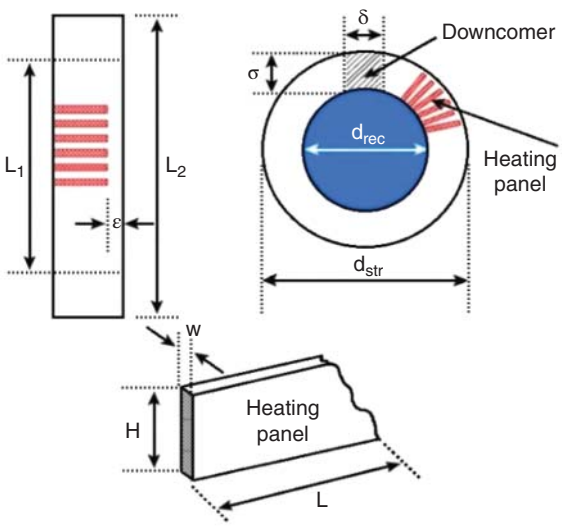

Figure 6.9 Geometrical analysis of concentric HIDiC configuration. Source: Gadalla et al. [3]. Reproduced with permission of Elsevier.

Table 6.6 Geometrical analysis of heat panels.

Variables	Units	Top-integrated configuration	Bottom-integrated configuration
d_{rec}	m	0.691	0.691
d_{str}	m	0.991	0.986
Σ	m	0.150	0.147
Δ	m	0.515	0.518
L	m	0.149	0.146
L_1	m	1.657	1.654
L_2	m	2.965	2.952
H	m	0.450	0.450
A_{HP}	m^2	0.134	0.132
A_i	m^2	42.00	74.45
N_{HP}		314	564
W	m	0.005	0.003
Total number of heat panels		1256	2256

Geometrical analysis of the concentric column is determined by using the model equations as proposed by Gadalla et al. [3]. The results of the geometrical analysis of concentric HIDiC configurations are presented in Table 6.6.

From Table 6.6, one observes that the diameter of the rectifying section, d_{rec}, remains the same, but the stripping diameter, d_{str}, differs slightly for different HIDiC configurations. However, the total number of heat panels in the bottom-integrated column configuration is 1.80 times higher than that in the

top-integrated column configuration, because the heat transfer area per stage, A_i, of the latter is way smaller than that of bottom-integrated column configuration.

6.5 Energy Savings and Economic Evaluation

Table 6.7 shows the energy savings and economic evaluation of top- and bottom-integrated column configurations as compared with that of conventional column.

As shown in Table 6.7, the reboiler duty of the conventional column is the highest as compared with other HIDiCs. When comparing the percentage of reduction in reboiler duty between top- and bottom-integrated configurations with respect to the conventional column, it is clearly observed that bottom-integrated configuration yields a higher reduction in reboiler duty (approximately 79.1%), as compared with top-integrated configuration (with 72.5% reduction). The reason for this difference is due to the larger surface area available for heat transfer between the rectifying and stripping columns in the bottom-integrated configuration, as compared with the top-integrated column configuration. Similar observation is found for the condenser duty, where the bottom-integrated

Table 6.7 Energy savings and economic evaluation of different column configurations.

Configuration type	Conventional	Top-integrated	Bottom-integrated
Comparison of loads			
Reboiler duty (MJ/h)	7314	2014	1531
Condenser duty (MJ/h)	7063	1807	1324
Compressor load (MJ/h)	—	615	549
Heater load (MJ/h)	—	38	23
Cooler load (MJ/h)	—	557	476
Energy saving			
Standard energy duty (MJ/h)	—	7314	7314
Energy duty of HIDiC (MJ/h)	—	2667	2103
Energy saving rate (%)	—	63.5	71.2
Cost of electricity and steam			
Peak period tariff rate ($/kWh)	—	0.08	
Off-peak period tariff rate ($/kWh)	—	0.05	
Medium pressure steam ($/t)	12		
Comparison of various costs for conventional column and HIDiC configurations			
TCC ($)	1.556E+07	1.610E+07	1.573E+07
TOC ($/yr)	2.954E+05	1.657E+05	1.367E+05
TAC ($/yr)	2.984E+06	2.949E+06	2.855E+06
Comparison in TCC (%)	100	103.47	101.09
Comparison in TOC (%)	100	56.09	46.28
Comparison in TAC (%)	100	98.83	95.68

configuration (with 81.3% reduction) has much higher reduction as compared with the top-integrated configuration (of approximately 74.4%). Temperature difference along the heat-integrated stages also plays an important role in the reduction of the reboiler and condenser duty. The total summation of the temperature difference in the bottom-integrated configuration is 23.8 °C, which is much lower than the total temperature difference of the top-integrated configuration, which is about 42.1 °C. The heat transfer per stage, Q_i, is inversely proportional to the total temperature difference, along the heat-integrated stages.

Total capital cost (TCC) of each column is calculated based on the battery limits investment, utility investment, off-site investment, engineering fees, and working capital by taking installation factors into consideration [13]. The main utility costs correspond to electricity cost (compressor power) and steam cost (reboiler and heater duty). The total operating cost (TOC) is taken to be identical to utility cost for the sake of simplicity. TAC determines the economic feasibility of HIDiC.

From Table 6.7, the TCC for top- and bottom-integrated configurations are higher by 3.47% and 1.09%, respectively, when compared with conventional column. The additional costs are due to the presence of compressor, heater, cooler, heat exchanger, and heat panels in the system with only smaller reboiler and condenser as compared with conventional column.

Bottom-integrated configuration shows the highest saving of 53.72% in TOC, while top-integrated column configuration shows 43.91% saving only. This is due to lower electricity consumption for compressor and lower steam consumption for heating in bottom-integrated configuration as compared with top-integrated configuration.

The payback period is set at seven years with a fixed interest rate of 5%. As shown in Table 6.7, top- and bottom-integrated configurations possess 1.17% and 4.32% reduction, respectively, in TAC when compared with that of conventional column. Hence, the bottom-integrated configuration (see Figure 6.10) is

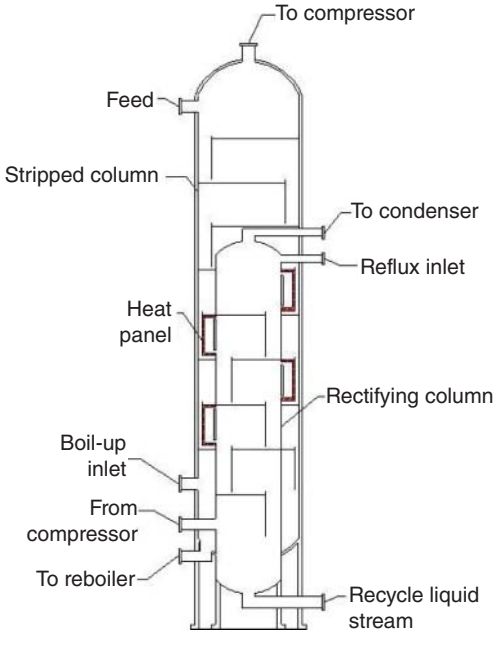

Figure 6.10 Bottom-integrated column configuration.

considered as the best option in terms of economic feasibility as the TAC is the lowest when compared with other column configurations.

6.6 Concluding Thoughts

This chapter presents the design procedure of an HIDiC with the aid of process simulation tools. It is shown that HIDiC indeed reduces reboiler and condenser duties significantly, as compared with the conventional column. For the example of methanol and water separation, the bottom-integrated configuration demonstrates higher energy saving as compared with the top-integrated configuration because it possesses larger heat transfer area for heat integration between the columns. Economic evaluation reveals that the TAC of HIDiC is lower than that of conventional column despite of its high capital cost. The reason for this is simply because of its low TOC due to heat integration between the columns.

References

1 de Rijke, A. (2007). Development of a concentric internally heat integrated distillation column (HIDiC). PhD thesis. Delft University of Technology.
2 Yala, O., Rouzineau, D., Thery-Hetreux, R., and Meyer, M. (2017). Design and optimization of Heat Integrated Distillation Column "HIDiC". *Computer Aided Chemical Engineering* 40: 1783–1788.
3 Gadalla, M., Jiménez, L., Olujic, Z., and Jansens, P.J. (2007). A thermo-hydraulic approach to conceptual design of an internally heat-integrated distillation column (i-HIDiC). *Computers and Chemical Engineering* 31 (10): 1346–1354.
4 Suphanit, B. (2010). Design of internally heat-integrated distillation column (HIDiC): uniform heat transfer area versus uniform heat distribution. *Energy* 35 (3): 1505–1514.
5 Fitzmorris, R.E. and Mah, R.S.H. (1980). Improving distillation column design using thermodynamic availability analysis. *AIChE Journal* 26 (2): 265–273.
6 Iwakabe, K., Nakaiwa, M., Huang, K. et al. (2006). An internally heat-integrated distillation column (HIDiC) in Japan. *IChemE Symposium Series* 152: 900–911.
7 Gutiérrez-Guerra, R., Murrieta-Dueñas, R., Cortez-González, J. et al. (2016). Design and optimization of HIDiC columns using a constrained Boltzmann-based estimation of distribution algorithm-evaluating the effect of relative volatility. *Chemical Engineering and Processing: Process Intensification* 104: 29–42.
8 Cong, H., Li, X., Li, H. et al. (2017). Performance analysis and structural optimization of multi-tube type heat integrated distillation column (HIDiC). *Separation and Purification Technology* 188: 303–315.
9 Rix, A., Hecht, C., Paul, N., and Schallenberg, J. (2019). Design of heat-integrated columns: industrial practice. *Chemical Engineering Research and Design* 147: 83–89.

10 Olujić, Ž., Sun, L., de Rijke, A., and Jansens, P.J. (2006). Conceptual design of an internally heat integrated propylene-propane splitter. *Energy* 31 (15): 3083–3096.
11 Gadalla, M.A. (2009). Internal heat integrated distillation columns (iHIDiCs) – new systematic design methodology. *Chemical Engineering Research and Design* 87 (12): 1658–1666.
12 Horiuchi, K., Yanagimoto, K., Kataoka, K., and Nakaiwa, M. (2006). Energy-saving characteristics of heat integrated distillation column applied to multi-component petroleum distillation. *IChemE Symposium Series* 152: 172–180.
13 Smith, R. (2016). *Chemical Process Design and Integration*, 2e. Chichester, West Sussex, UK: Wiley.

7

Graphical Analysis and Integration of Heat Exchanger Networks with Heat Pumps

Minbo Yang and Xiao Feng

Xi'an Jiaotong University, School of Chemical Engineering and Technology, No. 28, Xianning West Road, Xi'an, Shaanxi 710049, China

7.1 Introduction

Energy is integral to our life, economy, and civilizations. Fossil fuels including coal, petroleum, and natural gas are the leading sources for the global energy supply both now and in the coming decades [1]. However, these energy sources have limited reserves. Stimulated by the energy crises and environmental legislations, sustainable design and synthesis of energy systems has drawn great attention from industries and become an active research area [2].

Heat integration refers to the thermal combinations of process streams to achieve heat recovery via heat exchange [3]. It has been extensively used in the manufacturing industries (such as chemical, petrochemical, pulp and paper, food and drinks, steel making) and power generating industries. Over the last 40 years, many systematic approaches have been provided for *heat exchanger network* (HEN), including pinch analysis, mathematical programming methods, and hybrid techniques [3–6]. These methods can examine the potential for improving and optimizing the heat exchange between heat sources and sinks in order to reduce external hot and cold utilities, which then leads to reduced cost and emissions.

A heat pump is a device that transfers heat from a low temperature reservoir to a high temperature reservoir by consuming external high-grade energy. Thus, integration of HEN and heat pumps allows the transfer of heat from low temperature hot streams to high temperature cold streams, achieving further reduction of hot and cold utilities, and hence improves the overall energy efficiency. Townsend and Linnhoff [7] proposed that a heat pump should receive heat below the pinch temperature and deliver the heat above it; this is known as the "across-pinch rule." This rule is obviously correct because a net heat source exists in region below the pinch and a net heat sink exists above the pinch. The across-pinch rule has been successfully implemented in a number of studies on heat pump integration [8–10]. Bagajewicz and Barbaro [11] discussed the role of heat pumps in total site heat integration. They proposed four possible arrangements for a system of two heat pumps and found that heat pumps that do not transfer energy across

Process Intensification and Integration for Sustainable Design, First Edition.
Edited by Dominic C. Y. Foo and Mahmoud M. El-Halwagi.
© 2021 WILEY-VCH GmbH. Published 2021 by WILEY-VCH GmbH.

the pinch also save utility. This obviously contradicts with the across-pinch rule. A possible explanation for this interesting finding is that heat pumps change the pinch temperature.

Distillation is a technology for separating components from a mixture by using selective boiling and condensation. It is widely used in the chemical, petrochemical, and food industries. As distillation is a large energy consumer, many efforts have been devoted to reducing its energy consumption. The effective options focusing on operating parameters include preheating feed, changing operating pressure [12], and adjusting reflux ratio [13]. Other option for reducing energy consumption is through heat integration [14]. The well-known schemes include thermal coupling distillation [15], multiple effect distillation [16], distillation with heat pump [17], and setting intermediate reboiler and condenser [18]. Moreover, Linnhoff et al. [19] studied the integration of distillation and its background processes. They reported that distillation can be integrated into the overall process to save energy, by not placing it across the pinch. For distillation across the pinch, they proposed various ways to alter column conditions to make integration possible away from the pinch.

Introducing heat pumps into a process may change the pinch temperature of the process, which is an alternative to make the integration of distillation and its background processes. To achieve such integration, it is necessary to know how the pinch temperature is changed by heat pumps and how to systematically analyze heat integration involving heat pump, distillation, and their background processes.

In this chapter, we first introduce a graphical analysis method that combines the graphical representation of a heat pump with *grand composite curve* (GCC) to investigate the effects of heat pump placement on the GCC and pinch temperature. The insights of changes of GCC and pinch temperature are presented, and reasons for such changes are determined. On this basis, a systematic design methodology is presented for the use of heat pumps to assist heat integration of distillation column with the overall process.

7.2 Influences of Heat Pumps on HENs

In this chapter, the vapor compression heat pump is taken for illustration to simplify the analysis. Figure 7.1 shows the vapor compression heat pump system, which consists of four major devices, i.e. evaporator, condenser, compressor, and expansion valve. T_{con} and T_{eva} are the condensing and evaporating temperatures of the working fluid, respectively; Q_{re} and Q_{de} are the heat received and delivered by the heat pump, respectively; and W is the external power. The energy balance of the heat pump system can be described as Eq. (7.1).

$$Q_{de} = Q_{re} + W \tag{7.1}$$

In this section, the changes of the GCC and pinch temperature are analyzed based on seven cases when a heat pump is introduced into an HEN [20].

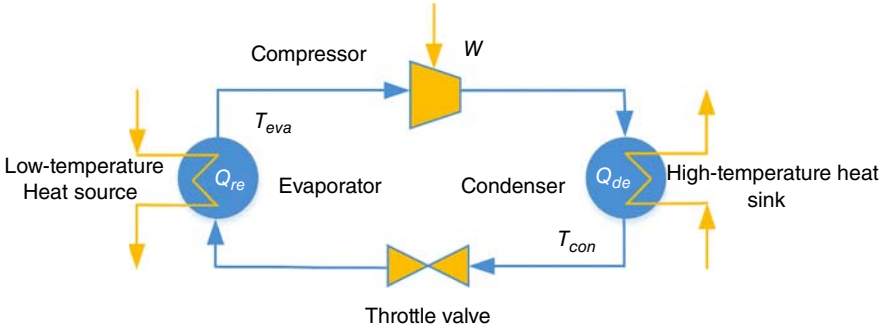

Figure 7.1 The vapor compression heat pump system.

Figure 7.2 Pinch location is unchanged after setting a heat pump.

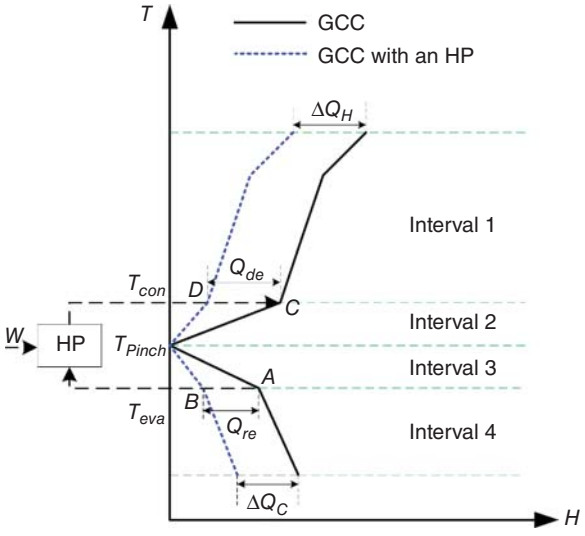

7.2.1 Case 1

In the first case shown in Figure 7.2, a heat pump is set to operate across the pinch temperature of a system. On the basis of T_{con}, T_{eva}, and T_{Pinch}, the GCC is divided into four intervals. When the heat pump receives heat (Q_{re}) from interval 3, the heat flux is reduced and the point A moves to B. After lifting the temperature, the heat pump delivers heat (Q_{de}) to interval 2, where a portion of the heat requirement is satisfied. Therefore, the heat flux is decreased, and the point C moves to D. The placement of heat pump does not affect the intervals 1 and 4, and thus the utility requirements in the two intervals remain unchanged. The original curves in the intervals 1 and 4 are shifted to the left horizontally until point C coincides with point D, forming a new GCC as depicted by the dotted line. Comparing the two GCCs, it can be found that the placement of heat pump does not change pinch location. The hot utility saving ΔQ_H is given by Q_{de}, and the cold utility saving ΔQ_C is given by Q_{re}.

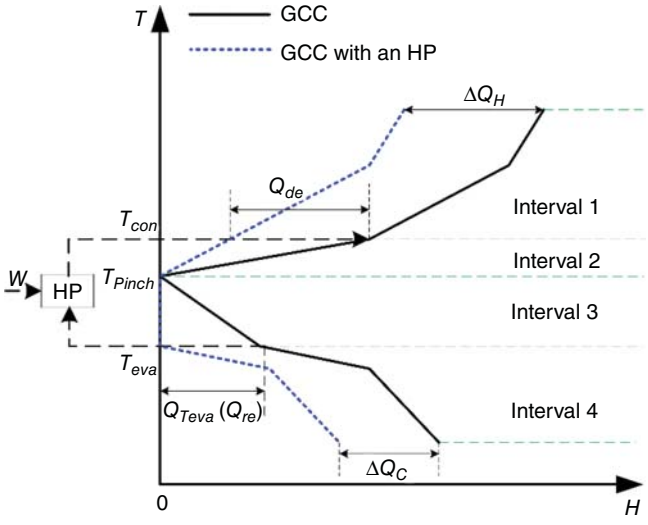

Figure 7.3 GCC with a pinch interval below the original pinch after placing a heat.

7.2.2 Case 2

A second case is shown in Figure 7.3, a heat pump is introduced into the system to receive heat (Q_{re}) at a temperature (T_{eva}) below the pinch, and Q_{re} equals the heat surplus ($Q_{T_{eva}}$) at T_{eva}. Similar to the first case, a new GCC can be formed as the dotted line. Figure 7.3 shows that the heat flux from the T_{Pinch} to T_{con} is zero, which can be defined as a pinch interval. In this case, ΔQ_C and ΔQ_H are equal to Q_{re} and Q_{de}, respectively.

7.2.3 Case 3

In the third case depicted in Figure 7.4, a heat pump is set to receive heat (Q_{re}) at a temperature (T_{eva}) below the pinch, and Q_{re} is larger than $Q_{T_{eva}}$. A new GCC is obtained as the dotted line in Figure 7.4a. It shows that a portion of the new GCC is located at the left side of the vertical axis, which means that the HEN is infeasible. To make the HEN feasible, the new GCC should be shifted to right side of the vertical axis totally as demonstrated in Figure 7.4b. The new GCC shows a pinch temperature, which is lower than the original pinch temperature. The placement of heat pump changes the pinch temperature of the system. In case 3, ΔQ_C is equal to $Q_{T_{eva}}$ but smaller than Q_{re}, while ΔQ_H is equal to $(Q_{T_{eva}} + W)$ but smaller than Q_{de}. The heat flux at the original pinch temperature is given by $(Q_{re} - Q_{T_{eva}})$ rather than zero.

In case 3, although the arrangement of the heat pump obeys the across-pinch rule, what obviously different from cases 1 and 2 is that the savings of cold and hot utilities are smaller than the heat received and delivered by the heat pump. With a further insight, a consequence of the decrease in pinch temperature is that the heat pump turns the interval 3 from a heat source to a heat sink. Thus, $(Q_{re} - Q_{T_{eva}})$ of the received heat below the original pinch is now found above

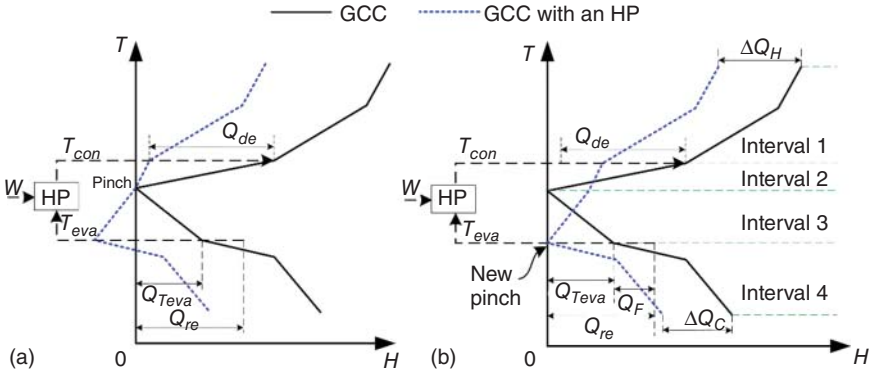

Figure 7.4 GCC with decreased pinch temperature after placing a heat pump: (a) intermediate GCC; (b) final GCC.

the new pinch, violating the across-pinch rule. As a result, this portion of heat $(Q_{re} - Q_{T_{eva}})$ cannot be used to reduce utility consumption.

7.2.4 Case 4

The fourth case is depicted in Figure 7.5, where a heat pocket is observed in the region below the pinch in the GCC. A heat pump is introduced into the system to receive heat (Q_{re}) at a temperature (T_{eva}) below the pinch, and Q_{re} is smaller than $Q_{T_{eva}}$ but larger than Q_P. A new GCC is formed as the dotted line given in Figure 7.5b. It indicates that a new pinch occurs and its temperature is lower than the original. As for utility savings, $\Delta Q_C = Q_P < Q_{re}$ and $\Delta Q_H = Q_P + W < Q_{de}$.

Because of the decrease in the pinch temperature, $(Q_{re} - Q_P)$ of the heat received by the heat pump from the original pinch now appears above the new pinch. Note that this is against the across-pinch rule. As a result, this portion of heat $(Q_{re} - Q_P)$ cannot be used for energy saving.

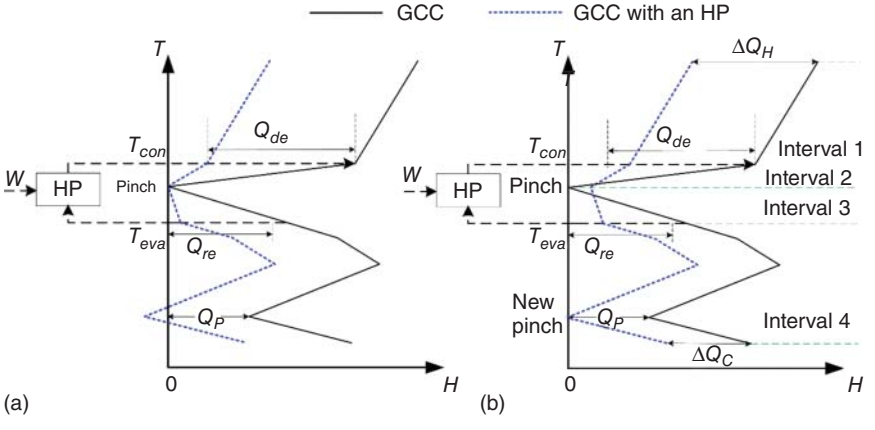

Figure 7.5 A heat pocket exists below the original pinch and GCC with decreased pinch temperature after placing a heat pump: (a) intermediate GCC; (b) final GCC.

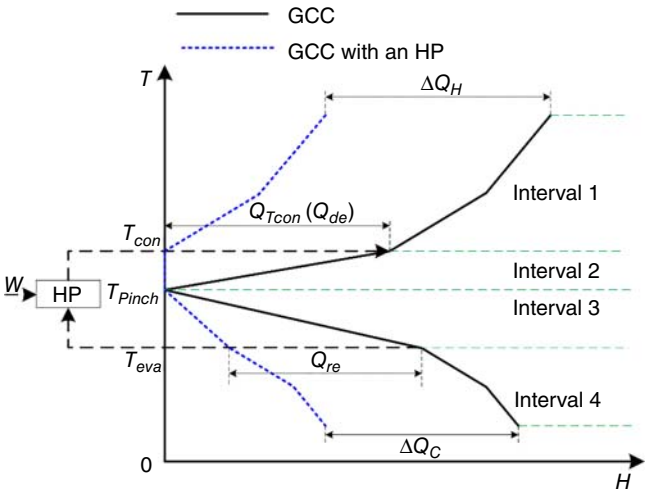

Figure 7.6 GCC with a pinch interval above the original pinch after placing a heat.

7.2.5 Case 5

In case 5, a heat pump delivers heat (Q_{de}) at the temperature (T_{con}) above the pinch, and Q_{de} is equal to $Q_{T_{con}}$. The new GCC is constructed as the dotted line in Figure 7.6. The heat flux from the T_{Pinch} to T_{con} is zero, forming a pinch interval, which is similar to that in case 2. In terms of the utility savings, ΔQ_C and ΔQ_H are also equal to Q_{re} and Q_{de}, respectively.

7.2.6 Case 6

Case 6 is given in Figure 7.7, where a heat pump delivers heat (Q_{de}) larger than $Q_{T_{con}}$ at the temperature (T_{con}) above the pinch. Similar to case 3, the initially constructed GCC is presented as the dotted line in Figure 7.7a and shifted to the right side of the vertical axis as shown in Figure 7.7b. It can be found that a new pinch appears above the original pinch after setting the heat pump. The placement of heat pump increases the pinch temperature of the system. The hot utility saving ΔQ_H is equal to $Q_{T_{con}}$, and the cold utility saving ΔQ_C is equal to $(Q_{T_{con}} - W)$. It is obvious that ΔQ_C and ΔQ_H are smaller than Q_{re} and Q_{de}, respectively. The reason is that the heat pump turns the interval 2 from a heat sink to a heat source, making $(Q_{de} - Q_{T_{con}})$ of the delivered heat below the new pinch. In other words, this violates the across-pinch rule. As a result, this part of heat $(Q_{de} - Q_{T_{con}})$ cannot be used to save utilities.

7.2.7 Case 7

In case 7, there is a heat pocket above the pinch in the GCC as illustrated in Figure 7.8. A heat pump is introduced into the system to deliver heat (Q_{de}) at a temperature (T_{con}) above the pinch. Q_{de} is smaller than $Q_{T_{con}}$ but larger than Q_P. This case is similar to case 5, and the new GCC is shown as the dotted line

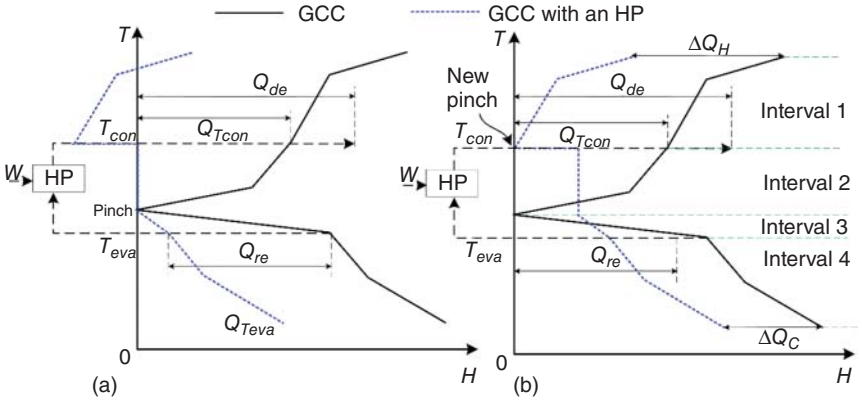

Figure 7.7 GCC with increased pinch temperature after placing a heat pump: (a) intermediate GCC; (b) final GCC.

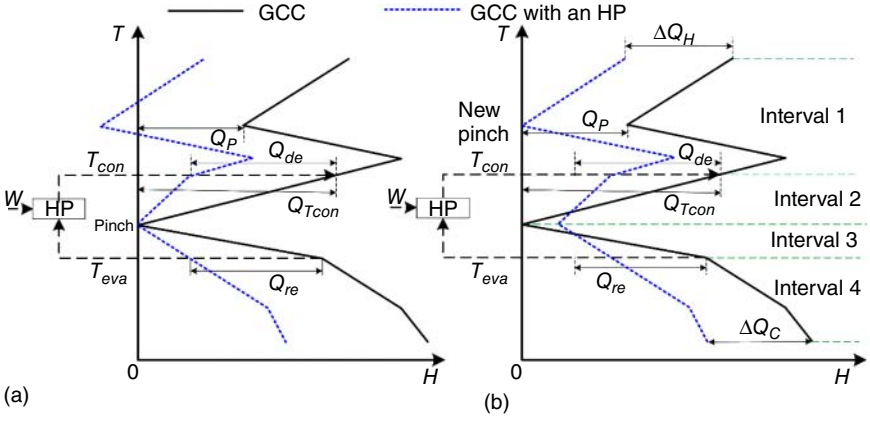

Figure 7.8 A heat pocket exists above the original pinch and GCC with increased pinch temperature after placing a heat pump: (a) intermediate GCC; (b) final GCC.

in Figure 7.8b. The placement of heat pump results in a new pinch temperature that is higher than the original one. It can be indicated that the heat pump turns the interval 2 from a heat sink to a heat source. Thus, $(Q_{de} - Q_P)$ of the delivered heat cannot save utilities. As for utility savings, $\Delta Q_C = Q_P - W < Q_{re}$ and $\Delta Q_H = Q_P < Q_{de}$.

Table 7.1 summarizes and compares all the results obtained from the seven cases. It can be found that when the original pinch is still the pinch after setting the heat pump, all the heat received and delivered by the heat pump can be used to save hot and cold utilities. Otherwise, there will be useless heat transfer although the heat pump is introduced following the across-pinch rule. Based on results summarized in Table 7.1, two following conditions can be derived when the original pinch remains unchanged after setting a heat pump.

Table 7.1 Summary of cases 1–7.

Cases	Pinch	Hot utility saving	Cold utility saving	Heat flux at original pinch	Reasons for pinch changes
1	No change	$\Delta Q_H = Q_{de}$	$\Delta Q_C = Q_{re}$	0	—
2	Pinch interval	$\Delta Q_H = Q_{de}$	$\Delta Q_C = Q_{re} = Q_{T_{eva}}$	0	—
3	Decrease	$\Delta Q_H = Q_{T_{eva}} + W < Q_{de}$	$\Delta Q_C = Q_{T_{eva}} < Q_{re}$	$Q_{re} - Q_{T_{eva}}$	$Q_{re} > Q_{T_{eva}}$
4	Decrease	$\Delta Q_H = Q_P + W < Q_{de}$	$\Delta Q_C = Q_P < Q_{re}$	$Q_{re} - Q_P$	$Q_{re} > Q_P$
5	Pinch interval	$\Delta Q_H = Q_{de} = Q_{T_{con}}$	$\Delta Q_C = Q_{re}$	0	—
6	Increase	$\Delta Q_H = Q_{T_{con}} < Q_{de}$	$\Delta Q_C = Q_{T_{con}} - W < Q_{re}$	$Q_{de} - Q_{T_{con}}$	$Q_{de} > Q_{T_{con}}$
7	Increase	$\Delta Q_H = Q_P < Q_{de}$	$\Delta Q_C = Q_P - W < Q_{re}$	$Q_{de} - Q_P$	$Q_{de} > Q_P$

(1) Heat (Q_{re}) received by a heat pump cannot exceed the heat surplus at temperature T_{eva}, which lies below the pinch temperature in the net GCC.
(2) Heat (Q_{de}) delivered by a heat pump cannot exceed the heat deficit at temperature T_{con}, which lies above the pinch temperature in the net GCC.

7.3 Integration of Heat Pump Assisted Distillation in the Overall Process

As presented by Linnhoff et al. [19], for a distillation column that is not located across the pinch of its background process, either the reboiler or condenser of the column can be integrated with hot or cold streams in the background process. To be specific, a reboiler of a column that is located in the region below the pinch can receive heat from the hot streams, thus reducing requirement of hot utility. Alternatively, a condenser of a column that is located in region above the pinch can reject heat to the cold streams, which also leads to reduced hot utility of the background process.

When a distillation process is located across the pinch, it can be considered to change the location of pinch so that both operating temperatures of its condenser and reboiler can lie above or below the new pinch. In Section 7.2, the changes of GCC were analyzed with a heat pump introduced into the system. In some cases, the pinch temperatures were changed due to the placement of heat pumps. Based on this observation, heat pumps can be strategically applied to change the pinch temperature of the background process for better heat integration [21].

7.3.1 Increase of Pinch Temperature

For a conventional distillation column, its reboiler absorbs heat Q_{reb} at temperature T_{reb} and the condenser rejects heat Q_{cond} at temperature T_{cond}. Assuming

that no subcooling or superheating for the condensation and evaporation, heat surplus and deficit of a distillation column can be represented as a quadrilateral box in the T–H diagram, as shown in Figure 7.9a [19]. The GCC of a background process is also depicted in Figure 7.9a, which illustrates the case in which a distillation column is located across the pinch and cannot be integrated with its background process directly. Thus, the total hot utility demand of the overall process is $Q_H = Q_{H,min} + Q_{reb}$, while the total cold utility demand is $Q_C = Q_{C,min} + Q_{cond}$.

A heat pump is introduced to change the pinch as shown in Figure 7.9b. The heat pump receives heat Q_{re} at temperature T_{eva} and delivers heat Q_{de} at temperature T_{con}. When Q_{de} is larger than the deficient heat $Q_{T_{con}}$ at temperature T_{con} in the GCC, the pinch is raised from P to P_1, and a new GCC is established. Consequently, the required hot utility for the background process is $Q_{H,\min} - Q_{T_{con}}$ and the required cold utility is $Q_{C,\min} + (Q_{de} - Q_{re}) - Q_{T_{con}}$. The distillation column is now located below the new GCC, as shown in Figure 7.9c. For the overall process, the total hot utility reduces to $Q_H = Q_{H,\min} - Q_{T_{con}}$ and the total cold utility is $Q_C = Q_{C,\min} + (Q_{de} - Q_{re}) - Q_{T_{con}} + Q_{cond} - Q_{reb}$. It should be noted that, in order to fully meet the heat demands of the distillation process, T_{con} should not be lower than T_{reb} and Q_{de} should be no less than $Q_{T_{con}} + Q_{reb}$.

Figure 7.10a shows a GCC of a background process with a heat pocket above the pinch, and a distillation column is located across the pinch. In Figure 7.10b, a heat pump is set across the pinch. Q_{re} is smaller than the $Q_{T_{eva}}$ at temperature T_{eva}, and Q_{de} is equal to $Q_{T_{con}}$ at temperature T_{con} but larger than Q_{P_1}. As a result, the pinch is now changed from point P to P_1. The new GCC shows that the new pinch temperature is higher than both T_{con} and T_{reb}. Heat integration between the distillation column and its background process can be achieved because the column is located below the new pinch of the updated GCC in Figure 7.10c. For

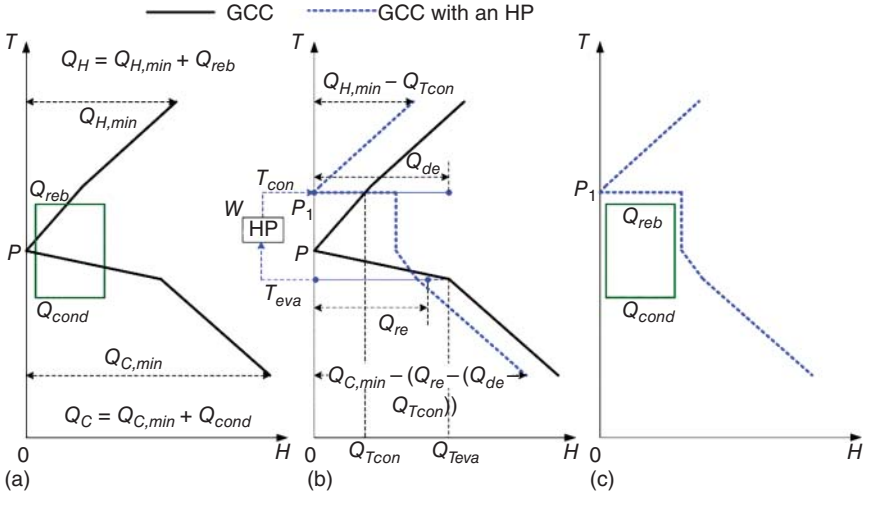

Figure 7.9 Heat integration based on the increased pinch temperature: (a) base case; (b) new GCC; (c) final integration.

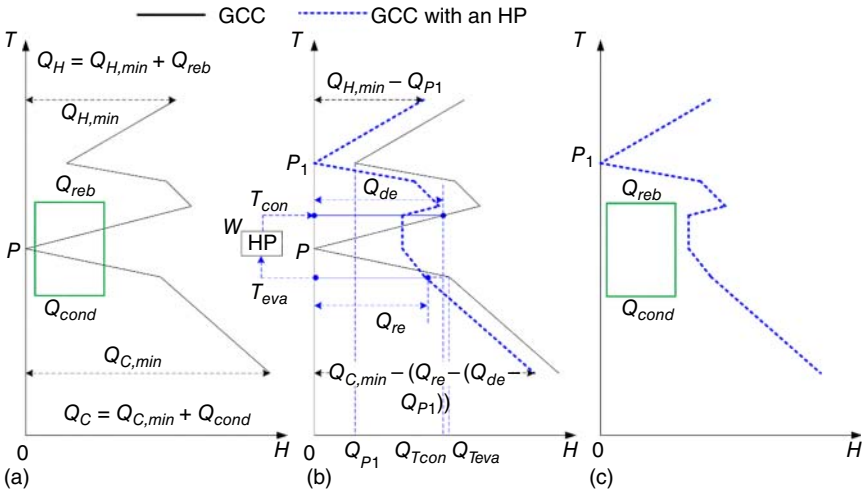

Figure 7.10 Heat integration based on the increased pinch temperature (a heat pocket above the original pinch): (a) base case: (b) new GCC; (c) final integration.

the overall process, the total hot utility is $Q_H = Q_{H,\min} - Q_{P_1}$ and the total cold utility is $Q_C = Q_{C,\min} + (Q_{de} - Q_{re}) - Q_{P_1} + Q_{cond} - Q_{reb}$.

Comparing the two cases in Figures 7.9 and 7.10, the reboiler of the distillation column in Figure 7.9 receives heat Q_{reb} from the heat pump, while in Figure 7.10, the reboiler receives heat Q_{reb} from the local heat source in the heat pocket. With the local heat source existing above the original pinch, the temperature lift for heat pumping is reduced. In this way, the heat in the pocket can be used for sinks with higher temperatures and better energy efficiency can be achieved.

7.3.2 Decrease of Pinch Temperature

Figure 7.11 illustrates the GCC for the case where the pinch is shifted downward for distillation column placement. In the base case, the column is located across the pinch. A heat pump is then set to operate across the pinch, as shown in Figure 7.11b. For this case, Q_{re} is larger than $Q_{T_{eva}}$ at temperature T_{eva}, and Q_{de} is equal to the deficient heat $Q_{T_{con}}$ at temperature T_{con}. With introduction of a heat pump, the pinch temperature is decreased from point P to P_1, and distillation column can be located above the new pinch, as shown in Figure 7.11c. For the overall process, the cold utility requirement is $Q_C = Q_{C,\min} - Q_{T_{eva}}$ and hot utility requirement is $Q_H = Q_{H,\min} - (Q_{de} - Q_{re}) - Q_{T_{eva}} + Q_{reb} - Q_{cond}$. It should be noted that the temperature T_{eva} cannot be higher than T_{cond} and Q_{re} cannot be smaller than $Q_{T_{eva}} + Q_{cond}$.

Similarly to the earlier scenario, here we look at the case of having a heat pocket below the pinch as well as a distillation column located across the pinch (Figure 7.12a). A heat pump is set to operate across the pinch, as shown in Figure 7.12b. When Q_{re} is larger than heat Q_P, the pinch is shifted downward from P to P_1 to achieve heat integration between distillation column and its background process, as shown in Figure 7.12c. For this case, T_{eva} is higher than T_{cond}

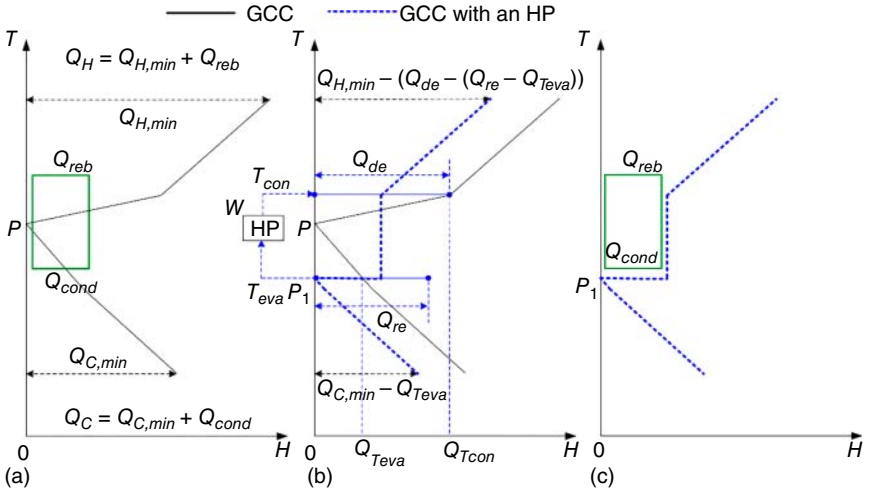

Figure 7.11 Heat integration based on the decreased pinch temperature: (a) base case; (b) new GCC; (c) final integration.

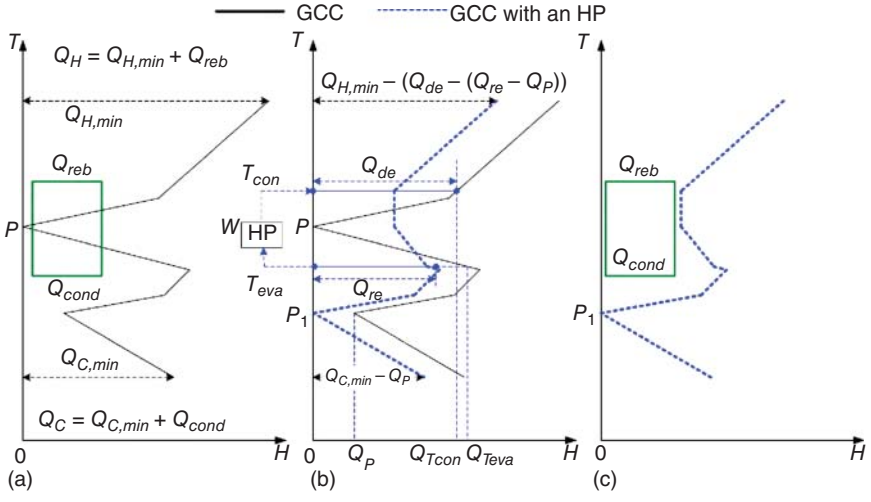

Figure 7.12 Heat integration based on the decreased pinch temperature (a heat pocket below the original pinch): (a) base case; (b) new GCC; (c) final integration.

but the new pinch temperature is lower than both T_{eva} and T_{cond}. For the overall process, the total hot utility is $Q_H = Q_{H,min} - (Q_{de} - Q_{re}) - Q_P + Q_{reb} - Q_{cond}$ and the total cold utility is $Q_C = Q_{C,min} - Q_P$.

7.3.3 No Change in Pinch Temperature

The previous text illustrates how to achieve integration between a distillation column and its background process by changing the pinch temperature. Additionally, there is potential for achieving better heat recovery without changing

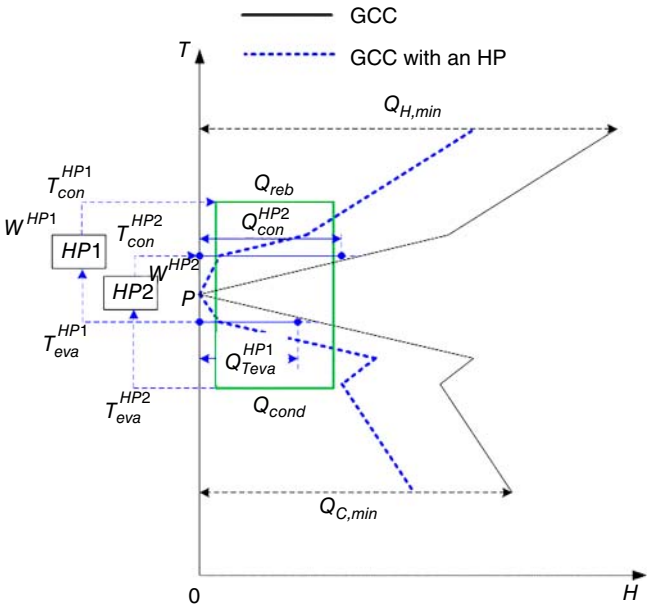

Figure 7.13 Heat integration with no change in pinch temperature.

the pinch temperature when heat pumps are integrated. As shown in Figure 7.13, heat pumps can be set at two different locations. Heat pump 1 receives heat from the background process and delivers heat to the reboiler of the distillation column, while heat pump 2 receives the heat from the condenser of the distillation column and delivers the heat to the background process. The amount of heat $Q_{T_{eva}}^{HP1}$ received by heat pump 1 is smaller than surplus heat of background process at temperature T_{eva}^{HP1}, and the amount of delivered heat Q_{con}^{HP2} of heat pump 2 is smaller than deficient heat at temperature T_{con}^{HP2}. Thus, pinch temperature remains the same for this case. Accordingly, the total hot utility required for the overall process is decreased from $(Q_{H,min} + Q_{reb})$ to $(Q_{H,\min} - T_{con}^{HP2})$ and the total cold utility is decreased from $(Q_{C,min} + Q_{cond})$ to $(Q_{C,\min} - Q_{T_{eva}}^{HP1})$.

Compared with cases in Sections 7.3.1 and 7.3.2, heat integration in this section is achieved without changes in the pinch temperature at the expense of an additional heat pump. For all heat pumps discussed in this section, their temperature lift can be smaller than the temperature difference between the reboiler and condenser of column. Besides, heat pumps are employed to supply heat for the distillation column as well as the background process. Such synergetic benefits gained from the proposed heat integration options provide more opportunities in heat recovery, leading to further energy savings. However, the specific characteristics of a distillation column and its background process will determine whether heat integration can be achieved and which is the better selection.

7.3.4 Heat Pump Placement

Heat integration of heat pumps, a distillation column, and its background process has been described in considerable detail. When designing or retrofitting an

HEN, the operating conditions of heat pumps and the streams matched with heat pumps need to be identified. These topics are discussed as follows.

A large temperature lift through a heat pump should be avoided because it reduces the *coefficient of performance* (COP) of the heat pump. To achieve the smallest possible temperature lift, an approach is presented to determine the energy-optimum operating conditions of a heat pump. For convenience, this design concept is illustrated with an example depicted in Figure 7.14.

Step 1:: Based on the GCC and the operating conditions of the distillation column, either Q_{re} or Q_{de} of a heat pump can be identified. As shown in Figure 7.14a, when Q_{de} is smaller than $Q_{reb} + Q_{T_{con}}$, the distillation column cannot be fully integrated into the overall process. On the contrary, when Q_{de} is larger than $Q_{reb} + Q_{T_{con}}$, this surplus heat $Q_{de} - (Q_{reb} + Q_{T_{con}})$ results in no savings for hot and cold utilities. Hence, the optimal Q_{de} is $(Q_{reb} + Q_{T_{con}})$. With this amount of heat available for heat integration, the lowest temperature T_{con} for the heat pump can be determined such that $Q_{T_{con}}$ is equal to Q_{de} from the GCC, as shown in Figure 7.14b.
In the GCC, the temperature of a cold stream is higher than its real value by $0.5\Delta T_{min}$ (minimum temperature difference for heat exchange), while the temperature of a hot stream is lower than its real value by $0.5\Delta T_{min}$. Therefore, Eqs. (7.2, 7.3) can be derived:

$$T_{con}^{real} = T_{con} + 0.5\Delta T_{\min} \tag{7.2}$$

$$T_{eva}^{real} = T_{eva} - 0.5\Delta T_{\min} \tag{7.3}$$

where the superscript *real* represents the actual stream conditions.

Step 2: Q_{re} and T_{eva} that correspond to Q_{de} at T_{con} can be estimated by simple empirical formulas or a rigorous mathematical model of heat pumps. One practical measure for evaluating the performance of a vapor compression heat pump is the COP, which is given in Eqs. (7.4, 7.5). Based on this, Q_{re} at T_{eva} can be expressed as Eq. (7.6). When T_{con} and Q_{de} are fixed, there is a positive linear correlation between Q_{re} and T_{eva}.

$$\mathrm{COP} = \frac{Q_{de}}{W} = \frac{Q_{de}}{Q_{de} - Q_{re}} \tag{7.4}$$

$$\mathrm{COP} = \eta_C \cdot \frac{T_{con} + 0.5\Delta T_{\min} + 273.2}{(T_{con} + 0.5\Delta T_{\min}) - (T_{eva} - 0.5\Delta T_{\min})} \tag{7.5}$$

$$\frac{Q_{de}}{Q_{de} - Q_{re}} = \eta_C \cdot \frac{T_{con} + 0.5\Delta T_{\min} + 273.2}{(T_{con} + 0.5\Delta T_{\min}) - (T_{eva} - 0.5\Delta T_{\min})} \tag{7.6}$$

where η_C is the Carnot efficiency.

Step 3: The GCC below the pinch shows that net heat surplus is in negative correlation to temperature. Based on Eq. (7.6) and the GCC, $Q_{re,}$ and T_{eva} can be determined. This allows integration between the distillation column and its background process, and the minimum temperature lift for the heat pump is identified.

Step 4: The next step is to select process streams to be integrated with the heat pump. Due to the high capital cost of heat pumps, and to reduce the

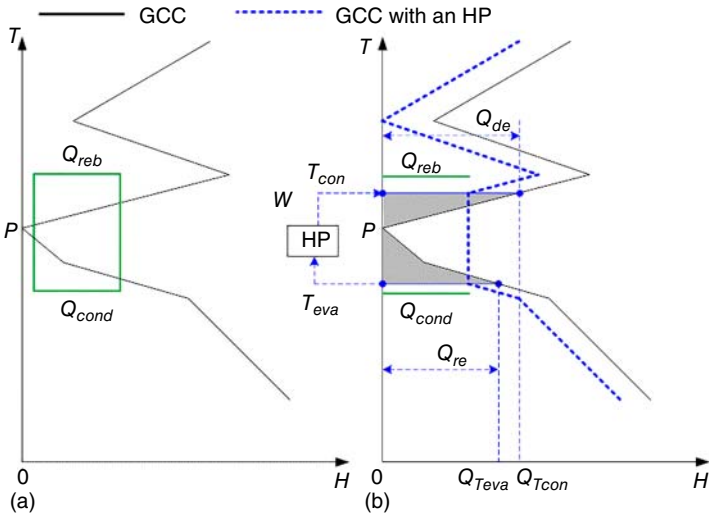

Figure 7.14 Example for identifying the operating parameters of heat pump.

number of heat pumps used, it is assumed that a heat pump is allowed to simultaneously receive heat from different hot streams and to deliver heat to different cold streams. Figure 7.15 shows the enlarged part of Figure 7.14 where the heat pump is integrated with GCC. The shaded parts represent the feasible regions for selecting hot and cold streams to be integrated with the heat pump. All hot and cold streams are expressed as a series of segments in the *T*–*H* diagram. A hot stream is expressed as a segment with a negative slope and a cold stream as a segment with a positive slope. If a hot or cold stream is desired to satisfy the corresponding heat demand of the heat pump, it is necessary to consider both its temperature and heat load. The procedure of selecting a stream is illustrated as below:

(1) Shift all segments of streams to the left until the right endpoint of these cold and hot streams coincide with the right end vertexes of the cold and hot shaded regions, indicated by points A and B, respectively. Any streams that cannot meet this requirement should not be considered for selection, e.g. cold stream 1.

(2) If the segment of a stream does not intersect with the vertical axis, for example, cold stream 2, the heat load of this stream is not big enough and this stream should not be considered as well.

(3) If a part of the segment appears outside of the shaded region, e.g. hot stream 1, this stream should also be excluded due to the infeasibility in heat exchange within the background process. Finally, hot stream 2 and cold stream 3 are the feasible streams for heat pump integration.

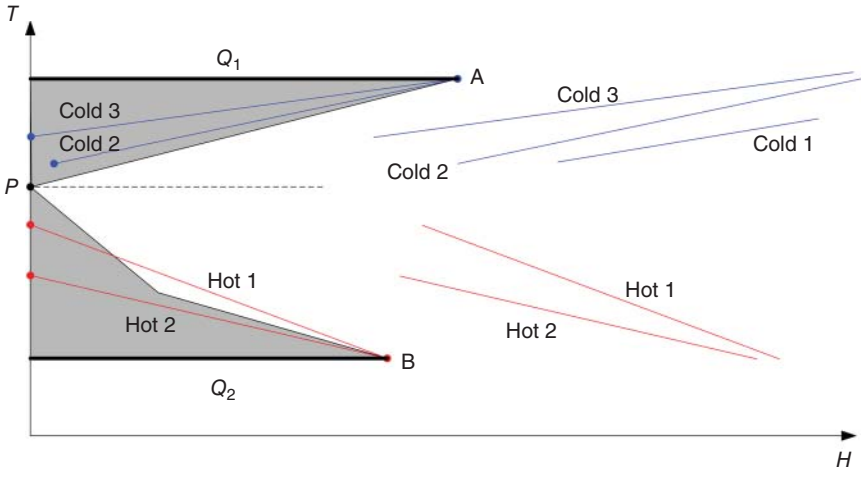

Figure 7.15 Determining the streams to be integrated with heat pump.

If a hot or cold stream cannot be selected for heat pump integration, combination of several streams is necessary. The way to select streams and to combine them should reflect the feasibility of heat transfer constrained by the shaded regions.

7.4 Case Study

This case study is used to illustrate the application of heat pump for achieving heat integration between a distillation process and its background process.

Table 7.2 shows the stream data of a chemical process. The energy performance of the background process is analyzed by pinch analysis. When ΔT_{min} is assumed to be 10 °C, the average pinch temperature is found to be 75 °C (i.e. 80 °C for hot streams and 70 °C for cold streams). The minimum hot and cold utilities are identified as 10 and 118 kW, respectively. When the distillation column is included, the total hot and cold utilities increase to 40 and 148 kW, respectively.

The GCC of the background process is given in Figure 7.16a. The latter also shows that the reboiler and condenser of a distillation column are located across the pinch. A vapor compression heat pump is introduced to facilitate heat integration. With the across-pinch rule, R142b with a critical temperature of 136.5 °C is chosen as the working fluid of the heat pump. Following the procedure described in Section 7.3.4, Q_{de} is found to be 48 kW, and T_{con} is determined as 92.2 °C (i.e. real temperature is 97.2 °C). It is assumed that the Carnot efficiency is 60%, when the heat pump receives heat from the heat source available in the background process. Hence, Q_{re} is determined as 38.9 kW and T_{eva} is 59.8 °C (i.e. real temperature is 54.8 °C). When the heat pump receives heat from the condenser of distillation column, T_{re} should be lower than 50 °C. It can be deduced that receiving heat from the background process is better than from the condenser. Although the operating conditions of the heat pump

Table 7.2 Stream data of the process.

Stream	Heat capacity flow rate (CP) (kW/°C)	T_{sup} (°C)	T_{tar} (°C)	Heat load (kW)
Hot 1	1	180	80	100
Hot 2	2	130	40	180
Hot 3	5	80	50	150
Cold 1	1.8	30	120	162
Cold 2	4	60	100	160
Column	Reboiler	130 (liquid)	130 (vapor)	38
	Condenser	60 (vapor)	60 (liquid)	40

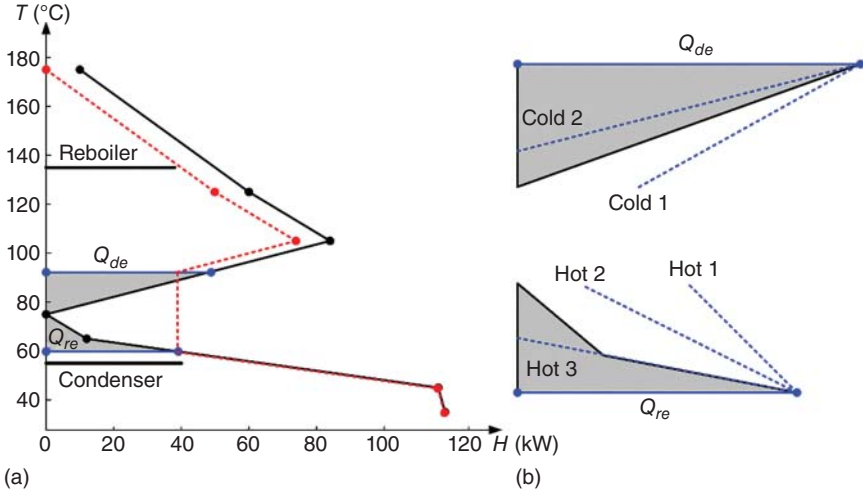

Figure 7.16 Identification of heat pump placement based on GCC: (a) determination of receiving and delivery temperatures; (b) selection of streams.

are determined by considering the minimum temperature lift for heat pumping, none of the hot streams can solely meet the heat duty required for integration with heat pump, as shown in Figure 7.16b. Note that the shade regions in Figure 7.16b are enlarged views of those in Figure 7.16a. It means that at least three heat exchangers (one condenser and two evaporators) are required in the heat pump system.

In Figure 7.16b, hot stream 3 is located close to the feasible region and thus it is selected as the heat source to supply heat to the heat pump. Now, new operating conditions for the heat pump are determined as Q_{re} equals 38.8 kW and T_{eva} (based on the actual temperature) equals 54.6 °C, as shown in Figure 7.17. The external energy supplied for the heat pump is 9.2 kW and the COP of the heat pump is 5.2. The heat pump receives 38.8 kW of heat from hot stream 3, and its temperature is reduced from 72.4 to 64.6 °C. The heat pump then rejects 48 kW

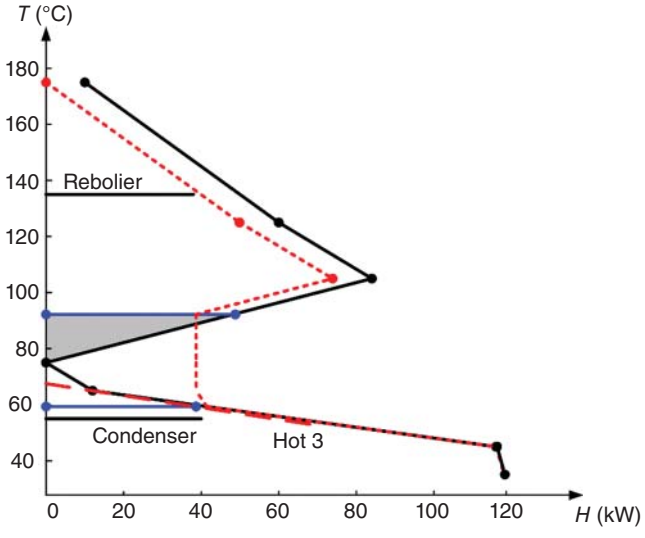

Figure 7.17 Improvement of heat pump placement.

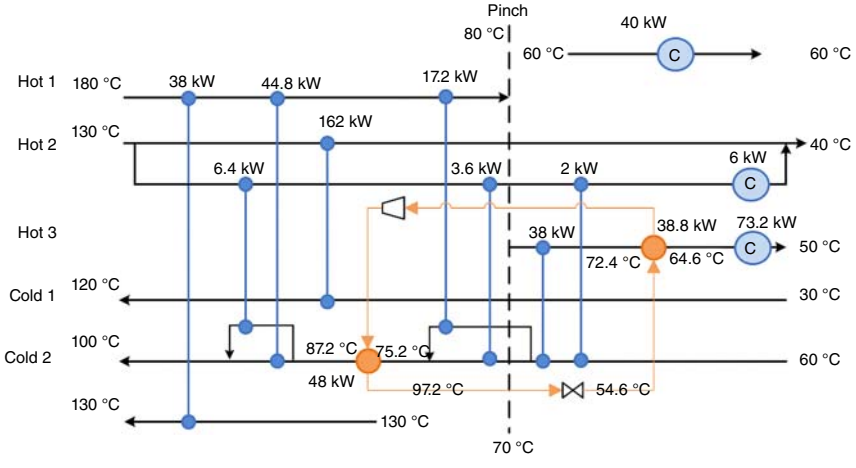

Figure 7.18 Resulting network after implementing the heat integration.

of heat to cold stream 2 and its temperature is increased from 75.2 to 87.2 °C. In this way, only two heat exchangers are required in the heat pump system, and a further increase in the temperature lift of heat pump is only 0.2 °C. Figure 7.18 shows the HEN after implementing the previous solutions. The total hot utility reduces to 0 kW and total cold utility decreases to 119.2 kW, i.e. reduction of 48 and 38.8 kW, respectively. The temperature lift of heat pump is 42.6 °C, which is smaller than the temperature difference between the reboiler and the condenser, i.e. 70 °C.

7.5 Conclusion

This chapter presents insightful analyses for integration of HEN and heat pumps. The pinch temperature of a process may be changed by setting a heat pump, which has implications for compliance with the across-pinch rule. The characteristics of variations on pinch temperature can be deduced from the net GCC. When a heat pump is integrated into a process, the pinch temperature will change if the delivered heat is larger than the net heat deficit at condensing temperature (in region above the pinch), or the received heat is larger than the heat surplus at evaporating temperature (in region below the pinch). With this principle, heat pumps can be used to facilitate heat integration between distillation and its background process. When a distillation process is located across the pinch, three possible scenarios for such heat integration are presented. The case study indicates that this method allows a smaller temperature lift for heat pump, compared with traditional heat pump assisted distillation, and provides more opportunities for energy saving.

References

1 U.S. Energy Information Administration (2019). International Energy Outlook 2019 with projections to 2050. https://www.eia.gov/outlooks/ieo/pdf/ieo2019.pdf (accessed 8 October 2019).
2 Gong, J. and You, F. (2015). Sustainable design and synthesis of energy systems. *Current Opinion in Chemical Engineering* 10: 77–86.
3 Klemeš, J.J. and Kravanja, Z. (2013). Forty years of Heat Integration: Pinch Analysis (PA) and Mathematical Programming (MP). *Current Opinion in Chemical Engineering* 2 (4): 461–474.
4 Grossmann, I.E., Caballero, J.A., and Yeomans, H. (2000). Advances in mathematical programming for the synthesis of process systems. *Latin American Applied Research* 30 (4): 263–284.
5 Kemp, I.C. (2011). *Pinch Analysis and Process Integration: A User Guide on Process Integration for the Efficient Use of Energy*. Butterworth-Heinemann.
6 Sreepathi, B.K. and Rangaiah, G.P. (2014). Review of heat exchanger network retrofitting methodologies and their applications. *Industrial and Engineering Chemistry Research* 53 (28): 11205–11220.
7 Townsend, D. and Linnhoff, B. (1983). Heat and power networks in process design. Part I: Criteria for placement of heat engines and heat pumps in process networks. *AIChE Journal* 29 (5): 742–748.
8 Becker, H., Vuillermoz, A., and Maréchal, F. (2012). Heat pump integration in a cheese factory. *Applied Thermal Engineering* 43: 118–127.
9 Wallerand, A.S., Kermani, M., Kantor, I., and Maréchal, F. (2018). Optimal heat pump integration in industrial processes. *Applied Energy* 219: 68–92.
10 Kang, L. and Liu, Y. (2015). Multi-objective optimization on a heat exchanger network retrofit with a heat pump and analysis of CO_2 emissions control. *Applied Energy* 154 (15): 696–708.

11 Bagajewicz, M.J. and Barbaro, A.F. (2003). On the use of heat pumps in total site heat integration. *Computers and Chemical Engineering* 27 (11): 1707–1719.

12 Liu, Z.-Y. and Jobson, M. (1999). The effect of operating pressure on distillation column throughput. *Computers & Chemical Engineering* 23: 831–834.

13 Abolpour, B., Abolpour, R., Shamseddini, A. et al. (2013). Optimization of the reflux ratio for methanol-water stage distillation column. *Research on Chemical Intermediates* 39 (2): 681–692.

14 Jana, A.K. (2010). Heat integrated distillation operation. *Applied Energy* 87 (5): 1477–1494.

15 Caballero, J.A. and Grossmann, I.E. (2014). Optimal synthesis of thermally coupled distillation sequences using a novel MILP approach. *Computers and Chemical Engineering* 61: 118–135.

16 Sayyaadi, H. and Saffari, A. (2010). Thermoeconomic optimization of multi effect distillation desalination systems. *Applied Energy* 87 (4): 1122–1133.

17 Fonyo, Z. and Mizsey, P. (1994). Economic application of heat pumps in integrated distillation systems. *Heat Recovery Systems and CHP* 14 (3): 249–263.

18 An, W., Yu, F., Dong, F., and Hu, Y. (2008). Simulated annealing approach to the optimal synthesis of distillation column with intermediate heat exchangers. *Chinese Journal of Chemical Engineering* 16 (1): 30–35.

19 Linnhoff, B., Dunford, H., and Smith, R. (1983). Heat integration of distillation columns into overall processes. *Chemical Engineering Science* 38 (8): 1175–1188.

20 Yang, M., Feng, X., and Chu, K.H. (2013). Graphical analysis of the integration of heat pumps in chemical process systems. *Industrial and Engineering Chemistry Research* 52 (24): 8305–8310.

21 Yang, M., Feng, X., and Liu, G. (2016). Heat integration of heat pump assisted distillation into the overall process. *Applied Energy* 162: 1–10.

8

Insightful Analysis and Integration of Reactor and Heat Exchanger Network

Di Zhang, Guilian Liu, and Xiao Feng

Xi'an Jiaotong University, School of Chemical Engineering and Technology, No. 28, Xianning West Road, Xi'an, Shaanxi 710049, China

8.1 Introduction

Energy is an important element for the development of the world economy. With global gross domestic product (GDP) rising by 3.6% each year, the world energy consumption will increase by 56% between 2010 and 2040 [1]. Hence, the contradiction between the demand and supply of energy will become more intense. Chemical production consumes high amount energy, whose cost accounts for 20–30% of its total production cost for most chemical products, and up to 70–80% for high-energy-consumption product [2]. It is hence necessary to reduce the energy consumption, in order to reduce the production cost.

Integration of *heat exchanger network* (HEN) is effective in reducing energy consumption and enhances economic and environmental performances of chemical processes. In the past four decades, HEN has been an active area of research. Many systematic methods have been developed based on pinch analysis techniques and mathematical programming methods [3–6].

In a chemical process, reactor is the core unit that converts raw material into desired product(s). Although hot and cold utilities are mainly consumed in the HEN, reactor should also be considered in the effort to reduce energy consumption. The reason is that inlet and outlet streams of the reactor are generally heat sink/source, which need to be heated/cooled, as shown by Figure 8.1. Hence, adjusting the reactor's parameters will affect the temperature and duty of its associated sink/source, as well as the HEN performance. Glavič et al. [7] analyzed the thermodynamic characteristic of reactors and integrated it with the overall background process and identified its appropriate placement based on the pinch method. In a later work, a method is proposed to match the temperature–reaction heat curve with the *heat recovery pinch diagram* (HRPD) [8]. Based on this concept, all energy-consuming units can be taken as hot/cold streams and be integrated with the overall process [9]. In a much later work, the integration of multiple reactors was also investigated [10].

Altering energy consumption of a chemical process might affect the yield of its desired product. Hence, increasing/reducing the energy consumption should be

Process Intensification and Integration for Sustainable Design, First Edition.
Edited by Dominic C. Y. Foo and Mahmoud M. El-Halwagi.
© 2021 WILEY-VCH GmbH. Published 2021 by WILEY-VCH GmbH.

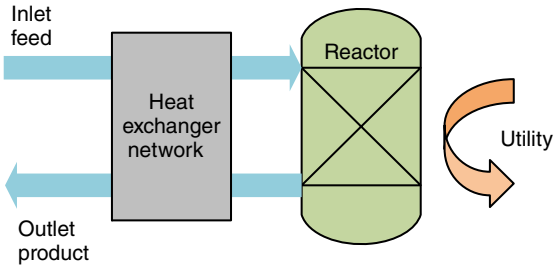

Figure 8.1 Interactions between HEN and reactor.

well balanced with the production of desired product. This can be achieved by evaluating the energy consumption of unit production, which is one of the key factors affecting the overall cost of the process. To achieve this, it is necessary to optimize the operating condition of the reactor and its energy consumption simultaneously.

This chapter introduces a pinch-based graphical methodology for the integration of HEN and reactor [11, 12]. By coupling the reactor model with pinch technique, the effect of temperature variation on HEN is analyzed for exothermic and endothermic reactions. Relations among temperatures, selectivity, utilities, energy consumption of unit product, and conversion are deduced and plotted in a *combined multi-parameter optimization diagram* (CMOD), which can be used to identify the optimal utilities, inlet/outlet temperature, selectivity, and conversion of the reactor.

8.2 Influence of Temperature Variation on HEN

8.2.1 Location of Cold and Hot Streams

In an HEN, there are multiple hot streams to be cooled and multiple cold streams to be heated. Within the HRPD, different streams lie in different segments in the hot and cold composite curves. The following rules can be used to identify their characteristics [13].

Rule 1: For two neighboring segments of the hot composite curve, the one with smaller slope indicates that it has an additional hot stream (SR_i) than the other. If SR_i lies below a turning point, the latter corresponds to its supply temperature, otherwise, it is its target temperature.

Rule 2: For two neighboring segments of the cold composite curve, the one with smaller slope has an additional cold stream (SK_j) than the other. If SK_j lies below the turning point, the latter corresponds to its target temperature, otherwise, it is its supply temperature.

According to these rules, it is easy to identify the location of the corresponding hot and cold streams in the HRPD. For example, for the hot and cold composite curves in Figure 8.2, it can be analyzed that point C corresponds to supply temperature of a hot stream that is found in segment BC. Note that this stream is not found in segment AB. On the other hand, point C′ corresponds to target temperature of a cold stream that appears in B′C′, but not in segment C′D′.

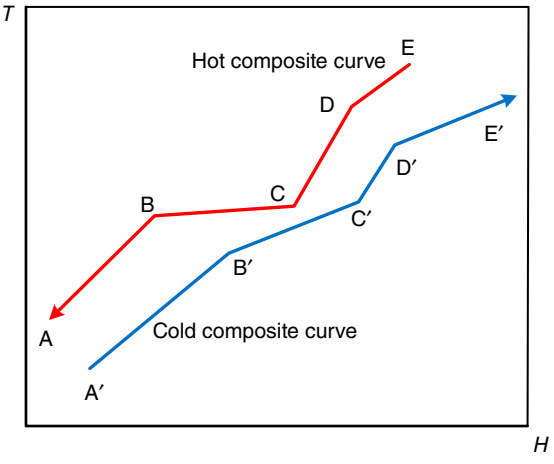

Figure 8.2 An HRPD with hot and cold composite curves.

8.2.2 Effect of Temperature Variation

For an exothermic reaction that is operated at high temperature, inlet stream of the reactor is usually a cold stream (SK_q), while its effluent acts as a hot stream (SR_p). Based on composite curves, the influence of the reactor's inlet and outlet temperature (T_0 and T) could be studied.

Figure 8.3 shows the HRPD for an illustrative example. In this figure, the pinch lies at point P. CDEPFGN and HIJKLM are the turning points of the hot and cold composite curves, respectively. The minimal hot and cold utilities are labeled as $Q_{H,min,}$ and $Q_{C,min}$, respectively. The reactor is operated at a high temperature in order to increase its reaction rate. As shown in Figure 8.3, both T and T_0 lie in region above the pinch, and they correspond to points D and J, respectively.

When T increases to T', the horizontal line corresponding to T' intersects the hot composite curve at point D′. In temperature interval $[T, T']$, the heat capacity flow rate (CP, the product of heat capacity and flow rate) corresponding to section DD′ increases by that of SR_p, as this hot stream exists in this interval. The segment in temperature interval $[T', T_C]$ is not affected, and thus point C should move rightward to point C′. It is noteworthy that the flow rate or composition of the outlet stream will alter along with the reaction conversion, which may vary the CP of this stream. The corresponding variation, ΔCP, can be calculated by Eq. (8.1). If ΔCP > 0, point D′ should move rightward to D″ by $\Delta CP \times (T' - T_E)$, and point C′ need to be shifted with the same distance to C″. If ΔCP < 0, they should be shifted leftward. Note that T_E represents the target temperature of SR_p.

$$\Delta CP = F_A^0 N(X' - X) \tag{8.1}$$

where, F_A^0 stands for the inlet molar flow rate of the key component A; N is the difference of heat capacity between the outlet and inlet stream of the reactor; X′ is the conversion of component A when T of SR_p increases to T'.

If there are other turning points between the supply and target temperatures of SR_p, each of these turning points should be shifted by $\Delta CP \times (T_{tur} - T_E)$. T_{tur} is the temperature of the turning point lies between the supply and target temperatures of SR_p.

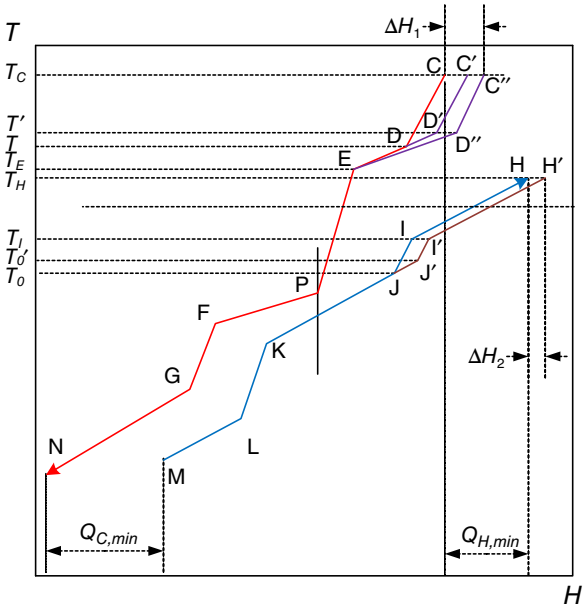

Figure 8.3 Variation of hot and cold composite curves when temperatures of SR_p and SK_q increase (exothermic reaction).

Consequently, in Figure 8.3, C″D″DEPFGN represents the new hot composite curve, and C″C indicates the incremental energy provided by hot streams, labeled as ΔH_1, which can be calculated by Eq. (8.2).

$$\Delta H_1 = \mathrm{CP}_{SR_p}(T' - T) + \Delta CP(T' - T_E) \tag{8.2}$$

If T_0 increases, the variation of cold composite curve can be identified in a similar way. H′I′J′JKLM represents the new cold composite curve when the target temperature of SK_q increases from T_0 to T_0'. H′H represents the incremental energy demanded by all cold streams and is denoted as ΔH_2, which also equals to that of SK_q. Hence, the variation of hot utility, ΔH, is

$$\begin{aligned}\Delta H &= \Delta H_2 - \Delta H_1 \\ &= \mathrm{CP}_{SK_q}(T_0' - T_0) - \mathrm{CP}_{SR_p}(T' - T) - \Delta CP(T' - T_E)\end{aligned} \tag{8.3}$$

As parameters of reactor change, the energy added or removed from the reactor will change correspondingly. The energy variation, denoted as ΔH_3, can be calculated by Eq. (8.4).

$$\Delta H_3 = (m_T' - m_T)\mathrm{CP}_T(T_{a2} - T_{a1}) = Q' - Q \tag{8.4}$$

where m_T' is the flow rate of utility stream and Q' is the heat supplied to reactor at temperature T'.

In conclusion, the change of composite curves and utility consumptions can be obtained followed by the steps shown in Figure 8.4.

For some cases, the inlet stream of the reactor is a heat source in the HEN and needs to be cooled to the specified inlet temperature of the reactor. The outlet stream of the reactor is a heat sink and needs to be heated. It is noteworthy that the inlet temperature is always the target temperature and the outlet temperature is the supply temperature, regardless of a cold or hot stream in the HEN. However,

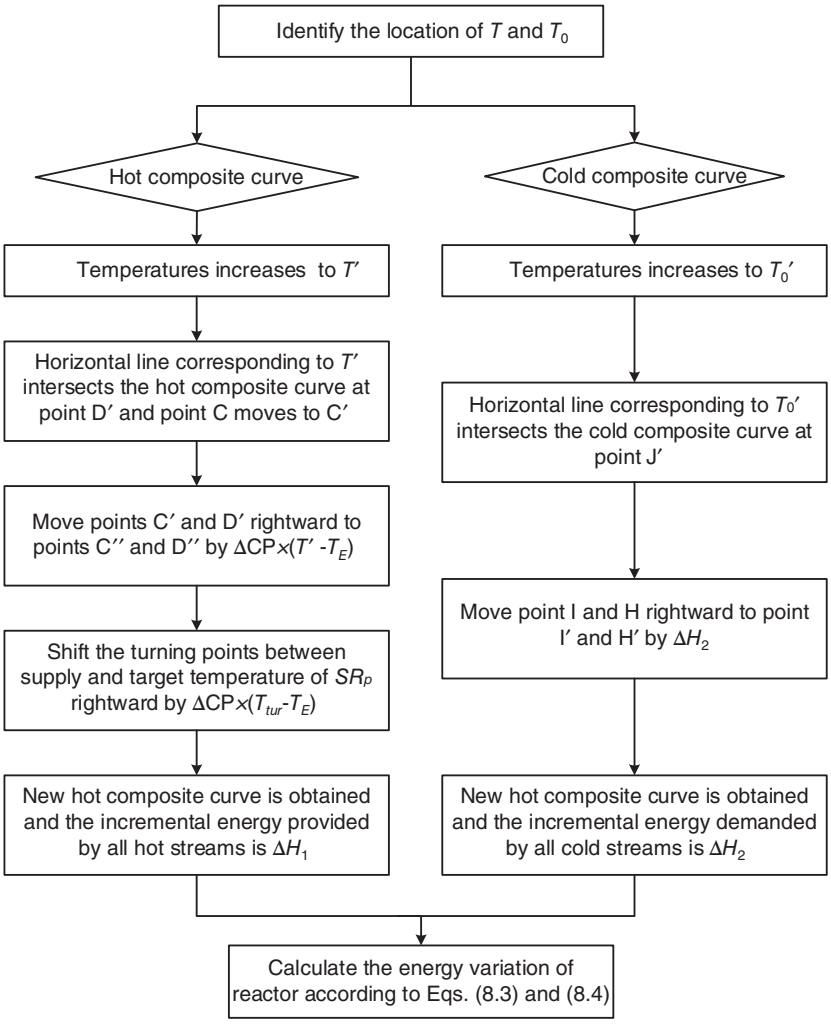

Figure 8.4 Procedure for determining the new composite curves and energy consumptions.

the location of this pair of hot and/or cold streams might be different in various chemical processes. Assuming that the pinch position stays unchanged, the variation of the energy consumption can be identified when the inlet and outlet streams of the reactor are different combinations of sink and/or source and with different relative locations to the pinch point. The results of utility variation for exothermic reaction are listed in Table 8.1.

For endothermic reactions, the variation of the utility consumption can be identified by the same method, and the results are listed in Table 8.2.

For some cases, the pinch position varies accordingly as the inlet and outlet temperatures change. The hot and cold composite curves should be shifted to meet the minimum approach temperature.

Table 8.1 Variation of energy consumptions for exothermic reaction.

			Utility variation	
Location	**Inlet stream**	**Outlet stream**	**Hot (ΔH_H)**	**Cold (ΔH_C)**
Above the pinch	Source	Source	$\Delta H_2 - \Delta H_1$	ΔH_3
	Source	Sink		
	Sink	Source		
	Sink	Sink		
Below the pinch	Source	Source	Unchanged	$\Delta H_1 - \Delta H_2 + \Delta H_3$
	Source	Sink		
	Sink	Source		
	Sink	Sink		
Across the pinch	Source	Source	$-\Delta H_1$	$\Delta H_3 - \Delta H_2$
	Source	Sink		
	Sink	Source		
	Sink	Sink		

Table 8.2 Variation of energy consumptions for endothermic reaction.

			Utility variation	
Location	**Inlet stream**	**Outlet stream**	**Hot (ΔH_H)**	**Cold (ΔH_C)**
Above the pinch	Source	Source	$\Delta H_2 - \Delta H_1 - \Delta H_3$	Unchanged
	Source	Sink		
	Sink	Source		
	Sink	Sink		
Below the pinch	Source	Source	$-\Delta H_3$	$\Delta H_1 - \Delta H_2$
	Source	Sink		
	Sink	Source		
	Sink	Sink		
Across the pinch	Source	Source	$-\Delta H_1 - \Delta H_3$	$-\Delta H_2$
	Source	Sink		
	Sink	Source		
	Sink	Sink		

8.3 Relation Among Reactor Parameters

For a reactor with series reactions, the inlet and outlet streams are sink/source of HEN in relation to both the conversion and selectivity of reactions. The relation among the reactor temperature, conversion, and selectivity is affected by the catalyst, type, and parameters of reactor.

8.3.1 Relation Among Temperatures, Selectivity, and Conversion of Reactor

For a system with multiple irreversible reactions described in the following, W and B represent raw materials, C is the desired product, and D is the byproduct. For convenience, the primary and secondary reactions are numbered as 1 and 2, respectively. The reaction rate of component W for reaction 1 (r_{1W}) is given as Eq. (8.5), and that of B for reaction 2 (r_{2B}) is represented by Eq. (8.6).

$$\text{Primary reaction } \ \mathrm{W} + \mathrm{B} \xrightarrow{1} \mathrm{C}$$

$$\text{Secondary reaction } \ \mathrm{B} + \mathrm{C} \xrightarrow{2} \mathrm{D}$$

$$-r_{1\mathrm{W}} = k_1 c_{\mathrm{W}}^{\alpha_1} c_{\mathrm{B}}^{\beta_1} c_{\mathrm{C}}^{\nu_1} \tag{8.5}$$

$$-r_{2\mathrm{B}} = k_2 c_{\mathrm{B}}^{\beta_2} c_{\mathrm{C}}^{\nu_2} c_{\mathrm{D}}^{\delta_2} \tag{8.6}$$

where k_1 and k_2 are the rate constants of reactions 1 and 2, respectively; c_{W}, c_{B}, c_{C}, and c_{D} are the molar concentration of species W, B, C, and D; α_1, β_1, and ν_1 are the reaction orders of species W, B, and C for reaction 1; β_2, ν_2, and δ_2 are the reaction orders of species B, C, and D for reaction 2.

The rate constants k_1 and k_2 are associated with the reactor temperature (T) and the activation energy, as represented by Eqs. (8.7) and (8.8).

$$k_1 = A_1 \exp\left(-\frac{E_1}{RT}\right) \tag{8.7}$$

$$k_2 = A_2 \exp\left(-\frac{E_2}{RT}\right) \tag{8.8}$$

where A_1 and A_2 are pre-exponential factors of reactions 1 and 2; E_1 and E_2 are the activation energy for these two reactions, respectively. The activation energy is mainly determined by the catalyst and temperature, and the influence of temperature on it can be ignored within a small temperature interval.

The reactors applied for the studied multiple reactions can be either a continuous well-mixed-reactor (CSTR) or a plug-flow reactor (PFR), and the corresponding design equations to achieve a specific conversion without pressure drop are shown by Eqs. (8.9) and (8.10), respectively.

$$\frac{V}{F_{\mathrm{W}}^0} = \frac{X}{-r_{1\mathrm{W}}} \tag{8.9}$$

$$\frac{V}{F_{\mathrm{W}}^0} = \int_0^X \frac{dX}{-r_{1\mathrm{W}}} \tag{8.10}$$

where V is the volume of the reactor; X and F_{W}^0 represent the conversion and the inlet molar flow rate of W, respectively.

The selectivity of component W (S) is directly relevant to the yield of product, and it can be calculated by Eq. (8.11).

$$\mathrm{S} = \frac{r_{1\mathrm{W}} - r_{2\mathrm{B}}}{r_{1\mathrm{W}}} \tag{8.11}$$

The concentration of each component at the outlet is related to the chemical stoichiometric factors, conversion, and selectivity and can be estimated according to Eqs. (8.12–8.15).

$$c_{\mathrm{W}} = c_{\mathrm{W}}^{0}(1 - X) \tag{8.12}$$

$$c_{\mathrm{B}} = c_{\mathrm{B}}^{0} - 2c_{\mathrm{W}}^{0}X + c_{\mathrm{W}}^{0}XS \tag{8.13}$$

$$c_{\mathrm{C}} = c_{\mathrm{C}}^{0} + c_{\mathrm{W}}^{0}XS \tag{8.14}$$

$$c_{\mathrm{D}} = c_{\mathrm{D}}^{0} + c_{\mathrm{W}}^{0}X(1 - S) \tag{8.15}$$

The relation among selectivity, conversion, activation energy, composition, and temperature can be represented by Eq. (8.16), which is derived based on Eqs. (8.5–8.15). Furthermore, for CSTR and PFR, Eqs. (8.17) and (8.18) describe the relation among conversion X, selectivity S, and reaction temperature T, respectively. Based on the activation energy and feed composition, the reaction temperature and selectivity at a specific conversion can be obtained by these equations. Note that the influence of temperature on active energy is ignored in the derivation.

$$S = 1 - \frac{k_2[c_{\mathrm{B}}^{0} - 2c_{\mathrm{W}}^{0}X + c_{\mathrm{W}}^{0}XS]^{\beta_2}[c_{\mathrm{C}}^{0} + c_{\mathrm{W}}^{0}XS]^{\nu_2}[c_{\mathrm{D}}^{0} + c_{\mathrm{W}}^{0}X(1 - S)]^{\delta_2}}{A_1 \exp\left(-\frac{E_1}{RT}\right)[c_{\mathrm{W}}^{0}(1 - X)]^{\alpha_1}[c_{\mathrm{B}}^{0} - 2c_{\mathrm{W}}^{0}X + c_{\mathrm{W}}^{0}XS]^{\beta_1}[c_{\mathrm{C}}^{0} + c_{\mathrm{W}}^{0}XS]^{\nu_1}} \tag{8.16}$$

$$\frac{V}{F_{\mathrm{W}}^{0}} = \frac{X_{\mathrm{W}}}{A_1 \exp\left(-\frac{E_1}{RT}\right)[c_{\mathrm{W}}^{0}(1 - X)]^{\alpha_1}[c_{\mathrm{C}}^{0} - 2c_{\mathrm{W}}^{0}X + c_{\mathrm{W}}^{0}XS]^{\beta_1}[c_{\mathrm{C}}^{0} + c_{\mathrm{W}}^{0}XS]^{\nu_1}} \tag{8.17}$$

$$\frac{V}{F_{\mathrm{W}}^{0}} = \int_{0}^{X_{\mathrm{W}}} \frac{dX_{\mathrm{W}}}{k_1[c_{\mathrm{W}}^{0}(1 - X)]^{\alpha_1}[c_{\mathrm{B}}^{0} - 2c_{\mathrm{W}}^{0}X + c_{\mathrm{W}}^{0}XS]^{\beta_1}[c_{\mathrm{C}}^{0} + c_{\mathrm{W}}^{0}XS]^{\nu_1}} \tag{8.18}$$

In addition to the operating parameters and the catalyst, the inlet temperature and energy added to the reactor also affect the outlet temperature. At steady state, when the reactants flow into the reactor at temperature (T_0), the relation among them is derived according to the energy balance, as shown by Eq. (8.19).

$$Q - W - F_{\mathrm{W}}^{0}\sum \frac{F_0^i}{F_{\mathrm{W}}^{0}}\mathrm{Cp}_i(T - T_0) - V[r_{1\mathrm{W}}\Delta H_{Rx1}(T) + r_{2\mathrm{B}}\Delta H_{Rx2}(T)] = 0 \tag{8.19}$$

where Q and W are the energy and work inlet into the reactor, respectively; i denotes species i; F_0^i is the molar flow rate of species i flowing into the reactor; Cp_i is the heat capacity of species i; ΔH_{Rx1} and ΔH_{Rx2} are the heat of reactions 1 and 2, respectively.

The heat of reactions 1 and 2, namely, ΔH_{Rx1} and ΔH_{Rx2}, can be estimated by Eqs. (8.20) and (8.21), respectively.

$$\Delta H_{Rx1}(T) = \Delta H_{Rx1}^{o}(T_R) + \Delta \mathrm{Cp}_1(T - T_R) \tag{8.20}$$

$$\Delta H_{Rx2}(T) = \Delta H_{Rx2}^{o}(T_R) + \Delta \mathrm{Cp}_2(T - T_R) \tag{8.21}$$

where $\Delta H^o_{Rx1}(T_R)$ and $\Delta H^o_{Rx2}(T_R)$ are the reaction heat at the reaction pressure and the reference temperature T_R (usually taken as 298.15 K); $\Delta \mathrm{Cp}_1$ and $\Delta \mathrm{Cp}_2$ are the difference of heat capacity between the products and reactants of reactions 1 and 2, respectively.

The utility stream is used to supply energy to the reactor or remove that from the reactor. It is assumed that the utility stream enters the external jacket of the reactor at flow rate m_T (with heat capacity of Cp_T) and temperature T_{a1} and leaves at temperature T_{a2} without phase transition. The heat transfer can be calculated by Eq. (8.22). If T_{a1} and T_{a2} are constant, the energy supplied to or removed from the reactor can be adjusted by controlling the flow rate of the utility stream, m_T.

$$Q = m_T \mathrm{Cp}_T (T_{a1} - T_{a2}) \tag{8.22}$$

For exothermic reactions, the reactor needs to be cooled down, and thus Q is negative. For endothermic reactions that need heat supply, Q is positive.

Since the temperature is identical within a CSTR, but varies along the radial direction in a PFR, these two types of reactors are analyzed separately, as follows.

8.3.1.1 CSTR

For exothermic reactions, $T > T_{a2} > T_{a1}$, while for endothermic reactions, $T_{a1} > T_{a2} > T$. With the assumption that T_{a1} and T_{a2} keep unchanged, the energy added to or removed from the reactor can be calculated by Eq. (8.23). The flow rate of utility stream m_T changes according to Eq. (8.22).

$$Q = \frac{UA(T_{a1} - T_{a2})}{\ln \frac{T - T_{a1}}{T - T_{a2}}} \tag{8.23}$$

where U is the total heat transfer coefficient and A is the heat transfer area.

For cases where $W_S = 0$, Eq. (8.19) can be written into Eq. (8.24) that shows the relation among the inlet and outlet temperatures (T and T_0) and the conversion (X).

$$T_0 = T - \frac{\frac{UA(T_{a1} - T_{a2})}{\ln \frac{T - T_{a1}}{T - T_{a2}}} - Vr_{1\mathrm{W}}[\Delta H^o_{Rx1}(T_R) + N_1(T - T_R)] - Vr_{2\mathrm{B}}[\Delta H^o_{Rx2}(T_R) + N_2(T - T_R)]}{F^0_{\mathrm{W}} M} \tag{8.24}$$

Define

$$M = \sum \frac{F^0_i}{F^0_{\mathrm{W}}} \mathrm{Cp}_i = \mathrm{Cp}_{\mathrm{W}} + \frac{F^0_{\mathrm{B}}}{F^0_{\mathrm{W}}} \mathrm{Cp}_{\mathrm{B}} + \frac{F^0_{\mathrm{C}}}{F^0_{\mathrm{W}}} \mathrm{Cp}_{\mathrm{C}} + \frac{F^0_{\mathrm{D}}}{F^0_{\mathrm{W}}} \mathrm{Cp}_{\mathrm{D}} \tag{8.25}$$

$$N_1 = \Delta \mathrm{Cp}_1 = \mathrm{Cp}_{\mathrm{C}} - \mathrm{Cp}_{\mathrm{B}} - \mathrm{Cp}_{\mathrm{W}} \tag{8.26}$$

$$N_2 = \Delta \mathrm{Cp}_2 = \mathrm{Cp}_{\mathrm{D}} - \mathrm{Cp}_{\mathrm{C}} - \mathrm{Cp}_{\mathrm{B}} \tag{8.27}$$

8.3.1.2 PFR

For a PFR with the utility stream flowing in parallel with the fluid in the reactor, the transferred heat can be calculated by Eq. (8.28). For endothermic reactions,

Q is positive, while for exothermic reactions, it is negative.

$$Q = \frac{UA[(T - T_{a2}) - (T_0 - T_{a1})]}{\ln \frac{T - T_{a2}}{T_0 - T_{a1}}} \tag{8.28}$$

On the basis of Eq. (8.19), the relation of T, T_0, and X can be obtained by Eq. (8.29).

$$\frac{UA[(T - T_{a2}) - (T_0 - T_{a1})]}{\ln \frac{T - T_{a2}}{T_0 - T_{a1}}} - F_W^0 M(T - T_0)$$
$$= Vr_{1W}[\Delta H^o_{Rx1}(T_R) + N_1(T - T_R)] + Vr_{2B}[\Delta H^o_{Rx2}(T_R) + N_2(T - T_R)] \tag{8.29}$$

8.3.2 Reactor Characteristic Diagram

For a CSTR, the variations of S, T, Q, and T_0 along with X can be analyzed by Eqs. (8.16), (8.17), (8.26), and (8.27). The corresponding S–X, T–X, Q–X, and T_0–X curves can be plotted in the same diagram, as shown by Figure 8.5. In this diagram, the far-right vertical axis represents the selectivity, while the other one on the right corresponds to temperature. The left vertical axis represents the absolute value of heat added to the reactor. For a PFR, such a diagram can be constructed based on Eqs. (8.16), (8.18), (8.28), and (8.29).

For a given conversion, X_A, the corresponding inlet temperature, outlet temperature, selectivity, and energy added to the reactor can be easily identified from Figure 8.4. The variation of the selectivity is affected by the relative values of r_{1W} and r_{2B}. If r_{2B} is great enough, the highest selectivity might exist, as shown in Figure 8.5. Note that in Figure 8.5, the outlet temperature of the reactor is always higher than the inlet temperature. This is the general case for exothermic reactions, while the opposite holds true for endothermic reactions.

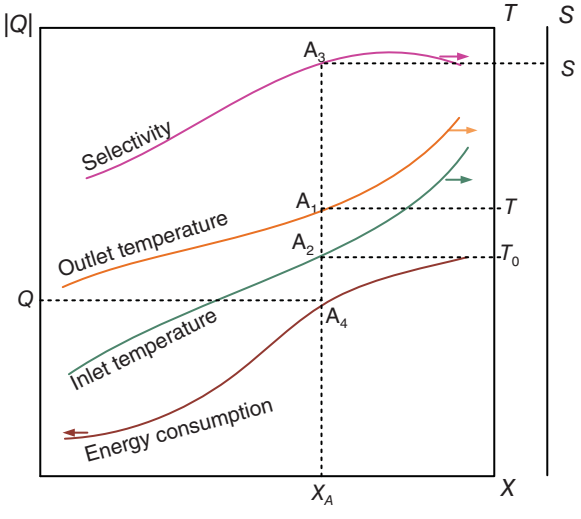

Figure 8.5 The reactor character diagram for reactor with exothermic reactions.

8.4 Coupling Optimization of HEN and Reactor

Reactor parameters affect not only the energy consumption but also the yield of desired product. Considering the trade-off between the energy consumption and the yield, their influence can be evaluated by the energy consumption of unit production, which is denoted as Y as in Eq. (8.30).

$$Y = \frac{h|Q_{C,min} + \Delta H_C| + g(Q_{H,min} + \Delta H_H)}{XSF_W^0} \tag{8.30}$$

where h and g are the coefficients of cold and hot utility for converting the energy consumption (kW) into standard coal (kg standard coal/kJ).

Based on Eqs. (8.3), (8.4), and (8.30), the variation of the energy consumption of unit product, hot and cold utilities along with conversion, can be plotted in the energy consumption analysis diagram for consumptions evaluation, as shown by Figure 8.6. Note that in this diagram, the cold and hot utility includes the energy supplied to the reactor (Q).

Figures 8.5 and 8.6 can be combined into the CMOD, as shown by Figure 8.7. Based on this diagram, the variation of energy consumption, selectivity, and temperature along with conversion can be identified simultaneously. Furthermore, the minimum energy consumption of unit product can be identified. The optimum conversion and selectivity, along with the corresponding optimum inlet temperature, can be identified using the corresponding curves in CMOD. For the given catalyst, the minimum energy consumption of unit product can be achieved through adjusting the inlet temperature to its optimal value and the integration with the HEN. Besides, the corresponding outlet temperature, minimum

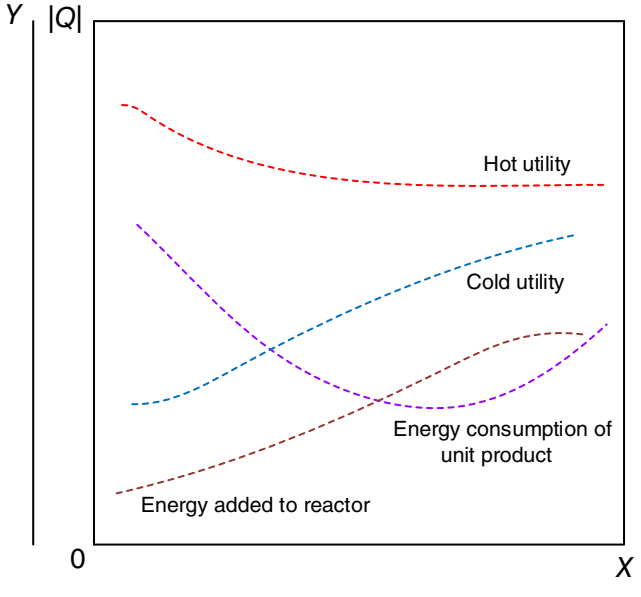

Figure 8.6 The energy consumption analysis diagram for consumptions evaluation.

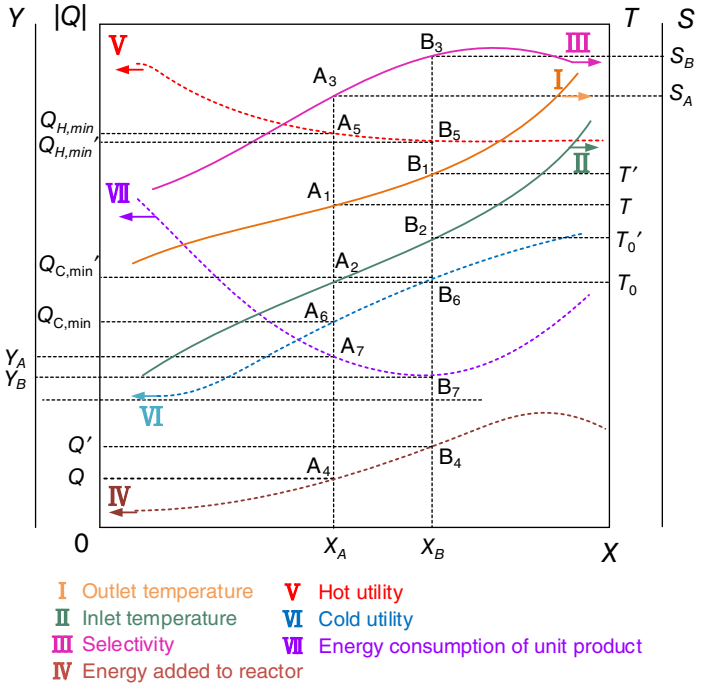

Figure 8.7 The combined multi-parameter optimization diagram (CMOD).

hot and cold utility consumption, and energy added to the reactor can be identified according to the corresponding curves in CMOD as well. For example, in Figure 8.7, when the process is operated at conversion X_A, points A_1, A_2, A_3, A_4, A_5, and A_6 stand for the corresponding outlet and inlet temperatures, selectivity, energy added to reactor, and hot and cold utility, respectively. A_7 corresponds to the energy consumption of unit production at this conversion. The lowest energy consumption of unit product appears at point B_7, and X_B and S_B are the optimal conversion and selectivity, respectively. Based on this figure, it can be identified that to achieve this energy consumption, the inlet temperature should be adjusted to the optimal value, T_0', and the HEN should be integrated. The corresponding outlet temperature, minimum cold utility consumption, and energy added to the reactor will increase to T', $Q'_{C,min}$, and Q', respectively, while the hot utility consumption will decrease from $Q_{H,min}$ to $Q'_{H,min}$.

It is noteworthy that the inlet temperature of the reactor should be adjusted within the limits determined by the catalyst and product properties. Otherwise, the catalyst will deactivate or the desired product will deteriorate. Besides, the energy variation of HEN demonstrated in Tables 8.1 and 8.2 are identified based on the assumption that pinch position keeps unchanged when temperatures of sink and source streams change. However, this assumption is not applicable for some cases. Therefore, it is necessary to determine if the pinch temperature will change. If the pinch temperature changes, the value identified according to

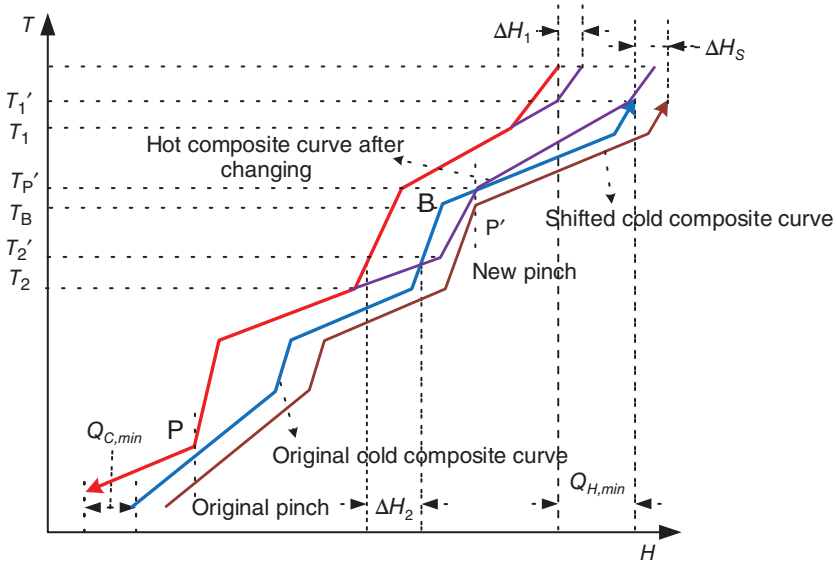

Figure 8.8 Variation of pinch position caused by the change of reactor temperatures.

Tables 8.1 and 8.2 should be revised by ΔH_S, which is the shifted distance of the hot or cold composite curve when the new pinch appears as shown in Figure 8.8.

8.5 Case Study

Figure 8.9 shows the simplified flowsheet of a process for selective hydrogenation of benzene to produce cyclohexene. The processing capacity of benzene is 1712.36 mol/min. R-104 is a PFR packed with catalyst. The selective hydrogenation of benzene to cyclohexene is a system of series reactions as shown follows.

$$\text{Primary reaction} \quad \text{BZ} + \text{H}_2(\text{g}) \xrightarrow{1} \text{HE}$$

$$\text{Secondary reaction} \quad \text{HE} + \text{H}_2(\text{g}) \xrightarrow{2} \text{HA}$$

where BZ is benzene, HE is cyclohexene, and HA is cyclohexane.

Based on the method introduced earlier and the reaction kinetics, the CMOD is plotted in Figure 8.10. For a given conversion, the corresponding hot and cold utility consumptions, outlet and inlet temperatures of the reactor, outlet temperature of the utility stream used in the reactor, and energy consumption of unit product can be identified directly from this diagram. When the conversion is 0.4, the corresponding outlet and inlet temperatures of the reactor, selectivity, heat supplied to reactor, and hot and cold utilities correspond to point A_1, A_2, A_3, A_4, A_5, and A_6, and are 393 K, 317 K, 0.53, 1094 kW, 7,202 kW, and 5,244 kW (including Q), respectively. A_7 corresponds to the energy consumption of unit product and equals 0.043 kg standard coal/mol.

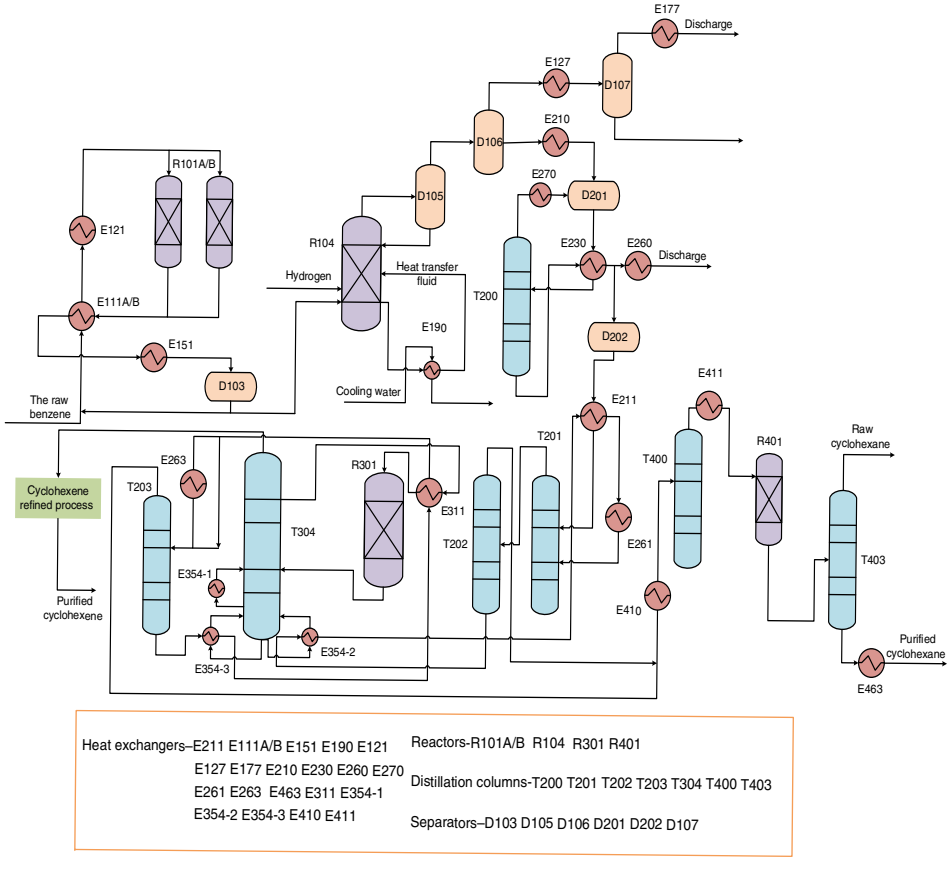

Figure 8.9 The flowsheet of benzene to cyclohexene process.

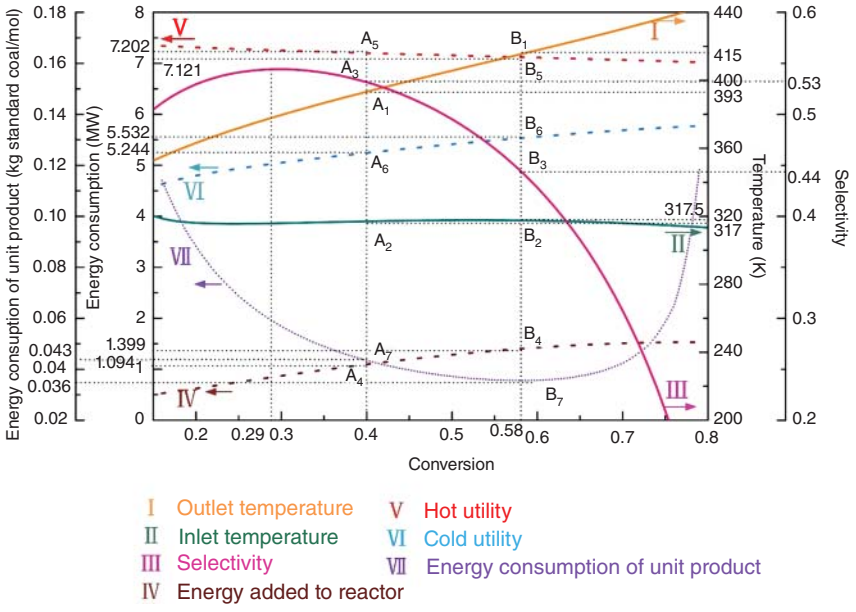

Figure 8.10 The CMOD for benzene to cyclohexene process.

The minimum energy consumption of the unit product is identified at the conversion of 0.58. When the conversion increases from 0.4 to the optimal value, the energy consumption of unit product decreases from 0.043 to 0.036 kg standard coal/mol. This corresponds to a reduction of 16.3%. In other words, 16.3% of energy can be saved by changing the reactor parameters. The outlet and inlet temperatures of the reactor, the heat supplied to reactor and cold utility consumption increase to 415 K, 317.5 K, 1399 kW, and 5532 kW (included Q), and correspond to point B_1, B_2, B_4, and B_6, respectively. Whereas, the hot utility decreases slightly to 7121 kW (point B_5) and the selectivity decreases to 0.44 (point B_3).

8.6 Conclusions

In this chapter, a graphic methodology is introduced to systematically integrate HEN and reactor with multiple reactions. In this method, the deduced equations clearly show the relationship among temperatures, selectivity, and conversion of the reactor, as well as energy consumption of unit production. The proposed CMOD can give clear insights into the variation of the energy consumption, inlet/outlet temperature, selectivity, and conversion of the reactor. Furthermore, the optimal point corresponding to the minimum energy consumption of unit product can be identified easily. With the energy consumption of unit production taken as the indicator of optimization, the energy efficiency can be well balanced with the production of the desired product.

References

1 British Petroleum Company (2019). *BP Statistical Review of World Energy*, 68e. London, UK: British Petroleum Company.

2 Smith, R. (2005). *Chemical Process Design and Integration*, 3e. West Sussex, UK: Wiley.

3 Grossmann, I.E., Caballero, J.A., and Yeomans, H. (2000). Advances in mathematical programming for the synthesis of process systems. *Latin American Applied Research* 30: 263–284.

4 Kemp, I.C. (2011). *Pinch Analysis and Process Integration: A User Guide on Process Integration for the Efficient Use of Energy*. Butterworth-Heinemann.

5 Klemeš, J.J. and Kravanja, Z. (2013). Forty years of heat integration: pinch analysis (PA) and mathematical programming (MP). *Current Opinion in Chemical Engineering* 2: 461–474.

6 Sreepathi, B.K. and Rangaiah, G.P. (2014). Review of heat exchanger network retrofitting methodologies and their applications. *Industrial and Engineering Chemistry Research* 53: 11205–11220.

7 Glavič, P., Kravanja, Z., and Homšak, M. (1988). Heat integration of reactors – I. Criteria for the placement of reactors into process flowsheet. *Chemical Engineering Science* 43: 593–608.

8 Glavič, P., Kravanja, Z., and Homšak, M. (1988). Modeling of reactors for process heat integration. *Computers & Chemical Engineering* 12: 189–194.

9 Kravanja, Z. and Glavič, P. (1989). Heat integration of reactors – II. Total flowsheet integration. *Chemical Engineering Science* 44: 2667–2682.

10 Lavric, V., Pleşu, V., and De Ruyck, J. (2005). Chemical reactors energy integration through virtual heat exchangers – benefits and drawbacks. *Applied Thermal Engineering* 25: 1033–1044.

11 Zhang, D., Wang, P., and Liu, G. (2018). A novel sensitivity analysis method for the energy consumption of coupled reactor and heat exchanger network system. *Energy & Fuels* 32: 7210–7219.

12 Zhang, D., Liu, G., and Li, Y. (2018). Graphical optimization method for coupled heat exchanger network and reactor. *Energy* 156: 635–646.

13 Zhang, D. and Liu, G. (2017). Integration of heat exchanger network considering the pressure variation of distillation column. *Applied Thermal Engineering* 116: 777–783.

9

Fouling Mitigation in Heat Exchanger Network Through Process Optimization

Yufei Wang[1] *and Xiao Feng*[2]

[1] *China University of Petroleum, Department of Chemical Engineering, State Key Laboratory of Heavy Oil Processing, Fuxue Road 18, Beijing 102249, China*
[2] *Xi'an Jiaotong University, Department of Chemical Engineering, School of Chemical Engineering and Technology, 28# Xianning West Street, Xi'an, Shaanxi 710049, China*

9.1 Introduction

Heat recovery through *heat exchanger network* (HEN) has been studied for several decades to satisfy energy saving in the process industries. There are two widely used methodologies for HEN synthesis, i.e. pinch analysis and mathematical programming [1].

One critical issue for HEN design and operation is fouling. Fouling in heat exchangers will severely affect the performance of an HEN, resulting in a reduction in energy recovery and operation stability. Note that different materials will have different fouling mechanisms, which entails different fouling models. Nevertheless, fouling is normally sensitive to velocity and temperature. Hence, even though the methodology presented in this chapter is based on crude fouling, the same physical insights are also applicable for other fouling mechanisms.

Research of crude oil fouling requires appropriate models for predicting the fouling behaviors, which have been developed by many researchers in last three decades. Ebert and Panchal [2] first introduced the concept of fouling threshold in 1995. Since then, several modified models were proposed to improve the prediction accuracy of crude oil fouling behavior. Panchal et al. [3, 4] made use of the Prandtl number to take thermal properties into account. In Polley's model [5], wall temperature and the Reynolds number were used instead of film temperature and shear stress term. As compared with Ebert and Panchal's model [2], Polley's model is more accurate and shear stress term is eliminated so that the calculation is easier. Yeap et al. [6] carried out a large number of studies to evaluate different threshold fouling models using various laboratory and plant data sets and proposed a more accurate and complex model compared with the other three models. Recently, *computational fluid dynamics* simulations were used to predict fouling behaviors [7] and its effect on heat transfer condition [8]. In addition, fouling behaviors under different surface roughness were studied through a number of experiments [9].

Process Intensification and Integration for Sustainable Design, First Edition.
Edited by Dominic C. Y. Foo and Mahmoud M. El-Halwagi.
© 2021 WILEY-VCH GmbH. Published 2021 by WILEY-VCH GmbH.

To address fouling problem in HEN through process optimization, there are basically three common methodologies, i.e. regular cleaning, parameter optimization, and new device technologies. Regular cleaning of fouled heat exchangers is a promising mitigation strategy for minimizing fouling issue. For optimizing cleaning schedule in a single heat exchanger, Ishiyama et al. [10] proposed a methodology to identify optimum cleaning cycles and optimal cleaning time between plant shutdowns, by idealizing the foulant deposit as two, the fresh and aged layers. In their work, they considered two available cleaning methods, i.e. chemical and mechanical cleaning, and introduced economic competition between the two methods [10]. Pogiatzis et al. [11, 12] successively established a nonlinear programming (NLP)-based approach and a mixed integer nonlinear programming (MINLP) model to optimize the schedule of cleaning actions of a heat exchanger subject to fouling and aging, considering the combinations of chemical and mechanical cleaning. For optimizing cleaning schedule in an HEN, Smaïli et al. [13, 14] optimized the scheduling problem for a large continuously operating HEN, and an MINLP model was introduced to optimize the cleaning schedule with the objective of minimizing the total operating cost. Aforementioned papers focused on the cleaning schedule problems. This kind of method can quickly restore the heat transfer capacity of heat exchanger, so it is very suitable for the processes with high fouling rate. However, this method cannot prevent fouling, and the interaction between fouling and network characteristics is ignored.

The second methodology for fouling mitigation is to consider parameter optimization in an HEN. Rodriguez and Smith [15] put forward a new proactive method by exploiting the effects of wall temperature on fouling to depress the occurrence of fouling deposition. The method combined the optimization of wall temperature with the optimal management of cleaning actions. The results indicated higher energy savings, lower operational costs, and fewer disturbances to the background process, as compared with optimizing cleaning schemes alone. The mean idea for wall temperature optimization is to make more crisscrossed matches to reduce wall temperature. Although this method reduces fouling, it also reduces heat recovery when all heat exchangers are clean (due to the crisscross effect). Ishiyama et al. [16] combined the desalter inlet temperature control with the cleaning schedule optimization to aid fouling management by using hot stream bypass. They considered hydraulic behavior [17] in their follow-up paper; a highly flexible preheat train simulator is developed in MATLAB/Excel to accommodate variable throughput in scheduling the cleaning operations. Biyanto et al. [18] developed an improved optimization problem for the cleaning schedule of heat exchangers in a crude preheat train considering the hydraulic impact of fouling through the additional pressure drops. A stochastic optimization method was proposed to solve the problem [18]. Several researchers found that optimizing flow velocity can be applied to fouling mitigation. Assis et al. [19] developed a constrained NLP formulation for fouling management considering the hydraulic behavior of an HEN. In their work, velocity is redistributed through optimizing the split ratio of parallel structures in HEN design. Another work is further extended to consider the dynamic nature of fouling [20]. In the work of Ishiyama

et al. [21], flow rate optimization is incorporated with cleaning of parallel heat exchangers.

The third way for solving fouling problem in an HEN is the application of new device technologies. It is found that applying heat transfer enhancement devices in the HEN is an effective strategy for fouling mitigation. Wang and Smith [22] proposed a simulated annealing (SA)-based method to solve HEN retrofit problems on the basis of heat transfer enhancement. The method is applied to retrofit HEN under fouling with different kinds of crude oils [22]. Pan et al. [23] developed a new mixed integer linear programming (MILP)-based iteration method for HEN retrofit by implementing tube-side intensification. They extended the work for more practical problems in retrofitting the HEN within the operating period, addressing fouling effects and pressure drop constraints in their follow-up work [24]. In addition, some researchers have found that a sol–gel coating can be used for fouling mitigation in heat exchangers, which focuses on the material and the interaction between crude oil fouling, but ignoring the network characteristics [25, 26].

Although a number of works have been reported for fouling consideration in HEN design and operation, due to the dynamic and complex nature of fouling and HEN, simultaneous consideration of fouling, pressure drop, and heat transfer has not been reported. In this chapter, a new velocity optimization-based methodology is presented for solving fouling problem in HEN. In particular, the aspects of fouling rate, heat transfer coefficient (HTC), and pressure drop are correlated through velocity. By using velocity as a critical link, pressure drop, HTC, and fouling can be adjusted through velocity variation, so that variables involved in the optimization can be significantly reduced, which in turn leads to simpler model. Next, the velocity optimization-based methodology is also combined with cleaning schedule optimization and backup heat exchangers.

9.2 Operation Parameter Optimization for Fouling Mitigation in HENs

9.2.1 Description on Velocity Optimization

Fouling rate, HTC, and pressure drop are three key aspects for the operation of heat exchangers. They significantly affect the performance of heat exchangers. It is found that velocity is a parameter that can affect all three aspects. With increased velocity, pressure drop and HTCs of the heat exchange will be increased, while its fouling rate will reduce. Therefore, velocity can be used to correlate the three aspects, so to reduce the complexity of the optimization model.

Figure 9.1 shows the detailed relation between velocity and the other aspects. From the figure, it can be seen that the interaction between velocity, pressure drop, heat transfer, and fouling is complicated. High velocity will inhibit the fouling process. With the accumulation of fouling deposition, the velocity will increase due to the reduction in the flow area. Furthermore, HTC has a positive relation with wall temperature; however it will be reduced when fouling

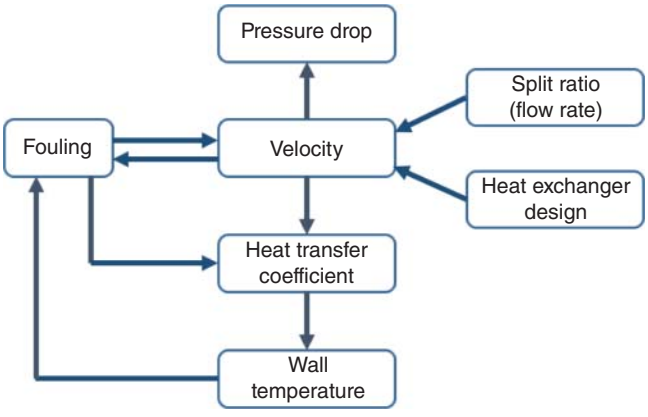

Figure 9.1 Velocity related performances of heat exchanger.

occurs. Wall temperature also has a relationship with fouling, i.e. higher wall temperature will lead to a severe fouling.

There are basically two ways to change the velocity in a heat exchanger. One option is to change the flow rate distribution in the splitter, which can only be done for heat exchangers with parallel structure. Due to the constant flow rate, flow rate increase in one branch will decrease the flow rate in other branches. The other way for changing velocity in a heat exchanger is to modify the detailed design of heat exchanger. For example, the number of tube pass can be increased to increase the velocity. This option is not as flexible as compared with the changing split ratio, but it may be applied to any heat exchanger in the HEN.

The objective for the velocity optimization is to find the most economical HEN design. As shown in Figure 9.2, with the raise of velocity, hot utility cost and fouling related loss are reduced; however with the price of higher capital and pump costs. Hence, an optimum velocity does exist that leads to the minimum total cost. Note that Figure 9.2 is meant for a single heat exchanger. For an HEN, there must be an optimal velocity distribution that leads to minimum total cost. It must

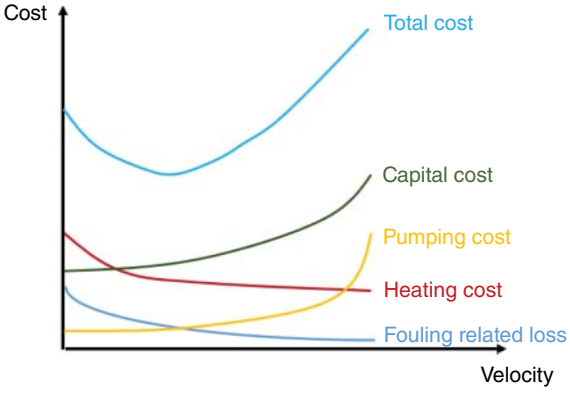

Figure 9.2 The relation between velocity and different cost elements.

be noted that to avoid practical problem, e.g. vibration issue, velocity must be limited for a given range.

9.2.2 Fouling Threshold Model

On the basis of fouling threshold concept introduced by Ebert and Panchal [27], several modified models were proposed. In these models, fouling rate of fluid at the tube side is a function of fluid velocity and wall (or surface) temperature. From the threshold model, fouling can be neglected for fluid with high velocity and low wall temperature. To avoid a severe fouling problem, operating conditions must be below the threshold line, as shown in Figure 9.3. Due to the difficulty of fouling materials clean-up on the shell side of heat exchangers, crude oil normally goes through the tube side. Model parameters vary for different crude oils and are usually obtained by regression of pilot data. Polley's threshold model [5] is used in this chapter to calculate the fouling rate. This model uses the Reynolds number [5], which is easy to correlate velocity rather than shear stress. The expression for Polley's model is given in Eq. (9.1). Note that the fouling rate of heat exchanger cannot be less than 0.

$$\frac{d\mathrm{Rf}}{dt} = \max\left\{\alpha Re^{-0.8}Pr^{-0.33}\exp\left(\frac{-E}{R_g T_w}\right) - \gamma Re^{0.8}, 0\right\} \tag{9.1}$$

where Rf is fouling resistance, Re and Pr are the Reynolds number and Prandtl number, respectively, α and γ are model parameters, E is activation energy, R_g is gas constant, and T_w represents wall temperature of heat exchanger.

As fouling is a dynamic process, fouling rate, velocity, wall temperature, pressure drop, and HTCs are all varied with time. In the presented methodology, the entire time zone is divided into n time intervals. Within each time interval, the process is assumed as steady state, where calculation is performed (see Figure 9.4). The overall performance of HEN (e.g. hot utility) is the sum of the performance in each time interval.

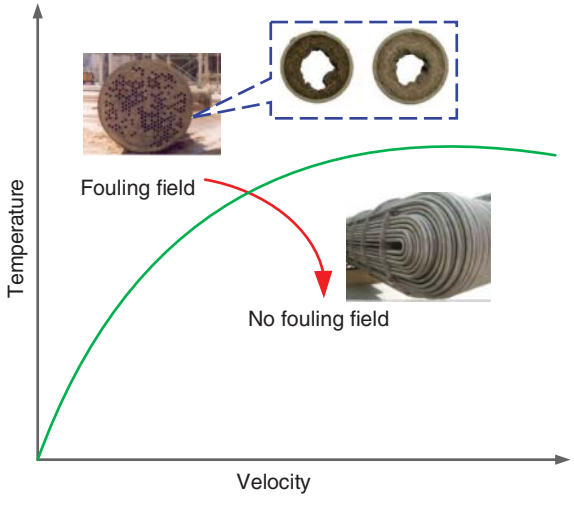

Figure 9.3 Fouling threshold curve.

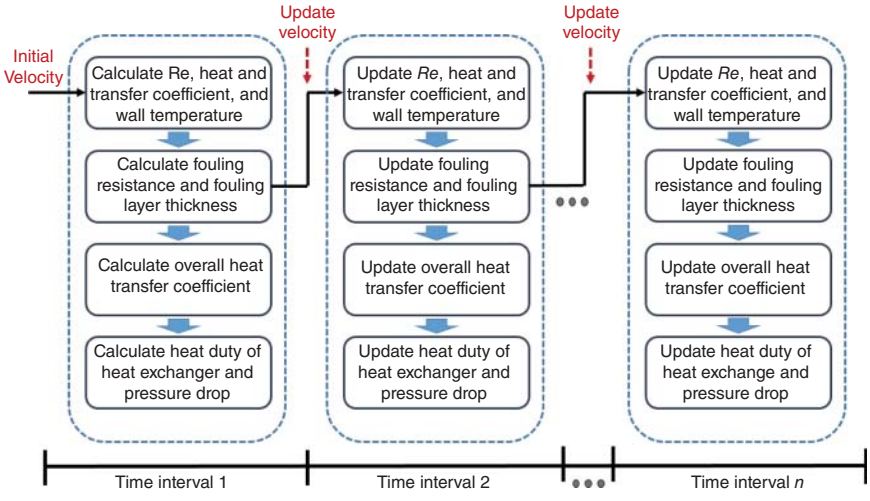

Figure 9.4 Pictorial representation of the heat exchanger fouling calculations.

The length of each time period must be well considered in order to maintain accuracy of the model, while keeping the number of binary variables at an acceptable level. In other words, if the time periods are too long, the model would deviate from the actual process. On the other hand, if the time periods are too short, solving the problem can be very difficult due to large number of variables.

9.2.3 Heat Transfer Related Models

Due to the variation of fouling layer and velocity, the HTC for tube side is changing with time during the operational period, which is calculated using Eqs. (9.2)–(9.4).

$$h_T = h_{T,n=0}(v_n/v_{n=0})^{0.8} \tag{9.2}$$

$$h_{T,n=0} = 0.023\frac{\lambda}{d}\left(\frac{d_{n=0}v_{n=0}\rho}{\mu}\right)^{0.8}\left(\frac{\mu\cdot\mathrm{CP}}{\lambda}\right)^{0.4} \tag{9.3}$$

$$v_n = v_{n=0}[d/(d-2\delta_{n-1})]^2 \tag{9.4}$$

In this chapter, the shell side convective HTC is assumed constant along the HEN, because streams prone to foul normally flow through the tube side. Equation (9.5) is used to calculate the overall HTC K, while Eq. (9.6) is used to calculate the wall temperature of heat exchanger. The latter is related to HTC of both sides and it has a close relation with the fouling rate of heat exchanger. For heat exchanger in series structure, the initial velocity $v_{n=0}$ can only be changed through modification of detailed heat exchanger design. On the other hand, for heat exchangers in parallel branches, the initial velocity $v_{n=0}$ of the tube side is co-determined by both the detailed design of heat exchanger and the mass flow rate of the branch obtained from optimization, as shown in Eq. (9.7). Detailed modification of shell side is not considered in this work, so the shell

side convective HTC for heat exchanger is only related to mass flow rate (i.e. split ratio), as presented in Eq. (9.8).

$$K = \left(\frac{1}{h_S} + \frac{1}{h_T} + \mathrm{Rf}_T + \mathrm{Rf}_S \right)^{-1} \tag{9.5}$$

$$T_w = T_{S,bulk} + \frac{h_S}{h_S + h_T} \times (T_{T,bulk} - T_{S,bulk}) \tag{9.6}$$

$$v_{n=0} = v'(M_{T,optimized}/M_{T,base}) \tag{9.7}$$

$$h_S = h_{S,base}(M_{S,optimized}/M_{S,base})^{0.6} \tag{9.8}$$

where h_T and h_S are convective HTC for tube and shell sides of heat exchanger, respectively, d is the inner diameter of tubes, λ is fluid heat conductivity, v is fluid velocity in the tube side, ρ is fluid density, μ is fluid viscosity, δ is the thickness of fouling layer, which can be calculated on the basis of fouling rate, Rf_S is the shell side fouling resistance, subscript $n = 0$ means the beginning of operation time period, $T_{c,bulk}$ and $T_{h,bulk}$ are bulk temperature of cold and hot streams, respectively, subscripts S and T represent shell and tube sides, respectively, v' is the velocity of heat exchanger considering only detailed design modification, M is the mass flow rate, and subscripts *base* and *optimized* represent base case before optimization and optimized case.

Number of transfer units (NTU) method is used to calculate heat transfer of heat exchanger in this chapter. It is assumed that the heat exchangers considered in this chapter are counter flow with single shell pass and two tube passes. The corresponding NTU expression is shown in Eq. (9.9). Note that in crude oil preheat train, heat capacity flow rate of crude oil is normally larger than those of the hot streams, so the parameters of cold streams are selected to express P, R_n, and NTU in NTU method.

$$P = 2\left\{ 1 + R_n + (1 + R_n^2)^{1/2} \times \frac{1 + \exp[-\mathrm{NTU}_n(1 + R_n^2)^{1/2}]}{1 - \exp[-\mathrm{NTU}_n(1 + R_n^2)^{1/2}]} \right\}^{-1} \tag{9.9}$$

where P is the thermal effectiveness, R is heat capacity flow rate ratio of cold stream to the hot stream, and NTU is heat transfer unit. They are described in Eqs. (9.10)–(9.12).

$$P = \frac{T_c^{\,out} - T_c^{\,in}}{T_h^{\,in} - T_c^{\,in}} \tag{9.10}$$

$$R_n = \frac{M_{c,n}\mathrm{CP}_{c,n}}{M_{h,n}\mathrm{CP}_{h,n}} \tag{9.11}$$

$$\mathrm{NTU}_n = \frac{K_n A}{M_{c,n}\mathrm{CP}_{c,n}} \tag{9.12}$$

where the superscripts *in* and *out* are inlet and outlet, respectively, A is heat transfer area of a heat exchanger, Cp is the specific heat capacity of a stream, subscripts c and h are cold and hot streams, respectively.

9.2.4 Pressure Drop Related Models

As the deposition of fouling is in tube side, the actual fluid flowing area constantly decreases, which promotes the fluid velocity and results in higher pressure drop. The total pressure drop for the tube side (ΔPf) of a heat exchanger consists of three parts, as shown in Eq. (9.13).

$$\Delta \mathrm{Pf}_{n=0} = \Delta \mathrm{Ps}_{n=0} + \Delta \mathrm{Pl}_{n=0} + \Delta \mathrm{Pn}_{n=0} \tag{9.13}$$

where $\Delta \mathrm{Ps}_n$, $\Delta \mathrm{Pl}_n$, and $\Delta \mathrm{Pn}_n$ represent straight pipe resistance, local resistance, and nozzle resistance, respectively. The three resistances can be calculated by Eqs. (9.14)–(9.17).

$$\Delta \mathrm{Ps}_{n=0} = \xi_{n=0} \frac{L}{d} \frac{\rho v_{n=0}^2}{2} N \tag{9.14}$$

$$\xi_{n=0} = 0.01227 + \frac{0.7543}{Re_{n=0}^{0.38}} \tag{9.15}$$

$$\Delta \mathrm{Pl}_{n=0} = \zeta \frac{\rho v_{n=0}^2}{2} N \tag{9.16}$$

$$\Delta \mathrm{Pn}_{n=0} = 1.5 \times \frac{\rho v_{n=0}^2}{2} \tag{9.17}$$

where ξ is friction coefficient, which can be calculated by Eq. (9.15), L is the length of tubes, N is the number of tube passes, and ζ in Eq. (9.16) is the local resistance coefficient, it values 3–4 for multiple tube passes, while it equals to 2 for single tube pass.

Once the initial (or base case) pressure drop is calculated through Eq. (9.13), change of pressure drop under fouling over the investigated time can be obtained from the correlation in Eq. (9.18).

$$\frac{\Delta \mathrm{Pf}_n}{\Delta \mathrm{Pf}_{n=0}} = \left(1 - \frac{\delta_n}{d}\right)^{-5} \tag{9.18}$$

In this chapter, pipeline pressure drop is not considered, so the total pressure drop ΔP_T for an HEN is the sum of pressure drop of heat exchangers in series and in parallel, as shown in Eq. (9.19).

$$\Delta P_T = \sum \Delta \mathrm{Pf}_{series} + \sum \Delta P_{parallel} \tag{9.19}$$

$$\Delta P_{T,parallel} = \max\{\Delta P_{T,branch,1}, \Delta P_{T,branch,2}, \ldots, \Delta P_{T,branch,j}\} \tag{9.20}$$

where $\Delta \mathrm{Pf}_{series}$ is the pressure drop of a heat exchanger in series and $\Delta P_{T,parallel}$ represents the pressure drop of parallel heat exchangers, which depends on the maximum pressure drop among all the branches, as shown in Eq. (9.20). In the equation, $\Delta P_{T,branch,j}$ is the sum of pressure drop of all the heat exchangers on branch j. For branches with lower pressure drop, throttle valves will be adjusted on these branches to ensure balanced pressure drop across all branches.

9.3 Optimization of Cleaning Schedule

The optimization of velocity across heat exchangers cannot prevent the accumulation of fouling deposits completely in HEN. Due to high temperature in the hot end and the limitation of velocity, not every heat exchanger can reach a non-fouling condition through velocity optimization. Therefore, off-line cleaning of fouled heat exchangers for mitigating fouling is necessary to further reduce the negative impact of fouling.

An alternative discretization approach is used to model the cleaning condition of exchangers after choosing the time horizon. As illustrated in Figure 9.5, the time horizon in Figure 9.4 is further discretized by two sub-periods, a cleaning sub-period (off-line) and a processing sub-period (on-line), with time lengths of t^{cl} and t^{pr}. Note that superscripts *cl* and *pr* represent cleaning sub-period and processing sub-period, respectively. Cleaning actions are required to be implemented only at cleaning sub-periods and all exchangers must be kept on-line at the processing sub-periods. The operating conditions are assumed to be constant in each time period. Binary variable $y_{i,n}$ is used to represent the cleaning condition of unit i over cleaning sub-period n ($y_{i,n} = 1$, on-line; $y_{i,n} = 0$, off-line). In the model, when a cleaning action is applied, velocity, fouling resistance, pressure drop, and HTC are set to be their initial value.

In the aforementioned method, flow velocities across the HEN and the scheduling of cleaning can be optimized simultaneously, which is a more comprehensive strategy as compared to conventional fouling mitigation methods. When a heat exchanger is taken off-line for cleaning, the duty of this heat exchanger in that period will be compensated by hot utility. Hence, the utility cost will be higher in the cleaning period. Meanwhile, after cleaning, the heat exchanger capacity will be restored. In other words, the trade-off among cleaning cost, benefits of mitigating fouling, pumping, and capital cost are considered in the model.

9.4 Application of Backup Heat Exchangers

In the food industry, the severe fouling situation leads to frequent cleaning actions. In this case, backup heat exchanger is considered to keep heat duty when the heat exchanger is taken off-line. For crude oil system, some heat exchangers at the hot end are also suffering from severe fouling. Backup heat exchanger can be an alternative option to avoid off-line loss when cleaning takes place.

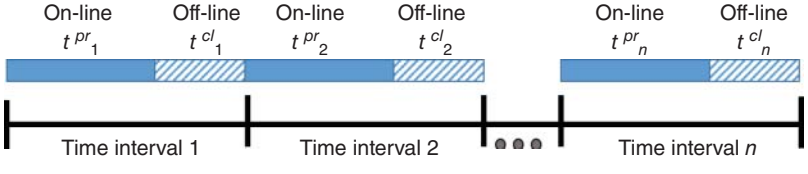

Figure 9.5 Time discretization for modeling cleaning condition.

When backup heat exchanger is considered in the optimization, trade-off between capital cost of backup heat exchanger and the off-line loss must be considered. In an HEN, the raise of hot utility is determined by the cleaning frequency and the duty of off-line heat exchangers. The frequency of cleaning depends on the fouling rate and heat duty of the heat exchanger, as well as the location of heat exchanger in the network. In this chapter, binary variables are used to define if backup heat exchanger existed.

9.5 Optimization Constraints and Objective Function

9.5.1 Optimization Constraints

The main optimization constraints are composed of bounds for velocity in tube side of a heat exchanger, bounds for mass flow rate of each branch, mass and energy balances, heat exchanger equations, and fouling rate model equations. To keep heat exchangers working away from vibration and abrasion problems, the fluid velocity must be limited to a certain range, which is represented by Eq. (9.21). Generally, the maximum flow velocity in a shell-and-tube heat exchanger can reach 3 m/s, while the minimum value cannot be less than 0.5 m/s [28]. The constraints for mass flow rate of each branch are shown in Eq. (9.22).

$$v_{LB} \le v \le v_{UB} \tag{9.21}$$

$$M_{LB} \le M_{branch} \le M_{UB} \tag{9.22}$$

where the subscripts *UB* and *LB* represent the upper and lower bounds, respectively.

The constraints for inlet and outlet temperatures of cold and hot streams of every heat exchanger are given in Eqs. (9.23)–(9.26). The outlet temperature of cold streams in hot utility heat exchanger must be equal to target temperature of cold streams, and the outlet temperature of hot streams in cold utility heat exchanger must be equal to target temperature of hot streams, as shown in Eqs. (9.27) and (9.28).

$$T_c^{\,out} \le T_h^{\,in} \le T_{h,supply} \tag{9.23}$$

$$T_{h,target} \le T_h^{\,out} \le T_h^{\,in} \tag{9.24}$$

$$T_{c,supply} \le T_c^{\,in} \le T_h^{\,out} \tag{9.25}$$

$$T_c^{\,in} \le T_c^{\,out} \le T_{c,target} \tag{9.26}$$

$$T_{c,hu}^{out} = T_{c,target} \tag{9.27}$$

$$T_{h,cu}^{out} = T_{h,target} \tag{9.28}$$

where subscripts *supply* and *target* represent the supply and target temperatures of the streams and subscripts *hu* and *cu* represent hot utility and cold utility, respectively.

Equations (9.29)–(9.32) show the mass balances and energy balances for splitters and mixers.

$$\sum M_{SP}^{in} = \sum M_{SP}^{out} \tag{9.29}$$

$$\sum M_{MX}^{in} = \sum M_{MX}^{out} \tag{9.30}$$

$$\sum (M\mathrm{Cp}T)_{SP}^{in} = \sum (M\mathrm{CP}T)_{SP}^{out} \tag{9.31}$$

$$\sum (M\mathrm{CP}T)_{MX}^{in} = \sum (M\mathrm{CP}T)_{MX}^{out} \tag{9.32}$$

where subscripts *SP* represents the splitter and *MX* represents the mixer.

9.5.2 Objective Function

The objective function in this work is to minimize the total annualized cost, which is the summation of cost for utility, power (electricity charges for pumps), cleaning, equipment capital cost, and detailed structure modification cost for heat exchangers, as shown in Eq. (9.33).

$$\mathrm{obj} = C_{utility} + C_{power} + C_{pump} + C_{ex,modify} + C_{ex} + C_{ex,clean} \tag{9.33}$$

where $C_{utility}$, C_{power}, C_{pump}, and C_{modify} are annualized cost for hot and cold utilities, power, pump investment, detailed structure modification cost, new heat exchanger investment, and total cleaning costs.

Equations (9.34) and (9.35) are the calculations of hot utility Q_{hu} and cold utility Q_{cu}, respectively, the price of utility cost $C_{utility}$ can be calculated by Eq. (9.36).

$$Q_{hu} = \sum_{i,hu} [M_c \mathrm{CP}_c \times (\mathrm{Tc}_{i,hu}^{out} - \mathrm{Tc}_{i,hu}^{in})] \tag{9.34}$$

$$Q_{cu} = \sum_{i,cu} [M_h \mathrm{CP}_h \times (\mathrm{Th}_{i,cu}^{out} - \mathrm{Th}_{i,cu}^{in})] \tag{9.35}$$

$$C_{utility} = \sum_{t} [\mathrm{hu} \times Q_{hu} + \mathrm{cu} \times Q_{cu}] \tag{9.36}$$

where hu and cu represent the unit price of hot utility and cold utility.

Power cost is related to volume flow rate of fluid and pressure drop, which can be calculated by Eq. (9.37) [29].

$$C_{power} = \sum_{t} \left(\mathrm{pc} \times \frac{V \times \Delta P_T}{\eta} \right) \tag{9.37}$$

where pc is the unit electricity cost, η represents the pump efficiency, and V is volumetric flow rate for a stream.

Pump investment meets exponential function of the flow rate and pressure drop, and annualized pump capital cost C_{pump} is calculated by Eq. (9.38) [29]. Heat exchanger annualized capital cost C_{ex} is related to its heat exchange area

and device lifetime, which can be calculated by Eq. (9.39). Equation (9.40) is used to calculate detailed structure modification cost $C_{ex,modify}$ for optimized cases.

$$C_{pump} = \frac{2.365 + 0.151 \times (V \times \Delta P_{T,n=m})^{0.86}}{\mathrm{Yr}_{pump}} \tag{9.38}$$

$$C_{ex} = \frac{a + bA^{\beta}}{\mathrm{Yr}_{ex}} \tag{9.39}$$

$$C_{ex,modify} = \sum_{ex} C_{ex} \cdot \theta \tag{9.40}$$

where Yr_{pump} is pump lifetime, subscript $n = m$ indicates the last time interval of the operational time horizon, Yr_{ex} is lifetime of heat exchanger, θ is structure modification cost coefficient, and a, b, and β are model parameters.

9.5.3 Optimization Algorithm

The presented method is to minimize total annualized cost. Due to the highly nonlinear property of fouling problems, SA algorithm is used to solve the optimization problem in this chapter. As compared with the deterministic methods, SA algorithm has better chance to escape from being trapped into local optimality. The proposed method can be used for both retrofit and grassroots design problems.

The optimization variables in this method are velocity of heat exchangers, split ratio of each splitter for both cold and hot streams, and binary variables for cleaning actions. The first variable refers to changing velocity through detailed design modification of heat exchangers. Obviously, the velocities for heat exchangers in series can only be changed by detailed design modification, while both split ratios optimization and detailed design modification are considered for parallel heat exchangers. These two control variables jointly determine the initial velocity distribution. Next, velocity distribution and cleaning schedule are optimized together to find the best design configuration of HEN under fouling consideration.

9.6 Case Studies

9.6.1 Case Study 1: Consideration of Velocity Optimization Alone

This section illustrates the application of the proposed optimization approach by using a simplified crude oil HEN, as shown in Figure 9.6. This case study is based on the work presented by Smaïli et al. [14], which is composed of nine shell-and-tube heat exchangers, four splitters, and four mixers. The HEN can be considered as two sections. The section in the upstream of the flash unit contains three heat exchangers in series, while the section in the downstream section of the flash contains six heat exchangers aligned equally in two parallel branches (i.e. branches A and B). The temperature change in flash is neglected, while there is a loss of 5–10% in flow rate [14]. The stream split ratios of base case for all splitters are equal to 0.5 over the whole operational period.

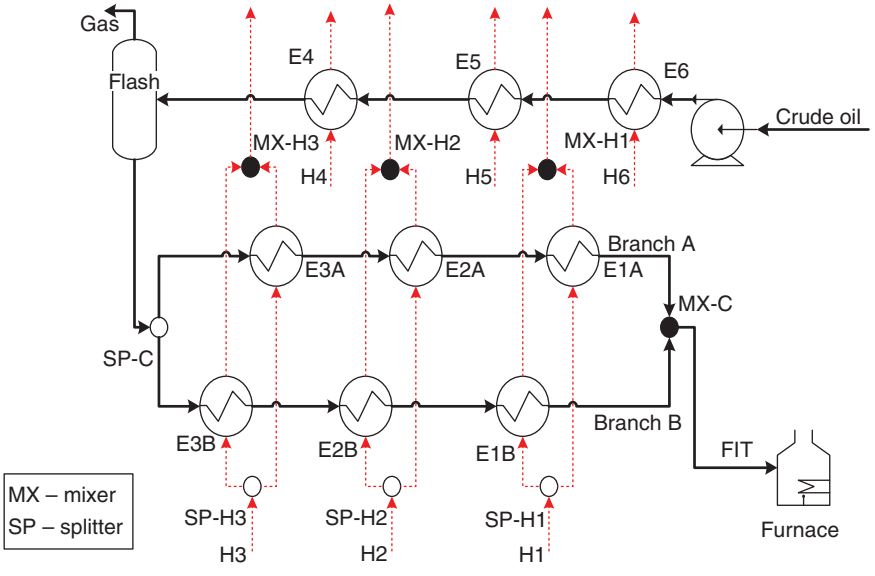

Figure 9.6 Diagram of crude oil preheat train for Case Study 1.

Table 9.1 Streams data for Case Study 1.

Streams	Mass flow rate (kg/s)	Specific heat (kJ/(kg K))	T_{supply} (°C)	T_{target} (°C)
H1	142.0	2.8	327	200
H2	127.0	2.9	292	200
H3	127.5	2.8	282	180
H4	63.2	2.9	251	150
H5	68.5	2.6	233	120
H6	70.9	2.8	205	100
Crude	95	2.3/2.4	135	385

Prefixes H indicate hot streams.

The mass flow rates, temperatures, and heat capacities of the process streams are presented in Table 9.1. Crude oil is the only cold stream in this case. The heat capacity of the hot streams are assumed as constants along the HEN, while the heat capacity of crude oil upstream the flash is taken as 2.3 kJ/(kg K) and crude downstream the flash has a heat capacity of 2.4 kJ/(kg K). The density of crude is 800 kg/m^3, the viscosity of crude is 1×10^{-3} Pa s, while the thermal conductivity of crude is 1×10^{-4} W/(m K). The heat capacity and other physical properties of process streams are assumed as constants along the HEN.

Table 9.2 displays the detailed data of the heat exchangers. The size of heat exchangers in branch B is larger than those in branch A. The heat of heat exchangers in Table 9.2 is the average heat duty during the operational time

Table 9.2 Heat exchangers data for Case Study 1.

Exchangers	ID (mm)	Area (m^2)	Heat duty (kW)	Initial velocity (m/s)		Shell side HTC ($kW/m^2/K$)
				Base case	Optimized case	
E1A	15.4	310	2648	1.5	2.84	0.451
E1B	15.4	360	2673	1.4	2.94	0.451
E2A	15.4	300	2388	1.4	2.12	0.523
E2B	15.4	350	2634	1.2	1.77	0.523
E3A	15.4	200	2400	1.1	1.55	0.482
E3B	15.4	250	2787	1.1	1.66	0.482
E4	15.4	600	5642	1.1	1.10	0.590
E5	15.4	300	5034	2.4	0.82	0.653
E6	15.4	400	5872	1.8	0.58	0.653

period. Fouling in heat exchangers is mainly due to the deposition of crude oil, and crude always flows in the tube side of heat exchangers in this case. Hence, only the tube side fouling is considered in this case, which is calculated by Polley's model [5]. The parameters of Polley's model (Eq. (9.1)) are set equal for all heat exchangers in this case study, i.e. $\alpha = 8 \times 10^5$ m^2 K/(kW h), $E = 55$ kJ/mol, $\gamma = 2 \times 10^{-9}$ m^2 K/(kW h). All heat exchangers are cleaned at the beginning of the operation time. The thermal conductivity of fouling resistance Rf is 0.5 W/m/K. Fouling resistances in shell side are assumed to stay constant along the HEN in the investigated time period. The detailed structure modification cost coefficient (Eq. (9.40)) for heat exchangers is set to be 0.02.

Figure 9.7 presents the conditions for all heat exchangers in the base case in the fouling threshold curve plot. The latter corresponds to the wall temperature and velocity, which can be determined at the condition with zero fouling rate. As discussed earlier, the heat exchanger will foul when it stays above the fouling threshold curve. Higher wall temperature and lower velocity will lead to more fouling deposition formed in the operation period. In Figure 9.7, all heat exchangers in the base case stay above the fouling threshold curve. Moreover, heat exchangers E1A and E1B stay farthest away from the threshold curve, indicating that these two heat exchangers will be severely fouled. The reason is that E1A and E1B are located at the hot end of the cold stream, where the wall temperatures are high and the initial velocities are low. Meanwhile, heat exchangers E5 and E6 are close to the threshold curve; because both heat exchangers are far from the hot end of the preheat train, hence their lower wall temperatures will not lead to severe fouling.

9.6.1.1 Optimization Results

By solving Eq. (9.33) (C_{clean} is not considered in this case) subject to Eqs. (9.1)–(9.32) and (9.34)–(9.40), the results of the stream split ratios over the whole operational period are described in Table 9.3. For example, the split ratio for SP-H1 is 0.473, representing that 43.7% of the mass flow rate of hot

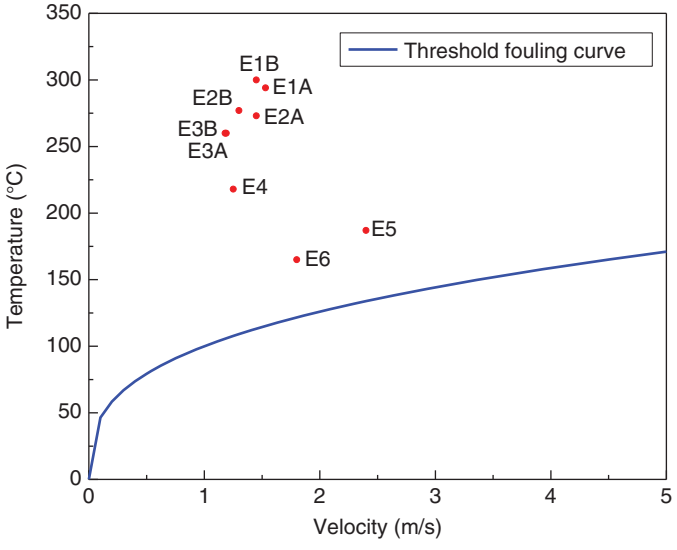

Figure 9.7 Fouling threshold curve and exchangers condition in base case (Case Study 1).

Table 9.3 Stream split ratio in the base and optimized case (the split ratio are calculated based on branch A).

Splitters	SP-C	SP-H1	SP-H2	SP-H3
Split ratio (base case)	0.5	0.5	0.5	0.5
Split ratio (optimized case)	0.475	0.473	0.493	0.468

stream H1 is distributed to the heat exchanger E1A in branch A. In other words, 56.7% of hot stream H1 is distributed to heat exchange E1B in branch B. As can be seen in Table 9.3, the values of all split ratios after optimization decrease as compared with the base case. For crude oil, the split ratio is mainly dependent on the difference of the fouling resistances and the heat duty between the parallel branches. Although all heat exchangers in this case are clean at the initial time, heat exchangers present different fouling rates due to different velocities and wall temperatures. The average fouling resistances of branches A and B during the investigated time horizon are 4.91 and 5.29 m^2 K/kW, respectively. This indicates that branch B is easier to foul, so greater mass flow rate is required to increase the velocity for fouling mitigation. Moreover, the increase in mass flow rate can positively affect the convective HTC, apart from fouling mitigation. The average heat duty of branch B is higher than that of branch A in the base case, which indicates that, with same increasing percentage of HTC, the increase of the heat duty in branch B is larger than that of branch A.

Figure 9.8 presents the initial crude oil velocity distribution in the base and optimized case. It can be seen from the figure, for heat exchangers upstream of the flash, the initial velocities of heat exchangers E6 and E5 after optimization

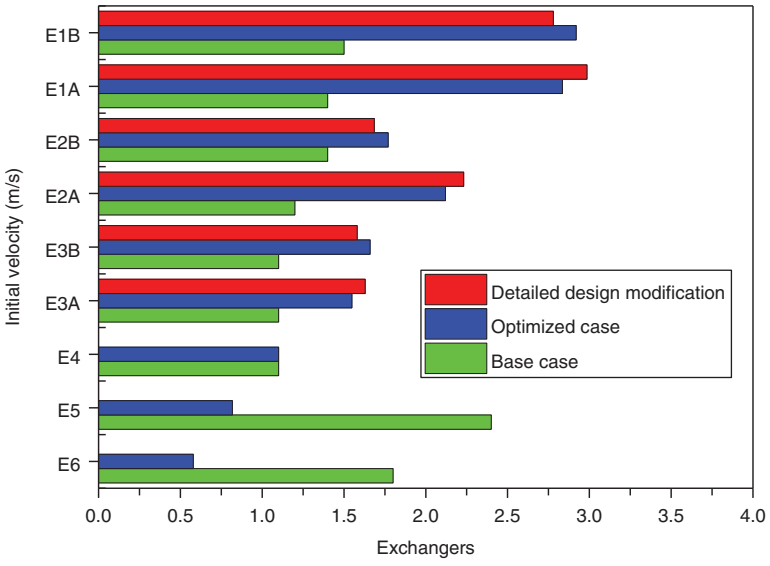

Figure 9.8 Initial velocity distribution in the base and optimized case.

decrease sharply. This is because E6 and E5 are far from the fouling region, and no severe fouling is expected for E6 and E5, even at low velocities. Thus, the velocities are decreased to save the pump capacity, while velocities are increased in other heat exchangers that are prone to fouling. It must be emphasized that the velocity has to be kept at a reasonable value to maintain the heat transfer efficiency. For E4, the initial velocity in the optimized case is the same as that in the base case mainly because it is near the optimal value in the base case when trade-off among fouling, pressure drop, and heat transfer is considered. For parallel heat exchangers downstream of the flash, velocities for these units are increased not only by changing the split ratios but also by detailed structure modification of the heat exchangers. Since the wall temperature is high, the velocity tends to be high to avoid fast fouling after optimization, especially for E1A and E1B (with the highest wall temperature). In Figure 9.8, the third column for parallel heat exchangers E3A through E1B represents the optimal velocity distribution through detailed structure modification only (the cold stream split ratio is set to be 0.5). The difference between the values of the second columns and the third columns is helpful for designers to observe the contribution of split fractions and detailed structure modification as compared with the initial velocity of the parallel heat exchangers. For example, the second columns are generally higher than the third columns for heat exchangers in branch B due to the increase of the mass flow rate of crude oil in branch B after optimization. It is worth noting that the initial velocities of heat exchangers in branch A are improved after optimization, even with a reduction in crude oil split fraction, this is due to the detailed design modification.

Figure 9.9 shows the initial and average heat duty of the heat exchangers in both the base and optimized cases. The index X represents the difference between the initial and average heat duty of every heat exchanger. The heat duty reflects the

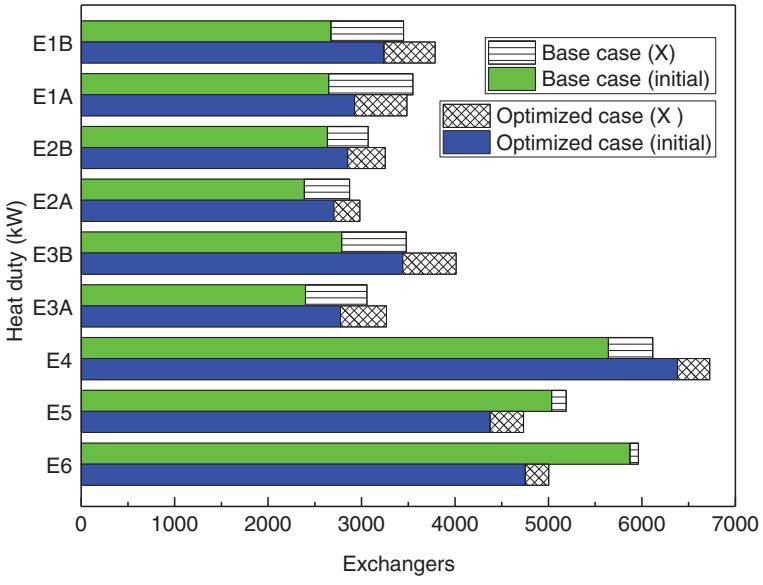

Figure 9.9 Initial and average heat duty of heat exchangers in base and optimized cases.

heat recovery and is directly related to the cost of utilities, which is the major component of the total cost. In Figure 9.9, both the initial and average heat duties of E6 and E5 in the optimized case decrease as compared with the base case, owing to the reduction in velocities. For E4, both the initial and average heat duty increase after optimization, even without a change in velocity. This is because of the up- and downstream relation between the heat exchangers. The inlet temperature of crude oil in E4 dropped due to the reduction of the heat duty in E6 and E5, so the heat transfer driving force in E4 is increased to have a larger heat duty. The reduction in duty of E1A can be also explained by the up- and downstream relation between the heat exchangers. In addition, the decrease in the flow rate in branch A makes the temperature change for both hot and cold streams more significantly, resulting in a reduction of heat transfer driving force. On the contrary, the increase in flow rate of branch B makes the heat duty of heat exchangers in branch B larger than those in branch A after optimization.

It is known that the heat duty of a heat exchanger decreases with time due to fouling in the operational period, so the difference (X) between initial and average heat duty can represent the severity of fouling in heat exchangers. It can be seen that the difference between the initial and average heat duty of the parallel heat exchangers decreases after optimization, due to the fouling mitigation.

Figure 9.10 presents the fouling rates of E6 and E1B during the investigated time, for both base and optimized cases. It can be seen in Figure 9.6 that the fouling rate of E1B is much higher than that of E6, and it decreases rapidly with time. This is because the increase of deposition of foulant leads to a decline of wall temperature and an increase in velocity, and both aspects decrease the fouling rate. It can be predicted that the fouling rate will become a constant value eventually, if the investigated period is long enough. It can be also seen that the

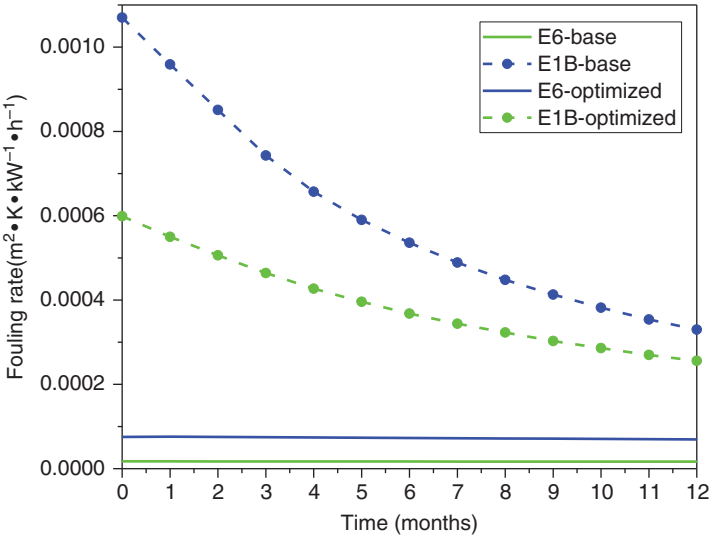

Figure 9.10 Fouling rates of E6 and E1A both in base and optimized cased.

fouling rate of E1B presents an apparent reduction after optimization, mainly due to the increase in velocity of E1B. On the contrary, the fouling rate of E6 in both cases is almost horizontal and on the verge of zero, which indicates that E6 is very unlikely in experiencing the fouling problem.

The furnace inlet temperature (FIT) profile is an important indicator for the performance of the crude oil preheat train, which can estimate the fuel consumption to meet the target temperature of the crude oil. Figure 9.11 shows the

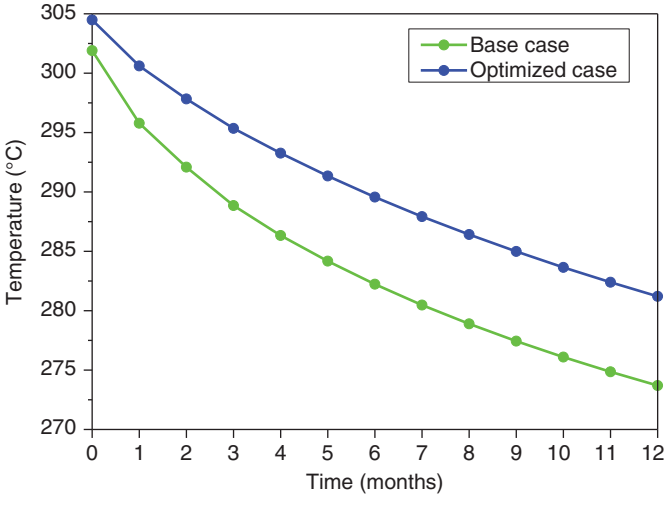

Figure 9.11 Comparison of FIT in the base and optimized cases.

comparison of FIT profiles between the base and optimized cases over the operational period (12 months). It can be seen that the trends of the two curves are similar, which are decreasing with time due to fouling. The decline rate of the FIT profile also gradually decreases with time, which can be explained on the basis of the interaction with fouling rates of heat exchangers. The FIT decreases by 23.3 °C (= 304.5 – 281.2 °C) during the operational period in the optimized case, while the FIT before optimization is determined as 28.3 °C (= 302.2 – 273.9 °C). The comparison of the FIT profiles clearly indicates a better HEN performance and appreciable energy savings after optimization.

Table 9.4 presents the cost related data. Utility cost used in this paper is taken from the work of Panjeshahi and Tahouni [30], power charge refers to current price in China. Table 9.5 presents the total annualized cost in the base, optimized, and two reference cases. Comparing the optimized case with the base case, the power costs after optimization change slightly, but total utility cost decreases sharply by US$193.03k per year. The lifetime for all pumps and heat exchangers is set to be five years. The total annualized cost is reduced from US$4677.87k to US$4535.00k per year, saving about US$142.87k per year. Two reference cases are performed to compare the optimization results. Reference case 1 is based on the method proposed by Assis et al. [19], which choose stream split ratios both for cold and hot streams as optimization variables and the hot utility cost is treated as objective function without considering the cost for power and pump. From the results, it can be seen that the total annualized cost has increased as compared with the base case, even with a reduction in the utility cost. This is because the changes in mass flow rate of the two parallel branches can cause very high pressure drop, which is not considered in this case. Reference case 2 is based

Table 9.4 Cost related data (Case Study 1).

Items	Values
Power cost ($/kW yr)	400
Cold utility ($/kW yr)	11.8
Hot utility ($/kW yr)	118
Pump efficiency (%)	70

Table 9.5 Economic efficiency in different cases (Case Study 1).

Items	Base case	Optimized case	Reference case 1	Reference case 2
Utility cost (k$/yr)	4423.51	4230.48	4410.20	4266.35
Power cost (k$/yr)	16.73	19.08	20.62	17.48
Pump capital cost (k$/yr)	237.62	272.00	282.95	252.15
Detailed structure modification cost (k$/yr)	0	13.44	0	13.44
Total cost (k$/yr)	4677.87	4535.00	4713.77	4549.43

on the work of Wang et al. [28], which mitigates fouling by optimizing velocity only through modifying detailed design of heat exchangers; with saving of about US$128.44k per year as compared with the base case (see Table 9.5). It can be seen that the presented work in this chapter has higher economic efficiency.

9.6.2 Case Study 2: Simultaneous Consideration of Velocity and Cleaning Schedule Optimization

Case Study 2 is taken from Rodriguez and Smith's work [15], with the HEN structure for a crude oil preheat train shown in Figure 9.12. The case is a simplified crude oil preheat train, the design and operation parameters for the HEN is summarized in Table 9.6.

Due to the different mechanisms for fouling deposition in the heat exchangers at the cold end of the network (E4–E11), the accumulation of fouling depends on physical deposition, where a constant value of fouling rate was used. At the hot end of the network (E1–E3), more severe fouling problem is caused by the chemical reaction. Polley's model [5] is used to describe the fouling rate. The division of hot end and cold end is based on temperature, as fouling mechanisms is different for different temperatures. As mentioned, fouling process can be mitigated through the changes of flow velocity, so the optimization of velocity is considered only at the hot end, giving three continuous decision variables. According to the operation conditions of the crude oil preheat in practical oil refinery, the velocity range of crude oil is set to be 0.5–3 m/s. The cost related data and property data are listed in Table 9.7.

The cleaning actions are carried out through off-line cleaning. During cleaning period, the hot and cold streams are bypassed to the next related unit and the rest of heat exchangers continue working on-line. Cleaning cost is assumed to be the same in every heat exchanger. In this case study, the optimal cleaning schedule and velocity distribution for the network are considered over a time

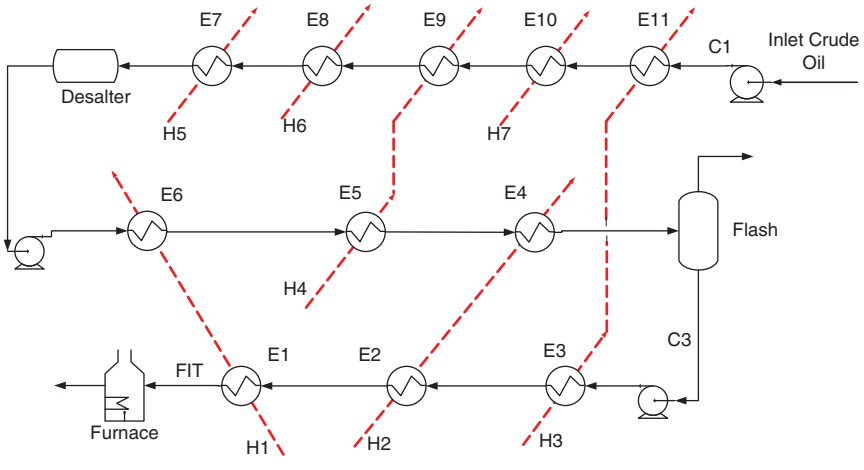

Figure 9.12 Diagram of crude oil preheat train for the Case Study 2.

Table 9.6 Design and operation parameters for Case Study 2.

Exchangers	Hot stream		Clod stream		K (kW/(m^2 °C))	A (m^2)	Heat duty (kW)
	T_{in} (°C)	$M_h Cp_h$ (kW/°C)	T_{in} (°C)	$M_c Cp_c$ (kW/°C)			
E1	334	97.4	210	220.8	0.5	111.2	4968.0
E2	286	132.0	191	220.8	0.5	122.6	4195.2
E3	249	53.2	178	220.8	0.5	182.0	2870.4
E4	254	132.0	167	218.5	0.5	67.1	2403.5
E5	205	145.1	161	218.5	0.5	67.2	1311.0
E6	285	97.4	135	218.5	0.5	110.1	5681.0
E7	237	129.2	116	182.4	0.5	121.6	3465.6
E8	170	129.2	101	182.4	0.5	112.9	2736.0
E9	197	145.1	50	182.4	0.5	208.3	9302.4
E10	296	9.6	45	182.4	0.5	8.9	912.0
E11	194	53.5	26	182.4	0.5	56.6	3465.6

Table 9.7 Cost and physical related data (Case Study 2).

Items	Values
Power cost ($/MW h)	45
Cleaning cost ($/cleaning action)	20 000
Hot utility ($/MW h)	15.5
Specific heat capacity of crude oil (J/kg °C)	2.4
Thermal conductivity of crude oil (W/m °C)	0.075
Fouling thermal conductivity (kW/m °C)	0.002

horizon of three years. The time horizon is divided into 36 equal periods (one month for a period), and length of each sub-period is 15 days ($t^{cl} = t^{pr} = 15$). The whole time horizon gives 396 binary variables for all heat exchangers. The inner diameter for tube sides is 0.025 m for all the heat exchangers. The parameters of fouling threshold model are given as follows [4]: $\alpha = 2.4 \times 10^7$ m^2 °C/(kW d), $\gamma = 3.6 \times 10^{-8}$ m^2 °C/(kW d), $E = 48$ kJ/mol.

In the base case, all binary variables $y_{i,n}$ are set to be 1, which means that no cleaning action is taken to mitigate fouling in the network. Three scenarios are implemented to compare the overall performance of HEN under different fouling mitigation strategy. In Scenario 1, only cleaning schedule optimization is considered, and the operation conditions of the network are not optimized. In Scenario 2, only velocity optimization is considered. In Scenario 3, the cleaning schedule and velocity distribution in the network are optimized simultaneously. The pump investment is only considered in Scenarios 2 and 3, where optimization of velocity is involved.

9.6.2.1 Constraints for Case Study

In continuous operation HENs, in order to meet the requirement of actual production process, some constraints must be applied to restrict the optimization parameters.

The NTU method is an area-based calculation process, where temperature differences of hot and cold streams are always larger than zero. Therefore, there is no minimum temperature approach constraint.

Since the interval between two adjacent cleaning sub-periods is short (one month), continuous cleaning actions are prevented with the constraint in Eq. (9.41).

$$y_{i,n} + y_{i,n-1} \geq 1 \tag{9.41}$$

In order to prevent the furnace load from reaching its operation limitation (but still satisfying the temperature range of the fluid entering the flash), the cleaning action for certain exchanger groups must be limited to ensure that the HEN is controllable. Corresponding constraints are shown in Eqs. (9.42)–(9.44).

$$y_{i=1,n} + y_{i=2,n} + y_{i=3,n} \geq 2 \tag{9.42}$$

$$y_{i=4,n} + y_{i=5,n} + y_{i=6,n} \geq 2 \tag{9.43}$$

$$y_{i=7,n} + y_{i=8,n} + y_{i=9,n} + y_{i=10,n} + y_{i=11,n} \geq 2 \tag{9.44}$$

As depicted in Figure 9.12, some hot streams pass through series exchangers in the HEN, the combination of cleaning actions of related exchangers should be limited to satisfy the target temperature of the hot streams, given by the constraints in Eqs. (9.45)–(9.47).

$$y_{i=1,n} + y_{i=6,n} \geq 1 \tag{9.45}$$

$$y_{i=2,n} + y_{i=4,n} \geq 1 \tag{9.46}$$

$$y_{i=3,n} + y_{i=11,n} \geq 1 \tag{9.47}$$

As stated earlier, pressure drop also imposes a constraint. For the exchangers at the hot end, the maximum pressure drop should be retrained to keep the total pressure drop lower than the pump capacity margin. In addition, because pressure drop is related to deposition layer thickness, the constraint can also be used to maintain the FIT by keeping the fouling at a certain level. The relevant constraint used in this work is given as in Eq. (9.48).

$$\Delta P_n = \Delta P_{i=1,n} + \Delta P_{i=2,n} + \Delta P_{i=3,n} \leq 1.5\Delta P_{n=0} \tag{9.48}$$

where ΔP_n represents the total pressure drop of E1–E3. If the pressure drop of exchanger E1–E3 cannot satisfy the aforementioned constraint, it indicates that cleaning actions must be implemented among these three exchangers.

Temperature target constraint on fluid entering into the furnace is considered, to avoid reaching its capacity limit for a given throughput, as shown in Eq. (9.49).

$$T_{1,n}^{c,out} \geq 200\ ^\circ\mathrm{C} \tag{9.49}$$

Owing to the disturbance of desalter on the temperature of crude oil, the temperature relation between E6 and E7 is considered by the following relationship in Eq. (9.50).

$$T_{6,n}^{c,in} = T_{7,n}^{c,out} - 10 \tag{9.50}$$

9.6.2.2 Results and Discussion

By solving Eq. (9.33) subject to Eqs. (9.1)–(9.32) and (9.34)–(9.50), the optimized cleaning schedules for Scenarios 1 and 3 are determined and shown in Tables 9.8 and 9.9. As illustrated in the schedules, exchangers at the hot end of the network (e.g. E1 and E2) require more frequent cleaning actions, as more severe fouling deposition is expected. It is notable that E3 is cleaned only once (Scenario 3) or twice (Scenario 1) even though it is at the hot end. This is because the heat duty of E3 is much lower as compared with E1 and E2. Too many cleaning actions are not economical since the restored heat recovery is low. Heat duty and heat exchange area of E2 and E9 are larger than those of E11. So cleaning E4 and E5 more frequently will benefit heat recovery of the hot streams. It can also be found that E8 is cleaned more frequently than the other exchangers at the cold end of the network. Compared with E3, E8 has same level of heat duty but with lower fouling rate. It is not very beneficial to clean E8 too many times merely for heat recovery. So the reason for frequent cleaning actions of E8 should be analyzed from the interaction between heat exchangers in the HEN. Due to the constraints of FIT and pressure drop, some exchangers must be taken out of service and cleaned in certain time periods to satisfy the constraints. Compared with other heat exchangers, E8 is only restricted by constraint in Eq. (9.44), so its frequent cleaning does not easily lead to constraints violation. In contrary, E3 is restricted by constraints in Eqs. (9.42) and (9.47); hence, frequent cleaning actions in E3 increase the possibility of constraints violation. Similar phenomenon occurs in E4 and E5. The heat duty and fouling rate in E4 and E5 are lower than those of E3, but they require more cleaning actions. There is one constraint that is effective for every exchanger, i.e. the temperature target constraint on fluid entering the furnace in Eq. (9.49). When the temperature entering the furnace violates Eq. (9.49), there must be some exchangers taken out for cleaning. So those heat exchangers with fewer constraints tend to be cleaned. Due to the constraints, the distribution of cleaning actions in the cleaning schedule obtained for a network may not show a strong regularity, but it does follow the rule that exchangers with higher fouling rate and larger heat duty tend to be cleaned more frequently.

From the cleaning schedules shown in Tables 9.8 and 9.9, 29 cleaning actions are required for Scenario 1, while only 20 cleaning actions are required for Scenario 3. It is worth nothing that for E1–E3, the sum of cleaning number is reduced by 5; this is because the fouling rate of E1–E3 has been significantly reduced by velocity optimization in Scenario 3, as shown in Table 9.10. In addition, velocity optimization improves the heat transfer across the network. So exchangers are not cleaned that frequently. It is also noted that the cleaning actions required in Scenario 3 are more concentrated in the middle of the time horizon. As less cleaning actions are needed in Scenario 3, it is more cost-effective to avoid cleaning actions near the start and end periods of the time horizon. This is because

Table 9.8 Optimized cleaning schedules for Scenario 1.

	Months																																		
HEX	**1**	**2**	**3**	**4**	**5**	**6**	**7**	**8**	**9**	**10**	**11**	**12**	**13**	**14**	**15**	**16**	**17**	**18**	**19**	**20**	**21**	**22**	**23**	**24**	**25**	**26**	**27**	**28**	**29**	**30**	**31**	**32**	**33**	**34**	**35**	**36**	**Total**
1							√				√								√									√					√				5
2			√										√				√					√								√							5
3										√													√														2
4									√									√												√							3
5																√								√													2
6														√												√											2
7												√																									1
8											√		√								√				√												4
9																			√																		1
10						√												√																			2
11																	√																	√			2
Cleans	0	0	1	0	0	1	1	0	1	1	2	1	2	1	0	1	2	2	2	0	1	1	1	1	1	1	0	1	0	1	1	0	1	1	0	0	29

Table 9.9 Optimized cleaning schedules for Scenario 3.

	Months																																
HEX	**1**	**2**	**3**	**4**	**5**	**6**	**7**	**8**	**9**	**10**	**11**	**12**	**13**	**14**	**15**	**16**	**17**	**18**	**19**	**20**	**21**	**22**	**23**	**24**	**25**	**26**	**27**	**28**	**29**	**30**	**31**	**32**	**33**	**34**	**35**	**36**	**Total**
1									√										√										√								3
2											√									√							√										3
3																	√																				1
4															√													√									2
5														√										√													2
6													√												√												2
7												√											√														2
8												√													√					√							3
9																		√																			1
10																					√																1
11																																					0
Cleans	0	0	0	0	0	0	0	0	1	0	1	2	1	1	1	0	1	1	1	1	1	0	1	1	2	0	1	1	1	1	0	0	0	0	0	0	20

Table 9.10 Fouling rate of different scenarios at hot end of the network.

		Initial fouling rate (m^2 K/(kW d))		
Exchangers	**Base case**	**Scenario 1**	**Scenario 2**	**Scenario 3**
E1	9.90×10^{-3}	9.90×10^{-3}	2.20×10^{-3}	3.22×10^{-3}
E2	7.07×10^{-3}	7.07×10^{-3}	1.48×10^{-3}	1.44×10^{-3}
E3	4.21×10^{-3}	4.21×10^{-3}	1.54×10^{-3}	2.18×10^{-3}

fouling deposition is not very severe near the initial several segments, and there is not enough time left to recover the heat after fouling removal near the final segments. That is the reason why the schedule of Scenario 3 shows a more concentrated distribution.

The optimization results are listed in Table 9.11. Comparison of hot utility cost for non-fouling condition and the base case indicates that fouling causes a significant increase in furnace duty during operation period. The hot utility cost under fouling condition is US$5 227 781, which is much higher than non-fouling condition (US$2 431 724). Due to velocity optimization, the power cost in Scenarios 2 and 3 have significantly increased, and extra pumps are required which incur higher capital investment. For Scenario 3, due to the simultaneous optimization of flow velocity and cleaning schedule, cleaning cost and pump investment are both reduced as compared with Scenarios 1 and 2. The total cost for Scenario 2 is lower than that in Scenario 1, indicating that the optimization of flow velocity is a more effective way as compared with cleaning schedule based on the network selected in this work. Fouling of different crude oil has different sensitivity on velocity, so in some other scenarios, cleaning schedule optimization may be

Table 9.11 Summary of optimized results for selected scenarios.

	Non-fouling condition	**Base case**	**Scenario 1**	**Scenario 2**	**Scenario 3**
Initial FIT (°C)	232	232	232	245	243
Final FIT (°C)	232	182	215	206	227
Number of cleaning actions	0	0	29	0	20
Pump investment ($)	0	0	0	454 098	336 164
Power cost ($)	20 665	30 245	24 032	76 140	57 160
Cleaning cost ($)	0	0	580 000	0	400 000
Hot utility cost ($)	2 431 724	5 227 781	3 692 140	3 320 781	2 532 884
Total cost ($)	2 452 389	5 258 080	4 296 171	3 851 020	3 326 210
Reduction in hot utility cost (%)	0	0	30	36	52
Reduction in operation cost (%)	0	0	18	27	37

more effective. For Scenario 3, although the costs of pump investment, power, and cleaning are high, its hot utility has a remarkable reduction. Due to simultaneous consideration of flow velocity and cleaning schedule, the total annualized cost in Scenario 3 is only US$3 326 210 , which is much lower than the other scenarios.

The FIT profiles for all scenarios are shown in Figure 9.13. In the figure, the temporary sharp drops in FIT profiles of Scenarios 1 and 3 indicate that groups of heat exchangers are out of service for cleaning in the corresponding time periods. Due to the improvement of HTC in velocity optimization, the initial FIT in Scenarios 2 and 3 is around 10 °C higher than that in the base case and Scenario 1. As observed, the FIT profile of base case decreases sharply from 232 to 182 °C during the operation period, i.e. a reduction of 50 °C. On average, the FIT of Scenario 3 (almost all above 215 °C) is higher than that in Scenario 2, so its energy cost is the lowest. Correspondingly, the energy cost is around US$3 692 140 by optimizing cleaning schedule in Scenario 1, and US$3 320 781 by optimizing velocity in Scenario 2, with a reduction of 30% and 36%. Since fewer cleaning actions are required, the FIT profile of Scenario 3 features fewer drops than that in Scenario 1.

This method considers fouling, heat transfer, and pressure drop simultaneously so that the design obtained from the method can be more practical. Simultaneously consideration of cleaning schedule and velocity can give a more

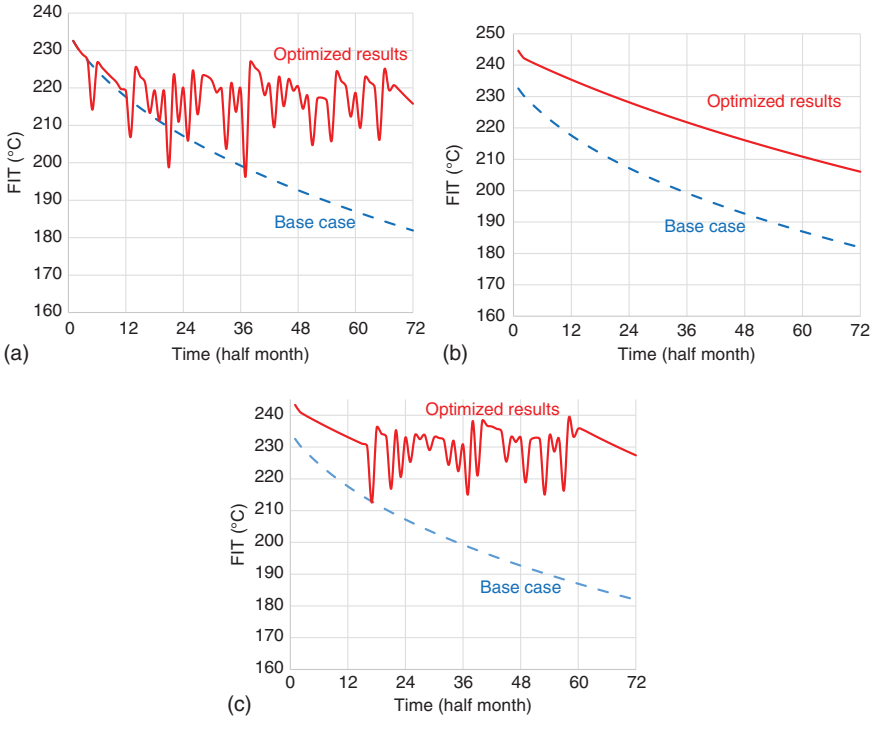

Figure 9.13 FIT profiles for selected scenarios over the whole time horizon. (a) Scenario 1, (b) Scenario 2, and (c) Scenario 3.

comprehensive consideration of fouling mitigation strategy. The results can give a guideline for retrofit and design of crude oil preheat train. The method can be applied to any crude oil preheat train, but it is noted that different crude oil has a different fouling threshold model parameter. Therefore, it is better to get the right parameter through experiments first, and then the proposed methodology can be applied.

9.6.2.3 Considering Backup Heat Exchanger

When backup heat exchanger is considered, the constraint must be adjusted. This is because when heat exchangers with backup units are taken off-line, heat duty is still maintained, and some binary variables need to be changed. In the case study, Eqs. (9.42), (9.45), and (9.46) are not applied, while Eq. (9.43) is modified as Eq. (9.51). The other constraints remain unchanged.

$$y_{i=4,n} + y_{i=5,n} \geq 1 \tag{9.51}$$

All heat exchangers in the case are simulated. By the trade-off between backup heat exchanger capital cost and heat duty loss in cleaning action, it is beneficial to install backup heat exchangers on E1, E2, and E6. Optimization is carried out to find the optimal cleaning schedule under two different situations, i.e. with and without backup heat exchangers. Table 9.12 shows the detailed cleaning schedule for the situation considering backup heat exchangers. Compared with the results shown in Table 9.8, the cleaning schedule for the heat exchangers with a backup unit is significantly changed. After installing backup heat exchangers on E1, E2, and E6, the number of cleaning actions is more frequent. The reason is that after installing the backup heat exchangers, cleaning actions will no longer lead to off-line heat duty loss. Meanwhile, because of cleaning cost, too many cleaning actions are not beneficial.

Figure 9.14 gives the FIT curve for the situation with and without backup heat exchangers. In the curve, every sudden drop indicates one or several clean actions in that period. When backup heat exchangers are applied, it can be clearly seen that the sudden drops are relieved, indicating a higher heat recovery during operation period.

9.7 Conclusion

Fouling is a crucial problem in HEN operation. In HEN synthesis, fluid velocity is a key variable that can correlate fouling, pressure drop, and heat transfer. Therefore, velocity is dealt as a key variable in the optimization to find the best velocity distribution in HEN. Further, cleaning schedule optimization and backup heat exchangers are considered simultaneously with velocity optimization.

From the case studies, it is found that velocity distribution is sensitive to fouling, duty of heat exchangers, and heat capacity flow rates. Exchangers with higher fouling rate, larger heat duty, and heat capacity flow rates tend to have higher velocity. It can be also found that the velocities of some heat exchangers are

Table 9.12 Cleaning schedule with back-up heat exchangers.

	Months																																			
HEX	**1**	**2**	**3**	**4**	**5**	**6**	**7**	**8**	**9**	**10**	**11**	**12**	**13**	**14**	**15**	**16**	**17**	**18**	**19**	**20**	**21**	**22**	**23**	**24**	**25**	**26**	**27**	**28**	**29**	**30**	**31**	**32**	**33**	**34**	**35**	**36**	**Total**
1				√				√			√				√				√					√				√					√				8
2				√					√				√				√					√					√				√					7
3										√													√														2
4																		√																			1
5																																					0
6									√									√										√									3
7												√																									1
8																		√																			1
9																			√																		1
10																																					0
11																																					0
Cleans	0	0	1	2	0	0	0	1	2	1	1	1	1	0	1	0	1	3	2	0	0	1	1	1	0	0	1	2	0	0	0	1	1	0	0	0	24

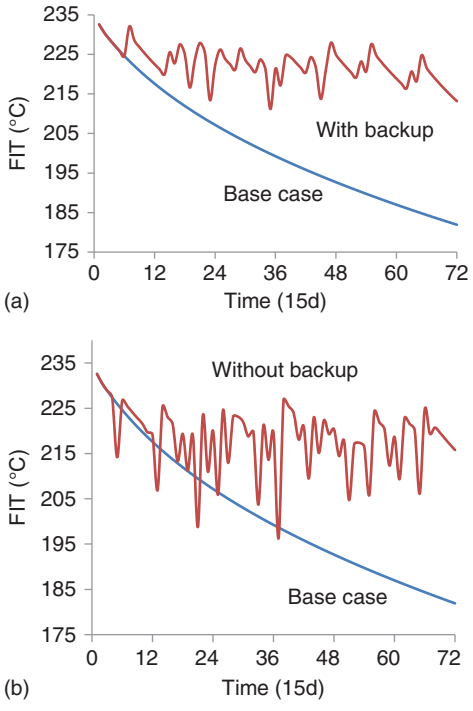

Figure 9.14 FIT profiles for selected scenarios over the whole time horizon: (a) with backup and (b) without backup.

reduced after optimization. The reason is that those heat exchangers are not sensitive to velocity, and pressure drop can be reduced in those heat exchangers to save pump power.

From the results of Case 2, it can be seen that the application of systematical cleaning actions can reduce the total cost (18.3% reduction in total cost), but it does not slow down the fouling rate, and the FIT has frequent and sharp fluctuation. When only velocity optimization is applied, total cost is further reduced compared with cleaning schedule optimization (26.8% reduction in total cost), indicating flow velocity optimization is more effective for this specified case. When cleaning schedule and flow velocity are optimized simultaneously, the results show a much higher energy saving and lower cost (36.7% reduction in total cost). With the reduction in fouling rate, the number of cleaning actions is lowered, which means fewer disturbances to the HEN during operation period. When backup heat exchanger is considered, it is found that it is benefit for installing backup heat exchangers when the heat exchanger has large heat duty and high fouling rate.

Acknowledgments

Financial supports from National Natural Science Foundation of China (No. 21576286) and Science Foundation of China University of Petroleum, Beijing (No. 2462017BJB03 and 2462018BJC004) are gratefully acknowledged.

Nomenclature

A	heat transfer area of a heat exchanger (m^2)
a	model parameter for calculating exchanger cost
b	model parameter for calculating exchanger cost
C	cost ($)
Cp	specific heat capacity of a stream (J/kg K)
cu	unit cost of cold utility ($/kW)
d	inner diameter of tube (m)
E	activation energy (kJ/mol)
h	convective heat transfer coefficient (W/(m^2 K))
hu	unit cost of hot utility ($/kW)
K	Overall heat transfer coefficient (W/(m^2 K))
L	The length of tubes in a heat exchanger (m)
M	mass flow rate (kg/s)
N	number of tube passes
n	number of time intervals
NTU	heat transfer unit in NTU method
P	thermal effectiveness in NTU method
pc	unit electricity cost
Pr	Prandtl number
Q	heat duty (kW)
R	heat capacity flow rate ratio of cold stream to the hot stream
Re	Reynolds number
Rf	fouling resistance (m^2 °C/W)
R_g	gas constant (J/(mol K))
T	temperature (°C)
t	time interval
V	volumetric flow rate (m^3/s)
v	tube side velocity (m/s)
v'	velocity of heat exchanger considering only detailed design modification (m/s)
y	binary variable representing the cleaning condition of heat exchanger
Yr	equipment life time
ΔPf	pressure drop of a heat exchanger (Pa)
ΔPl	local resistance of a heat exchanger (Pa)
ΔPn	nozzle resistance of a heat exchanger (Pa)
ΔPs	straight pipe resistance of a heat exchanger (Pa)
ΔP_T	total pressure drop of a stream (Pa)

Greek Letters

α	model parameter of fouling threshold model
β	model parameter for calculating exchanger cost
η	pump efficiency
γ	model parameter of fouling threshold model

ρ	fluid density (kg/m^3)
λ	fluid heat conductivity (W/(m^2 °C))
μ	fluid viscosity (Pa s)
δ	thickness of fouling layer (m)
ξ	friction coefficient
ζ'	local resistance coefficient
θ	structure modification cost coefficient

Subscripts

base	base case
branch	the branch in heat exchangers in parallel structure
bulk	bulk temperature
c	cold side
cu	cold utility
ex	heat exchanger
h	hot side
hu	hot utility
i	index for heat exchanger
j	index for branch
LB	lower bound
MX	mixer
modify	detail design modification for heat exchanger
optimized	optimized case
parallel	heat exchangers in parallel
S	shell side
series	heat exchangers in series
SP	splitter
supply	supply condition
T	tube side
target	target condition
UB	upper bound
w	tube wall

Superscripts

cl	cleaning sub-period
in	inlet
out	outlet
pr	processing sub-period

References

1 Klemeš, J.J., Varbanov, P.S., and Kravanja, Z. (2013). Recent developments in Process Integration. *Chemical Engineering Research and Design* 91 (10): 2037–2053.

2 Ebert, W. and Panchal, C. (1995). *Analysis of Exxon Crude-oil-slip Stream Coking Data*. Lemont, IL: Argonne National Laboratory.

3 Panchal, C.B., Kuru, W.C., Liao, C.F. et al. (1999). Threshold conditions for crude oil fouling. In: *Understanding Heat Exchanger Fouling and its Mitigation*, Proceedings of an International Conference on Understanding Heat Exchanger Fouling and Its Mitigation, 273–282. New York: Begell House. ISBN: 156700136X 9781567001365.

4 Asomaning, S., Panchal, C.B., and Liao, C.F. (2000). Correlating field and laboratory data for crude oil fouling. *Heat Transfer Engineering* 21 (3): 17–23.

5 Polley, G.T., Wilson, D.I., Yeap, B.L., and Pugh, S.J. (2002). Evaluation of laboratory crude oil threshold fouling data for application to refinery pre-heat trains. *Applied Thermal Engineering* 22 (7): 777–788.

6 Yeap, B.L., Wilson, D.I., Polley, G.T., and Pugh, S.J. (2004). Mitigation of crude oil refinery heat exchanger fouling through retrofits based on thermo-hydraulic fouling models. *Chemical Engineering Research and Design* 82 (1): 53–71.

7 Bayat, M., Aminian, J., Bazmi, M. et al. (2012). CFD modeling of fouling in crude oil pre-heaters. *Energy Conversion and Management* 64: 344–350.

8 Łopata, S. and Ocłoń, P. (2015). Numerical study of the effect of fouling on local heat transfer conditions in a high-temperature fin-and-tube heat exchanger. *Energy* 92 (Part 1): 100–116.

9 Bishara, E., Abd-Elhady, M.S., and Halim, M.A. (2015). Influence of thermal shock on fouling of smooth, rough and finned tubes. *Energy* 93 (Part 1): 354–360.

10 Ishiyama, E.M., Paterson, W.R., and Ian Wilson, D. (2011). Optimum cleaning cycles for heat transfer equipment undergoing fouling and ageing. *Chemical Engineering Science* 66 (4): 604–612.

11 Pogiatzis, T., Ishiyama, E.M., Paterson, W.R. et al. (2012). Identifying optimal cleaning cycles for heat exchangers subject to fouling and ageing. *Applied Energy* 89 (1): 60–66.

12 Pogiatzis, T.A., Wilson, D.I., and Vassiliadis, V.S. (2012). Scheduling the cleaning actions for a fouled heat exchanger subject to ageing: MINLP formulation. *Computers and Chemical Engineering* 39: 179–185.

13 Smaïli, F., Vassiliadis, V.S., and Wilson, D.I. (2001). Mitigation of fouling in refinery heat exchanger networks by optimal management of cleaning. *Energy and Fuels* 15 (5): 1038–1056.

14 Smaïli, F., Vassiliadis, V.S., and Wilson, D.I. (2002). Long-term scheduling of cleaning of heat exchanger networks: comparison of outer approximation-based solutions with a backtracking threshold accepting algorithm. *Chemical Engineering Research and Design* 80 (6): 561–578.

15 Rodriguez, C. and Smith, R. (2007). Optimization of operating conditions for mitigating fouling in heat exchanger networks. *Chemical Engineering Research and Design* 85 (6): 839–851.

16 Ishiyama, E., Heins, A., Paterson, W. et al. (2010). Scheduling cleaning in a crude oil preheat train subject to fouling: incorporating desalter control. *Applied Thermal Engineering* 30 (13): 1852–1862.

17 Ishiyama, E.M., Paterson, W.R., and Wilson, D.I. (2009). The effect of fouling on heat transfer, pressure drop, and throughput in refinery preheat trains: optimization of cleaning schedules. *Heat Transfer Engineering* 30 (10–11): 805–814.

18 Biyanto, T.R., Ramasamy, M., Jameran, A.B., and Fibrianto, H.Y. (2016). Thermal and hydraulic impacts consideration in refinery crude preheat train cleaning scheduling using recent stochastic optimization methods. *Applied Thermal Engineering* 108: 1436–1450.

19 Assis, B.C.G., Gonçalves, C.D.O., Liporace, F.S. et al. (2013). Constrained thermohydraulic optimization of the flow rate distribution in crude preheat trains. *Chemical Engineering Research and Design* 91 (8): 1517–1526.

20 Assis, B.C.G., Lemos, J.C., Liporace, F.S. et al. (2015). Dynamic optimization of the flow rate distribution in heat exchanger networks for fouling mitigation. *Industrial and Engineering Chemistry Research* 54 (25): 6497–6507.

21 Ishiyama, E.M., Paterson, W., and Wilson, D. (2008). Platform for techno-economic analysis of fouling mitigation options in refinery preheat trains. *Energy and Fuels* 23 (3): 1323–1337.

22 Wang, Y. and Smith, R. (2013). Retrofit of a heat-exchanger network by considering heat-transfer enhancement and fouling. *Industrial and Engineering Chemistry Research* 52 (25): 8527–8537.

23 Pan, M., Bulatov, I., and Smith, R. (2013). Exploiting tube inserts to intensify heat transfer for the retrofit of heat exchanger networks considering fouling mitigation. *Industrial and Engineering Chemistry Research* 52 (8): 2925–2943.

24 Pan, M., Bulatov, I., and Smith, R. (2016). Improving heat recovery in retrofitting heat exchanger networks with heat transfer intensification, pressure drop constraint and fouling mitigation. *Applied Energy* 161: 611–626.

25 Oldani, V., Sergi, G., Pirola, C., and Bianchi, C.L. (2016). Use of a sol-gel hybrid coating composed by a fluoropolymer and silica for the mitigation of mineral fouling in heat exchangers. *Applied Thermal Engineering* 106: 427–431.

26 Taylor, S.T., Jackowski, L., Losada, R. et al. (2017). Thin sol-gel coatings for fouling mitigation in shell-and-tube heat exchangers. In: *CORROSION 2017*, 2017. New Orleans, LA: NACE International.

27 Ebert, W.A. and Panchal, C.B. (1997). Analysis of Exxon crude-oil-slip stream coking data. In: *Fouling Mitigation of Industrial Heat Exchange Equipment* (eds. C.B. Panchal, T.R. Bott, E.F.C. Somerscales and S. Toyama), 451–460. New York, NY: Begell House.

28 Wang, Y., Zhan, S., and Feng, X. (2015). Optimization of velocity for energy saving and mitigating fouling in a crude oil preheat train with fixed network structure. *Energy* 93: 1478–1488.

29 Zhu, X.X. and Nie, X.R. (2002). Pressure drop considerations for heat exchanger network grassroots design. *Computers and Chemical Engineering* 26 (12): 1661–1676.

30 Panjeshahi, M.H. and Tahouni, N. (2008). Pressure drop optimisation in debottlenecking of heat exchanger networks. *Energy* 33 (6): 942–951.

10

Decomposition and Implementation of Large-Scale Interplant Heat Integration

Runrun Song[1], Xiao Feng[2], Mahmoud M. El-Halwagi[3], and Yufei Wang[4]

[1] *Sinopec Guangzhou Engineering Co., Ltd, 191# Tiyu West Road, Guangzhou 510620, China*
[2] *Xi'an Jiaotong University, School of Chemical Engineering and Technology, 28# Xianning West Road, Xi'an 710049, China*
[3] *Texas A&M University, Artie McFerrin Chemical Engineering Department, University Drive at Spence Street, College Station, TX, 77843, United States*
[4] *China University of Petroleum, State Key Laboratory of Heavy Oil Processing, 18# Fuxue Road, Beijing 102249, China*

10.1 Introduction

Process integration (PI) is a systematic methodology for resource saving and emission reduction that has been studied extensively over last 40 years [1]. *Heat integration* (HI) is the earliest PI trend, where a systematic method was developed for the synthesis of *heat exchanger networks* (HENs) for a process plant. The benefits for implementing HI include increased energy efficiency and reduced negative environment impacts [2]. Facility-wide HI or *total site heat integration* (TSHI) was first introduced by Dhole and Linnhoff [3] to determine additional reductions in energy use across multiple plants within an industrial site. TSHI is typically supported by a site utility system [1]. Within a TSHI, excess heat from a process can be transferred to another process via generated steam(s) or heat transfer fluid(s) [4]. Utilities, cogeneration, and emissions may be also taken into consideration in TSHI. As a subsection of TSHI, interplant heat integration (IPHI) [5–7] only focuses on the heat exchange opportunities across plants.

For IPHI (also for TSHI), especially for a large-scale problem, there are always several challenges that need to be solved.

(a) *Stream selection*: Which hot/cold streams should be extracted from individual plants and used for IPHI?
(b) *Plant selection*: Considering multiple alternative plants at a site, how many and which plants should be selected to undergo IPHI?
(c) *Plant integration*: In an IPHI scheme with multiple plants, how can we integrate the selected plants in order to recover energy across plants?

This work is determined to solve the problems earlier and to provide a feasible and practical solution for a large-scale IPHI problem. In Sections 10.1.1–10.1.3, the aforementioned problems are reviewed.

Process Intensification and Integration for Sustainable Design, First Edition.
Edited by Dominic C. Y. Foo and Mahmoud M. El-Halwagi.
© 2021 WILEY-VCH GmbH. Published 2021 by WILEY-VCH GmbH.

10.1.1 Reviews and Discussions for Stream Selection

To extract streams from individual plants for IPHI, researchers mainly use *grand composite curve* (GCC) to analyze the heat recovery potential across plants. Waste heat sources/sinks, which are currently serviced by utilities in the existing HENs, can be also directly used for IPHI. Besides, some researches also directly use process streams to conduct simultaneous intra- and interplant HI. These methods are reviewed in the following paragraphs respectively.

To facilitate better discussion, three definitions are first introduced, to differentiate how heat sources/sinks are extracted for IPHI study:

(a) *Waste heat source/sink*: Defined as the heat source/sink which is currently serviced by utilities in an existing HEN.
(b) *Surplus heat source/sink*: Defined as the remnant sections after removing the "pockets" below/above the pinch point on a GCC [3].
(c) *Nimiety heat source/sink*: Defined as the heat source/sink identified in our new proposed method, which is presented in Section 10.2.2.

A GCC is shown in Figure 10.1a. The three aforementioned heat sources/sinks are compared on the GCC as in Figure 10.1b. We can see from Figure 10.1b that surplus, waste, and nimiety heat sources/sinks have different temperature levels. For heat exchange system, high-temperature hot stream and low-temperature cold stream are preferred as they can provide a broader utilization space, which means they can offer more match options with more streams. We define the high-temperature hot stream and low-temperature cold stream as high-grade heat source/sink, respectively; correspondingly, the low-temperature hot stream

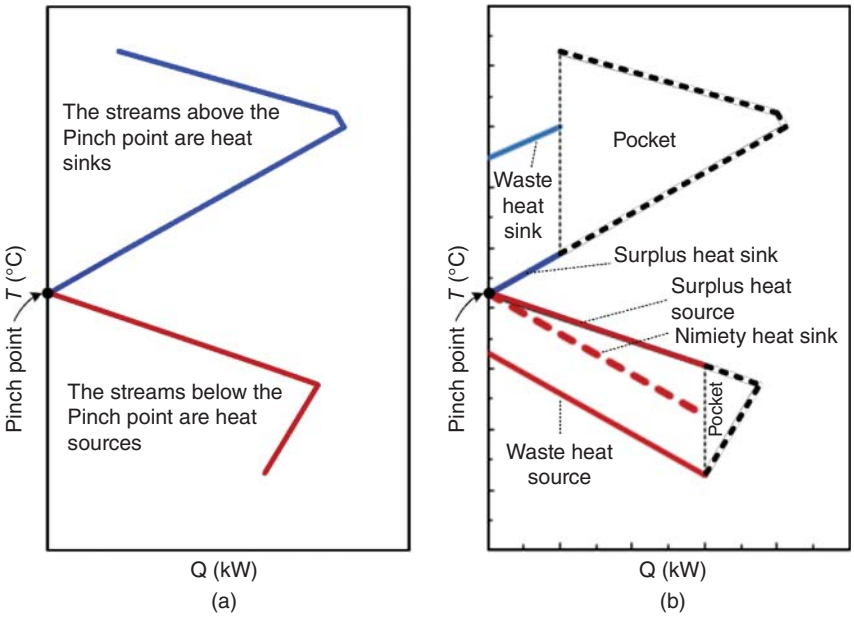

Figure 10.1 (a) GCC. (b) Comparison of different heat sources/sinks on a GCC.

and high-temperature cold stream are defined as low-grade heat source/sink, respectively. Therefore, the grades of surplus, nimiety, and waste heat source/sink are successively decreasing.

In the first effort of TSHI, Dhole and Linnhoff [3] proposed *site source sink profiles* (SSSPs), which was composed by the remained sections of the GCCs of individual plants, after their heat recovery "pockets" are removed. The SSSP is utilized to determine the different temperature levels of the generated steams. This pioneering work was then extended and developed by other researchers. Klemeš et al. [8] further developed SSSP to *total site profiles* (TSPs) and *site composite curve* (SCC). These new analytical tools can be used to identify the pinch temperature as well as heat recovery and cogeneration potential for a total site. Rodera and Bagajewicz [9] introduced a mathematical method to target energy savings for IPHI. They also first proposed the concepts of *assisted and unassisted heat transfer* [9], for which in certain cases, removing the "pockets" from GCCs reduce the energy recovery potential. Bandyopadhyay et al. [10] later contributed with a new graphical tool named *site grand composite curve* (SGCC). In essence, the SGCC provided a graphical expression for the concept of assisted heat transfer. Certainly, it was reported that these two methods showed the same heat recovery potential across plants.

In principles, the GCC provides the maximum possible heat recovery potential across plants. This potential is obtained through GCC, where surplus heat sources/sinks are identified. However, the utilization of surplus heat sources/sinks for IPHI may lead to complicated intra-plant HEN design or retrofit, which is often not easy and impractical [11]. The impracticality is mainly because it is difficult to conduct complicated intra-plant HEN retrofits for a well-established HEN. However, even for a grassroots design case, a complex and fixed HEN configuration has to be designated to extract surplus heat sources/sinks. An illustrative case of it can be seen elsewhere [11]. Besides, for a large-scale IPHI problem, more significant modifications will also need to be introduced for other systems apart from heat exchange system (e.g. piping and control system), which must be not easy and cautious to come by.

Note that the heat sources/sinks that are currently serviced by utilities in the existing HENs [12–15] can also be extracted for IPHI. It is technically easier than the utilization of surplus heat sources/sinks. However, using waste heat sources/sinks to implement IPHI may lead to a smaller interplant heat recovery potential than that of using surplus heat sources/sinks [11]. Hence, researchers need to make a trade-off between the interplant heat recovery potential and the complexity of intra-plant HENs.

Some researches [7, 16] have also reported the use of process streams to implement intra-plant HI and IPHI simultaneously. However, the practical IPHI problems present complexities as boundaries when simultaneous intra-plant HI and IPHI are considered, especially for a large-scale IPHI problem. One significant consideration for impracticality is the timeline at which different plants are developed, i.e. when plants are constructed at different time. Furthermore, when multiple plants are connected via a single IPHI system, process control and safety for individual plants remain as some important challenges.

10.1.2 Reviews and Discussions for Plant Selection

For a large-scale IPHI problem, the solution model may be very complicated, especially when it involves complex industrial sites. It is difficult to obtain an optimal result when there are too many plants (each with many streams) are involved, especially for the simultaneous intra- and interplant HI [5]. Even if a large-scale IPHI problem is solved, the results, in which multiple plants may be connected together via a single IPHI scheme, still present great challenges for process control and safety. The parameter fluctuations in a plant will influence the operation of other plant(s), which are in a same IPHI scheme.

Therefore, most reported researches on IPHI were implemented with only two or three plants. For an IPHI problem with more plants (e.g. four plants and above), researchers often selected a small group of streams for IPHI [16, 17]. Alternatively, they would use a step-wise method [18–20] to reduce the problem complexity.

Combining pinch analysis (PA) and mathematical programming (MP) has made HI even more robust and powerful in solving the large-scale IPHI problems [1]. The hybrid method for IPHI [21–25] usually comes to a step-wise method. Note that these methods are mainly used to reduce the calculation difficulties of a large-scale problem. As mentioned earlier, even if a large-scale IPHI problem can be solved, its results should be also considered for practical concerns. One solution that addresses the challenge is to divide a large-scale IPHI problem with multiple plants into several smaller subsections, instead of simultaneously considering all plants within an industrial site [5]. The detailed designs of these smaller sections can be then developed separately. Doing so facilitates easier calculation and avoids the non-convergence that is often encountered when attempting to solve a large-scale IPHI problem. However, the segregation must follow specific rules and give a reasonable result.

10.1.3 Reviews and Discussions for Plant Integration

If a plant provides its hot streams for IPHI, it is defined as a heat source plant. Similarly, it is defined as a heat sink plant if its cold stream(s) are used for IPHI [5]. Note that in some cases, the same plant can act as heat source and heat sink plants simultaneously. IPHI can be implemented either directly or indirectly. For a *direct IPHI* scheme, the process streams are used to transfer heat across the plants. On the other hand, *indirect IPHI* is implemented through the utility system [26] or heat transfer fluids, such as hot oil [27] and hot water [28].

For direct IPHI, the distance between heat source plant and heat sink plant is an important consideration [29]. When the distances across plants are long, capital investment for the interplant piping network may offset the savings gained from IPHI, which then lead to an impractical result [5]. For a reported case involving direct IPHI across four plants [30], five heat transfer zones exist in between every two plants. For another direct IPHI case across 7 plants [30], 17 heat transfer zones exist. Note that the required piping loop number may be far more than the number of heat transfer zones, as one piping loop needs to be built for every single stream participated in IPHI. Having long interplant piping distances and/or too

many interplant piping loops significantly increases the total capital investment for the interplant piping network and also possesses great challenge for process control and safety.

For indirect IPHI, the excess heat sources from a heat source plant are first transferred to one steam/heat transfer fluid line, before heat is transferred to a heat sink plant. Doing so can significantly decrease the number of interplant piping loops. Therefore, indirect IPHI is encouraged for large-scale IPHI problem, which allows for simple interplant piping network and practical result. Note that, since the heat is transferred two times in indirect IPHI, it may present a smaller interplant heat recovery potential than that of direct IPHI. This chapter focuses on indirect IPHI using heat transfer fluid (hot oil or hot water).

Connection pattern [29], which means the placement of heat transfer fluid loops across plants, is another significant factor where attention should be paid in indirect IPHI. Wang et al. [29] proposed three basic connection patterns for IPHI among three plants, i.e. parallel, split, and series connection patterns. These interplant connection patterns present differences in interplant heat recovery potential, pipeline costs, and reliability of the IPHI system [31].

10.2 Methodology

10.2.1 Strategy 1 – Overview

Strategy 1, which consists of three steps, is proposed to solve a large-scale IPHI problem. The overall procedure is shown in Figure 10.2. The details of Step 1 and Step 2 are described in Sections 10.2.2 and 10.2.3 respectively.

In Step 1, nimiety heat sources/sinks are extracted for IPHI from individual plants. Next, the large-scale IPHI problem is decomposed into smaller separated subsections in Step 2. In Step 3, it should be noted that researchers can build their

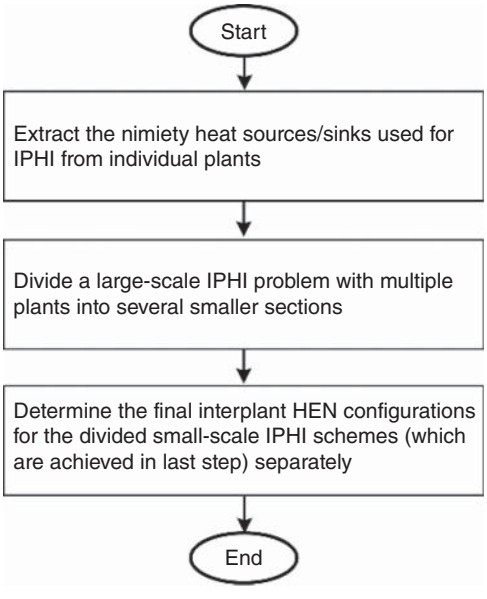

Figure 10.2 Flowchart of Strategy 1 for solving a large-scale IPHI problem.

own solving model of IPHI, either PA or MP, to determine the final interplant HEN configurations of the separated subsections. Since the divided small-scale IPHI schemes are independent, their final interplant HEN configurations can be determined one by one. This work also presented a *mixed integer nonlinear programming* (MINLP) mathematical model, which allowed for an objective of minimum *total annual costs* (TACs), to determine the final interplant HEN configurations. The details of the proposed MINLP model can be seen in [6].

10.2.2 Identification of Heat Sources/Sinks for IPHI from Individual Plants

A new method is introduced to extract nimiety hot/cold steams for IPHI from individual plants. This is illustrated in Figure 10.3b. Instead of extracting streams that were served by the utilities (see Figure 10.3a), the extraction points may be set before the utilities and the nimiety heat source/sink are then extracted (see Figure 10.3b).

There are two different scenarios where the nimiety heat source/sink may be extracted from individual plants.

Scenario 1: The existing hot and cold streams have been well matched according to Pinch principles. However, when one or more "pockets" appear on GCC above/below the pinch, the higher-grade stream(s) may not be fully utilized. This is because the heat supply and demand are self-sufficient within a "pocket," leaving the higher-grade stream(s) to be extracted; the latter is the nimiety heat source/sink as illustrated in Figure 10.3b.

Scenario 2: The existing individual HEN violates the Pinch principles, which means heat transfer across the pinch exists. Note that this includes the cold utility that is used above the pinch, and hot utility that is used below the pinch. For such cases, the higher-grade stream(s) is not fully utilized.

This is a new method to identify hot/cold streams from individual plants for IPHI [11]. Compared with the two traditional stream extraction methods

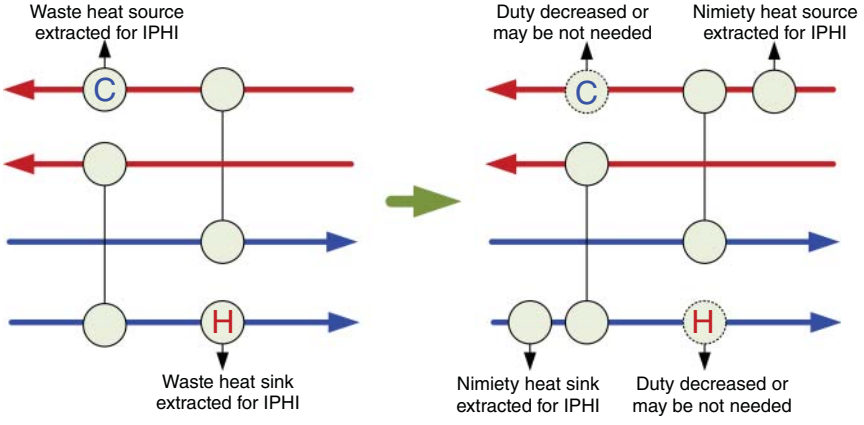

Figure 10.3 (a) Extraction of waste heat source/sink. (b) Extraction of nimiety heat source/sink.

(see Section 10.1.1), the new method presents unique advantages. Not only that it avoids the complex retrofits of individual HENs when using surplus heat source/sink for IPHI, it also provides higher-grade hot/cold streams than the waste heat sources/sinks. Note that this simple method can be applied to both grassroots design and retrofit projects. Furthermore, this method preserves the existing HEN structures when it is applied on a retrofit project.

In summary, the key point of the new stream extraction method is to set the extraction points before the utilities, which is applicable to both scenarios earlier. More details about it are found elsewhere [11].

10.2.3 Decomposition of a Large-Scale IPHI Problem into Small-Scale Subsections

A novel screening algorithm, i.e. *nearest and largest Q_{rec}-based screening algorithm* (NLQSA) [5], is proposed for practical IPHI problems. The NLQSA is established based on PA and the theoretical maximum interplant heat recovery potential (Q_{rec}^{max}) of total site. The overall procedure of NLQSA is shown in Figure 10.4. NLQSA helps to decompose a large-scale IPHI problem into several small-scale subsections, in which each of the subsections includes two or three plants.

In Figure 10.4, exergy loss is represented as ΔE and the maximum interplant heat recovery potential attained by each IPHI scheme is designated as Q_{rec}. Both Q_{rec} and Q_{rec}^{max} do not include the intra-plant heat recovery and can be easily achieved using *composite curves* (CCs). When constructing the interplant CC to determine Q_{rec} and Q_{rec}^{max}, the temperatures of hot streams should be shifted down by minimum temperature approach (ΔT_{min}) of their own plants. On the other hand, the temperatures of the cold streams should be shifted up by ΔT_{min} of their own plants.

For an IPHI scheme between two plants (one heat source plant and one heat sink plant), another heat source plant or heat sink plant can be added to this IPHI scheme to form a new IPHI scheme among three plants. If Q_{rec} of the new IPHI scheme among three plants is bigger than that of the original IPHI scheme between two plants, the newly added plant is defined as an assisted plant. Otherwise, the newly added plant is unassisted one if it has no effect on the total heat recovery potential.

Based on the "Plus–Minus principle" [32], the criteria to determine unassisted heat source/sink plants (UAPC) are summarized in Figure 10.5. Apparently, the left plants are the assisted ones. Note that T_{source}^{max} and T_{sink}^{min} shown in Figure 10.5 are the maximum temperature of hot streams in a heat source plant and the minimum temperature of cold streams in one heat sink plant, respectively. Both T_{source}^{max} and T_{sink}^{min} are shifted temperatures. They are shifted down/up by ΔT_{min} of their own plant, respectively. The pinch temperature shown in Figure 10.5 is also the shifted pinch temperature.

Theoretically, a large-scale IPHI problem can be divided into several smaller independent sections by using NLQSA. The latter allows easier calculation and improves total heat recovery potentials approaching to Q_{rec}^{max}.

Pinch/threshold problem, exergy analysis, and maximum number of participating plants are also taken into consideration for the IPHI scheme, which

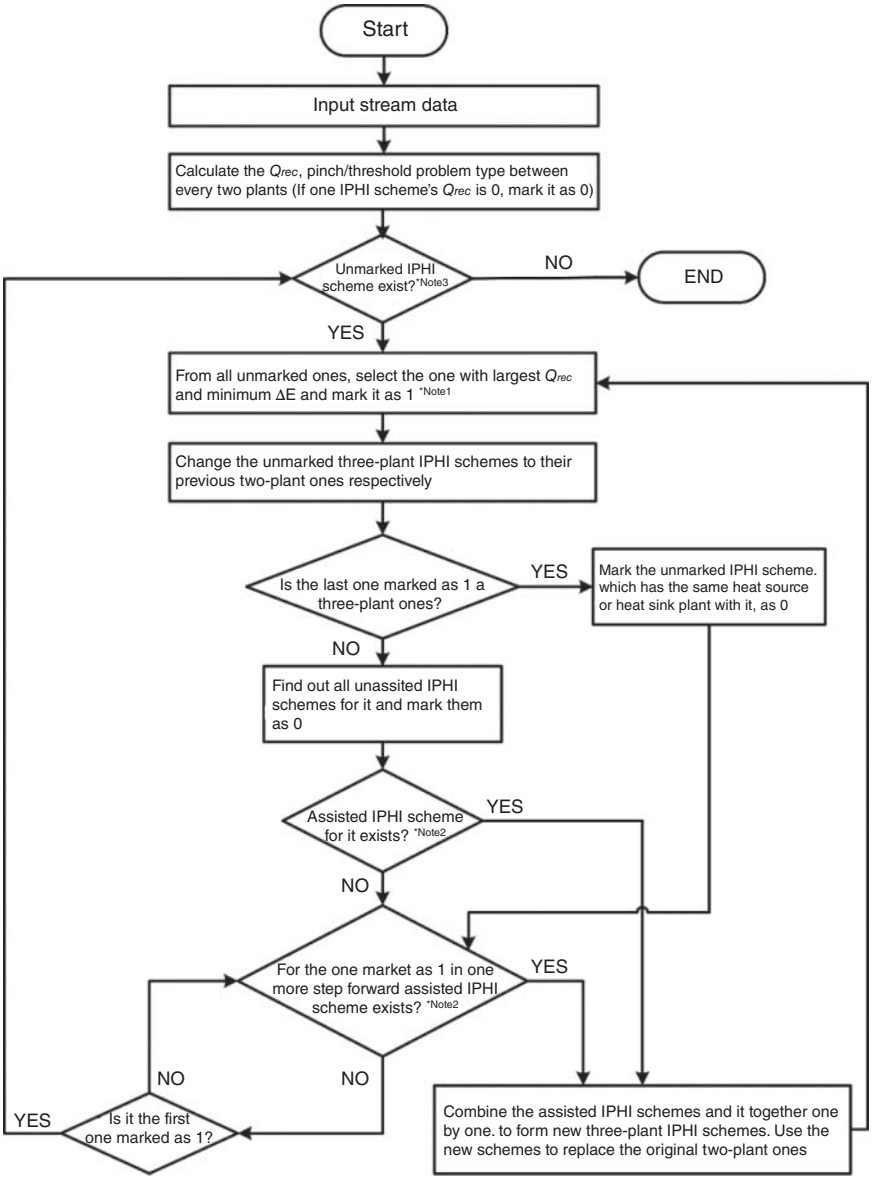

Figure 10.4 Complete flow diagram of NLQSA. Source: Song et al. 2017 [5]. Reproduced with permission of Elsevier. Note 1: Only in this step, for the new IPHI scheme among three plants, its Q_rec is the increment over the previous step. Note 2: Not including the ones which have the same heat source or heat sink plant with all the IPHI schemes marked as 1 before it. Note 3: The one marked as 1 means it is selected and the one marked as 0 means it is deleted from the screening list.

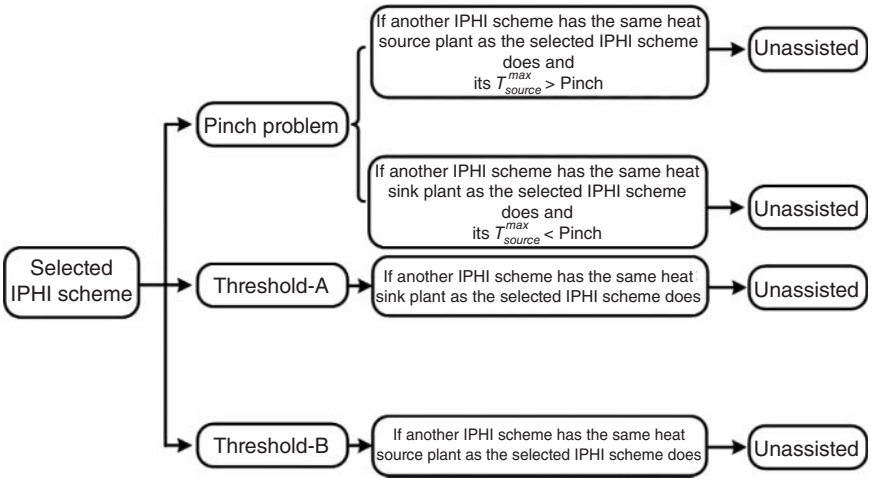

Figure 10.5 Criteria to determine unassisted heat source/sink plant (UAPC) [5].

make NLQSA more feasible and practical. In order to make NLQSA easy and convenient to use, the algorithm is coded via *visual basic for applications* (VBA) into a Microsoft Excel worksheet, which can be downloaded from [5].

More details about NLQSA are found elsewhere [5]. A case study by using NLQSA can be seen in Section 10.3.1.

10.2.4 Strategy 2 for Indirect IPHI

In Strategy 1, after a large-scale IPHI problem is decomposed by NLQSA (Step 2), users can utilize PA or MP methods to determine the final interplant HEN configurations for the subsections separately. However, the connection pattern, which is also a significant factor for indirect IPHI, is not taken into consideration in Strategy 1. Therefore, an additional step is now added to Strategy 2, to allow the determination of parallel connection pattern. The entire steps for Strategy 2 are shown in the flowchart in Figure 10.6.

Compared with serial/split connection patterns, parallel connection pattern presents two independent heat transfer fluid loops, which may reduce interactions among different plants in an IPHI scheme. Moreover, with a parallel connection pattern, two different heat transfer fluids may be used according to different stream temperature levels. Such an action can decrease the capital investment of interplant piping network to some extent. However, for serial/split connection pattern, only one intermedium is used in one IPHI scheme, and the selection of heat transfer fluid has to be made based on the highest temperature level of the stream participated in IPHI.

It is commonly thought that parallel connection pattern presents the longest interplant piping length for indirect IPHI. This increases the interplant piping costs as compared with serial/split connection patterns [29]. However, longest interplant piping length does not necessary mean that it has the highest piping cost, as the latter is also affected by piping size and its heat transfer fluids [31].

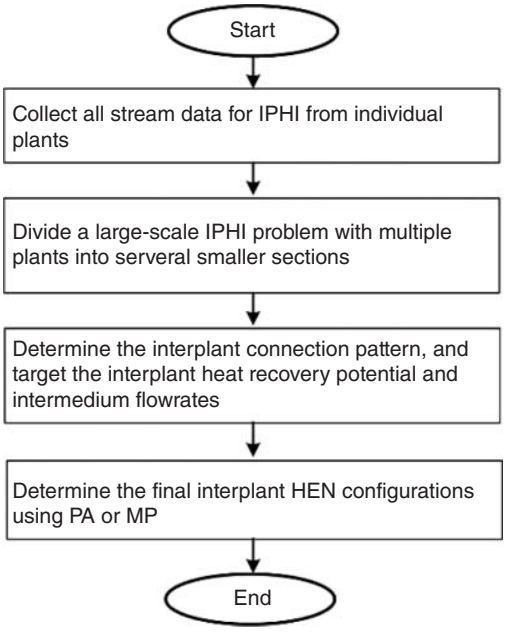

Figure 10.6 Flowchart for Strategy 2 considering connection pattern for solving a large-scale IPHI problem. Source: Song et al. 2018 [31]. Reproduced with permission of American Chemical Society.

For practical concerns, the parallel connection pattern for indirect IPHI shows significant advantages. This work will address the parallel connection pattern for it presents the maximum interplant heat recovery potential and is a flexible pattern.

A new graphical tool, i.e. *interplant composite diagram* (IPCD) (see Figure 10.7) [31] is proposed to target Q_{rec}^{max} for indirect IPHI among three plants and simultaneously minimizes the corresponding intermedium flow rates. The *interplant shifted composite curve* (ISCC) (Figure 10.7b) [11] is drawn based on each participating plant's shifted CCs (Figure 10.7a), which have been vertically shifted on the T–Q diagram by the minimum temperature approach (ΔT_{min}) of their own. As shown in Figure 10.7c, the IPCD is then combined by shifted CCs and ISCC.

Following the NLQSA procedure outline earlier, a large-scale IPHI problem is divided into two-plant or three-plant ones. The connection pattern does not exist in the two-plant IPHI problem; hence only parallel connection pattern within

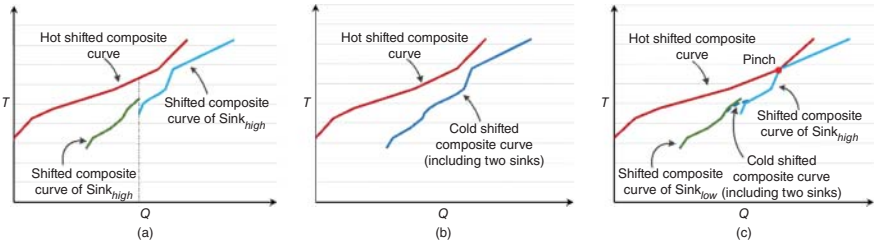

Figure 10.7 (a) Shifted composite curves. (b) ISCC [11]. (c) Interplant composite diagram (IPCD). Source: Song et al. 2018 [31]. Reproduced with permission of American Chemical Society.

three plants is discussed as follows. An illustrative example with one heat source and two heat sink plants is used to illustrate the IPCD. As shown in Figure 10.7, two shifted CCs belong to two heat sink plants respectively. The two shifted CCs are drawn by end to end along the x-axis. The segments with higher temperature among the two heat sinks is placed on the right side and is termed as Sink_{high}; while the other one on the left side is designated as Sink_{low}. For cases with both heat sink plants share the same highest temperature, the one with the lowest temperature among them is drawn on the left side (i.e. as Sink_{low}), while the other on the right side (as Sink_{high}). The two connected CCs are then shifted horizontally until they touch the hot CC at the pinch.

By utilizing the IPCD, one determining procedure for indirect IPHI has been proposed [31] and is summarized as a flowchart given in Figure 10.8, which presents a parallel connection pattern among one heat source plant and two heat sink plants. The procedure is conveniently illustrated on an IPCD, as shown in Figure 10.9.

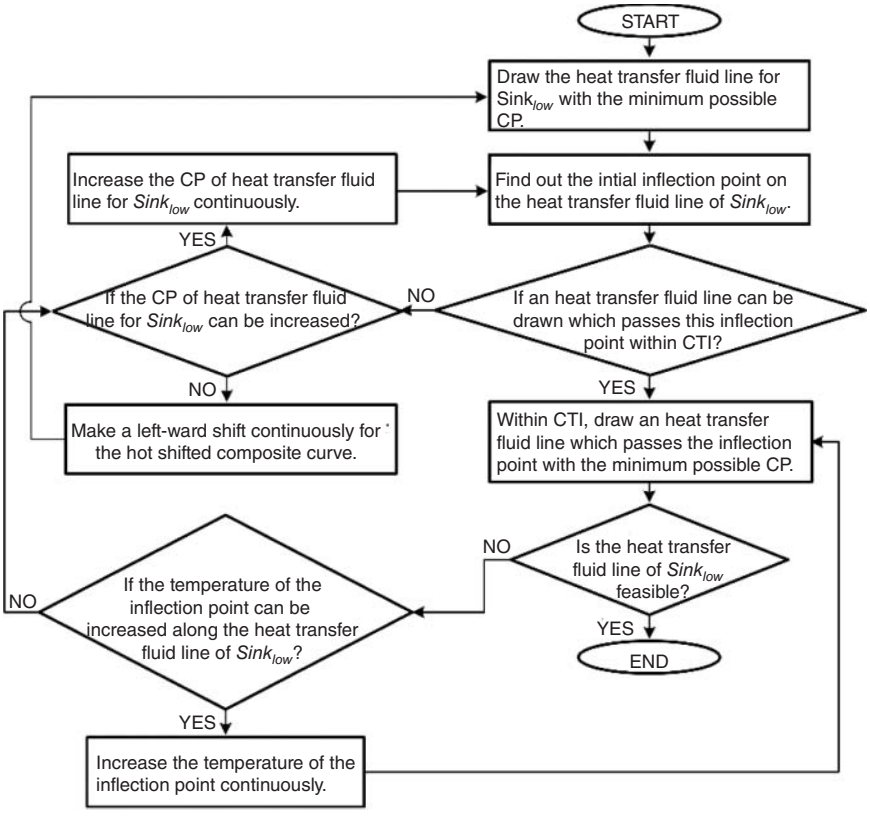

Figure 10.8 Flowchart to determine the indirect IPHI with a parallel connection pattern among one heat source plant and two heat sink plants. *Note*: The definitions of "inflection point," "*common temperature interval* (CTI)," and "*key region for determining parallel connection pattern* (KRP)" can be found in [31]. Source: Song et al. 2018 [31]. Reproduced with permission of American Chemical Society.

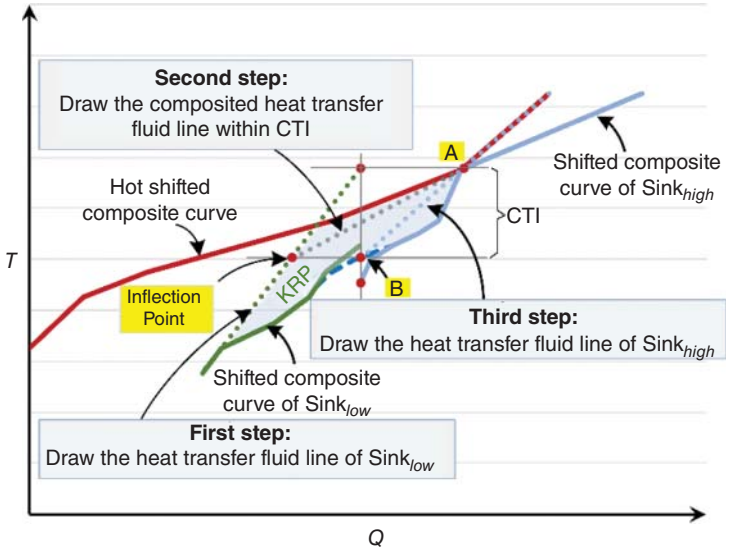

Figure 10.9 Graphical illustration on IPCD for the determination of indirect IPHI with a parallel connection pattern among one heat source plant and two heat sink plants. Source: Song et al. 2018 [31]. Reproduced with permission of American Chemical Society.

Compared with the scenario including one heat source plant and two heat sink plants, the scenario including two heat source plants and one heat sink plant can be determined by a similar way. The corresponding flowchart can be found in [31].

Besides, more details about IPCD and the targeting procedure of parallel connection pattern for indirect IPHI can be found elsewhere [31]. A case study for the proposed method in this section can be seen in Section 10.3.2.

10.3 Case Study

10.3.1 Example 1

This example involves seven plants, and 52 streams are presented to illustrate how NLQSA may be used to simplify a large-scale IPHI problem into smaller ones. The existing HENs of these plants can be found in [6]. The stream data were extracted for IPHI from these HENs using the method proposed in Section 10.2.2 and are listed in Table 10.1. Noted that in Table 10.1, T_s and T_t are supply and target temperatures of each stream, respectively. The heat capacity flow rate of each stream is represented as CP. The minimum approach temperature of each plant refers to ΔT_{min}.

Using NLQSA, the IPHI implementation results of Example 1 can be obtained as shown in Table 10.2. The net results are two IPHI schemes, each involving three plants respectively. The first IPHI scheme involves Plants 1, 4, and 5, where Plant 1 serves as heat source plant while Plants 4 and 5 are heat sink plants. On the

Table 10.1 The stream data of Example 1.

Stream	T_s (°C)	T_t (°C)	CP (MW/°C)	Enthalpy (MW)	Plant	Stream type	ΔT_{min} (°C)
H11	228.0	70.0	0.0338	5.3433	1	HOT	10
H12	228.0	80.0	0.0314	4.6431	1	HOT	
H13	228.0	190.0	0.1350	5.1300	1	HOT	
H14	228.0	190.0	0.0636	2.4182	1	HOT	
H15	137.2	45.0	0.1710	15.7646	1	HOT	
H16	140.5	80.0	0.1268	7.6716	1	HOT	
H17	250.0	128.0	0.0910	11.1000	1	HOT	
H18	70.0	60.0	0.0739	0.7385	1	HOT	
H19	155.0	80.0	0.0387	2.9000	1	HOT	
H110	145.0	50.0	0.0621	5.9000	1	HOT	
H111	90.8	60.0	0.3930	12.1051	1	HOT	
C11	348.0	384.0	0.5861	21.1000	1	COLD	
C12	303.2	361.0	0.7963	46.0262	1	COLD	
H21	347.4	113.8	0.0433	10.1047	2	HOT	8
H22	113.8	100.0	0.3205	4.4231	2	HOT	
H23	168.0	45.0	0.1485	18.2685	2	HOT	
H24	165.8	70.0	0.0293	2.8037	2	HOT	
C21	350.0	385.0	0.3457	12.1000	2	COLD	
H31	70.2	55.0	0.3240	4.9254	3	HOT	8
H32	71.2	54.0	0.2088	3.5905	3	HOT	
H33	89.4	36.0	0.0132	0.7026	3	HOT	
H34	72.2	35.0	0.1028	3.8253	3	HOT	
C31	181.1	311.0	0.0358	4.6521	3	COLD	
C32	181.4	311.0	0.0183	2.3774	3	COLD	
C33	174.6	311.0	0.0390	5.3143	3	COLD	
C34	238.0	280.0	0.3000	12.6000	3	COLD	
H41	67.1	35.0	0.2082	6.6831	4	HOT	6
H42	78.6	40.0	0.1191	4.5977	4	HOT	
C41	180.0	185.0	2.4762	12.3808	4	COLD	
H51	100.1	43.0	0.4246	24.2425	5	HOT	6
H52	106.0	53.0	0.0951	5.0386	5	HOT	
H53	119.0	45.0	0.0521	3.8542	5	HOT	
H54	116.5	60.0	0.0372	2.1000	5	HOT	
H55	90.0	45.0	0.6044	27.2000	5	HOT	
H56	78.0	45.0	0.1909	6.3000	5	HOT	
C51	360.0	375.0	0.9000	13.5000	5	COLD	

(Continued)

Table 10.1 (Continued)

Stream	T_s (°C)	T_t (°C)	CP (MW/°C)	Enthalpy (MW)	Plant	Stream type	ΔT_{min} (°C)
C52	330.0	367.0	0.0383	1.4181	5	COLD	
C53	330.0	367.0	0.0314	1.1603	5	COLD	
C54	341.0	367.0	0.1268	3.2976	5	COLD	
C55	347.0	352.0	1.6200	8.1000	5	COLD	
C56	290.0	319.3	0.7051	20.6593	5	COLD	
C57	130.0	142.0	0.1167	1.4000	5	COLD	
H61	80.0	45.0	0.0766	2.6800	6	HOT	7
H62	101.5	40.0	0.0265	1.6283	6	HOT	
H63	84.0	40.0	0.1294	5.6941	6	HOT	
H64	69.3	42.0	0.2304	6.2888	6	HOT	
H65	84.0	45.0	0.1733	6.7600	6	HOT	
H66	100.0	80.0	0.0750	1.5000	6	HOT	
C61	240.7	250.0	3.5109	32.6512	6	COLD	
C71	15.0	54.0	0.0019	0.0753	7	COLD	10
C72	53.3	55.1	0.0774	0.1392	7	COLD	
C73	94.0	94.5	8.2840	4.1420	7	COLD	

Table 10.2 The IPHI implementation result of Example 1.

Source plant	T^{max}_{source} (°C)	Sink plant	T^{min}_{sink} (°C)	IPHI schemes	Pinch (°C)	Q_{rec} (MW)	Final mark
1	240.0	3	182.6	1–3	218.0	4.9405	0
1	240.0	4	186.0	1–4	Threshold-A	12.3808	0
1	240.0	5	136.0	1–5	240.0	1.4000	0
1	240.0	7	25.0	1–7	Threshold-A	4.3565	0
2	339.4	1	313.2	2–1	313.2	1.1333	0
2	339.4	3	182.6	2–3	189.1	6.7547	0
2	339.4	4	186.0	2–4	186.0	6.6355	0
2	339.4	5	136.0	2–5	296.0	3.2773	0
2	339.4	6	247.7	2–6	247.7	3.9666	0
2	339.4	7	25.0	2–7	Threshold-A	4.3565	0
3	81.4	7	25.0	3–7	81.4	0.2145	0
4	72.6	7	25.0	4–7	72.6	0.2145	0
5	113.0	7	25.0	5–7	104.0	0.9249	0
6	94.5	7	25.0	6–7	94.5	0.2145	0
1	240.0	4 and 5	136.0	1–4 and 5	240.0	13.7808	1
2	339.4	3 and 7	25.0	2–3 and 7	189.1	11.1112	1

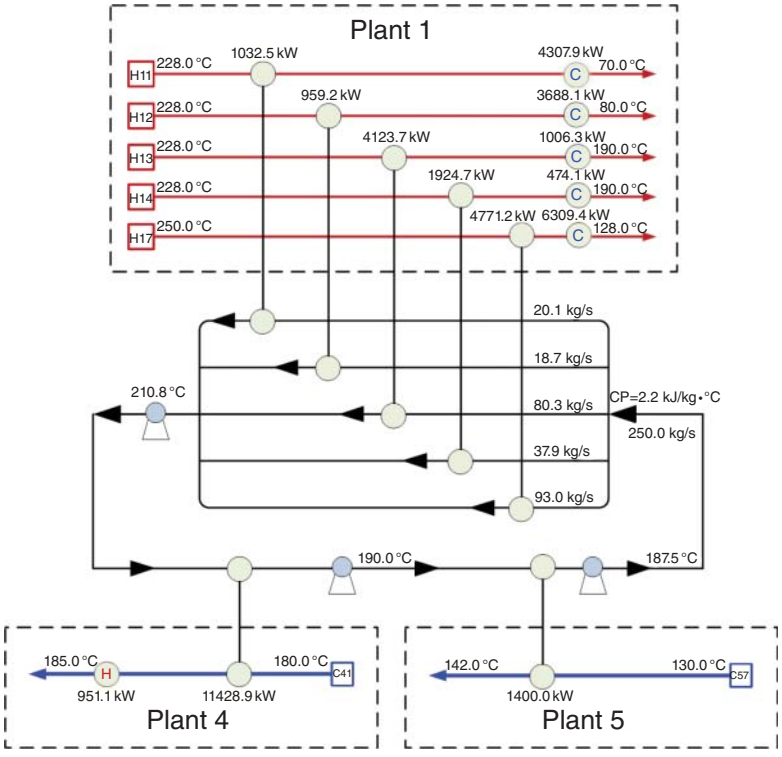

Figure 10.10 The final HEN configuration for IPHI scheme 1 involving Plants 1, 4, and 5.

other hand, second IPHI scheme involves Plants 2 as heat source, while Plants 3 and 7 as heat sinks. The total recovered heat is determined as 24.89 MW with the two IPHI schemes. The interplant HEN configurations for the two IPHI schemes, which are obtained by solving an MINLP model [6] for the minimum TACs, are shown in Figures 10.10 and 10.11, respectively.

More details and analyses about Example 1 can be found elsewhere [6].

10.3.2 Example 2

This example was originally reported by Wang et al. [29] and later modified by Song et al. [31]. It is used to illustrate the applicability and advantages of the proposed method of determining a parallel connection pattern for indirect IPHI. The stream data for Example 2 are listed in Table 10.3.

By using the newly proposed method in Section 10.2.4, the determination of parallel connection pattern on an IPCD is illustrated in Figure 10.12. For comparison purpose, another interplant HEN design with parallel connection pattern is also examined, by applying the method from Wang et al. [29]. The two results are compared as in Table 10.4. As shown, the interplant HEN design as a result of this work presents bigger heat recovery potential, however with less number of heat exchangers and lower overall CP of heat transfer fluid. This is because the method

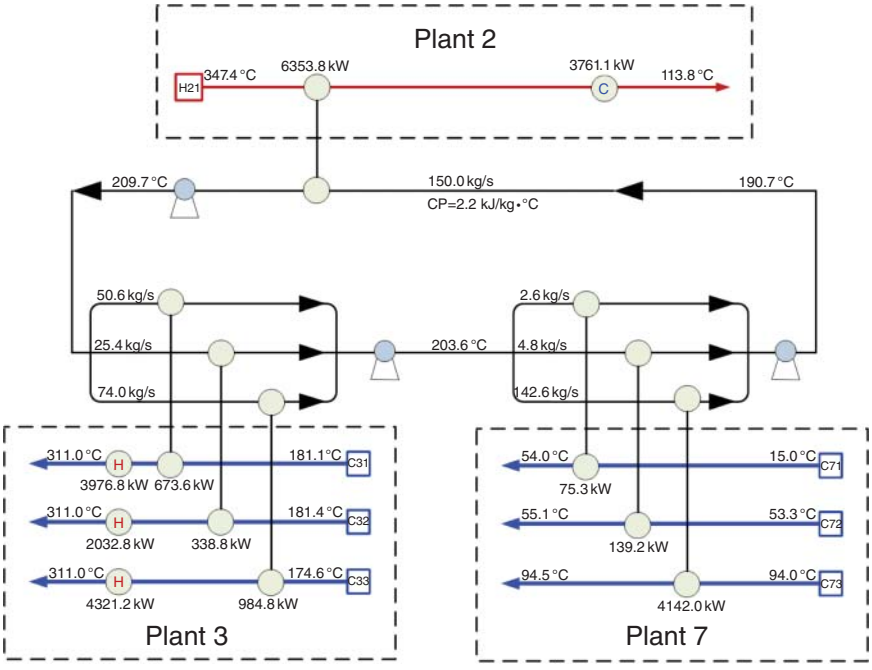

Figure 10.11 The final HEN configuration for IPHI scheme 2 involving Plants 2, 3, and 7. Source: Song et al. 2017 [6]. Reproduced with permission of Elsevier.

Table 10.3 The stream data of Example 2.

Stream	T_s (°C)	T_t (°C)	Duty (kW)
H1 (refinery)	162.5	95.0	9000
H2 (refinery)	135.0	75.0	6000
H3 (refinery)	115.0	65.0	8000
C1 (rubber plant)	115.0	135.0	6000
C2 (rubber plant)	105.0	120.0	1875
C3 (tank field)	55.0	70.0	1500
C4 (tank field)	65.0	80.0	1000
C5 (tank field)	65.0	90.0	2000
C6 (tank field)	85.0	105.0	2000

of Wang et al. [29] draws the simplified curves (which are also used as the heat transfer fluid lines) and thus fixates the flow rates of heat transfer fluid lines and interplant heat recovery potential in the very beginning. Doing so may mislead the maximum interplant heat recovery potential. However, multiple possibilities of heat transfer fluid lines and interplant heat recovery potential are presented in the certain case. The method of this work mitigates the drawbacks of previous

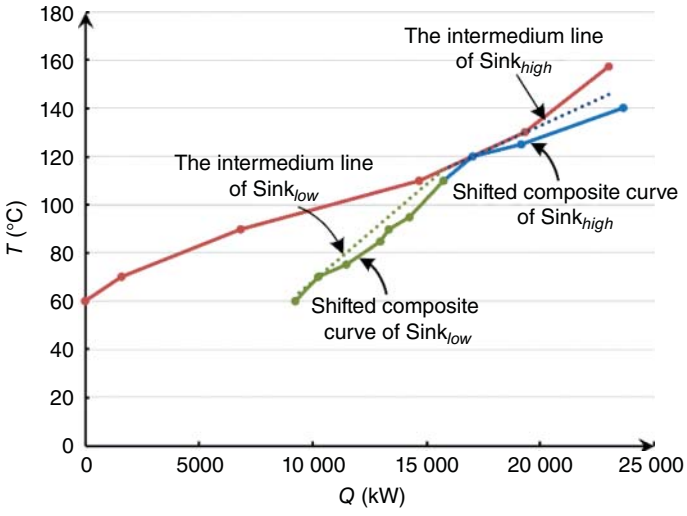

Figure 10.12 Determination of parallel connection pattern on IPCD for Example 2.

Table 10.4 Comparisons between the designs by utilizing different methods from Wang et al. [29] and from this work.

Item	Design by utilizing the method from [29]	This work
Connection pattern	Parallel	Parallel
Total number of interplant connections	4	4
Total number of heat exchangers	16	15
Overall CP of heat transfer fluid (kW/°C)	937.50	713.07
Total interplant heat recovery (kW)	13 380.5	13 750.0

Song et al. 2018 [31]. Reproduced with permission of American Chemical Society.

method [29] and achieves maximum heat recovery potential, and with minimum flow rates of heat transfer fluid.

More detailed analyses of this example can be found elsewhere [31].

10.4 Conclusion

This work presents two strategies to solve a large-scale IPHI problem. Strategy 1 involves steps such as the extraction of hot/cold streams for IPHI from individual plants, the decomposition of a large-scale IPHI problem, and the design of interplant HEN configurations. Strategy 2, on the other hand, involves the same steps earlier, along with another new step, i.e. determination of connection pattern for indirect IPHI. All efforts are dedicated to the finding of practical and cost effective implementation of IPHI problem, especially for a large-scale one.

List of Abbreviations and Symbols

CC	composite curve
CP	heat capacity flow rate of each stream (kW/°C)
CTI	common temperature interval
GCC	grand composite curve
HEN	heat exchanger network
HI	heat integration
IPCD	interplant composite diagram
IPHI	interplant heat integration
KRP	key region for determining parallel connection pattern
MINLP	mixed integer nonlinear programming
MP	mathematical programming
NLQSA	nearest and largest Q_{rec}-based screening algorithm
PA	pinch analysis
Q_{rec}	maximum interplant heat recovery potential via each IPHI scheme (kW)
Q_{rec}^{max}	theoretical maximum interplant heat recovery potential of a total site (kW)
SCC	site composite curve
SGCC	site grand composite curve
SSSP	site source sink profile
TAC	total annual cost
TSHI	total site heat integration
TSP	total site profile
T_s	supply temperature of each stream (°C)
T_t	target temperature of each stream (°C)
T_{source}^{max}	maximum temperature of hot streams in heat source plant (°C)
T_{sink}^{min}	minimum temperature of cold streams in heat sink plant (°C)
ΔT_{min}	minimum temperature approach of individual plant (°C)
UAPC	criteria to determine unassisted heat source/sink plants
VBA	visual basic for applications

References

1 Klemeš, J.J. and Kravanja, Z. (2013). Forty years of heat integration: pinch analysis (PA) and mathematical programming (MP). *Current Opinion in Chemical Engineering* 2 (4): 461–474.

2 Gundersen, T. (2000). *A Process Integration Primer-Implementing Agreement on Process Integration*, 34–47. Trondheim, Norway: International Energy Agency, SINTEF Energy Research.

3 Dhole, V.R. and Linnhoff, B. (1993). Total site targets for fuel, co-generation, emissions, and cooling. *Computers and Chemical Engineering* 17: S101–S109.

4 Liew, P.Y., Theo, W.L., Alwi, S.R. et al. (2017). Total Site Heat Integration planning and design for industrial, urban and renewable systems. *Renewable and Sustainable Energy Reviews* 68: 964–985.

5 Song, R., Tang, Q., Wang, Y. et al. (2017). The implementation of inter-plant heat integration among multiple plants. Part I: A novel screening algorithm. *Energy* 140: 1018–1029.

6 Song, R., Chang, C., Tang, Q. et al. (2017). The implementation of inter-plant heat integration among multiple plants. Part II: The mathematical model. *Energy* 135: 382–393.

7 Hong, X.D., Liao, Z.W., Sun, J.Y. et al. (2019). Transshipment type heat exchanger network model for intra- and inter-plant heat integration using process streams. *Energy* 178: 853–866.

8 Klemeš, J., Dhole, V.R., Raissi, K. et al. (1997). Targeting and design methodology for reduction of fuel, power and CO_2 on total sites. *Applied Thermal Engineering* 17 (8–10): 993–1003.

9 Rodera, H. and Bagajewicz, M.J. (1999). Targeting procedures for energy savings by heat integration across plants. *AIChE Journal* 45 (8): 1721–1742.

10 Bandyopadhyay, S., Varghese, J., and Bansal, V. (2010). Targeting for cogeneration potential through total site integration. *Applied Thermal Engineering* 30 (1): 6–14.

11 Song, R., Feng, X., and Wang, Y. (2016). Feasible heat recovery of interplant heat integration between two plants via an intermediate medium analyzed by Interplant Shifted Composite Curves. *Applied Thermal Engineering* 94: 90–98.

12 Walmsley, T.G., Walmsley, M.R., Tarighaleslami, A.H. et al. (2015). Integration options for solar thermal with low temperature industrial heat recovery loops. *Energy* 90: 113–121.

13 Oluleye, G., Jobson, M., Smith, R., and Perry, S.J. (2016). Evaluating the potential of process sites for waste heat recovery. *Applied Energy* 161: 627–646.

14 Stijepovic, V.Z., Linke, P., Stijepovic, M.Z. et al. (2012). Targeting and design of industrial zone waste heat reuse for combined heat and power generation. *Energy* 47 (1): 302–313.

15 Chang, C., Chen, X., Wang, Y., and Feng, X. (2016). An efficient optimization algorithm for waste Heat Integration using a heat recovery loop between two plants. *Applied Thermal Engineering* 105: 799–806.

16 Chang, C., Chen, X., Wang, Y., and Feng, X. (2017). Simultaneous optimization of multi-plant heat integration using intermediate fluid circles. *Energy* 121: 306–317.

17 Nemet, A., Klemeš, J.J., and Kravanja, Z. (2015). Designing a Total Site for an entire lifetime under fluctuating utility prices. *Computers and Chemical Engineering* 72: 159–182.

18 Pouransari, N. and Maréchal, F. (2014). Heat exchanger network design of large-scale industrial site with layout inspired constraints. *Computers and Chemical Engineering* 71: 426–445.

19 Pouransari, N. and Maréchal, F. (2015). Heat recovery networks synthesis of large-scale industrial sites: heat load distribution problem with virtual process subsystems. *Energy Conversion and Management* 89: 985–1000.

20 Nemet, A. and Kravanja, Z. (2017). Enhanced procedure for simultaneous synthesis of an entire total site. In: *27th European Symposium on Computer Aided Process Engineering* (ed. A. Espuña), 427–432. Barcelona: Elsevier.

21 Shang, Z. and Kokossis, A. (2005). A systematic approach to the synthesis and design of flexible site utility systems. *Chemical Engineering Science* 60 (16): 4431–4451.

22 Coetzee, S.W. and Majozi, T. (2008). Steam system network synthesis using process integration. *Industrial and Engineering Chemistry Research* 47 (13): 4405–4413.

23 Price, T. and Majozi, T. (2010). Synthesis and optimization of steam system networks. 2. Multiple steam levels. *Industrial and Engineering Chemistry Research* 49 (19): 9154–9164.

24 Luo, X., Zhang, B., Chen, Y., and Mo, S. (2012). Heat integration of regenerative Rankine cycle and process surplus heat through graphical targeting and mathematical modeling technique. *Energy* 45 (1): 556–569.

25 Kralj, A.K., Glavič, P., and Kravanja, Z. (2005). Heat integration between processes: integrated structure and MINLP model. *Computers and Chemical Engineering* 29 (8): 1699–1711.

26 Hu, C.W. and Ahmad, S. (1994). Total site heat integration using the utility system. *Computers and Chemical Engineering* 18 (8): 729–742.

27 Bade, M.H. and Bandyopadhyay, S. (2014). Minimization of thermal oil flow rate for indirect integration of multiple plants. *Industrial and Engineering Chemistry Research* 53 (33): 13146–13156.

28 Chang, C., Wang, Y., and Feng, X. (2015). Indirect heat integration across plants using hot water circles. *Chinese Journal of Chemical Engineering* 23 (6): 992–997.

29 Wang, Y., Feng, X., and Chu, K.H. (2014). Trade-off between energy and distance related costs for different connection patterns in heat integration across plants. *Applied Thermal Engineering* 70 (1): 857–866.

30 Rodera, H. (2001). *Heat Integration Across Plants in the Total Site[D]*. Norman: University of Oklahoma.

31 Song, R., Wang, Y., Panu, M. et al. (2018). Improved targeting procedure to determine the indirect interplant heat integration with parallel connection pattern among three plants. *Industrial and Engineering Chemistry Research* 57 (5): 1569–1580.

32 Linnhoff, B. and Vredeveld, R. (1984). Pinch technology has come of age. *Chemical Engineering Progress* 80 (7): 33–40.

11

Multi-objective Optimisation of Integrated Heat, Mass and Regeneration Networks with Renewables Considering Economics and Environmental Impact

So-Mang Kim[1], *Adeniyi J. Isafiade*[1], *and Michael Short*[2]

[1] *University of Cape Town, Department of Chemical Engineering, New Engineering Building, Madiba Circle, Rondebosch, Cape Town, 7701 South Africa*
[2] *University of Surrey, Chemical and Process Engineering Department, Stag Hill, Guildford, GU2 7XH UK*

11.1 Introduction

Over the past three decades, there exists extensive literature on the *heat exchanger network synthesis* (HENS) problem, where significant progress has been made within the process synthesis field. One of the essential operations in the process industries is that of mass exchange. This has motivated many recent studies to explore different synthesis methods on *mass exchange networks* (MENs). Pollutants are selectively removed from waste streams (*rich streams*) through mass-separating agents (MSAs), which are then regenerated or disposed of, depending on the economic and environmental consequences. There are a variety of mass exchange unit operations, such as absorption, adsorption, extraction, ion exchange, leaching, and stripping [1]. The studies of both heat exchanger networks (HENs) and mass exchanger network synthesis (MENs) are aimed to develop more sustainable chemical processes through optimized usage of utilities in each network. When these networks are integrated, i.e. in what is termed *combined heat and mass exchange network* (CHAMEN), heating and cooling, through an optimally integrated network of heat exchangers, can be used to improve mass absorption/stripping in the MEN subsystem. Such improvements can be accomplished by varying the equilibrium constant in mass transfer, which is a function of temperature [2]. Beyond just combining the synthesis of HEN and MEN, integrating regeneration of the MSAs with the combined network can significantly improve the sustainability of the overall process. Combined MENS and MSA regeneration has been presented in various works in the literature. However, the regeneration component of the combined networks has been limited to one MSA with a single regenerating unit. This chapter aims to explore the benefits of integrating a network of regeneration columns, in what is termed *regeneration exchange network* (REN) with CHAMEN synthesis.

Section 11.2 of this chapter begins with a brief review on regeneration in process synthesis, as well as a review on CHAMENs. Since there have been some attempts to include renewable energy, through process integration, to further

Process Intensification and Integration for Sustainable Design, First Edition.
Edited by Dominic C. Y. Foo and Mahmoud M. El-Halwagi.
© 2021 WILEY-VCH GmbH. Published 2021 by WILEY-VCH GmbH.

reduce the environmental impact of chemical processes, techniques that have been used in the context of CHAMENs are also briefly introduced in Section 11.3. Section 11.4 then discusses the synthesis method and the model formulation of CHAMENs with an REN extension. Furthermore, to find a network configuration that is simultaneously optimized in terms of both economics and environmental impact, multi-objective optimization (MOO) is implemented. Finally, case studies involving these extensions are presented in Section 11.5. This is followed by conclusions and recommendations on future work in Section 11.6.

11.2 Literature Review

11.2.1 Regeneration in Process Synthesis

Waste minimization in chemical industries is a significant concern, and the importance of extracting harmful pollutants from industrial effluents has resulted in the application of regeneration for waste minimization. Isafiade and Fraser [3] studied regeneration in CHAMENs where a single unit involving a single external MSA and a regenerating stream was implemented. There are few other papers that also considered regeneration, including El-Halwagi and Manousiouthakis [4], El-Halwagi et al. [5], Garrard and Fraga [6], and Chen and Hung [7].

El-Halwagi and Manousiouthakis [4] first presented the concept of regeneration of recyclable lean streams in MENs using a two-step sequential mathematical method. In the first step, the minimum operating cost is targeted, while in the second step, a network configuration featuring the minimum number of units is obtained. El-Halwagi et al. [5] presented a case study that is based on the methodology of El-Halwagi and Manousiouthakis [4]. The case study involves one recyclable lean stream and two stripping nitrogen gas streams at different temperatures. Limitations of this approach include the fact that the sequential nature of the model solution does not allow simultaneous trade-offs of competing costs and the match between the lean stream and the regenerating streams is preselected. In a later work by Garrard and Fraga [6], a number of exhausted lean streams are mixed into a single stream before being regenerated in a single unit. Chen and Hung [7] presented a set of regeneration network model in their work; however, the regeneration was not studied in a network context but rather in a single unit operation. Since MENs and RENs can interact through the recyclable lean streams, MENs involving regeneration increase the degrees of freedom and thus contribute to the difficulty in solving the combined networks. It is noted, however, that MEN and REN are very similar in principle; hence the analogy of the two systems is described in the next section.

11.2.2 The Analogy of MEN and REN

The fundamental principle of MENs and RENs is very similar in that both networks involve "rich" streams to be cleaned, while there exist "lean" streams to remove the wastes selectively. Looking at an individual mass exchanger, mass

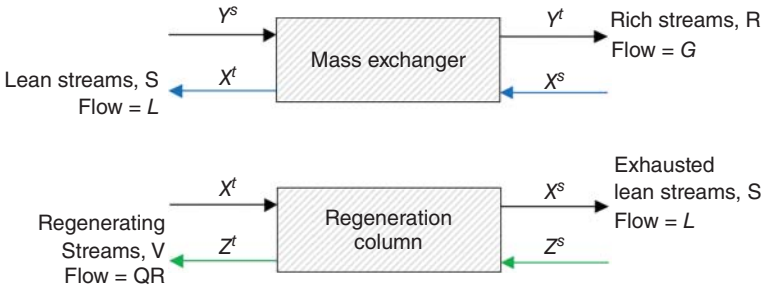

Figure 11.1 A mass exchanger and regeneration column.

transfer takes place between the rich stream of given supply and target compositions (y^s and y^t) and the lean stream with supply and the target compositions (x^s and x^t). The same principle applies in a regeneration column where the exhausted lean streams of primary mass exchanger are treated as "rich" streams, while the regenerating streams take the role of "lean" streams. The latter is also given the supply and target compositions (z^s and z^t). The principles of mass exchanger and regeneration column are illustrated in Figure 11.1.

Given enough time for mixing, the composition of a rich stream (y) and the composition of a lean stream (x) reach equilibrium. The equilibrium relation is governed by the expression in Eq. (11.1) [1]:

$$y^* = f(x) \tag{11.1}$$

where y^* represents the composition of a lean stream in equilibrium with the rich phase. The equilibrium relations can be found in the literature or can be obtained experimentally. The composition of regenerating streams is governed by the same relation. There are different options for regeneration, depending on the types of solutes, solvent, and economic/environmental considerations. One of the most widely used regeneration options is the stripping process. El-Halwagi [8] presented an equation to calculate the equilibrium constants for the stripping process as follows:

$$H = \frac{P_{total} \cdot y_i^{solubility}}{P^o_{solute}(T)} \tag{11.2}$$

where P_{total} is the total pressure of the stripping gas, $y_i^{solubility}$ is the liquid phase solubility of the solute at temperature T (in mole fraction of solute in the liquid effluent), $P^o_{solute}(T)$ is the vapor pressure of the solute at temperature T, and H is Henry's constant. The difference between the rich stream and the equilibrium composition is a measure of the mass transfer driving force and is used to size individual exchangers. When a problem of interest involves multiple streams, the problem goes beyond a single unit and expands into a network of exchangers. Since there exists the analogy of individual operation of the mass exchanger and regeneration columns, when designing a network, the methodology developed for a MEN can be adapted for the REN. Since this chapter proposes a synthesis method for CHAMENs involving a REN, a brief review on CHAMENs is presented next.

11.2.3 Combined Heat and Mass Exchange Networks (CHAMENs)

In many industrial applications, heat and mass exchangers are essential units. Having different mass exchange temperatures throughout a MEN can be beneficial since there is a strong interaction between energy and mass in a chemical process [1]. Intermediate heating/cooling of MSAs (lean streams) can enhance mass transfer and result in an improved overall process.

There are many methods available in the literature for the synthesis of HENs and MENs; however, few attempts at developing CHAMEN synthesis methods have been presented due to their complex nature. Some of the works on CHAMENs include the approaches of Edgar and Huang [9], Srinivas and El-Halwagi [10], Papalexandri et al. [11], Isafiade and Fraser [3, 12], and Liu et al. [13, 14].

Edgar and Huang [9] presented a sequential approach to study CHAMENs where the problem is divided into two sub-problems to simplify the solution process. In the first step, the operating temperature of the MEN is fixed, while the corresponding MEN is synthesized. In the second step, a HEN satisfying the thermal requirements of the previous step is synthesized. This is a good approach when the optimal MEN temperature is known before the synthesis; however, any design procedure involving preselection can result in sub-optimal results. Srinivas and El-Halwagi [10] studied the combined networks through a sequential mathematical approach, which is based on pinch technology to obtain the minimum annual operating costs (AOCs). The lean streams are divided into sub-streams to identify the optimal mass exchange temperatures. The primary shortcomings of the pinch-based approach are that the simultaneous trade-offs between competing variables cannot be studied and the solution procedure can become tedious. Papalexandri et al. [11] applied a hyperstructure to the CHAMENs problem. The model suffers from high nonlinearity, and therefore a special initialization technique is required. Isafiade and Fraser [12] followed the pinch technology approach to study CHAMENs where the minimum total annual cost (TAC) is targeted. Due to the shortcomings of the sequential model, the same authors developed a simultaneous mathematical model. They followed the lean sub-stream approach of Srinivas and El-Halwagi [10] to identify optimal MEN operating temperatures in a sequential manner [3]. This was done to simplify the highly combinatorial nature of CHAMENs. The most Recent CHAMENs studies were published by Liu et al. [13, 14]. In the earlier work of Liu et al. [14], the potential streams that would exchange heat prior to the network synthesis are first identified but the method is also based on pinch technology. In their later work, Liu et al. [13] developed a nonlinear programming (NLP) mathematical model to solve the CHAMENs through a genetic algorithm–simulated annealing (GA–SA) algorithm. It was noted that the model includes many nonlinear model equations and, therefore, obtaining a feasible solution can be difficult.

To conclude, there have been few attempts at synthesizing CHAMENs over the past 30 years. Despite the significant improvement in computing power, the synthesis of CHAMENs has received little attention in the process synthesis field due to the difficulties in the model formulations as well as the limitations on the current generation of mathematical solvers. Also, to the best knowledge

of the current authors, no literature has considered integrating RENs with CHAMENs. The works of Isafiade and Fraser [3] and Isafiade [15] included only a single regenerating unit with CHAMEN synthesis. Therefore, literature on regeneration in CHAMENs is even more scarce and, hence, requires more research. Before presenting the synthesis method of this chapter on the combined networks, selected literature in process synthesis, which considered environmental impact, are reviewed.

11.3 Environmental Impact in Process Synthesis

HENs and MENs can reduce both economic and environmental burdens of a process. However, most of the earlier publications focused on optimizing economic performance of the process. In recent years, there are some attempts that considered both economic and environmental performances. Some of the relevant studies include the papers of López-Maldonado et al. [16], Vaskan et al. [17], and Isafiade et al. [15]. In the works of López-Maldonado et al. [16] and Vaskan et al. [17], the authors aimed at synthesizing HENs to minimize TAC and environmental impact simultaneously through MOO. The environmental impact was calculated using life cycle assessment (LCA) principles. The shortcomings of these studies are that the models are based on HENS alone and no renewables are considered. Isafiade et al. [15] studied a simultaneous interaction between TAC and environmental impact in HENs, in which utilities generated from both fossil-based and renewable energy sources were considered. Environmental impact was calculated with the ReCiPe 2008 method in SimaPro [18] as the LCA method. LCA is discussed in the following section.

11.3.1 Life Cycle Assessment

LCA involves the factual analysis of a product system through all stages of its life cycle in terms of sustainability [19]. During decision making (on a product, process, or technology), LCA can provide information on the impacts to the environment and, therefore, prevents the shifting of environmental problems from one place to another [20]. The main stages considered in an LCA study are presented in Figure 11.2.

LCA allows the estimation of the cumulative environmental impacts throughout the manufacturing process including the gathering of raw materials, usage of the product, and lastly its disposal. LCA involves a step called life cycle impact assessment (LCIA) where inputs and outputs are interpreted in terms of environmental burdens, human health, and resources. According to ISO 14044 [22], LCIA requires four steps [23]:

1. Selection of impact categories and classification
2. Characterization
3. Normalization
4. Weighting

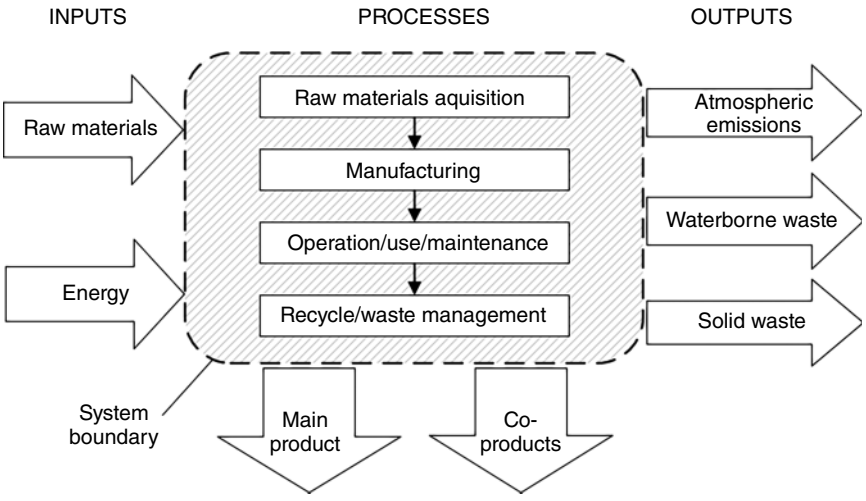

Figure 11.2 The stages involved in life cycle assessment. Source: From Fedkin 2018 [21].

There are various methods available to handle large amount of data and transform it into understandable information, which simplifies the LCA process. The LCIA methods can be classified further into midpoint and endpoint approaches. The former involves the quantification of impact using an indicator located somewhere along the impact pathways, such as climate change, acidification, and ecotoxicity. The endpoint approach quantifies through the endpoint categories, which includes human health, natural environment, and natural resources. The HENS model of López-Maldonado et al. [16] and Vaskan et al. [17], stated previously, selected the Eco-indicator 99 [24], which is an endpoint approach. On the other hand, the model of Isafiade et al. [15] selected the ReCiPe 2008 method [18] to quantify environmental impacts associated with hot utility (HU) and cold utility (CU) generation. Note that the ReCiPe methods combine midpoint and endpoint approaches. The ReCiPe 2008 method [18] was updated to ReCiPe 2016 [25] recently, which includes both midpoint and endpoint impact categories. The characterization factors represent the European scale in the previous version, while the global scale characterization factors are applied in ReCiPe 2016. ReCiPe 2016 is used in this study to calculate environmental impact of utilities in MENs, HENs, and RENs. The synthesis method of the combined networks is presented in the following section.

11.4 The Synthesis Method and Model Formulation

This section presents the combined network synthesis method considering utilities generated from both renewable and non-renewable energy sources. Most synthesis methods involving regeneration simplified the problem by using a single lean stream through a single regeneration unit, and in some cases, no consideration was given to enhancing the regeneration through heating/cooling. However, synthesizing a regeneration network allows the regeneration and

recycling of multiple MSAs to the MEN in a simultaneous manner. This allows the analysis of the interactions between MENs and RENs.

The main challenge in synthesizing the combined network of HEN, MEN, and REN is obtaining feasible solutions to the mixed integer nonlinear programming (MINLP) optimization problem. There have been significant challenges in obtaining globally optimal solutions in the process synthesis field, and many available methodologies require special initialization strategies to find feasible solutions. Reducing the complexity of a model can assist in finding the feasible solutions.

11.4.1 Synthesis Approach

Of the many existing MINLP formulations, the HENS model of Yee and Grossmann [26] and MENS model of Szitkai et al. [27] are selected, as these formulations are relatively simple and can be adapted for further modifications. The stages of the HEN and MEN models are defined using temperatures and compositions of streams. In order to overcome the challenges inherent in the multidimensional nature of the proposed multi-period CHAMEN problem, an initialization technique is introduced. A general overview of the methodology for this study is presented in Figure 11.3.

Given a scenario, the first step of the proposed method involves a gathering of relevant data such as heat capacity flow rates of streams, availability of process and external MSAs, types of utilities, operating hours/periods, and supply and target temperatures/composition of streams. The synthesis of the CHAMEN requires good initialization values to reduce challenges in obtaining feasible solutions. Therefore, relevant data for HEN, MEN, and REN are used to first synthesize the networks separately in three steps. In the first step, the MEN is synthesized to provide initialization values for the second step; which includes the MEN synthesis with the REN. Once a feasible MEN with REN solution is obtained, the HEN is synthesized separately to provide initialization values for the HEN aspect of CHAMEN. In the last step, the set of initial values that gave feasible solutions in the first two steps are used to initialize the CHAMEN model in the third step. These individual network syntheses of the first two steps ensures that data associated with each network is rational and able to generate feasible solutions before being used in the combined network synthesis.

To the best of the knowledge of the current authors, there is no literature considering detailed REN in CHAMENs. To include REN in CHAMENS, an analog of the MEN stage-wise superstructure (SWS) of Szitkai et al. [27] was applied. In MENs the MSAs serve as the lean streams, which absorb the pollutants in the waste streams (the rich streams). The REN follows the same logic as the MEN but the role of the MSAs change. The spent MSAs leaving the MEN are fed into the REN as the rich streams, and the regenerating streams serve as the lean streams. To link the MSA flow rates in the MEN and REN, the same index "l" is used in the model formulation. Besides, the optimal temperatures in MEN and REN are identified through the coupling methods presented by Srinivas and El-Halwagi [10]. In this method, each lean stream is divided into lean sub-streams. The number of lean sub-streams depends on the accuracy required for the problem. Each lean sub-stream is given a different temperature within a supply and a target value

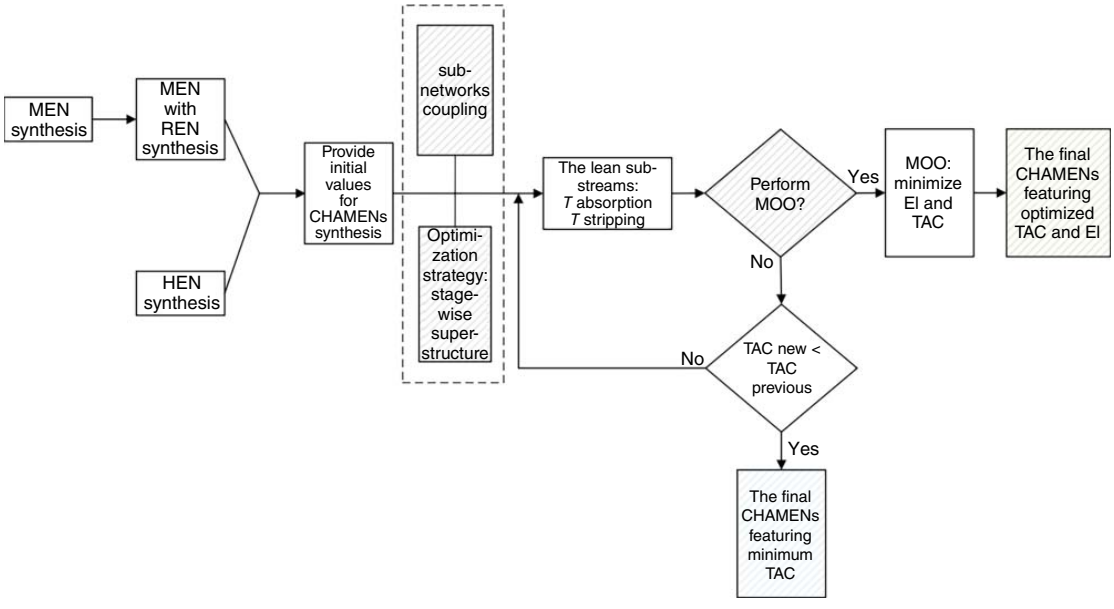

Figure 11.3 General proposed approach of the combined networks.

of the lean stream. The lean sub-streams do not exchange heat with each other, but each sub-stream temperature is used individually in the network synthesis to obtain a corresponding feasible solution. In this way, the optimal temperature that results in the minimum TAC of the combined network can be identified.

To simultaneously optimize the CHAMENs model in terms of both economics and environmental impact, an MOO method, i.e. the goal method [28], is implemented. Using the MOO, we wish to find the solution that optimally trades off the economic benefits and environmental impact of a chosen design.

Beyond the individual HENs, MENs, and RENs of the CHAMENs, additional model equations to handle multi-period operations are included. This is achieved by including the index "p" which accounts for different periods of solar irradiation availability. The extension of the model to handle multi-period operations allows incorporation of renewables, whose availability is time dependent. The incorporation of renewables introduces extra equations into the model formulations. These equations account for the optimal size of solar panels to capture heat for both direct and indirect heat integration [29]. The equations also include an expression to determine the volume of heat storage vessel. The vessel is included to make provision for indirect heat integration in the network. These equations are presented in the model formulation section.

Figure 11.4 shows a schematic of how the MEN involving multiple MSAs is linked to the REN involving multiple regeneration streams through the HEN. In this figure, the MSA streams are cooled in the HEN to temperature T^{MEN} to enhance absorption. The streams then flow at this temperature to the MEN with supply compositions x^s. In the MEN, the MSAs receive mass from the rich streams, which increases their compositions to x^t. The MSA streams then flow back to the HEN where their temperature is raised from T^{MEN} to T^{REN} to enhance regeneration in the REN. In the REN, the mass load in the MSA streams is transferred to the regenerating streams so that the compositions of the MSA streams decrease to x^s again. It is worth stating that a solar panel network, which includes heat storage vessel, is integrated with the HEN to offset the use of non-renewable energy sources as utilities.

11.4.2 Assumptions

A network involving heat and mass exchange is a complex system. The following simplifying assumptions are applied in the proposed CHAMENs synthesis model of this chapter:

1. For material balance purposes, the flow rate of any stream is to remain constant throughout the networks during each period.
2. The exchangers in the networks operate isothermally and isobarically. These assumptions ensure that the equilibrium functions used in the synthesis remain constant.
3. The split streams are mixed at the same composition and temperature in the SWSs. This allows intermediate compositions/temperatures of streams to be characterized by the compositions/temperatures at the superstructure stage boundaries.

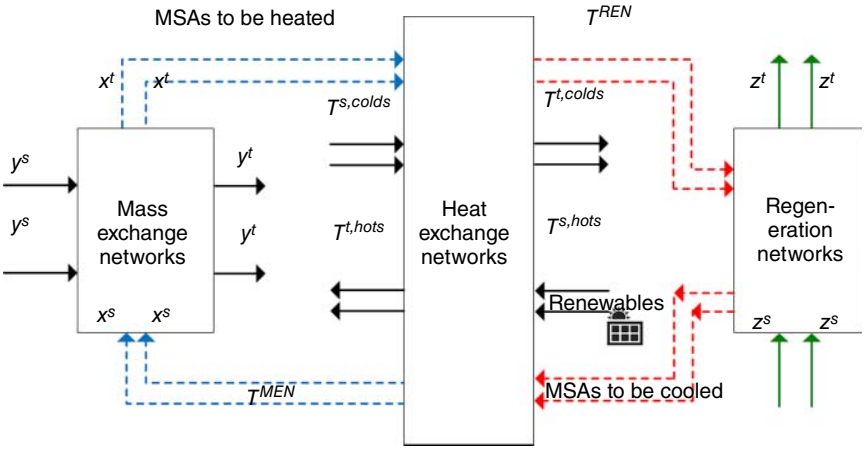

Figure 11.4 A schematic of combined heat, mass, and regeneration networks involving multiple streams.

4. The exchanger units are counter-current.
5. No mass exchange occurs among the rich streams.
6. The solubility of lean streams in rich streams is negligible.
7. Regeneration is perfect, and therefore, no solvent makeup is required.
8. The renewable energy source for solar panels, i.e. solar irradiation, is available at fixed periods per day which comprises day and night.

11.4.3 MINLP Model Formulation

This section focuses on the formulation of the proposed synthesis approach. The formulation is similar to that of Isafiade [15] in which the models of Szitkai et al. [27] and Yee and Grossmann [26] are used to formulate the MEN and HEN, respectively. Index "*p*" is included in the model equations to accommodate the multi-period profile of solar irradiation. The model equations of HEN are presented first, followed by MEN and REN.

11.4.3.1 HENS Model Equations

The HEN model consists of index *ih*, which denotes the hot streams given in set *H*, and *jc* representing cold streams given in set *C*. Index *kh* represents the superstructure stages given in set *KH*, and *p* represents the operation period given in set *P*. The superstructure is defined with the three indices: *ih, jc*, and *kh*. In each stage (*kh*) of the superstructure, a hot (*ih*) and a cold (*jc*) stream can exchange heat once. The model consists of the following mathematical equations and inequalities:

Overall Stream Heat Balance

$$(T^s_{ih,p} - T^t_{ih,p}) \cdot F_{ih,p} = \sum_{jc \in C} \sum_{kh \in Kh} q_{ih,jc,p,kh} \quad ih \in H, p \in P \tag{11.3}$$

$$(T^t_{jc,p} - T^s_{jc,p}) \cdot F_{jc,p} = \sum_{ih \in H} \sum_{kh \in Kh} q_{ih,jc,p,kh} \quad jc \in C, p \in P \tag{11.4}$$

Note that $T^s_{ih,p}$ and $T^t_{ih,p}$ in Eqs. (11.3) and (11.4) are supply and target temperatures of hot stream ih for period p, $T^t_{jc,p}$ and $T^s_{jc,p}$ are target and supply temperatures of cold stream jc for period p, $F_{ih,p}$ and $F_{jc,p}$ are the heat capacity flow rates of hot and cold streams in period p, and $q_{ih,jc,p,kh}$ is the amount of heat exchanged between hot stream ih and cold stream jc in temperature location kh and period p and is treated as a continuous variable.

Stage Heat Balance

$$(t_{ih,p,kh} - t_{ih,p,kh+1}) \cdot F_{ih,p} = \sum_{jc \in C} q_{ih,jc,p,kh} \quad ih \in H, kh \in Kh, p \in P \tag{11.5}$$

$$(t_{jc,p,kh} - t_{jc,p,kh+1}) \cdot F_{jc,p} = \sum_{ih \in H} q_{ih,jc,p,kh} \quad jc \in C, kh \in Kh, p \in P \tag{11.6}$$

In Eqs. (11.5) and (11.6), $t_{ih,p,kh}$ and $t_{ih,p,kh+1}$ are the temperatures of hot stream ih in temperature location kh for period p and the temperature of the same type of stream in the next temperature location $kh+1$ for period p. The same logic applies to $t_{jc,p,kh}$ and $t_{jc,p,kh+1}$ where the variables involve cold stream jc in temperature location kh and $kh+1$ for period p respectively.

Superstructure Inlet Temperature Assignment The first temperature location, $kh = 1$, is assigned to the supply temperatures of hot streams in each period, while the last temperature location, $kh = NOKh + 1$, is the location where the supply temperatures of each cold streams in each period is assigned. Equations (11.7) and (11.8) are used to assign the supply temperatures:

$$T^s_{ih,p} = t_{ih,1,p} \quad ih \in H, p \in P \tag{11.7}$$

$$T^s_{jc,p} = t_{jc,NOKh+1,p} \quad jc \in C, p \in P \tag{11.8}$$

Temperature Feasibility In the superstructure, temperatures of hot streams are designed to monotonically decrease from left to right, while cold stream temperatures increase from the right to left as described in Eqs. (11.9) and (11.10).

$$t_{ih,kh,p} \geq t_{ih,kh+1,p} \quad kh \in Kh, ih \in H, p \in P \tag{11.9}$$

$$t_{jc,kh,p} \geq t_{jh,kh+1,p} \quad kh \in Kh, jc \in C, p \in P \tag{11.10}$$

Logical Constraints When a hot stream exchanges heat with a cold stream in a temperature stage, then a match exists in that stage. The match is described by logical constraints and binary variables, $zhn_{ih,jc,kh}$. The logical constraint contains a parameter, which bounds the amount of exchangeable heat ($\Omega_{p,HEN}$). The upper bound can take the smaller value of the overall heat loads available in each of the streams involved in the match. The binary variable consists of "1" and "0" where the value of "1" indicates the existence of a match in a stage, while the value of "0" indicates no match. The logical constraint is shown in Eq. (11.11):

$$q_{ih,jc,kh,p} - \Omega_{p,HEN} \cdot zhn_{ih,jc,kh} \leq 0 \quad ih \in H, jc \in C, kh \in Kh, p \in P \tag{11.11}$$

When a match exists in a stage, the binary variable $zhn_{ih,jc,kh}$ has a value of "1" and the bounding variable ($\Omega_{p,HEN}$) becomes active. Equation (11.11) prevents deviant heat exchange between the streams in each period p.

Calculation of Driving Forces The heat exchange area requirement of each exchanger is included in the objective equation of the SWS model. The driving forces used to calculate the exchanger areas are determined in Eqs. (11.12) and (11.13). These constraints ensure feasible driving forces for exchangers selected in the optimization and activation of such equations is determined by the binary variables in the equations.

$$dt_{ih,jc,kh,p} \leq t_{ih,kh,p} - t_{jc,kh,p} + \Gamma_h(1 - zhn_{ih,jc,kh}) \quad ih \in H, jc \in C, kh \in Kh, p \in P \tag{11.12}$$

$$dt_{ih,jc,kh+1,p} \leq t_{ih,kh+1,p} - t_{jc,kh+1,p} + \Gamma_h(1 - zhn_{ih,jc,kh}) \quad ih \in H, jc \in C, kh \in Kh, p \in P \tag{11.13}$$

The upper bound (Γ_h) with the binary variables ($zhn_{ih,\,jc,\,kh}$) in Eqs. (11.12) and (11.13) deactivates the constraints if the value of the binary variable is zero, which implies that there is no match in temperature location *kh*. This deactivation ensures that no negative driving forces exist in the optimized network. To avoid infinite areas in the optimal network, an exchanger minimum approach temperature (EMAT) constraint is used as shown in Eq. (11.14):

$$dt_{ih,jc,kh,p} > \text{EMAT} \tag{11.14}$$

The temperature driving forces can be implemented in the logarithmic mean temperature difference (LMTD) expression (Eq. (11.15)) to calculate heat exchanger area. The LMTD is calculated by

$$\text{LMTD}_{ih,jc,kh,p} = \left[\frac{(dt_{ih,jc,kh,p}) \cdot (dt_{ih,jc,kh+1,p}) \cdot (dt_{ih,jc,kh,p} + dt_{ih,jc,kh+1,p})}{2}\right]^{\frac{1}{3}} \tag{11.15}$$

The LMTD equation is approximated by using Chen's first approximation [30]. Verheyen and Zhang [31] introduced a constraint to select the maximum area over each period as presented in Eq. (11.16):

$$A_{ih,jc,kh} \geq \frac{q_{ih,jc,kh,p}}{LMTD_{ih,jc,kh,p} \cdot U_{ih,jc}} \tag{11.16}$$

Note that the maximum area ($A_{ih,\,jc,\,kh}$) do not have index "p" since the maximum area over entire periods is selected in the optimization, while other parts of the equation contain the index "p" including heat requirements of each exchanger in each period $q_{ih,\,jc,\,kh,\,p}$ and the LMTD expression. $U_{ih,\,jc}$ is the overall heat transfer coefficient of the streams involved in a match. Equations (11.3–11.16) form the equations for the HEN part of the CHAMEN model. The next section introduces solar panel and heat storage design equations.

Solar Panel and Heat Storage Vessel Design Equation Isafiade [15] used utilities generated from solar thermal energy considering solar panel sizing in an attempt to reduce the environmental impact of a process. To allow a solar panel to be

effective across the periods, the maximum solar panel area ($ASC_{ih,\,jc,\,kh}$) is presented as shown in Eq. (11.17):

$$ASC_{ih,jc,kh} \geq \frac{q_{ih,jc,p,kh}}{\eta_o(GHI_p) - a_1(T_c - Ta_p) - a_2(T_c - Ta_p)^2} \tag{11.17}$$

where η_o is the efficiency factor of the solar panel, GHI_p is the global horizontal irradiation for the period p in the location where the chemical plant is situated, a_1 and a_2 are the thermal loss coefficients, which can be obtained experimentally, T_c is the average of the inlet and outlet temperatures of the solar panel capture fluid, and Ta_p is the ambient temperature at the plant location at period p. Isafiade [15] also integrated heat storage vessel with solar panel to preserve heat when solar irradiation is available and to use the heat from the vessels during night-time operation. The model equation to calculate the volume of the vessel is described in Eq. (11.18):

$$VTS_{ih,jc,kh} \geq \frac{q_{ih,jc,p,kh}}{C_p \cdot \rho(T^s_{ih} - T^t_{ih})} \tag{11.18}$$

where C_p and ρ are the heat capacity and density of the thermal storage fluid, and T^s_{ih} and T^t_{ih} are the supply and target temperatures of the thermal storage fluid in the vessel. The implementations of such infrastructures are usually perceived to exert less environmental impact.

11.4.3.2 MEN and REN Model Equations

The MEN and REN model equations consist of mass balances and constraints to govern the transfer of mass across the superstructure. In the MEN model, index r refers to rich process streams given in set R, while the lean streams (including process and external MSAs) are denoted by index l given in set S. The superstructure stages are denoted with the index k. In the REN, index l denotes the exhausted lean streams. Note that the flow rates of the regenerable lean streams are assumed to be constant throughout the networks, the same index l is used to link the MEN REN. Index v represents regeneration streams given in set V. The regeneration superstructure stages (kr) are used in the model formulation given in set KR. In both networks, the operation periods are denoted by index p given in set P. The model equations of the MEN and REN comprise the following expressions.

Overall Mass Balance for the Rich and Lean Streams The total amount of exchangeable mass is calculated by multiplying rich stream flow rates with the difference between their supply and target compositions. The same logic is applied to the lean streams. Equations (11.19) and (11.20) illustrate the mass balances.

$$(Y^s_{r,p} - Y^t_{r,p}) \cdot G_{r,p} = \sum_{k \in K} \sum_{l \in S} M_{r,l,k,p} \quad r \in R, p \in P \tag{11.19}$$

$$(Y^{*t}_{l,p} - Y^{*s}_{l,p}) \cdot L_{l,p} = \sum_{k \in K} \sum_{r \in R} M_{r,l,k,p} \quad l \in S, p \in P \tag{11.20}$$

In Eq. (11.19), $Y^{s}_{r,p}$ and $Y^{t}_{r,p}$ are supply and target compositions of rich streams in period p. For lean streams, $Y^{*t}_{l,p}$ and $Y^{*s}_{l,p}$ are supply and target equilibrium compositions of lean streams l in the rich phase in period p; these parameters can be found in Eq. (11.20). The composition differences in Eqs. (11.19) and (11.20) are multiplied with the flow rates $G_{r,p}$ and $L_{l,p}$ for rich and lean streams in period p, respectively. The mass exchanged between rich stream r and lean stream l in composition location k and period p is represented as $M_{r,l,k,p}$ in both equations.

In REN model equations, the MEN equations are adapted to handle exhausted lean streams and regenerating streams. The exhausted lean streams from the MEN are treated as "rich" streams in the REN, and the regenerating streams in the REN are used as "lean" streams. For the regenerating streams, $Z^{*s}_{v,p}$ and $Z^{*t}_{v,p}$ are used to denote supply and target equilibrium compositions of regenerating streams v in period p, and $\mathrm{QR}_{v,p}$ represents regenerating stream flow rates across the period p. The exchanged mass between exhausted lean stream l and regenerating stream v in composition location kr and period p of the REN superstructure is represented as $RM_{l,v,kr,p}$. The REN model equation follows the same structure as that of MEN and these are presented next.

Mass Balances for Rich and Lean Streams in Each Stage The compositions of streams at each stage boundary are determined using Eqs. (11.21) and (11.22):

$$(y_{r,k,p} - y_{r,k+1,p}) \cdot G_{r,p} = \sum_{l \in S} M_{r,l,k,p} \quad r \in R, k \in K, p \in P \tag{11.21}$$

$$(y^{*}_{l,k,p} - y^{*}_{l,k+1,p}) \cdot L_{l,p} = \sum_{r \in R} M_{r,l,k,p} \quad l \in S, k \in K, p \in P \tag{11.22}$$

where $y_{r,k,p}$ and $y^{*}_{l,k,p}$ are the compositions of rich and lean streams in composition location k and period p. The index "$k+1$" implies the composition of streams in the next stage boundary location.

Assignment of Target and Supply Concentrations The first composition location, $k = 1$, and the last composition location, $k = NOK + 1$, are the given supply composition of the rich streams in period p and the supply composition of the lean streams in period p, respectively. These are described in Eqs. (11.23) and (11.24):

$$Y^{s}_{r,p} = y_{r,1,p} \quad r \in R, p \in P \tag{11.23}$$

$$Y^{*s}_{l,p} = y_{l,NOK+1,p} \quad l \in S, p \in P \tag{11.24}$$

The target compositions of rich and lean streams are described using inequality constraints shown in Eqs. (11.25) and (11.26). The last composition location, $k = NOK + 1$ is assigned the target composition of the rich streams in period p

while the first composition location, $k = 1$ is provided with the target composition of the lean streams in period p.

$$Y^{t}_{r,p} = y_{r,NOK+1,p} \quad r \in R, p \in P \tag{11.25}$$

$$Y^{*t}_{l,p} = y_{l,1,p} \quad l \in S, p \in P \tag{11.26}$$

Feasibility of the Rich and Lean Stream Concentrations Equation (11.27) is a constraint, which determines the monotonic decrease of rich stream compositions along the stages of the superstructure, while the increase in lean stream compositions is illustrated by Eq. (11.28):

$$y_{r,k,p} \geq y_{r,k+1,p} \quad k \in K, r \in R, p \in P \tag{11.27}$$

$$y^{*}_{l,k,p} \geq y^{*}_{l,k+1,p} \quad k \in K, l \in S, p \in P \tag{11.28}$$

Relaxed Binary Variable To improve the numerical stability of the solution, the integer-infeasible path MINLP (IIP-MINLP) formulation of Soršak and Kravanja [32] as used by Szitkai et al. [27] is also adapted in this work. This formulation involves relaxing the binary variables as shown in Eq. (11.29):

$$zmn_{r,l,k} = bzmn_{r,l,k} + pzmn_{r,l,k} - srmn_{r,l,k} \quad r \in R, l \in S, k \in K \tag{11.29}$$

Equation (11.29) provides numerical stability during the optimization procedure by converting the actual binary variables ($bzmn_{r,\,l,\,k}$) into the relaxed versions ($zmn_{r,\,l,\,k}$). The motivation of this approach was to allow solvers to search for feasible solutions in both feasible and infeasible solution spaces and this can improve search speed. The relaxed binary variable is calculated by including a positive tolerance ($pzmn_{r,\,l,\,k}$) and a negative tolerance ($srmn_{r,\,l,\,k}$) in the actual binary variable.

Logical Constraints When there is no match in a stage of the superstructure, the binary variable ($zmn_{r,\,l,\,k}$) has a value of zero. This is used to set the exchanged mass of an exchanger ($M_{r,\,l,\,k,\,p}$) to zero; hence, the mass is exchanged only when there is a match. This is described in Eq. (11.30):

$$M_{r,l,k,p} - \Omega_{p,MEN} \cdot zmn_{r,l,k} \quad r \in R, l \in S, k \in K \tag{11.30}$$

The logical constraint presented in Eq. (11.30) also includes an upper bound ($\Omega_{p,\,MEN}$) on the exchangeable mass. The minimum mass load of any of the rich and lean streams involved in the match can be used as the upper bound.

Driving Force for Mass Exchange The driving forces at both ends of the mass exchangers are calculated when the matches exist. The rich end driving force is

described as shown in Eqs. (11.31) and (11.32):

$$dy_{r,l,k,p} \leq y_{r,k,p} - y^*_{l,k,p} + \Gamma_m(1 - zmn_{r,l,k}) \quad k \in K, r \in R, p \in P \tag{11.31}$$

$$dy_{r,l,k,p} \geq y_{r,k,p} - y^*_{l,k,p} - \Gamma_m(1 - zmn_{r,l,k}) \quad k \in K, r \in R, p \in P \tag{11.32}$$

The lean end driving force of the mass exchangers are calculated as shown in Eqs. (11.33) and (11.34):

$$dy_{r,l,k+1,p} \leq y_{r,k+1,p} - y^*_{l,k+1,p} + \Gamma_m(1 - zmn_{r,l,k}) \quad k \in K/\text{last}, r \in R, p \in P \tag{11.33}$$

$$dy_{r,l,k+1,p} \geq y_{r,k+1,p} - y^*_{l,k+1,p} - \Gamma_m(1 - zmn_{r,l,k}) \quad k \in K/\text{last}, r \in R, p \in P \tag{11.34}$$

In these constraints, the binary variable ($zmn_{r,l,k}$) activates the constraints when its value equals one. In this way, the upper bound (Γ_m) is canceled out in the constraints, and the driving forces are calculated by comparing differences between rich and lean stream compositions of a particular match. As it was done in the HEN model formulation, an exchanger minimum approach composition (EMAC) can be used as a lower bound to the driving forces. In the case of REN model, a regeneration exchanger minimum approach composition (REMAC) is used. This excludes infinite height/stages from the network configurations. This is represented as shown in Eq. (11.35):

$$dy_{r,l,k,p} \geq \text{EMAC} \tag{11.35}$$

Chen's approximation for the logarithmic mean concentration differences (LMCD) can be used to estimate driving forces for the sizing of mass exchangers [30]. This is shown in Eq. (11.36):

$$\text{LMCD}_{r,l,k,p} = \left[\frac{(dy_{r,l,k,p}) \cdot (dy_{r,l,k+1,p}) \cdot (dy_{r,l,k,p} + dy_{r,l,k+1,p})}{2}\right]^{\frac{1}{3}} \quad r \in R, l \in S, k \in K, p \in P \tag{11.36}$$

Szitkai et al. [27] implemented the capital costing estimation of Hallale [33] where the exchanger mass-based costing equations are used. The exchanged mass in an exchanger ($M_{r,l,k,p}$) is converted to the mass of the equipment ($mass_{r,l,k,p}$, in kg) in Eq. (11.37).

$$mass_{r,l,k,p} \cdot K_w \cdot LMCD_{r,l,k,p} = M_{r,l,k,p} \quad r \in R, l \in S, k \in K, p \in P \tag{11.37}$$

where K_w is the lumped mass transfer coefficient. The next section presents the combined objective function.

11.4.3.3 The Combined Economic Objective Function

The Economic Objective Function The economic objective function is used to simultaneously minimize the TAC of the combined networks. The objective function

also determines the optimal network configuration and utility consumptions for the CHAMENs. Equation (11.38) represents the economic objective function.

$$
\begin{aligned}
\min \Bigg\{ & \sum_{p\in P} \Bigg\{ \Bigg\{ \Bigg[\frac{\mathrm{DOP}_p}{\sum_{p=1}^{NOP} DOP_p} \cdot \sum_{r\in R} \sum_{l\in S} \sum_{k\in K} \mathrm{LSC}_l \cdot L_{l,p} \Bigg] \Bigg\} \\
& + \frac{\mathrm{DOP}_p}{\sum_{p=1}^{NOP} \mathrm{DOP}_p} \cdot \sum_{l\in S} \sum_{v\in V} \sum_{kr\in Kr} \mathrm{RSC}_v \cdot \mathrm{QR}_{v,p} \Bigg\} \\
& + \frac{\mathrm{DOP}_p}{\sum_{p=1}^{NOP} \mathrm{DOP}_p} \cdot \sum_{ih\in HU} \sum_{jc\in CP} \sum_{kh\in Kh} \mathrm{HUC}_{ih} \cdot q_{ih,jc,kh,p} \\
& + \frac{\mathrm{DOP}_p}{\sum_{p=1}^{NOP} \mathrm{DOP}_p} \cdot \sum_{ih\in \mathrm{HP}} \sum_{jc\in \mathrm{CU}} \sum_{kh\in Kh} \mathrm{CUC}_{jc} \cdot q_{ih,jc,kh,p} \Bigg\} \Bigg\} \\
& + \mathrm{AF}_{MEN} \Bigg\{ \sum_{r\in R} \sum_{l\in S} \sum_{k\in K} \mathrm{CF}_{l,s} \cdot zmn_{r,l,k} \\
& + \sum_{r\in R} \sum_{l\in S} \sum_{k\in K} \mathrm{ACH}_{r,l} \left[\frac{\mathrm{mass}_{r,l,k,p}}{K_w} \cdot \mathrm{LMCD}_{r,l,k,p} \right]^{D_{r,l}} \Bigg\} \\
& + \mathrm{AF}_{REN} \Bigg\{ \sum_{l\in S} \sum_{v\in V} \sum_{kr\in Kr} \mathrm{CF}_{l,v} \cdot zrn_{l,v,kr} \\
& + \sum_{l\in S} \sum_{v\in V} \sum_{kr\in Kr} \mathrm{ACH}_{l,v} \left[\frac{\mathrm{rmass}_{l,v,kr,p}}{K_w} \cdot \mathrm{LMCD}_{l,v,kr,p} \right]^{D_{l,v}} \Bigg\} \\
& + \mathrm{AF}_{HEN} \Bigg\{ \sum_{ih\in \mathrm{HP}} \sum_{jc\in \mathrm{CP}} \sum_{kh\in Kh} \mathrm{CF}_{ih,jc} \cdot zhn_{ih,jc,kh} \\
& + \sum_{ih\in \mathrm{HP}} \sum_{jc\in \mathrm{CP}} \sum_{kh\in KH} \mathrm{AC}_{ih,jc} \cdot \left[\frac{q_{ih,jc,kh,p}}{U_{ih,jc}(\mathrm{LMTD}_{ih,jc,kh,p})} \right]^{\mathrm{ACE}} \Bigg\} \\
& + \mathrm{AF}_{SP}(\mathrm{ACSC}_{ih,jc} \cdot \mathrm{ASC}_{ih,jc,kh}) + \mathrm{AF}_{ST}(\mathrm{ACTC}_{ih,jc} \cdot \mathrm{VTS}_{ih,jc,kh}) \\
& + w \sum_{r\in R} \sum_{l\in S} \sum_{k\in K} (pzmn_{r,l,kr} + szmn_{r,l,kr}) \\
& + w \sum_{l\in S} \sum_{v\in V} \sum_{kr\in Kr} (pzrn_{l,v,kr} + szrn_{l,v,kr}) \qquad (11.38)
\end{aligned}
$$

The combined economic objective function consists of AOCs of the external MSAs, regenerants and heating/cooling utilities, and annualized capital costs (ACCs) of the process equipment involved in the combined network. The first four terms of the objective function are the operating costs of the three networks. The next set of terms is the ACCs of the MEN, REN, and HEN as well as the ACC of solar panels and thermal storage vessels. In the MEN and REN, the equipment cost is defined in terms of shell mass [33]. The last two terms in Eq. (11.38) ensure numerical stability for the MEN and REN. w in these terms represents weighting factor, which is an arbitrarily large number.

In Eq. (11.38), DOP_p is the duration of each period within a day where solar irradiation is available or not available, while NOP is the number of periods considered for each day. AF_{MEN}, AF_{REN}, AF_{HEN}, AF_{SP}, and AF_{ST} are the annualization factors for the exchangers in the MEN, REN, HEN, solar panels, and heat storage tank, respectively. $\mathrm{CF}_{r,l}$, $\mathrm{CF}_{l,v}$, and $\mathrm{CF}_{ih,jc}$ are fixed costs for mass absorbers, regenerating columns, and heat exchangers, respectively. $zmn_{r,l,k}$, $zrn_{l,v,kr}$, and $zhn_{ih,jc,kh}$ are binary variables that indicate the presence of exchangers in a mass, regeneration, and heat exchange network, respectively. $\mathrm{ACH}_{r,l}$ and $\mathrm{ACH}_{l,v}$ are cost per unit of shell mass of columns. $\mathrm{mass}_{r,l,k,p}$ and $\mathrm{rmass}_{l,v,kr,p}$ are mass of shells in MEN and REN, respectively, while $q_{ih,jc,kh,p}$ is the amount of heat exchanged between hot and cold streams. U is the overall heat transfer coefficient and K_w is the lumped mass transfer coefficient [33]. $D_{r,l}$, $D_{l,v}$, and ACE are cost exponents for units in MEN, REN, and HEN, respectively. $\mathrm{AC}_{ih,\mathrm{jc}}$, $\mathrm{ACSC}_{ih,jc}$, and $\mathrm{ACTS}_{ih,jc}$ are the costs per unit area for heat exchangers, costs per unit area for solar panels, and costs per unit volume for heat storage tank, respectively. LSC_l is the cost per unit of external lean stream, while RSC_v is the cost per unit of regenerating stream. HUC_{ih} and CUC_{jc} are the costs per unit of hot and cold utilities respectively. $L_{l,p}$, $\mathrm{QR}_{v,p,}$ and $A_{ij,jc,kh}$ are the flow rates of external MSAs in period p, flow rates of regenerants in period "p" and maximum area (m^2) of heat exchangers.

Environmental Objective Function The environmental impact associated with the HEN (EI_{HEN}) can be obtained through Eq. (11.39):

$$\min \mathrm{EI}_{HEN} = H_Y \sum_{p\in P} \left\{ \left[\frac{\mathrm{DOP}_p}{\sum_{p=1}^{NOP} \mathrm{DOP}_p} \cdot \sum_{ih\in \mathrm{HU}} \sum_{jc\in \mathrm{CP}} \sum_{kh\in Kh} q_{ih,jc,kh,p} \cdot \mathrm{EIHU}_{ih} \right] + \left[\frac{\mathrm{DOP}_p}{\sum_{p=1}^{NOP} \mathrm{DOP}_p} \cdot \sum_{ih\in \mathrm{HP}} \sum_{jc\in \mathrm{CU}} \sum_{kh\in Kh} q_{ih,jc,kh,p} \cdot \mathrm{EICU}_{jc} \right] \right\} \tag{11.39}$$

Equation (11.39) is presented in the work of Isafiade et al. [15] for HENS, where H_Y is the operating time in a year. The term involving DOP_p is used to allow the model to consider the exact quantities of utilities in each period. The environmental impact is calculated by multiplying the heat exchanged between the hot utility (HU) and cold process (CP) streams in temperature location *kh* with the environmental impact of the hot utility (EIHU_{ih}) concerned. The same calculation is applied to the match involving the cold utility (CU) and hot process (HP) streams in which environmental impact of cold utility (EICU_{jc}) is used. The same logic is adapted and applied in this chapter to the MEN to calculate the associated environmental impact (EI_{MEN}) as shown in Eq. (11.40):

$$\min \mathrm{EI}_{MEN} = H_Y \sum_{p\in P} \left\{ \left[\frac{\mathrm{DOP}_p}{\sum_{p=1}^{NOP} \mathrm{DOP}_p} \cdot \sum_{r\in R} \sum_{l\in S} \sum_{k\in K} L_{l,p} \cdot \mathrm{EIMN}_l \right] + \left[\frac{\mathrm{DOP}_p}{\sum_{p=1}^{NOP} \mathrm{DOP}_p} \cdot \sum_{l\in S} \sum_{v\in V} \sum_{kr\in Kr} \mathrm{QR}_{v,p} \cdot \mathrm{EIRN}_v \right] \right\} \tag{11.40}$$

where the environmental impact of lean streams ($EIMN_l$) and environmental impact of regenerating streams ($EIRN_v$) are multiplied by the flow rate of lean and regenerating streams respectively. The ReCiPe method in SimaPro 2016 [25] for LCIA was used to quantify the environmental impacts of the utilities generated from both renewable and fossil-based energy sources for HEN. The same method was applied to obtain environmental impact (EI) of MSAs and regenerating streams in MEN. ReCiPe Endpoint (Egalitarian) V1.06m normalization/weighting set in SimaPro was selected. This option provides a single score that combines human health, ecosystem, and resources impacts.

Multi-objective Function In this chapter, the modified goal method presented in Gxavu and Smaill [34] is used to simultaneously optimize combined networks in terms of both economic and environmental objectives as shown in Eq. (11.41):

$$\min Z = R_g \times \frac{\text{TAC}}{\text{TAC}_{\min}} + (1 - R_g) \times \frac{\text{EI}}{\text{EI}_{\min}} \tag{11.41}$$

where R_g is a parameter, which can be used to allocate weightings to each of the objectives in the combined objective function. Note that TAC_{min} and EI_{min} are the minimum objectives for TAC and environmental impact, respectively. Equation (11.41) can minimize both objectives by calculating the ratio between the minimum objective values and the actual objectives, which becomes dimensionless.

The presented model, is solved as an MINLP problem in general algebraic modeling system (GAMS) environment with the DICOPT solver [35].

11.4.3.4 Initializations and Convergence

Attempting to obtain a feasible solution with the combined set of model equations for HENs, MENs, and RENs can be challenging as there are many unknown variables related through highly nonlinear constraints. Finding an initial value for such variables and the associated bounds is therefore essential. It is suggested to do an exploratory run of the separate MINLP models of the HEN, MEN, and REN in order to obtain initial values for the following variables/parameters:

- EMAC, REMAC, and EMAT
- $\Omega_{p,\,MEN}$ and $\Omega_{p,\,REN}$
- The upper and the lower initialization values of lean and regenerating streams
- The thermal flow rates of recyclable MSAs
- The number of temperature/composition locations in the superstructures

These initial values are inputted into the CHAMENs model and solved simultaneously. The models may require additional exploratory runs with slight changes of the variables/parameters listed earlier until the solver has produced the optimal solutions. Small changes in the values can have a significant influence on the direction of the search for the solvers. The initialization step is therefore likely to guide the solver to find the region, which contains feasible solutions.

In many complex problems, apart from the best network, several good alternatives may exist [36]. Therefore, in the next section, the developed CHAMEN synthesis approach is implemented to show its applicability in obtaining good solutions.

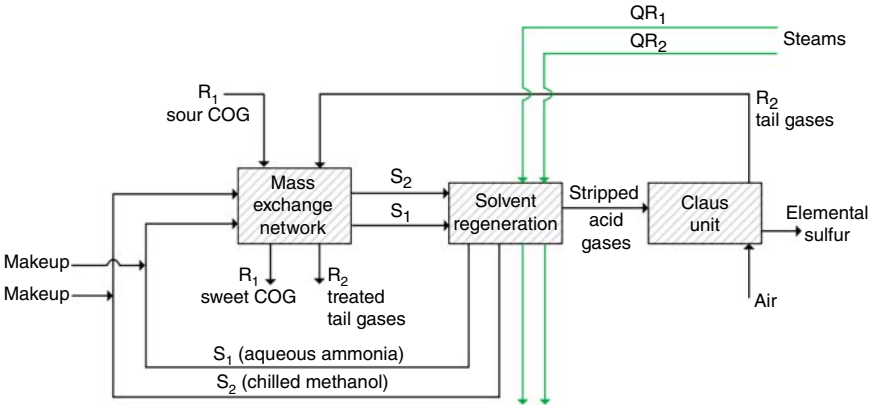

Figure 11.5 A schematic representation of H_2S removal process.

11.5 Case Study

A case study involving H_2S removal is presented in this section. The MEN model is first solved to obtain a feasible solution. The MEN model is then extended to include a REN, in which the recyclable external MSAs flow rates in the MEN are linked to the REN with the index "*l*." Having the same index ensures that the flow rates of the lean streams are the same throughout the networks, which allows the flow rates to be treated as variables during optimization. A feasible solution from this run can be used to obtain the initialization values. Once each network is initialized, the values are entered into the CHAMENs model to obtain a feasible solution. Note that exploratory runs may be required to obtain a solution in the combined model as well. The model's ability to handle regeneration networks involving multiple MSAs and multiple regeneration streams is presented in the case study as well. Also, multi-period operation of solar thermal energy and MOO of economic and environmental impact of CHAMENs is presented.

11.5.1 H_2S Removal

The coke-oven gas (COG) sweetening process [37] involving H_2S removal was adapted in this study. The original example, involving two rich streams and two lean streams, was solved by various authors including Hallale and Fraser [38] and Szitkai et al. [27]. The rich streams consist of a COG (R_1) and tail-gas from a Claus unit (R_2). The two lean streams used in the original example were aqueous ammonia (S_1), which is a process MSA, and chilled methanol (S_2). A schematic representation of this problem is presented in Figure 11.5.

Apart from the original lean streams (S_1 and S_2) used in the problem, an extra external MSA (S_3), which is 15 wt% methyl diethanolamine (MDEA), is introduced in the problem. Stream data of S_3 was obtained from Srinivas and

Table 11.1 The MEN stream data (concentrations given in mass fractions).

Rich streams	Flow (kg/s)	y^s	y^t	Lean streams	Flow (kg/s)	m	x^s	x^t
R_1	0.9	0.070	0.0003	S_1	2.3	1.45	0.0006	0.031
R_2	0.1	0.051	0.0001	S_2	∞	0.26	0.0002	0.0035
				S_3	∞	a)	0.001	0.01

a) S_3 equilibrium data is a function of temperature shown in Eq. (11.42).
Source: El-Halwagi and Manousiouthakis 1989 [37]. Reproduced with permission of John Wiley and Sons.

Table 11.2 The REN stream data (compositions given in mass fractions).

Regenerating streams	m	z^s	z^t
QR_1 (steam 1)	0.0131	4.504×10^{-4}	1.522×10^{-3}
QR_2 (steam 2)	0.008	1.25×10^{-4}	0.011

El-Halwagi [10] where a similar problem involving H_2S was presented. The stream data of rich and lean streams are summarized in Table 11.1.

The equilibrium data for S_3 was obtained from Srinivas and El-Halwagi [10] where the equilibrium data is a function of temperature, given as in Eq. (11.42):

$$m = (9.386410^{-10}) \cdot 10^{(0.0215 \times T)} \tag{11.42}$$

The MEN and HEN interact with each other through equilibrium relations influenced by varying temperature. Data for the regeneration streams are presented in Table 11.2.

The external MSAs can be regenerated using two kinds of regenerating streams, which are low-pressure steam (QR_1) and medium-pressure steam (QR_2). For the purpose of this chapter, the two regenerants are assumed to be generated and transported from a remote process nearby and used in the REN. The equilibrium constants of the regenerating streams are estimated using Eq. (11.2). The regeneration of S_3 can be achieved through a conventional steam stripping method, while the regeneration of S_2 requires a lower temperature of 100 °C or below. The relevant capital costs are summarized in Table 11.3.

Note that tray columns are used in MEN, while packed columns are used in REN. Equation (11.37) presented in Hallale [33] can be used to cost exchangers in terms of shell mass. The operating costs of the corresponding lean, regenerating, and heating/cooling utilities are presented in Table 11.4.

The ReCiPe method indicator values associated with the lean streams and regenerating streams are presented in Table 11.5. These values are used to obtain the environmental impact of a network. The values are used in Eq. (11.40) to compare the results of the MEN (i.e. the first step in the synthesis procedure) and the MEN–REN (i.e. the second step of the synthesis procedure).

Table 11.3 The capital costs of different networks.

Capital costs and sizing data	Values
MEN, tray column cost (installed)	US\$4552 N_{stages}/(stage · y) [11]
REN, shell cost (installed)	US\$1000 · $M^{0.66}$ (M in kg) [3]
Packing	2.54 mm Raschig rings
K_w	0.0254 kg of H_2S/s/kg exchanger mass
HEN, counter-current heat exchanger	$1200 \cdot A^{0.6} + 10\,000$ (A in m^2) [3]
Solar panel	US\$100/(yr m^2) [15]
Heat storage	US\$50/(yr m^3) [15]
Annualization factor	0.225
Annual operating time	8200 h/yr

Table 11.4 Operating costs of lean, regenerating, and utility streams.

Operating cost			Values
MEN	S_1	Process MSA (aqueous ammonia)	117 360 $\left(\frac{\$}{yr}\right)\left(\frac{kg}{s}\right)$ [27]
	S_2	External MSA (chilled methanol)	176 040 $\left(\frac{\$}{yr}\right)\left(\frac{kg}{s}\right)$ [37]
	S_3	External MSA (15 wt% MDEA)	295 200 $\left(\frac{\$}{yr}\right)\left(\frac{kg}{s}\right)$ [10]
	S_3 [a)]	External MSA (*N*-methyl-2-pyrrolidone)	206 640 $\left(\frac{\$}{yr}\right)\left(\frac{kg}{s}\right)$ [10]
REN	QR_1	Stripping steam	118 080 $\left(\frac{\$}{yr}\right)\left(\frac{kg}{s}\right)$
	QR_2	Stripping steam	312 811.63 $\left(\frac{\$}{yr}\right)\left(\frac{kg}{s}\right)$
	QR_2 [a)]	Inert gas stripping (N_2)	212 544 $\left(\frac{\$}{yr}\right)\left(\frac{kg}{s}\right)$ [8]
HEN	HU_1	Hot utility generated from solar thermal energy	US\$0/(kW yr)
	HU_2	Steam generated from the fossil-based source	US\$60/(kW yr)
	CU_1	Cooling water	US\$30/(kW yr)
	CU_2	Liquid nitrogen	US\$121.05/(kW yr)

a) S_3 data is used in the MOO problem presented later in this chapter.

11.5.1.1 Synthesis of MEN (The First Step)

Given all the relevant data, the MEN was first synthesized independently in the first step. The MEN configuration presented in Figure 11.6 was obtained at an EMAC value of 4.22×10^{-8} (wt fraction) and $\Omega_{p,\,MEN}$ value of 0.018 13. Lower bounds of 1.45, 0.26, and 0.003 kg/s were used for S_1, S_2, and S_3 flow

Table 11.5 The environmental impact of lean and regenerating streams for H_2S removal process.

Item			ReCiPe method indicator values (kg^{-1})
MEN	S_1	Aqueous ammonia	0.479
	S_2	Chilled methanol	0.204
	S_3	15 wt% MDEA	0.292
REN	QR_1	Stripping steam	0.0741
	QR_2	Stripping steam	0.0723

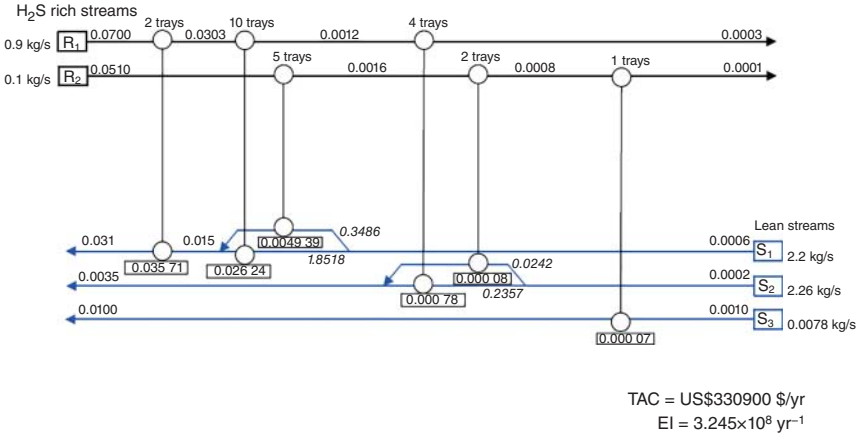

Figure 11.6 The MEN configuration of H_2S removal process (values above streams are composition in mass fractions; while values in boxes indicate mass load transferred in mass exchangers [kg/s]).

rates, respectively, while their upper bounds are set as 2.3, 2.6, and 3.3 kg/s, respectively. This case study is solved using DICOPT/GAMS with version 24.2.3, which uses CPLEX for the mixed integer linear programming (MILP) and CONOPT for the NLP sub-problems. The machine platform is an Intel® Core™ i5-7200U 2.70 GHz CPU with 4.00 GB of RAM.

In the MENS model, five superstructure stages were used to initialize the network. The optimized network consists of six mass exchangers. The MEN solution was then extended to include the REN model.

11.5.1.2 Simultaneous Synthesis of MEN and REN (The Second Step)

The regeneration streams were initialized at lower bound flow rates of 0.013 kg/s and 8×10^{-5} kg/s for QR_1 and QR_2, while upper bound flow rates are set to 10.72 and 7.2 kg/s, respectively. Note that the flow rates of lean streams through the MEN and REN and the flow rates of regenerating streams are variables in the optimization problem. The combined model was solved as an MINLP, and the configuration presented in Figure 11.7 was obtained. An exploratory run of the

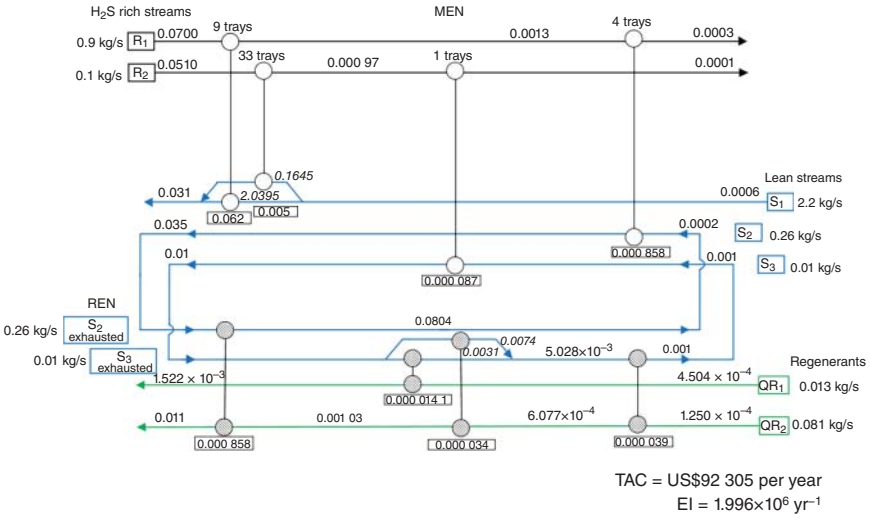

Figure 11.7 The MEN and REN configuration (values above streams are composition in mass fractions; while values in boxes indicate mass load transferred in mass exchangers [kg/s]).

model was necessary to solve the problem. Note that two of the matches (R_1–S_1 and R_2–S_2) obtained in the MEN case (Figure 11.6) do not appear in the combined MEN–REN solution of Figure 11.7. This is possible because the combined MEN–REN model is solved as an MINLP.

The network in Figure 11.7 has four mass exchangers in the MEN and four regeneration columns in the REN. Two-way stream splits were observed for S_1 in the MEN and S_3 in the REN. The environmental impact values presented in Figures 11.6 and 11.7 were obtained by implementing ReCiPe method indicator presented in Table 11.5 in Eq. (11.40). As expected, the network with regeneration (Figure 11.7) exerts less impact on the environment (1.996×10^6 yr^{-1}) compared with that in Figure 11.6 (3.245×10^8 yr^{-1}), which does not include regeneration. This is the case because the lean streams in the solution of Figure 11.6, which are used on a once-through basis, are regarded as being disposed of into the environment. To have a more accurate environmental impact, detailed LCIA is required. The next step involves expanding the combined MEN–REN model to include HEN. Note that relevant data associated with the HEN is used to synthesize a separate HEN prior to step three. This individual network synthesis ensures that HEN data is rational and able to generate feasible solutions before being used in the combined network synthesis.

11.5.1.3 Simultaneous Synthesis of MEN, REN, and HEN (The Third Step)

A regeneration temperature of 100 °C was used for S_3 in the REN, while an absorption temperature of 30 °C was used as initial value to find preliminary feasible solutions. In the case of chilled methanol (S_2), a temperature of 68 °C was used to boil the methanol solvent for regeneration [39], while −20 °C was used for absorption [40]. The equilibrium constant for regenerating streams was obtained using Eq. (11.2). Thermal data for the HEN is presented in Table 11.6.

Table 11.6 The HEN stream data for H_2S removal process.

Streams	T^s (°C)	T^t (°C)	F (kW/°C)	H	CP (kJ/kg K)	Costs ($/(kW yr))	ReCiPe values (kJ^{-1})
H_1	120	60	—	0.2	—	0	2.02×10^{-6}
H_2	135	134	—	0.2	—	60	1.36×10^{-4}
H_3	68	−20	a)	0.2	2.6	—	—
H_4	100	30	a)	0.2	3.7	—	—
C_1	−20	68	a)	0.2	2.6	—	—
C_2	30	100	a)	0.2	3.7	—	—
C_3	5	10	—	0.2	—	30	4.67×10^{-5}
C_4	−173	−173	—	0.2	—	121.05	0.0003

a) The mass flow rates of H_3, H_4, C_1, and C_2 are converted to the corresponding thermal flow rates using the C_p values presented in the earlier text.

H_1 and H_2 are hot utilities generated from solar thermal and fossil, respectively. H_3 and H_4 are chilled methanol (S_2) and MDEA (S_3) streams, respectively, which need to be cooled to meet the suitable absorption temperature in the MEN, while C_1 and C_2 are the same lean streams which need to be heated to optimal regeneration temperatures. There are two cold utilities used in this study, i.e. C_3 (cooling water) and C_4 (liquid nitrogen). The use of C_4 was necessary to cool S_2 stream to the desired temperature of −20 °C.

The ReCiPe method indicator values (kJ^{-1}) associated with the heating/cooling utilities are also presented in Table 11.6. These values are used in Eq. (11.39) to obtain the environmental impact of the HEN component of the combined network. Superstructures having 5, 3, and 4 stages were used to initialize MEN, REN, and HEN, respectively. An EMAT value of 10 °C was used for the HEN. The combined model has 1497 single equations, 1295 single variables, and 122 discrete variables. The network configuration is presented in Figure 11.8.

The network configuration in Figure 11.8 involves four, five, and five exchangers in the MEN, HEN, and REN, respectively. In the MEN, presented on the rightmost side of the figure, the external lean streams, S_2 and S_3, are fed into the MEN to remove H_2S from the rich streams. The spent external lean streams are sent to the REN, which is presented on the leftmost side of the figure. Before S_2 and S_3 enter the REN, they are heated in the HEN, which is situated in the center of the network configuration, to the desired stripping temperatures as specified in Table 11.6. At a fossil-based hot utility price of US$60/(kW yr), all hot utilities selected in the solution are fossil based (i.e. H_2). The heated streams are then fed into the REN for regeneration. It was assumed that all exchangers operate isothermally, and therefore, the stream temperatures remain constant through the networks unless the stream goes through a heat exchanger.

In the HEN, hot process streams H_3 and H_4, which are regenerated lean streams from the REN, are allowed to exchange heat with cold process streams C_1 and C_2, which are exhausted lean streams from the MEN. H_3 goes through a process heat exchanger to exchange heat with C_1 before entering cooler 1, while

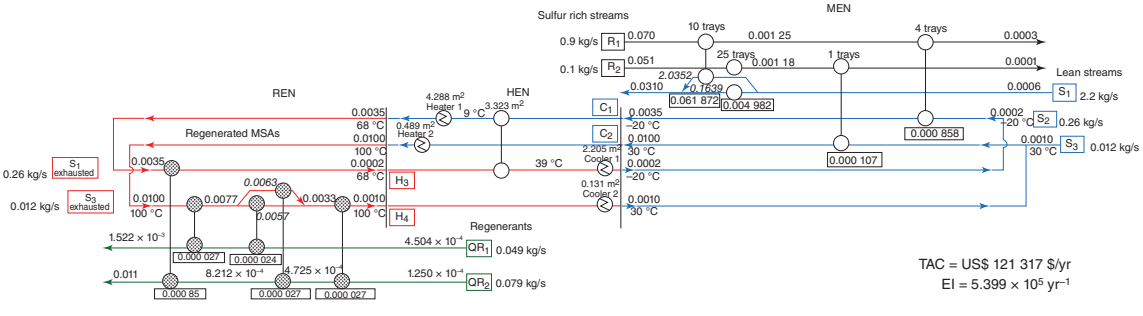

Figure 11.8 The CHAMEN configuration for H_2S removal process (values above streams are composition in mass fractions; while values in boxes indicate mass load transferred in mass exchangers [kg/s]).

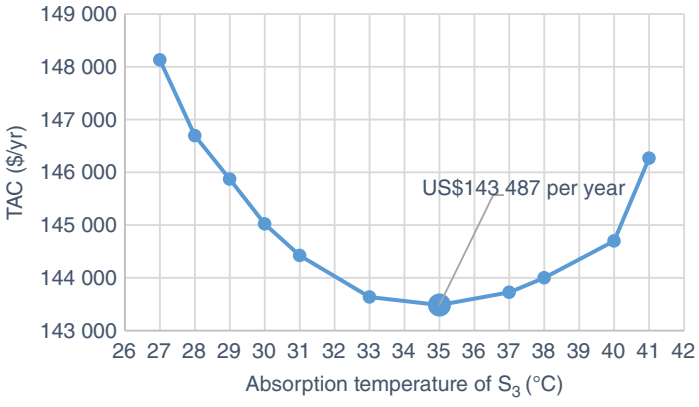

Figure 11.9 Variation of S_3 absorption temperatures and the resulting TAC.

H_4 achieves its target temperature via cooler 2 only. The cooled S_2 and S_3 lean streams then enter the MEN to complete the recycle procedure. As can be seen in the figure, the MEN and REN are connected through the lean streams S_2 and S_3. The optimal flow rates for the MSAs are found to be 2.2 kg/s (S_1), 0.26 kg/s (S_2), and 0.012 kg/s (S_3). For the regenerants, QR_1 and QR_2, the optimal flow rates of 0.049 and 0.079 kg/s were obtained, respectively. The resulting TAC of the combined network is determined as US$121 317 per year.

The CHAMEN model was then extended to handle multi-period operation by introducing index "*p*" in the model equations to allow fluctuations in solar irradiations. The model was then tested at different fossil-based hot utility prices to find the maximum price at which the usage of hot utility generated from fossil becomes uneconomical. At a price of US$1075/(kW yr), the solver switched from using the fossil-based utility, H_2, to utility generated from solar, H_1, for both heaters in the HEN. The resulting combined network TAC with solar panels is US$145 021 per year. This network is further optimized by implementing the previously optimized operating temperatures of the MEN and REN. The optimization procedure is discussed next.

11.5.1.4 Absorption and Regeneration Temperature Optimization

To further optimize the solar integrated network, an investigation was carried out to determine the optimal absorption and regeneration temperatures. The lean streams are divided into sub-streams having different temperatures, with that of S_3 being the first to be varied. Once the optimal absorption temperatures for S_2 and S_3 were identified, then the stripping temperature for S_3 was varied. Figures 11.9–11.12 show the TACs associated with the varying temperatures.

In Figure 11.9, the TAC of the network decreases as the S_3 absorption temperature increases from 27 to 34 °C. The TAC curve then goes through a minimum value of US$143 487 per year at the absorption temperature of 35 °C. Further increase in the absorption temperature from 35 to 41 °C showed an increasing trend in the TAC. These results were obtained through investigating 11 sub-stream temperatures. Note that the mass transfer equilibrium is a function

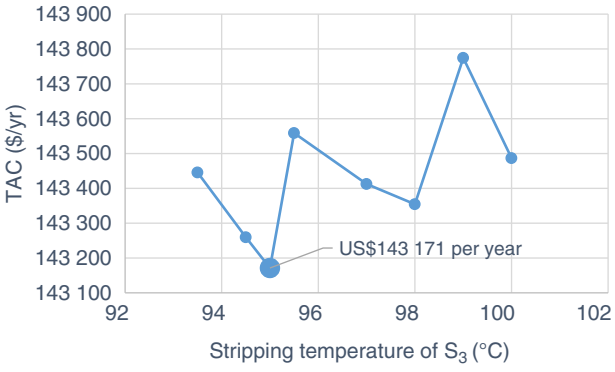

Figure 11.10 Variation of S_3 stripping temperatures and the resulting TAC.

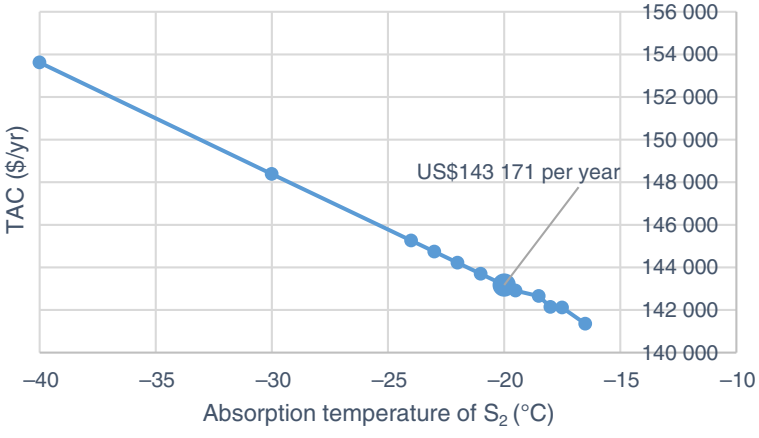

Figure 11.11 Variation of S_2 absorption temperatures and the resulting TAC.

of temperature as presented in Eq. (11.42). At each sub-stream temperature, a new equilibrium constant was calculated. These different equilibrium constants change the mass transfer driving forces, and therefore, it affects the optimization results.

The next step of the investigation involved varying the stripping temperature of S_3. Of the 10 sub-stream temperatures investigated, only 8 gave feasible solutions. The 8 sub-stream temperatures are plotted against their corresponding TACs in Figure 11.10.

Reducing the stripping temperature from 100 to 95 °C resulted in slight decrease in TAC values from US$143 487 per year to US$143 171 per year. Further temperature reduction, however, increased the TACs. Note that S_3 flow rate is low compared with the other lean stream flow rates, and therefore, change in S_3 stripping temperatures do not significantly affect the resulting TAC values. In general practice of steam stripping, the operating temperature is kept slightly below 100 °C to prevent corrosion [41]. The effects of compositions on stripping temperature were investigated, and it was found that increase in composition

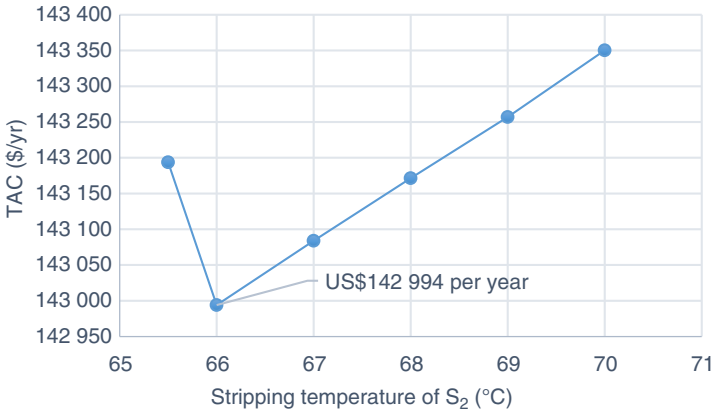

Figure 11.12 Variation of S_2 stripping temperatures and the resulting TAC.

resulted in better stripping at higher temperatures [41]. It should be noted that in this case study, the composition of H_2S in the streams is low, and therefore, the benefit of increasing the stripping temperature is not favorable. The study of Addington and Ness [41] thus validates our result in Figure 11.10.

The optimal operating temperature of S_3 was found to be 35 °C for the absorption process and 95 °C for the regeneration process. These values were fixed for the next investigation, which involves varying the temperature of S_2. The absorption temperature of S_2 was varied first while keeping the stripping temperature of S_2 and the best operating temperatures of S_3 obtained in Figures 11.9 and 11.10 constant. Due to the sequential nature of this investigation, the authors of this chapter are aware that depending on the order of investigations, the results may differ. The S_2 absorption temperature variations are presented in Figure 11.11.

The overall trend depicted through 12 sets of sub-streams in Figure 11.11 shows an increasing trend of TAC as absorption temperatures decreases. This is due to increasing cooling requirements to achieve low absorption temperatures. Note that S_2 is the chilled methanol, which is cooled below 0 °C for absorption. TAC values obtained in Figure 11.11 show a decreasing trend as absorption temperature increases; however, the minimum point was not depicted within the tested temperature values. Therefore, literature absorption temperature of −20 °C was selected for further investigation. The variations of the stripping temperature of S_2 are presented in Figure 11.12.

The investigation showed that there is a rapid decrease in TAC values over the temperature ranges of 70 and 67 °C. The minimum TAC of US$142 994 per year was obtained at the stripping temperature of 66 °C. Thereafter, the further reduction in temperature causes the TAC curve to slightly increase. The stripping temperature of 66 °C is within the good operating temperature as the boiling point of methanol is 64.7 °C. With these optimized operating temperatures, the optimized CHAMEN configuration was obtained as shown in Figure 11.13.

The optimized network in Figure 11.13 consists of four, five, and five exchangers in MEN, HEN, and REN, respectively. There is a two-way stream split involving S_1 in the MEN with the split flow rates of 2.0395 and 0.1645 kg/s. The exhausted S_3

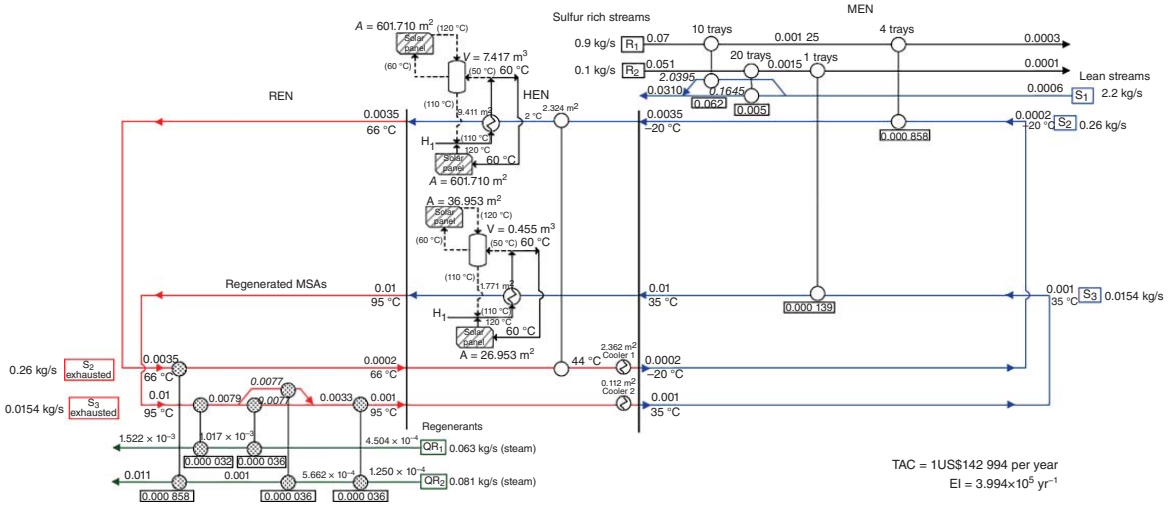

Figure 11.13 The optimized CHAMEN configuration (values above streams are composition in mass fractions; while values in boxes indicate mass load transferred in mass exchangers [kg/s]).

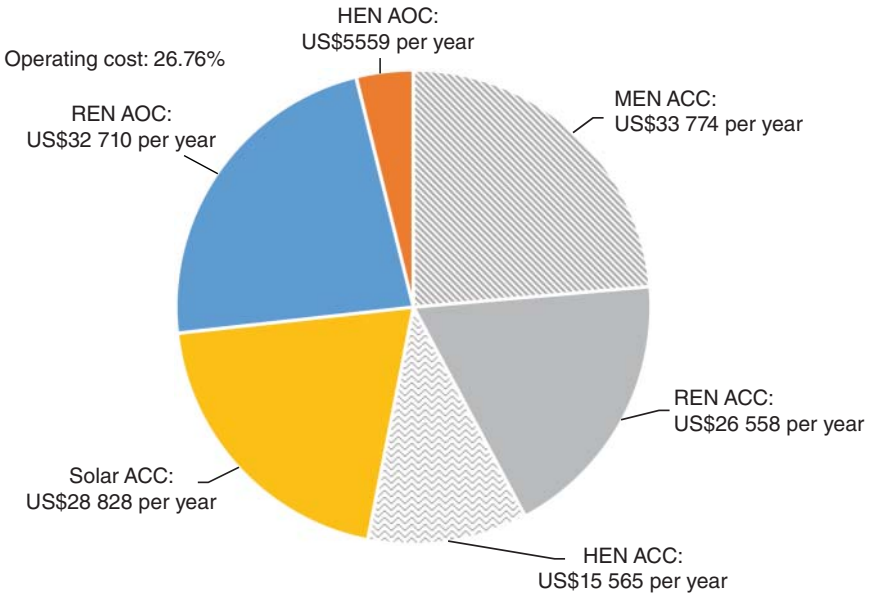

Figure 11.14 Detailed TAC for CHAMENs with solar panels.

in the REN also involves a two-way stream split. In the multi-period model, two discrete time intervals, day and night, were considered. The stream temperature during night time is shown in bracket the HEN of Figure 11.13. The optimized CHAMEN has a TAC of US$142 994 per year. The breakdown of the TAC of the network, which comprises the ACC and the AOC is presented in Figure 11.14.

In Figure 11.14 the operating costs, which comprises that of HEN and REN, contribute 26.76% to the TAC of the integrated network. The solar network capital cost, which comprises cost of solar panels and heat storage vessel, contributes 20.16% to the TAC. The combined networks without solar panels shown in Figure 11.8 are studied further, and the breakdown of the TAC is presented in Figure 11.15.

In Figure 11.15, the operating costs of the REN and HEN comprise 31.63% of the TAC. It can be observed that the resulting TAC of the network without solar panels (Figure 11.8) is 15% lower than the network with solar panels (Figure 11.13). However, implementation of solar panels can reduce the environmental impact of the process by 26%. Further, temperature optimization performed on the network (Figure 11.13) can result in a reduction in HEN capital cost as well. However, the MEN capital cost is higher in the combined network with solar panels. This may have resulted from the trade-offs between the competing variables and the temperature effects on the equilibrium relation which affects the sizing of the mass exchangers.

Note that during the temperature variation presented in Figures 11.9–11.12, the combined networks were optimized in terms of the TAC only. To optimize a network simultaneously in terms of both the TAC and environmental impact, the environmental objective function presented in Eq. (11.41) is used with the economic objective function in the model formulation.

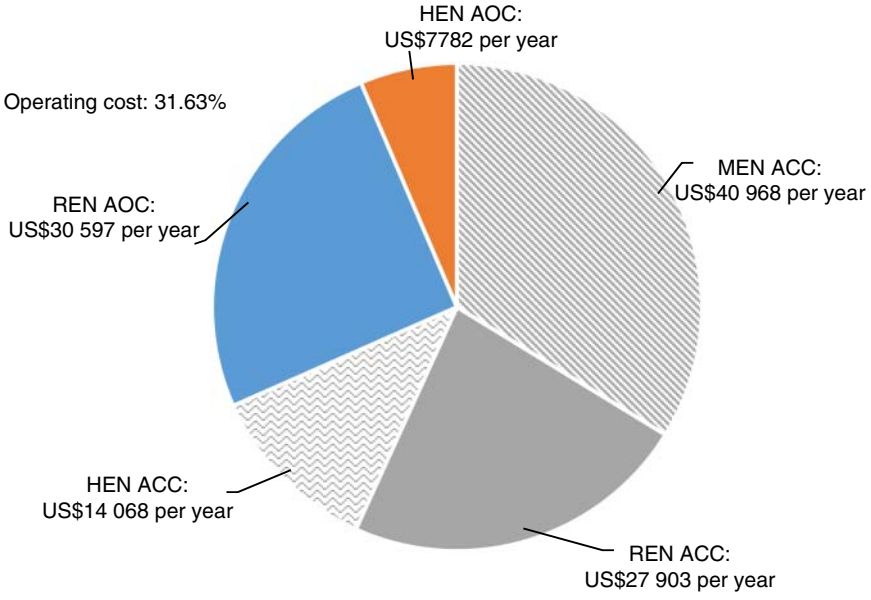

Figure 11.15 Detailed TAC for CHAMENs without solar panels.

Table 11.7 NMP lean stream data.

New lean stream data	M	z^s	z^t
S_3 (NMP)	–	1×10^{-5}	1×10^{-4}

Source: Srinivas and El-Halwagi 1994 [10]. Reproduced with permission of Elsevier.

11.5.1.5 The Synthesis of Combined Model Using MOO

The purpose of this section is to demonstrate the implementation of MOO in the context of the integrated CHAMEN model developed in this chapter. However, due to the multidimensional nature of the problem, and its highly nonlinear nature, implementing MOO gave infeasible solutions for some range of data used in the previous steps. Therefore, the stream data for S_3 is replaced with *N*-methyl-2-pyrrolidone (NMP) whose data were obtained from Srinivas and El-Halwagi [10]. Table 11.7 presents the stream data. The concentrations are given in mass fractions.

Srinivas and El-Halwagi [10] also presented the equilibrium relation of the NMP solvent as shown in Eq. (11.43):

$$m(T) = 1.1907 \cdot T - 332.0 \tag{11.43}$$

The absorption temperature of NMP was assumed to be 10 °C. The regeneration of the NMP solvent can involve either steam stripping or inert gas (N_2). The REN data is presented in Table 11.8 where the compositions are given in mass fractions. The equilibrium constants of QR_v were obtained using Eq. (11.2).

Table 11.8 The inert gas stripping stream data.

New lean stream data	*M*	z^s	z^t
QR_1	0.029 4	0.000 02	0.00068
QR_2	0.0022	0.00045	0.0423

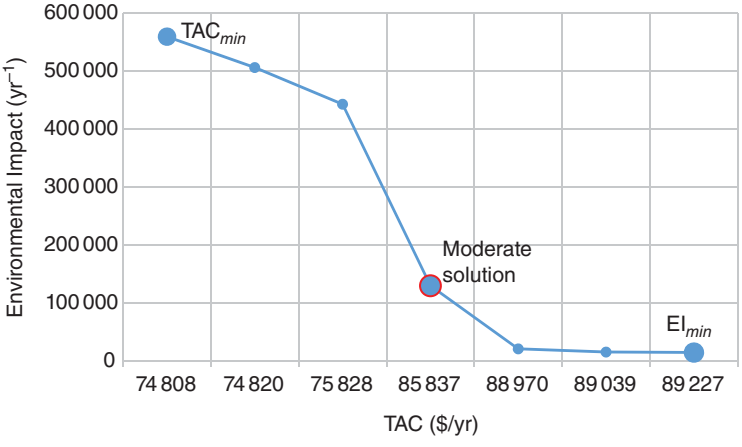

Figure 11.16 Pareto optimal of the combined networks with NMP as S_3 solvent.

The model was initialized at an EMAC value of 4.15×10^{-13} (wt fraction), an REMAC value of 7.7×10^{-8} (wt fraction), and an EMAT value of 5.1 °C. Some exploratory runs were necessary to get feasible solutions. The $\Omega_{p,\,MEN}$ value of 0.01811 and $\Omega_{p,\,REN}$ value of 0.008144 were used in this case. To obtain different network configurations with different TAC and environmental impact, the multi-objective function presented in Eq. (11.41) is used [34].

The TAC_{min} in Eq. (11.41) is obtained by optimizing the combined networks in terms of the TAC only. This was achieved by setting R_g, the weighting parameter to 1. In this way, the second term in the multi-objective function becomes zero. In the same way, the EI_{min} in Eq. (11.41) was obtained by using the weighting parameter value of 0. The network obtained at these extremes is presented in Figure 11.16.

Each data point in Figure 11.16 represents the different network configurations. The network representing TAC_{min} is shown at the left top corner of the Pareto optimal curve, while the network of EI_{min} is presented at the right bottom corner of the curve. It can be observed that the network with the minimum TAC exerts the most impacts on the environment. This is because the minimum TAC network uses utilities generated from the fossil-based energy source priced at US$60/(kW yr). The implementation of solar panels is, in general, relatively more expensive. However, the trade-off is that the implementation of such renewable infrastructures can reduce the environmental impact significantly.

The network with the minimum environmental impact has the highest TAC value because it includes solar panels and heat storage vessel. In practical process design context, it is desirable to synthesize networks with moderate levels of environmental impact and TAC. In Figure 11.16, the data points lying between the two extremes of the curve are obtained by varying the weighting term in Eq. (11.41) from 0 to 1.

For this case study, obtaining feasible solutions was not a trivial task; therefore, few points are presented in Figure 11.16. The solution highlighted with the tag "moderate solution" in the figure was selected as the optimal combined networks of HEN, MEN, and REN, which resulted in acceptable trade-off between of both TAC and EI. The optimized network configuration is presented in Figure 11.17.

Note that to obtain a moderate level of environmental impact, one of the heaters (matched with C_1) involves utility generated from solar thermal energy, while the other (matched with C_2) involves utility generated from fossil sources. The resulting configuration consists of five, six, and three exchangers in MEN, HEN, and REN, respectively. More accurate equilibrium relations for regenerating streams could also be used to make the REN more realistic. The network in Figure 11.17 has a TAC of US$85 837 per year and an associated environmental impact of 1.301×10^5 yr^{-1}. The breakdown of the TAC of Figure 11.17 is presented in Figure 11.18.

Compared with the previous problem data for MDEA solvent, NMP has lower operating cost. Also, the operating cost of inert gas is much lower than that of the stripping steam used in Section 11.5.1.4. The biggest contribution to the significant difference in TACs of the configuration presented in Figures 11.13 and 11.17 is the capital costs of solar panels and heat storage vessel. In Section 11.5.1.4, the resulting network configuration in Figure 11.13 involves solar panels and heat storage vessels in both heaters, while in Figure 11.17 only heater 1 involves solar panel infrastructures. Since a set of different S_3 data is used in the MOO model, the results in this section cannot be directly compared with the previous results. However, the resulting configuration in Figure 11.17 demonstrates that it was possible to extend the combined CHAMENs model to include MOO.

11.6 Conclusions and Future Works

This chapter presented a synthesis method for CHAMENs. The traditional MEN and HEN synthesis methods were extended with a newly developed REN model to handle CHAMEN problems involving multiple regenerable MSAs and multiple regenerating streams. Furthermore, solar thermal energy is integrated with the combined model to offset the environmental impact associated with the use of fossil-based energy sources. The "breadth first, depth later" approach is a key aspect of the overall design philosophy in this research field [8], and therefore, the model can be used to gain preliminary insights into the benefit of combining the synthesis of heat exchange networks with primary mass exchange and regeneration networks. The combined model was further extended to perform MOO of both economic and the environmental impact and the case study demonstrated

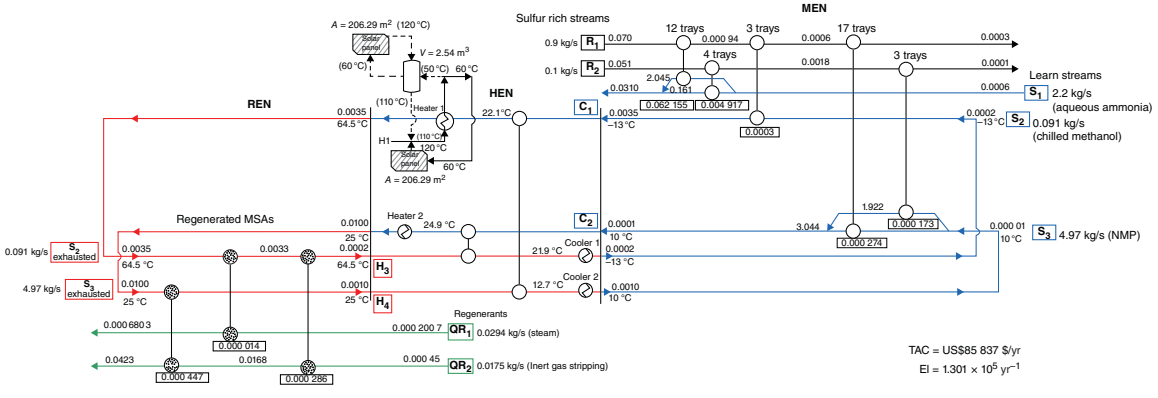

Figure 11.17 The combined networks with a moderate level of both TAC and EI (values above streams are composition in mass fractions; while values in boxes indicate mass load transferred in mass exchangers [kg/s]).

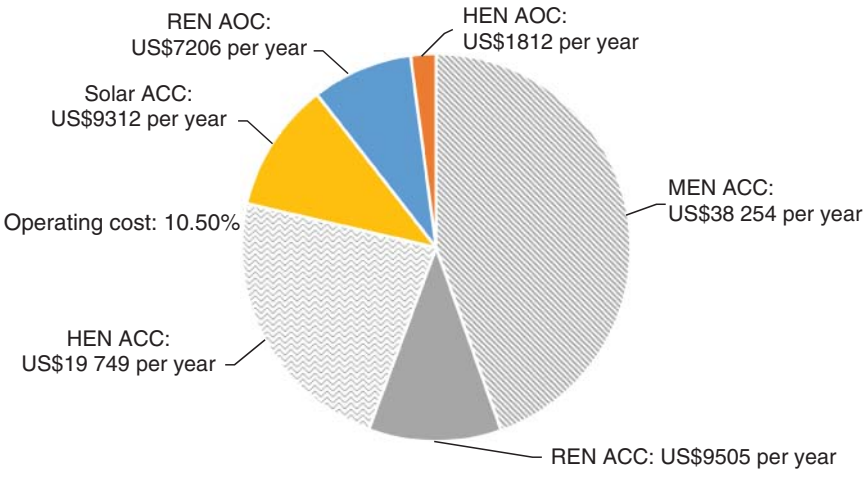

Figure 11.18 Detailed TAC for CHAMENs with NMP.

its ability to minimize both objectives simultaneously. However, it was noted that obtaining feasible solutions in the model was challenging especially when solving problems involving many streams.

The proposed combined model uses the sub-stream approach of Srinivas and El-Halwagi [10], which examines each sub-stream in a sequential manner. The same authors mentioned that a synthesis method of combining HEN and MEN should aim to search over all possible mass exchange temperatures and optimize network designs without preselecting the temperatures to study the economic trade-off between networks. Therefore, in future work, the optimization of operating temperatures ofMENs and RENs should be achieved without any preselecting of the temperature in a sequential way. Furthermore, regeneration stream data is very scarce, and it was challenging finding reasonable data. To obtain more practical REN configurations, it is suggested that more realistic regeneration data be implemented in a REN synthesis procedure.

It should be mentioned that the method presented in this chapter covered relatively simple cases, which involve linear equilibrium relations, single component problem, and simple LCIA. Also, detailed design criteria are not considered in the model formulation. Recently, Short et al. [42, 43] published several papers to update the exchanger configurations obtained from GAMS to include individual exchanger design heuristics which makes the individual exchanger in the network more realistic and practical. This will also be considered in future studies.

References

1 El-Halwagi, M.M. (1998). Pollution prevention through process integration. *Clean Products and Processes* 1: 5–19.

2 Seader, J.D., Henley, E.J., and Roper, D.K. (1998). *Separation Process Principles*. Wiley.

3 Isafiade, A. and Fraser, D. (2009). Interval based MINLP superstructure synthesis of combined heat and mass exchanger networks. *Chemical Engineering Research and Design* 87: 1536–1542.

4 El-Halwagi, M.M. and Manousiouthakis, V. (1990). Simultaneous synthesis of mass-exchange and regeneration networks. *AIChE Journal* 36: 1209–1219.

5 El-Halwagi, M., Hamad, A., and Garrison, G. (1996). Synthesis of waste interception and allocation networks. *AIChE Journal* 42: 3087–3101.

6 Garrard, A. and Fraga, E.S. (1998). Mass exchange network synthesis using genetic algorithms. *Computers and Chemical Engineering* 22: 1837–1850.

7 Chen, C.-L. and Hung, P.-S. (2005). Simultaneous synthesis of mass exchange networks for waste minimization. *Computers and Chemical Engineering* 29: 1561–1576.

8 El-Halwagi, M.M. (2017). *Sustainable Design Through Process Integration: Fundamentals and Applications to Industrial Pollution Prevention, Resource Conservation, and Profitability Enhancement*. Butterworth-Heinemann.

9 Edgar, T. and Huang, Y. (1993). Simultaneous recovery of waste chemicals and energy in an oil refinery. In: *ACS Special Symposium on Emerging Technologies for Hazardous Waste Management*, Book of Extended Abstracts, Atlanta, GA, 27–29 September (ed. D.W. Tedder), 27–29. American Chemical Society.

10 Srinivas, B. and El-Halwagi, M. (1994). Synthesis of combined heat and reactive mass-exchange networks. *Chemical Engineering Science* 49: 2059–2074.

11 Papalexandri, K., Pistikopoulos, E., and Floudas, A. (1994). Mass-exchange networks for waste minimization – a simultaneous approach. *Chemical Engineering Research and Design* 72: 279–294.

12 Isafiade, A. and Fraser, D. (2007). Optimization of combined heat and mass exchanger networks using pinch technology. *Asia-Pacific Journal of Chemical Engineering* 2: 554–565.

13 Liu, L., Du, J., and Yang, F. (2015). Combined mass and heat exchange network synthesis based on stage-wise superstructure model. *Chinese Journal of Chemical Engineering* 23: 1502–1508.

14 Liu, L., El-Halwagi, M.M., Du, J. et al. (2013). Systematic synthesis of mass exchange networks for multicomponent systems. *Industrial and Engineering Chemistry Research* 52: 14219–14230.

15 Isafiade, A.J., Short, M., Bogataj, M., and Kravanja, Z. (2017). Integrating renewables into multi-period heat exchanger network synthesis considering economics and environmental impact. *Computers and Chemical Engineering* 99: 51–65.

16 López-Maldonado, L.A., Ponce-Ortega, J.M., and Segovia-Hernández, J.G. (2011). Multiobjective synthesis of heat exchanger networks minimizing the total annual cost and the environmental impact. *Applied Thermal Engineering* 31: 1099–1113.

17 Vaskan, P., Guillén-Gosálbez, G., and Jiménez, L. (2012). Multi-objective design of heat-exchanger networks considering several life cycle impacts using a rigorous MILP-based dimensionality reduction technique. *Applied Energy* 98: 149–161.

18 Goedkoop, M., De Schryver, A., Oele, M. et al. (2008). *Introduction to LCA with SimaPro 7*. The Netherlands: PRé Consultants.

19 Jensen, A., Elkington, J., Christiansen, K. et al. (1997). *Life Cycle Assessment: A Guide to Approaches, Experiences and Information Sources*. Copenhagen: European Environment Agency.

20 US EPA (2006). *Life Cycle Assessment: Principles and Practice*. Cincinnati, OH: National Risk Management Research Laboratory.

21 Fedkin, M. (2018). *Life Cycle Assessment (LCA) Methodology*. College of Earth and Mineral Sciences, The Pennsylvania State University, Department of Mechanical and Nuclear Engineering.

22 International Organization for Standardization (2006). *Environmental Management – Life Cycle Assessments – Requirements and Guidelines*. ISO.

23 Institute for Environment and Sustainability (2010). *Framework and Requirements for LCIA Models and Indicators*. JRC, European Commission.

24 Goedkoop, M.J. (1999). *The Eco-indicator 99: A Damage Oriented Method for Life Cycle Impact Assessment Methodology Report*. PRé Consultants.

25 Huijbregts, M., Steinmann, Z., Elshout, P. et al. (2016). *ReCiPe 2016: A Harmonized Life Cycle Impact Assessment Method at Midpoint and Endpoint Level Report I: Characterization*. Bilthoven The Netherlands: National Institute for Public Health and Environment.

26 Yee, T.F. and Grossmann, I.E. (1990). Simultaneous optimization models for heat integration – II. Heat exchanger network synthesis. *Computers and Chemical Engineering* 14: 1165–1184.

27 Szitkai, Z., Farkas, T., Lelkes, Z. et al. (2006). Fairly linear mixed integer nonlinear programming model for the synthesis of mass exchange networks. *Industrial and Engineering Chemistry Research* 45: 236–244.

28 Miettinen, K. and Mäkelä, M. (1999). Comparative evaluation of some interactive reference point-based methods for multi-objective optimisation. *Journal of the Operational Research Society* 50: 949–959.

29 Isafiade, A.J. (2017). Integration of renewable energy into mass, heat and regeneration network synthesis. *Chemical Engineering Transactions* 61: 67–72.

30 Chen, J. (1987). Comments on improvements on a replacement for the logarithmic mean. *Chemical Engineering Science* 42: 2488–2489.

31 Verheyen, W. and Zhang, N. (2006). Design of flexible heat exchanger network for multi-period operation. *Chemical Engineering Science* 61: 7730–7753.

32 Soršak, A. and Kravanja, Z. (2002). Simultaneous MINLP synthesis of heat exchanger networks comprising different exchanger types. *Computers and Chemical Engineering* 26: 599–615.

33 Hallale, N. (1998). *Capital Cost Targets for the Optimum Synthesis of Mass Exchange Networks*. University of Cape Town.

34 Gxavu, S. and Smaill, P.A. (2012). Design of heat exchanger networks to minimize cost and environmental impact. BSc thesis. University of Cape Town.

35 Rosenthal, R. (2007). *GAMS – A User's Guide*. Washington, DC: GAMS Development Corporation https://www.gams.com/latest/docs/UG_MAIN.html.

36 Kemp, I. (2007). *Pinch Analysis and Process Integration: A User Guide on Process Integration for the Efficient Use of Energy*, 2e. Butterworth-Heinemann.

37 El-Halwagi, M.M. and Manousiouthakis, V. (1989). Synthesis of mass exchange networks. *AIChE Journal* 35: 1233–1244.
38 Hallale, N. and Fraser, D. (2000). Capital and total cost targets for mass exchange networks: Part 2: Detailed capital cost models. *Computers and Chemical Engineering* 23: 1681–1699.
39 Elvers, B. (2015). *Ullmann's Energy, 3 Volume Set: Resources, Processes, Products*. Wiley.
40 ProSim (2015). *Syngas Deacidification with Rectisol Process*. Laberge, France: ProSim.
41 Addington, L. and Ness, C. (2010). *An Evaluation of General "Rules of Thumb" in Amine Sweetening Unit Design and Operation*. Bryan Research and Engineering.
42 Short, M., Isafiade, A.J., Biegler, L.T., and Kravanja, Z. (2018). Synthesis of mass exchanger networks in a two-step hybrid optimization strategy. *Chemical Engineering Science* 178: 118–135.
43 Short, M., Isafiade, A.J., Fraser, D.M., and Kravanja, Z. (2016). Two-step hybrid approach for the synthesis of multi-period heat exchanger networks with detailed exchanger design. *Applied Thermal Engineering* 105: 807–821.

12

Optimization of Integrated Water and Multi-regenerator Membrane Systems Involving Multi-contaminants: A Water-Energy Nexus Aspect

Musah Abass and Thokozani Majozi

University of Witwatersrand, NRF/DST Chair in Sustainable Process Engineering, School of Chemical and Metallurgical Engineering, 1 Jan Smuts Avenue, Braamfontein, Johannesburg 2000, South Africa

12.1 Introduction

The increasing demand on water and energy resources combined with strict environmental regulations on effluent discharge limits necessitates sustainable use of both resources. The majority of water withdrawn for industrial and domestic use requires treatment. Enormous amount of energy is required in the treatment and distribution of water. Similarly, in the production of energy, large amounts of water are used. This inherent interdependence of energy and water is known as *water-energy nexus*. This presents important challenges, which require development of effective process integration techniques.

Within the realm of *process systems engineering*, process integration techniques have been developed for water minimization through reuse/recycle and regeneration reuse/recycle schemes. Achieving water minimization through regeneration reuse/recycle involves partial treatment of effluent using purification processes, which can be categorized as membrane and non-membrane operations. The worldwide acceptance of membrane regeneration systems for water network synthesis is due to increased regulatory pressure to meet portable water standards, increased demand for water and pressure on existing but overly exploited water bodies, and market forces governing the development and commercialization of membrane technologies [1]. However, using membrane technologies for water minimization is energy intensive; therefore, it is of significant importance to account for the system in detail so that an optimal network can be achieved. This study aims at exploring a detailed multi-regenerator membrane system to enhance water minimization considering the multi-contaminant characteristics of most effluent generated in process industries with focus on electrodialysis (ED) and reverse osmosis (RO) processes. These two membrane technologies are considered because ED is capable of handling ionic contaminants and RO works for both ionic and non-ionic contaminants.

Because of the interdependence of water and energy in process industries, several researches have been carried out in literature in which detailed analysis of the regeneration unit within the water network is explored to account for energy

Process Intensification and Integration for Sustainable Design, First Edition.
Edited by Dominic C. Y. Foo and Mahmoud M. El-Halwagi.
© 2021 WILEY-VCH GmbH. Published 2021 by WILEY-VCH GmbH.

requirement in water network optimization. Khor et al. [2] developed a detailed regeneration model, which was incorporated within a water network superstructure for water regeneration network. The work involved a rigorous nonlinear model of an RO unit with fixed design considerations for multi-contaminant case. The work did not, however, consider the possibility of different regenerators to explore their treatment capabilities. Yang et al. [3] considered multiple water treatment units for a case involving multi-contaminants using short-cut expressions with the purpose of gaining comprehensive understanding of trade-offs between removal efficiencies and the cost of the treatment units, as well as the impact on the units' designs but without capturing the detail regenerator design. According to Rangaiah and Wei [4], it is vital to take into consideration details of the network system with regeneration unit inclusive; such that the structural and parametric (design) optimization of the system is satisfied completely for true optimal water network to be attained.

Recent works on water network optimization through regeneration systems have incorporated detailed modeling with variable removal ratio of the regeneration units because it gives accurate cost representation and additional degree of freedom for better performance of the water network system. Buanbeng-Baidoo and Majozi [5] proposed a superstructure optimization that incorporates a detailed RO network model, which relied on the state-space approach developed by El-Halwagi [6], for simultaneous minimization of water and energy in a multi-contaminant water network. Mafukidze and Majozi [7] developed a similar approach using multiple ED membrane units focusing on a single ionic contaminant. Their approach enhanced the work of Khor et al. [2] to allow for series and parallel connection of membrane units in the treatment unit subnetwork. Abass and Majozi [8] also proposed an approach in which RO and ED membrane systems are employed but assuming a single contaminant scenario. As most of the researches earlier are related to continuous processes, Oke et al. [9, 10] employed the use of detailed membrane distillation model to simultaneously optimize water and energy usage in hydraulic fracturing process focusing on single contaminant. In their latter work, Oke et al. [11] extended the model to capture multi-contaminant characteristics of wastewater (WW) generated from hydraulic fracturing process using detailed ultrafiltration membrane technology model.

Despite the usefulness of the aforementioned formulations, most of the developed models are limited to single membrane technology, while those that considered two types of membrane technologies were limited to a single contaminant. Effluents from industries frequently comprise of various ionic and non-ionic contaminants. Given consideration to effluent with multi-contaminants (ionic and non-ionic) using combination of membrane technologies will allow for selection of the best technology for water network optimization. Therefore, the current work focuses on the development of detailed ED and RO regeneration models with the intention of addressing a problem involving multi-contaminants. The ED formulation in this work is specific to the case of a single contaminant; hence, sequence specific constraints are employed such that ionic contaminants that are specific to the ED unit are removed by it. The RO unit is, however, at liberty to treat both contaminants provided the optimization chooses that option.

A comparison between the variable removal ratio, blackbox formulation, and detailed model is conducted to provide accurate water network description in terms of design, cost, freshwater (FW) consumption, wastewater generation, and regeneration and energy costs.

12.2 Problem Statement

The problem addressed in this work can be stated as follows:

Given:

(i) A set of water sources, J, with known flowrates, Q_j, and known contaminant concentration $C^x_{j,co}$.
(ii) A set of water sinks, I, with known flowrates, Q_i, and known maximum permissible contaminant concentration, $C^U_{i,co}$.
(iii) Membrane regenerators capable of partial wastewater treatment from sources for reuse/recycle with important design parameters.
(iv) A freshwater source, FW, with known contaminant concentration and variable and unlimited flowrate.
(v) A wastewater sink, WW, with known maximum allowable contaminant concentration, $C^U_{i,co}$, and variable and unlimited flowrate.

Determine:

(i) Optimal water network configuration for minimum FW intake, wastewater generation, and energy usage.
(ii) Minimum annualized costs of the regeneration units.
(iii) Optimum design variables of the regeneration units.

12.3 Model Formulation

The model is formulated based on the water network superstructure depicted in Figure 12.1, which is an extension of the work, by Abass and Majozi [8]. Based on Figure 12.1, a *source* and *sink* approach is adopted. A source is a process unit that produces effluent, while a sink is a process unit that consumes water from other process units, FW source, and both permeate and reject stream of the regeneration units (provided that the streams meets the maximum allowable contaminant limit of the sink). The choice of superstructure and modeling technique in this work is motivated by the case study for this work. Since the case study explored in this work is multi-contaminant, the superstructure is developed such that streams from the reject streams of the RO unit should not be fed into the ED unit. This is to prevent fouling of membrane of the ED unit, as the contaminants from the reject stream of the RO unit are highly concentrated.

The mathematical formulation in this work is separated into three different sections. The first section consists of water network modeling, which is basically mass and concentration balance across the water network superstructure. The

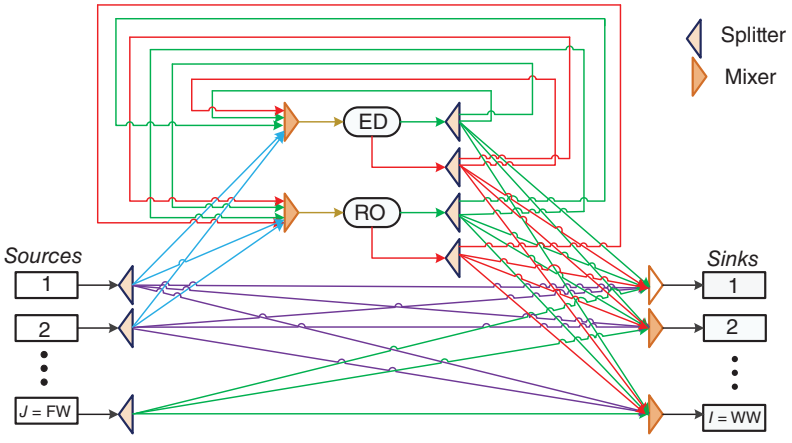

Figure 12.1 Superstructure representation of water network with multiple membrane regenerators.

second section consists of detailed mathematical model of both ED and RO units, which is incorporated into the objective function, which forms the third part of the model. The objective function is set to minimize the total network cost.

12.3.1 Material Balances for Sources

Figure 12.2 shows a schematic representation of water source, *j*, where a water source can split into many streams for reuse/recycle into sinks including the wastewater sink and regeneration units as shown in constraint (12.1). It is worth mentioning that the last sink, WW, represents the waste sink.

$$Q_j^x = \sum_{i \in I} Q_{j,i} + Q_j^{ro} + Q_j^{ed} \quad \forall j \in J \tag{12.1}$$

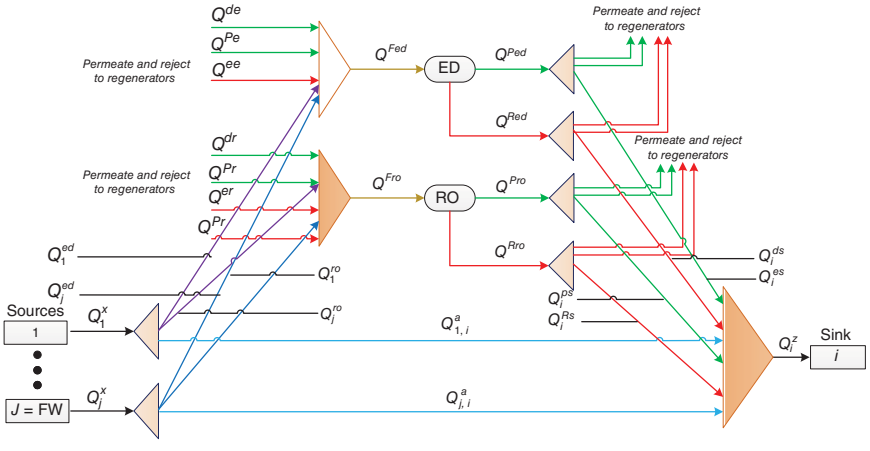

Figure 12.2 Schematic representations of a water source.

12.3.2 Mass and Contaminants Balances for Regeneration Units

Material balances are conducted for all streams entering the regeneration units. The streams from sources, as well as the permeate and reject streams of both regenerators, may be sent for reuse/recycle depending on the contaminant concentration limits of the regeneration units. Constraints (12.2) and (12.3) are the water balances around the mixer preceding the RO and ED units, respectively. The recycle term for the reject stream from RO unit into the ED unit is omitted in constraint (12.3) in order to prevent fouling of the ED membrane. Since the contaminants identified in the effluents for the case study consists of ionic and non-ionic contaminants, it is presumed that the reject stream of the RO unit will be highly contaminated hence not practically feasible to feed it into the ED unit.

$$\sum_{j\in J} Q_j^{ro} + Q^{dr} + Q^{er} + Q^{fr} + Q^{gr} = Q^{Fro} \tag{12.2}$$

$$\sum_{j\in J} Q_j^{ed} + Q^{de} + Q^{ee} + Q^{fe} = Q^{Fed} \tag{12.3}$$

A contaminant balance is conducted for the feed into the regeneration unit depending on the varying tolerance of contaminants of the ED and RO units, where the maximum contaminant for each unit is taken into consideration. Hence, constraints(12.4) and (12.5) represent the contaminant balance around the mixer of ED and RO, respectively.

$$C_{co}^{Ule} \geq \frac{\sum_{j\in J} Q_j^{ed} C_{j,co}^{x} + Q^{de} C_{co}^{Ped} + Q^{ee} C_{co}^{Red} + Q^{fe} C_{co}^{Pro}}{Q^{Fed}} \quad \forall co \in CO \tag{12.4}$$

$$C_{co}^{Ulr} \geq \frac{\sum_{j\in J} Q_j^{ro} C_{j,co}^{x} + Q^{dr} C_{co}^{Ped} + Q^{er} C_{co}^{Red} + Q^{fr} C_{co}^{Pro} + Q^{ge} C_{co}^{Rro}}{Q^{Fro}} \quad \forall co \in CO \tag{12.5}$$

12.3.3 Mass and Contaminant Balances for Permeate and Reject Streams

The water balances for permeate and reject streams of the ED unit that splits into sinks, which recycle into the ED and RO units, are represented by constraints (12.6) and (12.7).

$$Q^{Ped} = \sum_{i\in I} Q_i^{ds} + Q^{dr} + Q^{de} \tag{12.6}$$

$$Q^{Red} = \sum_{i\in I} Q_i^{es} + Q^{er} + Q^{ee} \tag{12.7}$$

Likewise, constraints (12.8) and (12.9) represent the water balances for permeate and reject streams of the RO unit.

$$Q^{Pro} = \sum_{i\in I} Q_i^{fs} + Q^{fr} + Q^{fe} \tag{12.8}$$

$$Q^{Rro} = \sum_{i\in I} Q_i^{gs} + Q^{gr} \tag{12.9}$$

12.3.4 Mass and Contaminant Balances for Sinks

Constraint (12.10) describes how a water sink can receive water from the water sources and from the permeate and reject streams of the membrane regenerators.

$$\sum_{j\in J} Q_{j,i}^{a} + Q_i^{ds} + Q_i^{es} + Q_i^{fs} + Q_i^{gs} = Q_i^{z} \quad \forall i \in I \tag{12.10}$$

It is worth mentioning that the last source FW signifies the freshwater source. Constraint (12.11) states that the maximum allowable contaminant concentrations into any sink, *i*, should not be exceeded.

$$\frac{\sum_{j\in J} Q_{j,i}^{a} C_{j,co}^{x} + Q_i^{ds} C_{co}^{Ped} + Q_i^{es} C_{co}^{Red} + Q_i^{fs} C_{co}^{Pro} + Q_i^{gs} C_{co}^{Rro}}{Q_i^{z}} \leq C_{i,co}^{Ul} \forall co \in CO, \ \ \forall i \in I \tag{12.11}$$

12.3.5 Modeling of the Regeneration Units

In modeling the ED and RO regeneration units, detailed mechanistic models of both regeneration units are considered in order to give a true representation of the operational conditions of the regeneration units. This is also done to show the synergy between the water network and the regeneration units. The detailed models of the RO and ED regeneration units by Abass and Majozi [8] are considered for this formulation. These models are presented in detail in the Appendix. The respective annualized costs are added to the objective function for optimal operation and capital costs of the water network superstructure. The model entails sequence specific constraints that allow the ED unit to remove only ionic contaminants prior to the RO unit that removes both organic and ionic contaminants. Consequently, the ED unit operates as a preprocessing step for the RO unit.

12.3.5.1 Performance of Regeneration Units

The performance of a membrane regeneration unit is typically described by the removal ratio and liquid recovery. The removal ratio refers to the fraction of mass load from the feed stream of the regeneration unit that exits the reject stream. This is represented by constraints (12.12) and (12.13) for the ED and RO units, respectively.

$$\mathrm{RR}_{ed} = \frac{Q^{Red} C_{co}^{Red}}{Q^{Fed} C_{co}^{Fed}} \quad \forall co \in CO \tag{12.12}$$

$$\mathrm{RR}_{ro} = \frac{Q^{Rro} C_{co}^{Rro}}{Q^{Fro} C_{co}^{Fro}} \quad \forall co \in CO \tag{12.13}$$

Most published work designates the removal ratio as a parameter [2, 12]. This work, however, sets the removal ratio of the organic contaminant chemical oxygen demand (COD) for the ED unit to be 0. This is done for ease of mathematical modeling and efficient operation of the ED unit. Setting the removal ratio of COD to 0 means the contaminant in any stream that feeds into the ED unit will exit as it entered since ED units are not capable of treating organic contaminants,

besides the formulation of the ED unit in this work is single contaminant based. The removal ratio for the ionic contaminants is set as variable and will be determined by the optimization model. Similarly the removal ratio for the RO unit is set as a variable for both contaminants, since the RO unit is capable of treating both contaminants. This also gives the optimization model the degree of freedom to select the fraction of contaminant that is optimally feasible to be removed.

The liquid recovery on the other hand represents the fraction of feed flowrate that exits through the permeate stream of the regeneration unit. This is shown by constraint (12.14) and (12.15) for ED and RO units, respectively.

$$\mathrm{LR}_{ed} = \frac{Q^{Ped}}{Q^{Fed}} \tag{12.14}$$

$$\mathrm{LR}_{ro} = \frac{Q^{Pro}}{Q^{Fro}} \tag{12.15}$$

12.3.6 Logical Constraints

Logical constraints are used to determine the existence of stream piping between units within the water network superstructure. This is done to prevent the existence of unnecessary streams and avoid water network complexity and unnecessary costs. Binary variables are introduced together with practical flowrates based on the case study to force constraints to be active or inactive. This is contrary to using Big-M constraints, where arbitrary maximum and minimum values are chosen to guide the existence of piping interconnections. The consequence for such a practice is the result of large search space, which inconsequently results in large computational time and many local or suboptimal solutions. Minimum flowrates are set such that flowrates below such bounds are deemed practically infeasible and therefore rejected. In order to achieve this, constraint (12.16), which defines the list of flowrates within the water network superstructure, is introduced for simplicity of the model formulation.

$$\text{Let } X = \{pr, pe, ps, Rr, Rs, dr, de, ds, er, ee, es\} \tag{12.16}$$

Constraint (12.16)–(12.20) are formulated are also used to control the structural design features.

$$Q^{aL} y^{a}_{j,i} \leq Q^{a}_{j.i} \leq Q^{a}_{j.i} y^{a}_{j,i} \quad \forall j \in J \ \ \forall i \in I \tag{12.17}$$

$$Q^{roL}_{j} y^{ro}_{j} \leq Q^{ro}_{j} \leq Q^{roU}_{j} y^{ro}_{j} \quad \forall j \in J \tag{12.18}$$

$$Q^{L} y^{X}_{i} \leq Q^{X}_{i} \leq Q^{U} y^{X}_{i} \quad \forall j \in J \ \ \forall i \in I \tag{12.19}$$

$$Q^{L} y^{X} \leq Q^{X} \leq Q^{U} y^{X} \quad \forall j \in J \tag{12.20}$$

12.3.7 The Objective Function

The objective function of the water network superstructure comprises of the annualized cost functions of the ED and RO units, which result in an overall

capital and operation costs function to be minimized. This is represented by constraint (12.21). The stream flow velocity, v, is assumed to be constant for all pipes with the same costs coefficients p and q. A 1-norm Manhattan distance, D, is adopted for all piping connections between units and AF is the annualization cost factor.

$$\text{Obj} = \min \left(\begin{array}{c} (K_{water}\text{FW} + K_{waste}\text{WW})\text{AOT} + \text{TAC}_{ed} + \text{TAC}_{ro} + \\ \text{AF}\left[\begin{array}{c} \sum_{j\in J}\sum_{i\in I} D_{j,i}\left(\frac{pQ^{a}_{j,i}}{3600v} + qY_{j,i}\right) + \sum_{j\in J} D^{ro}_{j}\left(\frac{pQ^{ro}_{j}}{3600v} + qY^{ro}_{j}\right) \\ \sum_{i\in I} D^{X}_{i}\left(\frac{pQ^{X}_{i}}{3600v} + qY^{X}_{i}\right) + D^{X}\left(\frac{pQ^{X}}{3600v} + qY^{X}\right) \end{array} \right] \end{array} \right) \tag{12.21}$$

The resultant model is an mixed integer nonlinear programming (MINLP) due to the presence of nonlinear terms, integer variables, and continuous variables. The MINLP model was solved using general algebraic modelling system (GAMS) 24.2 using the general-purpose global optimization solver branch and reduce optimization navigator (BARON). In this chapter, the piping connection distances were not considered; hence, only the first three terms of the objective function are taken into consideration.

12.4 Illustrative Example

The new mathematical model was applied to an illustrative example, with data given in Table 12.1. The example consists of a conceptual process water network, where water from sources including an FW source are sent to satisfy the demands of process water sinks including wastewater sinks. Process streams that require partial treatment are fed into the regeneration units to enhance their quality before being used in the sinks. Based on Table 12.1, five sources and sinks are

Table 12.1 Process data for water network.

Sources, *j*				Sinks, *i*			
		Concentration (mg/l)				Maximum concentration (mg/l)	
Source	Flowrate (t/s)	NaCl	COD	Sink	Flowrate (t/s)	NaCl	COD
1	0.384	0	600	1	0.247	34.22	34.22
2	0.040	30.02	30.02	2	0.040	0	60.03
3	0.160	0	120.07	3	0.028	0.37	20.41
4	0.861	498.28	498.28	4	0.861	0	54.03
FW	—	0	0	WW	—	600	600
Total	1.445				1.176		

found in the water network, including freshwater source and wastewater sink. Two contaminants, i.e. NaCl and COD, are identified for this example, with their concentrations given in Table 12.1. Table 12.2 shows the economic data for the example that is applied to the optimization models.

The example was analyzed in three scenarios and the results were compared. The first scenario consists of water integration without regeneration (i.e. with direct reuse/recycle scheme), and the second scenario represents water integration with a blackbox model regeneration system with variable removal ratio framework. The third scenario is water integration comprising of a detailed regeneration model system with a variable removal ratio framework.

In this current work the variable removal ratio is chosen over the more rigid fixed removal ratio for Scenarios 2 and 3 because it has proven to be the best method for optimal operation of the regeneration units within a water network superstructure optimization [3, 5, 7, 8]. Current research works have demonstrated that models with fixed removal ratios do not give the optimization a degree of freedom to explore and select the best performance for the regeneration units [3, 5, 7, 8].

Table 12.3 shows the optimal results of all scenarios in terms of FW consumption, wastewater generated, and total cost of water network. The optimal results for Scenarios 1, 2, and 3 are presented in Figures 12.1–12.3 accordingly. It is evident that Scenario 1 is the least optimal scenario since the amount of FW consumed is exceedingly higher compared with Scenarios 2 and 3. Both Scenarios 2 and 3 give better results in terms of water consumption and cost of water network. This shows that regeneration within a water network system is very important for

Table 12.2 Economic data for case study.

Parameter	Values
Annual operating time, AOT	870 h
Cost of electricity, C_{elect}	1.67×10^{-8} \$/(W s)
Unit cost of pretreatment of chemicals, C_{chem}	3×10^{-5} \$/kg
Annualization factor, AF	0.23
Unit cost of freshwater, C_{FW}	0.001 \$/kg
Unit cost of effluent treatment, C_{WW}	0.001 \$/kg

Table 12.3 Summary of results for all scenarios based on case study.

	Scenario 1 (recycle/reuse only)	Scenario 2 (blackbox model)	Scenario 3 (detailed model)
Freshwater (t/s)	1.134	0.989	1.00
Freshwater savings (%)	3.57	15.90	14.96
Wastewater (t/s)	0.861	0.716	0.729
Wastewater saving (%)	39.37	50.45	49.55

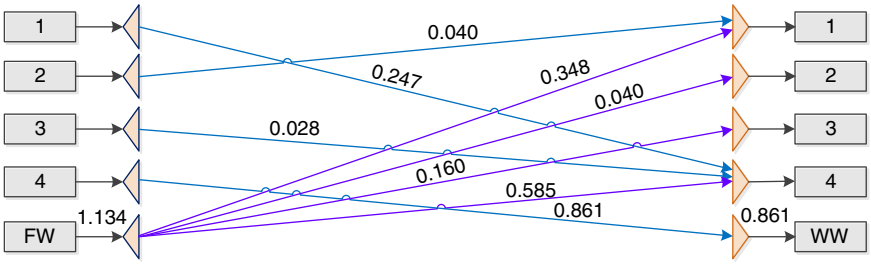

Figure 12.3 Optimum water network configuration for Scenario 1.

sustainable and cost effective use of water. Scenario 2, however, showed to be the best case scenario among the three scenarios in terms of saving in FW (15.9%) and wastewater (50.45%), compared with the base case scenario (i.e. without recycle and reuse). The results of Scenario 2 are, however, very deceptive and do not give a true representation of the water network cost. Scenario 2 also does not offer design opportunity of the regeneration units, and the type of regeneration is not known since the regeneration units in this case are simply characterized by the removal ratio and a linear cost function. This is misleading as the regeneration unit could be any unit ranging from membrane to non-membrane water regeneration units. In order to ascertain the better optimal solution among the three scenarios, a further analysis is conducted and the results are displayed in Table 12.4.

Table 12.4 details the results of the regeneration cost analysis. The total feed into the regeneration units based on the optimal design configurations of Figures 12.4 and 12.5 are represented together with regeneration cost of Scenarios 2 and 3, respectively. The regeneration cost of Scenario 2 is divided into estimated cost and true cost to aid comparison of the results. Estimated cost represents the costs of regeneration and total water network cost in Scenario 2, whereas true cost represent the cost of regeneration and total water network cost if the same amount of contaminated water is fed into a detailed model. From Table 12.4, it is evident that the cost of regeneration represented by the "estimated cost" blackbox model is much lesser than the true cost. This estimated cost shows a deviation of about 7% of the true cost of the water network. Based on the analysis in Table 12.4, it is evident that Scenario 3 with optimal configuration shown in Figure 12.5 is in fact the best case scenario for the case study. This is demonstrated by the 57.3% savings in regeneration and energy cost, and 2.5%

Table 12.4 Summary of regeneration cost analysis.

	Blackbox model		
	Estimated cost	**True cost**	**Detailed model**
Total regeneration feed (t/s)	0.848	0.848	0.747
Regeneration cost (million $)	0.099	3.68	1.573
Total cost (million $)	48.7	52.2	50.9

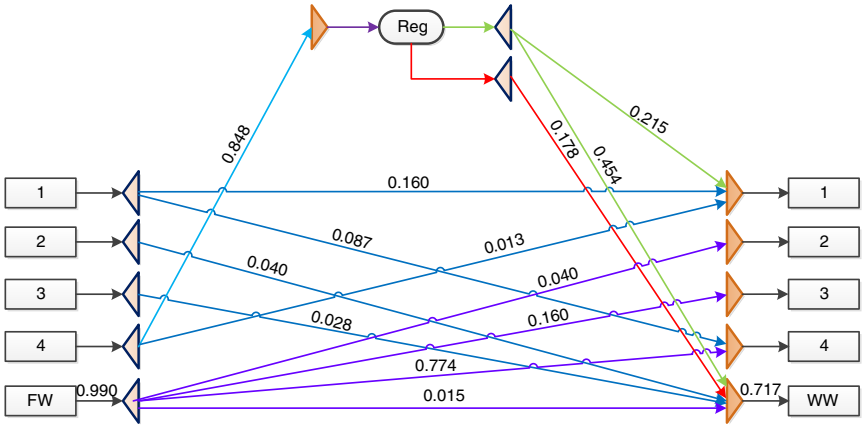

Figure 12.4 Optimum design configurations of the blackbox model.

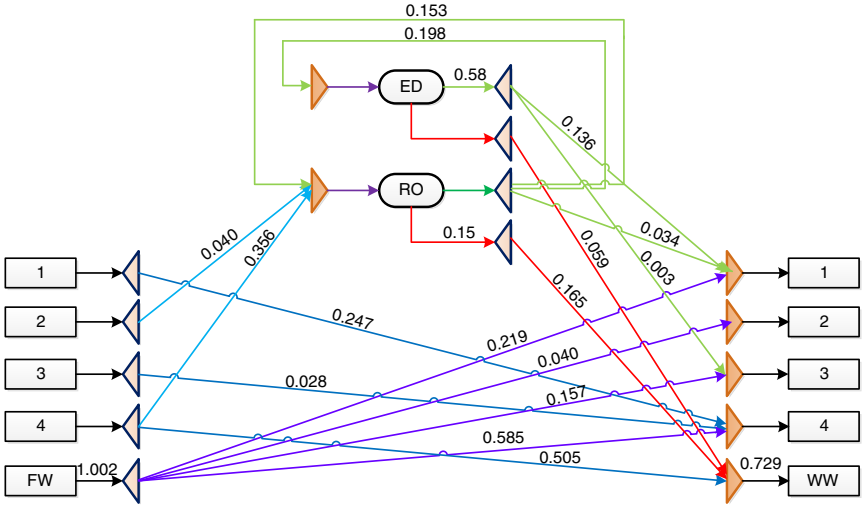

Figure 12.5 Optimum design configurations for detailed model.

savings in the total water network cost it offers compared to Scenario 2. The ED unit showed 0.95 removal ratio for the ionic contaminant (NaCl), whereas the RO unit showed 0.5 and 0.85 removal ratios for the ionic contaminant (NaCl) and organic contaminant (COD), respectively, for the detailed model.

Important model characteristics for all scenarios are presented in Table 12.5. The number of constraints, continuous variables, discrete variables, and computational times increases with the size of the models. Scenario 2 took a little bit over two minutes, whereas the detailed model requires over 16 hours to converge. The higher computational time of the detailed model is as a result of the nonlinear nature of the water network model. Tighter bounds were, however, imposed on certain variables of the regeneration units to aid convergence. The bounds imposed for the ED unit model included number of cell pairs, linear flow

Table 12.5 Summary of model characteristics for all scenarios.

	Base case	Blackbox model	Detailed model
Number of constraints	91	139	312
Number of continuous variables	73	117	241
Number of discrete variables	25	43	67
Tolerance	0	0.001	0.001
Time (s)	0	123	59 875

velocity, stacks length, and recovery rate to name but a few. The bounds on the RO regeneration unit model included but not limited to number of RO modules, permeate pressure, and retentate pressure. FW intake and wastewater generated flowrates for Scenario 1 were taken as upper bounds for Scenarios 2 and 3. This was done to ensure that the FW intake and wastewater discharge for Scenarios 2 and 3 should not exceed Scenario 1, otherwise there would be no need for regeneration. The complexity of the detailed model results in longer computational time needed to be solved; hence, insightful mathematical techniques are needed to reformulate the model for easier convergence. Powerful computers and robust mathematical solvers are needed to help the optimization and computation of MINLP problems.

12.5 Conclusion

This chapter has shown a mathematical formulation for detailed ED and RO units within a water network (WN) for a case study involving multi-contaminants. The developed model allowed ED unit to cater for the removal of ionic contaminants and RO unit for both ionic and organic contaminants. Incorporating the detailed models of regeneration units renders the model MINLP, which was solved using the GAMS\BARON. The developed model is applied to an illustrative example, with three scenarios. The detailed model showed 14.96% FW savings and 49.55% wastewater savings against the base case scenario. A further comparison was made between Scenarios 2 and 3, with Scenario 3 showing 57.3% saving in regeneration energy cost and 2.5% savings in total water network cost. The results shown in this work demonstrate that integrating regeneration units within a water network superstructure in a process unit will contribute immensely towards sustainable use of the overly burden global water resources. Incorporating detail models of regeneration units into the water network superstructure guides towards optimal design configuration of regeneration units that are environmentally sustainable and cost effective.

Acknowledgments

The authors would like to thank the Water Research Commission (WRC) and National Research Foundation (NRF) for funding this work under the NRF/DST Chair in Sustainable Process Engineering at the University of the Witwatersrand, South Africa.

12.A Appendix: Detailed Models for the ED and RO Modules

12.A.1 Electrodialysis Membrane Regeneration Unit

This section presents a detailed mechanistic model of a single stage ED regeneration unit based on the work of Tsiakis and Papageorgiou [13]. A single stage ED unit, Figure 12.A.1, is considered to demonstrate the interaction between the water network and the regeneration unit and also to enhance simplicity of the formulation.

In order to formulate the model for the regeneration unit, assumptions are made to describe the feed solution properties, hardware dimensions, and operating conditions [14].

The assumptions are:

(i) The diluate and concentrate cells are geometrically similar with identical flow patterns.
(ii) The flowrate in the diluate and concentrate compartments are equal and uniform$Q^d = Q^c$.
(iii) The fluid considered is Newtonian, i.e. the viscosity remains constant.
(iv) The unit is operated in a co-current flow.
(v) During operation the current should not exceed the limiting current density.
(vi) Water transport across the membrane is negligible compared with the flowrate in the diluate and concentrate streams.
(vii) Membrane thickness is negligible.
(viii) The concentration of the salt species is calculated using molar equivalents.

From the diagram Q^d is the diluate flowrate, Q^c is the concentrate stream flowrate, Q^{cr} is the concentrate stream recycle flowrate, Q^m is the flowrate from the feed stream that mixed with the concentrate stream to balance the flowrates, whereas C^{fc} is the feed concentration for the concentrate stream.

Physical parameters and necessary variables are incorporated to obtain an MINLP model. The total annualized cost TAC_e comprises of the electric current

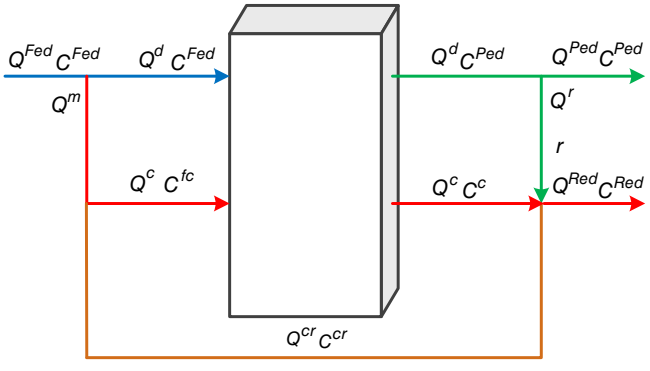

Figure 12.A.1 Schematic of a single stage ED plant.

through the ED unit, stack design considerations, desalination energy requirement, pumping energy requirement, and material balances and is formulated based on the following constraints.

12.A.1.1 Electric Current

The required electrical power through an ED unit is based on Faraday's law, which relates to the driving force that is required to transfer electrons from one stream to another in the ED unit as related in Lee et al. [14]. It also relates to the degree of desalination C^{Δ}, the flowrate of the diluate stream, and the number of cell pairs N in the stack as represented in constraint (12.A.1). ζ is the current utilization, and F is the Faraday's constant, which is required for the total current required to drive electrons from one stream to the other. The electrochemical valences of the ionic contaminants are represented by z.

$$I = \frac{Q^{d} F C^{\Delta} z}{\zeta N} \tag{12.A.1}$$

The degree of desalination is measured by the concentration difference between the diluate and concentrate streams across the ED unit as defined by the mass balance in constraint (12.A.2).

$$C^{\Delta} = C^{Fed} - C^{Ped} = C^{c} - C^{fc} \tag{12.A.2}$$

The limiting current density is determined by the mass transfer coefficient for the transport of ions across the membrane surface. This is difficult to determine theoretically, since it is a function of solution flow velocity, concentration, and stack and spacer configuration. Therefore, the limiting current density is determined experimentally for a certain flow velocity, concentration, and stack configuration as shown in Eq. (12.A.3).

$$I^{prac} = \varepsilon a^{LCD} C^{d} (u)^{b^{LCD}} \tag{12.A.3}$$

A safety factor, ε, within the range of 0.7–0.9, is used to adjust the practical limiting current density, which is dependent on the flow pattern. Constants a and b are determined by measuring the limiting current density under different flow conditions.

12.A.1.2 Stack Design Considerations

Efficient operation of an ED unit is dependent on the membrane area for a given feed solution, current density, number of cell pairs, and production rate [13]. Spacers are used to enhance mixing and attain uniform flow through the ED unit and also to separate and support the membranes. However, they reduce the volume of available cell, hence decreasing the flowrate. A safety factor, α, is included to cater for the corrections as shown in constraint (12.A.4). Here δ is the cell thickness, w is the diluate cell width, and v is the linear flow velocity.

$$Q^{Ped} = Nw\delta v\alpha \tag{12.A.4}$$

Membrane area is one of the design characteristics that determine the rate of desalination within an ED unit. The rate of desalination increases with the exposure of feed water on the membrane area. The presence of spacers reduces

the available area for current due to shadow effect. As a result the practically required membrane area is larger than the theoretically required area. A correction factor,β, is introduced to account for this effect as can be seen in constraint (12.A.5).

$$A = \frac{\left[\ln \frac{C^c C^{Fed}}{C^{Ped} C^{fc}} + \frac{\Lambda \rho^{AC} C^{\Delta}}{\delta}\right] C^{Ped} Q^{Ped} zF}{\left[\frac{C^{Ped}}{C^c} + 1 + \frac{\Lambda C^d}{\delta} \rho^{AC}\right] \varepsilon I^{prac} \beta \zeta} \tag{12.A.5}$$

From constraint (12.A.5), the parameter ρ^{AC} is the area resistance of the anion and cation exchange membranes and Λ is the equivalent electrical conductivity of the solution.

12.A.1.3 Energy Requirement

The energy required for the operation of an ED system is made of two components. The energy required for the transfer of ions from the solution across membrane material and the energy required for pumping the feed solution through the ED unit. The rate of consumption of either form of energy is dependent, among other factors, on the concentration of feed solution and the available membrane area to the feed solution.

Direct energy required in an ED unit is dependent on the voltage and current applied across the unit. The voltage drop across an ED unit is a result of resistance and potentials due to solutions of different salt concentration. The resistance is as a result of friction between ions with membrane matrix and water molecules. There is also energy loss due to electrode processes in the terminal compartments, although the energy loss due to resistance is much greater. It is, therefore, advisable to use membranes with low electrical resistance. Membranes should be closely arranged in order to reduce energy losses due to resistance of the cell pair unit as a result of salt transfer [14]. Based on Ohm's law, the voltage U, applied across an ED unit is shown in constraint (12.A.6).

$$U = \frac{C^{\Delta} N Q^{Ped} zF}{\zeta A} \left[\frac{\delta \ln \frac{C^c C^{Fed}}{C^{Ped} C^{fc}}}{\Lambda C^{\Delta}} + \rho^{AC}\right] \tag{12.A.6}$$

The voltage across an ED unit is, therefore, related to the total power,P_{ER}, required to produce a product capacity,Q^{Ped}. The specific energy required for desalination is represented by constraint (12.A.7).

$$E^{spec} = \frac{P_{ow}}{Q^{Ped}} \tag{12.A.7}$$

The pumping energy is the energy consumed in pumping the feed water into the ED unit. Since the membrane compartment is arranged in a rectangular form, the flows through the diluate and concentrate streams are considered to be passing through a rectangular channel. The geometry of the pipe is considered to be that of rectangular channel with a pressure drop ΔP, considered to be of a laminar flow as represented by constraint (12.A.8), which is a modified Hagen–Poiseuille equation for this type of geometry. The symbol μ is the viscosity of water, d is

the diameter of the rectangular channel of the ED unit, and L is the process path length of the ED unit.

$$\Delta P = \frac{12\nu\mu L}{d^2} \tag{12.A.8}$$

The pumping energy is, therefore, calculated based on the pressure drop as shown in constraint (12.A.9). Here Γ is a conversion factor available in literature, and η_p is the pumping efficiency.

$$E^{pump} = \frac{\Delta P \Gamma}{\eta_p} \tag{12.A.9}$$

12.A.1.4 Material Balances

Material balances are conducted around the ED unit in Figure 12.A.1 in order to conserve mass by accounting for materials entering, leaving, or mixing within the unit as shown in constraints (12.A.10)–(12.A.18).

$$Q^{Fed} = Q^{Ped} + Q^{Red} \tag{12.A.10}$$

$$Q^{Fed} = Q^{d} + Q^{m} \tag{12.A.11}$$

$$Q^{d} = Q^{Ped} + Q^{r} \tag{12.A.12}$$

$$Q^{c} = Q^{m} + Q^{cr} \tag{12.A.13}$$

$$Q^{Red} = Q^{c} + Q^{r} - Q^{cr} \tag{12.A.14}$$

Corresponding load balances are conducted across the ED unit in order to obtain the species balance in the streams and to demonstrate that the amount of contaminants removed from the diluate stream equals the amount of contaminants accumulated in the concentrate stream, for the case where $Q^c = Q^d$.

$$Q^{Fed}C^{Fed} = Q^{Ped}C^{Ped} + Q^{Red}C^{Red} \tag{12.A.15}$$

$$Q^{r}C^{Ped} + Q^{c}C^{c} = Q^{cr}C^{cr} + Q^{Red}C^{Red} \tag{12.A.16}$$

$$Q^{m}C^{Fed} + Q^{cr}C^{cr} = Q^{c}C^{fc} \tag{12.A.17}$$

$$Q^{d}C^{Fed} + Q^{c}C^{fc} = Q^{d}C^{Ped} + Q^{c}C^{c} \tag{12.A.18}$$

The liquid recovery rate, r, is the amount of product water that is directed to the recycle concentrate stream in order to reduce its salinity and is shown in constraint (12.A.19). It is required in order to avoid water transport due to osmosis across the membranes.

$$r = \frac{Q^{Ped}}{Q^{d}} \tag{12.A.19}$$

The purge concentrate is replaced by an amount of the less concentrated feed and is represented by the mixing ratio, m, in constraint (12.A.20).

$$m = \frac{Q^{d}}{Q^{Fed}} \tag{12.A.20}$$

Based on the formulation and physical design of the ED unit, it is assumed that both the diluate and concentrate maintain a constant flowrate. This is done in order to avoid strain on the membrane material.

The cost function of the ED regeneration unit, which is expressed as the TAC_e, comprises of the capital and operational costs. The capital cost consists of the costs associated with the purchase of pumping equipment and the establishment of the plant. The operating cost is the costs incurred due to day-to-day running of the plant over a specified time. It is associated with the electrical energy costs due to pumping of feed water into the system and desalination. Both costs are incorporated into a single function called TAC_e, which is synthesized to obtain optimal design parameters as shown in constraint (12.A.21). Here K^{mb} is the capital cost of membrane, $t^{\max}$ is the maximum equipment life, AOT is the annual operating time of the plant, and K^{el} represents the cost of the electrical power.

$$\mathrm{TAC}_e = \frac{K^{mb}A}{t^{\max}} + \mathrm{AOTK}^{el}Q^{Ped}[E^{Pump} + E^{spec}] \tag{12.A.21}$$

12.A.2 Reverse Osmosis Membrane Regenerator Formulation

Figure 12.A.2 is a schematic representation of a RO membrane regeneration unit based on the works of El-Halwagi [6] and Khor et al. [2]. Detailed synthesis of the membrane regeneration unit is conducted to obtain optimal design parameters based on number of membrane modules, feed flowrates, and energy required for pumping. In industrial applications, reverse-osmosis networks (RONs) are used for the separation processes. An RON comprises of multiple RO modules, pumps, and turbines to form a system. The aim of this section is to formulate a mathematical model of a hollow-fiber RON [6]. The formulated model is synthesized based on the pumps, reverse-osmosis modules, and energy recovery turbines from the high pressure reject side.

In modeling an RON there are two main considerations, such as membrane transport equations and the hydrodynamic modeling of the RON modules. The membrane equations have to do with water permeation and solute flux taking place at the membrane surface. Hydrodynamic modeling deals with microscopic transport of various species along with the momentum and energy associated with it. The separation efficiency of an RON is dependent on the influent solute concentration, pressure, and water flowrate.

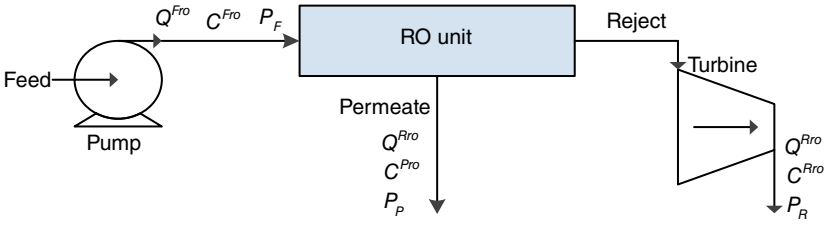

Figure 12.A.2 Schematic of a reverse osmosis unit.

12.A.2.1 Membrane Transport Equations

Transport equations are used to predict the flux of water and solute based on the work of Dandavati et al. [15] and Evangelista [16]. Both the water and solute flux equations are valid for all RO module configurations. The solute flux, N_{solute}, relates to the transport of solute by diffusion due to the transport of water across the membrane phase and is given by constraint (12.A.22), where $\left[\frac{D_{2M}}{K\delta}\right]$ the solute is flux constant and C_s is the average concentration on the feed side of the RO unit.

$$N_{solute} = \left[\frac{D_{2M}}{K\delta}\right] C_S \tag{12.A.22}$$

Water flux relates to rate at which water permeates through RO unit. It is directly related to the temperature and pressure as well as RO module dimensions and water properties as shown in constraint (12.A.23). Here A_P is the water permeability constant, ΔP is the pressure drop across the unit, π_F is the osmotic pressure on the feed side of the RO unit, and γ is a constant that represents the design features of the hollow fiber module.

$$N_{water} = A_P \left[\Delta P - \frac{\pi_F}{C^{Fro}} C_S\right] \gamma \tag{12.A.23}$$

12.A.2.2 Average Shell Side Concentration

The average concentration on the shell side of the membrane is the average of the feed and rejects concentration as represented in constraint (12.A.24).

$$C_S = \frac{C^{Fro} + C^{Rro}}{2} \tag{12.A.24}$$

12.A.2.3 Trans-Membrane Pressure

The pressure drop across the membrane is the difference in pressure between the feed side and the permeate side of the membrane unit. It is the driving force for membrane performance and product water production. The pressure difference across an RON increases with increasing flux across the membrane, which is represented by constraint (12.A.25). Here P_F, P_R, and P_P are the feed, retentate, and permeate pressures of the RO unit respectively.

$$\Delta P = \frac{(P_F + P_R)}{2} - P_P \tag{12.A.25}$$

The pressure on the shell side, ΔP_{shell}, of the RO hollow-fiber module is represented by the pressure difference between the feed side and the reject side of the RO unit.

$$\Delta P_{shell} = P_F - P_R \tag{12.A.26}$$

Substituting the shell side pressure drop into the pressure drop across the RO unit gives rise to the feed pressure applied to the RON.

$$P_F = \Delta P + \left[\frac{\Delta P_{shell}}{2} + P_P\right] \tag{12.A.27}$$

12.A.2.4 Power Across the RON

The power of turbine and pump across RON is represented by constraints (12.A.28) and (12.A.29), respectively. Here P_{atm} is the atmospheric pressure and ρ is the density of water.

$$\text{Pow}_{(turb)} = \frac{Q^{Rro}[P_R - P_{atm}]}{\rho} \tag{12.A.28}$$

$$\text{Pow}_{(pump)} = \frac{Q^{Fro}[P_F - P_{atm}]}{\rho} \tag{12.A.29}$$

12.A.2.5 Average Concentration on the Feed Side

The osmotic pressure on the feed side of RON is a function of the contaminant concentration. In this formulation the osmotic pressure on the permeate side is neglected since the concentration is assumed to be significantly lower. The osmotic pressure on the retentate side $\Delta\pi_{RO}$ is adopted from the formulation of Saif et al. [17] and is shown in constraint (12.A.30).

$$\Delta\pi_{ro} = \text{OS}C^{Fro} \tag{12.A.30}$$

The osmotic pressure coefficient,OS, ranges between osmotic pressure on the feed side and average solute concentration on the feed side. The average concentration on the feed side is reformulated based on the concentration on the permeate side as adopted from Khor et al. [2]. The pressures across the membrane material and membrane area are important parameters that determine the performance of the RON. Here S_C is the solute permeability coefficient.

$$C^{Fro} = \frac{C^{Pro}A_P\gamma[\Delta P - \Delta\pi_{ro}]}{S_C} \tag{12.A.31}$$

12.A.2.6 Permeate Flowrate

The permeate flowrate, described by Saif et al. [17], is related to the pressure drop across the membrane, the osmotic pressure on the reject side, and the number of modules present in the RON according to constraint (12.A.32). The parameter S_m is the membrane area per module.

$$Q^{Pro} = N_m S_m A_P \gamma[\Delta P - \Delta\pi_{ro}] \tag{12.A.32}$$

Constraint (12.A.32) is then reformulated based on the average solute concentration on the feed side to cater for the number of RO modules in the RON to yield constraint (12.A.33).

$$N_m = \frac{Q^{Pro}}{A_P S_m \gamma[\Delta P - \text{OS}C^{Fro}]} \tag{12.A.33}$$

The cost function of the RON comprises of variables and physical parameters of the RO membrane unit. It consists of the annualized fixed capital cost of turbine, pump, membrane modules, and operating costs for pump and pretreatment of chemicals. The operating revenue through energy recovery by the turbine at the

retentate side is also incorporated to supplement the cost of energy usage.

$$\begin{aligned}\mathrm{TAC}_r =& K_{mod}N_m + K_{pump}(\mathrm{Pow}_{(pump)})^{0.65} + K_{turb}(\mathrm{Pow}_{(turb)})^{0.43} \\ &+ \frac{\mathrm{Pow}_{(pump)}K_{elec}\mathrm{AOT}}{\eta_{pump}} + Q^{Fro}K_{chemicals}\mathrm{AOT} \\ &- \mathrm{Pow}_{(turb)}\eta_{turb}K_{chemicals}\mathrm{AOT} \end{aligned} \quad (12.A.34)$$

Nomenclature

Sets

J	$\{j \mid j = \text{water source}\}$
I	$\{i \mid i = \text{water sink}\}$
CO	$\{co \mid co = \text{contaminant}\}$

Parameters

AOT	annual operating time
K_{waste}	unit cost for waste treatment
K_{water}	unit cost for freshwater
p, q	parameter for carbon steel piping
RR_{ed}	removal ratio for ED unit
RR_{ro}	removal ratio for RO unit
LR_{ed}	liquid phase recovery for ED unit
LR_{ro}	liquid phase recovery for RO unit
Q_j	flowrate from source j
$C_{j,co}$	contaminant co from source j
Q_i^z	flowrate of sink i
$C_{i,co}^U$	maximum allowable contaminant concentration into sink i
Q^L	Minimum flowrate for piping interconnection between source and sink
Q^U	maximum flowrate for piping interconnection between source and sink
v	velocity of fluid in pipes
$D_{j,i}$	Manhattan distance from source j to sink i
D_j^{ro}	Manhattan distance from source j to RO unit
D_j^{ed}	Manhattan distance from source j to ED unit
D_i^X	Manhattan distance from permeate of ED unit to sink i
D^X	Manhattan distance from permeate stream of ED unit into ED unit

Continuous Variables

FW	freshwater flowrate
WW	wastewater flowrate
$Q_{j,i}$	flowrate from source j to sink i
Q_j^{ro}	flowrate from source j to RO unit

Q_j^{ed} flowrate from source *j* to ED unit
Q^{Fed} flowrate into the ED unit
Q^{Fro} flowrate into the RO unit
Q^{Ped} permeate flowrate of ED unit
$Q^{\mathrm{R}ed}$ reject flowrate of ED unit
$Q^{\mathrm{P}ro}$ permeate flowrate of RO unit
Q^{Rro} reject flowrate of RO unit
Q_i^{ds} flowrate from permeate stream of ED into sink *i*
Q^{de} flowrate from permeate stream of ED unit into ED unit
Q^{dr} flowrate from permeate stream of ED unit into RO unit
Q_i^{es} flowrate from reject stream of ED unit into sink *i*
Q^{ee} flowrate from reject stream of ED unit into ED unit
Q^{er} flowrate from reject stream of ED unit into RO unit
Q_i^{fs} flowrate from permeate stream of RO unit into sink *i*
Q^{fe} flowrate from permeate stream of RO unit into ED unit
Q^{fr} flowrate from permeate stream of RO unit into RO unit
Q_i^{gs} flowrate from reject stream of RO unit into sink *i*
Q^{gr} flowrate from reject stream of RO unit into RO unit
C_{co}^{Fed} concentration of contaminant *co* into ED unit
C_{co}^{Fro} concentration of contaminant *co* into RO unit
C_{co}^{Pro} concentration of contaminant *co* in the permeate stream of RO unit
C_{co}^{Rro} concentration of contaminant *co* in the reject stream of RO unit
C_{co}^{Red} concentration of contaminant in the reject stream of ED unit
C_{co}^{Ur} maximum allowable contaminant into RO unit
C_{co}^{Ue} maximum allowable contaminant into ED unit

Integer Variables

N_m number of reverse osmosis modules
N number of electrodialysis cell pairs

Binary Variables

$$y_{j,i} = \begin{cases} 1 \leftarrow \text{Existence of piping interconnection between source and sink} \\ 0 \leftarrow \text{Otherwise} \end{cases}$$

$$y_j^{ro} = \begin{cases} 1 \leftarrow \text{Existence of piping interconnection between source and RO unit} \\ 0 \leftarrow \text{Otherwise} \end{cases}$$

$$y_j^{ed} = \begin{cases} 1 \leftarrow \text{Existence of piping interconnection between source and ED unit} \\ 0 \leftarrow \text{Otherwise} \end{cases}$$

$$y_i^{X} = \begin{cases} 1 \leftarrow \text{Existence of piping interconnection between permeate of ED unit and ED unit} \\ 0 \leftarrow \text{Otherwise} \end{cases}$$

$$y^{X} = \begin{cases} 1 \leftarrow \text{Existence of piping interconnection between permeate of RO unit and ED unit} \\ 0 \leftarrow \text{Otherwise} \end{cases}$$

References

1 Mallevialle, J., Odendaal, P.E., and Wiesner, M.R. (1996). *Water Treatment Membrane Processes*. New York, NY: Lyonnaise des Eaux (LdE).

2 Khor, C.S., Foo, D.C., El-Halwagi, M.M. et al. (2011). A superstructure optimization approach for membrane separation-based water regeneration network synthesis with detailed nonlinear mechanistic reverse osmosis model. *Industrial and Engineering Chemistry Research* 11 (50): 13444–13456.

3 Yang, L., Salcedo-Diaz, R., and Grossmann, E.I. (2014). Water network optimization with wastewater regeneration models. *Industrial and Engineering Chemistry Research* 2014 (53): 17680–17695.

4 Rangaiah, G. and Wei, T. (eds.) (2010). *Advances in Process Systems Engineering: Stochastic Global Optimization, Techniques and Applications in Chemical Engineering*, vol. 2. Toh Tuck, Singapore: World Scientific Publishing Co. Pte. Ltd.

5 Buabeng-Baidoo, E. and Majozi, T. (2015). Effective synthesis and optimisation framework for integrated water and membrane networks: a focus on reverse osmosis membranes. *Industrial and Engineering Chemistry Research* 2016 (54): 9394–9406.

6 El-Halwagi, M.M. (1992). Synthesis of reverse-osmosis networks for waste reduction. *AIChE Journal* 38 (8): 1185–1198.

7 Mafukidze, N.Y. and Majozi, T. (2015). Synthesis and optimisation of an integrated water and membrane network framework with multiple electrodialysis regenerators. *Computers and Chemical Engineering* 85 (2016): 151–161.

8 Abass, M. and Majozi, T. (2016). Optimization of integrated water and multiregenerator membrane systems. *Industrial and Engineering Chemistry Research* 55: 1995–2007.
9 Oke, D., Majozi, T., Mukherjee, R. et al. (2018). Simultaneous energy and water optimization in shale exploration. *Processes* 6: 86.
10 Oke, D., Mukherjee, R., Sengupta, D. et al. (2019). Optimization of water-energy nexus in shale gas exploration: consideration of production to transmission. *Energy* 183: 651–669.
11 Oke, D., Mukherjee, R., Sengupta, D. et al. (2019). Using ultrafiltration for flowback water management in shale gas exploration: multicontaminant consideration. *Computer Aided Chemical Engineering* 47: 347–352.
12 Tan, R.R., Ng, D.K.S., Foo, D.C.Y., and Aviso, K.B. (2009). A superstructure model for the synthesis of single-contaminant water networks with partitioning regenerators. *Process Safety and Environmental Protection* 87 (9): 197–205.
13 Tsiakis, P. and Papageorgiou, L.G. (2005). Optimal design of an electrodialysis brackish water desalination plant. *Desalination* 173 (2): 173–186.
14 Lee, H.-J., Sarfert, F., Strathmann, H., and Moon, S.-H. (2002). Designing of an electrodialysis desalination plant. *Desalination* 142 (3): 267–286.
15 Dandavati, M.S., Doshi, M.R., and Gill, W.N. (1975). Hollow fiber reverse osmosis: experiments and analysis of radial flow systems. *Chemical Engineering Science* 30 (8): 877–886.
16 Evangelista, F. (1986). Improved graphical-analysis method for the design of reverse-osmosis plants. *Industrial Engineering Chemical Process* 25 (86): 366–375.
17 Saif, Y., Elkamel, A., and Pritzker, M. (2008). Optimal design of reverse-osmosis networks for wastewater treatment. *Chemical Engineering and Processing: Process Intensification* 47 (12): 2163–2174.

13

Optimization Strategies for Integrating and Intensifying Housing Complexes

Jesús M. Núñez-López[1] *and José M. Ponce-Ortega*[1]

[1] *Universidad Michoacana de San Nicolás de Hidalgo, Chemical Engineering Department, Av. Francisco J. Múgica, SN, Ciudad Universitaria, Boulding V1, Morelia, Michoacán 58060, México*

13.1 Introduction

The term "*process integration*" was introduced in the 1970s as a response to the oil crisis, caused by the shortage of this resource, which was reflected in a drastic increase in its price. Heat integration and energy efficiency were the first developments, such as the design of heat exchanger networks (HENs) [1, 2], combined heat and power (CHP) systems [3, 4], and refrigeration [5, 6]. Process integration is a holistic approach to process design, retrofitting, and operation, which emphasizes the unity of the process [7]. The main advantage of process integration is that it considers a whole system to improve the design and the operation, unlike an analytical approach that optimizes the process units separately.

Process integration can be mainly classified in two ways: mass and energy integration. Energy integration is a systematic methodology, which focuses primarily on the use of energy within the process where it is used for the optimization of heat and energy recovery systems. Likewise, mass integration is a systematic methodology; however, it focuses on the mass global flow within the process, which is used to identify redemption objectives and to optimize generation and routing throughout the process. Then, a new classification of process integration was proposed, where property integration was added to mass and energy integration. Property integration concept refers to a functionality-based holistic approach for the allocation and manipulation of streams and processing units, which is based on functionality tracking adjustment, and assignment throughout the process. Figure 13.1 shows some of the main uses for process integration and its classification.

Process integration involves the following activities:

1) *Task identification*: During the synthesis, the objective must be clearly established and described as a practical task. The actionable task should be defined in the way so to capture the essence of the original goal.
2) *Targeting*: Targeting is one of the strongest contributions of process integration. The concept of targeting refers to identifying the redirection reference

Process Intensification and Integration for Sustainable Design, First Edition.
Edited by Dominic C. Y. Foo and Mahmoud M. El-Halwagi.
© 2021 WILEY-VCH GmbH. Published 2021 by WILEY-VCH GmbH.

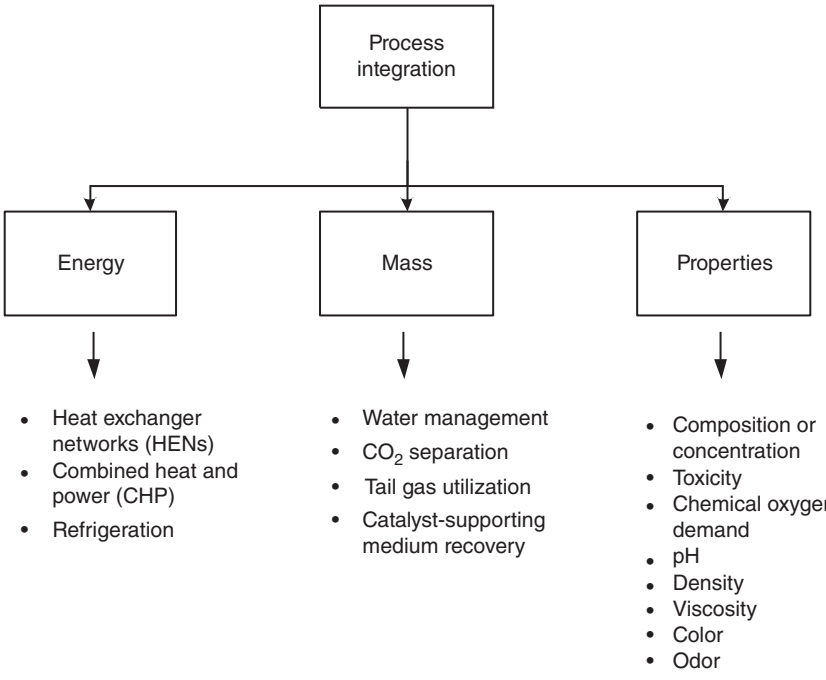

Figure 13.1 Process integration and its classification.

points before making a detailed design of the system. That is, we can find an answer without having to specify how to achieve it.

3) Due to the large number of possible solutions to achieve an objective, a framework that is rich enough to integrate all the configurations of interest should be used.
4) *Selection of alternative(s) (synthesis)*: Once all feasible alternatives are integrated, the optimal solution must be obtained between these alternatives.
5) *Analysis of selected alternative(s)*: Process analysis techniques can be used to evaluate the chosen solution. This may include performance prediction, a techno-economic assessment, a safety review, or an environmental impact assessment.

The fundamentals and applications of energy, mass, and property integration have been reviewed in literature [8–10].

On the other hand, just as the term process integration was introduced during the 1970s, the term process intensification was also introduced; however it was not until the 1990s that a certain interest began. In 1995 was the First International Conference on Process Intensification in the Chemical Industry, where Ramshaw, one of the pioneers in the field, defined process intensification as a strategy for making dramatic reduction in the size of a chemical plant to reach a given production objective. These reductions can come from shrinking the size of individual pieces of equipment and from cutting the number of unit operations or apparatuses involved; this definition is quite narrow, describing process

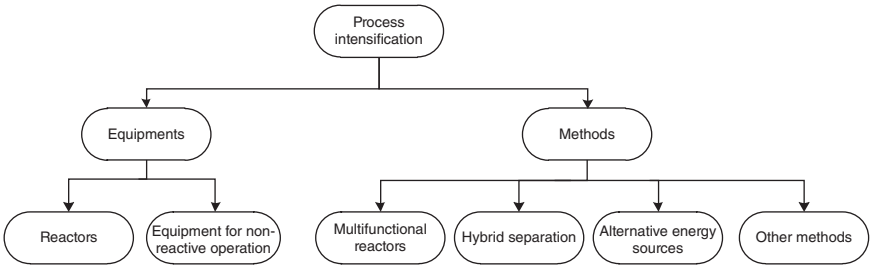

Figure 13.2 Process intensification classification.

intensification exclusively in terms of the reduction in plant or equipment size [11, 12].

Process intensification consists of developing new techniques and equipment that, compared with the existing ones, must present improvements in manufacturing and processing, which should lead to a decrease in the size ratio of the equipment and the production capacity of this and/or lower energy consumption and at a lower cost.

Otherwise, "*process intensification*" was defined as any chemical engineering development that leads to a substantially smaller, cleaner, and more energy efficient technology [13].

The whole field generally can be divided into two areas (see Figure 13.2): equipment and methods.

Process-intensifying equipments: Such as novel reactors, and intensive mixing, heat transfer and mass transfer devices; and

Process-intensifying methods: Such as new or hybrid separations, integration of reaction and separation, heat exchange, or phase transition, technologies using alternative energy sources, and new process control methods.

A promising intensified process should outperform the existing designs in at least one of the following aspects:

1) *Equipment number and size*: One of the main results that seek process intensification is the reduction in the number and size of equipment. There are several works that address these aspects.
2) *Energy consumption and cost*: Economics is often the main driver for widespread commercialization of new technologies. At the flowsheet level, intensification among various parts of a chemical process may require significant investment for mass and energy integration.

In 2011, a new classification of process integration was given [13]. Process intensification was classified in two main categories: unit intensification and plant intensification, each of the categories has different classes, which are shown in Figure 13.3.

It is worth mentioning that the classes presented in the new classification of the process intensification can be used to intensify new processes or existing ones. The goal of unit intensification is to intensify a single unit isolated from the rest of the process in order to minimize the size of this unit for a certain

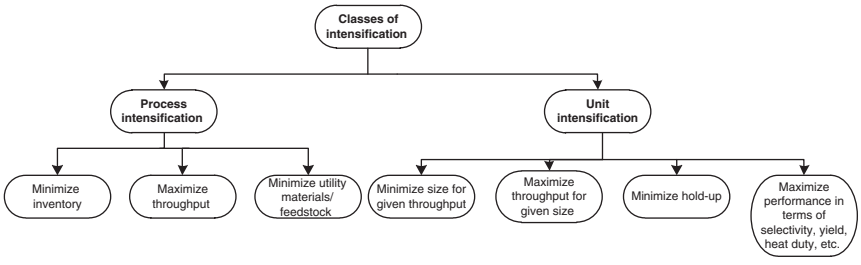

Figure 13.3 Process intensification classification. Source: Ponce-Ortega et al. 2012 [13]. Reproduced with permission of Elsevier.

performance or maximize the performance of the unit for a specified size. Plant intensification refers to maximizing the performance of a complete process by minimizing the inventory of the entire process or minimizing the raw material of the process. In this case the units to be intensified are not prespecified and can be intensified more than one unit at a time. In both industrial processes and housing complexes, we want to fully meet their needs, in the case of industry considering adequate sources of energy and heat for processes is essential, and example are heat exchange networks and cogeneration units. For housing complexes, the main resources to be satisfied are water, heat, and energy, the problem to be treated is to minimize the consumption of fresh resources and reducing the generated wastes by the inhabitants. An option for this is to treat the solid wastes and give it a use as fuel for the used process units. Another option is reuse wastewater and use it as irrigation in gardens. In general, process intensification at industrial level or in housing complexes is quite similar. The main difference is the considered resources and involved technologies.

In this chapter, a case study for a housing complex is presented to show the applicability of process integration and intensification, in Figure 13.4 a scheme of a house complex before and after the integration is shown, notice that an integration approach can reduce the fresh resources used to satisfy the needs of the inhabitants and to reduce the generated wastes in the complex, while process intensification helps to reduce the size and number of the process unit required in the proposed system.

13.2 Methods

An optimization model formulation for determining the optimal design of an integrated residential complex is presented. In this section only the objective functions are presented, while the constraints for the model are presented in the work by Núñez-López et al. [14]. There are considered three aspects in the integration of the complex, economic, environment, and social. For the economic objective, the total annual cost (TAC) and the sustainability return of investment are considered, for environmental aspects the fresh water consumption, the GHGE emissions, and the environmental impact are the objectives taken into account, while for social the process route healthiness index (PRHI) was used to

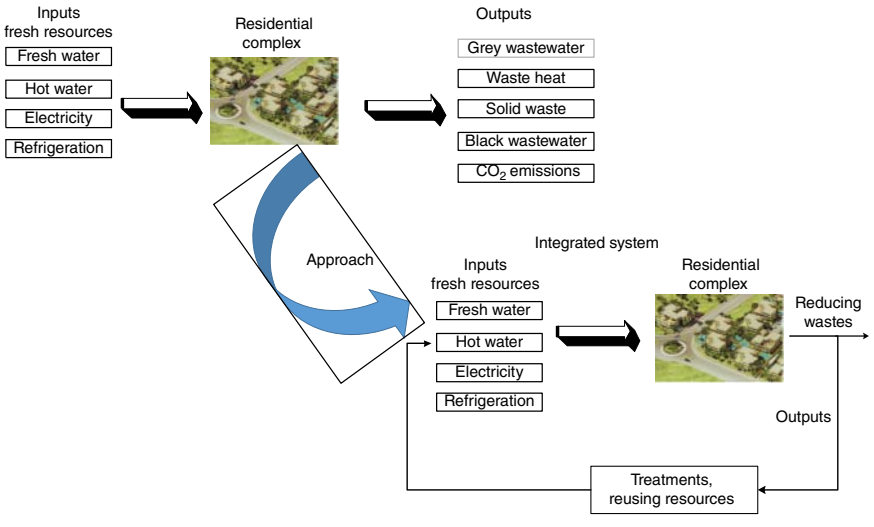

Figure 13.4 Proposed integration approach for a housing complex.

evaluate the occupational health (OH) of the inhabitants of the residential complex. The objective functions are described as follows.

13.2.1 Total Annual Cost for the Integrated System

The TAC is equal to the sum of the total operating cost (TotOpCost) and the total capital cost (TotCapCost) minus the total sales of the system (TotSales):

$$\text{TAC} = \text{TotOpCost} + \text{TotCapCost} - \text{TotSales} \tag{13.1}$$

The total operating cost is determinate by the cost of fresh resources, such as water, natural gas, and electricity for the right functionality of the units, while the total capital cost is calculated by the sum of the individual capital cost for the units used in the process. The individual capital cost for each unit is equal to the variable cost and for the fixed cost. There is a possibility that unit processes have greater capacities than necessary in certain periods of time, so the generation of resources may be greater than required, this way the sale of resources to an external company is also an option.

13.2.2 Fresh Water Consumption

The fresh water consumption (FFwTot) for the integrated system is equal to the sum of the fresh water consumed in each time period:

$$\text{FFwTot} = \sum_{t} \text{FFw}_{t} \tag{13.2}$$

13.2.3 GHGE Emissions

The greenhouse gas emissions that are discharged to the environment (GDischargeTotal) are equal to the emissions produced by the internal combustion engine (ICE; $\mathrm{Fg}_t^{Ice\text{-}Discharge}$) plus the emissions generates by the boiler ($\mathrm{Fg}_t^{Boiler\text{-}Discharge}$) and the gasification process ($\mathrm{Fg}_t^{Gasification\text{-}Discharge}$), respectively, as follows:

$$\mathrm{GDischargeTotal} = \sum_t \mathrm{Fg}_t^{Ice\text{-}Discharge} + \sum_t \mathrm{Fg}_t^{Boiler\text{-}Discharge} + \sum_t \mathrm{Fg}_t^{Gasification\text{-}Discharge} \tag{13.3}$$

13.2.4 Environmental Impact

The environmental impact (EnvImp) is quantified through the life cycle assessment (LCA) using the Eco-indicator 99 approach with the next equations:

$$\mathrm{EnvImp} = \mathrm{EI}^{HH} + \mathrm{EI}^{EQ} + \mathrm{EI}^{DR} \tag{13.4}$$

where EI^{HH} represents the human health damage, EI^{EQ} is the environmental impact that occurs in the ecosystem quality, and EI^{DR} is the damage to the resources, which are calculated as follows.

$$\begin{aligned}
\mathrm{EI}^{HH} =& \mathrm{EI}^{algae-HH}\mathrm{CTS}^{algae}\mathrm{Cap}^{algae} + \mathrm{EI}^{ARC\text{-}HH}\mathrm{CTS}^{ARC}\mathrm{Cap}^{ARC} + \mathrm{EI}^{boiler\text{-}HH}\mathrm{CTS}^{boiler}\mathrm{Cap}^{boiler} \\
&+ \mathrm{EI}^{WW\text{-}HH}\mathrm{CTS}^{WW}\mathrm{Cap}^{WW} + \mathrm{EI}^{gasification\text{-}HH}\mathrm{CTS}^{gasification}\mathrm{Cap}^{gasification} \\
&+ \mathrm{EI}^{GW\text{-}HH}\mathrm{CTS}^{GW}\mathrm{Cap}^{GW} \\
&+ \mathrm{EI}^{ICE\text{-}HH}\mathrm{CTS}^{ICE}\mathrm{Cap}^{ICE} + \mathrm{EI}^{NGT\text{-}HH}\mathrm{CTS}^{NGT}\mathrm{Cap}^{NGT} + \mathrm{EI}^{RWSS\text{-}HH}\mathrm{CTS}^{RWSS}\mathrm{Cap}^{RWSS} \\
&+ \mathrm{EI}^{FWSS\text{-}HH}\mathrm{CTS}^{FWSS}\mathrm{Cap}^{FWSS} + \mathrm{EI}^{biodisel\text{-}HH}\sum_t F_t^{biodisel} + \mathrm{EI}^{BWW\text{-}HH}\sum_t F_t^{treated\text{-}ww} \\
&+ \mathrm{EI}^{\mathrm{CO}_2\text{-}HH}\sum_t \left(G_t^{ICE} + G_t^{boiler} + G_t^{gasification}\right) \\
&+ \mathrm{EI}^{e\text{-}HH}\sum_t \left(E_t^{ICE} + e_t^{purchased\text{-}algae} + e_t^{purchased} + e_t^{purchased\text{-}GWT} + e_t^{purchased\text{-}WWT}\right) \\
&+ \mathrm{EI}^{water\text{-}HH}\sum_t F_t^{FW} + \mathrm{EI}^{GWW\text{-}HH}\sum_t F_t^{reclaimed\text{-}GW} \\
&+ \mathrm{EI}^{HW\text{-}HH}\sum_t \left(H_t^{ICE} + H_t^{HW\text{-}boiler} + h_t^{purchase\text{-}ARC}\right) \\
&+ \mathrm{EI}^{NG\text{-}HH}\sum_t \left(F_t^{NG\text{-}ICE} + F_t^{NG\text{-}boiler} + F_t^{NG\text{-}GWT} + F_t^{NG\text{-}WW}\right) \\
&+ \mathrm{EI}^{ref\text{-}HH}\sum_t \left(R_t^{ARC} + r_t^{purchased\text{-}residential}\right) \\
&+ \mathrm{EI}^{RW\text{-}HH}\sum_t F_t^{RW} + \mathrm{EI}^{SW\text{-}HH}\sum_t F_t^{solidwaste}
\end{aligned} \tag{13.5}$$

where CTS represents the energy needed to produce the construction material for each unit, and Cap corresponds to the capacities from each of the units. *G* represents the rates of CO_2 emissions that are generated in the ICE, the boiler, and the gasification process. *e* represents the electricity, *F* and *H* are the flows of fresh and hot water, respectively, and *r* refers to the refrigeration flows. It is the

same for Eqs. (13.6, 13.7).

$$\begin{aligned}
\mathrm{EI}^{EQ} =& \mathrm{EI}^{algae\text{-}EQ}\mathrm{CTS}^{algae}\mathrm{Cap}^{algae} + \mathrm{EI}^{ARC\text{-}EQ}\mathrm{CTS}^{ARC}\mathrm{Cap}^{ARC} + \mathrm{EI}^{boiler\text{-}EQ}\mathrm{CTS}^{boiler}\mathrm{Cap}^{boiler} \\
&+\mathrm{EI}^{WW\text{-}EQ}\mathrm{CTS}^{WW}\mathrm{Cap}^{WW} + \mathrm{EI}^{gasification\text{-}EQ}\mathrm{CTS}^{gasification}\mathrm{Cap}^{gasification} \\
&+\mathrm{EI}^{GW\text{-}EQ}\mathrm{CTS}^{GW}\mathrm{Cap}^{GW} \\
&+\mathrm{EI}^{ICE\text{-}EQ}\mathrm{CTS}^{ICE}\mathrm{Cap}^{ICE} + \mathrm{EI}^{NGT\text{-}EQ}\mathrm{CTS}^{NGT}\mathrm{Cap}^{NGT} + \mathrm{EI}^{RWSS\text{-}EQ}\mathrm{CTS}^{RWSS}\mathrm{Cap}^{RWSS} \\
&+\mathrm{EI}^{FWSS\text{-}EQ}\mathrm{CTS}^{FWSS}\mathrm{Cap}^{FWSS} + \mathrm{EI}^{biodisel\text{-}EQ}\sum_t F_t^{biodisel} + \mathrm{EI}^{BWW\text{-}EQ}\sum_t F_t^{treated\text{-}ww} \\
&+\mathrm{EI}^{\mathrm{CO}_2\text{-}EQ}\sum_t \left(G_t^{ICE} + G_t^{boiler} + G_t^{gasification}\right) \\
&+\mathrm{EI}^{e\text{-}EQ}\sum_t \left(E_t^{ICE} + e_t^{purchased\text{-}algae} + e_t^{purchased} + e_t^{purchased\text{-}GWT} + e_t^{purchased\text{-}WWT}\right) \\
&+\mathrm{EI}^{water\text{-}EQ}\sum_t F_t^{FW} \\
&+\mathrm{EI}^{GWW\text{-}EQ}\sum_t F_t^{reclaimed\text{-}GW} + \mathrm{EI}^{HW\text{-}EQ}\sum_t \left(H_t^{ICE} + H_t^{HW\text{-}boiler} + h_t^{purchase\text{-}ARC}\right) \\
&+\mathrm{EI}^{NG\text{-}HH}\left(\sum_t F_t^{NG\text{-}ICE} + F_t^{NG\text{-}boiler} + F_t^{NG\text{-}GWT} + F_t^{NG\text{-}WW}\right) \\
&+\mathrm{EI}^{ref\text{-}HH}\sum_t \left(R_t^{ARC} + r_t^{purchased\text{-}residential}\right) \\
&+\mathrm{EI}^{RW\text{-}EQ}\sum_t F_t^{RW} + \mathrm{EI}^{SW-EQ}\sum_t F_t^{solidwaste}
\end{aligned} \tag{13.6}$$

$$\begin{aligned}
\mathrm{EI}^{DR} =& \mathrm{EI}^{algae\text{-}DR}\mathrm{CTS}^{algae}\mathrm{Cap}^{algae} + \mathrm{EI}^{ARC\text{-}DR}\mathrm{CTS}^{ARC}\mathrm{Cap}^{ARC} + \mathrm{EI}^{boiler\text{-}DR}\mathrm{CTS}^{boiler}\mathrm{Cap}^{boiler} \\
&+\mathrm{EI}^{WW\text{-}DR}\mathrm{CTS}^{WW}\mathrm{Cap}^{WW} + \mathrm{EI}^{gasification\text{-}DR}\mathrm{CTS}^{gasification}\mathrm{Cap}^{gasification} \\
&+\mathrm{EI}^{GW\text{-}DR}\mathrm{CTS}^{GW}\mathrm{Cap}^{GW} \\
&+\mathrm{EI}^{ICE\text{-}DR}\mathrm{CTS}^{ICE}\mathrm{Cap}^{ICE} + \mathrm{EI}^{NGT\text{-}DR}\mathrm{CTS}^{NGT}\mathrm{Cap}^{NGT} + \mathrm{EI}^{RWSS\text{-}DR}\mathrm{CTS}^{RWSS}\mathrm{Cap}^{RWSS} \\
&+\mathrm{EI}^{FWSS\text{-}DR}\mathrm{CTS}^{FWSS}\mathrm{Cap}^{FWSS} + \mathrm{EI}^{biodisel\text{-}DR}\sum_t F_t^{biodisel} + \mathrm{EI}^{BWW\text{-}DR}\sum_t F_t^{treated\text{-}ww} \\
&+\mathrm{EI}^{\mathrm{CO}_2\text{-}DR}\sum_t \left(G_t^{ICE} + G_t^{boiler} + G_t^{gasification}\right) \\
&+\mathrm{EI}^{e\text{-}DR}\sum_t \left(E_t^{ICE} + e_t^{purchased\text{-}algae} + e_t^{purchased} + e_t^{purchased\text{-}GWT} + e_t^{purchased\text{-}WWT}\right) \\
&+\mathrm{EI}^{water\text{-}DR}\sum_t F_t^{FW} \\
&+\mathrm{EI}^{GWW\text{-}DR}\sum_t F_t^{reclaimed\text{-}GW} + \mathrm{EI}^{HW\text{-}DR}\sum_t (H_t^{ICE} + H_t^{HW\text{-}boiler} + h_t^{purchase\text{-}ARC}) \\
&+\mathrm{EI}^{NG\text{-}HH}\sum_t (F_t^{NG\text{-}ICE} + F_t^{NG\text{-}boiler} + F_t^{NG\text{-}GWT} + F_t^{NG\text{-}WW}) \\
&+\mathrm{EI}^{ref\text{-}HH}\sum_t (R_t^{ARC} + r_t^{purchased\text{-}residential}) \\
&+\mathrm{EI}^{RW\text{-}DR}\sum_t F_t^{RW} + \mathrm{EI}^{SW\text{-}DR}\sum_t F_t^{solidwaste}
\end{aligned} \tag{13.7}$$

Table 13.1 Eco-points for energy and resources for the proposed system [15].

Points			
Energy and resources	**Ecosystem quality**	**Human health**	**Damage resources**
Biofuel (kWh)	0.000 025	0.000 360	0.000 012
CO_2 (ton)	0.000 027	0.000 337	0.001 870
Electricity (kWh)	0.010 885	0.001 047	0.039 438
Gray water (m^3)	0.003 000	0.004 500	0.002 500
Hot water (m^3)	0.002 927	0.001 849	0.001 212
Natural gas (kWh)	0.005 384	0.000 616	0.024 764
Refrigeration (kWh)	0.001 283	0.000 808	0.004 003
Rainwater (m^3)	0.000 160	0.000 001	0.000 016
Solid wastes (kg)	0.020 200	0.008 807	0.000 756
Water (m^3)	0.013 854	0.006 497	0.011 885
Black water (m^3)	0.024 580	0.010 580	0.017 050

Table 13.2 Eco-points for the used material in the technologies production.

Points (pts/kg of material)			
Technology	**Ecosystem quality**	**Human health**	**Damage resources**
Algae system	3.00E−04	4.50E−04	2.50E−04
Absorption refrigeration cycle (ARC)	2.74E−10	2.70E−11	2.70E−11
Boiler	1.28E−03	8.08E−04	4.00E−03
Black water treatment	1.50E−04	1.00E−05	1.00E−05
Water storage tank	3.00E−03	4.50E−03	2.50E−03
Gasifier	1.74E−06	1.74E−06	1.74E−06
Gray water treatment	1.50E−04	1.00E−05	1.00E−05
ICE	2.74E−10	1.40E−10	2.50E−11
Natural gas treatment	3.00E−05	4.50E−04	2.50E−05
Rainwater collecting system	1.60E−04	1.00E−06	1.60E−06

where EI represents eco-points for each one of the fresh resources and the needed material for each of the process units. The eco-points for the fresh resources and for the process units are shown in Tables 13.1 and 13.2, respectively. Eco-points were obtained from the database SimaPro, a software used to quantify environmental impacts from different processes.

13.2.5 Sustainability Return of Investment

To evaluate the sustainability of a process, El-Halwagi [16] proposed the sustainability return of investment (SWSROIM), in this work it is determined as follows:

$$\text{SWSROIM} = \frac{\text{TAC}\left[1 + \sum_{i}^{N} w_i \left(\frac{\text{EnvImp}}{\text{Eco-indicator}^{ref}}\right)\right]}{\text{TAC}^{ref}} \tag{13.8}$$

where $\text{Eco-indicator}^{ref}$ and TAC^{ref} are the eco-indicator and the TAC, respectively, for the no-integrated system. w_i is the weighting factor to prioritize the associated units with the process.

13.2.6 Process Route Healthiness Index

A way to quantify the social impact of a residential complex is through the OH with the PRHI [17]. This index is a dimensionless number, which indicates the potential health hazard generated by a process. Higher PRHI numbers indicate larger hazards. The development of the PRHI takes into account all the factors that can potentially contribute to health hazards. The used data to assess this index was taken from the available data from Occupational Safety and Health Administration (OSHA) for the health effects and workplace exposure limit and from National Fire Protection Association (NFPA).

PRHI is evaluated for each process to identify the most hazardous process unit in the proposed superstructure:

$$\text{PRHI} = \text{ICPHI} \times \text{MHI} \times \text{HHI}\frac{\text{WEC}_{max}}{\text{OEL}_{min}} \tag{13.9}$$

where ICPHI is the inherent chemical and process hazard index, which is calculated by the sum of penalties for activities or operations and the penalties associated with process conditions and material properties. MHI is the material harm index based on the NFPA data, which evaluates the exposure limits that workers are exposed and the possible damage. Values can be assigned from 0 to 4, where 4 represents the maximum value. HHI is the health hazard index. For this, the Occupational Health Administration shows the main effects of exposure to substances that can generate irritation, sensitization, carcinogenicity, and physical hazards. WEC_{max} and OEL_{min} are the maximum concentration that a worker is exposed and the minimum permissible exposure limit, respectively.

Once the factors for each of the process units are calculated, they are multiplied by their respective flows to assess the OH:

$$\begin{aligned}\text{OH} = {} & \text{PR}^{BOILER} \times F_t^{\text{NG-boiler}} + \text{PR}^{GW} \times F_t^{\text{Inlet-GW}} + \text{PR}^{WW} \times F_t^{WW} + \text{PR}^{NGT} \times F_t^{\text{NGT-Inlet}} + \\ & \text{PR}^{ICE} \times F_t^{\text{NG-ICE}} + \text{PR}^{ALGAE} \times G_t^{algae} + \text{PR}^{GASIFICATION} \times F_t^{\text{NG-needed gasification}}\end{aligned} \tag{13.10}$$

The parameters obtained to calculate the OH for each process unit are shown in Table 13.3.

Table 13.3 Parameters to calculate the occupation health.

Process unit	Penalties for activities or operations (AP)	Penalties associated with process conditions and material properties (CP)	ICPHI = AP + CP	HHI	MHI	WEC_{max}	OEL_{min}	PRHI	$PRHI_{Scaled}$
Algae system	7	3	10	39.5	3	0.092 88	1.30E−06	84 401 040	0.028 991
Boiler	5	4	9	30.9	3	0.084 21	0.009	7 806	0.000 002
Black water treatment	8	5	13	100.8	20	2.558	2.30E−05	2 911 224 133	1
Gasifier	10	4	14	114.4	18	3.098 68	0.001 983	450 285 340	0.015 467
Gray water treatment	8	5	13	47	7	3.273 23	0.000 01	1 249 968 196	0.042 936 1
ICE	8	3	11	31.9	11	0.189 83	0.008	91 521	0.000 31
Natural gas treatment	7	2	9	55.8	7	0.145 99	0.000 01	45 824 701	0.015 74

13.2.7 Multistakeholder Approach

A *multistakeholder* optimization is proposed to determine the optimal design of the residential complex due to the number of objective functions. Mathematically it is modeled as follows:

$$\begin{aligned} f_j =& w_j^{TAC}\left(\frac{\mathrm{TAC}-\mathrm{TAC}^{LB}}{\mathrm{TAC}^{UB}-\mathrm{TAC}^{LB}}\right)+w_j^{FFwTot}\left(\frac{\mathrm{FFwTot}-\mathrm{FFwTot}^{LB}}{\mathrm{FFwTot}^{UB}-\mathrm{FFwTot}^{LB}}\right)\\ &+w_j^{GHGE}\left(\frac{\mathrm{GHGE}-\mathrm{GHGE}^{LB}}{\mathrm{GHGE}^{UB}-\mathrm{GHGE}^{LB}}\right)+w_j^{EnvImp}\left(\frac{\mathrm{EnvImp}-\mathrm{EnvImp}^{LB}}{\mathrm{EnvImp}^{UB}-\mathrm{EnvImp}^{LB}}\right)\\ &+w_j^{SWSROIM}\left(\frac{\mathrm{SWSROIM}-\mathrm{SWSROIM}^{LB}}{\mathrm{SWSROIM}^{UB}-\mathrm{SWSROIM}^{LB}}\right)+w_j^{OH}\left(\frac{\mathrm{OH}-\mathrm{OH}^{LB}}{\mathrm{OH}^{UB}-\mathrm{OH}^{LB}}\right) \end{aligned} \tag{13.11}$$

f_j is a new variable to optimize, which is called compromise solution, in this new variable all of the individual objectives are included. In calculating the compromise solution, the lower and upper points for each of the scenarios generated are needed for each one of the objectives. w_j represents the weighting factor for each one of the objectives, while superscripts *LB* and *UB* indicate the lower (Utopia point) and upper (Nadir point) bounds, respectively. These weighting factors are used to give a higher priority to one objective over another, the decision of which values to assign to these factors depends on the desired approach to each of the studied processes. Therefore, it is necessary to know in detail the case study.

To find a balance between the objectives, we propose to evaluate the total dissatisfaction of the system with the next equation:

$$\mathrm{dis}=\left(\frac{100}{6}\right)\left(\begin{array}{c}\left(\frac{\mathrm{TAC}-\mathrm{TAC}^{LB}}{\mathrm{TAC}^{UB}}\right)+\left(\frac{\mathrm{FFwTot}-\mathrm{FFwTot}^{LB}}{\mathrm{FFwTot}^{UB}}\right)+\left(\frac{\mathrm{GHGE}-\mathrm{GHGE}^{LB}}{\mathrm{GHGE}^{UB}}\right)\\ +\left(\frac{\mathrm{EnvImp}-\mathrm{EnvImp}^{LB}}{\mathrm{EnvImp}^{UB}}\right)+\left(\frac{\mathrm{SWSROIM}-\mathrm{SWSROIM}^{LB}}{\mathrm{SWSROIM}^{UB}}\right)+\left(\frac{\mathrm{OH}-\mathrm{OH}^{LB}}{\mathrm{OH}^{UB}}\right)\end{array}\right) \tag{13.12}$$

13.3 Case Study

A residential complex is located in the central-western region of Mexico, where it is sought to satisfy the fresh water, hot water, electricity, and refrigeration demands, as well as to treat the produced wastes by the complex. The residential complex consists of 1440 households, and it has an overall consumption of 538 376 m^3/yr of fresh water, 36 689 m^3/yr of hot water, 2400 kWh/yr of refrigeration, and 110 120 kWh/yr of electricity. In the same way, it generates 864 tons of solid waste per year that are treated by a gasification system to produce natural gas.

To satisfy the fresh water, we can obtain it by municipal network and by a rainwater collecting systems that are installed in the roof of the houses. For hot water, using a boiler and an ICE are the considered options. The ICE can be used to

generate the electricity needed by the complex and by other process units of the system. Electricity is also obtained by the grid. On the other hand, refrigeration is generated by an absorption refrigeration cycle. The gray and black water are treated by an aerobic treatment water plant, and the solid wastes are incinerated in a gasification system. A natural gas treatment is also proposed to use the gases produced by the treatment for other units, and an algae production system can be used to mitigate the CO_2 emissions.

13.4 Results

The addressed multi-objective optimization model consists of 1098 continuous variables, 3570 constraints, and 10 binary variables. The model was coded and solved in the software general algebraic modelling system (GAMS) [18]. Baron was the solver used, and it consumes approximately 15 minutes to find a solution. To assign random weights for objective functions, the Latin hypercube function in the software MatLab was implemented. A random generation is a representative option to show the effect of prioritizing one objective and to show the trade-offs of the considered objectives. We used an average data per hour throughout the day for each season, which is a representative way to model the needs that the residential complex has (Table 13.4).

The Utopia and Nadir points were calculated for each of the individual objective, as well as the solution with the multistakeholder optimization for 15 random scenarios, the results of this approach are shown in Table 13.5.

The results indicate that scenario 9 has the lowest global dissatisfaction. This represents an attractive solution for the design of the optimal residential complex. The values for this scenario of each individual objective are listed in Table 13.6.

We can observe in the scenario with the lowest dissatisfaction (Figure 13.5) that the OH is on the Utopia point. The TAC is only 0.06% far from its best solution; this is because not all the proposed units are selected, such as the ICE, the algae production system, and the natural gas treatment unit. In the same way the green house gas emissions (GHGE) is 0.52% far from the Utopia point. Otherwise, the consumption of fresh water and the environmental impact have an individual dissatisfaction of 21.25% and 17.56%, respectively. Furthermore, we can see that the sustainable return of investment is practically in its Nadir point with a dissatisfaction of 99.80%, which is because this is a system that is not focused on generating profits. It needs to satisfy the needs of the inhabitants, which represents huge costs compared with the incomes.

13.5 Conclusions

With the proposed case study, the applicability of process integration and intensification has been shown to yield significant benefits. In the case of housing

Table 13.4 Utopia and Nadir points for the random scenarios.

Scenarios	Weights (w_i)						Objectives						
	TAC ($US/yr) × 10^6	FFwTot (m^3/yr)	GHGE (tons CO_2/yr)	EnvImp	SWSROIM	OH	f_j	TAC ($US/yr) × 10^6	FFwTot (m^3/yr)	GHGE (tons CO_2/yr)	EnvImp	SWSROIM	OH
Utopia								16.73	523 971	974	58 252	0	191 205
Nadir								100.00	722 244	1 159	3 246 632	0	192 520
1	1	0	0	0	0	0	0	16.73	665 906	980	74 377	0	191 205
2	0	1	0	0	0	0	0	69.31	523 971	1 051	63 936	0	191 220
3	0	0	1	0	0	0	0	62.86	685 455	974	76 408	0	192 505
4	0	0	0	1	0	0	0	16.63	577 557	1 052	58 252	0	191 220
5	0	0	0	0	1	0	0.172	100.00	583 670	1 040	61 541	0	192 518
6	0	0	0	0	0	1	0	62.84	681 413	979	74 851	0	191 205
7	1	1	1	1	1	1	2.227	31.90	612 692	974	71 960	0	192 505
8	0.5	0	0	0	0	0.5	0	16.73	665 321	979	74 356	0	191 205
9	0.333	0	0	0.333	0	0.333	0.001	16.74	665 321	979	70 658	0	191 205
10	0.316	0.069	0.135	0.309	0.156	0.016	0.199	32.15	612 984	974	72 003	0	192 505
11	0.313	0.156	0.360	0.043	0.034	0.095	0.216	23.11	612 692	974	75 769	0	192 505
12	0.282	0.343	0.128	0.188	0.059	0.001	0.226	23.12	612 692	974	71 960	0	192 505
13	0.250	0.250	0	0	0.250	0.250	0.177	37.46	523 971	1 051	58 256	0	191 220
14	0.220	0.077	0.357	0.022	0.188	0.136	0.321	34.18	612 692	974	71 960	0	192 505
15	0	0.333	0.333	0	0.333	0.000	0.213	100.00	612 692	974	71 960	0	192 505

Table 13.5 Individual and total dissatisfaction for the proposed scenarios.

Scenarios	Dissatisfaction (%)						
	TAC	FFwTot	GHGE	EnvImp	SWSROIM	OH	Total
1	0	21.31	0.57	21.68	99.8	0.000 002	23.89
2	75.86	0	7.28	8.89	99.23	0.007 609	31.88
3	73.39	23.56	0	23.76	99.38	0.674 991	36.79
4	14.76	21.25	7.41	0	99.8	0.007 643	23.87
5	83.27	10.23	6.33	5.34	98.86	0.681 9	34.12
6	73.38	23.11	0.52	22.18	99.37	0	36.42
7	47.55	14.48	0	19.05	99.6	0.674 991	30.23
8	0	21.25	0.52	21.66	99.8	0	23.87
9	0.06	21.25	0.52	17.56	99.8	0	23.2
10	47.96	14.52	0	19.1	99.6	0.674 991	30.31
11	27.62	14.48	0	23.12	99.8	0.674 991	27.62
12	27.65	14.48	0	19.05	99.8	0.674 991	26.94
13	55.35	0	7.28	0.01	99.56	0.007 609	27.03

Table 13.6 Individual objective solutions for the scenario with lowest dissatisfaction.

Objective	Lowest dissatisfaction
TAC (US$/yr)	16 738 400
FFwTot (m^3/yr)	665 321
Gdischarge (tons/yr)	979
EnvImp	70 658
SWSROIM	0.002
OH	191 205

complexes, multiple units were integrated to satisfy the needs of the inhabitants of the complex while minimizing the amount of needed fresh resources through mass integration. Furthermore, symbiosis can be induced between the water and energy systems. For example, the fresh water needed for gardening can be obtained from the treatment of the graywater produced in the housing complex, in the same way the generated solid wastes are incinerated to minimize the outputs to the environment and the gases produced in this unit are used to operate other process units.

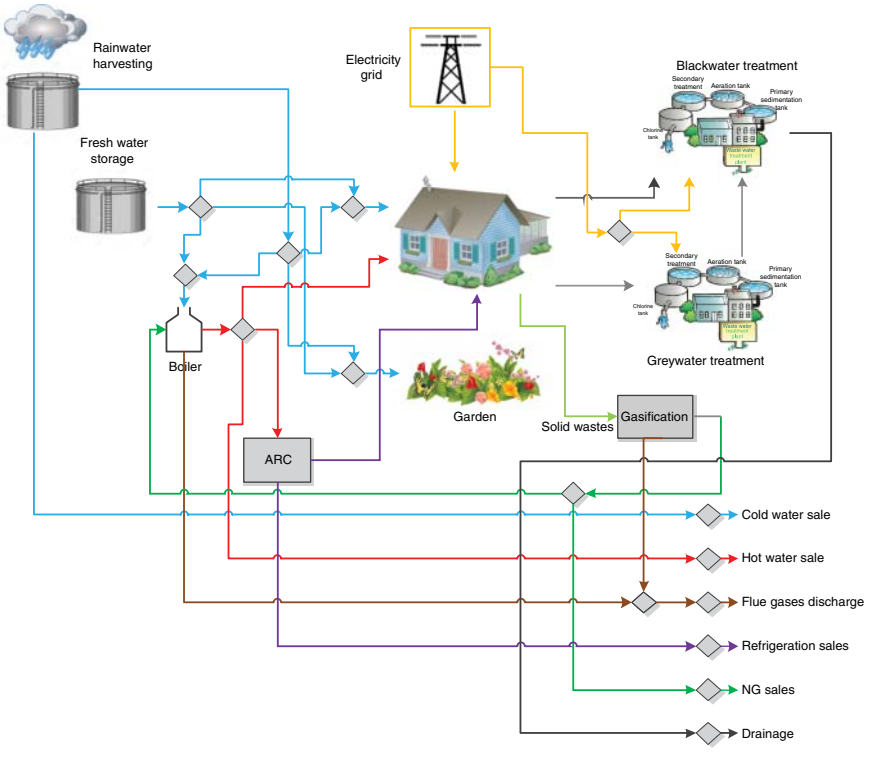

Figure 13.5 Distribution of process units for scenario with the lowest dissatisfaction. NG, natural gas.

References

1 Grossmann, I.E. and Sargent, R.W.H. (1978). Optimum design of heat exchanger networks. *Computers and Chemical Engineering* 2 (1): 1–7.

2 Floudas, C.A. and Grossmann, I.E. (1987). Synthesis of flexible heat exchanger networks with uncertain flowrates and temperatures. *Computers and Chemical Engineering* 11 (4): 319–336.

3 Murugan, S. and Horák, B. (2016). A review of micro combined heat and power systems for residential applications. *Renewable and Sustainable Energy Reviews* 64: 144–162.

4 Fuentes-Cortés, L.F., Ponce-Ortega, J.M., and Zavala, V.M. (2018). Balancing stakeholder priorities in the operation of combined heat and power systems. *Applied Thermal Engineering* 128: 480–488.

5 Misra, R.D., Sahoo, P.K., Sahoo, S., and Gupta, A. (2003). Thermoeconomic optimization of a single effect water/LiBr vapour absorption refrigeration system. *International Journal of Refrigeration* 26 (2): 158–169.

6 Lira-Barragán, L.F., Ponce-Ortega, J.M., Serna-González, M., and El-Halwagi, M.M. (2013). Synthesis of integrated absorption refrigeration systems involving economic and environmental objectives and quantifying social benefits. *Applied Thermal Engineering* 52 (2): 402–419.
7 El-Halwagi, M.M. (2006). *Process Integration*, vol. 7. Elsevier.
8 Núñez-López, J.M., Hernández-Calderón, O.M., Ponce-Ortega, J.M. et al. (2018). Optimal design of sustainable agricultural water networks. *ACS Sustainable Chemistry & Engineering* 7 (1): 440–457.
9 Ponce-Ortega, J.M., Mosqueda-Jiménez, F.W., Serna-González, M. et al. (2011). A property-based approach to the synthesis of material conservation networks with economic and environmental objectives. *AIChE Journal* 57 (9): 2369–2387.
10 Inman, R.H., Pedro, H.T., and Coimbra, C.F. (2013). Solar forecasting methods for renewable energy integration. *Progress in Energy and Combustion Science* 39 (6): 535–576.
11 Klemes, J.J. (ed.) (2013). *Handbook of Process Integration (PI): Minimisation of Energy and Water Use, Waste and Emissions*. Elsevier.
12 Keil, F.J. (2018). Process intensification. *Reviews in Chemical Engineering* 34 (2): 135–200.
13 Ponce-Ortega, J.M., Al-Thubaiti, M.M., and El-Halwagi, M.M. (2012). Process intensification: new understanding and systematic approach. *Chemical Engineering and Processing: Process Intensification* 53: 63–75.
14 Núñez-López, J.M., Villicaña-García, E., Cansino-Loeza, B. et al. (2018). Involving acceptability in the optimal design of total integrated residential complexes involving the water-energy-waste nexus. *ACS Sustainable Chemistry & Engineering* 6 (6): 7390–7402.
15 PRé Consultants. (2008). SimaPro software, SimaPro Version.
16 El-Halwagi, M.M. (2017). A return on investment metric for incorporating sustainability in process integration and improvement projects. *Clean Technologies and Environmental Policy* 19 (2): 611–617.
17 Hassim, M.H. and Edwards, D.W. (2006). Development of a methodology for assessing inherent occupational health hazards. *Process Safety and Environmental Protection* 84 (5): 378–390.
18 Brooke, A., Kendrick, D., and Meeraus, A. (2019). *Release 2.25 GAMS: A User's Guide*. Scientific Press.

14

Sustainable Biomass Conversion Process Assessment

Eric C. D. Tan

National Renewable Energy Laboratory, Center of Process Integration & Catalytic Carbon Transformation, 15013 Denver West Parkway, Golden, CO 80401, USA

14.1 Introduction

Human actions since the Industrial Revolution have become the main driver of global environmental change [1, 2]. There has been a flawed relationship between humans and the natural environment. The flawed relationship has caused us to face thresholds and tipping points within planetary boundaries such as biodiversity loss, ocean acidification, and climate change. Additionally, the mismanagement of natural resources is also not sustainable. As all forms of capital rely on natural capital (i.e. it takes something to make something), therefore, natural capital is non-substitutable. The take–make–use–disposal linear system has been the way for our society to grow and has triggered the exponential consumption of planetary resource (i.e. raw materials) and primary energy (i.e. fossil fuels). We are reminded that "we received this world as an inheritance from past generations, but also as a loan from future generations, to whom we will have to return it" [3]. In other words, we must attempt to minimize the impact of human activities on areas of protections (AoPs), namely, natural environment, human health, and natural resources [4]. Schaubroeck and Rugani suggest that sustainability is inherently anthropocentric, and human well-being is considered the primary AoP, i.e. the aspect that should primarily be sustained [1]. Their argument is supported through the original definition of sustainability, i.e. "the development that meets the needs of the present without compromising the ability of future generations to meet their own" [5].

During the last three decades, numerous studies on sustainability have been performed to understand and manage complex coupled human and natural systems (i.e. AoPs), and the design for sustainability and sustainability indicators have been identified as two of the seven functional approaches for addressing sustainability challenges [6]. Process intensification and integration (PII) for sustainable design is a pragmatic approach for developing environmentally sustainable processes and has recently gained momentum. PII aims to reduce the cost, energy intensity, emissions, and investment risk of a process [7], and the PII approach can also enable sustainable renewable fuels and chemicals manufacturing processes.

Process Intensification and Integration for Sustainable Design, First Edition.
Edited by Dominic C. Y. Foo and Mahmoud M. El-Halwagi.
© 2021 WILEY-VCH GmbH. Published 2021 by WILEY-VCH GmbH.

Hence, sustainable process design to convert biomass to fuels and chemicals plays an integral part in the bioeconomy sustainability.

The biorefinery concept is still in its nascent stage. It is recognized that the integration of sustainability in process design is desirable in developing renewable biofuels and should be considered a necessary practice in biorefinery design. Integrating a systematic and holistic framework in biorefinery process design can help understand the impact of design variation, evaluate alternative technologies, and track progress (i.e. vs. the baseline). We have recently explored and successfully implemented the multi-objective process sustainability evaluation methodology known as Gauging Reaction Effectiveness for ENvironmental Sustainability of Chemistries with a multi-Objective Process Evaluator (GREENSCOPE) for the production of biomass-derived ethanol [8] and gasoline-range hydrocarbon blendstock [9]. GREENSCOPE incorporates a wide range of sustainability indicators that allow for comprehensive direct comparison when evaluating design modifications and alternatives. To develop a more sustainable process, biorefinery design also adopts process intensification. Thus, the multi-objective process sustainability evaluation tools such as GREENSCOPE can also play a critical role in PII for sustainable design. The objective of this study is to demonstrate how the tool can help track progress on process sustainability performance attributed to conversion improvement using a high-octane gasoline (HOG) production from woody biomass feedstock as a case study.

14.2 Methodology and Assumptions

The GREENSCOPE methodology is a sustainability tool for process evaluation and design that was developed at the US Environment Protection Agency (EPA) [8, 9]. The sustainability is assessed by employing a set of indicators, categorized in four areas, i.e. economic, environmental, efficiency, and energy (Figure 14.1). Evaluating the process with a wide range of sustainability metrics allows GREENSCOPE to capture the multi-dimensional aspect of the process design and operation, as depicted in Figure 14.2. Equation (14.1) is used to calculate the sustainability score of each indicator [8, 9]:

$$\text{Sustainability score} = \frac{(\text{Actual\_value} - \text{Worst\_case})}{(\text{Best\_target} - \text{Worst\_case})} \times 100\% \tag{14.1}$$

The best target represents 100% sustainability and the worst-case scenario represents 0% sustainability. The sustainability reference values or scores allow for a direct assessment of the process sustainability status and for assessing how far the process is from achieving a more desirable sustainable state (i.e. potential). The selected indicators of interest represent only a subset of the entire GREENSCOPE indicators. The selected best-case (100% sustainability) and worst-case (0% sustainability) scenarios to establish the sustainability scale for each indicator are based on GREENSCOPE guidelines or default values. Users are encouraged to engage researchers and stakeholders to establish the sustainability scale for certain indicators and have the flexibility to refine the GREENSCOPE sustainability

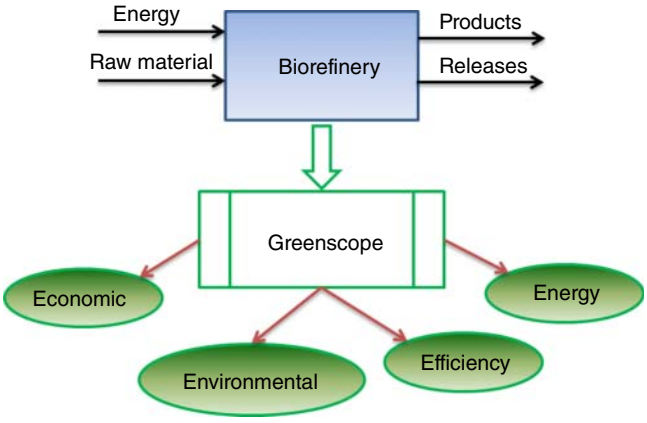

Figure 14.1 Implementing GREENSCOPE for sustainability performance assessment of biomass-to-fuel pathways.

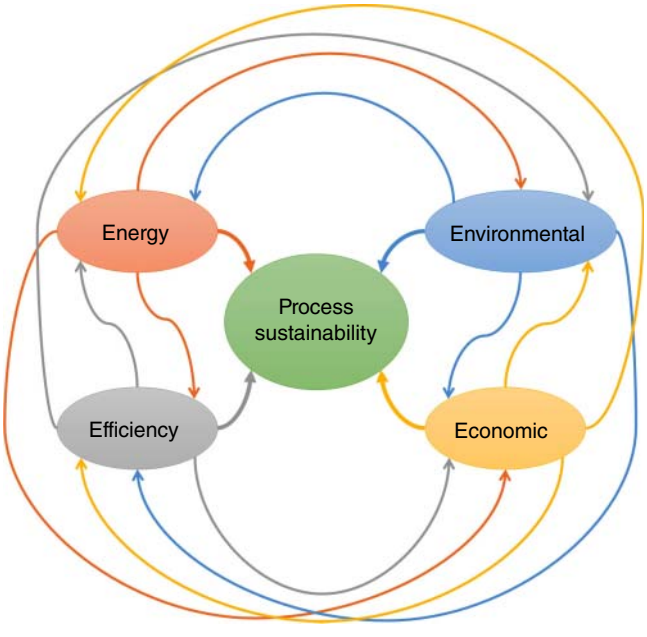

Figure 14.2 GREENSCOPE capturing the multi-dimensional aspect of the process design and operation.

indicators for better assessment. The definition and sustainability scale of each indicator in this study can be found in a recent work [9].

In this study, the production of HOG from woody biomass via a syngas conversion pathway through methanol and dimethyl ether (DME) intermediates is used for the case study [10]. The simplified process block flow diagram is shown in Figure 14.3. The detailed process description can be found in Refs. [10, 11]. The processing steps of this pathway include the conversion of biomass to syngas via

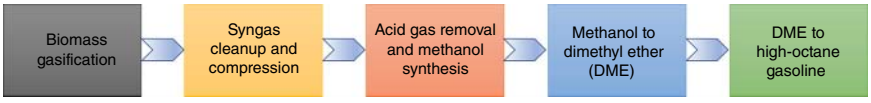

Figure 14.3 Simplified block flow diagram for the syngas conversion for high-octane gasoline production pathway.

indirect gasification, gas clean-up via reforming of tars and other hydrocarbons, catalytic conversion of syngas to methanol, methanol dehydration to DME, and homologation of DME over a zeolite-based catalyst to HOG range hydrocarbon products.

Biomass is indirectly gasified. The heat for the gasification reaction is supplied by circulating synthetic olivine sand that is preheated in a char combustor and fed to the gasifier. Conveyors and hoppers feed biomass to the low-pressure (18 psig/0.124 MPa) entrained flow gasifier. Steam is injected into the gasifier to stabilize the flow of biomass and olivine through the gasifier. Within the gasifier, biomass thermally deconstructs at 1598 °F (870 °C) to a mixture of syngas components (such as CO, H_2, CO_2, and CH_4), tars, and solid char containing residual carbon from the biomass and coke deposited on olivine.

Syngas clean-up in this design includes reforming of tars, methane, and other hydrocarbons followed by cooling, quenching, and scrubbing of the syngas for downstream operations. The water–gas shift reaction also occurs in the reformer. Raw syngas is reacted with the tar reforming catalyst (Ni/Mg/K supported on alumina) in an entrained flow reactor at (1670 °F/910 °C) and at a gas hourly space velocity of approximately 2500 h^{-1}.

The majority of the cleaned and conditioned syngas is further compressed to 735 psia (5.07 MPa) for methanol synthesis; the syngas is converted to methanol in a tubular, fixed-bed reactor containing a copper/zinc oxide/alumina catalyst.

Methanol dehydration to DME takes place in an adiabatic packed bed reactor with commercially available gamma alumina (γ-Al_2O_3) catalyst at 482 °F (250 °C) and 140 psia (0.965 MPa). Among various alumina-based catalysts, the γ-Al_2O_3 catalyst generally exhibits the best catalytic performance and hydrothermal stability for vapor-phase dehydration of methanol to DME. HOG is subsequently produced by the combination of acid-catalyzed homologation of DME and methylation of olefins. Hydrocarbon formation from DME is accomplished in two four-stage packed bed reactors containing National Renewable Energy Laboratory (NREL's) in-house developed metal modified β-zeolite (H-BEA) catalyst. The yields from the process are heavily weighted toward branched C_7 molecules, with octane ratings greater than 100.

The current GREENSCOPE sustainability assessment is focused on the biorefinery only (i.e. gate-to-gate) and does not include the biorefinery upstream (e.g. biomass feedstock harvesting) and downstream processes (e.g. biofuel transportation and distribution). The process sustainability performance is evaluated for the "base case" and the case with improved DME-to-HOG conversion (henceforward referred to as the "improved case"). The performance metrics comparison for the both cases is summarized in Table 14.1. The higher product yield (54.7 vs. 49.6 GGE/dry US ton; GGE, gasoline gallon equivalent) for the

Table 14.1 Key performance metrics comparison for the DME-to-HOG catalyst.

Metrics	Base case	Improved case
DME conversion (%)	38.9[a)]	40[a)]
C_{5+} C-selectivity (%)	72.3[b)]	86.7[b)]
Aromatics C-selectivity (%)	8.0	0.5
HOG hydrocarbon (HC) productivity (kg/kg cat/h)	0.073	0.1
HOG product yield (GGE[c)]/dry US ton)	49.6	54.7

a) Single-pass conversion.
b) Overall selectivity.
c) Gasoline gallon equivalent (GGE).
Source: From Tan 2018 [10].

improved case is resulted from the improved performance of the DME-to-HOG catalyst, which exhibits higher DME conversion, C_{5+} carbon selectivity, and hydrocarbon productivity, as well as lower aromatics (undesired component of the product) selectivity. The bioconversion process sustainability evaluation will quantify the overall process sustainability for the two cases.

Tables 14.2 and 14.3 show the required inputs for the GREENSCOPE, encompassing economic parameters and results (including production costs and revenues) and material and energy flows (such as biomass feedstock, releases, ancillary inputs, and process energy), respectively. Additionally, physicochemical, thermodynamics, and toxicological properties are also required for the calculation of environmental indicators with the potential data sourced detailed in Ruiz-Mercado et al. [12].

14.3 Results and Discussion

14.3.1 Environmental Indicators

The results of the environmental indicators are shown in Table 14.4 and Figure 14.4. Table 14.4 summarizes the associated sustainability indicators and the general characteristics for adopting the 0% and 100% sustainability reference values. The GREENSCOPE environmental indicator results are presented using a radar chart. The center of the radar graph represents a zero-sustainability value (i.e. worst-case scenario), and the external boundary of the graph represents a 100% sustainability value (i.e. best-case scenario). Sustainability percent scores are sorted in a descending order (decreasing clockwise) and result in a conch-shell configuration. Since the process sustainability is evaluated for the base case and the improved case, the ordering of indicators from largest to smallest score is done for the former, and the latter follows the set order.

As evident in Figure 14.4, the environmental scores for both the base case and the improved case are similar. The majority of the environmental indicators exhibits a relatively high level of sustainability (i.e. >50%) and is indicative of good process performance for many environmental aspects. However, there is

Table 14.2 Primary input data for economic indicator calculation.

Cases	Base case	Improved case
Annual salary ($/yr)	2 945 000	2 945 000
Land cost, C_{Land} ($)	1 610 000	1 610 000
Life of the plant, n (yr)	30	30
Fixed income tax rate given by the Internal Revenue Service (IRS), Φ (% or fraction)	0.21	0.21
Depreciation method	MACRS[a)]	MACRS[a)]
Plant startup at end of year	0	0
The year in which the first investment is made before the startup time, time zero, b (yr)	−2	−2
Cost of utilities, C_{UT} ($/yr)	250 808	234 266
Cost of waste treatment, C_{WT} ($/yr)	1 600 634	1 595 981
Cost of raw material, C_{RM} ($/yr)	60 449 000	57 465 734
Total income from all sales, S_m ($/yr)	118 587 000	130 701 000
Number of operators per shift, N_{OL}	7	7
Labor cost, C_{OL} ($/yr)	20 057 000	19 523 000
The capital cost (total module) of the plant, C_{TM} ($)	236 541 000	227 828 000
Fixed capital investment without including C_{land}, FCI_L($)	390 844 000	376 425 000
Working capital, WC ($)	19 542 000	18 821 000
Total capital investment, TCI ($)	411 996 000	396 856 000
Manufacturing cost without depreciation after startup, COM_m ($/yr)	82 059 000	78 609 000
Depreciation charge, d_m ($)	13 000 000	12 500 000
Salvage-value, rec_m ($)	0	0
Discount rate, r_d (%)	10	10

All currency in 2016 US dollars.

a) Modified accelerated cost recovery system (MACRS) depreciation schedule (year, %): 1 (14.29%), 2 (24.49%), 3 (17.49%), 4 (12.49%), 5 (8.93%), 6 (8.92%), 7 (8.93%), and 8 (4.46%).

one critical aspect, the one related to hazardous solid waste release (i.e. indicator #30, specific hazardous solid waste or $m_{s,haz.\ spec.}$). The corresponding specific hazardous solid waste sustainability scores for the base case and the improved case are 31% and 37%, respectively. The specific hazardous solid waste indicator is defined as the produced hazardous solid waste per unit mass of the product. The best target is 0, and the worst case is when all solid waste is considered hazardous and released to the environment. There are three major solid wastes from this process, i.e. spent catalysts, sand or olivine (a heat carrier) from the gasifier, and the char combustion ash. Only ash is considered a hazardous solid waste material here. Ash is minerals originated from the biomass. The minerals such as copper and chromium, as well as arsenic levels, concentrate in the ash and are toxic. As the amount of ash produced from the base case and the

Table 14.3 Material and energy flows for the syngas conversion process (gate-to-gate).

Cases	Base case Production rate	Improved case Production rate
Products		
High-octane gasoline (HOG)		
lb/h	28 015	30 768
MMBtu[a)]/h	529	583
By-product		
Sulfur (lb/h)	118	114
Resource consumption (lb/h)		
Blended woody biomass (30% moisture content)	262 455	262 455
Magnesium oxide (MgO)	23	23
Fresh olivine	527	527
Tar reformer catalyst	10	9
Methanol synthesis catalyst	5	5
DME catalyst	7	6
β-zeolite catalyst	45	34
Zinc oxide catalyst	2.5	2.5
Cooling tower water makeup	36 995	31 213
Boiler feed water makeup	89 723	86 887
Dimethyl disulfide (DMDS)	2.1	2.1
Methyl diethanolamine (MDEA) makeup	3.8	3.7
LO-CAT chemicals	118	114
Boiler feed water chemicals	2.9	2.7
Cooling tower chemicals	1.1	1.0
No. 2 diesel fuel	69	69
Excess electricity (kWh)	7	36
Waste streams (lb/h)		
Sand and ash purge	6 679	6 679
Tar reformer catalyst	8.7	8.7
Scrubber solids	7.8	8.8
Wastewater	16 369	14 845
Air emissions (lb/h)		
CO_2 (biogenic only)	250 142	241 844
NO_2	117	142
SO_2	43	51
H_2O	76 498	73 422

a) Lower heating value (LHV).
Source: From Tan 2018 [10].

Table 14.4 GREENSCOPE environmental indicators.

Indicator name	Indicator symbol	Units	Best case	Worst case	Base case	Improved case
Total mass of persistent, bio-accumulative and toxic chemicals used	1. $m_{PBT\,mat.}$	kg/h	0	539 625	0.0E+00	0.0E+00
Human health burden, cancer effects	2. $EB_{cancer\,eff.}$	kg/$	0	27.08	0.0E+00	0.0E+00
Stratospheric ozone-depletion potential	3. ODP	kg CFC-11 equivalent/kg prod	0	41.94	0.0E+00	0.0E+00
Stratospheric ozone-depletion intensity	4. ODI	kg CFC-11 equivalent/$	0	27.08	0.0E+00	0.0E+00
Aquatic acidification intensity	5. $WPI_{acid.\,water}$	kg H^+ equivalent/$	0	20.82	0.0E+00	0.0E+00
Aquatic acidification potential	6. $WP_{acid.\,water}$	kg H^+ equivalent/time	0	32.24	2.6E−05	2.1E−05
Toxic release intensity	7. TR	kg/$	0	27.08	1.0E−04	1.0E−04
Photochemical oxidation (smog) intensity	8. PCOI	kg ethylene equivalent/$	0	27.07	1.0E−04	1.0E−04
Specific toxic release	9. TR_s	kg/kg product	0	41.94	1.7E−04	1.4E−04
Aquatic basification potential	10. $WP_{basi.\,water}$	kg OH^- released/kg product	0	32.24	1.4E−04	1.1E−04
Photochemical oxidation (smog) potential	11. PCOP	kg ethylene equivalent/kg product	0	41.93	1.9E−04	2.1E−04
Aquatic basification intensity	12. $WPI_{basi.\,water}$	kg OH^- released/$	0	20.82	1.0E−04	1.0E−04
Ecotoxicity to aquatic life intensity	13. $WPI_{tox.\,other}$	kg formaldehyde equivalent/$	0	20.82	1.0E−04	1.0E−04
Ecotoxicity to aquatic life potential	14. $WP_{tox.\,other}$	kg formaldehyde equivalent/time	0	32.24	1.9E−04	1.6E−04
Eutrophication potential	15. EP	kg PO_4^{3+} equivalent/kg product	0	32.24	8.8E−04	9.6E−04
Eutrophication potential intensity	16. EPI	kg PO_4^{3+} equivalent/$	0	20.82	6.0E−04	7.0E−04

Table 14.4 (Continued)

Indicator name	Indicator symbol	Units	Best case	Worst case	Base case	Improved case
Atmospheric acidification intensity	17. API	kg SO_2 equivalent/$	0	27.08	3.0E−03	3.6E−03
Atmospheric acidification potential	18. AP	kg SO_2 equivalent/time	0	41.94	4.7E−03	5.1E−03
Aquatic oxygen demand potential	19. $WP_{O_2\ dem.}$	kg O_2 equivalent/time	0	9.26	1.7E−03	1.7E−03
Environmental hazard, water hazard	20. EH_{water}	kg/kg product	0	10 0000	3.3E+02	2.8E+02
Mass of hazardous materials input	21. $m_{haz.\ mat.}$	kg/h	0	53 9625	2.7E+03	2.7E+03
Specific hazardous raw materials input	22. $m_{haz.\ mat.\ spec.}$	kg hazardous input/kg product	0	42.29	2.1E−01	1.9E−01
Specific liquid waste volume	23. $V_{l,spec.}$	m^3/kg product	0	0.005 145	5.8E−04	4.8E−04
Polluted liquid waste volume	24. $V_{l,poll.}$	m^3	0	65.65	7.4E+00	6.7E+00
Safety hazard, acute toxicity	25. $SH_{acute\ tox.}$	m^3/kg	0	1 000 000	2.1E+05	1.9E+05
Global warming intensity	26. GWI	kg CO_2 equivalent/$	0	27.08	5.7E+00	5.6E+00
Global warming potential	27. GWP	kg CO_2 equivalent/kg product	0	41.94	8.9E+00	7.8E+00
Health hazard, chronic toxicity factor	28. $HH_{chronic\ toxicity}$	m^3/kg	0	10 000 000	2.2E+06	2.0E+06
Number of hazardous material inputs	29. $N_{haz.\ mat.}$	Dimensionless	0	12	3.0E+00	3.0E+00
Specific hazardous solid waste	30. $m_{s,haz.\ spec.}$	kg hazardous solid/kg product	0	0.087 15	6.0E−02	5.5E−02

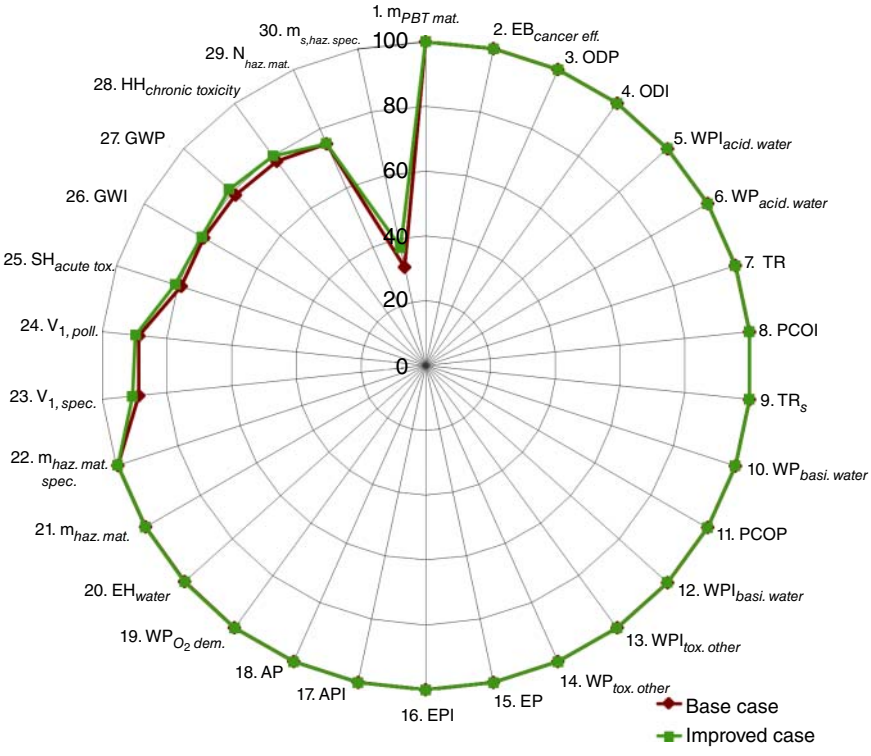

Figure 14.4 GREENSCOPE environmental indicators.

improved case are identical (Table 14.3), higher $m_{s,haz.\,spec.}$ sustainability score for the improved case is attributed only to its higher product yield (Table 14.1). Nevertheless, to improve this indicator score, one can choose to use the biomass feedstock with lower ash content. This study illustrates that by having this information from the GREENSCOPE sustainability evaluation, we can identify opportunities for achieving improved sustainability for the process.

14.3.2 Energy Indicators

The results of the energy-based indicators are shown in Table 14.5 and Figure 14.5. Indicator #7, resource-energy efficiency (η_E), is identified to exhibit low sustainability, 36% for the base case and 40% for the improved case. η_E is a ratio between the energy content of the product (i.e. HOG) to the total energy content of the feedstock (i.e. heating values of the biomass feedstock) that defines the quantity of the raw material energy that is remaining in the desired product. The energy balance analysis reveals that higher product yield and better process heat integration hold the keys to improving this aspect of sustainability, as depicted in Figure 14.6.

Table 14.5 GREENSCOPE energy indicators.

Indicator name	Indicator symbol	Units	Best case	Worst case	Base case	Improved case
Renewability-energy index	1. RI_E	Fraction	1	0	1.0	1.0
Waste treatment energy	2. WTE	MJ/kg	0	7.19	0.14	0.13
Total energy consumption	3. E_{total}	MJ/h	557 938	6 150 047	917 634	838 220
Specific energy intensity	4. R_{SEI}	MJ/kg	43.72	439.04	71.91	59.84
Energy intensity	5. R_{EI}	MJ/$	37.09	370.98	61.01	50.56
Solvent recovery energy	6. SRE	MJ/kg	0	7.19	1.58	1.37
Resource-energy efficiency	7. η_E	Fraction	1	0	0.4	0.4

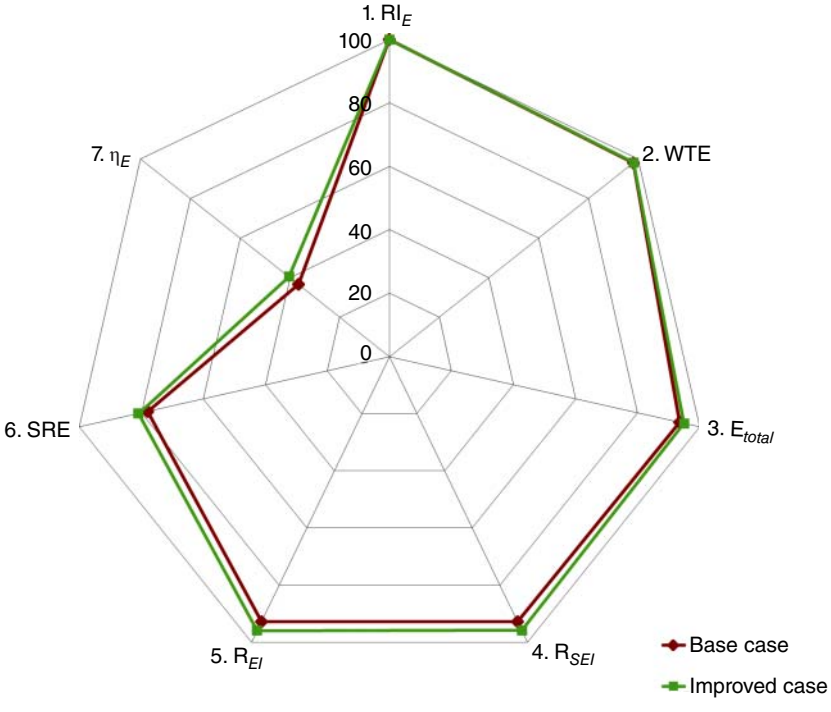

Figure 14.5 GREENSCOPE energy indicators.

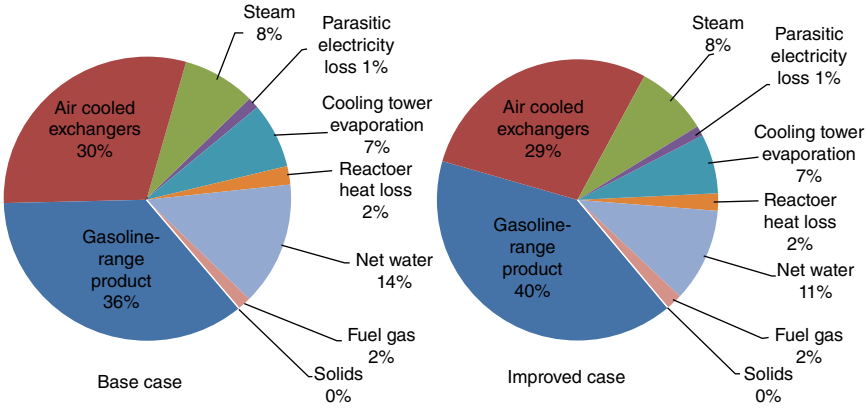

Figure 14.6 Energy analysis based on the dry biomass lower heating value (LHV) basis. Biomass LHV = 7856 Btu/lb. Source: From Tan 2018 [10].

Table 14.6 GREENSCOPE material efficiency indicators.

Indicator name	Indicator symbol	Units	Best case	Worst case	Base case	Improved case
Effective mass yield	1. EMY	kg/kg	0	40	0.014 0	0.012 0
Renewability-material index	2. RI_M	kg/kg	1	0	1.00	1.00
Fractional water consumption	3. FWC	m^3/kg	0	2.95	0.007 87	0.006 87
Water intensity	4. WI	m^3/$	0	1.55	0.006 67	0.005 80
Environmental factor	5. *E*	kg/kg	0	39	3.17	2.97
Mass loss index	6. MLI	kg/kg	0	100	12.9	11.4
Value mass intensity	7. MI_v	kg/$	0	52	11.8	10.4
Mass intensity	8. MI	kg/kg	1	40	13.9	12.4
Carbon efficiency	9. CE	kmol/kmol	1	0	0.247	0.271
Mass productivity	10. MP	kg/kg	1	0	0.157 0	0.173 0

14.3.3 Efficiency Indicators

Material efficiency indicators quantify the extent of the consumption and conversion of material inputs to the biorefinery for producing the hydrocarbon blendstock. An overall higher level of material efficiency sustainability of a process is typically associated with higher product yield and lower environmental impacts, such as raw material usage, greenhouse gas (GHG) emissions, fossil energy consumption, and consumptive water use. Consequently, material efficiency sustainability has a direct influence in other areas of process sustainability. The results of the material efficiency indicators are shown in Table 14.6 and Figure 14.7. The two critical aspects in the material efficiency sustainability area are carbon efficiency

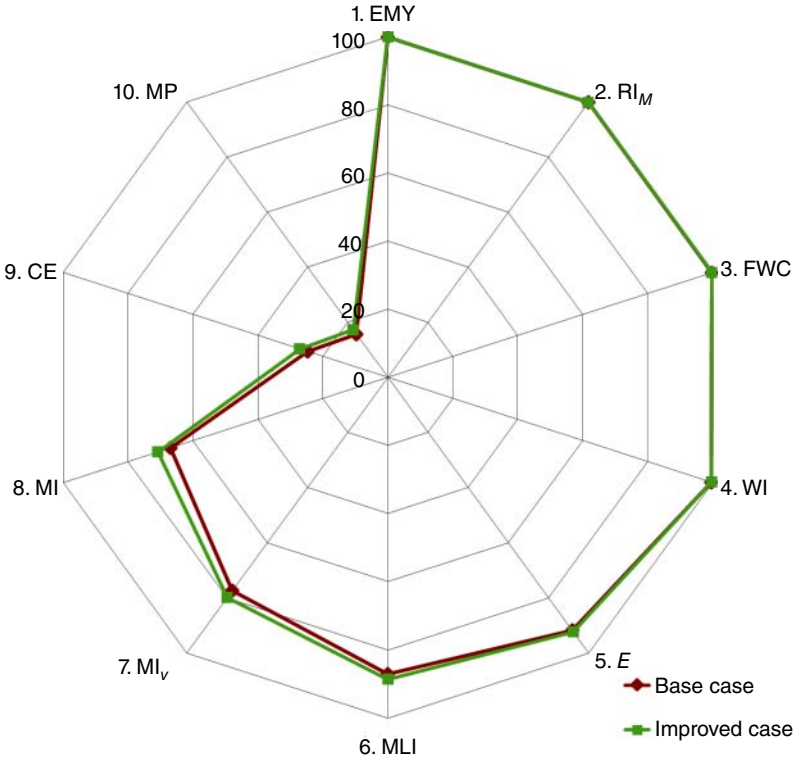

Figure 14.7 GREENSCOPE material efficiency indicators.

(CE) (indicator #9) and mass productivity (MP) (indicator #10). The sustainability scores for CE and MP are 24.7% and 15.7%, respectively, for the base case, and higher, 27.1% and 17.3%, respectively, for the improved case. Higher product yield for the improved case contributes to both higher CE and MP sustainability scores. Earlier analysis study suggested that the utilization of CO_2 from the acid gas removal (AGR) can improve the CE of the process by (i) recovering of the AGR CO_2 for dry reforming to produce additional syngas, (ii) using the CO_2-rich syngas (in the absent of an AGR system) for direct production of methanol and DME – the intermediates for HOG synthesis, and (iii) directly converting the CO_2-rich syngas into gasoline-range hydrocarbons [9]. MP is the ratio between the mass of the desired product (hydrocarbon blendstocks) over the ash and moisture free biomass total mass fed to the process. The woody biomass feedstock content is about 41% of oxygen, which eventually ends up as combustion CO_2 emission, AGR CO_2, and reaction by-product water, and is partly responsible for the abysmal MP sustainability scores.

14.3.4 Economic Indicators

The current process is based on a conceptual process design. An economic analysis for a conceptual process of new technology is more challenging than one for

an existing process. Thus, the inputs for the calculation of economic indicators are derived from the techno-economic analysis (TEA) of the process, which uses *n*th-plant economics. The summary of assumptions for the *n*th-plant economic analysis applied in this study can be found in Tan et al. [13]. The primary inputs for the calculation of the economic indicators are summarized in Table 14.2. If not otherwise mentioned, all currency is in 2016 US dollars. As shown in Table 14.3, the biorefinery produces HOG as the main product and sulfur as a by-product. At a fuel selling price of US$3.30 per GGE and sulfur co-product value of 4.4 ¢/kg, the total annual income from all sales (S_m) is determined to be US$118.6 MM and US$130.7 MM for the base case and the improved case, respectively. Note that the contribution of sulfur co-product credit to the total sales is mere 0.01% or less for both cases.

The results of the economic indicators are shown in Table 14.7 and Figure 14.8. Five out of fifteen economic indicators exhibit sustainability scores below 50%. The economic indicators with the lowest sustainability percent score are (ranked by indicator symbol, % scores for base case/improved case) total material cost ($C_{mat,tot.}$, 30%/34%), specific raw material cost (C_{SRM}, 30%/41%), turnover ratio (TR, 24%/28%), rate of return on investment (ROI, 13%/22%), and discounted payback period (DPBP, 0%/42%). These indicators are a function of fixed capital investment and product sales or revenues. In comparison to the base case, the higher product yield due to better DME-to-hydrocarbons catalyst performance and thus higher sales revenue for the improved case is responsible for the higher level of process sustainability in these economic sustainability aspects.

Lowering the capital cost will improve the economic aspect of the process sustainability. As an illustration, a single-point sensitive study for the improved case on the plant size of the biorefinery is conducted. As the biomass conversion process is capital intensive and with the average scaling factor of 0.6, increasing the plant size will leverage the economies of scale. Figure 14.8 shows that when the plant size is increased from the base case of 2000–10 000 dry metric tons/d, many of the economic indicators are noticeably improved, particularly the five indicators with scores lower than 50%: $C_{mat,tot.}$, from 34% to 45%; C_{SRM}, from 41% to 50%; TR, from 28% to 38%; ROI, from 22% to 43%; and DPBP, from 42% to 88%. Note that varying the plant size will only impact the economic indicators and will not affect the other three areas of process sustainability. Additionally, the biomass availability and logistics for biorefinery scaling, which can impact the feedstock cost [14–16], are not taken into consideration for the sensitivity study.

14.4 Conclusions

The present work evaluates the syngas conversion pathway to produce HOG blendstock from woody biomass via methanol and DME intermediates. The successful implementation and use of GREENSCOPE for a sustainability performance assessment for the conversion pathway has been demonstrated. Integrating sustainability in process design should be completed in the early stages of development to improve the overall sustainability of the process and

Table 14.7 GREENSCOPE economic indicators.

Indicator name	Indicator symbol	Units	Best case	Worst case	Base case	Improved case
Revenue fraction of eco-products	1. REVeco-prod	\$/\$	1	0	1.00	1.00
Revenues from eco-products	2. REV	1×10^6 \$/yr	118.59[a]/130.70[b]	0	118.57	130.70
Total liquid waste cost	3. $C_{l\,tot.}$	1×10^6 \$/yr	0	766.88	0.34	0.31
Production cost	4. E_{pc}	1×10^6 \$/yr	5.88	559.93	68.24	68.24
Total product cost	5. TPC	1×10^6 \$/yr	58.82	349.95	102.57	98.26
Manufacturing cost	6. COM	1×10^6 \$/yr	42.02	291.63	82.06	78.61
Capital cost	7. C_{TM}	1×10^6 \$/yr	187.08	1 022.06	410.39	395.25
Total water cost	8. $C_{water\,tot.}$	\$/yr	0	453 158	168 122	156 687
Total solid waste cost	9. $C_{s\,tot.}$	1×10^6 \$/yr	0.00	47.86	21.97	21.97
Specific biomass feedstock revenue	10. $REV_{biomass\,spec.}$	\$/dry ton	302.90	0.00	163.75	180.48
Total material cost	11. $C_{mat\,tot.}$	1×10^6 \$/yr	9.83	82.06	60.45	57.47
Specific raw material cost	12. C_{SRM}	\$/kg product	0.09	0.82	0.60	0.52
Turnover ratio	13. TR	\$/\$	1.25	0	0.30	0.35
Rate of return on investment	14. ROI	Fraction or %	0.4	0	0.05	0.09
Discounted payback period	15. DPBP	yr	1	30	>30	17.87

a) Base case.
b) Improved case.

identify key areas where further research and development (R&D) is needed. The conceptual process exhibits high sustainability in every aspect of the sustainability areas. Results from the current sustainability evaluation identify process areas (i.e. "hot spots") that need sustainability improvement. The other outcome of the GREENSCOPE sustainability evaluation is the identification of the challenges and opportunities for achieving the best possible sustainability targets. The process sustainability assessment results can help decision-makers to set priorities and allocate resources and to serve as the baseline for future comparison and as a basis for comparing this process to other biomass-to-liquid fuel pathways. The base case and the improved case exhibit similar sustainability performance for most of the indicators. However, the higher yield of the improved case (due to better DME-to-hydrocarbons catalyst performance) and the resulting higher sales revenue impact most on the economic sustainability and contribute to higher sustainability scores for about one-third of the economic indicators.

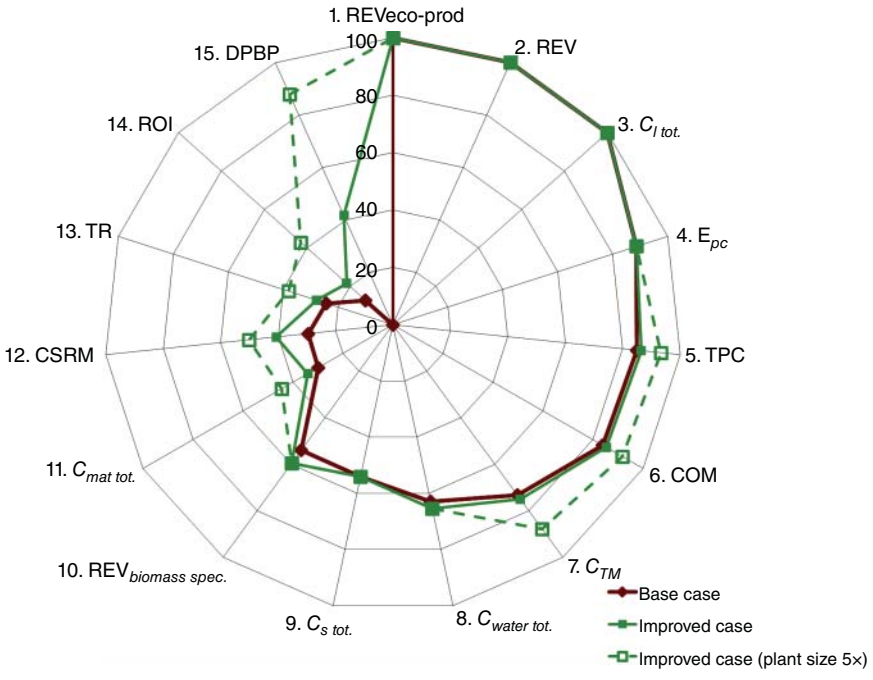

Figure 14.8 GREENSCOPE economic indicators.

Considering multiple metrics for evaluation when comparing technologies and design modifications can help make more informed decisions by looking at the design more holistically. GREENSCOPE can be an effective tool for biomass-to-fuels/chemicals process sustainability evaluation and design. With the incorporation of a wide range of indicators, GREENSCOPE can capture the multi-dimensional aspect of the process design and operation, as opposed to just limited economic and environmental aspects from TEA and life cycle assessment, and therefore can enable PII for sustainable design.

Acknowledgments

This work was authored by the National Renewable Energy Laboratory, operated by Alliance for Sustainable Energy, LLC, for the US Department of Energy (DOE) under Contract No. DE-AC36-08GO28308. Funding was provided by the US Department of Energy Office of Energy Efficiency and Renewable Energy Bioenergy Technologies Office. The views expressed in the article do not necessarily represent the views of the DOE or the US government. The author would like to thank Ling Tao at NREL and Alicia Lindauer and Kristen Johnson of BETO for their support.

References

1 Schaubroeck, T. and Rugani, B. (2017). A revision of what life cycle sustainability assessment should entail: towards modeling the net impact on human well-being. *Journal of Industrial Ecology* 21 (6): 1464–1477.

2 Wikipedia. (2019). Planetary boundaries [Internet]. https://en.wikipedia.org/w/index.php?title=Planetary_boundaries&oldid=917379662 (cited 2 October 2019).

3 Yardley, J. (2015). Pope Francis, in Ecuador, calls for more protection of rain forest and its people [Internet]. *The New York Times*. https://www.nytimes.com/2015/07/08/world/americas/pope-francis-in-ecuador-calls-for-more-protection-of-rain-forest-and-its-people.html (cited 2 October 2019).

4 Dewulf, J., Benini, L., Mancini, L. et al. (2015). Rethinking the area of protection "natural resources" in life cycle assessment. *Environmental Science and Technology* 49 (9): 5310–5317.

5 World Commission on Environment and Development (WCED) (1987). *Report of the World Commission on Environment and Development: Our Common Future*. Oxford, UK: World Commission on Environment and Development https://sustainabledevelopment.un.org/content/documents/5987our-common-future.pdf.

6 Lu, Z., Broesicke, O.A., Chang, M.E. et al. (2019). Seven approaches to manage complex coupled human and natural systems: a sustainability toolbox. *Environmental Science and Technology* 53 (16): 9341–9351.

7 Shonnard, D. (2019). Advanced manufacturing progress: RAPID steps toward sustainability. *Chemical Engineering Progress* 18: 7.

8 Smith, R.L., Tan, E.C.D., and Ruiz-Mercado, G.J. (2019). Applying environmental release inventories and indicators to the evaluation of chemical manufacturing processes in early stage development. *ACS Sustainable Chemistry & Engineering* 7: 10937–10950.

9 Tan, E.C.D. (2019). An integrated sustainability evaluation of high-octane gasoline production from lignocellulosic biomass. *Biofuels, Bioproducts and Biorefining* 13 (6): 1439–1453.

10 Tan, E.C.D., Ruddy, D., Nash, C., et al. (2018). High-Octane Gasoline from Lignocellulosic Biomass via Syngas and Methanol/Dimethyl Ether Intermediates: 2018 State of Technology and Future Research [Internet]. Report No. NREL/TP-5100-71957. Golden, CO: National Renewable Energy Laboratory. https://www.nrel.gov/docs/fy19osti/71957.pdf (accessed 23 April 2019).

11 Tan, E.C.D., Talmadge, M., Dutta, A., et al. (2015). Process Design and Economics for the Conversion of Lignocellulosic Biomass to Hydrocarbons via Indirect Liquefaction: Thermochemical Research Pathway to High-Octane Gasoline Blendstock Through Methanol/Dimethyl Ether Intermediates [Internet]. Report No. NREL/TP-5100-62402. Golden, CO: National Renewable Energy Laboratory. http://www.nrel.gov/docs/fy15osti/62402.pdf (accessed 23 April 2019).

12 Ruiz-Mercado, G.J., Smith, R.L., and Gonzalez, M.A. (2012). Sustainability indicators for chemical processes: II. Data needs. *Industrial and Engineering Chemistry Research* 51 (5): 2329–2353.
13 Tan, E.C., Talmadge, M., Dutta, A. et al. Conceptual process design and economics for the production of high-octane gasoline blendstock via indirect liquefaction of biomass through methanol/dimethyl ether intermediates. *Biofuels, Bioproducts and Biorefining* 10 (1): 17–35.
14 Muth, D.J., Langholtz, M.H., Tan, E.C.D. et al. (2014). Investigation of thermochemical biorefinery sizing and environmental sustainability impacts for conventional supply system and distributed pre-processing supply system designs. *Biofuels, Bioproducts and Biorefining* 8 (4): 545–567.
15 Argo, A.M., Tan, E.C., Inman, D. et al. (2013). Investigation of biochemical biorefinery sizing and environmental sustainability impacts for conventional bale system and advanced uniform biomass logistics designs. *Biofuels, Bioproducts and Biorefining* 7 (3): 282–302.
16 Lamers, P., Tan, E.C.D., Searcy, E.M. et al. (2015). Strategic supply system design – a holistic evaluation of operational and production cost for a biorefinery supply chain. *Biofuels, Bioproducts and Biorefining* 9 (6): 648–660.

Index

Process Intensification and Integration for Sustainable Design, First Edition.
Edited by Dominic C. Y. Foo and Mahmoud M. El-Halwagi.
© 2021 WILEY-VCH GmbH. Published 2021 by WILEY-VCH GmbH.